Transactions of the ASME®

Journal of Engineering for Gas Turbines and Power

Published Quarterly by The American Society of Mechanical Engineers

VOLUME 114 • NUMBER 4 • OCTOBER 1992

Technical Editor,
G. K. SEROVY
Associate Technical Editors
Advanced Energy Systems
M. J. MORAN
Environmental Control
H. E. HESKETH (1995)
Fuels and Combustion Technologies
D. W. PACER (1994)
Gas Turbine
L. S. LANGSTON (1993)
Internal Combustion Engine
J. A. CATON (1995)
Nuclear Engineering
S. M. CHO (1992)
Power
P. H. GILSON (1995)

BOARD ON COMMUNICATIONS
Chairman and Vice-President
R. D. ROCKE

Members-at-Large
T. BARLOW, W. BEGELL, T. F. CONRY, T. DEAR, J. KITTO, R. MATES, W. MORGAN, E. M. PATTON, S. PATULSKI, R. E. REDER, A. VAN DER SLUYS, F. M. WHITE

President, **J. A. FALCON**
Executive Director,
D. L. BELDEN
Treasurer, **ROBERT A. BENNETT**

PUBLISHING STAFF
Mng. Dir., Publ.
CHARLES W. BEARDSLEY
Managing Editor,
CORNELIA MONAHAN
Sr. Production Editor,
VALERIE WINTERS
Production Assistant,
MARISOL ANDINO

Transactions of the ASME, Journal of Engineering for Gas Turbines and Power (ISSN 0742-4795) is published quarterly (Jan., Apr., July, Oct.,) for $130.00 per year by The American Society of Mechanical Engineers, 345 East 47th Street, New York, NY 10017. Second class postage paid at New York, NY and additional mailing offices. POSTMASTER: Send address changes to Transactions of the ASME, Journal of Engineering for Gas Turbines and Power, c/o THE AMERICAN SOCIETY OF MECHANICAL ENGINEERS, 22 Law Drive, Box 2300, Fairfield, NJ 07007-2300. **CHANGES OF ADDRESS** must be received at Society headquarters seven weeks before they are to be effective. Please send old label and new address. **PRICES:** To members, $40.00, annually: to nonmembers, $136.00. Add $24.00 for postage to countries outside the United States and Canada.

STATEMENT from By-Laws. The Society shall not be responsible for statements or opinions advanced in papers or . . . printed in its publications (B 7.1, para. 3), **COPYRIGHT © 1992** by The American Society of Mechanical Engineers. Authorization to photocopy material for internal or personal use under circumstances not falling within the fair use provisions of the Copyright Act is granted by ASME to libraries and other users registered with the Copyright Clearance Center (CCC) Transactional Reporting Service provided that the base fee of $3.00 per article plus $.30 per page is paid directly to CCC, 27 Congress St., Salem, MA 01970. Request for special permission or bulk copying should be addressed to Reprints/Permission Department.

INDEXED by Applied Mechanics Reviews and Engineering Information, Inc. Canadian Goods & Services Tax Registration #126148048

TECHNICAL PAPERS

(Contents continued on page 620)

Downloaded 03 Jun 2010 to 171.66.16.159. Redistribution subject to ASME license or copyright; see http://www.asme.org/terms/Terms_Use.cfm

Contents (continued)

ANNOUNCEMENTS

The Rational Efficiency of Power Plants and Their Components

J. H. Horlock
Whittle Laboratory,
Cambridge, United Kingdom

The use of a rational efficiency for a power plant (the work output divided by the maximum possible reversible work output) is well established for conventional and combined plants. However, there are in the literature several proposals for "second-law" efficiencies of power plant components and no universally agreed practice. The paper discusses these various proposals and recommends particular definitions for the efficiency of components. These definitions are consistent with the universally agreed definition for overall plant rational efficiency. The approach is illustrated by a numerical example.

Introduction

The use of exergy in the analysis of power plant performance is now well established (see Haywood, 1980; Kotas, 1985; El-Masri, 1985; Tsatsaronis and Winfold, 1985). The rational efficiency of a power plant is defined as

$$(\eta_R)_{PP} \equiv \frac{W}{W_{\mathrm{REV}}} \tag{1a}$$

where W is the shaft work output and W_{REV} is the maximum possible work output from the fuel supplied. This definition is valid for open circuit internal combustion plants (with $W_{\mathrm{REV}} = (G_{R_o} - G_{P_o})$, the change in the Gibbs function from reactants to products at temperature T_o and pressure p_o) and for external combustion [boiler]/closed circuit plants (with W_{REV} equal to the decrease in the Gibbs function of the reactants supplied to the boiler). There is general agreement on this definition of rational efficiency; strictly the final state of the products used in the definition should be the completely dead state (with products in chemical equilibrium with the atmosphere, i.e., with individual product gases in unrestricted equilibrium at the corresponding partial pressures of the atmosphere). The extra exergy associated with this is usually neglected, G_{P_o} being the exergy at the "environmental state" (Kotas, 1985), with individual gases in restricted equilibrium, at atmospheric temperature T_o but each at atmospheric pressure p_o. Here we shall use

$$(\eta_R)_{PP} = \frac{W}{(G_{R_o} - G_{P_o})} = \frac{W}{(-\Delta G_o)}. \tag{1b}$$

However, there is not universal agreement on the best definition of the "second-law" efficiency of components. The purpose of this paper is to relate selected "second-law" efficiencies to the agreed and well-defined rational efficiency of the power plant.

Second Law Efficiencies of Components

We first review various proposals for second-law efficiencies. Subsequently we recommend the use of particular definitions for various components, to be employed with the rational efficiency of power plants that we have discussed and accepted above.

Haywood's Definition of Component Rational Efficiency. For a process involving flow of a fluid through a component (CP) from one (inlet) stable state to another (outlet) stable state, Haywood has unequivocally defined the *rational efficiency* of the component as

$$(\eta_R)_{CP} = \frac{W_{CP}}{(W_{\mathrm{REV}})_{CP}} \tag{2a}$$

where W_{CP} is the actual work output and $(W_{\mathrm{REV}})_{CP}$ is the maximum possible work output between the two states in the presence of an environment at temperature T_o. The maximum possible work output is the exergy difference (Fig. 1),

$$(W_{\mathrm{REV}})_{CP} = E_{IN} - E_{\mathrm{OUT}},$$

and parallels the definition for the power plant as a whole. For an actual process with heat transfer from the control surface surrounding the component (see Horlock and Haywood, 1985, and Horlock, 1987),

$$E_{IN} = E_{\mathrm{OUT}} + (E^Q)_{CP} + (I^C)_{CP} + W_{CP} \tag{3}$$

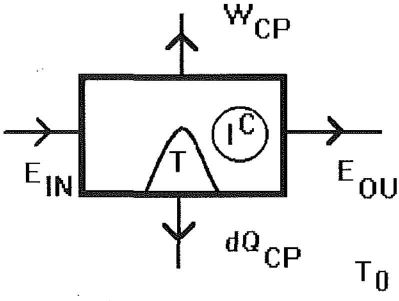

Fig. 1 Exergy fluxes

Contributed by the International Gas Turbine Institute and presented at the ASME Cogen-Turbo V, Budapest, Hungary, September 3-5, 1991. Manuscript received by the International Gas Turbine March 1991. Associate Technical Editor: L. S. Langston.

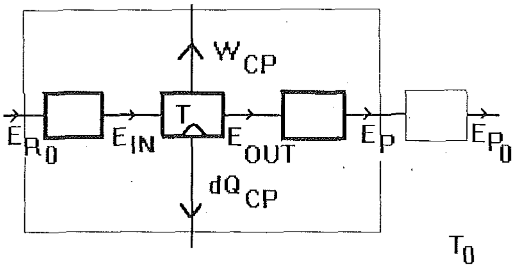

Fig. 2 Exergy fluxes through power plant

where

$$(E^Q)_{CP} = \int \frac{(T-T_o)}{T}\, dQ$$

is the work potential of the heat transferred out ($\approx \int dQ$) at (variable) temperature T. The lost work due to internal irreversibility is

$$(I^C)_{CP} = T_o\ (\Delta S^C)_{CP}$$

where $(\Delta S^C)_{CP}$ is the entropy created within the control surface surrounding the component (CP).

E^Q is sometimes called the thermal exergy (Kotas, 1985). If the heat ($\int dQ$) is unused (i.e., if its work potential is lost by heat transfer to the atmosphere) then we may write $(E^Q)_{CP} = (I^Q)_{CP}$ where $(I^Q)_{CP}$ is the lost work due to irreversibility external to the component (equal to the product of the temperature T_o and the entropy increase of the environment). Thus

$$(\eta_R)_{CP} = W_{CP}/(E_{IN} - E_{\text{OUT}})$$

$$= 1 - \frac{(I^Q + I^C)_{CP}}{(E_{IN} - E_{\text{OUT}})}. \qquad (2b)$$

If the exergy dropped steadily, in a series of work producing components through the whole producing components through the whole power plant [Fig. 2], then it would be simple to relate the plant efficiency

$$(\eta_R)_{PP} = \sum_{CP} W_{CP}/(-\Delta G_o) = 1 - \sum_{CP} \delta_{CP}, \qquad (4a)$$

where

$$\delta_{CP} = \frac{(I^Q + I^C)_{CP}}{(E_{R_o} - E_{P_o})}, \qquad (4b)$$

to the rational efficiency of the components, since

$$(E_{R_o} - E_{P_o}) = \sum_{CP} (E_{IN} - E_{\text{OUT}})_{CP}. \qquad (5)$$

Here we have included a final (hypothetical) component to reduce the exergy leaving the plant E_P to E_{P_o}, as shown in Fig. 2.

Defining the fractional exergy drop in a component as

$$\lambda_{CP} = \frac{(E_{IN} - E_{\text{OUT}})_{CP}}{(E_{R_o} - E_{P_o})} \qquad (6)$$

it follows from Eq. (4a) that

$$(\eta_R)_{PP} = \sum_{CP} \frac{W_{CP}}{(E_{IN} - E_{\text{OUT}})_{CP}} \frac{(E_{IN} - E_{\text{OUT}})_{CP}}{(E_{R_o} - E_{P_o})}$$

$$= \sum_{CP} (\eta_R)_{CP}\, \lambda_{CP}. \qquad (7)$$

Alternatively, since for component CP

$$(I^Q + I^C)_{CP} = (1 - (\eta_R)_{CP})\lambda_{CP}(E_{R_o} - E_{P_o})$$

then for all components

$$\sum_{CP} \frac{(I^Q + I^C)_{CP}}{(E_{R_o} - E_{P_o})} = \sum_{CP} \left[1 - (\eta_R)_{CP} \right] \lambda_{CP} \qquad (8)$$

since $\Sigma\lambda_{CP} = 1$. Hence from Eq. (4b)

$$(\eta_R)_{PP} = 1 - \sum_{CP} (I^Q + I^C)_{CP}/(E_{R_o} - E_{P_o})$$

$$= 1 - (1 - \sum_{CP} (\eta_R)_{CP}\lambda_{CP})$$

$$= \sum_{CP} (\eta_R)_{CP}\, \lambda_{CP} \qquad (7)$$

as before.

The plant rational efficiency is thus made up of a series of "weighted" component rational efficiencies. In this case if all components had the same efficiency $(\eta_R)_{CP}$ then the plant rational efficiency $(\eta_R)_{PP}$ would be equal to the component rational efficiency $(\eta_R)_{CP}$. However, power plant analysis is more complicated than implied in Fig. 2; there are work inputs to components as well as work outputs, there may be neither,

Nomenclature

E = exergy
E^Q = thermal exergy
G = gibbs function
ΔG = change in Gibbs function
H = enthalpy
I^C = lost work due to internal irreversibility
I^Q = lost work due to external irreversibility
n = number of moles
Q = heat transferred
S = entropy
ΔS^C = entropy creation
T = temperature
W = work
δ = $(I^C + I^Q)/(E_{R_o} - E_{P_o})$
ϵ = specific exergy
η_R = rational efficiency (Eqs. (1) and (2))
η_ξ = exergetic efficiency (Eq. (13))
η_e = exergetical efficiency (Eq. (15a))
λ = fraction of $(E_{R_o} - E_{P_o})$
μ' = first degree of quality (Eq. (10))
μ'' = second degree of quality

Subscripts

A = hot stream
B = cold stream
C = compressor
AC = air compressor
GC = gas compressor
CC = combustion chamber
CP = component
CON = condenser
DOWN = exergy decreasing
FP = feed pump
GT = gas turbine
$HRSG$ = heat recovery steam generator
IN = entry to component
OUT = exit from component
P = products
PP = power plant
R = reactants
S = steam cycle
ST = stack
T = turbine
TS = steam turbine
UP = exergy increasing
X = heat exchanger
0 = ambient conditions
1, 2,... = state points (gas turbine plant)
1S,2S,... = state points (steam cycle)

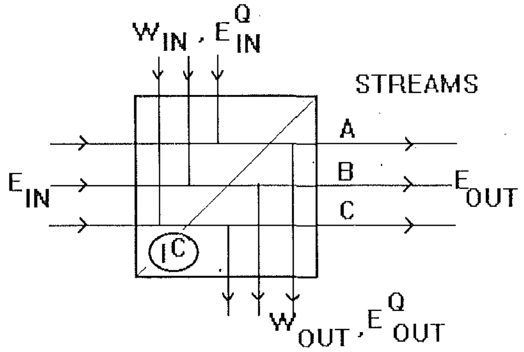

Fig. 3 Exergy fluxes for several streams

and there may be several fluid streams flowing in to and out of a component. We therefore consider other definitions of "second-law" efficiencies for components.

Fratzscher's Definition of Degree of Quality: Fratzscher (1961) has introduced two additional steps in the definition of components efficiency (Fig. 3). First, he considered the possibility of several fluid streams [$i=A, B, C,..$] entering and leaving the component. Second, he linked together the exergy, the work transfer, and the thermal exergy E^Q, summing them for input and output. Thus

$$(\xi)_{IN}=(E+E^Q+W)_{IN},$$

$$(\xi)_{\mathrm{OUT}}=(E+E^Q+W)_{\mathrm{OUT}}, \tag{9}$$

noting that E, E^Q, W are all positive quantities in these equations. E^Q is now associated with positive heat transfer into or out of the component and W with positive work input or output. Following Bosnjakovic (1935), Fratzscher defines a *"first degree of quality"* for the component

$$(\mu')_{CP}=\sum_i (\xi)_{\mathrm{OUT}}/\sum_i (\xi)_{IN}. \tag{10}$$

But

$$\sum_i (\xi)_{IN}=\sum_i (\xi)_{\mathrm{OUT}}+(I^C)_{CP} \tag{11}$$

where $(I^C)_{CP}$ is the lost work due to internal irreversibility within the control surface surrounding the component. Thus

$$1-(\mu')_{CP}=\frac{(I^C)_{CP}}{\sum_i (\xi)_{IN}}=\frac{T_o(\Delta S^C)_{CP}}{\sum_i (\xi)_{IN}}. \tag{12}$$

Haywood (1980), following Riekert (1974), has adopted a similar (but not identical) approach in defining the exergetic efficiency of a chemical process. Haywood allows for work transfer in and out, and fluxes of "available work," which he defines as $\Sigma_i\, \eta_i\, \epsilon_i$, where ϵ_i is the specific molar work equivalent and η_i is the number of moles of gas i flowing. His ϵ_i allows for the "exergy of extraction" from the atmosphere (and/or for return to the atmosphere).

Haywood then defines the exergetic efficiency of the component as

$$(\eta_\xi)_{CP}=\frac{\sum_i [\eta_i\epsilon_i)_{\mathrm{OUT}}+(W_i)_{\mathrm{OUT}}]}{\sum_i [(\eta_i\epsilon_i)_{IN}+(W_i)_{IN}]} \tag{13}$$

and shows that

$$1-(\eta_\xi)_{CP}=\frac{T_o(\Delta S^C)_{CP}}{\sum_i [\eta_i\epsilon_i)_{IN}+(W_i)_{IN}]}. \tag{14}$$

If his flux of "available work" includes E^Q, then Haywood's definition of component exergetic efficiency is the same as Fratzscher's first degree of quality. Alternatively, if the processes considered are adabiatic [$E^Q=0$] then again Haywood's η_ξ is identical to Fratzscher's μ'. (Fratzscher also defines a second degree of quality μ'', which we shall refer to briefly later, but it is not widely used.)

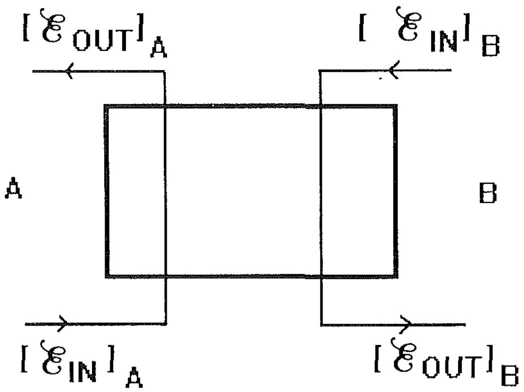

Fig. 4 Exergetical efficiency

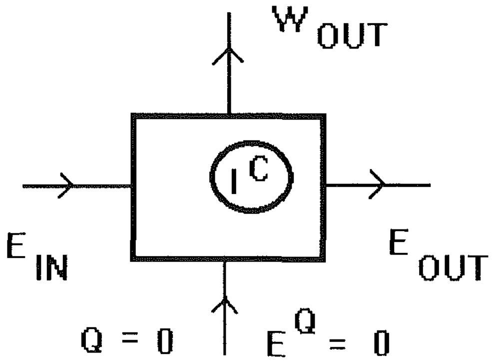

Fig. 5 Exergy flux though adiabatic turbine

Fratzscher's Definition of Exergetical Efficiency. Fratzscher next introduces the concepts of a desired output and an input that is regarded as expenditure, both of which are expressed in terms of differences.

Figure 4 shows two streams of fluid passing through a component; stream A is associated with the desired output or production and the expenditure comes from stream B. Fratzscher defines the exergetical efficiency of the component as

$$(\eta_e)_{CP}=\frac{(\Delta\xi)_A}{(\Delta\xi)_B}=\frac{(\xi_{\mathrm{OUT}})_A-(\xi_{IN})_A}{(\xi_{IN})_B-(\xi_{\mathrm{OUT}})_B} \tag{15a}$$

$$=1-(I^C)_{CP}/((\xi_{IN})_B-(\xi_{\mathrm{OUT}})_B). \tag{15b}$$

Fratzscher points out that this definition "assumes that use and expenditure can be clearly characterized" and that "the question cannot be answered so simply for complicated processes." (Neither can it be for flow of a single stream.) Nevertheless Fratzscher's approach has been extensively used by Tsatsaronis and Winhold (1985) in their comprehensive "thermo-economic" analyses of a range of power plants, and in particular of the integrated gasification combined "cycle" (IGCC) plant.

A difficulty in applying Fratzscher's definition of exergetical efficiency may be illustrated by the example of adiabatic flow of a single stream through a turbine (Fig. 5). Fratzscher suggests that the desired output is the work $W_{\mathrm{OUT}}=W_{CP}$ and the expenditure is $(E_{IN}-E_{\mathrm{OUT}})$. The exergetical efficiency then becomes

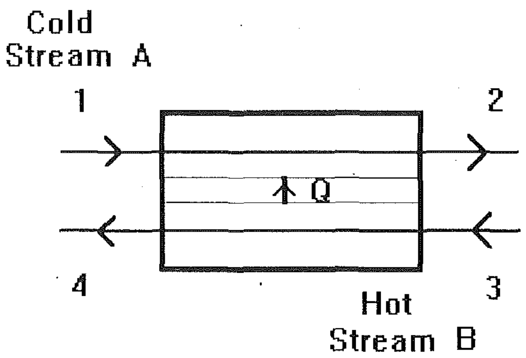

Fig. 6 Heat exchanger

$$(\eta_e)_{CP}=\frac{W_{CP}}{(E_{IN}-E_{OUT})}=1-\frac{T_o(\Delta S^C)_{CP}}{(E_{IN}-E_{\mathrm{OUT}})}. \qquad (16a)$$

In fact, this form is now the rational efficiency defined by Haywood, and earlier called the effectiveness by Keenan (1941), following a proposal by Darrieus (1930); it is also one of two component efficiency definitions, the extraction method, used by Kotas (1985).

A logical inconsistency in Fratzscher's approach to this example lies in treating the desired output for a component as the work output $W_{\mathrm{OUT}}=W_{CP}$, in view of his original definition of exergetical efficiency, (15*a*), which suggests that the output should be $(\Delta\xi)_B$.

We may note that Kotas introduces another definition of the turbine's second-law efficiency, by the "equality" method,

$$\psi=\frac{W_{CP}+E_{\mathrm{OUT}}}{E_{IN}}=1-\frac{T_o(\Delta S^C)_{CP}}{E_{IN}} \qquad (16b)$$

which he again calls a rational efficiency. This is closer to Fratzscher's original definition of degree of quality.

The author concludes that Fratzscher's exergetical efficiency has more value when two separate streams are indeed involved, and the desired output and "expanded" input are more readily identified. A boiler, with a water/steam stream *A* ["cold side"] and a gas stream *B* ["hot side"] and a gas stream *B* ["hot side"] is an example where its application appears sounder (Fig. 6). Following Fratzscher, the exergetical efficiency is then

$$\eta_e=\frac{(\Delta\xi)_A}{(\Delta\xi)_B}=\frac{(\xi_2-\xi_1)}{(\xi_3-\xi_4)}. \qquad (17)$$

No work transfers are involved, and if there are no heat losses overall then $E^Q=0$ for the complete component; further $(H_2-H_1)=(H_3-H_4)$, where H relates to the enthalpy fluxes. Hence

$$\eta_e=\frac{(E_2-E_1)}{(E_3-E_4)}=1-\frac{(E_3-E_4)-(E_2-E_1)}{(E_3-E_4)}$$

and

$$(1-\eta_e)=\frac{T_o[(S_2+S_4)-(S_1+S_3)]}{(E_3-E_4)}$$
$$=\frac{T_o(\Delta S^C)_{CP}}{(E_3-E_4)}. \qquad (18)$$

A heat exchanger, or a heat recovery steam generator, can be treated similarly. But if the heat exchanger is contained in an open circuit or closed cycle plant (both cold side and hot side) then the author's preference is to treat it as two separate components, for reasons which will become apparent below.

Summary of Definitions. These main definitions of "second-law" efficiency for a component are summarized in Table 1.

Table 1 Second-law component efficiencies

Author	Second-law efficiency	Definition
Haywood	Rational efficiency $(\eta_R)_{CP}$	$\frac{W_{CP}}{(W_{\mathrm{REV}})_{CP}}$
Fratzscher	Degree of quality $(\mu')_{CP}$	$\frac{\sum_i(\xi_i)_{\mathrm{OUT}}}{\sum_i(\xi_i)_{IN}}$
[also used by Kotas, Haywood, and Riekert]		
Fratzscher	Exergetical efficiency $(\eta_e)_{CP}$	$\frac{(\Delta\xi)_B}{(\Delta\xi)_A}$
[also used by Kotas, and Tsatsaronis and Winhold]		
Fratzscher	Alternative degree of quality $(\mu'')_{CP}$	$\frac{(\Delta\xi)_B}{(\xi)_{IN}}$

Choice of Component Rational Efficiency for Power Plant Analysis

As explained in the introduction, the definition of the rational efficiency of a power plant (internal combustion/open circuit or external combustion "boiler"/closed cycle) is well established as

$$(\eta_R)_{PP}=\frac{\sum_{CP}W_{CP}}{(-\Delta G_o)}=1-\frac{\sum_{CP}(\mathrm{I}^Q+\mathrm{I}^C)_{CP}}{(-\Delta G_o)} \qquad (4a)$$

noting that the exergies of extraction and return to the atmosphere have been neglected, and that a hypothetical component has been introduced to return products of combustion (exhaust gases from an open circuit plant or flue gases from a boiler or external heater) to the product state p_o (at environmental pressure and temperature).

This form of rational efficiency has been used by Meyer et al. (1959); Traupel (1957), and Horlock (1963), all of whom simply tabulated values of

$$\delta_{CP}=(\mathrm{I}^Q+\mathrm{I}^C)_{CP}/(-\Delta G_o)$$

for each of the components. However this approach, while locating the size of the various losses, does not give their relative magnitudes in terms of the changes in exergy across components.

Use of Fratzscher's exergetical efficiency (by Tsatsaronis and Winhold, for example) means that the values of $(\eta_e)_{CP}$ determined are not numerically related to the plant rational efficiency, and this approach is not entirely satisfactory either.

The method we adopt here is to use Haywood's original definition of rational efficiency $(\eta_R)_{CP}$ for a component with a single fluid stream, and to use Fratzscher's exergetical efficiency $(\eta_e)_{CP}$ for a boiler (i.e., for external combustion) and for a heat recovery steam generator (HRSG) in a combined power plant.

The exergy does not always drop progressively through the components of a power plant (for example, it increases in an adiabatic compression process); it decreases across some components and increases across others (Fig. 7). We must therefore note that

$$E_{R_o}-E_{P_o}=\sum_{\substack{CP\\ \mathrm{DOWN}}}(E_{IN}-E_{\mathrm{OUT}})_{CP}-\sum_{\substack{CP\\ UP}}(E_{\mathrm{OUT}}-E_{IN})_{CP} \qquad (19)$$

where $(E_{IN}-E_{\mathrm{OUT}})_{CP}$, $(E_{\mathrm{OUT}}-E_{IN})_{CP}$ are both positive quantities, in "down" components (exergy dropping) and "up" components (exergy rising), respectively. We shall treat the fractional exergy change as a positive quantity for both down and up components, so that

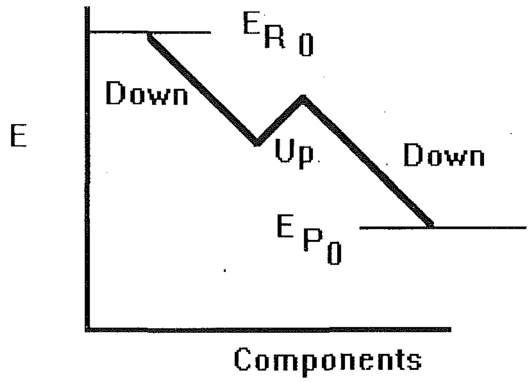

Fig. 7 Exergy changes through plant

$$(\lambda_{CP})_{\mathrm{DOWN}}=\frac{(E_{IN}-E_{\mathrm{OUT}})_{CP}}{(E_{R_o}-E_{P_o})},\ (\lambda_{CP})_{UP}=\frac{(E_{\mathrm{OUT}}-E_{IN})_{CP}}{(E_{R_o}-E_{P_o})} \tag{20}$$

and

$$\sum_{\substack{CP\\ \mathrm{DOWN}}}(\lambda_{CP})_{\mathrm{DOWN}}-\sum_{\substack{CP\\ UP}}(\lambda_{CP})_{UP}=1. \tag{21}$$

We also have to define the rational efficiency for an "up" component through which exergy increases. For such a component (e.g., a compressor with heat loss Q)

$$(\eta_R)_{CP}=\frac{(E_{\mathrm{OUT}}-E_{IN})_{CP}}{W_{IN}}$$

$$=\frac{1}{1+\left(\frac{(I^Q+I^C)_{CP}}{(E_{\mathrm{OUT}}-E_{IN})_{CP}}\right]} \tag{22}$$

so that

$$(I^Q+I^C)^{CP}=\left[\frac{1}{(\eta_R)_{CP}}-1\right](E_{\mathrm{OUT}}-E_{IN})_{CP}. \tag{23}$$

Thus the overall plant rational efficiency may be determined as

$$(\eta_R)_{PP}=\frac{\sum_{CP}[(W_{\mathrm{OUT}})_{CP}-(W_{IN})_{CP}]}{(E_{R_o}-E_{P_o})}$$

$$=\sum_{\substack{CP\\ \mathrm{DOWN}}}(\eta_R)_{CP}\lambda_{CP}-\sum_{\substack{CP\\ UP}}\lambda_{CP}/(\eta_R)_{CP}. \tag{24a}$$

Alternatively

$$(\eta_R)_{PP}=1-\sum_{CP}(\mathrm{I}^Q+\mathrm{I}^C)_{CP}/(E_{R_o}-E_{p_o})$$

$$=1-\left\{\sum_{\substack{CP\\ \mathrm{DOWN}}}(1-(\eta_R)_{CP}\lambda_{CP})+\sum_{\substack{CP\\ UP}}\left(\frac{1}{(\eta_R)_{CP}}-1\right)\lambda_{CP}\right\}$$

$$=\sum_{\substack{CP\\ \mathrm{DOWN}}}(\eta_R)_{CP}\lambda_{CP}-\sum_{\substack{CP\\ UP}}\lambda_{CP}/(\eta_R)_{CP} \tag{24b}$$

since

$$\sum_{\substack{CP\\ \mathrm{DOWN}}}\lambda_{CP}-\sum_{\substack{CP\\ UP}}\lambda_{CP}=1.$$

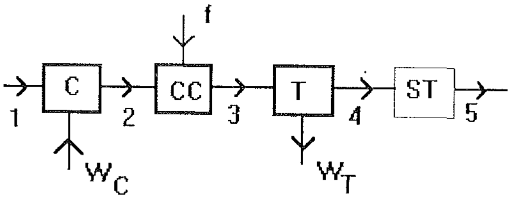

Fig. 8 Simple gas turbine

Exergy Analysis of Various Power Plants Using Component Efficiencies

Open Circuit Simple Gas Turbines. In the analysis of the last section, we assumed that exergy fluxes were associated with single stream flows, with the entering reactant flow of exergy E_{R_o}. In fact, in an open circuit power plant such as a simple gas turbine (Fig.8), the fuel does not enter the first component (compressor C) but the second (combustion chamber CC), separately from the compressed air. Our analysis is simply modified.

For the four components, including the turbine T and a hypothetical stack cooler ST (reducing the exergy of the gases from that at entry to the exhaust stack), we may write

$$(\eta_R)_{PP}=\frac{W_T-W_C}{E_{R_o}-E_{P_o}} \tag{25a}$$

$$=(\eta_R)_T\lambda_T-\lambda_C/(\eta_R)_C \tag{25b}$$

where

$$\lambda_T=(E_3-E_4)/(E_{R_o}-E_{P_o})_1$$

$$\lambda_C=(E_2-E_1)/(E_{R_o}-E_{P_o}).$$

More fully

$$(I^Q+I^C)_C=[1/(\eta_R)_C-1](E_2-E_1)$$

$$(I^Q+I^C)_{CC}=[1-(\eta_R)_{CC}](E_f+E_2-E_3)$$

$$(I^Q+I^C)_T=[1-(\eta_R)_T](E_3-E_4)$$

$$(I^Q+I^C)_{ST}=[1-(\eta_R)_{ST}](E_4-E_5).$$

Here CC, T, and ST are "down" components and C is an "up" component. Further, $E_{R_o}=E_f+\mathrm{E}_1$, and $E_{P_o}=E_5$. We can sum these "losses" to obtain $(\eta_R)_{PP}$

$$(\eta_R)_{PP}=1-\frac{\sum_{CP}(I^Q+I^C)_{CP}}{(E_{R_o}-E_{P_o})} \tag{4b}$$

$$=\sum_{CP=CC,T,ST}(\eta_R)_{CP}\lambda_{CP}-\lambda_C/(\eta_R)_C \tag{24b}$$

where

$$\lambda_{CC}=\frac{E_f+E_2-E_3}{E_f+E_1-E_5},$$

$$\lambda_{ST}=\frac{E_4-E_5}{E_f+E_1-E_5}.$$

But the combustion chamber and the hypothetical stack cooler [both "down" components] are not work producing and $(\eta_R)_{CC}$, $(\eta_R)_{ST}=0$. For in the former $E_f+E_2-E_3=(I^C)_{CC}$ and in the latter $E_4-E_5=(I^C)_{ST}$. Hence

$$(\eta_R)_{PP}=(\eta_R)_T\lambda_T-\lambda_C/(\eta_R)_C. \tag{25b}$$

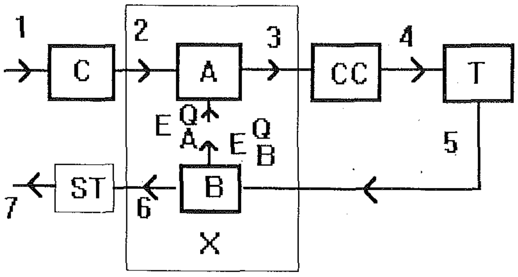

Fig. 9 Gas turbine with heat exchanger

At first sight it would appear that the irreversibility in the (adiabatic) combustion chamber and the discharge of exhaust gases at temperature T_5 (above $T_o = T_1$) has not involved a cost in plant rational efficiency. However, this is not so, for both λ_{CC} and λ_{ST} are nonzero; they lower the plant rational efficiency $[(\eta_R)_{PP}]$ by reducing the remaining balance,

$$\lambda_T - \lambda_C = 1 - \lambda_{CC} - \lambda_{ST}.$$

Open Circuit Gas Turbine With Heat Exchanger. Figure 9 shows a diagram of an open circuit gas turbine with a heat exchanger. Let us now consider the exchanger as involving two components, A and B; we assume no heat losses external to the whole heat exchanger (X).

For the cold stream (A)

$$E_3 = E_A^Q + E_2 - I_A^C \tag{26}$$

where E_A^Q is a positive quantity, associated with the heat input (Q), transferred in from the hot stream; and I_A^C is the internal irreversibility of the cold side.

For the hot stream (B)

$$E_5 = E_B^Q + E_6 + I_B^C \tag{27}$$

where E_B^Q is also positive, associated with Q transferred out from the hot side. Combination of these two equations gives

$$(E_5 - E_6) = (E_3 - E_2) + I_X^C \tag{28}$$

where

$$I_X^C = I_A^C + I_B^C + E_A^Q - E_B^Q$$

$$= T_o[(S_3 + S_6) - (S_2 + S_5)]$$

$$= T_o(\Delta S^C)_X$$

is the total loss of work due to all irreversibilities in the heat exchangers.

We can define two rational efficiencies, using Haywood's definition (2a). For the cold side (A), an "up" component, $W_{\mathrm{OUT}} = 0$, so that $(\eta_R)_A = 0$. For the hot side (B), a "down" component, $W_{IN} = 0$, so that $(\eta_R)_B = 0$. Hence the two components in the heat exchanger do not appear to make a direct contribution to the plant rational efficiency through the terms $(\eta_R)_B\, \lambda_B$ and $\lambda_A/(\eta_R)_A$. As with the combustion chamber and the hypothetical stack cooler, their effect is in reducing the net $(\lambda_T - \lambda_C)$ of the work transferring components. Hence the rational efficiency of the whole gas turbine plant will again be

$$(\eta_R)_{PP} = (\eta_R)_T \lambda_T - \lambda_C/(\eta_R)_C \tag{29}$$

but the values of λ_T and λ_C will be different from those for the simple gas turbine, for now

$$\lambda_T - \lambda_C = 1 - \lambda_{ST} - \lambda_{CC} + \lambda_A - \lambda_B. \tag{30}$$

A full numerical calculation for a gas turbine plant with two heat exchangers is given in the appendix, using an example originally given by Kotas (1985).

Had Fratzscher's exergetical efficiency for the whole heat exchanger been used, we would have written

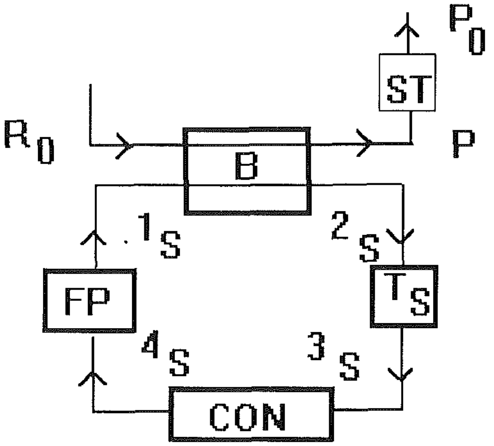

Fig. 10 Boiler/steam cycle

$$\eta_e = \frac{(E_3 - E_2)}{(E_5 - E_6)} \tag{31a}$$

$$= 1 - \frac{I_X^C}{(E_5 - E_6)} \tag{31b}$$

and

$$\delta_X = \frac{I_X^C}{(E_{R_o} - E_{P_o})} = \lambda_{56}\ (1 - \eta_e)$$

where

$$\lambda_{56} = (E_5 - E_6)/(E_{R_o} - E_{P_o}).$$

Effectively all the irreversibility is now loaded on the hot side, for accounting purposes. The plant rational efficiency can then be written

$$(\eta_R)_{PP} = \frac{\sum\limits_{\substack{CP\\ \mathrm{DOWN}}} (E_{IN} - E_{\mathrm{OUT}}) - \sum\limits_{\substack{CP\\ UP}} (E_{\mathrm{OUT}} - E_{IN}) - \sum\limits_{CP} (I^Q + I^C)_{CP}}{(E_{R_o} - E_{P_o})}$$

$$= (\eta_R)_T \lambda_T - \lambda_C/(\eta_R)_C + \eta_e \lambda_{56} - \lambda_{32} \tag{32}$$

where

$$\lambda_{32} = (E_3 - E_2)/(E_{R_o} - E_{P_o}).$$

It would now appear that we are allowing directly for the exergetical efficiency η_e in $(\eta_R)_{PP}$. However, we should note that the last two terms in Eq. (32) are

$$\eta_e \lambda_{56} - \lambda_{32} = \frac{(E_3 - E_2)\,(E_5 - E_6)}{(E_5 - E_6)\,(E_{R_o} - E_{P_o})} - \frac{(E_3 - E_2)}{(E_{R_o} - E_{P_o})} = 0$$

and the rational efficiency is again

$$(\eta_R)_{PP} = (\eta_R)_T \lambda_T - \lambda_C/(\eta_R)_C. \tag{29}$$

The irreversibility in the heat exchanger again appears only indirectly through reduction of $(\lambda_T - \lambda_C)$. There is no significant advantage or increased understanding that follows from use of η_e.

Open Circuit Boiler/Closed Steam Turbine Cycle. Next we consider the case of a power plant with an open circuit boiler and a closed water/steam cycle; we use the subscript S for the steam cycle (Fig. 10). We *shall* now use Fratzscher's exergetical efficiency for the complete boiler (B) so that

$$\eta_e = \frac{(\xi_{2S} - \xi_{1S})}{(\xi_{R_o} - \xi_P)} = \frac{(E_{2S} - E_{1S})}{(E_{R_o} - E_P)} \qquad (33a)$$

and

$$(1 - \eta_e) = T_o(\Delta S^C)_B/(E_{R_o} - E_P) \qquad (33b)$$

if there is no external heat loss. For the simple closed cycle, with turbine (*T*), condenser (CON), and feed pump (*FP*),

$$\frac{(E_{2S} - E_{1S})}{(E_{R_o} - E_{P_o})} = \frac{(E_{2S} - E_{3S})}{(E_{R_o} - E_{P_o})} + \frac{(E_{3S} - E_{4S})}{(E_{R_o} - E_{P_o})} - \frac{(E_{1S} - E_{4S})}{(E_{R_o} - E_{P_o})}$$

$$= \lambda_{TS} + \lambda_{CON} - \lambda_{FP}. \qquad (34)$$

But

$$(E_{R_o} - E_{P_o}) = (E_{R_o} - E_P) + (E_P - E_{P_o})$$

$$= \frac{(E_{2S} - E_{3S}) + (E_{3S} - E_{4S}) - (E_{1S} - E_{4S})}{\eta_e}$$

$$+ (E_P - E_{P_o})$$

and dividing by $(E_{R_o} - E_{P_o})$ we obtain

$$(\lambda_{TS} + \lambda_{CON} - \lambda_{FP})/\eta_e + \lambda_{ST} = 1 \qquad (35a)$$

where

$$\lambda_{ST} = (E_P - E_{P_o})/(E_{R_o} - E_{P_o})$$

Thus

$$\lambda_{TS} + \lambda_{CON} - \lambda_{FP} = \eta_e\ (1 - \lambda_{ST})$$

The rational efficiency of the components in the closed cycle are as we have defined them before [e.g., $(\eta_R)_{TS} = W_{TS}/(E_{2S} - E_{1S})$] and the rational efficiency of the total plant is

$$(\eta_R)_{PP} = \frac{W_{TS} - W_{FP}}{(E_{R_o} - E_{P_o})}$$

$$= (\eta_R)_{TS} - \lambda_{FP}(\eta_R)_{FP}. \qquad (36a)$$

An alternative form is

$$(\eta_R)_{PP} = [(\eta_R)_{TS}\lambda'_{TS} - \lambda'_{FP}\ (\eta_R)_{FP}]\ \eta_e(1 - \lambda_{ST}) \qquad (36b)$$

where

$$\lambda'_{TS} = \frac{(E_{2S} - E_{3S})}{(E_{2S} - E_{1S})},$$

$$\lambda'_{FP} = \frac{(E_{1S} - E_{4S})}{(E_{2S} - E_{1S})}.$$

The effect of the boiler performance is thus either through Eq. (36*b*), with λ'_{TS}, λ'_{CON}, λ'_{FP} being defined as fractions of $(E_{R_o} - E_{P_o})$ and summing to $\eta_e\ (1 - \lambda_{ST})$.

But

$$(\eta_R)_{TS}\ \lambda'_{TS} - \lambda'_{FP}/(\eta_R)_{FP} = (\eta_R)_S \qquad (37)$$

the rational efficiency of the steam cycle.

Hence

$$(\eta_R)_{PP} = (\eta_R)_S\ (1 - \lambda_{ST})\eta_e. \qquad (38)$$

It is tempting to define $(1 - \lambda_{ST})\ \eta_e$ as a rational efficiency for the boiler, but that would not be consistent with our recommendations for second law efficiencies.

Combined Open Circuit/Closed Cycle Combined Plant. Finally we consider a combined power plant in which heat is transferred from the exhaust gases of a "higher" simple gas turbine plant to raise steam in the "lower" steam cycle, in a heat recovery steam generator (HRSG); see Fig. 11. We now use Fratzscher's exergetical efficiency for the HRSG,

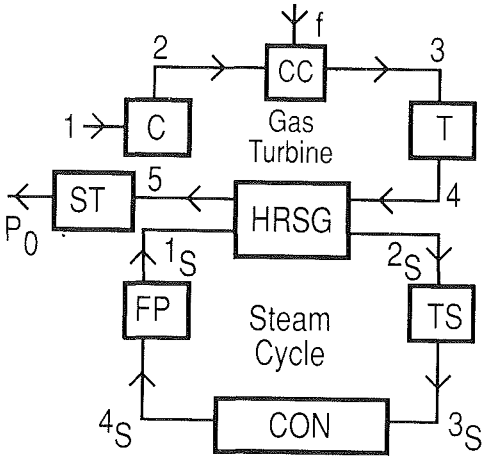

Fig. 11 Combined power plant

$$\eta_e = (E_{2S} - E_{1S})/(E_4 - E_5). \qquad (39a)$$

For the "higher" open circuit gas turbine plant

$$(\eta_R)_{GT} = (W_T - W_C)/(E_{R_o} - E_{P_o})$$

$$= (\eta_R)_T\ \lambda_T - \lambda_C/(\eta_R)_C. \qquad (40)$$

We note that a hypothetical cooling stack is included in the gas turbine plant, the exergy being reduced by $(E_P - E_{P_o}) = (E_5 - E_{P_o})$. Again a rational efficiency for the stack does not appear in the expression for $(\eta_R)_{GT}$, for its efficiency would be zero. But its effect on the plant efficiency is through the reduction of $(\lambda_T - \lambda_C)$.

For the steam cycle

$$(\eta_R)_S = (W_{TS} - W_{FP})/(E_{2S} - E_{1S})$$

$$= (\eta_R)_{TS}\ \lambda'_{TS} - \lambda'_{FP}/(\eta_R)_{FP}. \qquad (37)$$

where

$$\lambda'_{TS} = (E_{2S} - E_{3S})/(E_{2S} - E_{1S})$$

$$\lambda'_{FP} = (E_{1S} - E_{4S})/(E_{2S} - E_{1S}).$$

But

$$(E_{2S} - E_{1S}) = \eta_e\ (E_4 - E_5) \qquad (39b)$$

and

$$\frac{(E_{2S} - E_{1S})}{(E_{R_o} - E_{P_o})} = \frac{(E_{2S} - E_{1S})}{(E_4 - E_5)}\ \frac{(E_4 - E_5)}{(E_{R_o} - E_{P_o})} = \eta_e\ \lambda_{45}. \qquad (41)$$

Hence the rational efficiency of the whole combined plant is

$$(\eta_R)_{PP} = (W_T + W_C + W_{TS} - W_{FP})/(E_{R_o} - E_{P_o})$$

$$= [(\eta_R)_T\ \lambda_T - \lambda_C/(\eta_R)_C]$$

$$- [(\eta_R)_{TS}\ \lambda'_{TS} - \lambda'_{FP}/(\eta_R)_{CP}]\eta_e\lambda_{45}$$

$$= (\eta_R)_{GT} + (\eta_R)_S\ \eta_e\ \lambda_{45} \qquad (42)$$

where *GT* refers to the gas turbine plant and *S* to the steam turbine cycle.

Equation (42) may be written

$$(\eta_R)_{PP} = (\eta_R)_{GT} + (\eta_R)_S\ \eta_e\ [1 - (\eta_R)_{GT} - \delta_H]$$

$$= (\eta_R)_{GT} + \eta_e\ (\eta_R)_S - \eta_e\ (\eta_R)_{GT}\ (\eta_R)_S$$

$$- \eta_e\ (\eta_R)_S\ \delta_H \qquad (43)$$

where $\delta_H = (I_C + I_{CC} + I_T + I_S^Q)/(E_{R_o} - E_{P_o})$, and I_S^Q is now

$(E_5 - E_{P_0})$. This has some similarity to the form of expressions for overall efficiency η_o (see Horlock, 1992), such as

$$(\eta_o)_{PP} = (\eta_o)_{GT} + \eta_S - (\eta_o)_{GT}\,\eta_S - \nu_{UN}\,\eta_S \tag{44}$$

where

$$\nu_{UN} = (H_5 - H_{P_0})/(H_{R_0} - H_{P_0}).$$

Discussion and Conclusions

We have considered a range of definitions of "second-law" efficiencies of components that can be found in the literature. In attempting to relate these component efficiencies to the well-defined and widely accepted definition of plant rational efficiency, none of the component efficiencies proves entirely satisfactory. The most logical approach, to define the component efficiency as the ratio of the work output to the maximum possible (reverisible) work output, as for the power plant itself, proves to be somewhat barren since many component efficiencies then have values of zero or infinity and therefore do not appear explicitly in the expressions for plant rational efficiency that are derived.

A combination of rational efficiency defined in this way (for components with work inputs or outputs) with Fratzscher's definition of exergetical efficiency (for components such as boilers, heat exchangers, and HRSGs) proves more informative for several power plants and it is recommended that this method be adopted as a general practice.

However, it has to be said that the practice in which the sum of the fractional irreversibilities is subtracted from unity to give the plant rational efficiency, while not giving a very good estimate of individual component performance, does not have logical inconsistencies.

References

Bosnjakovic, F., 1935, *Technische Thermodynamik*, Steinkopf, Germany.

Darrieus, G., 1930, "Determination of Thermodynamic Efficiency of a Steam Turbine," *Engineering*, Vol. 130, pp. 283-285.

El-Masri, M. A., 1985, "On Thermodynamics of Gas-Turbine Cycles—Part I, Second Law Analysis of Combined Cycles," ASME *Journal of Engineering for Gas Turbines and Power*, Vol. 107, pp. 880-889.

Fratzscher, W., 1961, "Exergetical Efficiency," *Brennstoff-Wärme-Kraft*, Vol. 13, No. 11, pp. 486-493 [CE Trans. 2399].

Haywood, R. W., 1980, *Equilibrium Thermodynamics*, Wiley, Chichester, United Kingdom.

Horlock, J. H., and Haywood, R. W., 1985, "Thermodynamic Availability and Its Application to Combined Heat and Power Plant," *Proc. I Mech E.*, Vol. 199, No. C1, pp. 11-17.

Horlock, J. H., 1987, *Cogeneration—Combined Heat and Power*, Pergamon, Oxford, United Kingdom.

Horlock, J. H., 1992, *Combined Power Plants*, Pergamon Press, Oxford, United Kingdom.

Keenan, J. H., 1941, *Thermodynamics*, Wiley, New York.

Kotas, T. J., 1985, *The Exergy Method of Thermal Power Analysis*, Butterworths, London, United Kingdom.

Meyer, G. J., Silvestri, F., and Martin, J. A., 1959 "Availability Balance of Steam Power Plants," ASME *Journal of Engineering for Power*, Vol. 81, pp. 35-41.

Riekert, L., 1974, "The Efficiency of Energy Utilization in Chemical Processes," *Chem. Eng. Sci.*, Vol. 29, p. 1613.

Traupel, W., 1957, "Reciprocating Engine and Turbine in Internal Combustion Engineering," *Proc. C.I.M.A.C.*, p. 39.

Tsatsaronis, G., and Winfold M., 1985, "Exergoeconomic Analysis and Evaluation of Energy-Conversion Plants: I—A New General Methodology; II—Analysis of a Coal-Fired Steam Power Plant," *Energy*, Vol. 10, pp. 69-80, 81-94.

APPENDIX

An Illustrative Calculation

Kotas (1985) has given an example of how the rational efficiency of a gas turbine plant can be calculated using exergy analysis. Figure 12 shows a diagram of the plant, with states indicated by 1, 2, 3, ..., 12 and components *GC*, *AC*, *GX*, *AX*, *CC*, *T*. The plant burns blast furnace gas, and has two heat exchangers (*GX*) and (*GA*), to preheat the compressed gas and the compressed air separately before combustion.

The exergy flows through the plant are illustrated in Table 2, which is based on calculations given by Kotas. He takes the exergy of the air as zero at entry, and the final exergy of products $[E_{P_0}]$ also as zero, i.e., cooling and expansion of the gases discharged could take place to the final dead state, in unrestricted equilibrium with the atmosphere. Thus the exergy difference on which the plant rational efficiency is based is $(E_{R_0} - E_{P_0}) = E_1 + E_4 - E_{P_0} = E_4$, since E_1 and E_{P_0} are zero.

Table 2 also shows the exergy changes across the six components, together with values of λ_{CP}, λ_{CP}, and component rational efficiency $(\eta_R)_{CP}$. Plant rational efficiency is given by either

$$\begin{aligned}(\eta_R)_{PP} &= 1 - \Sigma\,\delta_{CP}\\ &= 1 - 0.751\\ &= 0.249,\end{aligned}$$

or by

$$\begin{aligned}(\eta_R)_{PP} &= \lambda_T(\eta_R)_T - \lambda_{AC}/(\eta_R)_{AC} - \lambda_{GC}/(\eta_R)_{GC}\\ &= 0.766 - 0.463 - 0.0534\\ &= 0.249\end{aligned}$$

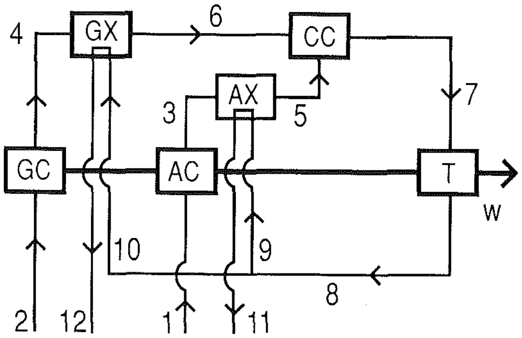

Fig. 12 Gas turbine example

Table 2 Gas turbine calculation

Component	Exergy Flux (kW) In	Exergy Flux (kW) Out	Down $\dot{E}_{IN}-\dot{E}_{OUT}$	Up $\dot{E}_{OUT}-\dot{E}_{IN}$	W_{IN}	W_{OUT}	I^C, I^Q	δ_{CP}	λ_{CP} Down	λ_{CP} Up	$(\eta_R)_{CP}$ Down	$(\eta_R)_{CP}$ Up	$(\eta_R)\lambda_{CP}$ Down	$\frac{\lambda_{CP}}{(\eta_R)_{CP}}$ Up
AC	$\dot{E}_1=0$	$\dot{E}_3=4997$		4997	5604		$I^C=607$	0.050		0.413		0.892		0.463
GC	$\dot{E}_2=12{,}077$	$\dot{E}_4=12{,}650$		573	651		$I^C=78$	0.006		0.047		0.880		0.0534
GX cold side	$\dot{E}_4=12{,}650$	$\dot{E}_6=13{,}010$		360			$I^C=89$	0.007		0.030				
Hot side	$\dot{E}_{10}=727$	$\dot{E}_{12}=278$	449						0.037					
AX cold side	$\dot{E}_3=4997$	$\dot{E}_5=8116$		3119			$I_C=741$	0.061		0.258				
Hot side	$\dot{E}_9=6248$	$\dot{E}_{11}=2388$	3860						0.320					
CC	$\dot{E}_6=13{,}010$ $+\dot{E}_5=8116$	$\dot{E}_7=16{,}930$	4196				$I^C=4196$	0.347	0.347					
T	$\dot{E}_7=16{,}930$	$\dot{E}_8=6995$ $=\dot{E}_9+\dot{E}_{10}$	9955			9256	$I^C=699$	0.058	0.824		0.930		0.766	
S	$\dot{E}_{11}=2388$ $+\dot{E}_{12}=278$	$\dot{E}_{P_o}=0$	2666				$I^Q=2666$	0.221	0.221					
Total	$\dot{E}_2-\dot{E}_{P_o}=12{,}077$		$\sum_{CP}(E_{IN}-E_{OUT})=12{,}077$		$\Sigma(W_{OUT}-W_{IN})=3001$		$\Sigma I=9076$	$\Sigma\delta_{CP}=0.750$	1.749 $\Sigma\lambda_{CP}=1.0$	0.748			0.766	0.517 $(\eta_R)_{PP}=0.249$

G. J. Silvestri

R. L. Bannister

Westinghouse Electric Corporation,
Orlando, FL 32826

T. Fujikawa

Mitsubishi Heavy Industries, Ltd.,
Nagasaki, Japan

A. Hizume

Kobe University,
Kobe, Japan

Optimization of Advanced Steam Condition Power Plants

The modern pulverized-coal power plant is the product of continuous design experience and component improvement in the 20th century. In recent years, studies of the effect of high temperatures on turbine materials have led to major worldwide research and development programs on improving the thermal cycle by raising turbine-inlet pressure and temperature. This paper reviews the importance of various parameters in trying to optimize a turbine cycle designed for advanced steam conditions. Combinations of throttle pressure (between 3500 psi [24.1 MPa] and 10,000 psi [70 MPa]), throttle and reheat temperature (1000°F [538°C] to 1400°F [760°C]), and number of reheats are explored to establish a realistic turbine cycle design. Assessments and trade-offs are discussed, as applicable. Critical cycle components, feedwater cycle arrangements, and reheat pressure selections are analyzed in establishing an optimized steam turbine-boiler cycle for a 1000 MW turbine-generator. Applicability of results to smaller advanced steam turbines is given. A brief update on the high-temperature Wakamatsu turbine project in Japan is also given.

Introduction

Today's pulverized-coal power plant is the product of nine decades of experience and component improvement (Bannister and Silvestri, 1989). Steam inlet conditions, starting at 155 psig (1.07 MPa) and 410°F (210°C) in 1902 for a 2000 kW Westinghouse unit, peaked at 5000 psig (34.5 MPa), 1200°F (649°C), and two reheats to 1050°F (565°C) for Philadelphia Electric Company's cross-compound, five-cylinder, double flow exhaust design (Campbell et al., 1957).

Eddystone 1 established a world-record annual plant performance level of 8534 Btu/kWh (9003 kJ/kWh) in 1962. Problems were encountered at Eddystone 1, although few were caused by the high temperatures and pressures. A number of the difficulties were in areas where limited or no operating experience existed (Chamberlain, 1983). For many years Eddystone 1 has operated under throttle steam conditions of 4700 psig (32.4 MPa) and 1130°F (510°C) and is currently scheduled to operate until the year 2005. In the early 1960s, experience was gained in operating this unit at a throttle pressure of 5000 psig (34.5 MPa) and inlet steam temperatures of 1140°F (621°C) and 1200°F (649°C) (Harlow, 1962).

The economic incentive to continue lowering heat rate diminished in the 1960s and early 1970s because of the anticipated increase in nuclear power generation for baseload operation and the availability of relatively inexpensive fossil fuel. In recent years, heat rates of existing fossil plants (including Eddystone 1) have increased due to the impact of environmental controls.

For the past 13 years, EPRI has funded a series of programs aimed at determining the feasibility of developing, designing, and building an advanced pulverized-coal steam plant in the pioneering spirit of the 1950s. Westinghouse, involved in one of the initial studies, recommended a turbine-generator designed for steam conditions of 4500 psi, 1100°F/1050°F/1050°F (31 MPa, 593°C/565°C/565°C) (Bennett and Bannister, 1981).

Today, in Japan, Mitsubishi Heavy Industries (MHI) is working on an extensive material verification and design program sponsored by the Electric Power Development Company (EPDC). The output of this program will support the design of a high-temperature, supercritical steam turbine-generator being considered for Japan within the next decade. Inlet steam conditions of 4500 psig (31 MPa) to 5000 psig (34.5 MPa) and 1000°F (538°C) to 1200°F (649°C) are being considered for this 600 MW to 1000 MW unit (Bannister et al., 1987).

Advanced Steam Conditions

The basic reason for raising steam pressure and temperature is to improve the potential efficiency of the thermal cycle. Pressure and temperature are not two completely independent variables. They should be combined so that turbine exhaust stage steam is neither superheated (a possibility with reheating) nor contains excessive moisture (a possibility with no reheating in the cycle). A good part of the thermal gain with better inlet steam conditions comes from a reduction in exhaust steam volumetric flow and resulting heat rejection to the condenser per kilowatt-hour generated. Higher initial steam pressure also justifies more steam extraction for regenerative feedwater heating, again decreasing exhaust flows. Where exhaust stage blading limitation is a factor in determining maximum economic unit loading, any manner of reducing exhaust flow volume per kilowatt hour generated will permit greater generator loading.

It should be noted that pressure and temperature should be increased in tandem to realize the maximum heat rate benefit. For a given set of throttle and reheat temperatures, increases

---

Contributed by the Power Division and presented at the Joint ASME-IEEE Power Generation Conference, Philadelphia, Pennsylvania, September 23–25, 1988. Manuscript received by the Power Division March 21, 1990. Associate Technical Editor: R. W. Porter.

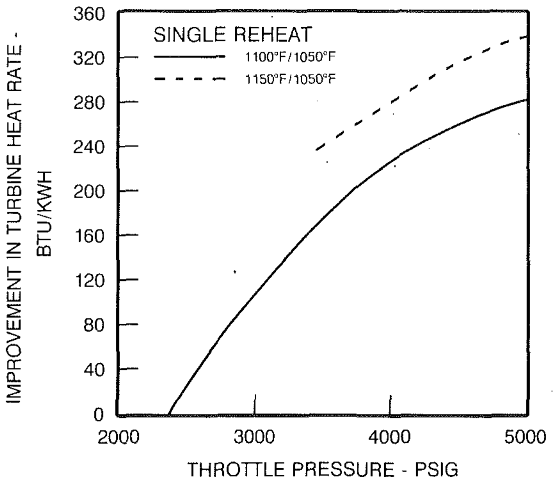

Fig. 1 Δ **heat rate versus throttle pressure**

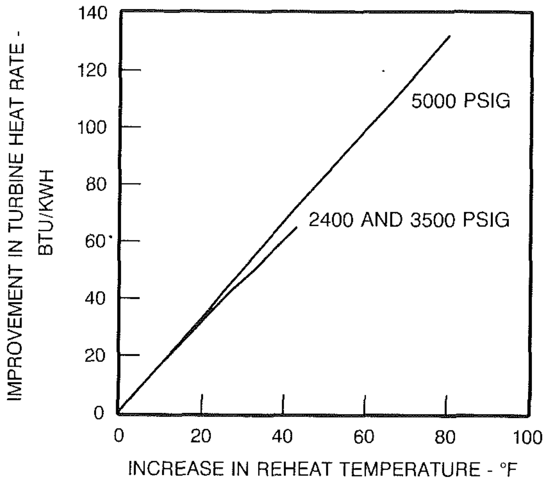

Fig. 2 Δ **heat rate versus reheat temperature**

in throttle pressure will initially result in decreases in cycle heat rate for a given plant configuration.[1] However, each successive increase in pressure results in progressively smaller decreases in heat rate. In like manner, higher pressure cycles can more effectively convert higher temperatures into increased plant efficiency as shown in Fig. 1. There is a pronounced decrease in the upward slope of the 1100°F/1050°F (593°C/565°C) (throttle and reheat temperatures) heat rate improvement curve as pressure is increased.

The improvements in heat rate in Fig. 1 reflect the kilowatt rating of the turbine and the cycle thermodynamics. With a given rating, high-pressure (HP) section volumetric flow decreases with increasing throttle pressure, thereby increasing leakage and other blading losses. Moreover, successive incremental increases in many cycle parameters result in diminishing improvements for such things as number of reheats, number of feedwater heaters, final feedwater temperature, and throttle temperature.

Conversely, the 5000 psig (34.5 MPa) value shows a larger improvement with steam temperatures of 1150°F/1050°F (621°C/565°C) than the 3500 psig (24.1 MPa) value when compared to the 1100°F/1050°F (593°C/565°C) values. The increase in throttle temperature from 1100°F (593°C) to 1150°F (621°C) not only increases the HP section efficiency of the 5000 psig (34.5 MPa) design because of the increase in volumetric flow, but also results in a greater increase of the available energy of the HP section. For a 5 to 1 HP section pressure ratio, the available energy increase related to an increase from 1100°F (593°C) throttle temperatures to 1150°F (621°C) is 6.5 percent for 5000 psig and 5.3 percent for 3500 psig (24.1 MPa).

Each 50°F (28°C) increase in reheat temperature improves heat rate by 60 to 70 Btu/kWh [63 to 74 kJ/kWh] (Fig. 2). The improvement is slightly pressure dependent. The absolute level of temperature can modify the gain slightly by producing variations in feed system losses. A second-order effect of fine tuning of reheat pressure selection, when varying either throttle or reheat temperature, can cause a slight raising or lowering of the lines of constant throttle pressure. Other contributors to the greater heat rate improvement for the 5000 psig (34 MPa) cycle with increased reheat temperature are reduced leakage and blading losses and increased cycle available energy. These effects in the intermediate pressure (IP) section are considerably more modest than with the HP section.

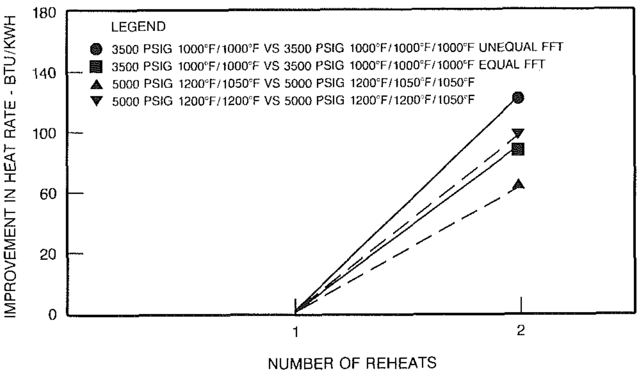

Fig. 3 Improvement in heat rate versus number of reheats

The incorporation of a second reheat will improve the cycle performance by 90 to 152 Btu/kWh (95 to 160 kJ/kWh), as shown in Fig. 3. The magnitude of the gain is dependent upon the respective final feed temperatures (FFTs) of the single and double reheat cycles. For example, the 3500 psig (24.1 MPa) double reheat case, denoted by a circle, has a 50°F (28°C) higher final feed temperature than the single reheat case. When a heater is added to the single reheat cycle to raise the final feedwater temperature 50°F (28°C), the heat rate improvement is reduced to 119 Btu/kWh [126 kJ/kWh].

An additional thermodynamic variable of potential interest is the ratio of throttle pressure to first reheat pressure. Normally, these parameters are ratioed approximately 4 or 5 to 1. The optimum value of this ratio is affected by throttle pressure, throttle temperature, reheat temperature, number of reheats, and feedwater heater configuration. However, the potential gain from such an optimization process would be small relative to other variables and the effort required to optimize the ratio will be significant. Details of the optimization are described in this paper.

Additional heat rate improvements can be obtained by modification of the thermodynamic cycle. Four types of heat exchangers having improvement potential are: a very high pressure heater, topping desuperheaters, crossover heaters, and intermediate desuperheaters.

Potential heat rate improvements for increasing steam temperature and pressure are illustrated in Table 1. A unit with steam conditions of 3500 psi 1000°F/1025°F/1050°F (24.1 MPa, 538°C/552°C/565°C) was chosen as the base design. Units with these steam conditions have accumulated many unit years of operation and have, as a class, achieved operating availabilities at the leading edge of industry practice.

---

[1] Heat rates discussed in this paper represent an estimate sufficient to present an engineering assessment. This is not, or is it intended to be, actual information representative of Westinghouse practice in connection with the heat rates of large turbine generators.

Table 1 Combined effect of throttle pressure and temperature and reheat temperature on heat rate

Throttle		Reheat Temperature		Heat Rate
Pressure (psig)	Temp (°F)	No. 1 (°F)	No. 2 (°F)	Increment (Btu/kWh)
3500	1000	1025	1050	---
4000	1050	1050	1050	116
4000	1100	1050	1050	170
4500	1100	1050	1050	203
4500	1200	1050	1050	310
5000	1200	1050	1050	344
5000	1200	1100	1100	390
5500	1200	1100	1100	410

Table 2 Combined effect of throttle and reheat temperature on heat rate for a 8000 psig throttle pressure

Throttle	Reheat Temperature		Heat Rate
Temp. (°F)	No. 1 (°F)	No. 2 (°F)	Increment (Btu/kWh)
1200	1400	1100	---
1400	1400	1100	223
1400	1400	1100	---
1400	1400	1200	5
1400	1400	1400*	68

* Includes a Crossover Heater

The 3500 psi, 1000°F/1025°F/1050°F (24.1 MPa, 538°C/552°C/565°C) design is in service and available today. For a 750 MW unit, with an eight heater cycle that uses a limestone flue-gas desulferization (FGD) gas clean-up system, a heat rate of approximately 9200 Btu/kWh (9700 kJ/kWh) is possible. This unit is significantly superior to the 2400 psi, 1000°F/1000°F (16.6 MPa, 538°C/538°C) unit whose heat rate of approximately 10,000 Btu/kWh (10,550 kJ/kWh) is often used as a basis of comparison with more advanced steam turbine designs.

For a given cycle configuration, results in Table 1 show the potential heat rate gains for varying inlet pressure (between 3500 psi (24.1 MPa) and 5500 psi (37.9 MPa)) and throttle and reheat temperature (1000°F to 1200°F) (538°C to 649°C).

Table 3 Effect of throttle pressure on heat rate for elevated throttle and reheat temperature

Throttle		Reheat Temperature		Heat Rate
Pressure (psig)	Temp (°F)	No. 1 (°F)	No. 2 (°F)	Increment (Btu/kWh)
6000	1400	1400	1100	---
7000	1400	1400	1100	56
8000	1400	1400	1100	77
10000	1400	1400	1100	85

A second set of advanced steam conditions is used to determine the lowest heat rate for which there is a possibility of designing an advanced steam turbine-generator plant. A comparison of throttle temepratures at 1200°F and 1400°F (649°C and 760°C) (Table 2) shows a significant heat rate improvement in going to 1400°F (760°C) (223 Btu/kWh) (235 kJ/kWh). Also in Table 2, the benefit of increasing the second reheat temperature above 1100°F (593°C) is modest for the problems involved in finding a rotor material for the size that would be required.

For a 1400°F (760°C) throttle temperature and reheat temperatures of 1400°F and 1100°F (760°C and 593°C), respectively, Table 3 shows the benefit of increasing throttle from 6000 psi to 10,000 psi [41.4 MPa to 70 MPa]. A gain of 56 Btu/kWh (59 kJ/kWh) occurred when the pressure is increased from 6000 psi to 7000 psi (41 MPa to 48.3 MPa), but only an additional 21 Btu/kWh (22 kJ/kWh) from 7000 psi to 8000 psi (48.3 to 55.2 MPa), and only an additional 8 Btu/kWh (8.4 kJ/kWh) between 8000 psi and 10,000 psi (55.2 to 70 MPa).

As noted earlier, increases in some cycle parameters resulted in minor heat rate improvements while others produced substantial improvement. In these latter instances, an assessment was also made of the relative degree of technical and economic difficulty (risk) to produce a viable design for the five alternatives developed from the screening studies. Figures 4 and 5 present the comparative risk for the cycles listed in Table 4. The object was to select a design that balanced the potential heat rate improvements with prudent economic and technical risk. It should also be noted that the assessment of risk factors has considerably more uncertainty than the heat rate predictions.

Based upon the potential heat rate improvements for elevated steam conditions in Tables 2, 3 and 4, there is no reason to elevate the steam conditions beyond 7000 psi, 1400°F/1400°F/1100°F (48 MPa, 760°C/760°C/593°C).

To retain a major fraction of the theoretical efficiency gains with initial steam conditions of 4500 psig, 1100°F (31 MPa, 593°C) a minimum turbine rating in the 400 to 450 MW range is needed. At a rating of 700 MW the heat rate gains from increased unit size have been substantially realized with a cross compound design using high-speed (3600 rpm), low-pressure elements. Where higher ratings are desired or lower exhaust pressures are practical, a cross compound design in which the high-temperature elements operate at high speed, 3600 rpm, and the low pressure elements operate at low speed, 1800 rpm, is the preferred choice.

Reheat Pressure Selections. There is a wide range over which first and second reheat pressures can be varied while having minimal effect on heat rate. Figure 6 illustrates the range of the two reheat pressures that can be selected while

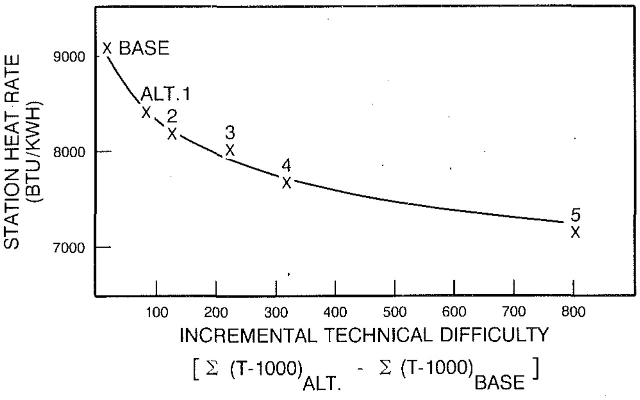

Fig. 4 Incremental technical difficulty for alternatives

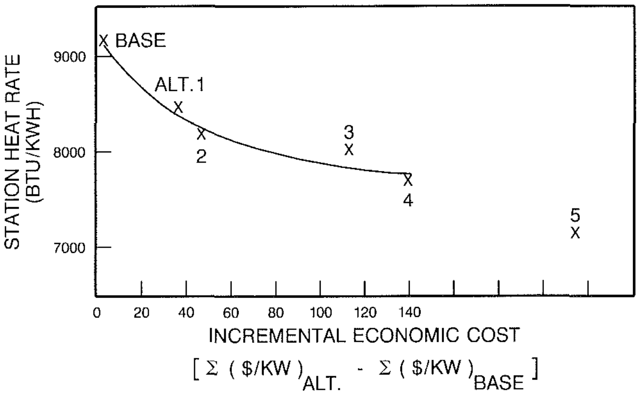

Fig. 5 Incremental economic cost for alternatives

Table 4 Summary of design alternatives

		Alternative					
		BASE	1	2	3	4	5
Throttle pressure	(psig)	3500	4000	4500	5000	5500	7000
Throttle temperature	(°F)	1000	1050	1100	1200	1200	1400
RH 1 temperature	(°F)	1025	1050	1050	1050	1100	1400
RH 2 temperature	(°F)	1050	1050	1050	1050	1100	1100
FFWT*	(°F)	550	610	610	650	650	750
Boiler excess air	(%)	22	15	15	15	12	12

*Final feedwater temperature

maintaining the heat rate change within 4 Btu/kWh (4.2 kJ/kWh) for steam conditions of 4500 psig, 1100°F/1050°F/1050°F (31 MPa, 593°C/565°C/565°C). For example, with a first reheat pressure of 1450 psia (10 MPa), second reheat pressure can be varied between 250 and 360 psia (1.72 and 2.48 MPa) with less than 4 Btu/kWh (4.2 kJ/kWh) change in heat rate.

In the past, double reheat units have experienced considerable second reheat temperature droop (decrease) as load was reduced. The choices of reheat pressure will also affect the droop. Fortunately, the availability of boilers that can vary or slide throttle pressure at lower loads, particularly operation in the hybrid sliding pressure mode, reduces boiler droop and improves efficiency.[2] This is especially advantageous on units that must cycle.

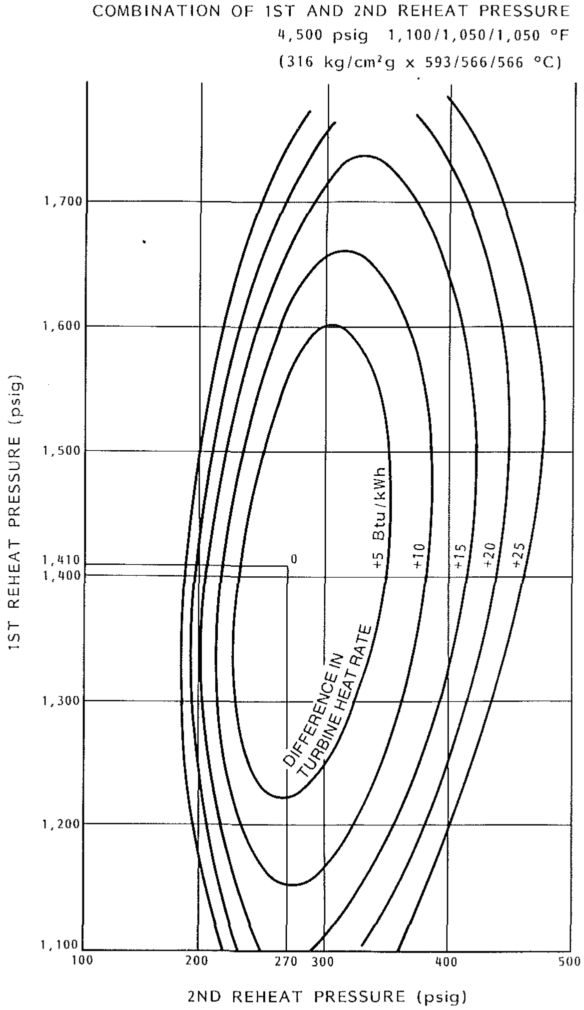

Fig. 6 Combination of first and second reheat pressure

Second Reheat Pressure Selection. Too low a second reheat pressure, although it may still be within the optimum range, might result in superheated exhaust at part load as shown in Fig. 7. In addition, it would increase the low-pressure (LP) inlet temperature and could result in temper embrittlement even if the improved LP rotor steels, which have higher temperature capability than conventional NiCrMoV steels, were used.

First Reheat Pressure Selection. After a viable second reheat pressure is chosen, unless Fig. 6 is interpreted judiciously, too high a first reheat pressure may be selected. There is a limitation on the final feedwater temperature established by the boiler design. If the top (highest extraction pressure) feedwater heater is supplied from the very-high-pressure (VHP) turbine exhaust, the first reheat pressure will be dictated by the limitation on the final feedwater temperature. If the top heater is supplied by steam from an upstream location of the

---

[2] Hybrid sliding pressure is applied with partial-arc admission turbines by maintaining constant pressure in the upper load ranges and modulating control valves and by holding valve position constant and varying throttle pressure in the lower load ranges.

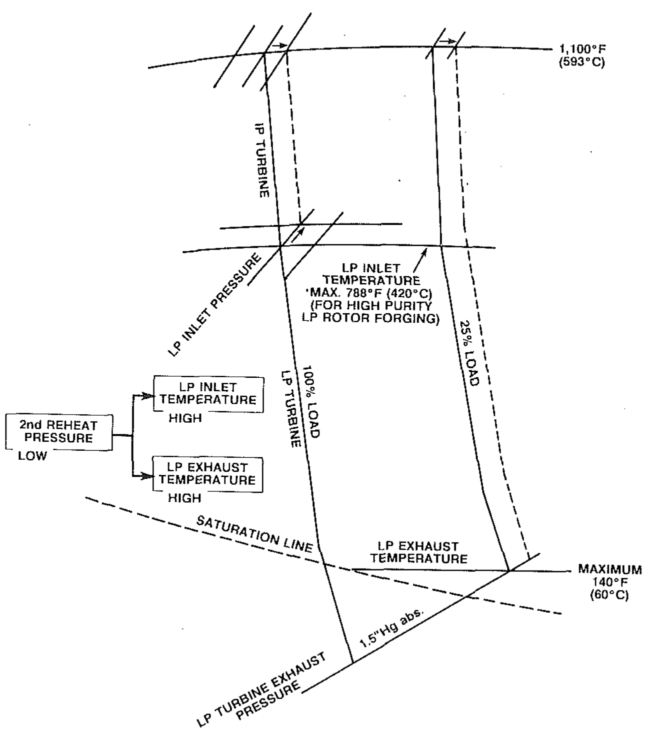

Fig. 7 Second reheat pressure and LP turbine inlet/exhaust temperature

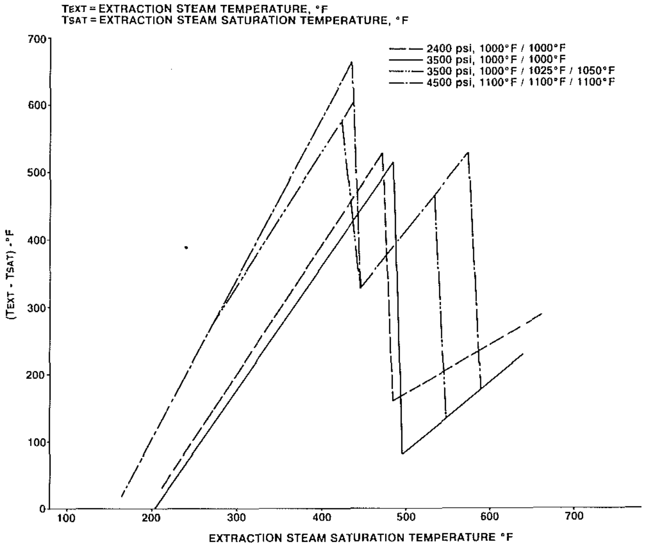

Fig. 8 Comparison of the difference between turbine steam temperature and the saturated steam temperature for a given turbine inlet pressure

VHP turbine, a HARP (heater above the reheat point) cycle, the optimum first reheat pressure is lower than when the top heater is supplied from the cold reheat point. In this instance another optimization study for the first reheat pressure must be done by fixing the top heater extraction pressure and the second reheat pressure.

In like manner, if topping desuperheaters are used, the first reheat pressure should be reduced as is the case with the HARP cycle.

Optimum Final Feedwater Temperature. The final feedwater temperature selection must include not only the effect on turbine heat rate but also the effect on boiler design. Experience has shown that the maximum practical limit of effectiveness of air heaters is in the range of 92 to 93 percent.

Higher effectivenesses are difficult to obtain or justify because of the inevitable nonuniformity of the effectiveness in the circumferential direction of the air heater and the huge increases in heat transfer area that result when effectivenesses above 93 percent are selected.

For a coal-fired boiler with an ambient air temperature of 68°F (20°C) and an air heater exit flue gas (stack) temperature in the 265°F to 285°F (129°C to 141°C) range, the air heater inlet flue gas temperature would be 680°F to 700°F (360°C to 371°C) with an air heater effectivenesses of 93 percent. For a temperature difference of 75°F (42°C) or more between the economizer exit gas temperature and the final feedwater temperature, the maximum final feedwater temperature would be 600°F ± 10° (316°C ± 6°).

Additional Feedwater Train Optimization. If regenerative feedwater heating were incorporated on a 4500 psig, 1100°F (31 MPa, 593°C) nonreheat Rankine cycle, there would also be an improvement in heat rate. If the straight condensing nonreheat cycle incorporated two stages of reheat to 1100°F (593°C), there would also be an improvement in heat rate. Then, if the 4500 psig, 1100°F (31 MPa, 593°C) two-stage reheat cycle incorporated feed heating, the resulting heat rate would be poorer (higher) than the heat rate obtained when numerically combining the improvements from separately incorporating regenerative feedwater heating and separately incorporating reheat. The reason for this is that reheat results in higher extraction steam temperatures at feedwater heaters. That is, regenerative feedwater heating is an inferior option when applied on reheat cycles than when applied on nonreheat Rankine cycles, particularly with very high reheat temperatures. This does not suggest that regenerative feedwater heating should not be used on high-temperature reheat cycles. But it should be recognized that the second reheat, in particular, results in large differences between the saturation temperature in the feedwater heater and the incoming extraction steam temperature.

Figure 8 compares the difference between the turbine steam temperature and the saturated steam temperature at the same pressure for a conventional 2400 psig, 1000°F/1000°F/1000°F cycle (16.6 MPa, 538°C/538°C/538°C), a 3500 psig, 1000°F/1000°F (24.1 MPa, 538°C/538°C) single reheat cycle, a double reheat cycle with steam conditions of 3500 psig, 1000°F/1025°F/1050°F (24.1 MPa, 538°C/552°C/565°C) (ascending reheat), and the 4500 psig, 1100°F/1100°/1100°F (31 MPa, 593°C/593°C/593°C) cycle.

Note that the differences between the extraction steam temperature and the feedwater heater saturation temperature are similar on 2400 psig, 1000°F/1000°F (16.6 Mpa, 538°C/538°C) single reheat units and 3500 psig, 1000°F/1000°F (24.1 MPa, 538°C/538°C) single reheat units. Also, the temperature comparison is similar for the initial expansion of the 3500 psig and 4500 psig (24.1 MPa and 31 MPa) double reheat designs. However, the addition of a second reheat causes large increases in the extraction temperatures, even without significant changes in reheat temperature.

In the latter part of the 1950s, a considerable number of units used noncondensing turbines as the boiler feed pump drives. The drive turbine received steam from the cold reheat point, supplied one or more feedwater heaters, and exhausted to a line connected to the IP turbine exhaust and the deaerator (Olmstead, 1958). A heat rate improvement of 15 to 20 Btu/kWh (15.8 to 21 kJ/kWh) was claimed as compared to a motor drive. In addition, plant investment costs were reduced and starting problems with large motors were eliminated. With the passage of time, the condensing turbine drive displaced the noncondensing turbines as the boiler feed pump drive (Frankenberg and Tillinghast, 1964).

A portion of the heat rate gain resulting from the use of noncondensing drives is attributable to the lesser temperature difference between the extraction steam supplied by the drive turbine and the heater saturation temperature. In the case of the advanced plant, this temperature difference would be reduced by as much as 300°F (149°C), if steam from the second cold reheat were supplied to a noncondensing drive turbine.

Even if the expansion efficiency of the noncondensing drive were lower than the condensing drives of the advanced steam plant, it would reduce the entropy increases (availability losses) in the affected feedwater heaters. In addition, it would reduce the amount of steam requiring reheating and could result in less second reheat temperature droop at part load. The high reheat steam temperatures of the advanced cycle make the noncondensing turbine drive a potential candidate for inclusion in the cycle.

Turbine Design and Materials

For a high-temperature, supercritical steam turbune, new elements must be developed, but temperature requirements are sufficiently similar to those of current units for the parts to be modeled after current designs for turbine throttle pressures and temperatures between 3500 psi to 5500 psi, and 1000°F to 1200°F (24.1 MPa to 37.9 MPa, 538°C to 649°C), respectively (Bannister et al., 1982). Because of higher throttle and reheat steam temperatures, it may be necessary to use separate VHP and HP elements. The rotors for the VHP, HP, and IP elements are probably the most critical turbine components that will have to be upgraded. Turbine cycles incorporating 1100°F (593°C) throttle steam have been built using standard CrMoV materials. However, these units are significantly smaller than the advanced design.

If an 1100°F (593°C) reheat temperature is adopted, or the design of the IP blading necessitates a higher LP element inlet pressure, the LP inlet temperature will exceed 775°F (413°C). The material used for the LP rotor must therefore be resistant to temper embrittlement. A high-purity, 3.5 NiCrMoV steel of low manganese and silicon content is a promising candidate for this application (Hizume et al., 1987; Fujita et al., 1986).

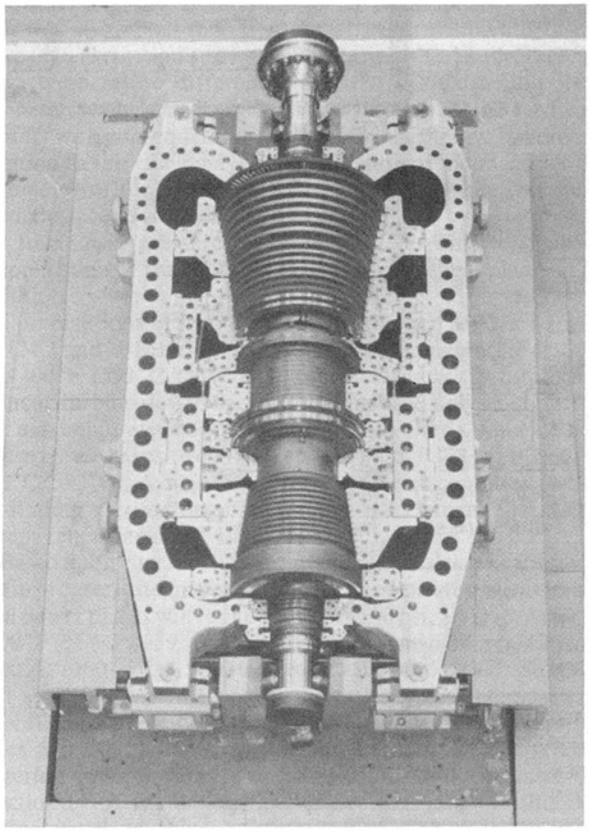

Fig. 9 Base half of Wakamatsu HP/IP turbine with rotor in place

Austenitic steel has been used with reasonable success to manufacture high-temperature steam piping. In recent years, however, distress has been found in several 15- to 20-year-old units, primarily in the transition piece, where the steam inlet pipe penetrates the ferritic turbine casing (Argo et al., 1984). The replacement of austenitic pipe with a newly developed 9Cr could eliminate the need for a transition piece.

For the VHP element a partial-arc method of load control, in conjunction with sliding throttle pressure, is preferable both at full and at part loads. Hybrid sliding pressure enhances the operational flexibility of the plant, and, compared with full-arc admission and sliding-pressure operation, the ability to transfer from full- to partial-arc admission can enhance turbine life (Silvestri and Martin, 1987).

The VHP inner cylinder must be made of a casting alloy with good weldability, high creep-rupture strength, and excellent resistance to oxidation and spalling in steam. In a VHP rotor of advanced 12-percent-Cr steel, it would be desirable to have a material with a thermal expansion coefficient similar to ferritic steels so as to minimize differential thermal expansion between the rotor and stationary parts.

If the steam conditions were increased to 7000 psi, 1400°F/1400°F/1100°F (48.3 MPa, 760°C/760°C/593°C), the major concern would be the 200°F (93°C) step change in temperature. A major issue would be finding a rotor material for the HP element that would accept reheat steam at 1400°F (760°C). If an acceptable material could be found, the pacing problem could be the inlet design to direct the steam flow (i.e., piping, inner cylinder). The lower pressure at the first reheat might make 1400°F (760°C) more achievable than at the throttle.

Wakamatsu Project

In Japan, the Electric Power Development Company (EPDC) is sponsoring an extensive material verification and design program to support the manufacture of a 1000 MW, high-temperature, supercritical-pressure steam power plant. Elevated steam conditons for such a unit will be specified by EPDC after the R&D program is reviewed. The steam conditions being considered for this unit range between 4500 psi and 1100°F/1100°F/1100°F (31 MPa and 593°C/593°C/593°C), and 5000 psi and 1200°F/1100°F/1100°F (34.5 MPa and 649°C/593°C/593°C).

A major part of EPDC's R&D program is the design and material verification project at Wakamatsu No. 2. Mitsubishi Heavy Industries has converted a 1450 psig, 1000°F/1000°F (10 MPa, 538°C/538°C), 75 MW commercial turbine generator to a 50 MW, high-temperatue unit (Fig. 9). Two HP/IP designs will be evaluated at 1100°F and 1200°F over a five-year period (Nakabayashi et al., 1986a). New HP/IP elements for each step (1450 psi, 1100°F/1100°F (10 MPa, 593°C/593°C) and 1450 psi, 1200°F/1200°F (10 MPa, 649°C/649°C)) are designed to simulate, respectively, the VHP element of an 1100°F (593°C) turbine and the super-pressure (SP) or VHP element of a 1200°F (649°C) turbine.

Design and material features of the HP/IP turbine for the 1100°F (593°C) test include: main steam radial inlet sleeves with flexible skirts made of dissimilar metal joints; HCM9M welded type center support nozzle chamber with cylindrical cross section; newly developed 12 Cr rotor; triple-pin type Curtis stage blade made of Refractory 26; newly developed 12 Cr cast inner cylinders and blade rings, nozzle chamber flow separator; IP inlet rotor cooling system with adjustable cooling steam temperature by HP dummy ring leakage steam bypass valves; and integral shroud HP and IP rotating blades (Nakabayashi et al., 1986b).

For the 1100°F (593°C) evaluation, the HP/IP cross section (Fig. 10) shows the ferritic materials selected for various turbine components. For the 1200°F (649°C) evaluation, various turbine components will be replaced with austenitic steels.

The Wakamatsu turbine, placed in operation during Dec. 1986, started the materials verification test at 1100°F (593°C) in Mar. 1987. The 1100°F (593°C) evaluation was completed in Mar. 1989. Installation of austenitic componenets started in Apr. 1990, and operation at 1200°F (649°C) started in Oct. 1990. Completion of the 1200°F (649°C) test is slated for Mar. 1992 (Ikeda et al., 1991).

In addition to the usual supervisory instruments, a number of instruments have been installed in the turbine to measure steam pressures and temperatures, metal temperatures of stationary parts, rotor temperatures at surface and bore, and bolt stresses. The temperature of the rotor cooling steam is also adjustable.

A data acquisition system gathers and stores the measured data and performs some on-line stress analysis (Kinoshita et al., 1987). This information will reveal actual operating conditions, such as the rotor cooling effect, thermal stress of the rotor, castings, and valve chests, and loosening of bolts over time (Bannister et al., 1983).

An example of on-line temperature and strain measurements is illustrated in Fig. 11 for the main steam inlet of the HP/IP turbine, which shows the temperature and stress in the various materials that are used in this critical component with the unit loaded at 37 MW. An example of on-line supervisory type measurements is given in Fig. 12, which shows the thrust loads (calculated and measured) at various points along the HP/IP and LP turbine elements. Also, calculations such as a turbine heat balance diagram can be performed on-line as shown in Fig. 13.

Conclusions

The basic reason for raising steam pressure and temperature is to improve the potential efficiency of the thermal cycle. Pressure and temperature should be increased in tandem to realize the maximum heat rate potential. They should be combined so that turbine exhaust stage stesm is neither superheated nor contains excessive moisture. Variables that are important in establishing maximum heat rate cycle improvement were reviewed in this paper.

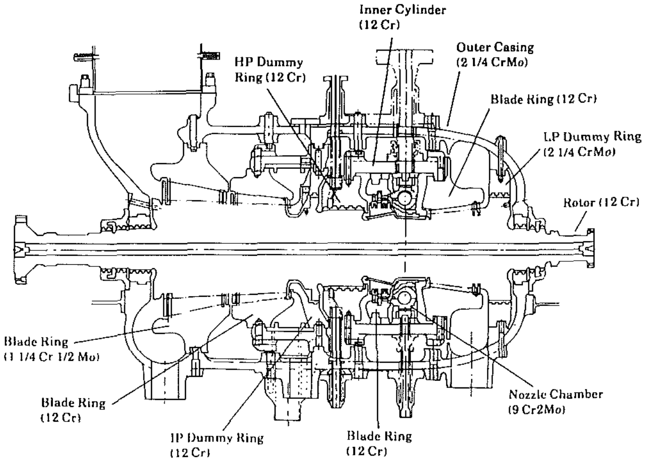

Fig. 10 Wakamatsu HP/IP turbine cross section for 1450 psig, 1100°F/1100°F (19 MPa, 593°C/593°C) evaluation

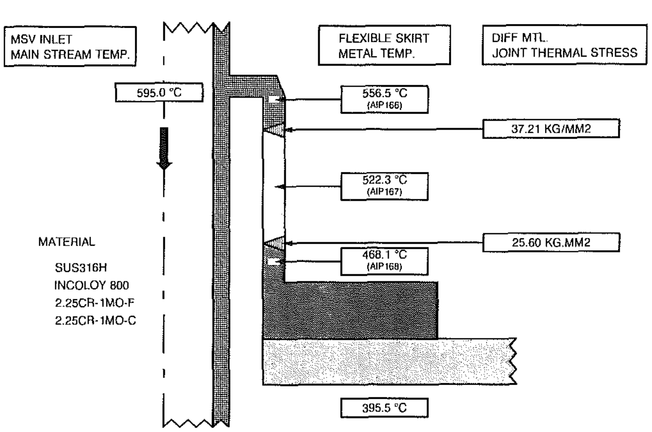

Fig. 11 Main steam inlet sleeve thermal stress

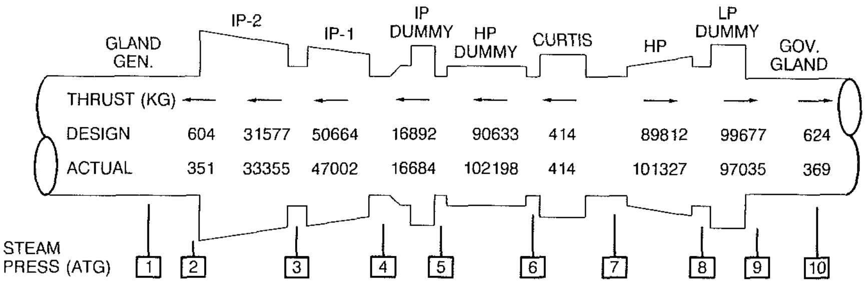

THRUST (KG)	←	←	←	←	←	←	→	→	→
DESIGN	604	31577	50664	16892	90633	414	89812	99677	624
ACTUAL	351	33355	47002	16684	102198	414	101327	97035	369

STEAM PRESS (ATG)	1	2	3	4	5	6	7	8	9	10
DESIGN	0.26	0.85	5.74	(15.3)	(18.3)	46.0	(45.6)	18.4	(0.87)	0.26
ACTUAL	0.42	0.77	5.93	(14.8)	(17.7)	49.0	(48.5)	17.8	(0.78)	0.42

LOAD 36 MW

THRUST BRG TEMP (°C)

	GOV	GEN
METAL	50	48
OIL	51	51

ROTOR POSITION
GOV -0.01 MM

TOTAL THRUST FORCE
DESIGN GEN 716 KG
ACTUAL GEN 1272 KG (WITH CURTIS)
ACTUAL GEN 858 KG (WITHOUT CURTIS)

CALCULATED THRUST INTENSITY
DESIGN GEN 0.76 KG/CM2
ACTUAL GEN 1.36 KG/CM2 (WITH CURTIS)
ACTUAL GEN 0.92 KG/CM2 (WITHOUT CURTIS)

Fig. 12 Turbine thrust and thrust bearing

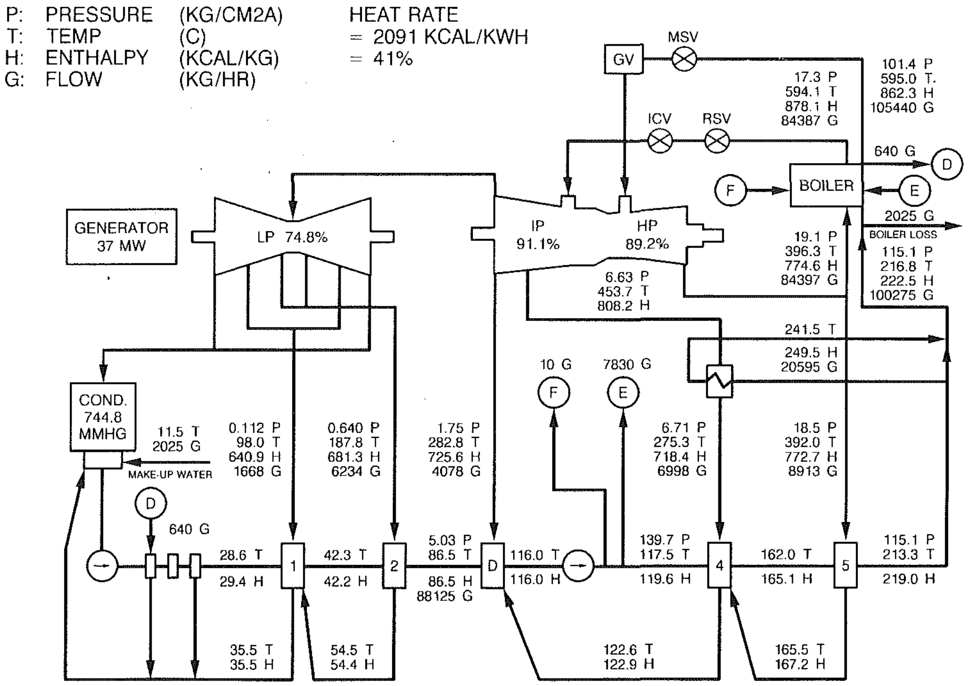

Fig. 13 Turbine heat balance diagram

Performance analyses, for example, demonstrated that first and second reheat pressures can be varied over an appreciable range with minimal increase in heat rate. However, equipment designs and operating concerns place limits on the selection. Where there are lower limits on second reheat pressure related to the avoidance of superheated exhaust from the LP turbine at part load and excessive LP inlet temperature, there is an upper limit on first reheat pressure because of boiler inlet feedwater temperature and air heater constraints.

It was also noted that high reheat steam temperatures produce high extraction steam temperatures. As a result, there are large temperature differences between the extraction steam temperature and the saturation temperature in the feedwater heaters with consequent losses in available energy. A potential solution to this dilemma would be the use of a noncondensing turbine drive for the boiler feed pump, which receives steam from the second cold reheat point and supplies extraction steam for four lower pressure feedwater heaters. This concept is a reapplication of that used on several single reheat plants in the 1960s.

Combinations of throttle pressure (between 3500 and 10,000 psi (24.1 and 70 MPa)), throttle and reheat temperature (1100°F to 1400°F (593°C to 760°C)) were evaluated to establish a realistic turbine design cycle. Performance analyses show that the maximum elevated steam conditions that should be considered are 7000 psi, 1400°F/1400°F/1100°F (48 MPa, 760°C/760°C/593°C). A major issue for these steam conditions would be finding a rotor material for the HP element that would accept reheat steam at 1400°F (760°C).

Based upon current knowledge and material verification testing in progress, steam conditions for the next step in pulverized coal power plants will range between 4500 psi, 1100°F/1100°F/1100°F (31 MPa, 593°C/593°C/593°C) and 5000 psi, 1200°F/1100°F/1100°F (34.5 MPa, 649°C/593°C/593°C). Selection and availability of the proper materials is the foremost consideration to make high-temperature, supercritical steam turbines a reality. The properties and behavior of the selected materials under elevated temperatures must be determined. The practicality of the design, manufacturing, and metallurgical testing of these turbines is being studied. The testing program outlined for the Wakamatsu project is determining and evaluating the properties of several new high-temperature materials that may have applications in existing turbines operating at temepratures below 1100°F (593°C) and up to 1200°F (649°C) for new turbine designs.

References

Argo, H. C., Delong, J. F., Kadoya, Y., Nakamura, M., and Ando, K., 1984, "Eddystone Experience on Long-Term Exposed 316 SS Steam Turbine Valve Components," ASME Paper No. 84-JPGC-Pwr-15.

Bannister, R. L., Bennett, S. B., Silvestri, G. J., Covell, R. B., and Phillips, N. A., 1982, "Material and Design Developments Needed for Next Step in Pulverized Coal Power Plants," *Power Engineering*, Vol. 86, No. 5, pp. 64-68.

Bannister, R. L., Bellows, J. C., and Osborne, R. L., 1983, "Steam-Turbine Generators-on-Line Monitoring and Availability," *Mechanical Engineering*, Vol. 105, No. 7, pp. 55-59.

Bannister, R. L., Silvestri, G. J., Hizume, A., and Fujikawa, T., 1987, "High-Temperature, Supercritical Steam Turbines," *Mechanical Engineering*, Vol. 109, No. 2, pp. 60-65.

Bannister, R. L, and Silvestri, G. J., 1989, "The Evolution of Central Station Steam Turbines," *Mechanical Engineering*, Vol. 111, No. 2, pp. 70-78.

Bennett, S. B., and Bannister, R. L., 1981, "Pulverized Coal Power Plants: The Next Logical Step," *Mechanical Engineering*, Vol. 103, No. 12, pp. 18-24.

Campbell, C. B., Franck, C. C., and Spahr, J. C., 1957, "The Eddystone Superpressure Unit," *Transactions of the ASME*, Vol. 79, pp. 1431-1446.

Chamberlain, H. G., 1983, "The Eddystone Experience—An Overview of Experience in the First Twenty-Four Years," presented at the EPRI Advanced Pulverized Coal Power Plant, Utility Advisory Committee Meeting, July, Washington, DC.

Frankenberg, T. T., and Tillinghast, J. A., 1964, "Seven Years' Experience With Turbine-Driven Feed Pumps Serving Large Generating Units," *Proceedings American Power Conference*, Vol. 26, pp. 435-446.

Fujita, T., Nakabayashi, Y., Hizume, A., Takeda, Y., Fujikawa, T., Takano, Y., Suzuki, A., Kinoshita, S., Kohno, M., and Tsuchiyama, T., 1986, "An Advanced 12Cr Steel Rotor (TMK1) for EPDC Wakamatsu's Step 1 (593/593°C)," presented at the Cost-EPRI Workshop 9-12Cr Steel for Power Generation, Oct., Schaffhausen, Switzerland.

Harlow, J. H., 1962, "Observations Regarding Eddystone No. 1—First Year of Operation at 5000 psi and 1150°F," *Combustion*, Jan., pp. 37-48.

Hizume, A., Takeda, Y., Yokota, H., Takano, Y., Suzuki, A., Kinoshita, S., Kohno, M., and Tsuchiyama, T., 1987, "An Advanced 12Cr Steel Rotor Applicable to Elevated Steam Temperature 593°C," ASME *Journal of Engineering Materials and Technology*, Vol. 109, pp. 319-325.

Ikeda, S., Hizume, A., Fujikawa, T., Yolkota, H., Kokubu, T., Takeda, Y., and Meshii, T., 1991, "Operating Experience of EPDC's Wakamatsu 50 MW High-Temperature Turbine Step 2 (649°C/593°C)," *Proceedings, EPRI sponsored Third International Conference on Improved Coal-Fired Power Plants*, Apr., Palo Alto, CA.

Kinoshita, S., Kohno, M., Honjo, T., Suzuki, A., Hizume, A., Takeda, Y., Yokota, H., and Fujita, A., 1987, "Effect of Freckles on Mechanical Properties of Large A286 Alloy Forging," *Proceedings, ASM International Conference on the Advances in Materials Technology for Fossil Power Plants*, Sept., Chicago, IL.

Nakabayashi, Y., Hizume, A., Fujikawa, T., Yokota, H., Kokubu, T., and Takeda, Y., 1986a, "Design and Test Program of EPDC's Wakamatsu 50 MW High-Temperature Turbine Step 1 (593/593°C)," *Proceedings, EPRI sponsored First International Conference on Improved Coal-Fired Power Plants*, Nov., Palo Alto, CA.

Nakabayashi, Y., Hizume, A., Nakamura, M., Takeda, Y., Fujikawa, T., Yokota, H., 1986b, "Materials/Components of EPDC's Wakamatsu 50 MW High Temperature Turbine Step 1 (593/593°C)," *Proceedings, EPRI sponsored First International Conference on Improved Coal-Fired Power Plants*, Nov., Palo Alto, CA.

Olmstead, L. N., 1958, "Turbines Gain as B-F Pump Drives for Large Units but Motors Still Hold the Lead," *Electrical World*, Mar. 17.

Silvestri, G., Jr., and Martin, H. F., 1987, "Recent Developments in the Application of Partial-Arc Turbines to Cyclic Service," presented at the EPRI sponsored Fossil Plant Cycling Seminar, Oct. 20–22, Princeton, NJ.

Condensing the Dumped Steam During a Turbine Bypass

W. Kals
Niagara Blower Co.,
Hastings-on-Hudson, NY 10706

The reaction of water-cooled and wet-surface air-cooled condensers to a bypass of the steam turbine is analyzed by the introduction of an indicant. Gas dynamics considerations for designing the breakdown of the steam pressure are included. SI metric units are compared with gravitational metric units in order to clarify the fundamental difference between these two systems of measure. Conditioning the steam before admission to the condenser involves desuperheating, which is analyzed on the basis of a heat balance.

A bypass system involving a breakdown of the steam pressure and the injection of water to desuperheat the steam permits full production of steam by the boiler during a turbine trip (Martin and Holly, 1973; Reason, 1984; Gardner, 1984; Kueffer, 1990). When bypassing the turbine, the steam pressure is reduced and the mass of steam that would be exhausted by the turbine is increased by the mass of injected water. With all conditions remaining unchanged, the increased mass of steam directed to the condenser will raise the condensing temperature. In this respect a wet surface aircooled condenser reacts in almost the same manner as a water-cooled condenser. This reaction is analyzed by the introduction of an indicant, which is expressed in strikingly similar terms for the two types of heat transfer mechanisms. Basic features of these two types of condenser are compared.

In the case of a water-cooled condenser, the performance is governed by the temperature of the entering cooling water, whereas the condensing temperature produced by the wet surface air-cooled condenser is determined by the enthalpy of the entering atmospheric air. It is assumed that the mass flow and temperature of water supplied to a water-cooled condenser and the mass flow and enthalpy of air supplied to a wet surface air-cooled condenser will remain unchanged at the bypass. The potential for surrendering heat to water by a water-cooled condenser is the temperature gradient between steam and water. The condensing temperature is determined by this potential. The potential for surrendering heat to air by a wet surface air-cooled condenser is the temperature gradient between steam and a boundary layer of air saturated at the temperature of the water that deluges the turbular surface. This temperature is essentially constant (Kals, 1971, 1972). The condensing temperature is determined by this potential.

Before examining the dynamics of the flow of steam it seems necessary to clarify the dimensions of the various physical magnitudes and their units of measure. The first section of this paper therefore discusses the subject under the heading "Units of Measure and Their Symbols."

Units of Measure and Their Symbols

Comparison between the British and the Technical Metric systems of units is quite simple because, except for the measurement of temperature, the units are converted by numerical multipliers. Both systems use force as "basic" and compare it with the force of gravity. They are both gravitational. British units, principally used in the U.K. and in the U.S.A., can be easily derived from metric units as long as both refer either to units of weight or to units of mass. Weight and force are synonymous in the gravitational system because both refer to the force of gravity. In the gravitational system the unit of mass is derived from the basic units of force as being the amount of substance that is accelerated g $\mathrm{m \cdot s^{-2}}$ by the unit of force $g = 9.80665$ being the standardized acceleration of gravity.

In the SI system, or international system of units (Kayan, 1959; Adams, 1974; Raznjevic, 1976) the unit of mass is the basic unit. The unit of force is derived as imparting the acceleration of 1 $\mathrm{m \cdot s^{-2}}$ to the unit of mass. No matter how the mass is measured, either as a derived or a basic unit, it is still the same amount of substance, either the substance of 1 $\mathrm{dm^3}$ pure water at 4°C, or the substance of a prototype. The basic unit of mass in the SI system is called kilogram (kg). In the past the gravitational system used this name for the unit of force and the name kilopond (kp) has therefore been adopted instead. Thus, 1 kp is the basic unit of force in the gravitational system. It is identical with the weight of 1 kg mass measured in a locality where the acceleration of gravity g has the standard value.

The relation between force and mass is

$$\text{force} = \text{mass} \times \text{acceleration}$$

Therefore, the derived unit of mass in the gravitational system is the constant of proportionality between force and g, having the dimension $\mathrm{kp \cdot m^{-1} \cdot s^2}$. The derived unit of force in the SI system is called newton (N). Its dimension is $\mathrm{kg \cdot m \cdot s^{-2}}$. Other units used in the SI system are the unit of energy (work) called joule (J) and the unit of pressure called pascal (Pa). Since

$$\text{work} = \text{force} \times \text{length}$$

$$\text{pressure} = \text{force per unit area}$$

the dimension of joule is $\mathrm{N \cdot m}$ and the dimension of pascal (Pa) is $\mathrm{N \cdot m^{-2}}$. The molecular weight or molar mass M is

---

Contributed by the Power Division for publication in the JOURNAL OF ENGINEERING FOR GAS TURBINES AND POWER. Manuscript received by the Power Division September 15, 1990. Associate Technical Editor: R. W. Porter.

dimensionless. It is the sum of the atomic weights (or masses) of the atoms in the molecule and the atomic weight (mass) is determined in proportion to the mass of one of the isotopes of carbon, taken as 12.

Reference is made to Table 1, which identified other magnitudes, their symbols, and dimensions. As seen from Table 1, the dimensions of measurements as weight are converted into measurements as mass simply by multiplying the weight appearing in these dimensions by g^{-1}, the reciprocal of the acceleration of gravity. This is important because all equations that generally refer to the mass of the substance will then be dimensionally correct. The unit of force, which is used to measure p, must not also be used as the unit of mass to measure v.

The product $p \times v$ is considered as an example. It represents work (sometimes called internal energy) per unit of mass. In the gravitational system v is the volume per unit of weight $m^3 \cdot kp^{-1}$ and is introduced as $g \times v$ $m^4 \cdot kp^{-1} \cdot s^{-2}$; p is the force per unit of area $kp \cdot m^{-2}$.

The product $p \times v$ therefore has the same dimensions as w^2, namely $m^2 \cdot s^{-2}$. Representing work or internal energy per unit of mass, it can be added to $1/2 \times w^2$, which represents the kinetic energy per unit of mass. The sum of these two energies, both per unit of mass, is constant along the flow of a fluid (Bernoulli constant). In the SI system v is introduced as $m^3 \cdot kg^{-1}$ and p is introduced as $N \cdot m^{-2}$ or $kg \cdot m^{-1} \cdot s^{-2}$. The product $p \times v$ therefore has again the same dimension as w^2, namely $m^2 \cdot s^{-2}$, and can be added to $1/2 \times w^2$ of identical dimension.

The pressure is often expressed as the height of a vertical column of mercury. This is a gravitational unit because it is the weight of a column of the same vertical height per unit area of its horizontal base. The pressure of 760 mm mercury is called "standard atmosphere" or "standard barometric pressure." The pressure of 10 m water or 735.559 mm mercury is called a "technical atmosphere" equivalent to a pressure of 1 $kp \cdot cm^{-2}$ in the gravitational system.

In the SI system the bar is frequently used as a unit of pressure

$$1 \text{ bar} = 10\ N \cdot cm^{-2} = 10.10^4 \cdot N \cdot m^{-2} = 10^5 \cdot Pa = 10^2 \cdot kPa$$

Since

$$1\ N = g^{-1} \times kp = 0.101972\ kp$$

$$1 \text{ bar} = 1.01972\ kp \cdot cm^{-2} = 750 \text{ mm Hg}$$

which closely resembles the "technical atmosphere."

Velocity and Mass Flow

In its approach to each orifice of a pressure letdown station the steam accelerates from a velocity w_1 during the approach to a velocity of w_2 at the orifice exit. The steam pressure drops from p_1 in the approach to p_2 at the orifice exit while the specific volume increases from v_1 and v_2 between these two points. Neglecting the heat of friction and potential energy, the expansion from p_1, v_1, to p_2, v_2 can be assumed isentropic.

Beyond the orifice exit, the energy generated by the isentropic expansion is again converted into heat, so that the enthalpy between the approach to the orifice and beyond the orifice exit will be unchanged (Schuele, 1930).

The isentropic expansion from the approach to the orifice to the orifice exit will follow the relation

$$p_1 v_1^k = p_2 v_2^k$$

$$v_2 = \left(\frac{p_1}{p_2}\right)^{\frac{1}{k}} v_1$$

The velocity w_2 at the orifice exit and the mass flow G' through orifice exit area F will then be

$$w_2 = \left(2\,\frac{k}{k-1}\right)^{0.5} (p_1 v_1)^{0.5} \left[1 - \left(\frac{p_2}{p_1}\right)^{\frac{k-1}{k}}\right]^{0.5}$$

$$G' = F\left(2\,\frac{k}{k-1}\right)^{0.5} \left(\frac{p_1}{v_1}\right)^{0.5} \left[\left(\frac{p_2}{p_1}\right)^{\frac{2}{k}} - \left(\frac{p_2}{p_1}\right)^{\frac{k+1}{k}}\right]^{0.5}$$

For superheated steam, $k = 1.3$, the velocity w_2 and the mass flow G' will be

$$w_2 = 2.944 (p_1 v_1)^{0.5} \left[1 - \left(\frac{p_2}{p_1}\right)^{0.231}\right]^{0.5}$$

$$G' = 2.944 F \left(\frac{p_1}{v_1}\right)^{0.5} \left[\left(\frac{p_2}{p_1}\right)^{1.54} - \left(\frac{p_2}{p_1}\right)^{1.769}\right]^{0.5}$$

These equations will yield the same answers with either system of units, as long as units of the same system are used consistently and as long as all symbols refer to the mass of the substance. These equations will then be dimensionally correct. G' will be expressed as mass flow per second. In order to express it as weight flow per second, both sides of the equation must be multiplied by g.

Equation of State of Gases

The involvement with the dynamics of gases requires a brief discussion of their equation of state. This equation introduces the gas constant R as the factor of proportionality between pressure p, volume V, amount of substance G, and temperature T. It is written in the form

Nomenclature

A = surface area for transferring heat
c_p = specific heat of the cooling medium (water or air) at constant pressure
D_S = small temperature difference between steam and leaving cooling water
D_L = large temperature difference between steam and entering cooling water
D_M = mean temperature difference between steam and cooling water
f = dimensionless indicant correction factor (wet-surface air-cooled condenser)
G = hourly mass flow of the cooling medium (water or air); 1 hour = 3600 seconds
H = enthalpy of 1 kg dry air in mixture with various kilogram amounts of water vapor
H_1 = the above at the condenser inlet
H_2 = the above at the condenser outlet
H_W = the above in mixture with saturated water vapor
I = indicant
Q = heat transferred by the condenser
s_H, s_t = scales of the enthalpy and temperature coordinates, unit of length per unit of the magnitude
t_1 = water temperature at the condenser inlet
t_2 = water temperature at the condenser outlet
t_s = steam temperature
t_W = temperature of the cascading water (wet-surface air-cooled condenser)
U = overall heat transfer coefficient, steam to water

$$pV = GRT \text{ or } R = \frac{pV}{GT}$$

R represents the work done by the unit of substance with a temperature change of one degree and it depends on the nature of the gas.

Whereas the quantity of G is measured in units of weight or mass, the quantity G^* is measured in mol. The mole is defined as the amount of a pure substance that contains Avogadro's number of molecules, this number being the same for any gas. Therefore, M measures the weight or mass of 1 mole of any gas and

Table 1 Symbols and dimensions

Note: The acceleration of gravity $g = 9\ 80664\ \mathrm{m \cdot s^{-2}}$ is applied if the force is the force of gravity, also called weight.

	Metric gravitational	Metric SI
Length	m	m
Area F	$\mathrm{m^2}$	$\mathrm{m^2}$
Volume V	$\mathrm{m^3}$	$\mathrm{m^3}$
Time	s	s
Temperature T	K (°C) *	K (!C) *
Force	kp Often called kg weight, if it is the force of gravity	N; $\mathrm{kg \cdot m \cdot s^{-2}}$
Mass	$\mathrm{kp \cdot m^{-1} \cdot s^2}$	kg
Work	$\mathrm{kp \cdot m}$	J; $\mathrm{N \cdot m}$; $\mathrm{kg \cdot m^2 \cdot s^{-2}}$
Pressure (force per unit area) p	$\mathrm{kp \cdot m^{-2}}$	Pa; $\mathrm{N \cdot m^{-2}}$; $\mathrm{kg \cdot m^{-1} \cdot s^{-2}}$
Specific volume v		
Volume per unit weight	$\mathrm{m^3 \cdot kp^{-1}}$	----
Volume per unit mass	$\mathrm{g \times m^3 \cdot kp^{-1}}$ $\mathrm{m^4 \cdot kp^{-1} \cdot s^{-2}}$	$\mathrm{m^3 \cdot kg^{-1}}$
Velocity w	$\mathrm{m \cdot s^{-1}}$	$\mathrm{m \cdot s^{-1}}$
Acceleration	$\mathrm{m \cdot s^{-2}}$	$\mathrm{m \cdot s^{-2}}$
Molecular weight; molar mass M	-----	-----
Amount of molecular substance G^*		
1 mol is the substance of 1 gram molecular weight, 1 gram molar mass; mol as mass; molwt as weight		
Measured as weight	kmolwt; $\mathrm{kp \cdot M^{-1}}$	------
Measured as mass	$g^{-1} \times$ kmolwt $\mathrm{kmolwt \cdot m^{-1} \cdot s^2}$	kmol; $\mathrm{kg \cdot M^{-1}}$
Substance $G = M \times G^*$		
Measured as weight	$\mathrm{M \cdot kmolwt}$ kp Often called kg weight if by gravity	-----
Measured as mass	$g^{-1} \times$ kp $\mathrm{kp \cdot m^{-1} \cdot s^2}$	$\mathrm{M \cdot kmol}$ kg
Rate of flow $G' = G \times s^{-1}$		
Measured as weight	$\mathrm{kp \cdot s^{-1}}$ Often called $\mathrm{kg \cdot s^{-1}}$ if by gravity	------
Measured as mass	$\mathrm{kp \cdot m^{-1} \cdot s}$	$\mathrm{kg \cdot s^{-1}}$
Universal Gas Constant $R^* = p \cdot V \cdot G^{*-1} \cdot T^{-1}$		
Measured as weight	$\mathrm{m \cdot M \cdot K^{-1}}$ 847.834	-----
Measured as mass	$g \times 847.834$ $\mathrm{m^2 \cdot s^{-2} \cdot M \cdot K^{-1}}$ 8314.7	$\mathrm{J \cdot kmol^{-1} \cdot k^{-1}}$ $\mathrm{J \cdot kg^{-1} \cdot M \cdot K^{-1}}$ With $\mathrm{J = N \cdot m}$, $\mathrm{N = kg} \times g$ $\mathrm{m^2 \cdot s^{-2} M \cdot K^{-1}}$ 8314.7
Gas Constant $R = R^* \times M^{-1}$		
Measured as weight	$\mathrm{m \cdot K^{-1}}$	-----
Measured as mass	$g \times \mathrm{m \cdot K^{-1}}$ $\mathrm{m^2 \cdot s^{-2} \cdot K^{-1}}$	$\mathrm{m^2 \cdot s^{-2} \cdot K^{-1}}$

* °C = 273.15 K; 100°C = 373.15 K

$$G^* = \frac{G}{M}$$

measures the amount (weight or mass) of any gas as the number of mol. With $G = G^* \times M$

$$R = \frac{pV}{G^*MT}; \quad MR = \frac{pV}{G^*T}$$

By definition

$$R^* = MR = \frac{pV}{G^*T}$$

is called the Universal Gas Constant. It is the same for any substance if the amount of substance is measured in mol. For $G^* = 1$ mol of any substance

$$R^* = \frac{pV^*}{T}$$

V^* is then the molal volume at a certain pressure and temperature. For one kmol of oxygen having a molecular weight (molecule mass) of 32, R^* was measured to be

$$8{,}314.448 \text{ kJ} \cdot \text{kmol}^{-1} \cdot T^{-1}$$

in metric SI units, the force being measured in N; or

$$847.834 \text{ kp} \cdot \text{m} \cdot \text{kmol}^{-1} \cdot T^{-1}$$

in metric gravitational units, the force being measured in kp. Since 1 kp $= g \times$ N

$$847.834 \times g = 8{,}314.448$$

Critical Pressure Ratio

The ratio of pressures at the exit and before entering an orifice that results in the maximum rate of flow through that orifice is called the "critical pressure ratio."

If the pressure p_1 at the approach to the orifice remains constant, the mass flow can increase to a maximum as the pressure p_2 at the orifice exit drops to a minimum, but will remain at maximum if the pressure p_3 beyond the orifice drops further. This minimum pressure at the orifice exit at which the mass flow is at its maximum is determined by the critical pressure ratio

$$\frac{p_2}{p_1} = \left(\frac{2}{k+1}\right)^{\frac{k}{k-1}}$$

With $k = 1.3$ for superheated steam this critical pressure ratio is

$$\frac{p_2}{p_1} = 0.546$$

This means that the minimum pressure at the orifice exit will be 0.546 times the inlet pressure. The mass of steam flowing through the orifice will be at a maximum and will have a maximum velocity, namely the sonic velocity of

$$w_s = (kRT)^{0.5}$$

R will be measured as mass (see Table 1).

In metric SI units, with $k = 1.3$ and $R = 8314.4/18$ for superheated steam

$$w_s = 24.5T^{0.5}$$

measured in $\text{m} \cdot \text{s}^{-1}$.

The maximum mass flow at sonic velocity through the flow area F at the nozzle exit is calculated from

$$G'_{\text{MAX}} = F\left(\frac{2}{k+1}\right)^{\frac{1}{k-1}} \left(\frac{p_1}{v_1}\right)^{0.5} \left(\frac{2k}{k+1}\right)^{0.5}$$

With $k = 1.3$ for superheated steam

$$G'_{\text{MAX}} = 0.667\, F\left(\frac{p_1}{v_1}\right)^{0.5}.$$

Again, these equations will yield the same answers with either system of units, as long as units of the same system are used consistently and as long as all symbols refer to the mass of the substance. These equations will then be dimensionally correct.

If the pressure p_3 at which the orifice discharges the steam is less than the critical pressure p_2 at the orifice exit, the steam will expand after leaving the orifice, but the sonic velocity at the orifice exit, and therefore the maximum mass flow through the orifice, will remain unchanged. The velocity will not increase further.

This consideration applies to orifices used for the pressure breakdown of the bypass steam. It does not apply to converging–diverging nozzles first introduced for DeLaval Steam Turbines. The velocity in the narrowest portion or throat of these nozzles cannot be supersonic and the energy potential for producing the velocity is still limited by the critical ratio of pressures in the throat and at the approach to the orifice. However, the gradually diverging portion permits a further expansion of the steam to a supersonic exit velocity with a corresponding energy gain. This exit velocity depends on the ratio of the flow areas at the nozzle exit and in the nozzle's throat. This ratio can be such that the steam will expand to any desired final pressure as long as the divergence is sufficiently long and gradual (Schuele, 1930).

The Pressure Letdown Station

Reducing the steam pressure from the pressure at the throttle to the vacuum at the condenser is performed in several successive stages. The reduction at each stage is governed by the critical pressure ratio. The initial reduction of the throttle pressure can be performed by a pressure control valve with an integral temperature-controlled injection of water. The pressure at the outlet of the valve is controlled by the position of the valve plug. The movement of the valve stem opens successively a number of calibrated orifices through which water is admitted to desuperheat the steam. Control of the flow of water supplied to these orifices establishes the temperature of the steam at the reduced pressure usually at a superheat of not less than 8°C. The valve plug can be of the perforated cage type and one or two additional diffuser plates can be used for further pressure reduction. Each stage of reduction is designed to be above critical pressure ratio of 0.546.

An arrangement showing a further reduction of the steam pressure by a sequence of performated pipes and plates called "breakdown diffuser" is shown in Fig. 1. According to recommendations by the Electric Power Research Institute (Electric Power Research Institute, 1982) the steam entering the condenser should have an enthalpy below 2800 kJ per kg and a temperature below 150°C. This is accomplished by a direct spray type desuperheater at the location where the final pressure reduction has been completed. Water and steam will mix at a constant pressure (Kueffer, 1991; VanBlarcom, 1921). For a complete evaporation of the injected water it is recommended to control the water supply so that a 28°C superheat is established. The desuperheater shown in Fig. 1 progressively uncovers a series of water inlet orifices in response to the valve actuator as the temperature transmitter calls for more desuperheating water.

Installations using separate high-pressure and low-pressure turbines employ a separate bypass control valve with integral spray water injection for each turbine. This arrangement provides great flexibility for a variety of operating conditions. Details are disclosed by the references cited at the beginning of this paper. The high-pressure bypass control also cools the

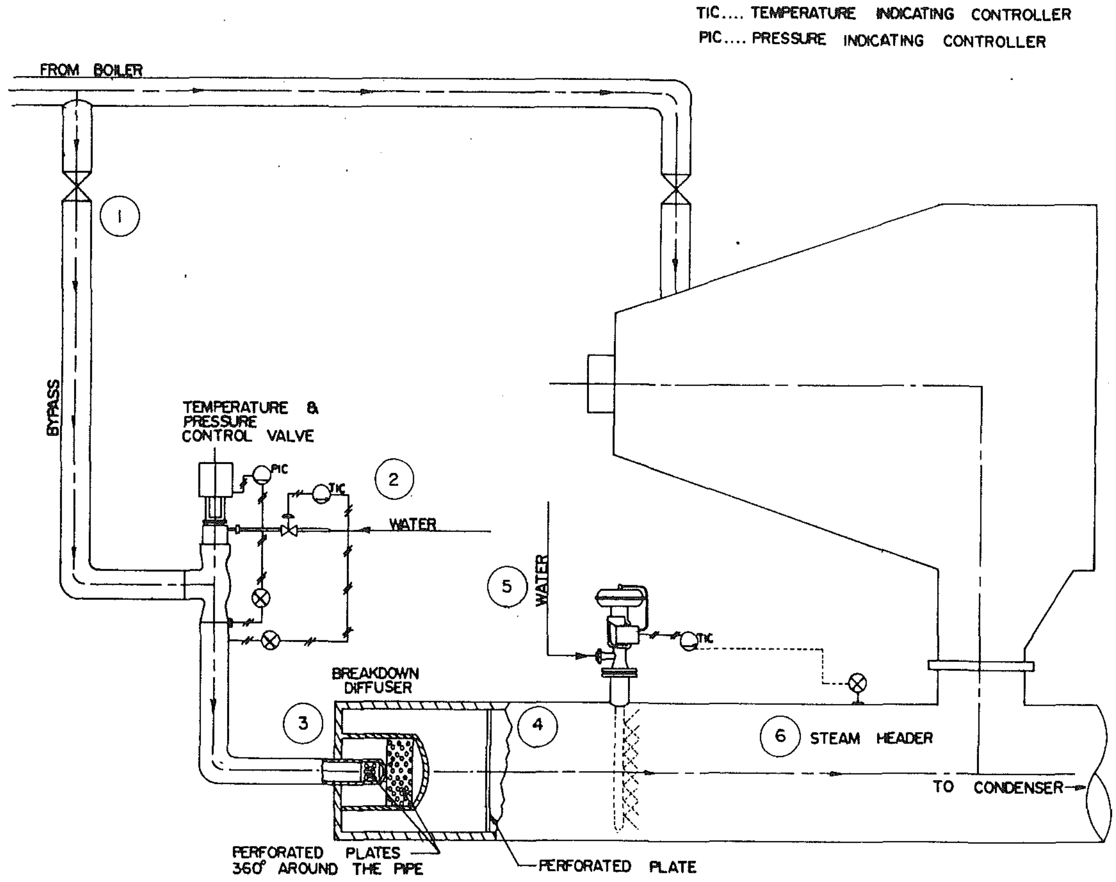

Fig. 1 Steam turbine bypass (schematic)

Table 2 Conditions of steam and water at six locations

	Locations (see Fig. 1)					
	1	2	3	4	5	6
Medium	Steam	Water	Steam	Steam	Water	Steam
Mass flow, kg/h	127,500	29,016	156,516	156,516	9562	166,078
Pressure, bar	64	39	11.4	0.165	17	0.165
Temperature, °C	487.8	56	193	160	56	84
Superheat, °C	208	-	7.4	104	-	28
Enthalpy, kJ/kg	3,390	234.4	2805	2805	234.4	2657

reheater between the two turbines. The low-pressure bypass usually has two stages of pressure and temperature reduction. The provision of an auxiliary bypass from the high-pressure turbine into the condenser would be independent from the exhaust of the low-pressure bypass into the condenser. The cited references analyze the economy of less than 100 percent bypass applicable to large power-generating stations.

Dispersion of the Dumped Steam

The "breakdown diffuser" shown in Fig. 1 in accordance with recommendations by the Electric Power Research Institute (EPRI, 1982) can be located at the neck of a water-cooled condenser, either outside or inside, as long as sufficient internal space is provided to prevent damage to the condenser tubes by a high steam velocity or by impingement of entrained water drops. The steam temperature and pressure should be well equalized inside the exhaust hood of the turbine. For this type of installation it would hardly be possible to use a spray type desuperheater after the final pressure reduction as shown in Fig. 1. However, a temperature of 160°C with an enthalpy of 2805 kJ per kg can probably be tolerated if the various recommendations have been followed. Otherwise, a device is available that expands the superheated steam with a nozzle and at the same time cools it by introducing spray water around the circumference of the spray nozzle. This device seems to assure complete mixing of steam and water. It is attached to a multihole pipe mounted inside the condenser neck.

No such problems exist when using the arrangement of Fig. 1 in connection with a wet surface air-cooled condenser because the breakdown diffuser can be suitably distanced from the exhaust hood of the turbine and from the condenser tubes. The vapor duct to the wet surface air-cooled condenser is simply sized for the mass flow of the dumped steam.

Thermal Duty of the Condenser

For a specific condition the total mass of bypass steam is calculated by a numerical example. As will be seen, the mass of steam that would have passed through the turbine is increased by the mass of water which is added to the steam to desuperheat it. An increase of the condensing pressure from 0.1 bar to about 0.17 bar was found by a preliminary scan and condensate at a temperature of 56°C is therefore used for desuperheating.

The amount of water required to desuperheat the steam is calculated by a simple heat balance (Bowie, 1985). As an example, the conditions of steam and water at the locations

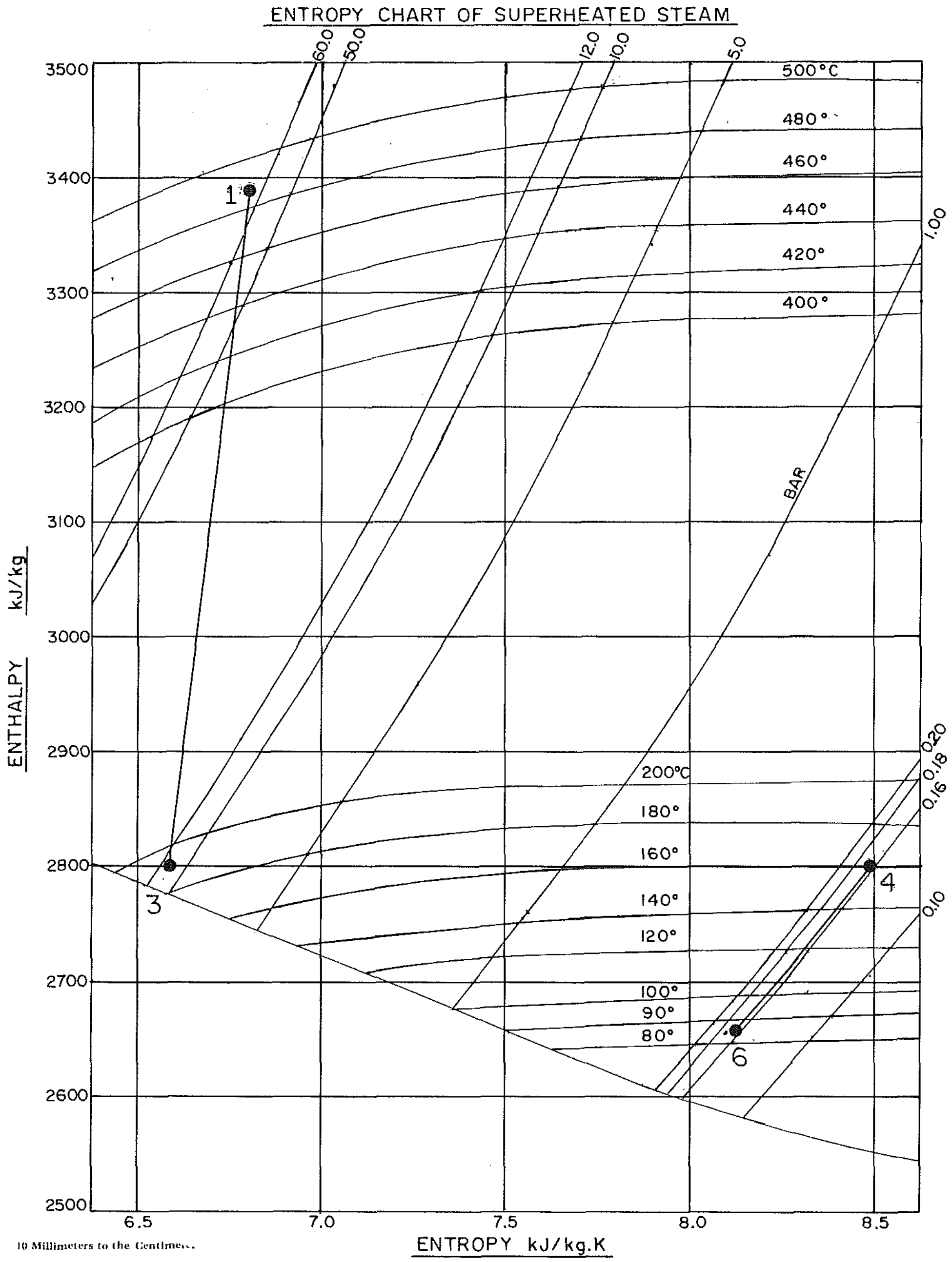

Fig. 2 Conditions of the bypassed steam before entering the condenser (entropy chart)

enumerated 1 to 6 on Fig. 1 are listed in Table 2. The conditions of steam at the locations 1, 3, 4, and 6 are marked on the entropy chart, Fig. 2. The flow rates per hour imply that 1 h = 3600 s. For this example the design throttle flow is 127,500 $\mathrm{kg \cdot h^{-1}}$. Its heat loss when passing from location 1 to location 3 is

$$127{,}500\ \mathrm{kg \cdot h^{-1}} \times (3390-2805)\ \mathrm{kJ \cdot kg^{-1}} = 74{,}587{,}500\ \mathrm{kJ \cdot h^{-1}}$$

An equal amount of heat gained by the water passing from location 2 to location 3 is

$$W_1\ \mathrm{kg \cdot h^{-1}}\ \text{water} \times (2805-234.4)\ \mathrm{kJ \cdot kg^{-1}} = 74{,}587{,}500\ \mathrm{kJ \cdot h^{-1}}$$

Therefore

$$W_1 = \text{approximately } 29{,}016\ \mathrm{kg \cdot h^{-1}}$$

The initial mass flow of steam being 127,500 $\mathrm{kg \cdot h^{-1}}$, it has now increased to

$$(127{,}500+29{,}016) = 156{,}516\ \mathrm{kg \cdot h^{-1}}$$

The heat lost by the steam when passing from location 3 to location 6 is

$$156{,}516\ \mathrm{kg \cdot h^{-1}} \times (2805-2657)\ \mathrm{kJ \cdot h^{-1}} = 23{,}164{,}368\ \mathrm{kJ \cdot h^{-1}}$$

An equal amount of heat gained by the water passing from location 5 to lcoation 6 is

$$W_2\ \mathrm{kg \cdot h^{-1}}\ \text{water} \times (2657-234.4)\ \mathrm{kJ \cdot kg^{-1}} = 23{,}164{,}368\ \mathrm{kJ \cdot h^{-1}}$$

Therefore,

$$W_2 = \text{approximately } 9562\ \mathrm{kg \cdot h^{-1}}$$

The mass flow of bypass steam to the condenser has now increased to

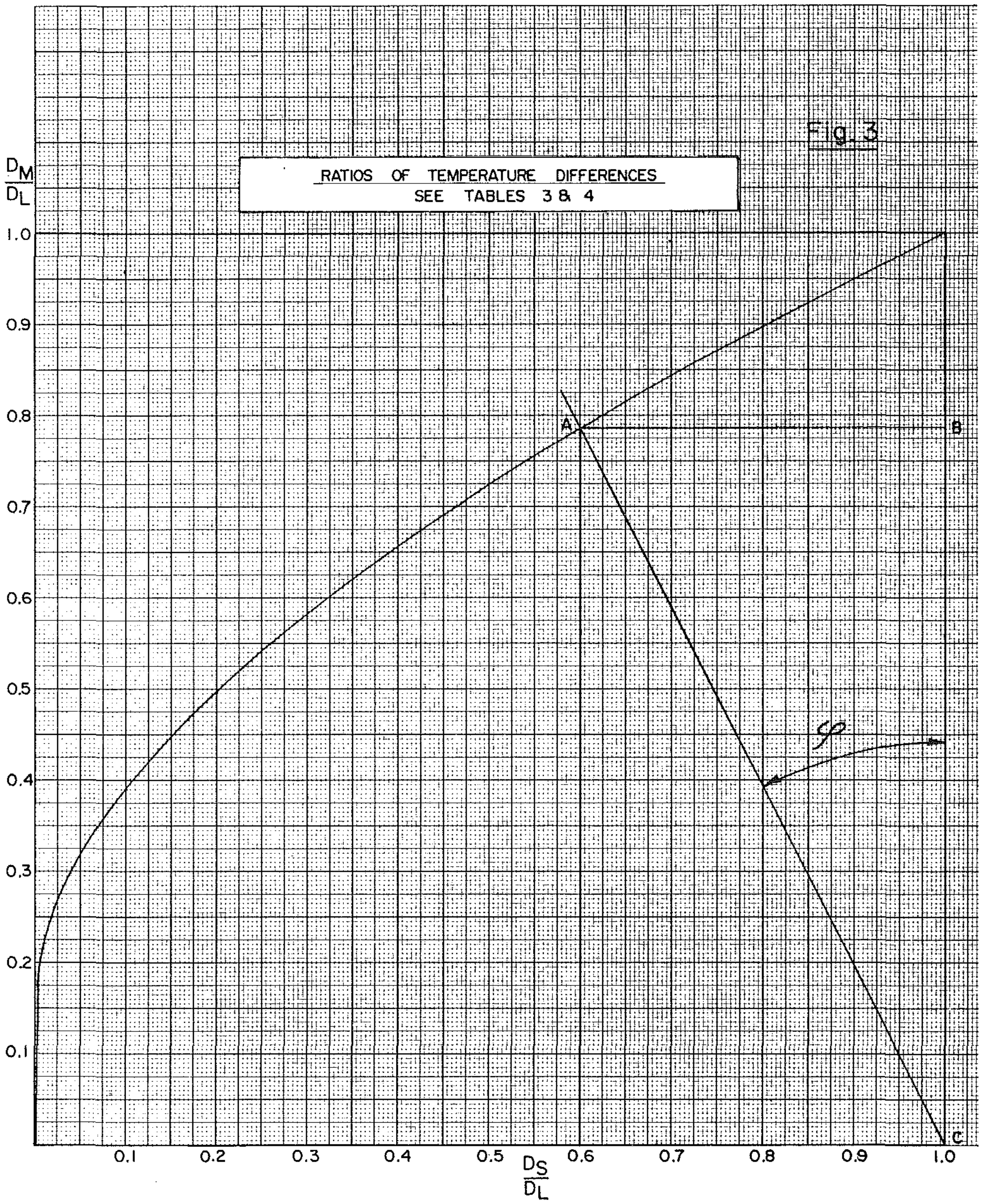

Fig. 3 Water-cooled steam condenser: ratios of temperature differences

$$156{,}516+9562=166{,}078\ \mathrm{kg\cdot h^{-2}}$$

If the condenser was designed to condense 127,500 $\mathrm{kg\cdot h^{-1}}$ steam exhausted by the turbine at 0.1 bar pressure and 90 percent quality, it will be shown that the dumped bypass steam of 166,078 $\mathrm{kg\cdot h^{-1}}$ will be condensed at about 0.16 to 0.18 bar under equal conditions.

For the design condition of 0.1 bar condensing pressure the condensing temperature is approximately 46°C and the enthalpy of the entering steam was assumed to be 2345 $\mathrm{kJ\cdot kg^{-1}}$ corresponding to a 90 percent steam quality. The enthalpy of the condensate being 191.9 $\mathrm{kJ\cdot kg^{-1}}$, the heat to be transferred for condensening 127,500 $\mathrm{kJ\cdot h^{-1}}$ steam is therefore figured as

$$Q=127{,}500\ \mathrm{kg\cdot h^{-1}}\times(2{,}345-191.9)$$
$$=274{,}520{,}000\ \mathrm{kJ\cdot h^{-1}}\text{ or }76{,}256\ \mathrm{kW}$$

Assuming that the bypassed steam of 166,078 $\mathrm{kg\cdot h^{-1}}$ can be condensed at 0.165 bar, 56°C, the enthalpy of the steam and condensate are 2602 and 234.4 $\mathrm{kJ\cdot kg^{-1}}$, respectively. The heat to be transferred is

$$Q'=166{,}078\ \mathrm{kg\cdot h^{-1}}\times(2602-234.4)$$
$$=393{,}206{,}000\ \mathrm{kJ\cdot h^{-1}}\text{ or }109{,}224\ \mathrm{kW}$$

This represents an increase of about 43.2 percent.

The preceding numerical example gives no consideration to the usual practice of extracting steam from the turbine for feedwater heating (about 6 percent at 0.55 bar) and for deaeration (about 3.8 percent at 2 bar). This extracted steam, available at the turbine throttle, would also have to be bypassed if the turbine is inoperative. However, the example is still valid if the steam is generated by a boiler that recovers heat from the exhaust of a gas turbine. These heat recovery boilers cool the exhaust gas in stages, first by superheating the subsequently generated high-pressure steam, then by generating intermediate pressure steam for the deaerator, and finally by heating the feedwater in an economizer section. Thus, no steam will be extracted from the turbine.

Considering about 9.8 percent steam extraction from the turbine, while still assuming that 127,500 $\mathrm{kg\cdot h^{-1}}$ would be exhausted to the condenser, the mass of steam to be bypassed

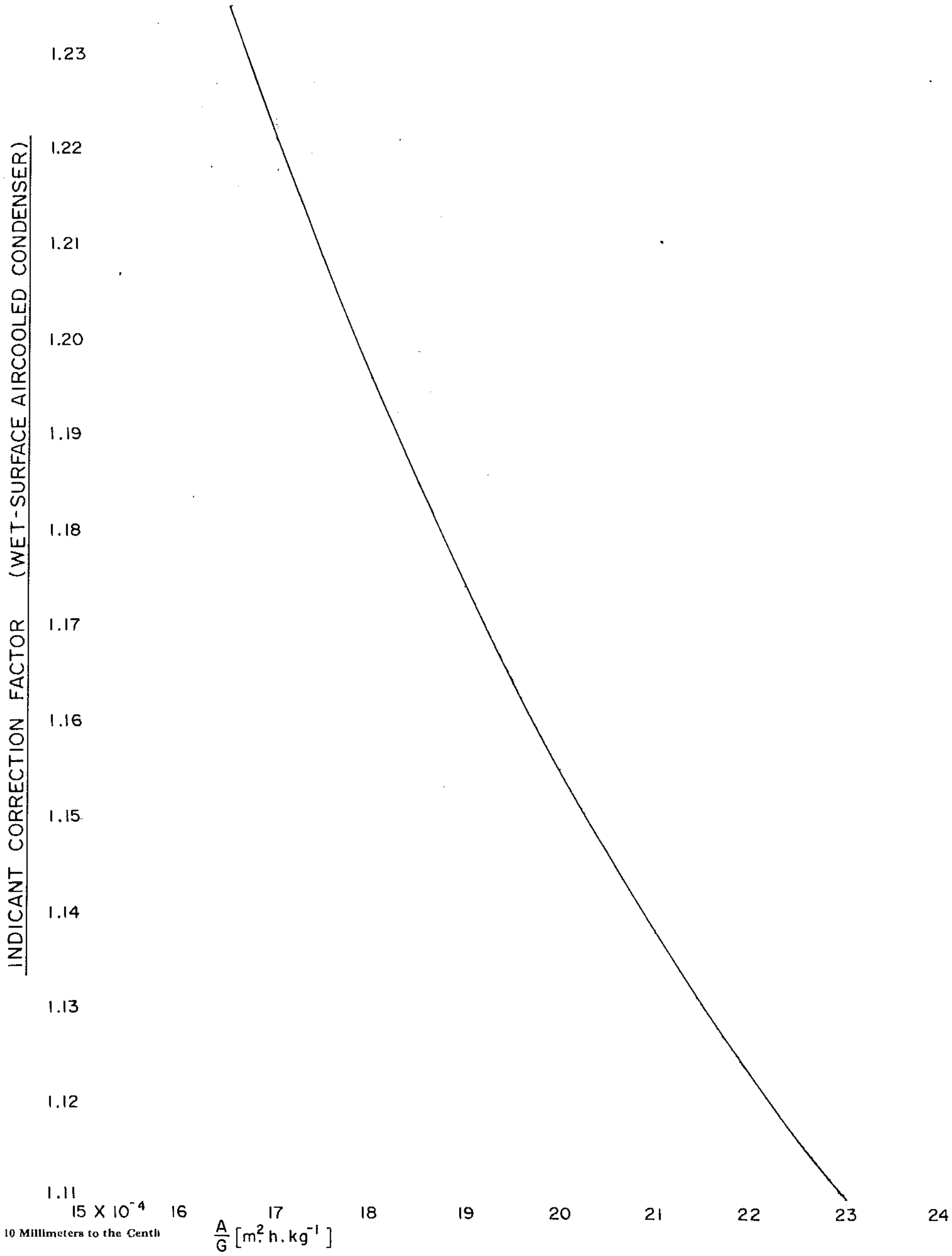

Fig. 4 Wet-surface air-cooled condenser: indicant correction factor

would be 140,000 $kg \cdot h^{-1}$. Retaining the steam conditions at the locations numbered in Figs. 1 and 2 and Table 1, the heat lost by the throttle steam when passing from "1" to "3," the corresponding mass of water W_1 to be injected, the subsequent increase of the flow of steam, the heat that the increased steam flow will lose when passing from "3" to "6," the mass of water W_2 to be injected, and the mass of steam to be eventually bypassed will all be 9.8 percent higher than the figures of the example, which gives no consideration to steam extraction. Therefore, the heat to be transferred by the condenser during the bypass event would also be 9.8 percent higher, or

$$Q' = 109{,}224 \times 1.098$$
$$= 119{,}928 \text{ kW, presumably at 2602 and 234.4 } kJ \cdot kg^{-1}$$

entering and leaving enthalpies, these values to be corrected after having determined the reaction of the heat transfer mechanism. This represents a 57 percent increase of the thermal load for which the condenser was designed.

The Mechanism of Heat Transfer

An analysis of the increase in condensing pressure due to an increase in steam flow reveals striking similarities between water-cooled and wet surface air-cooled condensers. These similarities are demonstrated by Table 3 and the related charts on Figs. 3, 4, and 5. The letter symbols are explained in the Nomenclature.

The equations used for the water-cooled condenser are elementary. Verification of those used for the wet surface air-cooled condenser is given by the referenced literature (Lewis, 1922; Merkel, 1927; Goodman, 1936, 1938; Kals, 1971, 1972). The indicant, which is introduced for both types of heat transfer mechanism, has the design parameters A, G, and U of both types of condenser in identical algebraic relationship. In the case of the water-cooled condenser, it includes the specific heat of the cooling medium (c_p of water = 4.19 $kJ \cdot kg^{-1} \cdot K^{-1}$) and is therefore dimensionless. In the case of the wet surface air-

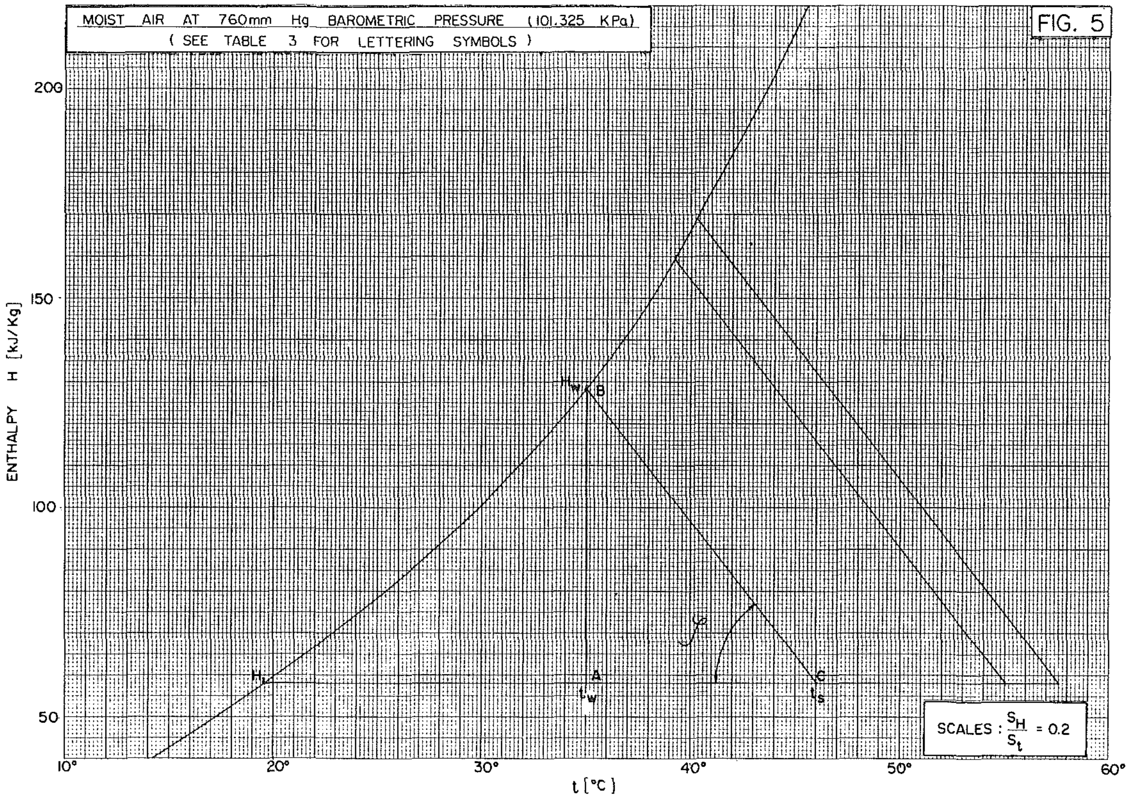

Fig. 5 Wet-surface air-cooled condenser: reaction to the dumped bypass steam

cooled condenser, the indicant includes a dimensionless correction factor f (Fig. 4), which is determined by tests of a specific mechanism, and its dimension is given in Table 3.

The reaction of each of these two types of condenser to a 43.2 percent and a 57 percent increase of the thermal load is illustrated by the following example.

(A) Water-Cooled Condenser

Design Data:

Atmospheric wet bulb temperature 20°C
$Q = 76{,}256\ \text{kW} = 274{,}521{,}600\ \text{kJ}\cdot\text{h}^{-1}$
$G = 8{,}193{,}000\ \text{kg}\cdot\text{h}^{-1}$
$c_p = 4.19\ \text{kJ}\cdot\text{kg}^{-1}\cdot\text{K}^{-1}$ (water)
$t_1 = 26°\text{C}$
$t_s = 46°\text{C}$ (0.1 bar)
$U = 3\ \text{kW}\cdot\text{m}^{-2}\cdot\text{K}^{-1}$or $(3 \times 3600)\ \text{kJ}\cdot\text{h}^{-1}\cdot\text{m}^{-2}\cdot\text{K}^{-1}$
$t_2 - t_1 = Q/c_pG = 8°\text{C}$
$t_2 = 26 + 8 = 34°\text{C}$
$D_L = 46 - 26 = 20°\text{C}$
$D_S = 46 - 34 = 12°\text{C}$
$D_M = 15.66°\text{C}$
$A = Q/UD_M = 1623\ \text{m}^2$
$A/G = 1.98 \times 10^{-4}\ \text{m}^2\cdot\text{kg}^{-1}\cdot\text{h}$
$I = 0.51$
$\varphi = 27$ deg
Fig. 3: $D_M/D_L = 0.783$; $D_S/D_L = 0.6$

Thermal Load Increased by 43.2 Percent
$D_M' = 15.66 \times 1.432 = 22.43$
$D_L' = D_M'/0.783 = 28.64°\text{C}$
$t_s' = t_1 + D_L' = 26 + 28.64$
$= 54.64°\text{C}$ (approximately 0.155 bar)

Thermal Load Increased by 57 Percent
$D_M' = 15.66 \times 1.57 = 24.59°\text{C}$
$D_L' = D_M'/0.783 = 31.40°\text{C}$
$t_s = t_1 + D_L' = 26 + 31.4 = 57.4°\text{C}$ (approximately 0.178 bar)

(B) Wet-Surface Aircooled Condenser

Design Data

Atmospheric wet bulb temperature 20°C
$Q = 76{,}250\ \text{kW} = 274{,}521{,}600\ \text{kJ}\cdot\text{h}^{-1}$
$H_1 = 57.555\ \text{kJ}\cdot\text{kg}^{-1}$
$t_s = 46°\text{C}$ (approximately 0.1 bar)
$U = 0.852\ \text{kW}\cdot\text{m}^{-2}\cdot\text{K}^{-1}$or $(0.852 \times 3600)\ \text{kg}\cdot\text{h}^{-1}\cdot\text{m}^{-2}\cdot\text{K}^{-1}$
$A/G = 0.00184\ \text{m}^2\cdot\text{kg}^{-1}\cdot\text{h}$
$f = 1.187$ (from Fig. 4)
$I = 6.7\ \text{kJ}\cdot\text{kg}^{-1}\cdot\text{K}^{-1}$
$\tan\varphi = s_H/s_t \times 6.7 = 0.2 \times 6.7 = 1.34$ (Fig. 5)
$\varphi = 53.5$ deg
Fig. 5: $t_w = 35°\text{C}$, $t_s - t_w = 11°\text{C}$
$A = Q/U(t_s - t_w) = 8.137\ \text{m}^2$
$G = 8{,}137/0.00184 = 4{,}422{,}283\ \text{kg}\cdot\text{h}^{-1}$

Thermal Load Increased by 43.2 Percent
$(t_s' - t_w') = 1.432 \times 11 = 15.75°\text{C}$
Fig. 5: $t_s' = 55.0°\text{C}$ (0.157 bar); $t_w' = 39.2°\text{C}$ (t_s is raised at constant φ until the above temperature difference is reached)

Thermal Load Increased by 57 Percent
$(t_s' - t_w') = 1.57 \times 11 = 17.27°\text{C}$
Fig. 5: $t_s' = 57.6°\text{C}$ (0.178 bar); $t_w' = 40.3°\text{C}$ (t_s is raised at constant φ until the above temperature difference is reached)

As can be seen from these examples, the water-cooled and wet surface air-cooled condensers will react in an almost identical manner to the increased thermal load during a bypass event. Introducing the bypassed steam into the neck of a water-cooled condenser will require various precautions, whereas the steam header or vapor duct leading from the turbine to a wet surface

Table 3 See Nomenclature for letter symbols

Water-cooled condenser G kg/h cooling water	Wet-surface air-cooled condenser G kg/h coolant air
$D_M=\dfrac{D_L-D_S}{\ln\dfrac{D_L}{D_S}}$	With t_s = const it can be assumed with good approximation that t_W = const and therefore H_W=const. The transfer of heat from the cascading water to the air will then be
$\dfrac{D_M}{D_L}=\dfrac{1-\dfrac{D_S}{D_L}}{\ln\dfrac{D_L}{D_S}}$ (see Fig. 3)	$Q=\dfrac{G}{f}(H_W-H_1)$ (Fig. 4)
$Q=AUD_M$ $Q=c_p(D_L-D_S)$	An equal amount of heat is transferred in a steady state from the condensing steam to the cascading water, namely $Q=AU(t_s-t_w)$
$\dfrac{D_L-D_S}{D_M}=\dfrac{AU}{Gc_p}$	By equating these two expressions, the indicant is $I=f\dfrac{AU}{G}=\dfrac{H_W-H_1}{t_s-t_W}$ (Fig. 4)
$\dfrac{1-\dfrac{D_S}{D_L}}{\dfrac{D_M}{D_L}}=\dfrac{AU}{Gc_p}$	The correction factor f being dimensionless, I has the same dimension as the specific heat, namely $\mathrm{kJ\cdot kg^{-1}\cdot K^{-1}}$
Triangle ABC on Fig. 3	Triangle ABC on Fig. 5
Side $\overline{AB}$: $1-\dfrac{D_S}{D_L}$	Side $\overline{AB}$: $(H_W-H_1)s_H$
Side $\overline{BC}$: $\dfrac{D_M}{D_L}$	Side $\overline{BC}$: $(t_s-t_W)s_t$
$\tan\varphi=\dfrac{\overline{AB}}{\overline{BC}}=\dfrac{AU}{Gc_p}=I$	$\tan\varphi=\dfrac{\overline{AB}}{\overline{AC}}=f\dfrac{AU}{G}\dfrac{s_H}{s_t}=I\dfrac{s_H}{s_t}$
The indicant I is dimensionless. It remains unchanged, regardless of operating conditions (U assumed to remain constant). Different performances can be analyzed by changing the design parameters A and G.	The indicant I has the dimension shown above. It remains unchanged regardless of operating condition (U assumed to remain unchanged). Different performances can be analyzed by changing the design parameters A and G.

air-cooled condenser provides a convenient location for dumping the bypassed steam.

Comparison of Water-Cooled and Wet Surface Air-Cooled Condensers

These two types of heat transfer mechanism are evaluated as viable alternatives because they are both applicable to the small and medium size power plants that are being built in ever-increasing numbers. Independent power producers are attracted by a shortfall of the capacity available from the regulated utilities and by the possibilities offered by gas turbines and by combined power cycles, which recover the heat loss of gas turbines as the energy source of steam turbines. Plants of this kind will often benefit from wet surface air-cooled steam turbine condensers.

By comparison wet surface air-cooled condensers require a lower capital investment. They can use 2 in. o.d. carbon steel tubes hot dip galvanized on the outside for the heat transfer surface, whereas water-cooled condensers served by a cooling tower circuit must use tubes of a copper-nickel alloy or of stainless steel. The much larger surface area required by the wet surface air-cooled condenser to transfer an equal amount of heat is therefore still less costly.

Wet surface air-cooled condensers are usually more energy efficient because they can consistently produce a higher vacuum and will require less parasitic energy. Experience has also shown that they require less maintenance. The vulnerability to fouling of the external tube surface is a lesser problem than fouling of the internal tube surface in contact with water of a water cooled condenser. Water utilities (cooling tower, pumping station, and piping) are avoided.

On the other hand, water-cooled steam turbine condensers have fewer physical limitations and will therefore remain the choice for the large power plants of the public utilities with capacities of more than 1000 MW.

References

Adams, H. F. R., 1974, *SI Metric Units, An Introduction*, McGraw-Hill Ryerson Ltd., Toronto, Canada.

Bowie, G. E., 1985, "Specifying and Operating Desuperheaters," *Chemical Engineering*, May 27, pp. 119–124.

Electric Power Research Institute, 1982, "Recommended Guidelines for the Admission of High Energy Fluids to Steam Surface Condensers," CS-2251, Research Project 1689-1, Palo Alto, CA.

Gardner, D. E. A., 1984, "How to Apply Existing Bypass Technology to Drum Boilers," *Power*, July, pp. 95–98.

Goodman, W., 1936, "Dehumidification of Air With Coils," *Refrigerating Engineering*, Oct., pp. 225–274.

Goodman, W., 1938, "The Evaporative Condenser," *Heating, Piping and Air Conditioning*, Mar., pp. 165–168; Apr., pp. 255–258; May, pp. 324–328.

Kals, W., 1971, "Wet-Surface Aircoolers," *Chemical Engineering*, July, pp. 90–94.

Kals, W., 1972, "Wet-Surface Aircoolers: Characteristics and Usefulness, ASME Paper No. 72-HT-28.

Kayan, C. F., 1959, "Systems of Units, National and International Aspects," American Association for the Advancement of Science, Publication #57.

Kueffer, M., 1990, "Exploit Turbine Bypass Systems for Improvement in Operation," *Power*, Oct., pp. 71–74.

Kueffer, M., 1991, "Make Use of Today's Technology in Taming Steam/Water Mixtures," *Power*, May, pp. 41–45.

Lewis, W. K., 1922, "The Evaporation of a Liquid Into a Gas," *Transactions of the ASME*, Vol. 4, pp. 325–340; correction published in *Mechanical Engineering*, Sept. 1933, p. 567.

Martin, P., and Holly, L., 1973, "Bypass Stations for Better Coordination Between Steam Turbine and Steam Generator Operation," American Power Conference, 35th Annual Meeting, May, Chicago, IL, pp. 1–18.

Merkel, F., 1927, "Der Berieselungsverfluessiger," *Zeitschrift fuer die gesamte Kaelteindustrie*, Feb., pp. 21–28; Mar., pp. 47–55.

Raznjevic, K., 1976, *Handbook of Thermodynamic Tables and Charts*, Hemisphere Publishing Gorporation, Washington, DC.

Reason, J., 1984, "Steam Bypass Systems for Drum Boilers and Turbines, How Much Capacity Do You Need?" *Power*, July, pp. 73–79.

Schuele, W., 1930, *Technische Thermodynamik*, Julius Springer, Berlin.

Van Blarcom, P. P., 1921, "Using Desuperheaters for Steam Temperature Control," *Plant Engineering*, Sept.

Effect of Drift Eliminator Design on Cooling Tower Performance

B. R. Becker
Assistant Professor of Mechanical
and Aerospace Engineering,
University of Missouri—Kansas City,
Independence, MO 64050-1799

L. F. Burdick
Project Engineer,
Marley Cooling Tower Company,
Mission, KS 66201

In the use of wet cooling towers, drift refers to small droplets of circulating water that are carried out of the cooling tower by the saturated exhaust air. Inertial impaction separators, known as drift eliminators, are used to strip the water droplets from the exhaust air. To achieve peak cooling tower operating efficiency, it is desirable that losses in fan system performance due to the drift eliminators be minimized. Therefore, an experimental program was developed and executed to evaluate the effect of drift eliminator design on cooling tower fan system performance. Flow visualization studies were used to gain insight into the flow patterns within the cooling tower plenum as influenced by drift eliminator design. A fully instrumented fan test cell was used to investigate the effects upon fan system performance resulting from two different styles of drift eliminators. The effect of drift eliminator discharge angle upon fan system total efficiency was investigated and the optimal discharge angle determined.

1 Introduction

In the use of wet cooling towers for waste heat rejection, drift refers to the small droplets of circulating water that are carried out of the cooling tower by the saturated exhaust air. These drift droplets contain corrosion control chemicals and other solids, which precipitate and damage the environment. Thus, inertial impaction separators, known as drift eliminators, are used to strip the water droplets from the warm air for the purposes of pollution reduction, water preservation, and conservation of corrosion and algae control chemicals. In this type of separator, the two-phase exhaust flow is forced to change direction abruptly, causing the dense drift droplets to impact the eliminator walls and become trapped inside the cooling tower.

Drift eliminators have evolved from the early single-pass wood lathe, to multiple pass wood, and then to sinusoidal wave. These were followed by combinations of sinusoidal and honeycomb shapes such as used on the Chalk Point cooling tower and reported by Holmberg (1974). Currently, various styles of cellular drift eliminator packs are constructed from thermoformed sheets of polyvinylchloride.

The performance of these various styles of drift eliminator pack is measured by two criteria: droplet collection efficiency and system pressure loss due to the eliminator pack. High droplet collection efficiency is desirable for all the reasons stated above. However, to achieve peak operating efficiency of the overall cooling tower system, it is desirable that the system pressure loss due to the eliminators be minimized. As an example of the importance of efficient air handling, consider a typical cooling tower operating in an ambient wet bulb of 80°F with a 12,750 gallon per minute water loading of 108°F hot water, which is to be cooled to 88°F. A typical cooling tower operating at these conditions might require 150 brake hp to operate the fan. With these conditions as input to a thermal design computer program (Marley, 1968), it can be calculated that a 2 percent decrease in air flow rate would increase the cold water temperature about 0.3°F. If the fan blade pitch was increased to maintain the original air flow rate, the power requirements of the fan would increase approximately 8 percent to 162 hp. Thus, drift eliminator design can impact the operating efficiency of the overall cooling tower system. Also, if a power plant or other type of process plant is operating at the maximum horsepower of its cooling tower fan motors, then inefficient air handling through the drift eliminators would result in unattainable fan horsepower requirements. This would reduce the capacity of the cooling tower system, thereby limiting the production capability of the entire plant.

In spite of this significant impact upon cooling tower efficiency, drift eliminator design has received limited attention in the literature. Chilton (1952) constructed an apparatus to test different counterflow fill and eliminator schemes for resistance to air flow and effectiveness of drift elimination. Flow resistance measurements were taken at three nominal air velocities for each eliminator scheme. Drift carryover was determined by measuring the amount of water collected by a scrubber during a known time period. Chilton concluded that redwood louver type eliminators could be oriented to be effective at stripping air borne water and produce low airflow resistances as well as being the most practical and economical choice.

Chan and Golay (1976) developed a numerical model to calculate the collection efficiency for various droplet sizes using different eliminator geometries. Their experimental work (Chan and Golay, 1977) was conducted in a test chamber having counterflow orientation and used water laden air as the working fluid. They compared the results of their numerical model

---

Contributed by the Power Division for publication in the JOURNAL OF ENGINEERING FOR GAS TURBINES AND POWER. Manuscript received by the Power Division April 22, 1991. Associate Technical Editor: R. W. Porter.

to these laboratory tests. A laser light scattering technique was utilized to obtain the size distribution of the drift droplets that passed through the eliminator section. Pressure drop between the inlet and outlet of the eliminator test section was measured via electronic manometer. Calculations and experimental results were not in agreement due to wake turbulence and recirculation in the more complicated eliminator shapes. However, they did have close correlation for more elementary shapes.

Yao and Schrock (1976) devised a numerical technique for optimizing the aerodynamic design of counterflow drift eliminators. The best design was chosen to be the one of minimum cost, which produced acceptable collection efficiency and pressure drop. However, their computer model lacked the ability to account for flow separation within the eliminator pack.

Thus, due to the lack of available information on drift eliminator design, the project reported in this paper was initiated. This project focuses upon the problem of identifying and minimizing the pressure loss through crossflow cooling tower plenums because of variations in drift eliminator design. In the crossflow cooling tower configuration, ambient air enters through the louver face and travels horizontally through the fill media. Meanwhile, hot water is falling vertically through the fill media, thus providing the crossflow pattern. After the water droplet laden air exits the fill packing, it traverses the drift eliminators, which are positioned approximately perpendicular to the air flow direction. The air then passes through a plenum, turns, and exits vertically through a fan and fan stack to the ambient.

The study reported in this paper investigated the plenum pressure loss characteristics of two styles of commercially available crossflow cooling tower drift eliminators. This study also investigated the effects of the air discharge angle at the eliminator face. Typically, drift eliminator design is optimized with respect to collection efficiency and pressure drop across the eliminator pack. The findings of this study demonstrate the importance of designing drift eliminators that also provide better air handling through reduction of plenum turning losses. An optimal discharge angle was determined so as to reduce the pressure drop resulting from turning losses as the exiting air moves toward the axial flow fan at the top of the plenum chamber prior to exhaust into the environment.

2 Experimental Facility

This study was performed using a three-dimensional scale model of a crossflow cooling tower, which was constructed in a wind tunnel so that operating conditions could be fluctuated to cover the possible points of application. The model was based upon an existing dual inlet crossflow cooling tower design that has a 36 foot fill height and length. This tower design has a 32 foot wide by 6 foot tall open plenum, which extends from directly below the fan deck to just above the drift eliminator discharge face. The drift eliminator sections in this cooling tower design are not vertical but rather slope inward at the base toward the center of tower. The cooling tower fan is 28 feet in diameter and operates inside a cylinder, which has an inlet bell and velocity recovery stack.

2.1 Model Cooling Tower. The model cooling tower was constructed around a three foot diameter fan making the model a 3/28 scale version of the full size tower. Figures 1 and 2 present top and side view schematic drawings of the cooling tower model. Due to the orientation of the wind tunnel, the model tower was rotated 90 deg so that the model fan operated in a vertical plane. The cell length was thus measured in the vertical direction and the fill height in the horizontal direction. The model was constructed from plywood with a plexiglass top and back to allow for flow visualization studies. Commercially available drift eliminator packs were installed in the model tower. A filter material was used as the pressure drop medium to simulate the fill and falling water of an actual tower.

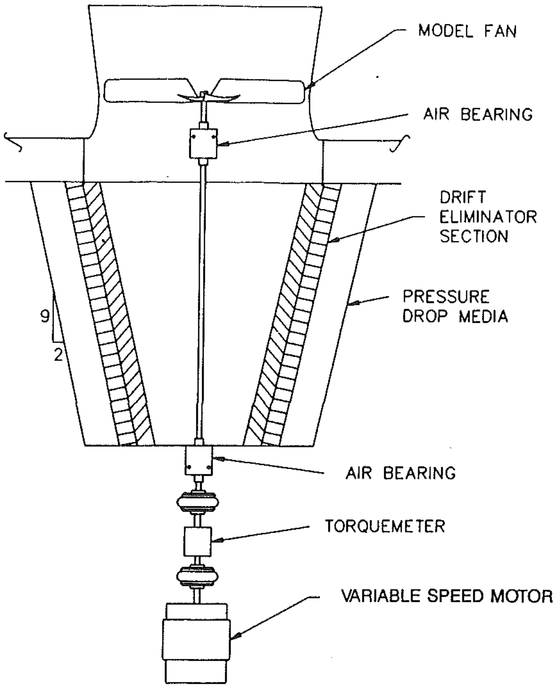

Fig. 1 Top view schematic of model cooling tower

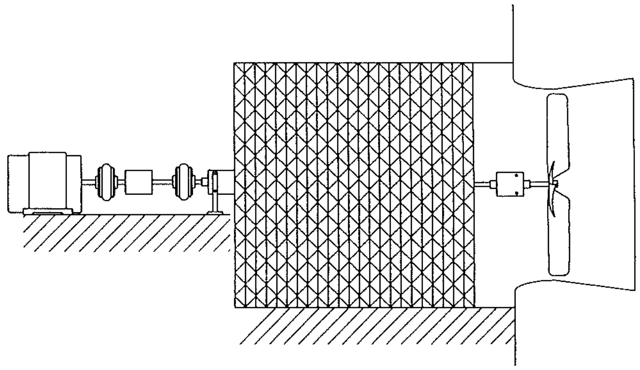

Fig. 2 Side view schematic of model cooling tower

2.2 Wind Tunnel and Instrumentation. As shown in Fig. 3, the model was positioned in a wind tunnel similar to that shown in Fig. 14 of the AMCA/ASHRAE Standard 210-85/51-1985 (1985). Air enters the test cell at the supply blower through a damper, which is used to adjust the air flow rate through the system. The air then moves through a duct containing straighteners, which leads into the nozzle. As it moves

Nomenclature

A = fan system outlet discharge area
P_S = fan system static pressure
P_T = fan system total pressure
P_V = fan system velocity pressure
$\dot{Q}$ = fan flow rate
$\dot{W}_I$ = fan power input
$\dot{W}_O$ = fan power output
η_T = fan system total efficiency
ρ = fan air density

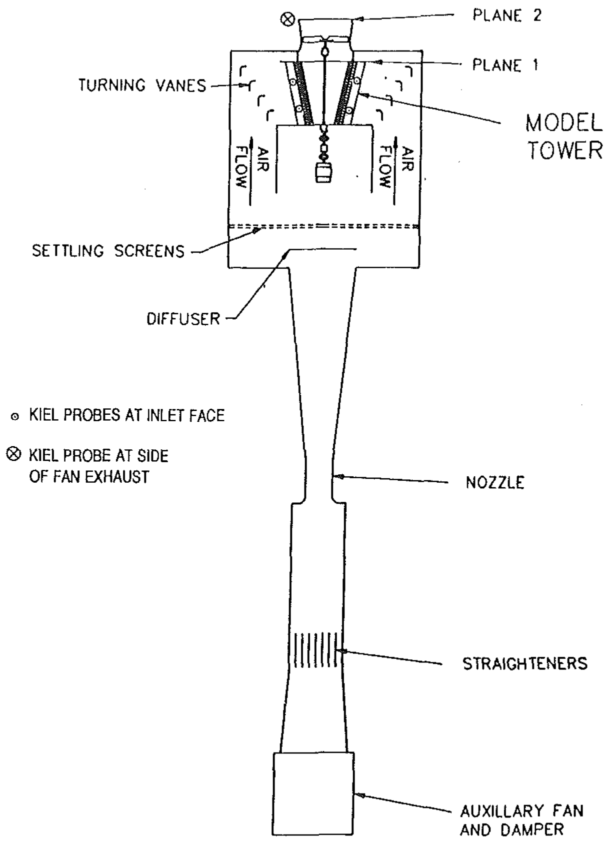

Fig. 3 Top view schematic of wind tunnel

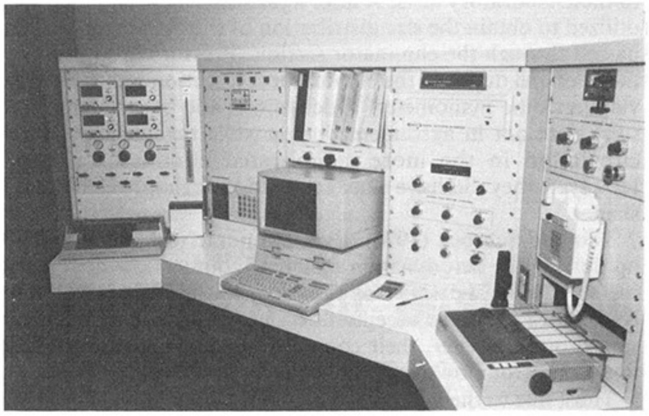

Photo 1 Test cell control panel

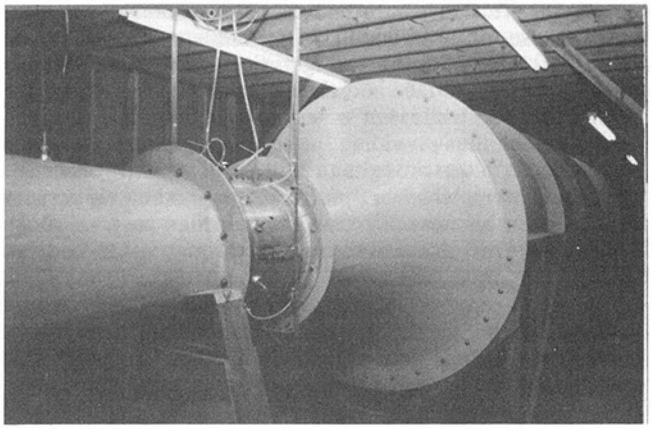

Photo 2 Flow measurement nozzle

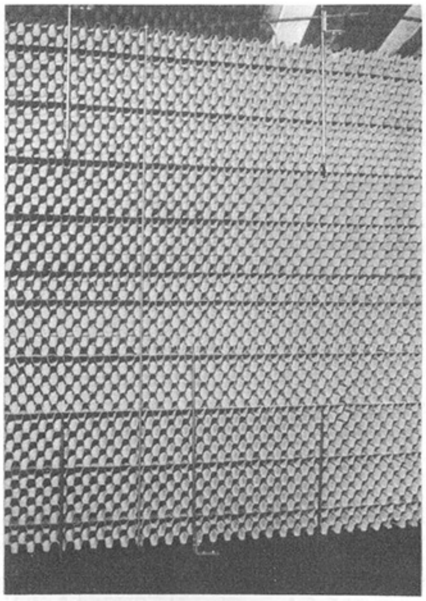

Photo 3 Static pressure probes

downstream, the air enters the sealed pressure room and impinges upon a distribution baffle or diffuser followed by settling screens. The air then flows along the walls of the pressure room through the turning vanes and approaches the cooling tower model, thereby simulating an operating cooling tower system. The exhausted air returns to the supply system along the outside walls of the test section.

A Hewlett Packard 9836 computer interfaces with a Hewlett Packard 3497A data acquisition system to access all test parameters electronically (barometric, flow, and system pressures; air temperature; and, fan torque and speed). The wind tunnel and instrumentation control panel are shown in Photo 1.

Air flow rate measurement is obtained from the pressure differential monitored by static wall taps in the nozzle throat and large diameter duct shown in Photo 2. The throat of the nozzle is constructed of aluminum, which is machined to an exact diameter. Two sets of throat taps connected by a piezometric ring provide individual signals for electronic manometers, which are read through the data acquisition system into the computer and used to establish the velocity head.

A total of eight Kiel probes were located at the two drift eliminator inlet faces: four probes on each inlet face. As shown in Photo 3, the probes were located at the centers of the four quadrants of each drift eliminator face. A ninth Kiel probe was located outside the exhaust air stream at Plane 2 (see Fig. 3). The differential pressure between each inlet probe and the single exhaust probe was monitored. These eight differential pressures were then averaged to yield the fan system static pressure. All of these pressures are sensed electronically and read through the data acquisition system into the computer.

A variable frequency drive motor powers the model fan transmitting the torque through a transducer indicating speed and torque. The shaft between the torquemeter and fan is supported by air bearings virtually eliminating frictional bearing losses. The six-blade, axial-flow model fan and its velocity recovery stack are shown in Photo 4.

Wet bulb and dry bulb temperatures are measured slightly upstream of Plane 1 (see Fig. 3). Dry bulb temperatures are monitored downstream of Plane 2 and downstream of the nozzle throat. The wet and dry bulb temperatures in the pressure room are used to calculate specific humidity and air density at the nozzle throat in order to determine the air flow rate.

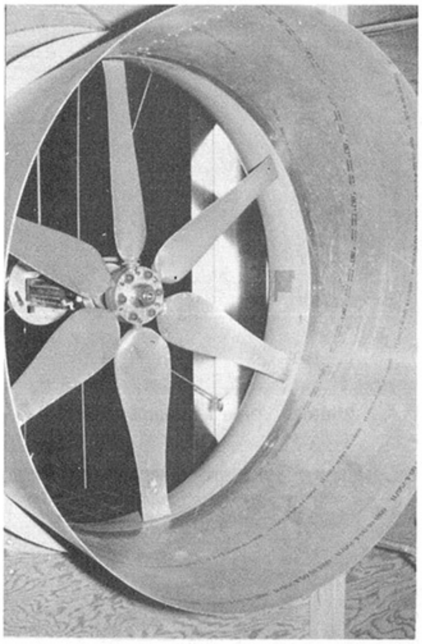

Photo 4 Model axial fan

They are also used to determine the fan air density at the fan discharge. A barometric pressure reading is also acquired electronically to aid in the calculation of the air density.

Temperature measurements are made via Rosemont Series 78S platinum resistance temperature sensors connected to the data acquisition system through four-wire cables. Two leads of each cable are used to transmit the precision current and two leads are used to sense the voltage drop across the resistance elements.

Torque measurements are sensed through a Himmelstein MCRT 24-02 (2-2) noncontact torquemeter transducer providing a signal to a Model 6-201 amplifier. The signal voltage, proportional to torque, is read into the computer via the data acquisition system. The torque transducer provides a speed pickup producing 60 pulses per revolution, which is processed by a counter card in the data acquisition unit.

The barometric pressure is sensed by a Setra Systems Model 361, which is also read electronically. Pressure differentials are sensed by Datametrics 590d barocels coupled to a Model 1400 signal conditioner. Model 525 thermal bases are mounted to the barocels for temperature stability. Once again the voltage output is read through the data acquisition device into the computer.

2.3 Validation of Test Facility. Before establishing a data acquisition procedure, all instruments were calibrated and least-squares relationships developed for each test parameter as a function of its signal voltage. Also, stability and response studies were performed on the test facility to ensure reliability and repeatability of accumulated data. These studies were done by setting a test condition and monitoring each test parameter a sufficient length of time to determine whether cyclic patterns exist that would cause variability in the reading. This method was also used to determine an acquisition period duration adequate to obtain a true mean value.

Rather than accepting a single point of measurement for the fan system static pressure and the pressure differential across the nozzle, redundant readings are taken for both pressures by using several different probes and wall taps. These redundant readings are then checked for consistency. To enable acquisition of these readings without an unreasonable number of sensors, leak-proof pneumatically operated valves are utilized to switch from one pressure measurement to another. When redundant measurements agree and two consecutive groups of data agree then the point is accepted as valid. A similar technique of data averaging is utilized for speed and torque measurements.

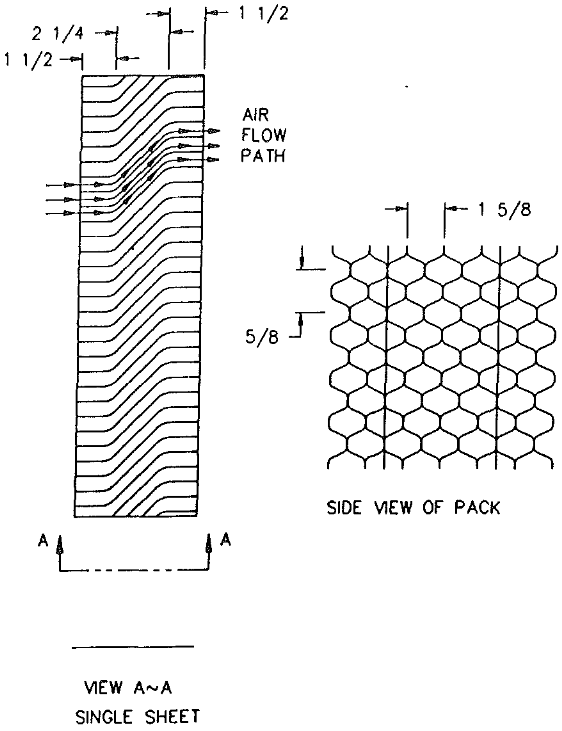

Fig. 4 Schematic of the Type Z drift eliminator

2.4 Uncertainty Analysis of Test Facility. An error analysis consistent with AMCA/ASHRAE Standard 210-85/51-1985 (1985) was performed on the test facility. It was found that for a single measurement, the flow and fan characteristic errors were on the order of 1.00 percent each. The error in power measurement was found to be less than 0.50 percent. In the experimental program, several redundant measurements are taken and then averaged for each data point, yielding highly reliable data.

3 Experimental Program and Results

The experimental program reported in this paper is composed of three studies. In the first two studies, flow visualization and drift eliminator performance comparisons were made between two different styles of commercially available drift eliminators. Both styles are widely used in existing crossflow cooling towers; however, their designs differ significantly.

The first style drift eliminator pack, which will be referred to in this paper as the Type Z eliminator, is constructed of thin plastic sheets, as shown in Fig. 4. If the eliminator pack was installed in a true vertical position, then the plastic sheets would measure 5 in. wide in the horizontal direction and their height would vary to fit the construction. These plastic sheets are molded to contain a uniform "wave pattern" so that when the sheets are bonded together, the "crests" of the waves of two adjacent sheets touch and the "troughs" form air flow channels. The cross-sectional opening of these air flow channels is oblong in shape with a height of approximately 0.63 in. and width of approximately 1.63 in. With the eliminator pack in a true vertical position, air would enter the pack and maintain a horizontal direction for 1.50 in., then the air flow channel ramps up at 45 deg for 2.25 in. and then returns to horizontal for the last 1.25 in. Thus the air flow must enter and exit normal to the drift eliminator face and change direc-

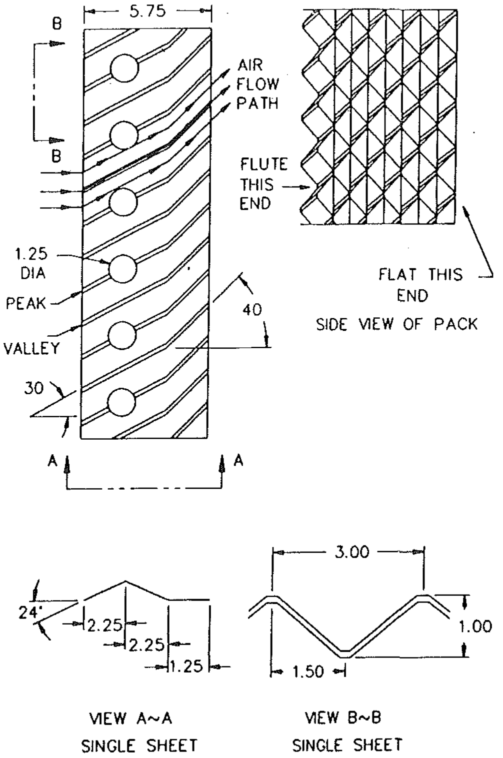

Fig. 5 Schematic of the Type T drift eliminator

tion twice within the drift eliminator pack. Also, when mounted in a typical crossflow cooling tower, the water entrained in this type of drift eliminator pack will drain back toward the inlet face subjecting it to possible re-entrainment.

The second style of drift eliminator pack, which will be referred to in this paper as the Type T eliminator, is constructed of PVC sheets that are 5.75 in. wide, as shown in Fig. 5. Again, these sheets are molded to contain a uniform wave pattern. However, in this case, when the PVC sheets are stacked together, the resulting air flow channels are triangular shaped in the cross section with a 3 in. height and a 1 in. width. Also, the wave pattern in these PVC sheets is such that the air flow must change directions in both the vertical plane, as in the Type Z eliminator, and in the horizontal plane. With the Type T eliminator pack in a true vertical position as shown in Fig. 5, air would enter the pack horizontally and immediately ramp upward at 30 deg in the vertical plane for 4.50 in. During this initial 4.50 in., the air flow path initially turns 24 deg "out-of-the-paper" for 2.25 in. and then 48 deg back toward the plane of the paper for another 2.25 in. In the final 1.25 in., the air flow path turns 24 deg to return to its initial vertical plane and ramps upward in that vertical plane an additional 10 deg for a total vertical slope of 40 deg.

Two other unique features are exhibited by the Type T drift eliminator packs: (*a*) They are self-sealing; and, (*b*) an internal drain is present. The packs are self-sealing by virtue of their three dimensionality, which permits adjacent packs to nestle together in service, thus providing drift elimination at the seam. Packs such as the Type Z, which are strictly two dimensional in nature, do not possess the ability to be self sealing and, unless they are tightly squeezed together, water-laden air will be able to leak through the seams between them. Holes in the Type T sheets at the peak of the first pass act as internal drains, which allow water to fall downward to a drain gutter at the bottom of the peak, thus avoiding re-entrainment.

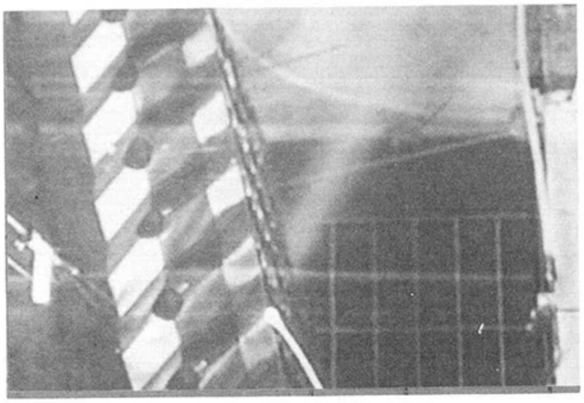

Photo 5 Type T streamline—top

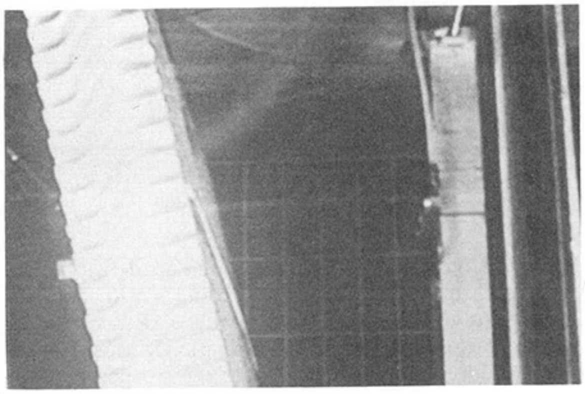

Photo 6 Type Z streamline—top

3.1 Flow Visualization. As described in Section 2.1, the model cooling tower was rotated 90 deg so that the model fan operated in a vertical plane. The cell length was thus measured in the vertical direction and the fill height in the horizontal direction. The top horizontal plane of the model (which would be a vertical end of the tower in a true operating position) was made of plexiglass to permit visualization of the flow as it exited from the drift eliminator packs. Therefore, the view presented in the flow visualization study is similar to that shown in Fig. 3, the top view schematic of the wind tunnel, with the drift eliminator packs being shown in an end view.

In this study, smoke bombs were released at the inlet side of the drift eliminator pack so as to visualize the air flow streamlines as they exit from the pack and move toward the axial flow fan. The purpose of this study was to compare the cooling tower internal flow field resulting from the Type Z drift eliminator versus that resulting from the Type T eliminator. In this study, the fan blade pitch and air flow rate were held constant and the smoke bombs were released at exactly the same position for both types of eliminator.

The smoke bombs were released at three positions along the midline between the floor and plexiglass top of the model. This midline would be the vertical midline of the drift eliminator face if the tower was in a true operating position. The smoke bombs were located at the "top," "center," and "ground level" along this vertical midline with reference to the drift eliminator face in a true operating position.

Photo 5 shows a streamline that exits near the "top" of the Type T drift eliminator pack while Photo 6 shows a similar streamline for the Type Z pack. Comparison shows that the streamline from the Type Z eliminator exits the pack closer to the fan deck and has a greater horizontal velocity component than does the Type T streamline. Photos 7 and 8 show streamlines that exit at the "center" position of the Type T and Type Z packs, respectively. Comparison again shows a much more substantial horizontal velocity component in the case of the Type Z pack. Finally, Photo 9 shows a streamline that exits

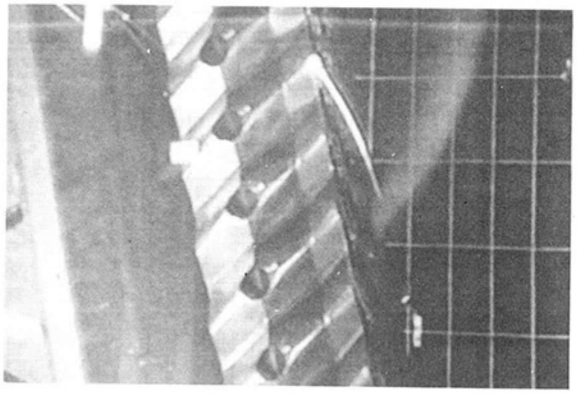

Photo 7 Type T streamline—center

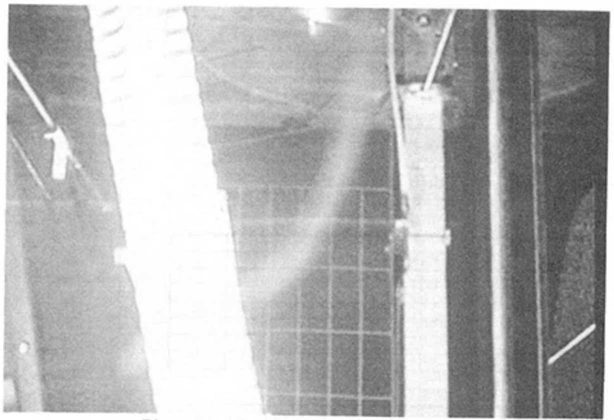

Photo 8 Type Z streamline—center

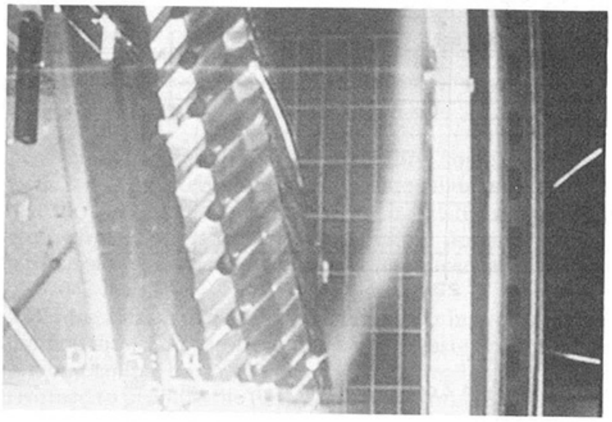

Photo 9 Type T streamline—bottom

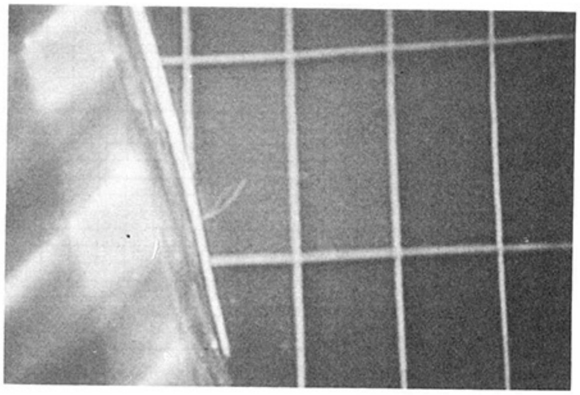

Photo 10 Type T streamer

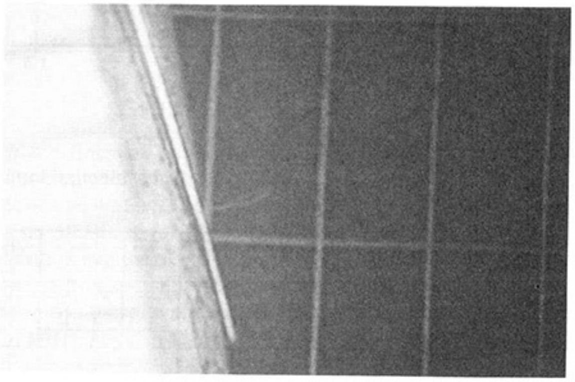

Photo 11 Type Z streamer

near "ground level" of the Type T eliminator. Photo 9 shows that, with the Type T eliminator, the "ground level" streamline angles toward the center of the cooling tower and feeds the axial flow fan along its centerline.

Photos 10 and 11 show a thread attached to an eliminator support rod near the center point of the Type T and Type Z eliminator faces, respectively. This thread indicates the angle of the streamline as it exits from the eliminator face. Comparison shows that the air leaves the Type T eliminator at a more vertical angle.

The results of the flow visualization study show that the air exiting from the Type Z drift eliminator pack has a substantial horizontal velocity component, which must be overcome before the air can move upward toward the axial flow fan. This horizontal velocity component produces higher turning losses when the Type Z eliminator is installed in a crossflow cooling tower than would be realized with the Type T eliminator. The flow visualization study also suggests that the Type Z drift eliminator causes the air flow to be concentrated toward a longitudinal central section of the cooling tower midway between the two opposing eliminator faces. This distorted air flow distribution degrades the efficiency of the axial flow fan. For such a fan to operate at peak efficiency, the approaching flow must be uniformly distributed across the fan inlet. Thus, the Type Z drift eliminator produces a fan inlet velocity distribution that tends to diminish fan performance.

In addition to this adverse effect upon fan system performance, the central air flow concentration produced by the Type Z drift eliminator implies an inefficient utilization of the cooling tower fill. In order to utilize the cooling tower fill fully, the air flow must be uniformly distributed throughout the fill. However, the flow visualization study suggests that the Type Z drift eliminator pack tends to produce a nonuniform air flow distribution through the fill and, hence, may have adverse effects upon the cooling tower's thermal performance.

3.2 Drift Eliminator Performance Comparison. In this portion of the experimental program, the performance of the Type T and Type Z drift eliminators was compared by evaluating the effects of the two eliminator types upon the total fan system performance.

The fan system performance was evaluated in accordance with the procedures specified in the AMCA/ASHRAE Standard 210-85/51-1985 (1985). As specified in this standard, fan system performance is determined as the relationship between the three basic parameters: fan power input, fan system static pressure, and fan flow rate.

The fan power input is the power required to drive the fan. The fan system static pressure, P_S, is defined to be the difference between the static pressure at the fan system outlet and

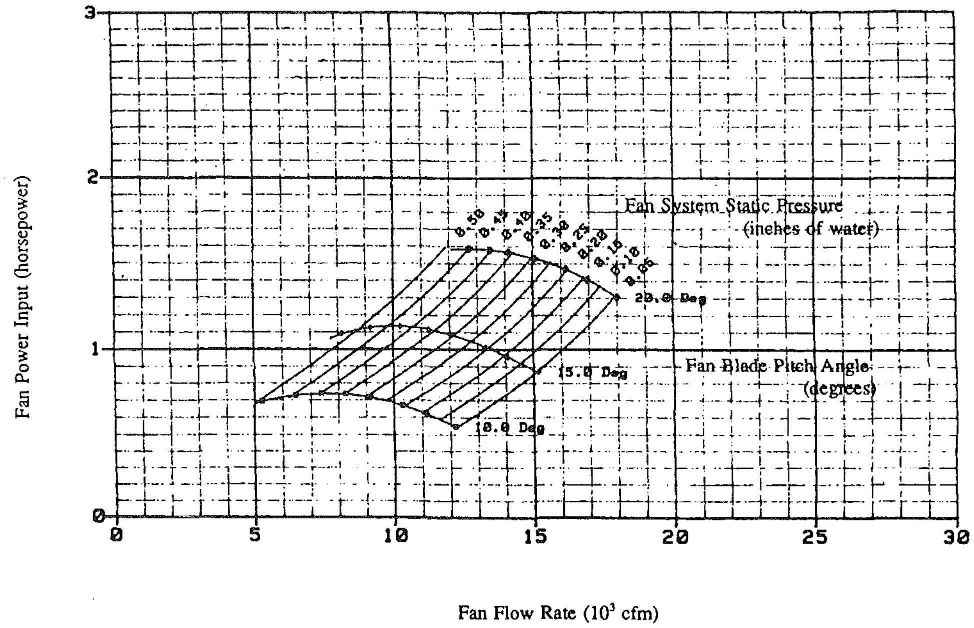

Fig. 6 Fan system performance curves for the Type T drift eliminator

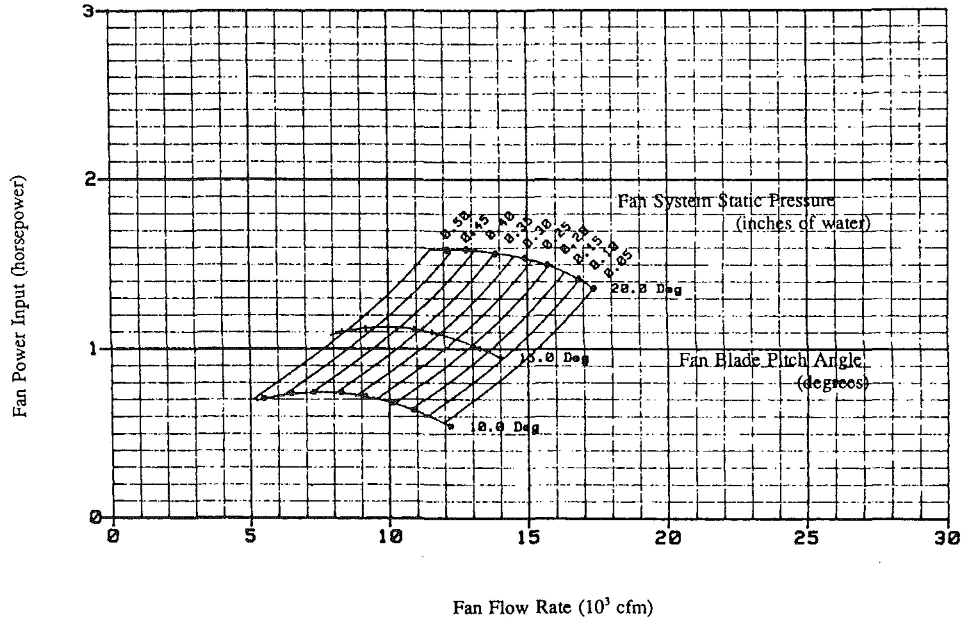

Fig. 7 Fan system performance curves for the Type Z drift eliminator

the total pressure at the fan system inlet. The fan flow rate, Q, is defined as the volumetric flow rate at the fan air density, ρ, which in turn is defined as the density of air corresponding to the total pressure and total temperature at the fan system inlet.

As stated above, the fan system performance is determined as the relationship between these three basic parameters: fan power input, fan system static pressure, and fan flow rate. For each data point taken in the experimental program, the fan blade pitch and wind tunnel supply damper were adjusted to approach the desired test conditions, then the resultant values of these three parameters were measured. Fan data were obtained along a constant blade pitch line at various fan flow rates while the fan system static pressure was varied from the stall region to free air. At a low fan flow rate, the fan system static pressure is high and as the fan flow rate increases, the fan system static pressure decreases. Also, as the flow rate is increased along a constant pitch line by opening the wind tunnel supply damper, not only does the fan system static pressure decrease, but also the fan power input changes as well. The change in fan power input along a constant pitch line is not nearly as dramatic as the change in the other two parameters. After data were accumulated at all applicable fan flow rates along a constant pitch line, the blade pitch setting was readjusted and another region of application analyzed. Ideally, throughout the experimental procedure, the fan rotational speed and fan air density were to have been held constant.

In this comparison study of drift eliminator performance, approximately 25 data points were taken with each type of drift eliminator to determine the corresponding set of fan system performance curves. A nominally constant fan rotational speed of 1062 rpm was maintained during testing and an average fan air density of 0.072 lb_m/ft^3 was experienced. Ideally there would be no fluctuation in these values throughout the

Table 1 Coefficients for the fan system performance relationship

Coefficient	Type T Drift Eliminator	Type Z Drift Eliminator
a_0	-0.31572 E + 01	-0.20796 E + 01
a_1	0.93544 E + 01	0.61517 E + 01
a_2	0.62461 E - 03	0.41296 E - 03
a_3	-0.10554 E - 02	-0.62555 E - 03
a_4	-0.85791 E + 01	-0.57166 E + 01
a_5	-0.39265 E - 07	-0.25573 E - 07
a_6	0.58238 E - 03	0.36869 E - 03
a_7	0.39275 E - 07	0.25377 E - 07
a_8	0.36711 E + 01	0.30510 E + 01
a_9	0.10238 E - 11	0.70213 E - 12

Table 2 Comparison of fan power input

Fan Flow Rate (10^3 cfm)	Fan System Static Pressure (inches of water)	Fan Power Input (horsepower)		
		Type T Eliminator	Type Z Eliminator	Difference[1] (%)
7.00	0.450	0.7997	0.8166	2.11
8.00	0.400	0.8086	0.8291	2.53
9.00	0.340	0.7971	0.8217	3.09
10.00	0.300	0.8254	0.8563	3.74
11.00	0.220	0.7710	0.8091	4.94
12.00	0.170	0.7758	0.8245	6.28
13.00	0.120	0.7791	0.8413	7.98
9.00	0.470	1.0763	1.1020	2.39
10.00	0.420	1.0856	1.1183	3.01
11.00	0.370	1.0971	1.1381	3.73
12.00	0.310	1.0867	1.1371	4.64
13.00	0.250	1.0771	1.1391	5.75
14.00	0.200	1.0924	1.1689	7.00
15.00	0.150	1.1089	1.2030	8.49
12.00	0.430	1.3994	1.4597	4.31
13.00	0.400	1.4807	1.5590	5.29
14.00	0.320	1.4175	1.5065	6.28
15.00	0.250	1.3866	1.4904	7.49
16.00	0.150	1.2678	1.3859	9.32
17.00	0.050	1.1446	1.2852	12.29

[1] Difference = $((hp)_Z - (hp)_T)/(hp)_T$

Table 3 Comparison of fan flow rate

Fan Power Input (horsepower)	Fan System Static Pressure (inches of water)	Fan Flow Rate (cfm)		
		Type T Eliminator	Type Z Eliminator	Difference[2] (%)
1.50	0.20	16435.1	15806.9	3.97
1.50	0.30	14792.2	14281.6	3.57
1.50	0.40	13109.9	12703.7	3.20
1.50	0.50	11358.4	11057.7	2.72
1.25	0.10	16754.6	16048.0	4.40
1.25	0.20	15042.2	14494.4	3.78
1.25	0.30	13323.0	12901.9	3.26
1.25	0.40	11569.2	11255.0	2.79
1.25	0.50	9750.4	9538.4	2.22
1.00	0.10	15148.0	14510.9	4.39
1.00	0.20	13322.6	12858.5	3.61
1.00	0.30	11508.5	11172.4	3.01
1.00	0.40	9681.4	9441.5	2.54
1.00	0.50	7815.0	7657.9	2.05
0.75	0.10	13141.0	12620.5	4.12
0.75	0.20	11192.6	10854.9	3.11
0.75	0.30	9308.8	9087.0	2.44
0.75	0.40	7468.7	7317.1	2.07
0.75	0.50	5644.2	5545.6	1.78

[2] Difference = $((cfm)_T - (cfm)_Z)/(cfm)_Z$

experimental program. However, in reality, some fluctuations did occur. Therefore, in order to evaluate all data on the same basis, the Fan Laws (Buffalo Forge Co., 1970) were used to correct all data so as to reflect the desired nominal value of fan rotational speed and a typical cooling tower fan air density of 0.07042 lb_m/ft^3.

After the measured values of the fan power input, fan system static pressure, and fan flow rate were adjusted to reflect the common nominal basis, a multivariable regression analysis was performed to produce the fan system performance relationship that specifies the fan power input, $\dot{W}_I$, as a function of the fan system static pressure, P_S, and fan flow rate, $\dot{Q}$. This relationship takes the following form:

$$\dot{W}_I = a_0 + a_1 P_S + a_2 \dot{Q} + a_3 P_S \dot{Q} + a_4 P_S^2 + a_5 \dot{Q}^2 + a_6 P_S^2 \dot{Q} + a_7 P_S \dot{Q}^2 + a_8 P_S^3 + a_9 \dot{Q}^3 \quad (1)$$

wherein the $\{a_i\}$ are constants determined by the multivariable regression analysis. The values of these $\{a_i\}$ for both the Type T and Type Z drift eliminators are given in Table 1.

With the appropriate values of the $\{a_i\}$, Eq. (1) can be plotted to produce the fan system performance curves corresponding to the two types of drift eliminators. The performance curves for the Type T eliminator are given in Fig. 6, while those for the Type Z eliminator are given in Fig. 7.

In Figs. 6 and 7, the vertical axis is the fan power input, while the horizontal axis is the fan flow rate. In these two plots, the lines of constant fan blade pitch, which run from left to right, are labeled with the corresponding blade pitch angle in degrees. The lines that run from lower left to upper right are lines of constant fan system static pressure, which are labeled with the corresponding fan system static pressure in inches of water. The measured data points appear along the lines of constant fan blade pitch.

Using these two fan system performance relationships and curves as a basis, the effects of the two different types of drift eliminators were evaluated in four different ways:

1 Difference in fan power input as a function of fan flow rate and fan system static pressure.
2 Difference in fan flow rate as a function of fan power input and fan system static pressure.
3 Difference in fan system static pressure as a function of fan flow rate and fan power input.
4 Difference in fan system static pressure as a function of fan flow rate along a line of constant fan blade pitch.

The results of the first evaluation are shown in Table 2. In this comparison the fan flow rate is held constant, thereby maintaining the same cooling capability for the cooling tower system. As shown in Table 2, the Type Z drift eliminator consistently requires a greater fan power input than does the Type T eliminator to achieve the same fan flow rate and fan system static pressure. The percentage increase in power requirement ranges from 2.11 to 12.29 percent.

As an example, assume that a cooling tower system containing the Type T eliminators is operating in the field at a fan flow rate of 14,000 cfm, a fan system static pressure of 0.39 in. of water, and requires a fan power input of 1.4 hp. Then, the fan power input penalty for converting to the Type Z eliminators would be over 6 percent. However, in most applications, the cooling tower fan motor is operating at full nameplate load. Therefore, if the fan blade pitch was increased to draw the additional fan power input necessary, it would result in overloading the fan motor.

The results of the second comparison are given in Table 3. This comparison is a more realistic comparison for the evaluation of the field retrofit scenario because the fan power input and fan system static pressure are held constant. As shown in Table 3, the Type Z eliminator consistently produces a lower fan flow rate than does the Type T eliminator. The percentage decrease in fan flow rate ranges from 1.78 to 4.40 percent. For the field example cited above, the decrease would be approximately 3 percent. Since the thermal capacity of a cooling tower is closely related to its fan flow rate, conversion to the Type Z drift eliminators would result in approximately a 3 percent decrease in cooling capacity.

Table 4 shows the difference in fan system static pressure when the fan power input and fan flow rate are held constant.

Table 4 Comparison of fan system static pressure

Fan Power Input (horsepower)	Fan Flow Rate (10^3 cfm)	Fan System Static Pressure (inches of water)		
		Type T Eliminator	Type Z Eliminator	Difference[3]
0.80	8.00	0.3960	0.3860	0.0100
0.80	9.00	0.3418	0.3296	0.0122
0.80	10.00	0.2878	0.2729	0.0149
0.80	11.00	0.2344	0.2159	0.0185
0.80	12.00	0.1816	0.1588	0.0228
1.00	10.00	0.3827	0.3680	0.0147
1.00	11.00	0.3280	0.3101	0.0179
1.00	12.00	0.2729	0.2512	0.0217
1.00	13.00	0.2178	0.1915	0.0263
1.00	14.00	0.1628	0.1381	0.0317
1.20	11.00	0.4123	0.3955	0.0168
1.20	12.00	0.3563	0.3357	0.0206
1.20	13.00	0.2995	0.2746	0.0249
1.20	14.00	0.2420	0.2123	0.0297
1.20	15.00	0.1843	0.1491	0.0352
1.40	12.00	0.4303	0.4099	0.0204
1.40	13.00	0.3728	0.3482	0.0246
1.40	14.00	0.3142	0.2850	0.0292
1.40	15.00	0.2547	0.2205	0.0342
1.40	16.00	0.1946	0.1549	0.0397

[3] Differnce = $(P_S)_T - (P_S)_Z$

The Type Z eliminator consistently produces a lower fan system static pressure when the other parameters are held constant.

The results of the fourth comparison are shown in Fig. 8 where the fan system static pressure is plotted versus the fan flow rate for a constant fan blade pitch angle of 20 deg. This figure shows that at all fan flow rates, the Type T drift eliminator provides a higher fan system static pressure than does the Type Z eliminator. This figure also shows that the Type T eliminators produce higher fan flow rates and hence higher cooling tower thermal performance for a given fan system static pressure.

A final aspect of the drift eliminator performance comparison concerns the distributions of fan system static pressure and fan flow rate across the drift eliminator inlet face. As described in Section 2.2 and shown in Photo 3, there was one Kiel probe located in the center of each quadrant of both drift eliminator inlet faces for a total of eight probes. A ninth probe was located outside the exhaust air stream (Plane 2, Fig. 3). The differential pressure between each of these eight inlet probes and the single exhaust probe was monitored. These eight differential pressures were then averaged to yield the fan system static pressure.

In order to investigate the distribution of the fan system static pressure across the drift eliminator inlet faces, each of the eight individual measurements as well as their average were recorded. These data were taken at various fan flow rates with the fan blade pitch angle set to 20 deg. At each of these fan flow rates, the difference between the maximum and minimum fan system static pressure readings was determined. This difference is plotted versus the average fan system static pressure in Fig. 9.

Figure 9 shows that, at all fan flow rates, the Type Z eliminator produces a greater variation in fan system static pressure than does the Type T eliminator. It also shows that the variation increases as the average fan system static pressure decreases. Since the average fan system static pressure decreases as the fan flow rate increases, Fig. 9 implies that the fan system static pressure distribution becomes more skewed as the fan flow rate increases.

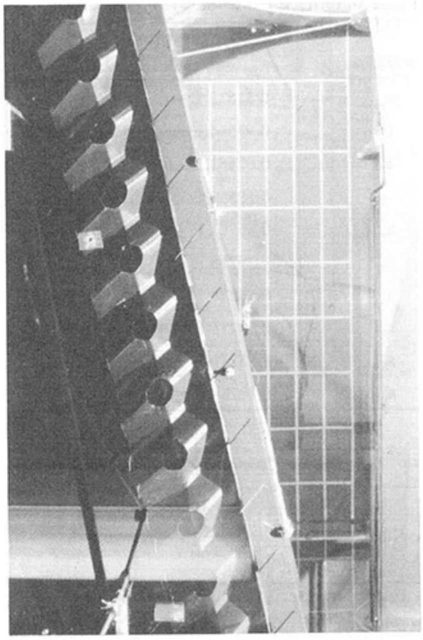

Photo 12 Guide vanes—top view

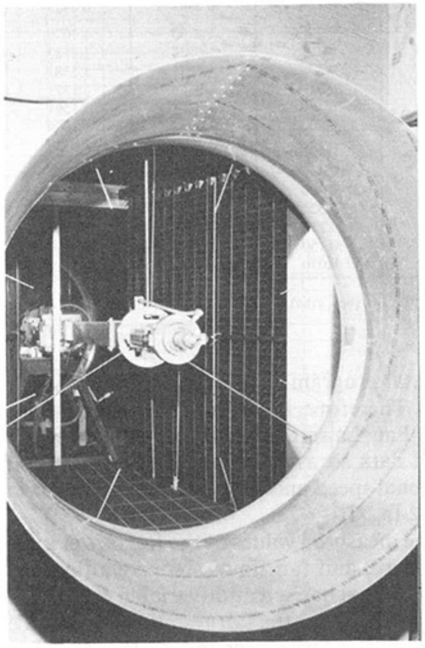

Photo 13 Guide vanes—outlet

This skewed distribution of fan system static pressure also reflects a skewed distribution of fan flow rate across the drift eliminator face. Details of the Type Z data indicate that the air flow through the Type Z eliminator is concentrated in those regions nearest the fan deck and becomes more skewed as the fan flow rate increases. Thus the Type Z drift eliminator causes a higher percentage of the air flow to move through the upper portion of the fill material than through the lower portion. This results in an underutilization of the cooling capacity of the fill material.

These skewed distributions of fan system static pressure and fan flow rate collaborate the results of the flow visualization studies, which indicated that the flow through the Type Z eliminator had a substantial horizontal velocity component. This high horizontal velocity caused the flow to move too far inward toward the tower centerline, thus starving the fan blade tips near the inlet sides of the plenum. Flow from the upper portion of the fill material and drift eliminator, which should supply the outer perimeter of the fan ring next to the air inlet sides of the plenum, was instead supplying the middle portion of the fan near the tower centerline, which is more suitably supplied by flow through the lower portion of the fill material

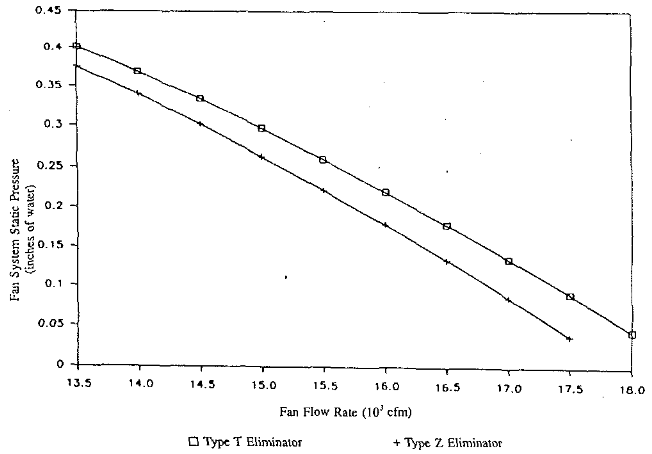

Fig. 8 Comparison of fan system static pressure at a fan blade pitch angle of 20 deg

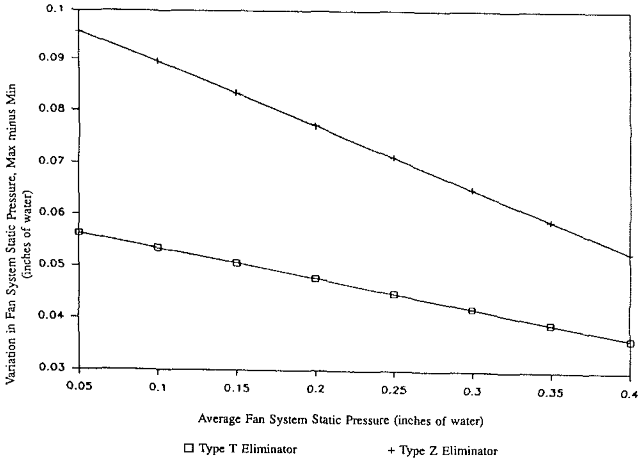

Fig. 9 Variation in fan system static pressure across the drift eliminator inlet face

and drift eliminator. The results of this condition are uneven flow distributions through the fill material and at the fan ring, which reduce the cooling capacity of the fill and the performance of the fan.

3.3 Optimization of Drift Eliminator Discharge Angle. From the results of the first two studies in this experimental program, it became apparent that the angle at which the flow exits from the drift eliminator has a substantial impact upon cooling capacity and fan performance. In the Type Z eliminator, this discharge angle gives the flow its detrimental horizontal velocity component. In the Type T eliminator, this discharge angle tends more properly to direct the flow to produce a more uniform velocity distribution at the fan inlet. Therefore, the purpose of this final study was to determine the optimal drift eliminator discharge angle that will produce the highest fan system total efficiency.

Fan system total efficiency, η_T, is defined as the ratio of the fan power output, $\dot{W}_O$, divided by the fan power input, $\dot{W}_I$ (AMCA/ASHRAE, 1985):

$$\eta_T = \dot{W}_O / \dot{W}_I \tag{2}$$

The fan power output is the product of the fan flow rate, $\dot{Q}$, times the fan system total pressure, P_T, which is defined to be the sum of the fan system static pressure, P_S, and the fan system velocity pressure, P_V:

$$\dot{W}_O = \dot{Q}(P_S + P_V) \tag{3}$$

The fan system velocity pressure is defined as the pressure corresponding to the average velocity at the fan system outlet, which has a discharge area, A:

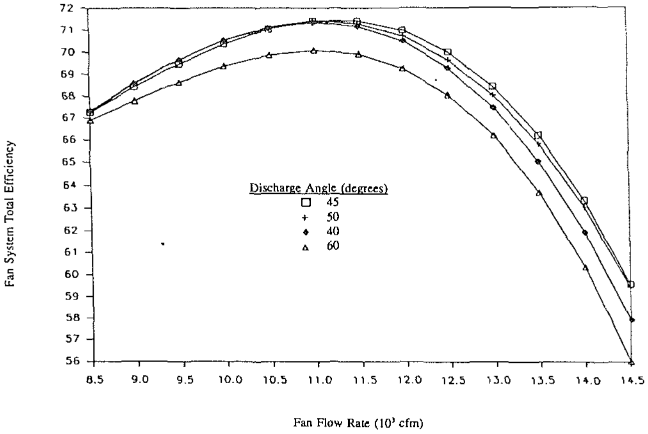

Fig. 10 Variation in fan system total efficiency as influenced by the drift eliminator discharge angle

$$P_V = (\rho/2)(\dot{Q}/A)^2 \tag{4}$$

Substituting Eqs. (3) and (4) into Eq. (2) gives the final expression for the fan system total efficiency:

$$\eta_T = \frac{\dot{Q}[P_S + (\rho/2)(\dot{Q}/A)^2]}{\dot{W}_I} \tag{5}$$

In this study, the final 1.25 in. section was cut off the exhaust side of the Type T drift eliminator (see Fig. 5). This section was replaced with equal width, sheet metal guide vane strips, which could be positioned to produce various drift eliminator discharge angles. Photo 12 is a top view of the drift eliminator section, which shows an end view of the guide vanes. Photo 13 is a view through the model fan opening with the fan removed. It shows an elevation view of the drift eliminator discharge with the sheet metal guide vanes in position.

Four different drift eliminator discharge angles were tested using a fan blade pitch angle of 15.0 deg. For each discharge angle, the fan system total efficiency was determined as a function of the fan flow rate. The results of this study are shown in Fig. 10.

As shown in Fig. 5, the original discharge angle of the Type T eliminator is 50 deg from the vertical (shown as 40 deg from the horizontal in Fig. 5). The four discharge angles tested in this study were 60, 50, 45, and 40 deg as measured from the vertical. The 50 deg discharge angle was used to replicate the original Type T results. In analyzing the results of this study, one must keep in mind that the eliminator packs are positioned at an angle of 12.5 deg from true vertical when installed in the cooling tower (see Fig. 1). Therefore, the upward deflection of the air stream increases as the discharge angle decreases with 12.5 deg being a true vertical discharge.

To determine the optimal guide vane angle, one would compare the fan system total efficiencies at a constant fan flow rate. As shown in Fig. 10, the 60 deg discharge angle underperforms at all fan flow rates. Figure 10 also shows that there is little difference in the performance of the 40, 45, and 50 deg discharge angles for fan flow rates between 8500 cfm and 11,000 cfm. However, from 11,000 cfm to 14,000 cfm, the 45 deg discharge angle produces the highest fan system total efficiency followed by the 50 and then the 40 deg discharge angles. According to these results, the performance of the Type T drift eliminator, measured in terms of fan system total efficiency, could be improved approximately one half of one percent by changing its discharge angle from 50 to 45 deg.

4 Conclusions

An experimental program consisting of three different studies was developed and executed to evaluate the effect of drift eliminator design upon cooling tower fan system performance:

1 The flow visualization study was used to gain insight into the flow patterns within the cooling tower plenum as influenced by two different styles of drift eliminators. This study showed that the Type Z eliminator produced a flow field that tended to diminish fan system performance and cooling tower thermal capacity while the Type T eliminator produced a flow field that tended to enhance both of these factors.

2 The drift eliminator performance comparison evaluated the effects of the two eliminator types upon fan system performance. The Type Z eliminator consistently underperformed the Type T. The measured distributions of the fan system static pressure across the inlet faces of the drift eliminator packs collaborated the results of the flow visualization study.

3 The optimal drift eliminator discharge angle for the Type T eliminator was determined to be 45 deg for the plenum dimensions tested.

In addition, a more general conclusion can be drawn from the results of this study: The evaluation of cooling tower components needs to be done in the context of the total cooling tower system. For example, the results of this study clearly show that the Type T drift eliminator outperforms the Type Z eliminator in terms of system pressure loss and fan system performance. However, a superficial comparison could be made in terms of the pressure loss across just the drift eliminator pack without regard for the fan system in toto. Such a comparison would incorrectly indicate that the Type Z eliminator is the best performer.

References

AMCA/ASHRAE, 1985, *ANSI/AMCA Standard 210-85 and ANSI/ASHRAE Standard 51-1985, Laboratory Methods of Testing Fans for Rating*, Air Movement and Control Association, Inc., and American Society of Heating, Refrigeration and Air Conditioning Engineers, Inc., Atlanta, GA.

Buffalo Forge Co., 1970, *Fan Engineering*, Buffalo, NY.

Chan, J., and Golay, M. W., 1976, "Numerical Simulation of Cooling Tower Drift Eliminator Performance," *Numerical/Laboratory Computer Methods in Fluid Mechanics*, A. A. Pouring, ed., ASME, New York, pp. 229-241.

Chan, J., and Golay, M. W., 1977, "Comparative Performance Evaluation of Current Design Evaporative Cooling Tower Drift Eliminators," *Atmospheric Environment*, Vol. 11, pp. 775-781.

Chilton, H., 1952, "Elimination of Carryover From Packed Towers With Special Reference to Natural Draught Water Cooling Towers," *Transactions of the London Institute of Chemical Engineers*, Vol. 30, pp. 235-250.

Holmberg, J. D., 1974, "Drift Management in the Chalk Point Cooling Tower," The Marley Company, Mission, KS.

Marley Cooling Tower Company, 1968, "TOPS, Thermal Operating Performance System," The Marley Company, Mission, KS.

Yao, S. C., and Schrock, V. E., 1976, "Aerodynamic Design of Cooling Tower Drift Eliminators," ASME JOURNAL OF ENGINEERING FOR POWER, Vol. 98, pp. 450-456.

Repowering Application Considerations

J. A. Brander
Application Engineer.

D. L. Chase
Manager, Combined Cycle Technology.

GE Industrial and Power Systems,
Schenectady, NY 12345

As utilities plan for load growth in the 1990s, they are faced with the difficulty of choosing the most economic generation while subject to a number of challenging constraints. These constraints include environmental regulations, particularly the new Clean Air Act, risk aversion, fuel availability and costs, etc. One of the options open to many utilities with existing steam units is repowering, which involves the installation of gas turbine(s) and heat recovery steam generator(s) (HRSG) to convert the steam plant to combined-cycle operation. This paper takes an overall look at the application considerations involved in the use of this generating option, beginning with a summary of the size ranges of existing steam turbines that can be repowered using the GE gas turbine product line. Other topics covered include performance estimates for repowered cycles, current emissions capabilities of GE gas turbines, approximate space requirements and repowering economics.

Introduction

As utilities plan for load growth and new environmental regulations in the 1990s, they are faced with the question of what to do with the large fleet of small nonreheat and reheat units that are still in operation. For example, there are currently almost 30 GW of nonreheat units 30 years of age or older in domestic utility service (representing over 4 percent of the current U.S. generating capability). Should this capacity be retired, upgraded, repowered, or operated as is? The answer to this question depends on many factors, which are both utility and site specific, and each must be evaluated on a case-by-case basis. While not all of the 30 GW are economic candidates for repowering, it is reasonable to assume that a significant number of utilities will at least consider this generation addition option. The objective of this paper is to review some of the more significant considerations when evaluating repowering, and present relevant application information about the GE gas turbine product line.

Description of Repowering Cycles

Combined-cycle repowering is defined as the integration of gas turbine generator units and heat recovery units into an existing steam power plant. Repowering of an existing steam power plant is a generation option that should be considered by utilities since it provides highly efficient capacity addition and improves the efficiency of existing capacity. All existing steam power plants are candidates for repowering, although not all will prove to be economically feasible.

There are three repowering approaches:

1 Feedwater heating repowering
2 Boiler repowering
3 Heat recovery repowering

Feedwater heater repowering systems utilize gas turbine exhaust gas to heat feedwater in the existing steam plant. In addition to incremental power supplied by the gas turbine generator, about 15 percent additional steam turbine power may be made available by elimination of steam extraction for feedwater heating or by increased power boiler steam flow reflecting increasing final feedwater temperature. Cycle diagrams of feedwater heater repowering systems are presented in Figs. 1 and 2.

Boiler repowering systems utilize gas turbine exhaust gas for combustion air in the existing boiler. Here, the gas turbine performs the function of the forced draft fan and air heater.

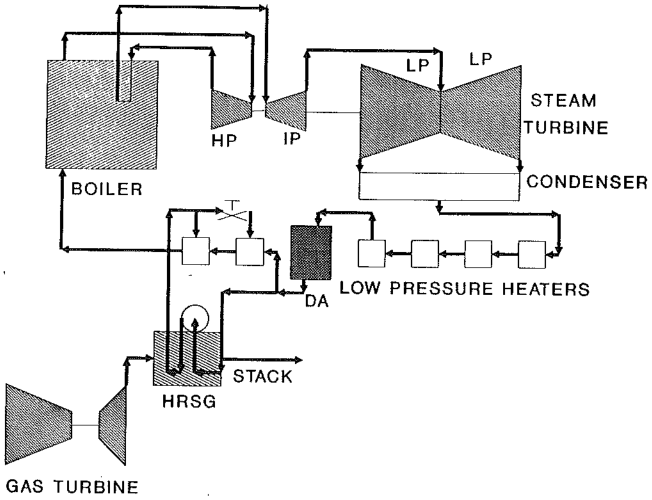

Fig. 1 **Feedwater heating repowering—existing extractions eliminated**

Contributed by the International Gas Turbine Institute and presented at the 36th International Gas Turbine and Aeroengine Congress and Exposition, Orlando, Florida, June 3-6, 1991. Manuscript received at ASME Headquarters March 4, 1991. Paper No. 91-GT-229. Associate Technical Editor: L. A. Riekert.

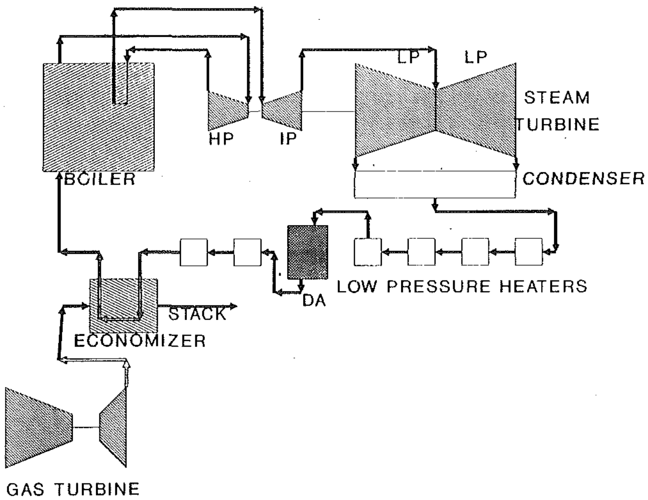

Fig. 2 Feedwater heating repowering—final feedwater temperature increased

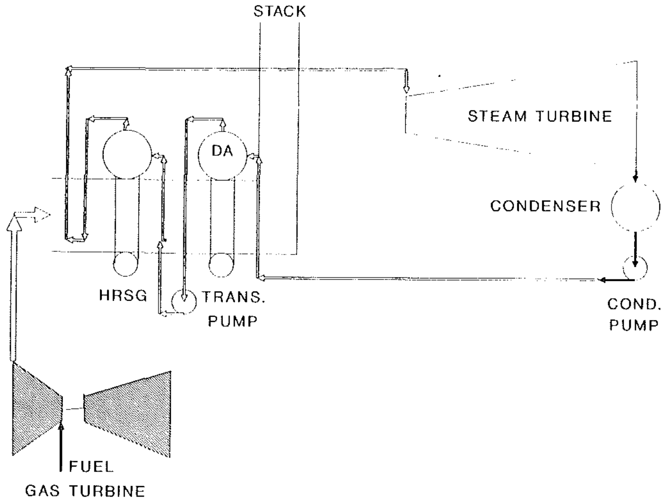

Fig. 4 Heat recovery repowering

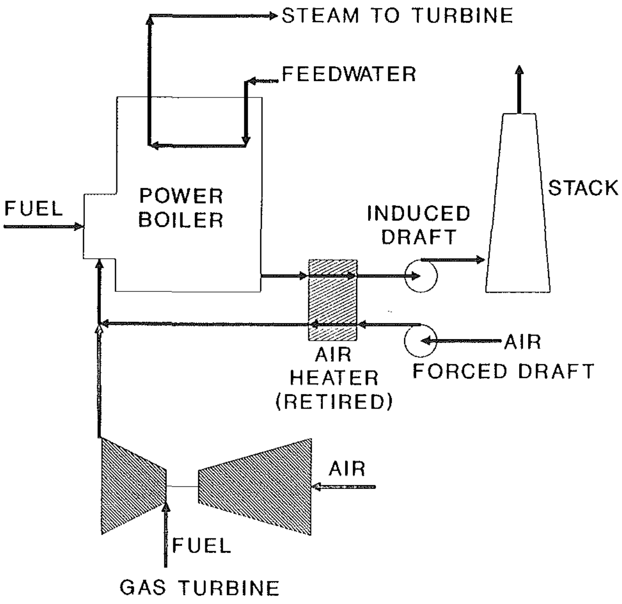

Fig. 3 Boiler repowering

A cycle diagram of a boiler repowering system is presented in Fig. 3.

Heat recovery repowering systems utilize gas turbines and heat recovery steam generators (HRSGs) to replace the power boiler in the existing steam plant as shown in Fig. 4. Here, the steam supply to the existing steam turbine is generated in the HRSG by energy recovered from the gas turbine exhaust gas.

The repowered plant configuration and the combined-cycle plant capacity and thermal efficiency achieved by repowering are dependent on several variables:

- Condition of existing plant equipment
- Ability to remove existing regenerative feedwater heaters from service
- Match between existing steam turbine operating envelope and gas turbine HRSG steam supply capability
- Space available for repowering equipment
- Fuel cost
- Duty cycle
- Environmental considerations

Candidate units for repowering impose design restraints relative to new combined-cycles since an existing steam turbine generator is used. However, various application techniques can be applied to mitigate the consequences of those limitations.

While all three cycles have potential applications in the United States, it is likely that heat recovery repowering will have the most favorable economics in the majority of cases, and will be the most commonly used form of repowering. As a result, this paper will concentrate on this option. Bear in mind that much of the information contained in this document will apply to the other repowering cycle options as well.

Since repowering results in a combined-cycle plant, it will be useful to give a brief description of some of the factors influencing the overall design of such cycles.

Combined-Cycle System

Combined-cycle development has proceeded in parallel with gas turbine development. The key performance characteristic of the gas turbine that influences combined-cycle plant performance is specific power, where specific power is the power produced by the gas turbine per unit of air flow (kW output per lb per s of compressor air flow). Combined-cycle system thermal efficiency increases with gas turbine specific power, with gas turbine firing temperature the primary determinant of specific power. The increase in gas turbine firing temperature and, therefore, gas turbine specific power, has resulted from development of high-temperature/high-strength materials, oxidation/corrosion resistant coatings, and improved surface cooling technology and their application in gas turbine hot gas path sections. Further improvement in combined-cycle efficiency will be based on future gas turbine development, fuel availability, and economics.

Most combined-cycle power generation systems installed during the 1950s and early 1960s included conventionally fired boilers. These systems were basically adaptations of conventional steam plants with the gas turbine exhaust serving as combustion air for the boiler. The efficiency of this type of combined-cycle was approximately 5–6 percent higher than that of conventional steam plant.

During the 1960s, the heat recovery type of combined-cycle became dominant. Its initial application was in power and heat applications where its power-to-heat ratio was favorable to many chemical and petrochemical processes. A small number of heat recovery type combined-cycles were installed in power generation applications in the 1960s. When gas turbines over 50 MW in capacity were introduced in the 1970s, the heat recovery combined-cycle experienced rapid growth in electric utility applications. These have developed into the most efficient fossil fuel fired power systems currently in commercial operation.

(A) SINGLE PRESSURE

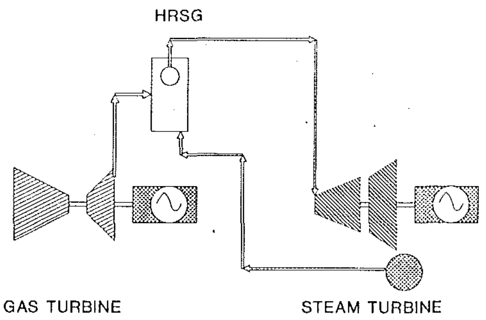

(B) TWO PRESSURE

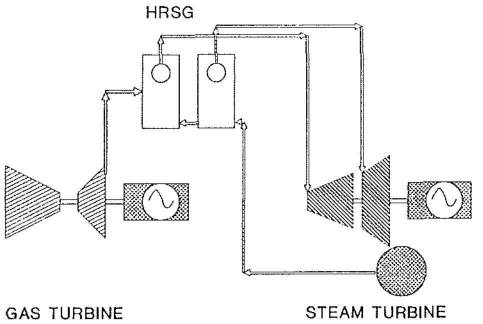

(C) TWO PRESSURE WITH FEEDWATER HEATING

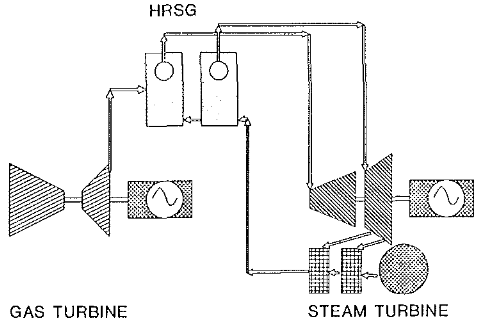

(D) THREE PRESSURE REHEAT

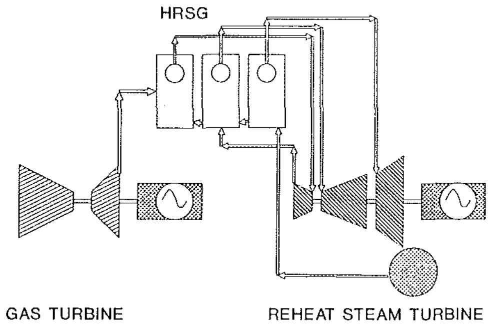

Fig. 5 Typical gas turbine combined-cycle systems

For power generation, the unfired heat recovery combined-cycles are the most efficient, and together with a standardized design using modular components that results in low installed costs, make these economical power plants. Steam cycles used for unfired heat recovery feedwater heating combined-cycles are simple, straightforward systems, which utilize modest steam conditions. Steam is generated in one, two, or three-pressure unfired HRSGs for delivery to a straight condensing steam turbine-generator. There are no steam turbine extractions for feedwater heating because gas turbine exhaust energy is sufficient to perform all steam generation and feedwater heating.

Combined-cycle systems with nonreheat steam cycles are generally applied in plants in which the gas turbine exhaust gas temperature is typically 1000°F or less. Cycle diagrams with unfired single-pressure and two-pressure heat recovery feedwater heating systems are presented in Figs. 5(*A*) and 5(*B*). The total fuel consumed by the unfired combined-cycle power plant is fuel burned in the gas turbine and the total energy supplied to the steam cycle is gas turbine exhaust energy. The single pressure steam cycle has the lowest capital cost and provides the lowest plant capacity and efficiency with stack gas temperatures typically greater than 340°F. These systems may be the economic choice in stations where fuel cost is low, operating hours are low (less than 1500 hours per year), or when operating with ash-bearing high-sulfur fuels.

A two-pressure steam cycle is expected to be the economic choice for midrange and base load service when burning higher priced low-sulfur fuels such as natural gas. Here, additional HRSG heat transfer surface is installed to reduce stack gas temperature to about 200°F and additional power generation is provided without additional fuel consumption. Extraction feedwater heaters may be added to optimize plant performance as presented in Fig. 5(*C*) when burning high-cost, high-sulfur-content fuels.

Combined cycles with reheat system cycles as shown in Fig. 5(*D*) are utilized in plants with gas turbines having exhaust gas temperatures around 1100°F. These systems utilize a three-pressure steam cycle to achieve low stack gas temperature and maximum plant thermal efficiency.

Repowered Cycle Design

The same gas turbine and heat recovery equipment configurations used to optimize "grass-roots" combined-cycle plants may be directly applied to repower existing steam power plants. In addition to flexibility in the design of the existing equipment, there is flexibility in the equipment configuration of the existing steam system. This additional flexibility arises from the ability to remove existing feedwater heaters from service and the ability to upgrade existing steam turbine steam path design to achieve maximum output and efficiency. Possible heat recovery feedwater heater repowered plant cycle diagrams are presented in Fig. 6. Figure 6(*A*) shows the repowered plant configuration with all existing feedwater heaters in service. This represents the minimum capital cost approach, which also results in the lowest output, lowest thermal efficiency alternative. If sufficient steam turbine low-pressure section flow passing capability is available, the top heaters (extraction feedwater heaters above the deaerator) or all heaters may be removed from service as shown in Figs. 6(*B*) and 6(*C*). These systems require additional heat transfer surface to be installed in the HRSG, which adds to capital expenditure, however. The increased plant output and efficiency may justify the added expense. Still further performance improvement can be achieved by adding a second low-pressure steam section to the HRSG and admitting the low-pressure steam to the appropriate section of the steam turbine, which gives the cycle shown in Fig. 5(*B*).

With cycle configurations shown in Figs. 6(*B*), 6(*C*), and 5(*B*), modifications have been made to an existing steam turbine, one that was designed for single-pressure steam admission and extractions for several stages of feedwater heaters. Steam flows though the latter stages of the turbine have risen, resulting in increased stage loadings, greater turbine-generator output, and higher condenser steam loads. Each of these must be checked to determine whether the increased loadings would exceed allowable limits. It becomes difficult to do this with equipment that is 30 or more years old, since there will be

(A) ALL FEEDWATER HEATERS IN SERVICE

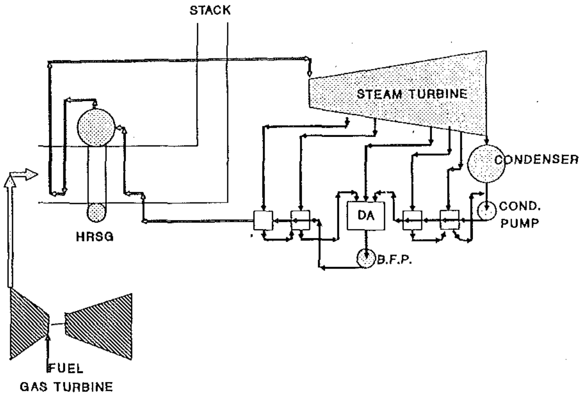

(B) LOW PRESSURE FEEDWATER HEATERS IN SERVICE

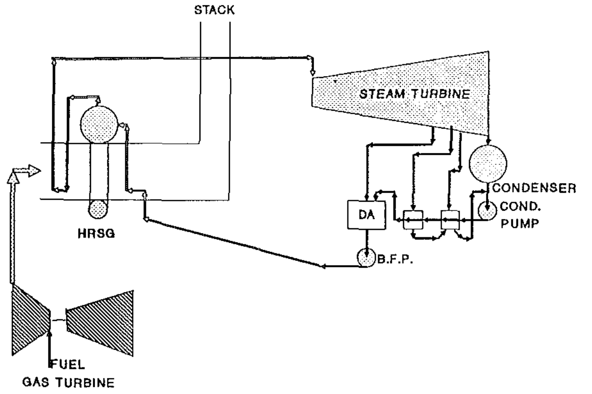

(C) NO FEEDWATER HEATERS IN SERVICE

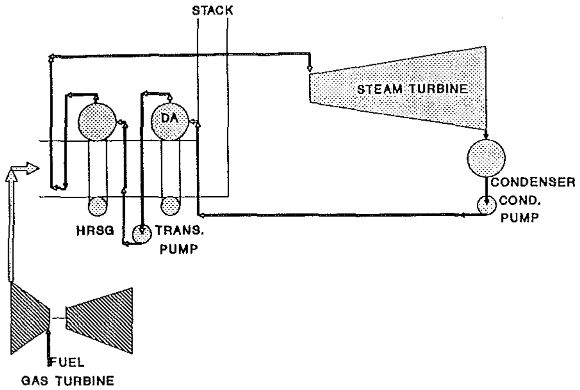

Fig. 6 Repowering cycle configurations

considerable uncertainty regarding materials properties and how much of the fatigue life might have already been expended over the years. Another possibility is to replace the steam path with a modern design that takes into account the increased steam flows. Not only would it be designed for the cycle, but it would use modern designs and materials for the nozzles, buckets, rotors, etc., that will have significantly better efficiency, lower stresses, and better reliability than the original parts. Upgrades to the generator and condenser may also be required to handle the additional loads.

Another consideration is the match between the steam and gas turbines, since gas turbines are available in discrete sizes. The optimal cycle results when there is an exact match between the steam turbine steam requirements and the gas turbine/HRSG steam production capabilities, such as occurs when designing a new combined-cycle plant. Since this is unlikely when repowering, there can be economic and performance penalties arising from the mismatch. For example, if the available gas turbines are too large, some of the exhaust heat will not be utilized unless power augmentation of the gas turbine is used. On the other hand, if the gas turbine is too small, not all of the capability of the steam turbine will be used unless the HRSG is supplementary fired or fully fired to increase steam production. In these situations the retrofit and/or operating cost will be increased in order to integrate the two cycles more fully.

The optimal repowered plant configuration must be determined based on economic analysis that considers the condition of the existing steam turbine and balance of plant equipment, steam path flow passing capability, generator, and cooling water system capability. Bear in mind that repowered units, because of their improved performance, will be dispatched more that the original steam unit and will operate at higher capacity factor. This change must be estimated and used in the economic evaluations.

GE Gas Turbine Repowering Capabilities

Table 1 presents data on the performance and typical steam generation from the gas turbines and HRSGs available in GE's product line. For example, an MS7001EA has an exhaust flow of 2,295,200 lb/hr at a temperature of 989°F in an unfired cycle. When combined with a single-pressure HRSG, 379,500 lb/hr of steam at 160 psig/371°F can be produced. When used with a two-pressure HRSG, steam output will be 253,500 lb/hr at 1525 psig/955°F and 90,100 lb/hr at 160 psig/371°F. When combined with to estimated steam turbine performance, these data can be used to determine the size of the steam turbine that can be repowered with each model gas turbine and an unfired HRSG. The curves in Figs. 7 and 8 show this as a function of steam conditions and cycle design. In each of these plots, the lower curve was calculated assuming that the steam turbine-generator limitations (e.g., stage loadings) were so severe that the repowering was a simple replacement for the boiler. For this case, the existing feedwater heater string was retained, and the HRSG was designed to produce steam only at the rated throttle conditions of the turbine, resulting in the cycle in Fig. 6(*A*). The upper curve was calculated assuming no steam turbine-generator limitations, so that all feedwater heaters could be eliminated and a two pressure HRSG used. The resulting cycle (see Fig. 5B) is identical to a new, optimized combined-cycle using those throttle steam conditions. (A completely new combined-cycle unit may have even better efficiency than this, however, since the optimal throttle steam conditions may differ from those of the existing unit.) Bear in mind that these two curves are estimates calculated using a simplified steam turbine performance estimation method for new units, no steam or water injection for NO_x controls, and with certain assumptions about cycle conditions. The actual repowering capabilities of the gas turbines in a given situation may be higher or lower, depending on factors such as ambient temperature and elevation, use of steam or water injection for NO_x control, condenser pressure, feedwater heating cycle design, amount of degradation present in the existing steam turbine, relative performance of new units with modern aerodynamic design advances as compared to original unit design, etc. For example, typical effects of degradation and design advances can total approximately 3 percent. Finally, supplemental firing of the gas turbine exhaust or power augmentation of the gas turbine can be used to increase cycle output and may be justified in some circumstances (for a discussion of these, see [1]).

Since these assumptions represent the upper and lower bounds, the actual repowering capabilities will fall between these two curves. As an example, consider a Frame 7EA gas turbine. Referring to Fig. 8, it is capable of repowering turbines

Table 1 Steam generation with gas turbines and exhaust heat boilers

Gas Turbine Type	MS5001 (PA)	MS6001 (B)	MS7001 (EA)	MS7001 (F)	LM2500-PE	LM5000-PC
ISO Base Rating, kW	26,300	38,340	83,500	150,000	21,790	33,060
Performance at 59°F, Sea Level, Natural Gas Fuel						
Output, kW	25,890	38,000	82,670	146,800	21,540	32,640
Fuel, MMBtu/Hr (HHV)	344.6	462.3	967.8	1645	236.2	356.3
Exhaust Flow, lb/Hr	971,400	1,083,000	2,295,200	3,307, 500	524,300	957,400
Exhaust Temperature, °F	906	1007	989	1091	992	845
HRSG Output, Thousands of lb/Hr						
Steam Conditions						
Single Pressure, psig/°F						
160/371	143.4	193.2	397.5	676.0	91.5	125.4
420/655	114.4	159.0	325.5	567.0	75.0	97.3
630/755	104.4	148.0	302.0	534.0	69.6	87.3
895/830	96.2	139.4	283.5	509.0	65.4	--
Two Pressure, psig/°F						
1) 895/830	96.2	139.4	283.5	509.0	65.4	--
2) 160/371	32.3	27.6	68.2	84.5	15.5	--
1) 1315/905	--	130.8	264.5	487.0	--	--
2) 160/371	--	34.3	83.2	98.1	--	--
1) 1525/955	--	125.8	253.5	471.5	--	--
2) 160/371	--	37.8	90.1	104.4	--	--

- Gas turbines fueled with natural gas and all fuel data based on higher heating value (HHV)
- Single pressure boilers have 92% effectiveness for superheater and evaporator
- For two pressure boilers, criteria of minimum 300°F stack temperature may require less than 92% low pressure boiler effectiveness
- Assumes 0% exhaust bypass stack damper leakage, 3% blowdown, 1.5% radiation and unaccounted losses and 228°F feedwater for all cases
- Gas turbine pressure drops: Inlet - 4" H_2O, Exhaust - 10" H_2O
- No water or steam injection for NO_x control
- LM2500 and LM5000 values based on guarantee, not average performance

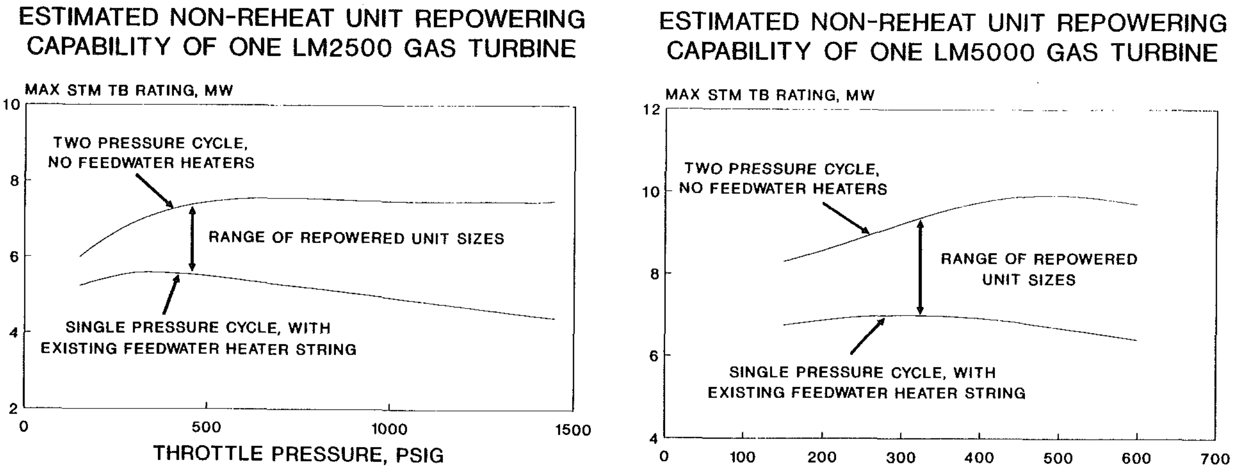

Fig. 7 Estimated unfired repowering capabilities of GE aeroderivative gas turbines

ranging from approximately 26 to 40 MW at 1250 psig throttle conditions. Adding the gas turbine output of 82.7 MW (from Table 1) gives a repowered cycle output ranging from 109 to 122 MW. Note that in the first case, the gas turbine rating is about three times that of the steam turbine, while in the latter the ratio is about two-to-one, the figure commonly used when referring to new combined-cycles.

Finally, since the 7F gas turbine has an exhaust temperature of 1091°F, it can be used to repower reheat turbines with throttle and reheat temperatures of up to 1000°F. A single 7F can satisfy the steam requirements of a 55 MW steam turbine if a straight boiler replacement is done. If the cycle can be optimized using three steam pressures and no feedwater heater, such as the cycle shown in Fig. 5(*D*), the corresponding unit size is approximately 75 MW.

Other Repowering Issues

As with any of the generation options available to the utility industry, there are a number of factors that must be considered in any evaluation to determine the economic choice. When evaluating repowering, the utility must also consider the following:

Reliability. Since the boiler is usually the plant component with the highest outage rates, replacing it with a modern, reliable GT/HRSG will result in higher reliability and availability. Furthermore, since the gas turbine can be operated independently of the steam turbine if equipped with an exhaust gas bypass, the plant can be used (at reduced capacity and efficiency) even if the steam turbine has an outage.

Environmental Issues. Combustion turbines have low

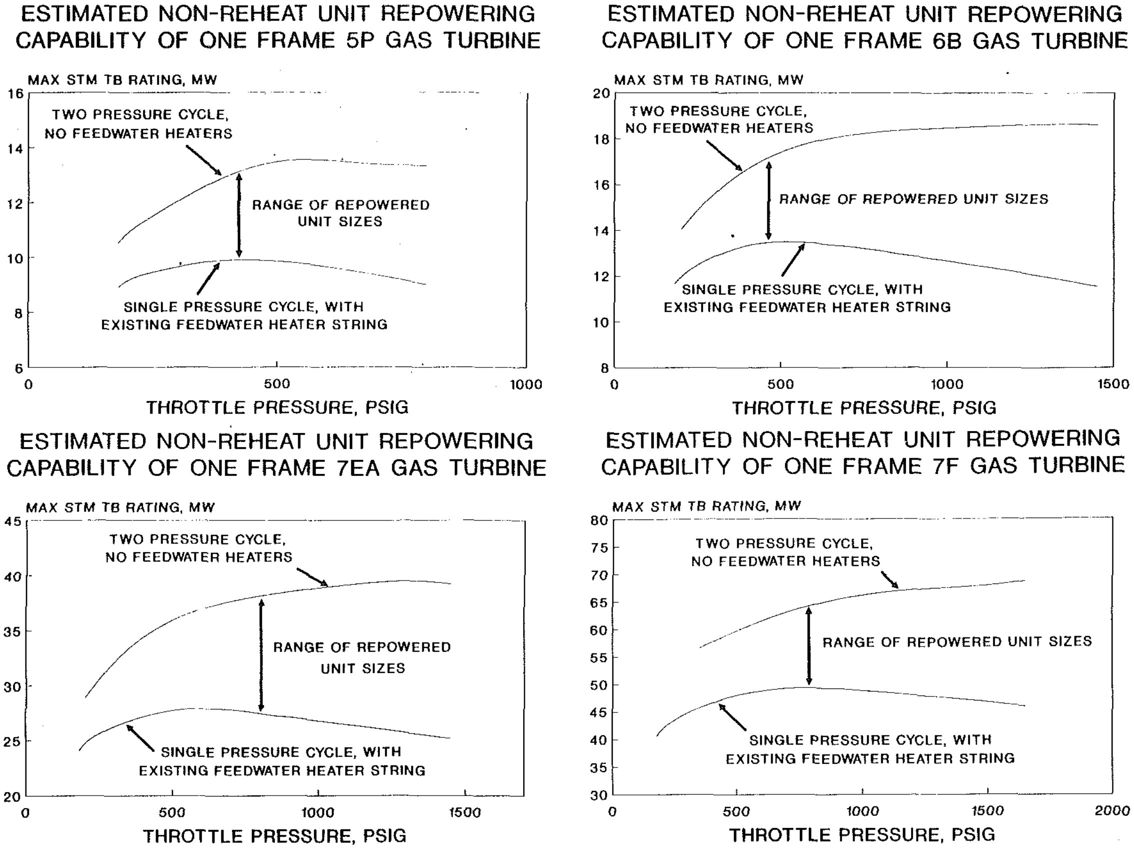

Fig. 8 Estimated unfired repowering capabilities of GE heavy-duty gas turbines

Table 2 GE gas turbine emissions with no steam or water injection

Model	Fuel	Rating,* kW	NO_X, ppm	Co, ppm
MS5001	Nat. Gas	26,300	135	10
	Distillate	25,800	202	10
MS6001	Nat. Gas	38,340	148	10
	Distillate	37,520	267	10
MS7001EA	Nat. Gas	83,500	154	10
	Distillate	82,100	228	10
MS7001F	Nat. Gas	150,000	179	25
	Distillate	147,210	276	25
LM2500PE	Nat. Gas	21,780	173	5
	Distillate	21,810	344	23
LM5000PC	Nat. Gas	33,070	216	3

* Rating at ISO Conditions in simple cycle application

Table 3 GE gas turbine emissions with steam injection

Model	Fuel	Rating,* kW	Steam Injection, lb/hr**	NO_X, ppm	CO, ppm
MS5001	Nat. Gas	27,680	15,900	42	10
	Distillate	27,380	18,180	65	10
MS6001	Nat. Gas	40,630	23,150	42	10
	Nat. Gas	42,720	44,978	25	40
	Distillate	40,230	27,620	65	10
	Distillate	41,400	40,600	42	10
MS7001EA	Nat. Gas	88,410	51,160	42	10
	Nat. Gas	90,030	68,400	25	25
	Distillate	87,640	57,820	65	10
	Distillate	89,170	74,270	42	10
MS7001F	Nat. Gas	160,580	95,853	42	25
	Distillate	159,160	111,420	65	25
LM2500PE	Nat. Gas	24,380	19,360	25	139
	Distillate	23,310	10,780	106	32
LM5000PC	Nat. Gas	39,820	36,620	25	84

* Rating at ISO Conditions in simple cycle application.
** Approximate flow rates

emissions of NO_x, CO, and SO_2, in most cases significantly lower than the emissions from conventional boilers This is a significant advantage to utilities having plants situated in pollution nonattainment areas or to utilities that will be affected by acid rain legislation, particularly if the steam plant currently uses sulfur-bearing fuels. With repowering, the unit capacity and output can be increased with a reduction in emissions. The actual emissions levels depend on the model gas turbine used, the type of fuel, and whether steam or water injection is utilized. Tables 2, 3, and 4 show the current emissions from GE gas turbines as a function of these parameters. These may then be compared to the existing unit emissions to determine the changes that will occur with repowering. The results of such a comparison will be site specific, depending on the existing fuel, type of firing, etc. and wide variations can be expected. Further reductions in combustion turbine NO_X emissions (to approximately 9 ppm with natural gas) are possible through the use of Selective Catalytic Reduction (SCR), although the use of this technology is costly.

Site Utilization. Repowering allows the utility to use a site already permitted for use as a generating station. This may simplify permitting, since the addition of the new equipment is a modification to an existing use rather than a new use for the site. This does not eliminate the need for new permits at the site, but could reduce the number required. In fact, it may

Table 4 GE gas turbine emissions with water injection

Model	Fuel	Rating,* kW	Water Injection, lb/hr**	NO_x, ppm	CO, ppm
MS5001	Nat. Gas	27,340	10,990	42	10
	Distillate	27,100	14,110	65	10
MS6001	Nat. Gas	40,050	16,020	42	10
	Distillate	39,340	17,460	65	10
MS7001EA	Nat. Gas	87,080	35,420	42	10
	Nat. Gas	88,360	46,200	25	25
	Distillate	85,450	33,730	65	10
	Distillate	86,650	45,970	42	25
MS7001F	Nat. Gas	158,100	58,860	42	25
	Distillate	155,630	61,660	65	25
LM2500PE	Nat. Gas	23,180	9,650	42	22
	Distillate	23,770	13,340	42	64
LM5000PC	Nat. Gas	35,680	15,690	42	13

* Rating at ISO Conditions in simple cycle application.
** Approximate flow rates

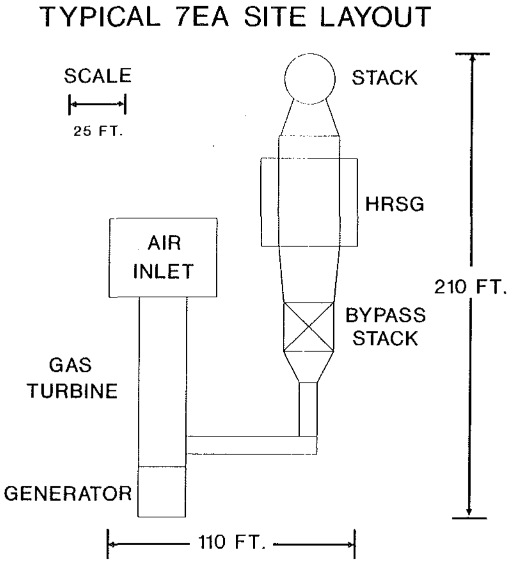

Fig. 9 Typical 7EA layout and space requirements

allow the utility to use a site that would not be permitted under current regulations.

Site Location. Many older plants are located closer to the load centers than the larger, newer plants on the utility system. If a plant is retired, rather than repowered, the capacity and energy it supplied must now be brought in from some other generation source. This could mean new investment in transmission lines and transformers. Further, the utility may need to install some form of voltage support, such as capacitors or Static Var Control (SVC), near the load center to compensate for the loss of the retired generator. However, if the unit is repowered, the additional generator will provide increased voltage support from the site.

Fuels. Since gas turbines require liquid or gaseous fuels, only natural gas, oil, or gasified coals can be used at the repowered unit. Because of the expense of the gasifier and associated equipment, and the additional space required for their installation, it is unlikely that coal gasification would be economic in repowering applications. This would force coal-fired sites to convert to either gas or oil. Natural gas use would depend on sufficient pipeline capacity located at a reasonable distance from the plant so that it would be economic to bring the fuel to the site. Conversion to oil would require the installation of new fuel handling, treatment, and storage facilities.

Since oil-fired steam plants commonly use lower grades of oil, additional fuel treatment equipment would be required in order to use these fuels in the combustion turbine, and unit performance will be poorer than with natural gas or distillate. Another option is to convert to distillate oil, but this would likely require some modifications to the existing fuel handling and storage facilities. A gas conversion is possible, although the economics are unlikely to be favorable because of the cost of a pipeline to the plant. Finally, even if the site will use the fuel currently burned, the adequacy of the fuel supply must be verified since the repowered cycle will burn approximately 75 percent more fuel than the existing steam plant.

Steam/Turbine and BOP Equipment. Even though the boiler has been replaced, the existing equipment being used in the repowered plant is likely to date back to the original startup date. Since equipment life is difficult to predict, the uncertainty associated with this will adversely affect the repowering economics. To counter this, the utility should consider upgrades to existing equipment being used in the repowered plant. For example, a new steam path or last-stage turbine buckets will improve the turbine reliability by using components with modern materials and design features that reduce stress levels. Efficiency will increase because modern steam path designs have better performance than the original and because the unrecoverable losses in the old components can be eliminated. Additional gains are possible if the new steam path will allow better integration of the GT/HRSG into the plant. In many instances, the economic benefits of the efficiency and reliability improvements will be great enough to justify the upgrade, particularly since the repowered unit will likely operate at a higher capacity factor than the original steam unit. The BOP should also be studied to identify other equipment that should be upgraded or replaced, particularly those that would force the steam unit out of service should they fail.

Site Space. Since new equipment is to be installed at an existing site, it is likely that site space will be at a premium. There is considerable flexibility in the arrangement of the GT, HRSG, and associated equipment and this will ease the difficulty of installation somewhat. However, installation costs will increase as the amount of space decreases and more complicated layouts are required. For particularly tight sites the boiler may have to be demolished to make room, with demolition complicated if asbestos removal is needed. (Recognize that the utility would eventually have to do this even if the unit were retired, so that the penalty arises from having to do the work now, rather than being able to delay it for several years.)

Typical layouts and component sizes for GE Frame 7EA and 7F gas turbines are shown in Figs. 9 and 10. The data in Table 5, which gives typical values for the effects of pressure drops on performance, can be used in determining the effects of plant layout on the overall plant performance.

All the preceding factors must be considered in an overall economic evaluation of repowering at a specific site. Depending on the unit, there may be other factors not mentioned that could have a significant impact. The results of any such evaluation will vary from site to site.

Repowering Economics

As described in this paper, many factors must be considered when evaluating the overall economics of repowering a given site. Because of the variability from site-to-site, it is clear that there will be a wide range in the results of economic evaluations.

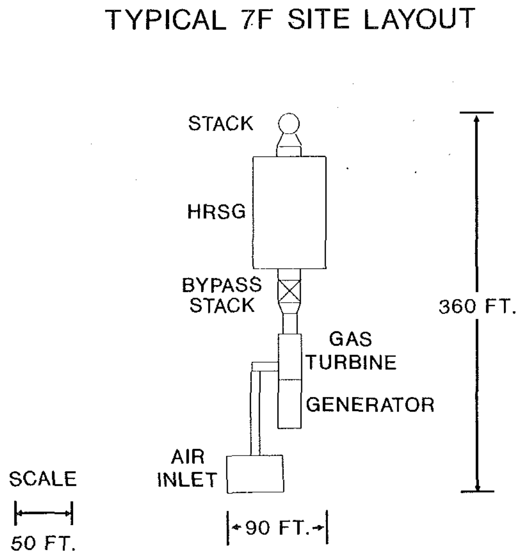

Fig. 10 Typical 7F layout and space requirements

Table 5 Typical pressure drop effects

Effect	4"H2O Inlet Pressure Drop Produces	4" H2O Outlet Pressure Drop Produces
Power Output Loss	1.42%	0.42%
Heat Rate Increase	0.45%	0.42%
Exhaust Temp Increase	1.9°F	1.9°F

Table 6 Repowered and combined-cycle data

Gas Turbine Data
Gas Turbine Model - 7EA
Gas Turbine Rating - 82.7 MW
Gas Turbine Heat Rate - 11,707 Btu/kWh (HHV)

New Combined-Cycle Data
Combined-Cycle Designation - STAG 107EA
Net Cycle Output - 123.5 MW
Combined-Cycle Heat Rate - 7870 Btu/kWh (HHV)
Estimated Installed Cost - $80.3 Million ($650/kW)

Steam Turbine Data	Minimum Case	Maximum Case
Throttle Pressure, psig	1250	1250
Unit Rating, MW	26	39
Heat Rate, Btu/kWh	11,500	11,500

Repowered Unit Data	Minimum Case	Maximum Case
Rating, MW	109	122
% Change from St Rating	+319	+209
Heat Rate, Btu/kWh (HHV)	8915	7920
% Change from St Heat Rate	-22	-31
Estimated Installed Cost (With AFUDC & Overheads)	$44.9 M	$48.0 M
Estimated Installed Cost (Based on total plant kW)	$413/kW	$393/kW
Estimated Installed Cost (Based on incremental kW)	$543/kW	$580/kW

As an example, consider a utility that is currently operating a gas or oil-fired steam plant that has a boiler that is in poor condition but with significant useful life left in the rest of the plant. This utility is evaluating repowering the steam turbine versus retiring the steam plant and replacing it with new generation. As shown in Figs. 7 and 8, there is a range of steam turbines that can be repowered with each GE gas turbine, with the actual rating depending on the steam conditions of the cycle and steam turbine-generator flow and loading limitations. Consider a 7EA gas turbine and a steam turbine operating at 1250 psig throttle conditions. Figure 8 shows that for the most restrictive condition, with a direct replacement of the boiler by the gas turbine/HRSG and no modifications to either the steam turbine or the feedwater heating system, a 26 MW steam turbine can be repowered (this will be called the "minimum case"). On the other hand, if the steam turbine has sufficient design margins so that it can be incorporated into a two-pressure cycle with no feedwater heating, the maximum steam turbine rating is 39 MW (this will be referred to as the "maximum case"). The performance of the alternative cycles is shown in Table 6. As shown in the table, the 13 MW difference in the repowered plant outputs results in a 995 Btu/kWh (11.2 percent) difference in heat rate.

Most utilities are finding that for new applications in which the capacity factor exceeds 15 percent, combined-cycle plants are the most economic type of capacity addition. Therefore, the economic comparison will be between a repowered plant and a new combined-cycle plant. The performance data for a new STAG 107EA unit are also included in Table 6. Comparing them to the repowered cycles, the outputs are higher by 1.2 to 13 percent. Estimated costs, which include AFUDC (Allowance for Funds Used During Construction) and overheads, are shown for the three alternatives. The cost difference between the two repowering options is due to the larger and more complex HRSG that must be supplied with the maximum case steam turbine. The economic analysis to be presented later in this paper will allow the utility to estimate how much incremental investment can be justified to get the additional output. Finally, plant costs for the repowered cycles are expressed as dollars per incremental kW of the resulting plant, and these range from $543/kW to $580/kW as compared to $650/kW for the new plant.

Although a power generation system planning study, using a generation planning decision simulation computer model, is the most accurate way to evaluate the repowering option, it is often useful to approximate the results with an analytic economic evaluation method. This is done as follows: Because of the high heat rate of the original steam plant, it is likely that it was used for peaking duty, with an annual capacity factor approximately 10 percent. If it is repowered or replaced with a new combined-cycle, the plant will run at higher capacity factors (approximately 50 percent) since it will have one of the best heat rates on the system. The economic evaluation must compare the total costs of operating the different generation options given this assumed dispatch. Included in these costs are the following:

1 **Fuel Costs.** Since all three cycles use the same gas turbine and operate at the same capacity factors, fuel costs will be the same.

2 **Replacement Energy Cost.** Since the three options have different capacities, they will produce differing amounts of energy (MWh) when run at the same capacity factor. If the new combined-cycle is taken as the basis of comparison, then the two repowering options will generate fewer MWh. In order to meet its energy demand, the utility must generate the difference with some other unit on the system, at a higher cost. This cost, the replacement (or incremental) energy cost, is the $/MWh cost of producing one additional MWh from the system. In a system with multiple generating units, the replacement energy cost is equal to the operating cost of the most expensive (last unit dispatched) unit operating on the system at that time. The value will fluctuate during the day as well as during the year, being greatest during the peak periods. For

Table 7 Economic evaluation data

Unit Fuel Cost	$3.00/MMBtu
System Replacement Energy Cost	
At Peak	$36/MWh
Off-Peak	$30/MWh
Economic Evaluation Period	20 Years
Present Worth Discount Rate	10%/Year
Inflation Rate	5%/Year
Levelized Fixed Charge Rate	18%/Year

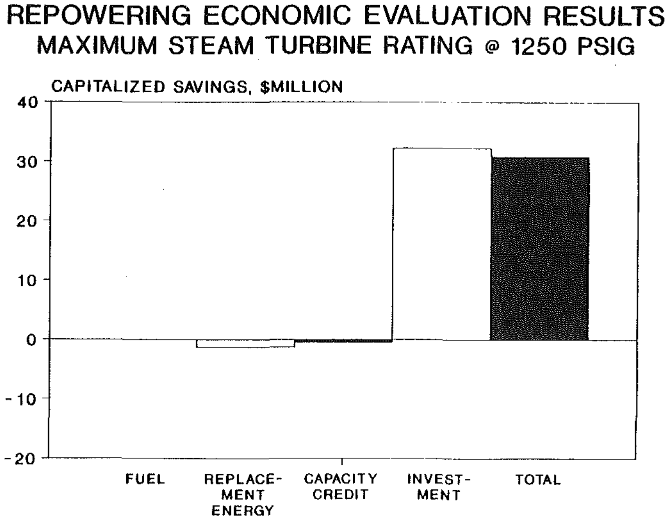

Fig. 11 Maximum case evaluation results

example, during peak periods, the energy might be generated by units with heat rates of 12,000 Btu/kWh (HHV), while at other times it might be produced by units operating with 10,000 Btu/kWh heat rates. With fuel costs of $3/million Btu (typical of gas or oil), the replacement energy costs are $36/MWh and $30/MWh, respectively. In calculating this cost, all units are assumed to run at 50 percent annual capacity factor, with 10 percentage points occurring during the peak periods, and the balance during off-peak times.

3 **Capacity Cost.** In order to maintain the same system reserve margin, the generation options must have the same capacity. If not, additional capacity must be installed to put them on the same basis. This additional capacity is typically based on the installed cost of new peaking gas turbines ($350/kW).

4 **Investment.** This is the cost of installing each option. The economic data used in the evaluation are given in Table 7. The evaluation results are shown in Fig. 11 for the maximum case, and the capitalized advantage for repowering is $30.9 million. Because the performance of the maximum case unit is so close to that of a new combined-cycle the replacement energy and capacity costs are less than 10 percent of the total evaluation. This means that the results are affected only by the relative installation costs of the two options. Even large changes in the other economic assumptions will have little effect on the results. For this situation, the utility can justify the expenditure of another $30.9 million (or a total of $78.9 million) for the repowering and still have evaluated costs equal to those of a new combined-cycle.

On the other hand, even though the replacement energy and capacity charges are a relatively small fraction of the total evaluation, they still amount to $1.8 million. Therefore, the utility would be justified in spending up to that amount if it could increase the unit performance to that of a new combined-cycle unit. Therefore, upgrades of the steam turbine generator should also be studied when the repowering option is considered, since it can be economically attractive.

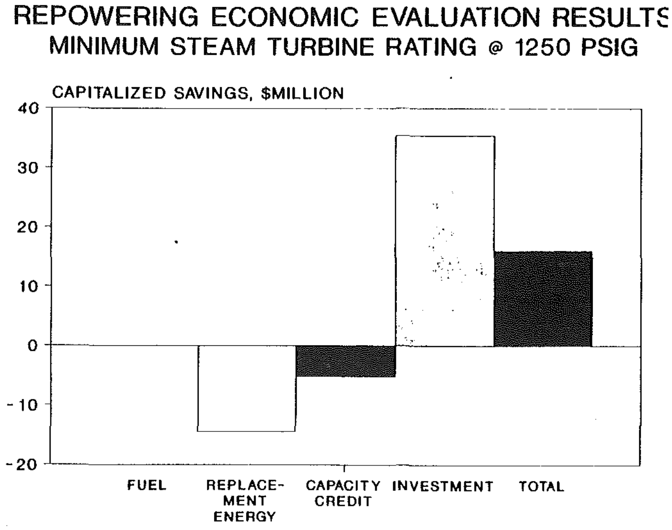

Fig. 12 Minimum case evaluation results

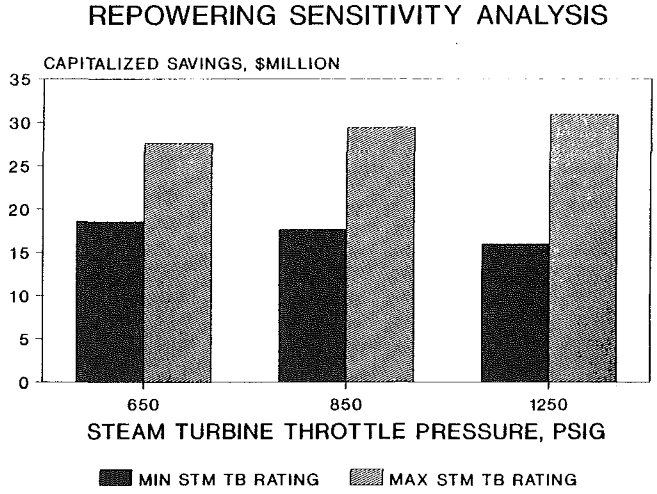

Fig. 13 Sensitivity analysis versus throttle pressure

Similar information for the minimum case is shown in Fig. 12, with the benefits totalling $16.0 million. In this case, replacement energy and capacity costs are significant because of the large performance difference relative to the new combined-cycle. For example, if capacity were valued at the cost of a combined-cycle plant, rather than gas turbines, the overall benefits would drop to $11 million. A similar effect would result if fuel prices were to rise to $4/MMBtu.

Finally, comparing the results of the minimum and maximum cases, the incremental benefit of the larger capacity repowered unit is $30.9 − 16.0 or $14.9 million. Therefore, the utility could justify the expenditure of up to $14.9 million to convert the steam turbine to two-pressure steam admission with no feedwater heater extractions.

Since the evaluation is strongly affected by the performance of the repowered cycle, the evaluations were repeated using the 7EA gas turbine, but with steam turbines having other throttle pressures. Figure 13 shows the results for minimum and maximum cases at pressures of 650 psig and 850 psig, as well as the 1250 psig pressure previously discussed. Savings are greatest for the highest throttle pressure in the maximum case, and the lowest throttle pressure in the minimum case.

Also, since the difference in savings between the maximum and minimum cases increases with throttle pressure, the utility can justify higher incremental expenditures for conversion to a two-pressure system with no feedwater heating at 1250 psig than at 650 psig.

Conclusions

Repowering can be an economically attractive generation option for electric utilities that have existing older steam units still in service. In the United States, there are almost 30 GW of nonreheat and reheat steam turbines 30 years of age or older that are potential repowering candidates. A site-specific evaluation that considers such factors as the condition of the existing equipment that will be used in the repowered plant, match between the steam turbine and available gas turbines and heat recovery equipment, fuel availability and cost, site space, etc., will be required to determine the overall economics. While not all of the 30 GW are going to have positive economics, it is clear that given the right situation, repowering can result in significant savings for the utility.

Conversion Factors for Tables and Figures

$k_g/hr = lb/hr \times 0.4536$

$°C = (°F - 32) \times 5/9$

$k_j/hr = Btu/hr \times 1.055$

$kPa = in.\ H_2O \times 0.2488$

$kPa = (psig + 14.7) \times 6.895$

References

1 Kovacik, J. M., and Stoll, H. G., "The Economics of Repowering Steam Turbines," presented at the American Power Conferences, April 1990.

2 Chase, D. L., et al., "GE Combined-Cycle Product Line and Performance," GER-3574A.

3 Allen, R. P., and Triassi, R. P., "GE Gas Turbine Performance Characteristics," GER-3567.

4 Schorr, M. M., "Legislation and Regulations Affecting Power Generation Systems," GER-3575A.

5 Schorr, M. M., "NO_x Control for Gas Turbines: Regulations and Technology," presented at the Association of Energy Engineers World Energy Engineering Congress, Oct. 11, 1990.

6 Kaupang, B. M., "Combined-Cycle Economics," GER-3584A.

H. H. Finckh
Head of Department,
Gas Turbine and Combine Cycle Technology,
Siemens AG, KWU Group,
Erlangen, Federal Republic of Germany
Mem. ASME

H. Pfost
Professor, Director,
Institute of Energy Technology,
Ruhr-University,
Bochum, Federal Republic of Germany

Development Potential of Combined-Cycle (GUD) Power Plants With and Without Supplementary Firing

Unfired combined cycles achieve superior efficiencies at low emission levels. The potential and efficiency limits are investigated and the possibilities for enhancing efficiency are described. It is demonstrated that limited supplementary firing of the heat recovery steam generator can be an interesting alternative and that this allows efficiency and plant size to be increased. The effects of supplementary firing on NO_x *emissions are also shown.*

Introduction

Large-output combined cycle (*CC*) plants achieve maximum efficiency at low emission values and low investment costs. They are therefore superior to all other fossil-fired power plants and still have the potential for further efficiency improvements in the future. The construction of such plants presupposes, however, the availability of oil or natural gas as high-grade fuels for the gas turbine.

From the thermodynamic point of view, the high efficiency potential of the *CC* plant is attributable to two inherent characteristics of the gas turbine:

- In simple cycle gas turbines, efficiency is improved by the fact that, for the sake of maximum Carnot efficiency, the fuel heat is transferred directly to the working fluid at a high upper process temperature [1].
- The high exhaust gas temperature of the gas turbine, which at first glance appears to be a drawback, actually opens up an additional source of high-exergy heat, which is exploited in a bottoming water/steam cycle.

The superiority of this type of power plant is the result of decades of development and has been influenced by energy crises, environmental problems, public attitudes and, last but not least, by competition among manufacturers.

Figure 1 shows, as an example, a general view of the 1350-MW GUD® combined-cycle power plant at Ambarli, Turkey [2]. It consists of three parallel blocks with a total of six gas turbines, six heat recovery steam generators, and three condensing turbines. The plant is operated on natural gas as its primary fuel, but heavy residual oil is available as an alternative.

This paper attempts to establish the limits to which efficiency can be improved while keeping expenditure to a reasonable level. The cycle concepts compared are currently feasible unfired combined-cycle configurations.

Since the maximum output rating of any gas turbine is governed by the size of the manufacturer's model, it is evident that larger plant outputs can only be achieved by combining a number of single units. This means that the plant size can be increased in large steps only. The question is considered to what degree the introduction of supplementary firing permits fine adjustment of the plant size without loss of efficiency. The effects of supplementary firing on emissions are investigated, too.

Mention should also be made in this context of the steam injection gas turbine (STIG) concept, which results in a limited increase in gas turbine output while reducing NO_x emissions. If this method is applied in an unfired combined cycle, however, both steam turbine output and overall plant efficiency decrease. There is therefore no economic advantage to be expected, as a recent EPRI study reports [3].

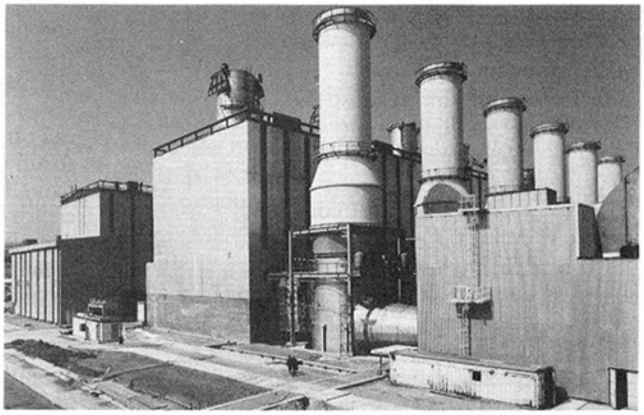

Fig. 1 The 1350-MW Ambarli GUD power plant under construction

---

Contributed by the International Gas Turbine Institute and presented at the 36th International Gas Turbine and Aeroengine Congress and Exposition, Orlando, Florida, June 3-6, 1991. Manuscript received at ASME Headquarters March 4, 1991. Paper No. 91-GT-227. Associate Technical Editor: L. A. Riekert.

Thermodynamic Limits

In any thermal power plant, including the combination of gas and steam cycles, the aim is to make the maximum possible use of the convertible portion of the energy, i.e., the exergy of the fuel. In the simplest form of combined cycle, the unfired type, fuel energy is released in the gas turbine combustion chamber only. The specific thermal energy fed into the process at constant pressure in the form of fuel is

$$q=\int_{T_2}^{T_3} c_p\,dT. \tag{1}$$

A more general equation for the heat input, which is valid for any change of state and describes the entropy increase, is

$$dq=T\,ds \tag{2}$$

Applied to the gas turbine combustion chamber and the entire combined cycle shown in the T,s diagram in Fig. 2, the equation is

$$q=\int_{s_2}^{s_3} T\,ds=T_m(s_3-s_2) \tag{3}$$

where T_m is the average heat input temperature.

The quality of the thermal energy and the limits of convertibility into mechanical energy can be illustrated by means of the Carnot process.

The Carnot efficiency η_c depends on the one hand on the upper temperature level T, at which the heat is input, and on the other on the level of T_l, at which the portion of the nonconvertible rejected heat has to be released to the environment. The following applies:

$$\eta_c=1-\frac{T_l}{T}. \tag{4}$$

η_c reaches its highest value when T is as high as possible and T_l as close to the ambient temperature T_a as possible. If this principle is applied to the CC process, the maximum recoverable specific work, under ideal conditions, i.e., with no internal losses, is, in differential form

$$dw_c=\eta_c dq \tag{5}$$

In greater detail, this is

$$dw_c=\left(1-\frac{T_a}{T}\right)c_p\,dT. \tag{6}$$

and, for the entire idealized CC process, with heat input from T_2 to T_3 in accordance with Fig. 2

$$w_c=\int_{T_2}^{T_3}\left(1-\frac{T_a}{T}\right)c_p\,dT. \tag{7}$$

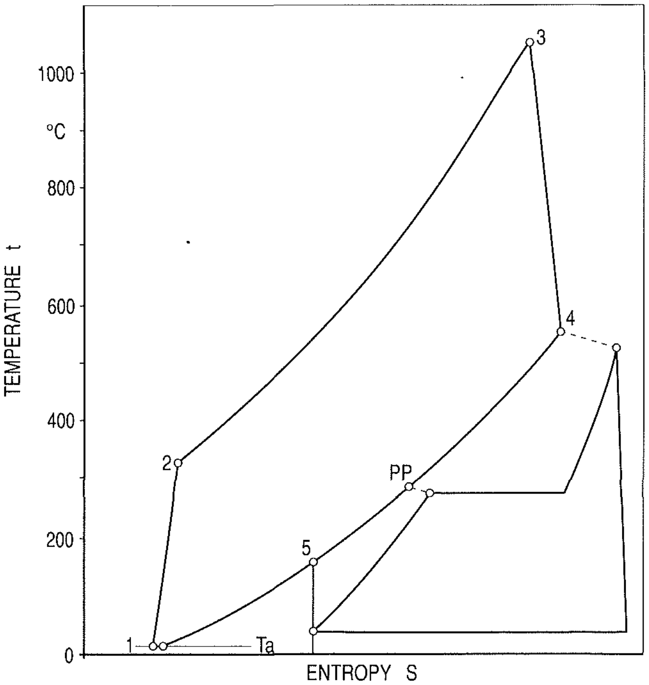

Fig. 2 ***T,s* diagram of the unfired combined cycle**

This equation corresponds to the exergy of the heat input. On the basis of the above equations, the maximum CC efficiency is

$$\eta_{c,\max}=\frac{w_c}{q}. \tag{8}$$

If this equation is applied to an advanced gas turbine where the temperature limits are $t_2=400°\mathrm{C}$ and $t_3=1250°\mathrm{C}$, at full utilization of the exergy down to an ambient temperature of $t_a=15°\mathrm{C}$, a Carnot efficiency of $\eta_{c,\max}\simeq 73$ percent could be achieved.

With a given gas turbine plant, the interesting question is how much of the energy in the gas turbine exhaust gases can be converted into mechanical energy in a bottoming steam cycle.

In Fig. 2 the cooldown curve runs from T_4 to T_5, where T_4 is fixed, being the gas turbine exhaust temperature. The closer T_5 is to the ambient temperature T_a, the more heat can be transferred in the heat recovery steam generator. In accordance with Eq. (7), but with the limits T_4 and T_5, the specific work that can theoretically be recovered from the gas turbine exhaust gas in the heat recovery steam generator is

Nomenclature

c_p = specific heat capacity
$\dot{m}_C$ = compressor air flow
$\dot{m}_S$ = mainsteam flow
$\dot{m}_T$ = gas turbine exhaust flow
P_G = gas turbine output
P_S = steam turbine output
P_{CC} = combined cycle output
P^* = specific output of combined cycle = $P_{CC}/\dot{m}_C$
q = specific heat flow
$\dot{Q}_G$ = heat flow to the combustion chamber
$\dot{Q}_F$ = heat flow to the duct burner
s = specific entropy
S = entropy
t = temperature
T = absolute temperature
w_c = specific work
η_B = efficiency of heat recovery steam generator
η_G = gas turbine cycle efficiency
η_S = steam cycle efficiency
η_{CC} = overall combined cycle efficiency
η_{CCF} = overall plant efficiency of combined cycle with supplementary firing
η_T = isentropic steam turbine efficiency
λ = air ratio of available air to air required for stochiometric combustion

Subscripts

a = ambient
c = Carnot
C = compressor
l = low
m = mean
MS 1 = high-pressure main steam
MS 2 = low-pressure main steam
S = steam

Abbreviations

CC = combined cycle
HRSG = heat recovery steam generator
PP = pinch point
LP = low pressure
HP = high pressure

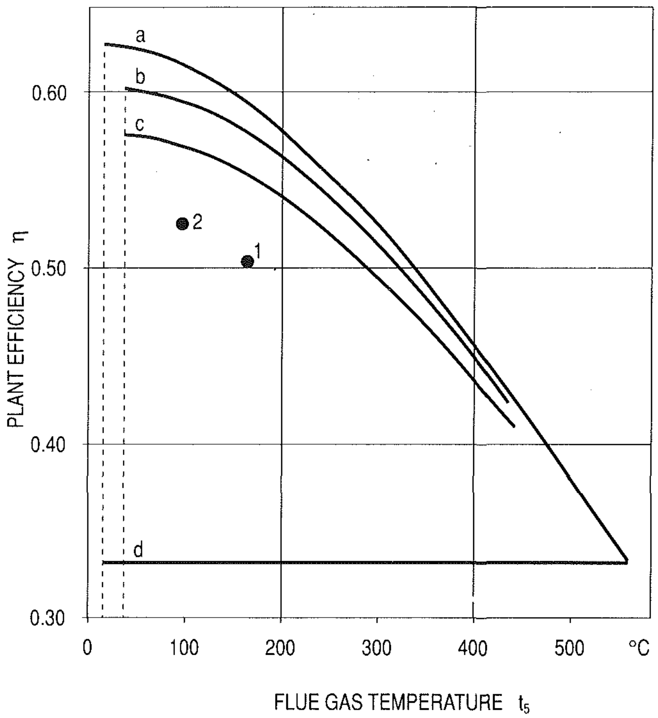

Fig. 3 Theoretical efficiencies of combined cycles as a function of the temperature at the flue gas outlet and comparison with values achieved. Curve (*a*): heat removal from the ideal heat recovery cycle at $t_l = t_a = 15°C$; curve (*b*): heat removal at $t_l = 35°C$, ideal heat recovery cycle; curve (*c*): heat removal at $t_l = 35°C$, ideal heat transfer, losses in the heat recovery cycle only allowed for steam turbine ($\eta_T = 90$ percent); curve (*d*): gas turbine cycle efficiency η_T without exhaust heat recovery; point 1: single-pressure combined cycle; point 2: dual-pressure combined cycle.

$$w_{c,\max} = \int_{T_5}^{T_4} \left(1 - \frac{T_a}{T}\right) c_p \, dT. \tag{9}$$

Considering the mass flow $\dot{m}_T$ of the gas turbine exhaust, the maximum achievable output of the steam cycle can therefore be obtained as

$$P_{s,\max} = \dot{m}_T \, w_{c,\max}. \tag{10}$$

With the output P_G of the gas turbine, the maximum output of the *CC* plant is

$$P_{CC,\max} = P_G + P_{S,\max}. \tag{11}$$

With the efficiency η_G of the gas turbine cycle, the associated plant efficiency is

$$\eta_{CC,\max} = P_{CC,\max}/\dot{Q} = \eta_G (1 + P_{S,\max}/P_G). \tag{12}$$

This equation can be solved for a given gas turbine. What first becomes apparent is that the maximum overall efficiency $\eta_{CC,\max}$ depends to a large degree on the efficiency of the gas turbine cycle. It is therefore here that efficiency improvements have top priority. In this context, the main development objectives are:

- Raising the turbine inlet temperature where the compression ratio as an optimizing parameter has only a minor effect on the overall process.
- Improving the component efficiencies of both the compressor and the turbine, and the overall efficiency of the entire gas path.

On the basis of Eq. (12), the question now considered is the maximum plant efficiency that can theoretically be attained in a *CC* plant with a known gas turbine output and efficiency.

In Fig. 3, curve (*a*) represents the upper limit of the theoretical *CC* efficiency, with complete utilization of the exhaust gas energy, as a function of the exhaust gas temperature at the steam generator outlet. It is shown that, after virtually complete cooling of the exhaust gases to the ambient temperature of $t_a = 15°C$, the efficiency is nearly 63 percent. The exhaust gas from the heat recovery steam generator can, however, not be released at ambient temperature.

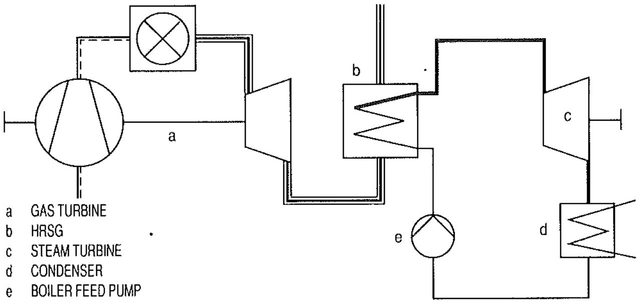

Fig. 4 Simplified flow diagram of combined cycle plant with single-pressure steam cycle

Taking into account a practicable temperature difference of $\Delta t = 20$ K in the cooling system at a realistic condenser pressure but otherwise idealized steam cycle, the theoretical curve (*b*) is obtained. These values can of course not be attained, as they presuppose components without any internal losses. Taking a steam turbine efficiency of $\eta_T = 0.9$ into account, the result is curve (*c*).

The fact that transfer of the exhaust gas heat to the water/steam cycle in the steam generator can only take place in the presence of a temperature difference results in further energy losses. Taking into account the finite temperature differences and the variable heat capacity on the water/steam side, the temperature at the boiler outlet is Δt_a above the ambient temperature, i.e, $t_5 = t_a + \Delta t_a$. At $t_5 = 90°C$, curve (*c*) shows a maximum figure of 57 percent.

When the efficiencies achieved by existing, modern plants are entered in this diagram, it becomes apparent that they still fall short of the theoretical limit represented by curve (*c*). The challenge faced by design engineers is to minimize these differences, while nonetheless further improving the cost-effectiveness of the plant. Simple measures for improving the process are investigated below.

Technology of Combined-Cycle Configurations

These considerations are based on a combined cycle with a single pressure stage heat recovery steam generator (HRSG) as shown in Fig. 4. In order to get as close as possible to the exhaust gas temperature, high main steam temperatures are advantageous. The first question to be considered is what optimum main steam pressure should be selected. The main steam pressure dictates the temperature at which evaporation sets in, i.e., the pinch point, thereby also determining the main steam mass flow that can be generated. Finally, the extent of exhaust gas cooling is also determined by the main steam pressure selected.

A diagram showing *t,q* interdependences illustrates this point. Figure 5(*a*) is a standard *t,q* diagram, which plots temperature profiles to show the heat flow from the flue gas to the water/steam cycle. It is apparent that the flue gas can be cooled further when the main steam pressure is kept low. The integral

$$\int (1 - T_l/T) \, dq \tag{13}$$

describes the maximum exergy, where the ratio T_l/T is a measure of the exergy loss. In Fig. 5(*b*) T_l/T is plotted as a function of q.

It can be seen that at high main stream pressure, the losses in the low-temperature range (area A) are dominant. At low main stream pressures the losses in the high-temperature range

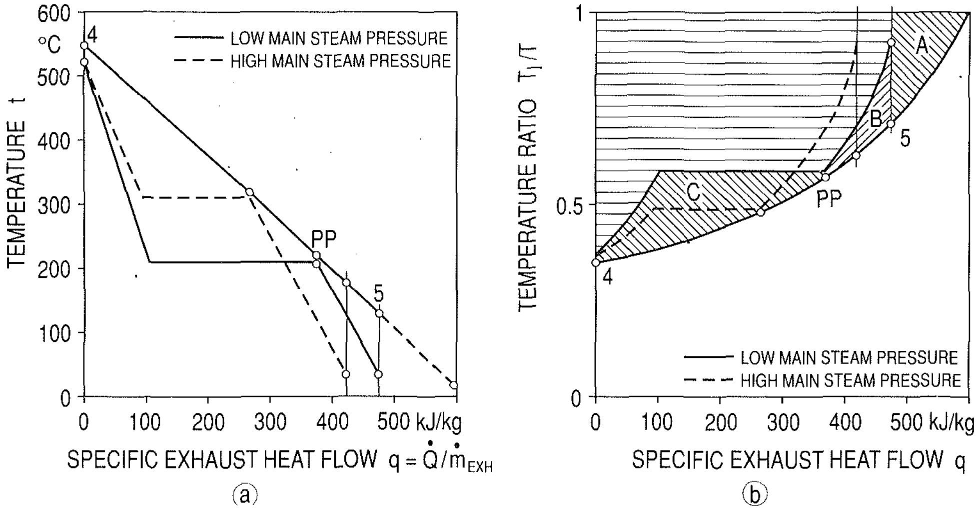

Fig. 5 Exhaust heat transfer in t,Q diagram (a) and in $T_l/T,Q$ diagram (b) as a representation of the exergy loss

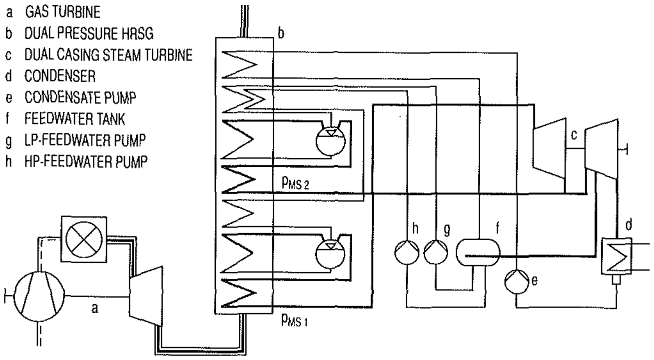

Fig. 6 Flow diagram of a dual-pressure unfired combined cycle

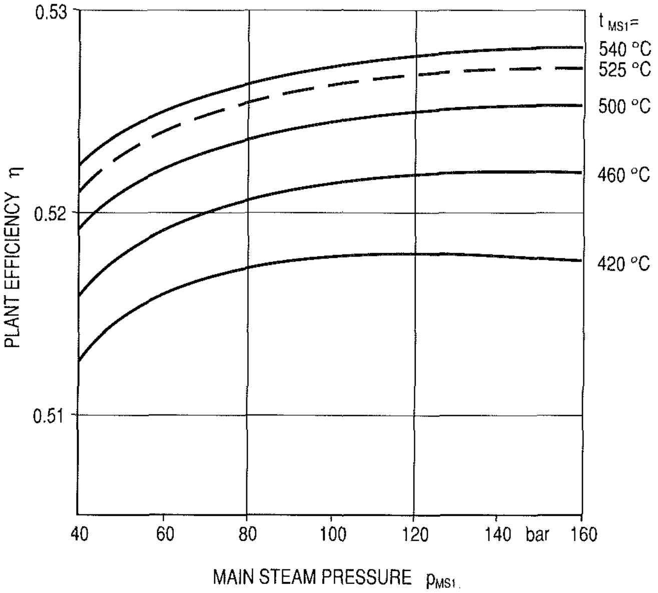

Fig. 7 Efficiency of the combined cycle with dual-pressure steam cycle as a function of the main steam pressure $p_{MS\,1}$ and for various main steam temperatures $t_{MS\,1}$

(area C) prevail. The optimum main steam pressure has been reached when the sum of the areas A + B + C is at a minimum, thus also minimizing the exergy losses.

On the basis of this premise, there are two ways of improving efficiency:

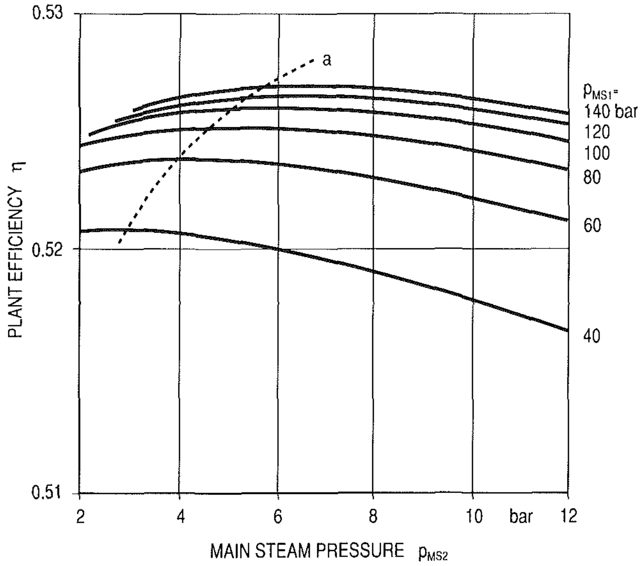

Fig. 8 Efficiency of the combined cycle with dual-pressure steam cycle as a function of the pressure $p_{MS\,2}$ of the secondary steam for various main steam pressures $p_{MS\,1}$

- In the low-temperature region the introduction of a second pressure stage with low main steam conditions ensures more extensive utilization of the exhaust heat than in the single-pressure cycle. Figure 6 shows the configuration for a dual-pressure combined cycle. Figure 7 represents the efficiency patterns as a function of the HP main steam pressure. As the influence of losses in the low-temperature range is reduced by the second pressure stage, the optimum main steam pressure shifts to a higher level. Fine adjustment of plant efficiency takes into consideration, as shown, in Fig. 8, the fact that the optimum second pressure also increases as the main steam pressure rises (curve a).
- In the high-temperature range, as much heat as possible should be fed into the steam cycle. This can be achieved by incorporating a reheat stage. As is the case with pressure increase, the introduction of a reheat system also reduces the heat transfer losses in the high-temperature range. Figure 9 shows the efficiency increases attained with a reheat system.

Supplementary Firing

The output of an unfired combined-cycle plant is determined by the rating of the gas turbine and by the amount of usable

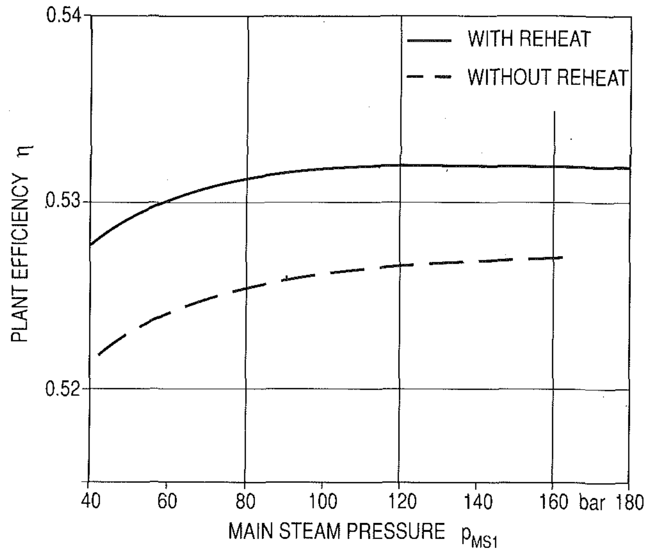

Fig. 9 Efficiency of the combined cycle with dual-pressure steam cycle as a function of the main steam pressure with and without reheat system

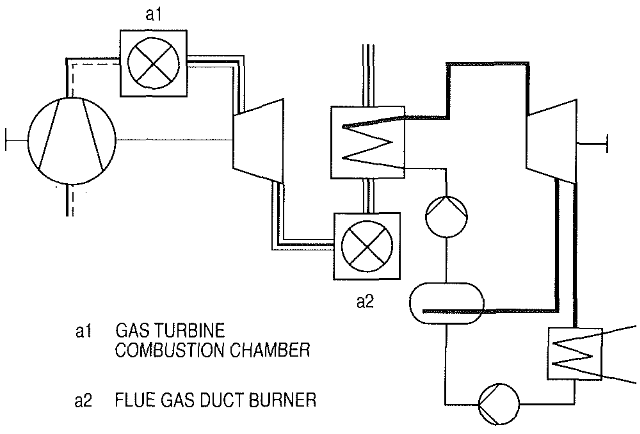

Fig. 10 Simplified flow diagram of a combined-cycle plant with supplementary firing

exhaust heat that can be exploited in a bottoming steam cycle, and can be influenced to a limited degree only by the thermal cycle configuration. Lower unit ratings can only be achieved by running in part-load operation. This, however, always results in reduced efficiency.

An increase in power plant output would normally mean adding a second unit, thus doubling the output. Finer upward adjustment of the design rating can be achieved by introducing supplementary firing in the exhaust gas duct of the heat recovery steam generator (Fig. 10). Natural-gas-fired duct burners are suitable for this purpose as they can easily be operated in an exhaust gas atmosphere with an oxygen content of 15.6 percent.

The efficiency equation for this extended cycle is now

$$\eta_{CCF}=\frac{P_G+P_S}{\dot{Q}_G+\dot{Q}_F}. \tag{14}$$

$\dot{Q}_G$ is the heat added in the gas turbine combustion chamber; $\dot{Q}_F$ is the heat input of the duct burner. The efficiency of the unfired *CC* can be derived from this equation by taking $\dot{Q}_F$ to be zero.

It is well known that conventional steam power plants, even of advanced design, do not achieve the same degree of efficiency as unfired combined cycles. One would therefore initially expect supplementary firing, by increasing the output of the steam cycle, to lower the plant efficiency. This is not necessarily the case.

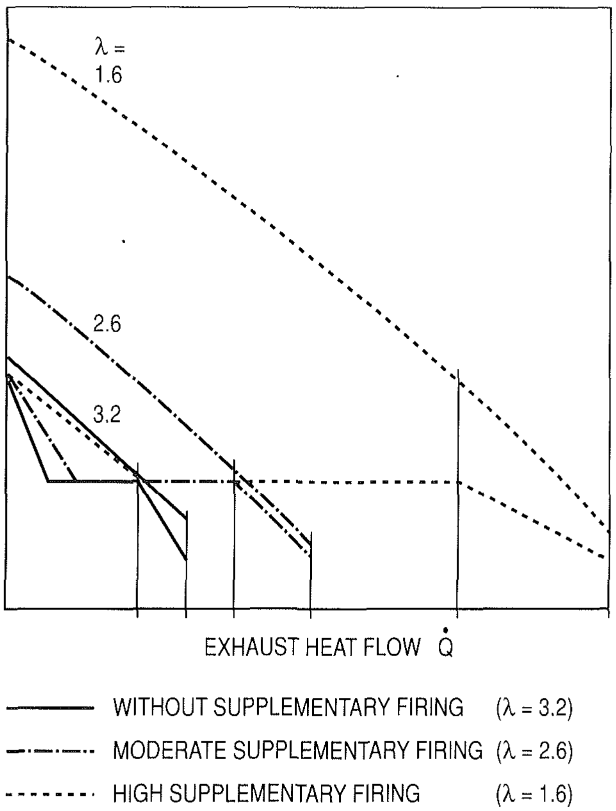

Fig. 11 *t*,*Q̇* diagram for transfer of exhaust heat to a single-pressure cycle at various degrees of supplementary firing (without supplementary firing (*SF*): λ = 3.2; low *SF*: λ = 2.6; high *SF*: λ = 1.6)

This can be illustrated by considering the efficiency in detail, taking into account the $t,\dot{Q}$ diagram for the heat recovery steam generator as shown in Fig. 11.

The extended equation for overall plant efficiency reads

$$\eta_{CCF}=\frac{\eta_G\dot{Q}_G+\eta_S\eta_B[(1-\eta_G)\dot{Q}_G+\dot{Q}_F]}{\dot{Q}_G+\dot{Q}_F}. \tag{15}$$

It includes the efficiencies of the gas turbine cycle η_G, of the steam cycle η_S, and of the heat recovery steam generator η_B.

Figure 11 shows how the exhaust gas cool-down curve and the feedwater heat-up curve approach each other with moderate supplementary firing. The curves are parallel and the distance between them is at its smallest when the heat capacities on the water side and on the flue gas side are about the same, that is, when

$$\dot{m}_G c_{pG}=\dot{m}_S c_{pS}. \tag{16}$$

This is the case in the present example of a single-pressure cycle at an air-to-fuel ratio of λ about 2.6. Thanks to extensive cool-down of the flue gas, the boiler efficiency has now reached its maximum value.

As long as η_B can be raised significantly and the steam cycle efficiency η_S does not decrease dramatically, supplementary firing can result in an efficiency gain.

In Fig. 12 the overall efficiency of a single-pressure reheat cycle is plotted as a function of the specific output. It can be seen that with supplementary firing of as much as $\dot{Q}_F/\dot{Q}_G \simeq 0.3$, and with high main steam pressures, the efficiency rises.

In the case of a dual-pressure reheat cycle, as shown in Fig. 13, the efficiency increase at high main steam pressure is hardly noticeable. Nonetheless, supplementary firing of up to 30 percent can also be applied here without resulting in a loss of efficiency.

Emissions and Byproducts

In view of anthropological climatic changes, the reduction of emissions, exhaust heat, and other byproducts from fossil-fired power plants has become a top priority objective. The emissions from combustion processes depend on the design of the power plant, on the type and quality of the fuel, on the application of fuel conditioning (primary measures) and flue gas cleaning (secondary measures).

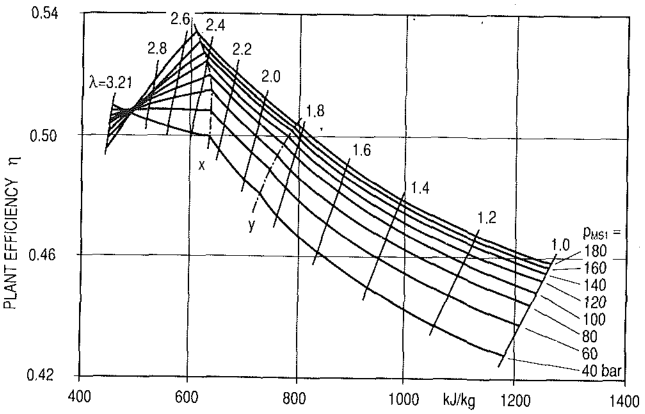

Fig. 12 **Efficiency of the combined cycle with single-pressure reheat cycle as a function of the overall specific output at various supplementary firing fractions and various main steam pressures**

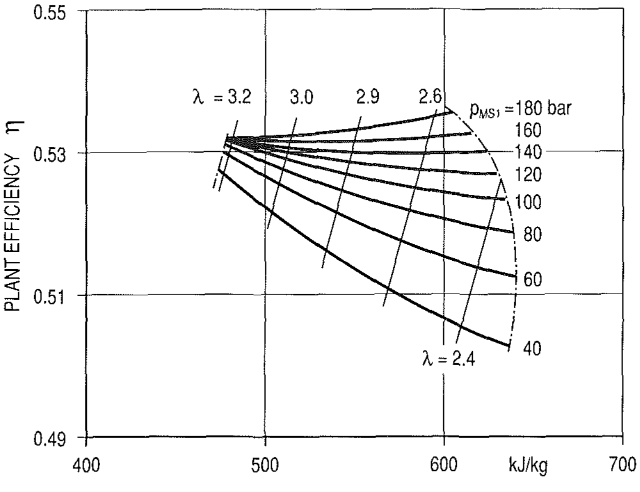

Fig. 13 **Efficiency of the combined cycle with dual-pressure cycle and reheat as a function of the overall specific output at various degrees of supplementary firing and various main steam pressures**

In view of the fact that CO_2 in the stratosphere contributes to the greenhouse effect, special attention must be paid to reducing CO_2 emissions in power plants. Fuels with a high hydrogen-to-carbon ratio, such as natural gas, produce less CO_2 when combusted than coal. Natural gas should therefore be utilized wherever possible. The other effective way of reducing CO_2 emissions is to raise the generating efficiency of the power plant, i.e., the percentage of chemical energy in the fossil fuel that is converted into electricity.

In the thermal cycle configurations described above, the availability of the high-grade fuel natural gas is presupposed. The emissions resulting from its combustion are restricted to CO_2, H_2O, NO_x, and exhaust heat. Other byproducts such as SO_2, ash, and gypsum, which are produced in the combustion of coal, do not occur.

In order to arrive at a meaningful comparison of the individual power plant types, the data on emissions and byproducts are referred to 1 kWh of generated electric power. Figure 14 compares the various natural-gas-fired combined-cycle plants, i.e.,

- the fully fired combined cycle
- the unfired combined-cycle power plant
- the unfired combined-cycle unit with supplementary firing

The combustion product and exhaust heat figures of a modern hard-coal-fired unit with desulfurization and $DeNO_x$ are taken as a reference [4].

It is apparent that natural-gas-based fully fired combined-cycle plants release about 50 percent and unfired combined cycles with and without supplementary firing only around 40 percent of the CO_2 emissions produced by the hard-coal-fired unit.

As a result of advances in gas turbine burner technology, NO_x emissions from unfired and fully fired plants are down to less than 50 percent of modern coal-fired plants.

In the case of *CC* plants with supplementary firing, the specific NO_x emissions remain more or less on the same level as for an unfired *CC* power plant without supplementary firing. This is due to the fact that extra NO_x produced by the duct burners is compensated by the extra output generated by the steam turbine cycle.

In a comparison of the exhaust heat figures, the combined-cycle plants show better results on account of their greater efficiency level.

Conclusions

1 Investigation of the exergy limits for combined cycles

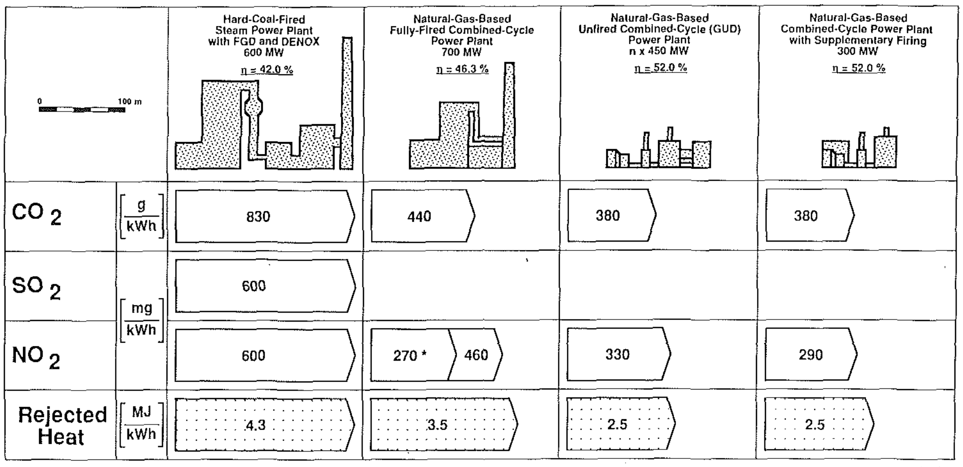

		Hard-Coal-Fired Steam Power Plant with FGD and DENOX 600 MW η = 42.0 %	Natural-Gas-Based Fully-Fired Combined-Cycle Power Plant 700 MW η = 46.3 %	Natural-Gas-Based Unfired Combined-Cycle (GUD) Power Plant n x 450 MW η = 52.0 %	Natural-Gas-Based Combined-Cycle Power Plant with Supplementary Firing 300 MW η = 52.0 %
CO_2	[g/kWh]	830	440	380	380
SO_2	[mg/kWh]	600			
NO_2		600	270 * 460	330	290
Rejected Heat	[MJ/kWh]	4.3	3.5	2.5	2.5

* best measured value

Fig. 14 **Comparison of emissions and rejected heat from various types of power plant**

shows that there is a usable efficiency potential of about 60 percentage points.

2 This also applies where an existing gas turbine is involved. In this instance, fine adjustment of the main steam pressure and the introduction of a reheat system are of great significance.

3 The introduction of supplementary firing permits, within certain limits, an increase in unit output without a reduction in overall plant efficiency, provided that boiler efficiency is improved and the main steam conditions raised.

4 In spite of the supplementary firing, there is no more than a negligible change in CO_2 and NO_x emissions per kWh of electricity generated, as compared with an unfired combined cycle.

Acknowledgments

This investigation was carried out at the suggestion of Mr. Albert Kreutzer, Senior Director, Thermal Power Plants, Engineering, and Marketing of the Siemens Power Generation Group KWU. The authors would like to thank Mr. Kreutzer for his encouragement and support. They are also grateful to H. Brueckner, W. Empsperger, H. J. Heinecke, and Dr. B. Rukes for their valuable advice.

References

1 Baehr, H. D., *Thermodynamik*, Springer, Berlin-New York, 1989, pp. 96-100.

2 Devizci, Y., and Hamann, B., "Design and Operation of Ambarli Combined Cycle Power Plant," *International Joint Power Generation Conference*, ASME Book No. G00519, Boston, Oct. 1990.

3 "Technology Assessment for Advanced Fossil Power Systems," EPRI GS-6165, Special Report, Dec. 1989.

4 Haupt, G., Joyce, J. S., and Kuenstle, K., "Combined Cycles Permit the Most Environmentally Benign Conversion of Fossil Fuel to Electricity," ASME Paper No. 90-GT-367, 1990.

Gas Turbines Above 150 MW for Integrated Coal Gasification Combined Cycles (IGCC)

B. Becker

B. Schetter

Siemens AG, KWU Group,
Gas Turbine Technology,
Mülheim a.d. Ruhr,
Federal Republic of Germany

Commercial IGCC power plants need gas turbines with high efficiency and high power output in order to reduce specific installation costs and fuel consumption. Therefore the well-proven 154 MW V94.2 and the new 211 MW V94.3 high-temperature gas turbines are well suited for this kind of application. A high degree of integration of the gas turbine, steam turbine, oxygen production, gasifier, and raw gas heat recovery improves the cycle efficiency. The air use for oxygen production is taken from the gas turbine compressor. The N_2 fraction is recompressed and mixed with the cleaned gas prior to combustion. Both features require modifications of the gas turbine casing and the burners. Newly designed burners using the coal gas with its very low heating value and a mixture of natural gas and steam as a second fuel are developed for low NO_x and CO emissions. These special design features are described and burner test results presented.

Introduction

Over the past two decades, the efficiency of the gas turbine has been improved and its reliability verified, with the result that it has gained considerable significance as a means of generating electricity. Where natural gas or fuel oil are used, the most economical type of power plant is either a gas turbine alone, as a peak load plant, or a combined gas and steam (GUD) cycle as an intermediate and baseload plant. By dividing the process into two temperature ranges, 1100 to 550°C in the gas turbine and 530°C to ambient temperature in the steam turbine, high overall efficiencies exceeding 50 percent are now being achieved [1]. Even with the most complex configurations, the straight steam cycle power plant will never be able to reach this level.

For that reason the gas turbine has gained a significant fraction of the market in recent years. The gas turbine is dependent on the availability of low-cost, clean fuel because of the direct combustion of the fuel in compressed air. The chief objective of the coming decade is utilization of coal for the combined cycle process. At present both direct combustion in a pressurized fluidized bed and gasification and cleanup of fuel gas prior to combustion are being investigated simultaneously to achieve this end.

New IGCC Demonstration Power Plants

Since the plants Cool Water and Dow Chemical, Plaquemine, in the USA verified the suitability of the integrated coal gasification combined cycle (IGCC) several years ago, several large European utilities are now showing interest in this new technology. In Europe, fuel costs have always been relatively high. For this reason, plant efficiency is a far more important consideration here. Furthermore, German coal-fired power plants have been fitted with flue gas desulfurization and $deNO_x$ plants at high capital costs. Any new plant designs to be installed are therefore expected to meet, preferably even to surpass, the emissions performance achieved in these plants.

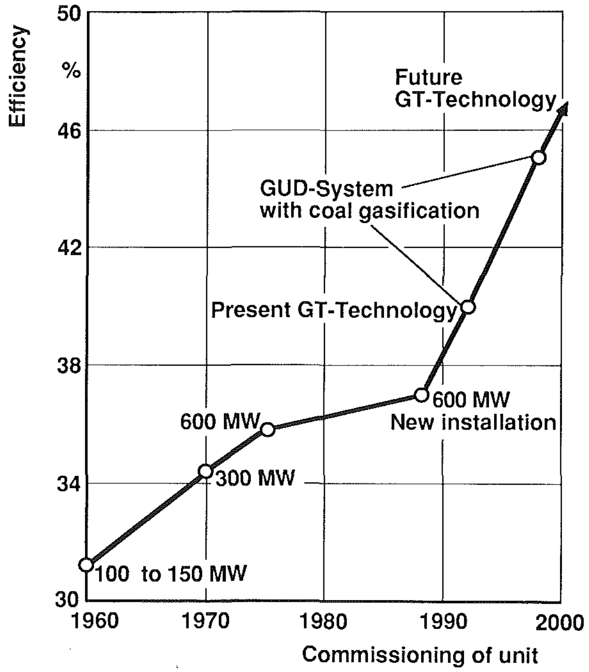

Fig. 1 New efficiency of RWE-bituminous coal power plants

Contributed by the International Gas Turbine Institute and presented at the 36th International Gas Turbine and Aeroengine Congress and Exposition, Orlando, Florida, June 3-6, 1991. Manuscript received at ASME Headquarters March 4, 1991. Paper No. 91-GT-256. Associate Technical Editor: L. A. Riekert.

Table 1 Thermodynamic data

1	Type		V64.3	V84.2	V84.3	V94.2	V94.3
2	Frequence	s^{-1}	50/60[1]	60		50	
3	Turbine inlet temperature according to ISO 2314	°C	1120	1040	1120	1050	1120
4	Power output at terminals (ISO-Base load)[2]	MW	60	103	139	150	200
5	Pressure ratio	-	15.6	10.9	15.6	10.9	15.6
6	Exhaust mass flow	kg/s	187	355	420	509	605
7	Exhaust temperature	°C	534	532	534	538	534
8	Efficiency at terminals (ISO-Base load)[2]	%	35.2	33.8	35.7	33.8	35.7

1) With gear (Gas turbine: 90 s^{-1})

2) ISO-Conditions, $\Delta p_{VI} = \Delta p_{TII} = 0$

Fuel : Natural gas

The largest German utility, RWE, operates primarily lignite-fired power plants in the baseload range. As shown in Fig. 1, published a year ago, the development of this configuration as a straight steam cycle power plant over the past decades has culminated in a 600 MW unit with about 38 percent net efficiency (based on the lower heating value) [2]. Since further improvements in steam cycle efficiency by increasing pressure and temperature are possible, but require substantial capital investments and longer start-up times, the present design can be regarded as fully optimized in economic terms.

Further significant efficiency improvements can only be achieved by utilizing the combined cycle process. Even implementation of today's standard gas turbines would substantially improve these performance levels. Since the 300 MW "Projekt KoBra" demonstration power plant calls for full exploitation of the efficiency potential of the increased turbine inlet temperature, RWE opted for the newly developed 211 MW Siemens V94.3 gas turbine.

In the neighboring Netherlands, the decision to build a 283 MW hard-coal-fired demonstration power plant was made some six months earlier. In this case, proven technology was given a high priority and the Siemens V94.2 gas turbine was selected. The V94 has been in commercial service since 1974, and by Sept. 1990, 37 V94 gas turbines had begun operation in 16 power plants, amassing some 400,000 operating hours. The Buggenum IGCC power plant (in Dutch KV-STEG) will be built by Demcolec B.V. adjacent to the existing "Maascentrale" (Maas power station) at Buggenum, near Roermond, Province of Limburg in the south of the Netherlands. Start-up and operation are scheduled for mid-1993. During the demonstration period, which will span about three years, the IGCC plant will be tested under different conditions and with various types of coal.

Gas Turbines

Table 1 lists the thermodynamic data of the two gas turbine designs under standard ISO conditions with natural gas fuel. Development of the new gas turbine model series has been described in several publications [3, 4]. Since the V64.3 model is smaller than the V94.3 by a factor of 1.8, but thermodynamically similar, and its efficiency and output potential have been demonstrated in both test-bed and commercial power plant operation, it was possible to increase the performance specs of the 50-Hz turbine over those previously published.

Figure 2 compares the longitudinal sections of the V94.2 and V94.3 gas turbines. The distance between bearings is virtually identical, but the blading diameter of the higher-output V94.3 was increased by about 10 percent to allow efficient exploitation of the increased enthalpy difference. To achieve a pressure ratio increase in the compressor from 10.9 to 15.6, it was therefore only necessary to adjust the number of compressor stages from 16 to 17. In the case of the turbine, the previous four stages represented an optimum.

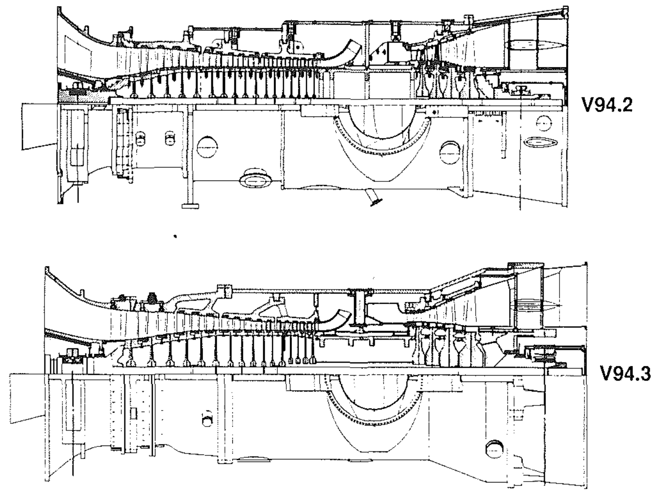

Fig. 2 Comparison of longitudinal cross sections

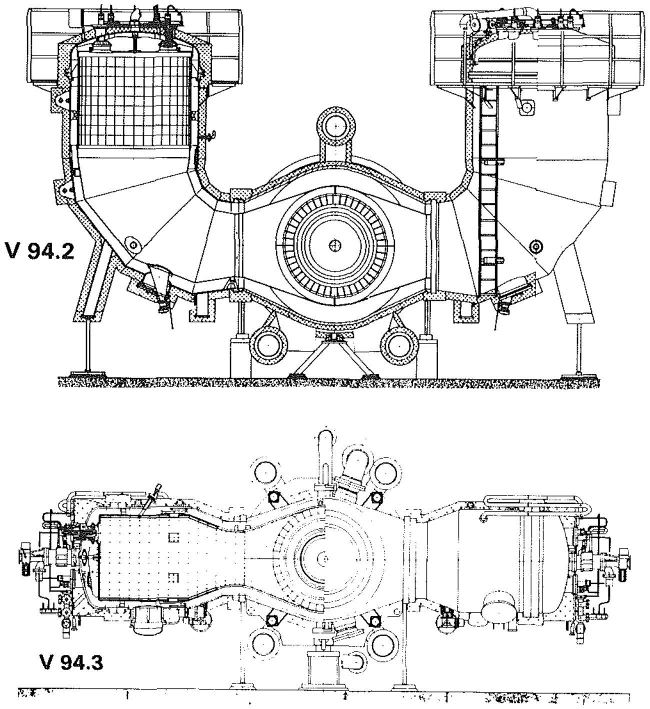

Fig. 3 Comparison of combustor cross sections

Since the new gas turbine is primarily envisaged for GUD power plant applications, particular emphasis was placed on high part-load efficiency. Four rows of variable-pitch compressor blade rows ensure a wide range of mass flow adjustment, making it possible to maintain a constant exhaust gas temperature from approximately 50 percent load to baseload. In a power plant with at least two gas turbines, it is therefore possible to maintain a constant steam temperature from 100 to 25 percent load, since one of the gas turbines can be shut down after simultaneously reducing the load of both to 50 percent. The other continuing operation with inlet blading fully open at 100 percent power output still has a further 50 percent power reduction reserve.

Adjustable pitch stator blading and three bleed points (as compared to the previous two of the V94.2) ensure unproblematic start-up of the compressor, which has a very high pressure ratio for a single-shaft axial compressor.

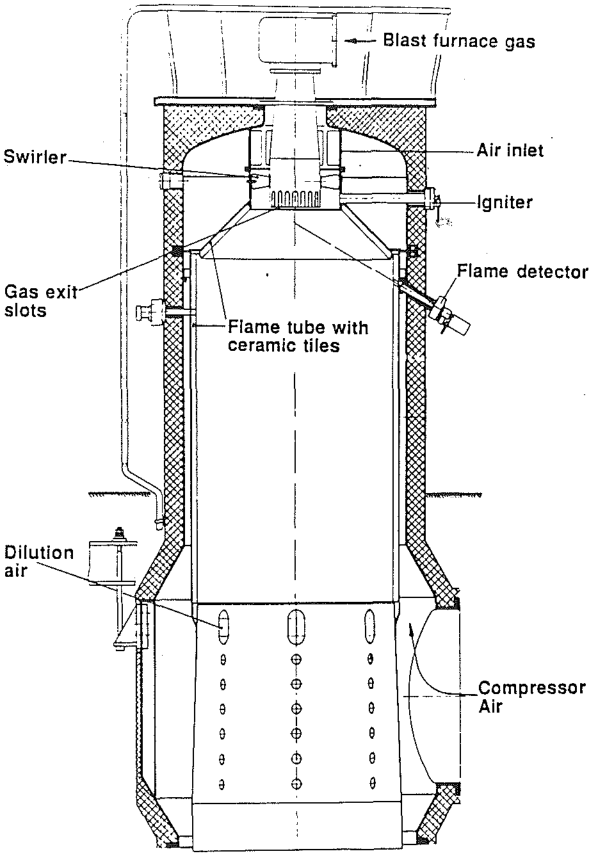

Fig. 4 Combustion chamber for low-BTU gas

By careful selection of the extraction pressures, it was possible to optimize the supply of cooling air to the turbine blading. In concrete terms, the second row of turbine vanes is supplied from the last extraction point and the third row from the middle extraction point. Two different cooling air flows were selected for supplying the rotor. Whereas the first row of both the stator and rotor blading is supplied with precooled air, subsequent stages are cooled with air extracted downstream of the 13th compressor stage. The pressure drop of this flow, which travels from the perimeter inward, in opposition to centrifugal force, is minimized by long bores oriented obliquely to the circumference. A cooling system design of such complexity is surely only possible where single disks and hollow shaft elements are used.

Figure 3 compares the combustion chamber arrangement. The number of burners of the V94.3 ($2\times 8=16$) corresponds to that of the V94.2. Owing to the higher pressure, it was possible to reduce the flame cylinder diameter slightly in spite of the higher burner power. At baseload the average flame temperature is kept so low, for reasons of NO_x reaction kinetics, that no dilution air other than cooling air is required to achieve a mean gas temperature of about 1300°C at the turbine inlet. This made it possible to reduce the combustion chamber volume and simplify geometry.

Combustor Design for Coal Gas

In high-output boilers for steam turbines it has always been standard practice to work with high residence times, i.e., with large combustion chamber volumes, in order to reduce CO emissions. This was especially important when gas turbines for blast-furnace gas were constructed in Europe in the early sixties [5]. The coal gas generated during steel production has a heating value approximately 5 percent of that of natural gas. The combustion temperatures are accordingly lower, thus delaying the reaction of CO with O_2 to form CO_2 and rendering good burn-out impossible in the small can-type combustion chambers of an aircraft derivative engine.

Figure 4 shows the combustion chamber of a 7 MW gas turbine that was developed for blast-furnace gas and is still functional after 83,000 hours of operation. This combustion chamber was fitted with a ceramic lining of the type used in present-day turbines, with the tiles suspended in such a way that thermal expansion and contraction are permitted. The immediate vicinity of the burner is also fitted with suspended ceramic tiles, which form a barrier between the metal wall behind them and the radiant heat of the hot gases. There are no instances of a hole being burned through a flame cylinder protected in this manner.

As the development of gas turbine technology has progressed, there has been a step-by-step increase in the maximum output. Maintaining the principle of one burner in one combustion chamber means that the burner becomes extremely large, resulting in long residence times in the near-stoichiometric range and thus in increased NO_x formation. This effect can be minimized by using several burners per combustion chamber, which also permits much more even temperature distribution [6].

With the exception of one manufacturer whose gas turbines have burners with thermal outputs ranging from less than 1 MW to more than 400 MW [7], the typical thermal output per burner in gas turbines with electrical outputs of over 30 MW is between 15 and 30 MW. Different gas turbine outputs are achieved by fitting various numbers of similar burners, thereby making use of the results achieved in the development of individual components. Consequently, each of the 16 V94.2 burners has a thermal output of 28 MW.

The thermal output of the old blast-furnace gas burner is 24 MW. If one allows for the increase of pressure ratio from about 4 to 11, thermal output can be increased without changing burner dimensions. On the basis of this comparison it is evident that the design of burners developed some 30 years ago does not differ significantly from coal gas burners of today's large gas turbines.

Burner Design for Several Fuels

A large percentage of the V94.2 gas turbines now in service are equipped with burners (Fig. 5), which permit the following three modes of operation:

1 Natural gas diffusion burner operation
2 Natural gas premix burner operation
3 Fuel oil diffusion burner operation

The switchover from one mode to another can be made without interruption of the plant process. Natural gas and fuel oil can be combusted simultaneously in diffusion burner operation in nearly all possible combinations (natural gas >20 percent, fuel oil >10 percent). Natural gas premix burners achieve NO_x concentrations below 25 ppm without water or steam injection [8]. H_2O is used with diffusion burners to control NO_x emissions.

For the IGCC plants, this burner was to be equipped with a coal gas injection system in addition. Since the fuel has a very low heating value (LHV approximately 4300 to 5000 kJ/kg), a fuel volume is required that is equivalent to 47 percent of the primary air that passes through the outer swirler during baseload operation. This made modification of the air flow patterns around the central diffusion nozzle system unavoidable. Furthermore, at the high H_2 concentration of the coal gas, spontaneous combustion of the air and fuel would occur on premixing. It was therefore necessary to arrange the coal gas nozzle system such that ignitable fuel–air mixtures cannot form near the walls.

The design developed with these parameters (Fig. 6) has an additional concentric ring of coal gas nozzles, which open into

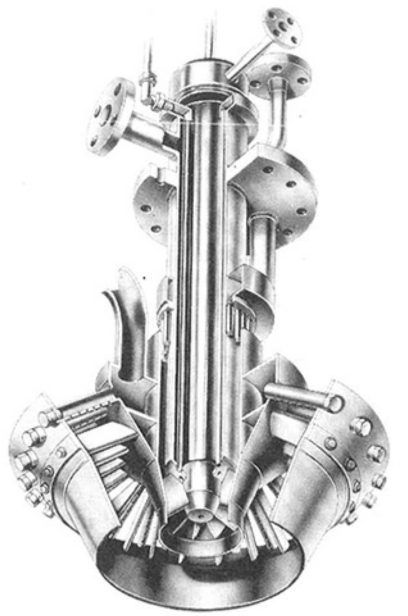

Fig. 5 Hybrid burner for low NO_x and CO emissions

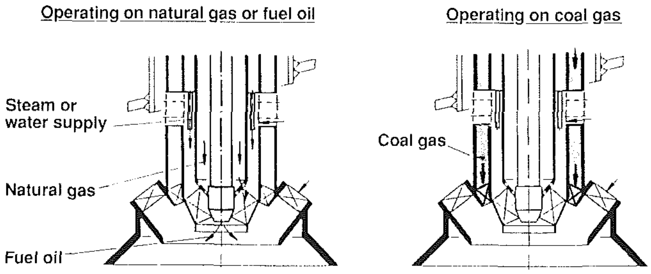

Fig. 6 Burner for coal gas and conventional fuels

the primary air duct downstream of the outer swirler. Since localized recirculation occurs in this region during natural gas operation, air–natural gas premixing is not performed for safety reasons. The additional coal gas duct does not, however, influence operation of diffusion burners with natural gas or fuel oil. This burner is therefore suitable for operation with three fuels, even any two simultaneously. In the Buggenum plant, the fuel oil system is not required. In the KoBra plant, fuel oil will possibly be the second fuel. It had to be demonstrated by 1 July 1990 that these burners can operate reliably with coal gas and in a manner that is benign to the environment. For gas turbine start-up and for achieving instantaneous load rejection to station service load, the alternative fuel natural gas may be used. The aim here is, however, to accommodate these operating conditions under operations with coal gas alone.

Results of Burner Testing

Investigations with the newly developed coal gas burner were conducted on a low-pressure burner test rig (Fig. 7) at the Mülheim Works at atmospheric pressure. This test equipment permits preheating the combustion air to 230°C to investigate the effects of elevated temperatures in the gas turbine on stability and emissions. Considerable effort was required to provide the equipment for the supply of coal gas to the test rig. This gas, synthesized from CO, H_2, and N_2, is stored in a 95 m^3 vessel. Maximum vessel pressure was 45 bar. This vessel pressure and volume did limit burner operation to around 40 minutes at an excess air ratio equivalent to baseload. Gas volumes required for filling the vessel, in particular CO, could only be delivered once a week within Western Europe.

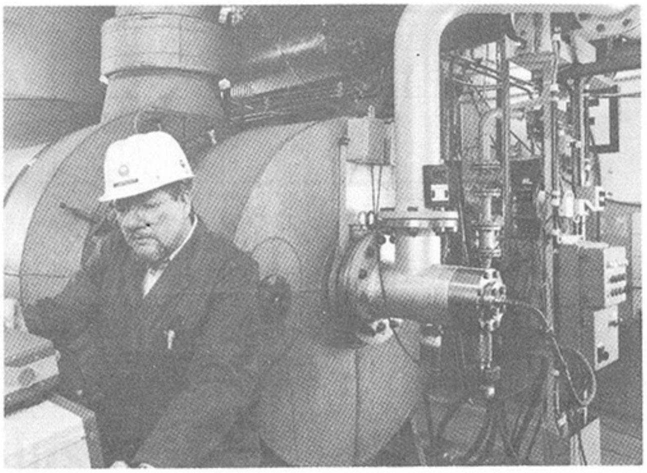

Fig. 7 Coal gas burner and test rig

Tests were conducted both with and without air preheating. It was demonstrated that the coal gas burner can be operated from gas turbine start-up, through idling and up to peak load stably and reliably. Natural gas or propane is required only for burner ignition since the spark igniter used is located in front of the nozzles of the central natural gas diffusion burner.

Other special measures are, however, necessary to accommodate load rejection. When the gas turbine is suddenly isolated from the grid, trip should not be initiated, but operation continued under the control of the speed governor to cover plant auxiliary requirements. Before this new steady-state condition is achieved, non-steady-state speed increases occur, which are limited and controlled by reducing the fuel flow to below the amount required for idling. Under such conditions the air flow in the combustion chambers increases slightly and the fuel flow is reduced to about 10 percent of the baseload flow rate. Excess air in the primary zone reaches extremely high levels and there is a risk that flame-out will occur, and the flame monitors will then initiate trip.

Tests with the coal gas burner have demonstrated that the stability range of the coal gas flame can be extended significantly by also feeding coal gas to the centrally located natural gas nozzles. Results of tests conducted at 1 bar are not adequate, however, for making definitive predictions on the effectiveness of the process envisaged for implementation in the power plant. For this reason, alternative plans call for injection of a small volume of natural gas or other fuels with high heating value on load rejection. Many V94.2 gas turbine plant tests have repeatedly demonstrated that load rejections can be accommodated with a natural gas flame.

When operating in the gas turbine load range, the burner can be switched over from coal gas to natural gas or vice versa in less than five seconds. This permits continued operation of the turboset at load and operating speed on loss of coal gas supply or shutdown at a rate that minimizes life-limiting effects on the plant without tripping.

Results of NO_x measurements taken during tests at atmospheric pressure with air preheating are compared with calculated reaction kinetics data in Fig. 8. Measured NO_x levels were achieved without the addition of water or steam for reduction. Emissions measured with synthetic coal gas (3846 kJ/kg) were below 2 ppm, therefore in the range of the zero drift of the instrumentation equipment used. NO_x levels in a V94 at a much higher pressure can therefore be expected to be below 20 ppm.

Carbon monoxide emissions of the burner were also very low. In spite of the comparatively low heating value of the coal gas, less than 10 ppm CO were measured at excess air ratios equivalent to 40–100 percent gas turbine load. When used in the gas turbine, the low-emissions operating range of this burner is more likely to become even greater due to the increased pressure level.

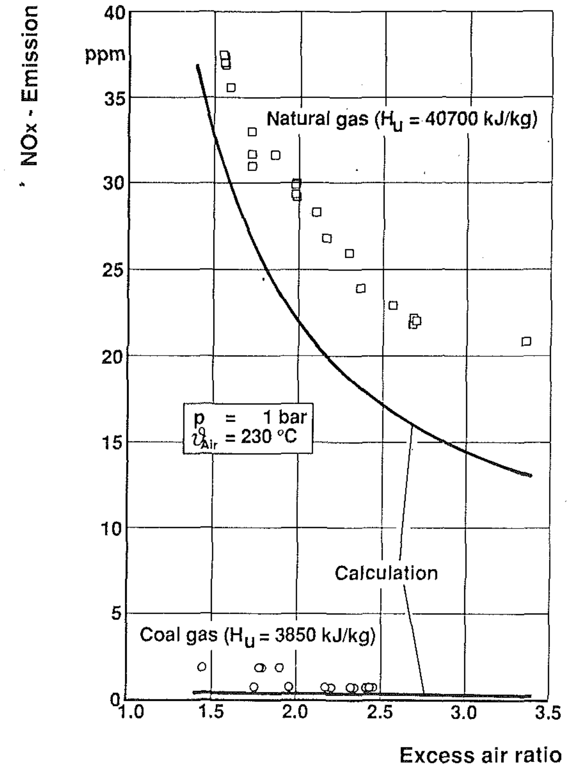

Fig. 8 NO$_x$ emissions of the coal gas burner in atmospheric burner test rig

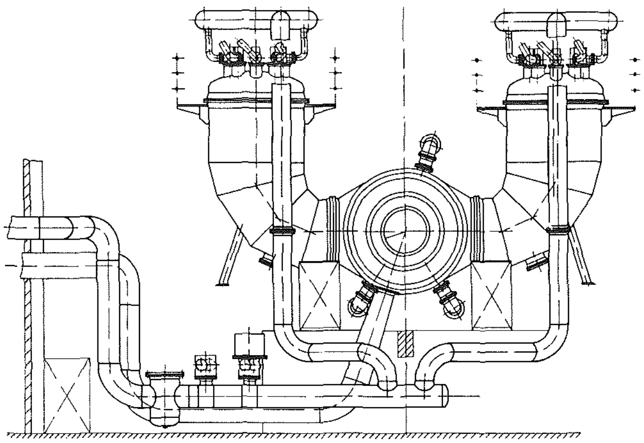

Fig. 9 V94.2 Buggenum, coal gas piping

Investigations included varying coal gas composition. Particular attention was directed to operation with a nearly nitrogen and steam-free clean gas with a heating value of about 9960 kJ/kg. Gas of this composition is produced in Buggenum on gasifier start-up and during certain faults when the admixture of the N_2 fraction produced by the air separation unit or the coal gas saturator has not yet begun operation. This high heating value coal gas can also be reliably combusted under all operating conditions.

These investigations have demonstrated that the requirements specified by Demkolec B.V. in the letter of intent have been satisfied on schedule. In the meantime, the contract for the supply of the gas turbine generator has been awarded.

Integration of the Gas Turbine Into the IGCC Power Plant

The air separation unit in the Buggenum plant is supplied with compressed and recooled air from the gas turbine compressor during normal operation. The gas turbine must therefore be equipped with an air bleed point located on the lower part of the outer casing (Fig. 9).

In the Buggenum plant the gas turbine and steam turbine have only one common generator. The compressor end is rigidly coupled to the high-pressure stage of the steam turbine by an intermediate shaft that passes through the air intake duct.

In the KoBra plant, an existing steam turbine will be used in the combined cycle. Details of the coal gasification system designed by Rheinbraun have not yet been published.

Conclusion

Two IGCC power plants will be built in the next two years in the Netherlands and Germany with efficiencies of 43–46 percent; these plants will operate more efficiently than conventional lignite or hard-coal fired plants.

Extremely low environmental impact will be achieved because of the very efficient desulfurization and cleanup of the coal gas in the gas clean-up system. This fuel will be free of fuel-bound nitrogen and because of the low combustion temperature only small amounts of thermal NO$_x$ will be formed. Due to the long residence time in the primary zone, the low combustion temperature will not lead to formation of significant amounts of CO in the normal operating range of the combined cycle.

The successful demonstration of the 283 MW Buggenum ICG-GUD block with the 154 MW V94.2 from 1993 onward and of the 300 MW KoBra IGCC block with the 211 MW V94.3 from 1995 onward will provide a decisive argument for the adoption of coal gasification for central power station generation. Just as combined cycles have already replaced straight steam cycles when noble fuels, i.e., natural gas or distillate oils, are utilized to generate electric power, they are likely to become predominant also when coal is the fuel, because integrated gasification into a combined cycle yields higher operating efficiency as well as the most environmentally benign conversion of coal to electricity.

References

1 Joyce, J. S., and Hamann, B., "World's Largest Gas Turbines for Ambarli Combined Cycle," *Modern Power Systems*, Vol. 9, No. 5, May 1989.

2 Hlubek, W., and Kallmeyer, D., "Maßnahmen der Elektrizitätswirtschaft zur Luftreinhaltung in der Bundesrepublik Deutschland," *Brennstoff-Wärme-Kraft*, Vol. 41, No. 9, Sept. 1989.

3 Becker, B., and Ziegner, M., "Die neue Siemens/KWU-Gasturbine V64.3," *Motortechnische Zeitschrift*, Vol. 49, 1988.

4 Becker, B., "Development of Gas Turbines in Germany," EPRI Seminar on Technologies for Generating Electricity in the 21st Century, San Francisco, CA, Oct. 1989.

5 Friedrich, R., "Gas Turbine for an Iron and Steel Works," *Siemens Review*, Vol. XXIX, 1962.

6 Jeffs, E., "New Low-NO$_x$ Combustors in European Service," *Gas Turbine World*, Sept.-Oct. 1987.

7 Angello, L., and Lowe, P., "Dry Low NO$_x$ Combustion Development for Electric Utility Gas Turbine Applications. A Status Report," ASME Paper No. 89-GT-254, 1989.

8 Maghon, H., "An Economic Solution to the NO$_x$ Problem in Gas Turbines," *VGB Kraftwerkstechnik*, Vol. 68, No. 8, Aug. 1988.

9 Dorstewitz, U., and Wien, H., "Die KDV-Anlage Lünen," *Kohlevergasung in der Energietechnik*, VGB-TD 201, VGB-Kraftwerkstechnik GmbH, Essen, Germany, 1979.

10 Joyce, J. S., "The Development of Integrated Coal-Gasification Combined-Cycle (ICC-GuD) Power Plants," presented at the Seminar on Coal Gasification for Generation of Electricity, Arnheim, Netherlands, Apr. 1990.

Biomass-Gasifier/Gas Turbine Cogeneration in the Pulp and Paper Industry

E. D. Larson
Center for Energy and
Environmental Studies,
School of Engineering and Applied Science,
Princeton University,
Princeton, NJ 08544

Increasing atmospheric carbon dioxide from fossil fuel combustion is raising new interest in using renewable biomass for energy. Modest-scale cogeneration systems using air-blown gasifiers coupled to aeroderivative gas turbines are expected to have high efficiencies and low unit capital costs, making them well-suited for use with biomass. Biomass-gasifier/gas turbine (BIG/GT) technology is not commercial, but efforts aimed at near-term commercialization are ongoing worldwide. Estimated performance and cost and prospects for commercial development of two BIG/GT systems are described, one using solid biomass fuel (e.g., wood chips), the other using kraft black liquor. At an energy-efficient kraft pulp mill, a BIG/GT cogeneration system could produce over three times as much electricity as is typically produced today. The mill's on-site energy needs could be met and a large surplus of electricity would be available for export. Using in addition currently unutilized forest residues for fuel, electricity production would be nearly five times today's level. The total cost to produce the electricity in excess of on-site needs is estimated to be below 4 cents per kWh in most cases. At projected growth rates for kraft pulp production, the associated biomass residue fuels could support up to 100 GW of BIG/GT capacity at kraft pulp mills worldwide in 2020 (30 GW in the US). The excess electricity production worldwide in 2020 would be equivalent to 10 percent of today's electricity production from fossil fuels.

Introduction

Biomass energy substituted for fossil fuels could help reduce carbon dioxide emissions that are contributing to the greenhouse warming of the earth, since biomass absorbs the same amount of carbon in growing as it releases when consumed as fuel. A major challenge to using biomass for energy is to identify conversion technologies for providing more convenient energy forms, like electricity or liquid fuels, at competitive costs and at the modest scales dictated by the low efficiency of photosynthesis. Power generation and cogeneration systems using pressurized, air-blown biomass gasifiers integrated with power cycles involving aeroderivative gas turbines are one promising set of technologies for "modernizing" bioenergy. These technologies have the potential for high efficiency and low unit capital cost at modest scale (Larson et al., 1989; Larson and Williams, 1990).

Biomass-gasifier/gas turbine (BIG/GT) systems might eventually be fueled by biomass grown on dedictated energy plantations (Hall et al., 1990), but initial applications are likely to be where biomass fuels already exist as residues of industrial processes. One potentially large market for BIG/GT units is in the sugar cane processing industries, where bagasse (residues left after crushing the cane) and barbojo (the tops and leaves of the cane plant) could be used as fuel. The 1987 global level of cane production could support 95 GW of BIG/GT cogeneration capacity, which would permit large quantities of electricity in excess of on-site process needs to be produced competitively (Ogden et al., 1990). The pulp and paper industry represents another possible near-term application of BIG/GT technology where processing by-products would be the fuel. This paper assesses the performance, cost, and prospects for commercialization of BIG/GT technologies for kraft pulp mills and explores the potential for cogenerating electricity in excess of on-site needs.

BIG/GT Technology

Two BIG/GT technologies are described here. One would use solid fuels (e.g., wood chips, wood waste, crop residues, etc.); the other, black liquor from kraft pulp production. Steam-injected gas turbines (STIGs) and intercooled steam-injected gas turbines (ISTIGs) are alternative aeroderivative turbine cycles that are considered (Larson and Williams, 1987; Williams and Larson, 1989). Gas-turbine/steam-turbine combined

---

Contributed by the International Gas Turbine Institute and presented at the 36th International Gas Turbine and Aeroengine Congress and Exposition, Orlando, Florida, June 3-6, 1991. Manuscript received at ASME Headquarters March 4, 1991. Paper No. 91-GT-280. Associate Technical Editor: L. A. Riekert.

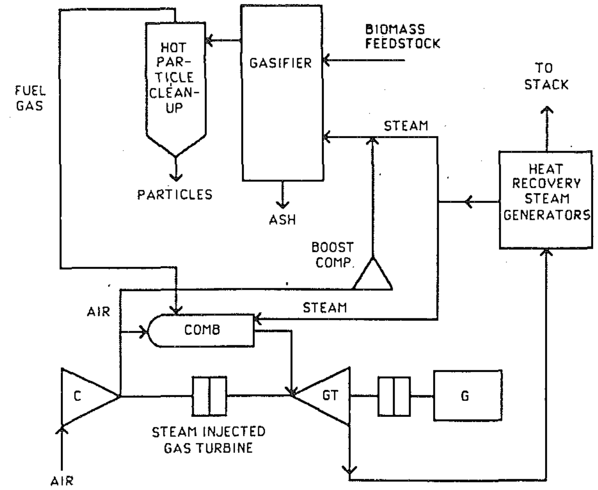

Fig. 1 Biomass-gasifier/steam-injected gas turbine cycle

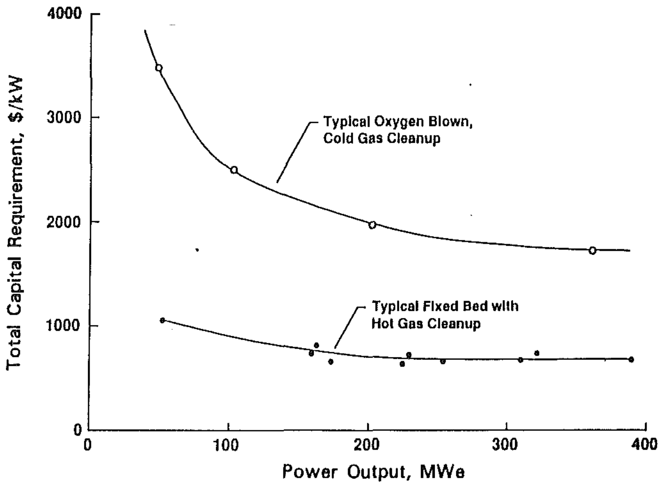

Fig. 2 Cost comparison (in 1988 $) of coal-gasifier/gas turbine power plants (Pitrolo and Graham, 1990). The upper curve represents technology like the Cool Water commercial demonstration plant that uses a Texaco entrained-bed gasifier, cold-gas cleanup, and a combined cycle. The lower curve represents systems using air-blown fixed-bed gasification with hot gas clean up and either combined cycles or steam-injected gas turbines. The points on this curve are calculated costs for specific plants using integral numbers of gasifiers and commercial gas turbines. See also Synthetic Fuels Associates (1983) for additional discussion of effects of scale on the cost of Cool Water technology.

cycles based on advanced aeroderivative turbines are also potential candidates.[1]

Solid-Biomass Gasifier/Gas Turbines. A biomass-gasifier/steam-injected gas turbine (BIG/STIG) fueled with solid biomass (Fig. 1) would be similar in many respects to the more familiar coal-gasifier/gas turbine (IGCC) technology commercially demonstrated at Cool Water (Clark, 1988). Important differences would include the use of air-blown instead of oxygen-blown gasification and a steam-injected gas turbine instead of a combined cycle. The sensitivity to scale of oxygen plants and conventional combined cycles makes the Cool Water technology uneconomic for relatively smaller applications (Fig. 2). Also, while the gas exiting the gasifier must be cleaned, so doing would not require developing advanced cleanup technologies (as required for hot sulfur removal from coal), because most biomass contains negligible sulfur. Furthermore, biomass is more reactive than coal and thus easier to gasify (Fig. 3), so that fixed-bed and fluidized-bed gasifiers, which operate at lower average temperatures than entrained beds such as the one at Cool Water, can provide essentially complete carbon conversion and high gasification efficiency (Larson et al., 1989).

Gasifier Design Options. The fixed-bed gasifier is attractive for relatively dense fuels (wood chips, hog fuel, or densified biomass) because of its simplicity and high efficiency (Larson et al., 1989). Among several fixed-bed units on which there has been development work during the last decade, the Lurgi dry-ash gasifier appears to be a good candidate for biomass applications (Corman, 1987). Its use in coal-IGCC applications has been extensively evaluated (Corman, 1986). Limited pilot-scale testing has been carried out by the General Electric Company using biomass pellets and RDF/coal briquettes (Larson et al., 1989). More extensive testing is required to determine the degree of fuel processing (e.g., densification) needed to make alternative biomass feedstocks acceptable for this gasifier and the suitability of this design for biomass/gas turbine applications.

Fluidized-bed gasifiers have higher throughput capabilities and greater fuel flexibility than fixed-beds, including the ability to handle low-density feedstocks like undensified crop residues or sawdust (Larson et al., 1989). A major drawback of fluidized-beds is the higher level of particulates in the raw gas, which makes gas cleanup more challenging. Large-scale atmospheric-pressure fluidized-bed gasifiers are commerically operating with biomass fuels to produce boiler fuel, and a significant amount of work was also done in the late 1970s and early 1980s on pressurized biomass-fueled units designed for use in methanol production.

Perhaps the most important development issue for BIG/GT technology relating to gasifier design is gas cleanup, specifically removal of alkali compounds (formed primarily from potassium and sodium in the feedstock) and particulates at elevated temperatures. Estimates of the tolerable concentration of alkali vapors in fuel gas for gas turbine applications are very low—100 to 200 parts per billion (Horner, 1985; Scandrett and Clift, 1984). The extent of alkali production and required removal from biomass gas has not been measured. Based on coal-related work, however, the gasifier exit temperature appears to be the most important controlling parameter. At fixed-bed gasifier exit temperatures (500–600°C) most of the alkalis appears to condense on particulates and can thus be controlled by controlling particulates. Particulate cleanup with fixed-bed gasifiers appears possible using cyclones, based on data for coal (Corman and Horner, 1986). Alkali that manages to reach the combustor would be in a chemically bound form and would not vaporize in short residence-time combustors (Corman, 1989). With fluidized-bed gasifiers (800–900°C exit temperatures), some cooling of the gas would be required to condense alkalis. Also, more efficient particle removal technology would be needed, e.g., barrier filters. Demonstration of a significant new design for ceramic barrier filters, intended in part to overcome the problems that traditional candle filters have in withstanding thermal and mechanical shock, is ongoing in Finland (Isaksson, 1989). Other designs are under development in the US (Pitrolo and Graham, 1990).

---

[1] Some advanced aeroderivative turbines with low expected costs will be better suited to combined cycles than to steam injection. For example, the LM-6000, which will enter commercial service in 1992, will produce 42.4 MW at a simple-cycle efficiency greater than 36 percent (HHV basis, natural gas fuel) and will have an estimated gen-set equipment price of $230/kW to $250/kW (de Biasi, 1990), much less than the $400/kW price for the most efficient (33 percent) aeroderivative gas turbine available today (Jersey Central, 1989). An LM-6000 based combined cycle would produce 53.3 MW at an expected efficiency of some 48 percent (HHV). Because the gas turbine involved in this combined cycle would be cheap and because the steam turbine would provide only 1/5 of the output (compared to 1/3 for a combined cycle based on the use of industrial gas turbines), the LM6000 combined cycle may prove competitive with much larger combined cycles based on industrial turbines. See Stambler (1990) for discussion of other advanced aeroderivative engines.

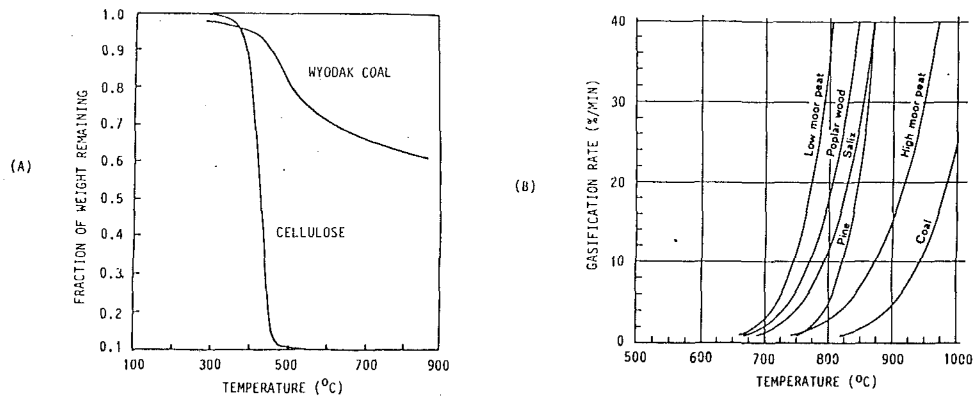

Fig. 3 Comparison of gasification characteristics of biomass and coal (Larson et al., 1989): (*a*) weight loss as a function of pyrolysis temperature for coal and cellulose (a major component of biomass); (*b*) gasification rates in steam of chars from different feedstocks

Table 1 Performance and capital cost estimates of biomass power generating systems[a]

	Cogeneration Performance				*Full Electricity Performance*		*Installed Capital Cost*[f]
	Electricity		*Maximum Process Steam*				
	(MW)	(%Effic.)	(kg/hr)	(%Effic.)	(MW)	(%Effic.)	(1990 $/kW)
15% mc Fuel							
BIG/ISTIG[b]							
LM-8000	97	37.9	76,200	25.4	111.2	42.9	890
BIG/STIG[c]							
LM-5000	39	31.3	47,700	30.0	53	35.6	1150
LM-1600	15	29.8	21,800	33.8	20	33.0	1420
LM-38	4	29.1	5,700	32.4	5.4	33.1	1900
50% mc Fuel							
BIG/STIG[d]	38.3	29.5	47,700	28.9	52.3	33.5	1250[g]
CEST[e]	37	10.0	319,000	52.1	77	20.9	1560

(a) All efficiencies are based on the higher heating value of the fuel. The indicated fuel moisture contents (mc) of 15% and 50% are fractions of the wet weight of the biomass.

(b) Preliminary performance estimate derived from performance with coal (Ogden et al., 1990). In the "full electricity performance" mode no process steam is produced.

(c) A previous estimate of BIG/STIG efficiency (Larson and Williams, 1990) was conservative, due largely to use of a conservative gasification efficiency. However, it appears that gasifier efficiency with biomass should be at least as high as with coal. The estimates here are based on gasifier efficiency equal to that estimated for a coal-gasifier/STIG. In the "full electricity performance" mode no process steam is produced.

(d) The lower efficiencies and slightly lower electricity production compared to the case with 15% mc fuel reflect the estimated energy use associated with drying the fuel to 15–20% mc. See footnote 12 for additional discussion of the drying technology assumed to be used here.

(e) This is a double-extraction/condensing steam turbine, with assumed boiler efficiency 68%, feedwater temperature 182°C, turbine inlet steam conditions 6.2 MPa, 400°C. Maximum process steam corresponds to operation with minimum flow to the condenser. Saturated process steam conditions are 12.9 bar (119 t/hr) and 4.4 bar (300 t/hr). Maximum electricity corresponds to minimum required extraction of 72 t/hr of saturated steam at 4.4 bar.

(f) The unit installed costs for the BIG/ISTIG, BIG/STIG and CEST are given by the following equations (Larson, 1990); $(\$/\mathrm{kW})_{\mathrm{ISTIG}} = 2516(\mathrm{MW})^{-0.22}$, $(\$/\mathrm{kW})_{\mathrm{STIG}} = 2746(\mathrm{MW})^{-0.22}$, and $(\$/\mathrm{kW})_{\mathrm{CEST}} = 6279(\mathrm{MW})^{-0.32}$.

(g) Includes $86/kW for a steam-based drier (see footnote 12).

System Performance and Cost. Table 1 gives estimates of the performance of BIG/STIG and BIG/ISTIG systems in cogeneration and power-only modes of operation assuming biomass fuel input with 15 percent moisture content (mc).[2] Gasifiers for BIG/GT systems require fuel with less than about 25 percent mc to produce a gas of acceptable quality for gas turbines.

Table 1 also compares the performance of a BIG/STIG and a double-extraction condensing steam turbine (CEST) system (a commercially available option for biomass cogeneration), taking account of the energy losses associated with drying the fuel for the BIG/STIG. Both CEST and BIG/STIG technologies offer flexibility in handling variable process steam demands (Larson and Williams, 1987). Operated in the cogeneration mode, the gas turbine systems would produce much less steam (as a fraction of fuel input) than the CEST. Operated in either cogeneration or power-only modes, the gas turbine is a more efficient electricity producer.

Gas turbine systems would also have capital cost advantages over CEST systems (Table 1). A 53-MW BIG/STIG based on the LM-5000 gas turbine would have a total installed cost of $1150/kW (or $1250/kW if costs for drying equipment are included).[3] The BIG/GT cost estimates are based on detailed cost estimates for similar systems using coal as fuel, from which

---

[2] Unless indicated otherwise, higher heating values are used for fuels throughout this paper.

[3] Unless indicated otherwise, all costs in this paper have been converted to first-quarter 1990 dollars using the US GNP deflator.

the costs for sulfur removal have been subtracted (Table 2).[4] For comparison, a natural-gas LM-5000 STIG is estimated to cost \$650/kW to \$760/kW (Larson, 1990). The cost advantage of the BIG/GT units would increase over the CEST, the smaller the plant size, because of the lower sensitivity of gas turbine system costs to scale (Larson and Williams, 1990).

Table 2 Cost estimates for coal and biomass-gasifier STIGs and ISTIGs (1990\$/kW).

	STIG		*ISTIG*	
	Coal[a]	Bio[b,c]	Coal[a]	Bio[b,c]
I. *Process Capital Cost*				
Fuel handling	45.9	45.9	42.5	42.5
Blast air system	15.6	15.6	11.1	11.1
Gasification plant	186.4	186.4	96.3	96.3
Raw-gas physical cleanup	10.2	10.2	8.9	8.9
Raw-gas chemical cleanup	202.8	0.0	174.8	0.0
Gas turbine/HRSG	341.1	341.1	297.1	297.1
Balance of plant				
Mechanical	46.6	46.6	38.2	38.2
Electrical	75.3	75.3	56.1	56.1
Civil	75.9	75.9	70.3	70.3
SUBTOTAL	999.8	797.0	795.3	620.5
II. *Total Plant Cost*				
Process plant cost	999.8	797.0	795.3	620.5
Engineering home office (10%)	100.0	79.7	79.5	62.1
Process contingency (6.2%)	62.0	49.4	49.3	38.5
Project contingency (17.4%)	174.0	138.7	138.4	108.0
SUBTOTAL	1,335.8	1,064.8	1,062.5	829.1
III. *Total Plant Investment*				
Total plant cost	1,335.8	1,064.8	1,062.5	829.1
AFDC (1.8%)	24.0	19.2	19.1	14.9
SUBTOTAL	1,359.8	1,084.0	1,081.6	844.0
IV. *Total Capital Requirement*				
Total plant investment	1,359.8	1,084.0	1,081.6	844.0
Preproduction costs (2.8%)	38.1	30.4	30.3	23.6
Inventory capital (2.8%)	38.1	30.4	30.3	23.6
Initial chemicals, catalysts	2.9	0.0	2.7	0.0
Land	1.6	1.6	1.5	1.5
TOTAL	**1440**	**1,146**	**1,146**	**893**

(a) From (Corman, 1986) for 2 parallel gasifier/LM-5000 gas turbine trains (total output 101 MW) for the STIG and a single gasifier/LM-8000 gas turbine for the ISTIG (109 MW).

(b) Costs for the biomass-based plants are assumed to be the same as for coal, except that the raw-gas chemical cleanup needed with coal is excluded since it would not be needed for most biomass.

(c) Assuming a single gasifier/LM-5000 gas turbine for the STIG, the net power output would be 53 MW (see Table 1). The unit costs for this arrangement would not be substantially different from a system with double the output using two parallel trains (Corman, 1990). The net power output of the BIG/ISTIG is 111 MW (see Table 1).

Commercialization Prospects. At least four major initiatives bearing on the commercial development of BIG/GT technology are under way or have recently been announced worldwide.[5] Ahlstrom, a Finnish producer of biomass gasifiers, plans to build a 6–10 MW_e BIG/GT cogeneration demonstration plant in Southern Sweden in collaboration with Sydkraft, a major Swedish electric utility (Ahlstrom and Sydkraft, 1990). The plant will use an Ahlstrom pressurized circulating fluidized-bed gasifier, a proprietary alkali removal system, and ceramic filters for particulates. The plant will begin operating in 1993.

In Brazil, a major electric utility in the Northeast has an ongoing R&D program to develop biomass from planted forests as a major fuel source for power generation, with conversion to electricity using BIG/GT units (Carpentieri, 1990). As part of the overall program initiated in 1982, the utility is currently planning a BIG/GT demonstration at the 18 MW_e level. The overall program goal is commercial implementation of plantation-based BIG/GT systems starting in 1998.

In the US, the Department of Energy (DOE) announced in late 1990 a major new program initiative to commercialize BIG/GT technology (San Martin, 1990). Specific program goals were not announced, but the overall target is commercialization of BIG/GT technology by the late 1990s. The USDOE also recently selected the pressurized bubbling-fluidized bed RENUGAS gasifier developed by the Institute of Gas Technology (IGT) for a large-scale gasification demonstration (Babu, 1990). A pressurized pilot-scale RENUGAS unit has extensive operating experience on a variety of biomass feedstocks (Evans et al., 1988). The scaled-up unit will be built in Hawaii and be run initially on sugarcane bagasse (100 tonne per day capacity). Start-up is anticipated in late 1992.

Also in the US, the Vermont Department of Public Service, in cooperation with in-state electric utilities, is exploring possibilities for a commercial demonstration of BIG/GT technology fueled by wood chips derived from forest management operations (Sterzinger, 1990). The DOE, US Environmental Protection Agency, and the US Agency for International Development are jointly supporting pre-project gasification tests of the proposed fuels. The General Electric Company has proposed undertaking these studies using the pilot-scale fixed-bed gasifier and gas turbine simulator facility at its corporate research headquarters.

Kraft Black Liquor Gasifier/Gas Turbines. Worldwide some 2.6 billion GJ of black liquor were produced in 1988 at kraft pulp mills, 40 percent of this in the US (Larson, 1990). Black liquor is the most important source of both energy and chemicals in the pulp and paper industry. It will continue to play a significant role in the US and other industrialized countries, as the pulp and paper industry is one of the few basic-materials processing industries that has strong growth potential in these regions (Williams et al., 1987). Although most pulp is made in industrialized countries today, production growth rates are highest in the developing world (FAO, 1982), so black liquor will grow rapidly in importance in many of these regions as well.

Black liquor is typically consumed today in Tomlinson recovery boilers, a technology commercialized in the early 1900s. Steam is raised (usually to drive a steam turbine cogeneration system) and a chemical smelt is produced containing $NaCO_3$

---

[4] The BIG/STIG cost estimate is consistent with the estimated cost for a 37-MW BIG/combined-cycle plant designed in a feasibility study carried out at the Shell International Petroleum Company (Elliott and Booth, 1990). The Shell design consisted of an Ahlstrom circulating fluidized-bed gasifier with ceramic-filter gas cleanup feeding a Rolls Royce RB211 aeroderivative gas turbine, which would provide 27 MW of the plant's output. Overall efficiency on 15 percent moisture content wheat straw was estimated to be 38–40 percent (HHV). The total installed capital cost was estimated to be \$1200–1300/kW for plants built subsequent to the demonstration plant, which was estimated to cost \$1600/kW to \$1700/kW.

[5] In addition to the development efforts described here dedicated to biomass, there are additional coal-related efforts ongoing with possible significance for biomass. In Germany, the Rheinbraun/Uhde company recently joined with the Lurgi Company to plan construction of a 275 MW coal-IGCC demonstration plant in Germany that will use a pressurized gasifier marrying Rheinbraun/Uhde's HTW (High Temperature Winkler) design to Lurgi's circulating fluidized bed technology (Anon., 1990). The plant is scheduled for startup in 1995. Currently, a pressurized (13.5 bar) commercial HTW unit is operating on peat in Finland for chemical synthesis (Larson et al., 1989). A 25-bar HTW coal-fueled pilot plant has been running since Nov. 1989 in Germany.

Tampella, a Finnish company, recently entered into a licensing agreement with the Institute of Gas Technology (IGT) to commercialize IGT's U-GAS fluidized-bed gasifier, the technology from which IGT's biomass gasification process, RENUGAS, was derived (Salo, 1990). Tampella is now building a 10 MW_{fuel}, 35-bar demonstration unit at its research headquarters in Tampere, Finland. Startup is scheduled for early 1991. Coal will be the primary fuel, but some biomass testing may also be undertaken. Tampella is planning to construct, starting in 1993, a commercial-scale unit (150 MW_{fuel}) that will fuel a gas turbine. The plant will most likely be located at one of Tampella's own pulp mills, using coal, waste bark, and pulp mill waste sludge for fuel.

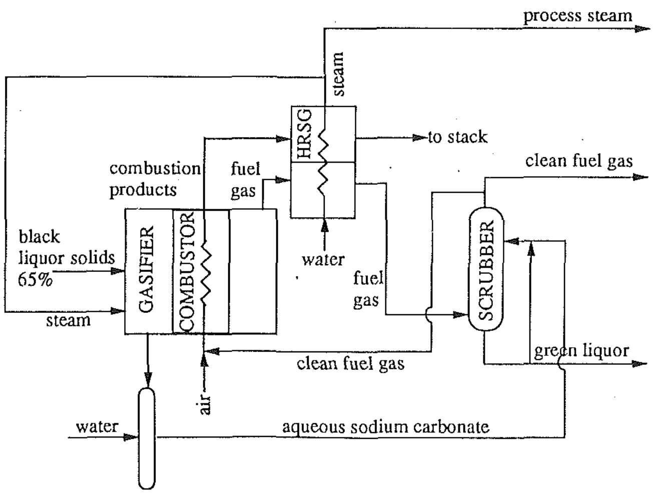

Fig. 4 Schematic MTCI black liquor gasification system (MTCI, 1990)

and Na_2S. The smelt is converted into NaOH and Na_2S, which is recycled for use in the pulping process (Grace and Malcolm, 1989). The high capital costs and smelt-water explosion risks of Tomlinson recovery boilers and an interest in increasing the electrical output from pulp mill cogeneration systems have motivated R&D work during the last 20 years on black liquor gasification for energy recovery. The market potential for retrofit applications alone is quite large, because many existing recovery boilers will be due for replacement within the next decade or so (Jaakko Poyry, 1989).

Gasification Technologies. Promising development efforts ongoing today are on an entrained-bed gasifier by Chemrec, a Swedish company (Stigsson, 1989), and on a fluidized-bed unit by MTCI, an American company (Durai-Swamy et al., 1989). In both cases the work is aimed at the near-term development of modular atmospheric-pressure gasifiers that can be used to expand the black liquor processing capacity of a pulp mill without the capital-intensive replacement of the complete recovery boiler. The Chemrec and MTCI technologies are at roughly the same stage of development. A Chemrec pilot plant processing 3 tons per hour (dry black liquor solids) is currently under construction at a mill in Sweden, with a larger commercial-scale unit planned for installation in a US mill in the mid-1990s. A 1 ton per hour MTCI gasifier will be installed at a US mill in late 1991. Pressurized versions of these technologies appear to be good candidates for gas turbine applications, e.g., see Kignell (1990) and Kelleher (1985).[6] Given black liquor's chemical composition, particular development effort should be focused on alkali removal from the fuel gas to make it suitable for gas turbine use.

Performance and Costs. Estimates of the performance and costs of the MTCI technology are used here for a preliminary evaluation of gas turbine applications of black liquor gasification. The MTCI gasifier uses a pulse combustor with in-bed heater tubes providing heat to gasify the black liquor (Fig. 4). A product gas cooler and flue gas heat recovery steam generator produce steam. Dry $NaCO_3$ is discharged from the gasifier, diluted with water and used in the product gas scrubber to recover H_2S and Na_2S, which are recycled to the pulping process as green liquor. The expected performance of the pilot-scale MTCI plant is shown in Table 3. Assuming all carbon is converted, the overall gasification efficiency would be 60 percent on a higher heating value basis. Firing gas turbines with the gas would give estimated black liquor-to-electricity conversion efficiencies of 21 percent for an LM5000 STIG and 25 percent for an LM8000 ISTIG.[7] At a kraft pulp mill producing 1000 tonnes of air-dry pulp per day (tpd), the available black liquor would be sufficient to support 55 MWs of STIG or 64 MWs of ISTIG capacity.

Table 3 Heat balance for the MTCI pilot plant black liquor gasifier with cold-gas cleanup[a]

	Mass flow (kg/hr)	*Energy flow* (GJ/hr)	*Energy per tonne pulp*[b] Hard (GJ/tp)	Soft (GJ/tp)
Inputs				
Black liquor dry solids[c]	909	13.93	19.9	23.3
Outputs				
Fuel gas (10.6 MJ/Nm^3 HHV)	518.5	7.884	11.2	13.16
Export steam (42 bar, sat.)	950	2.557	3.65	4.27
Carbon recoverable	15	0.516	0.74	0.86
Losses				
Flue at stack	3171	1.586	2.27	2.65
Hot salts discharge	392	0.265	0.378	0.44
Process gas to scrubber	1222	0.925	1.32	1.54
Heat loss from gasifier	--	0.193	0.276	0.32

(a) From (MTCI, 1990).

(b) Assuming 1.3 and 1.55 tonnes of dry black liquor are available per tonne of air-dry pulp produced from hardwood and softwood feedstock, respectively (Jaakko Poyry, 1989).

(c) The dry black liquor has a heating value of about 15 GJ/dry tonne (MTCI, 1990). The liquor is input to the gasifier as a 65% solids solution, the typical concentration of black liquor from evaporators at a kraft pulp mill.

A preliminary estimate of the installed cost of an MTCI gasification unit for a 1000 tpd pulp mill is \$60-80 million (Warren, 1990), which is essentially the cost of a new Tomlinson recovery boiler (Hunter, 1990). For purposes of preliminary economic analysis later in the paper, the cost for the gasifier is charged to chemical recovery rather than cogeneration, giving rise to installed capital costs of \$770/kW for the non-gasifier portion of a 55-MW black-liquor BIG/STIG and \$750/kW for a 64-MW BIG/ISTIG.[8]

BIG/GT Application at Kraft Pulp Mills

Most kraft pulp mills today are designed to meet their onsite steam and electricity needs using all of the biomass fuels currently available at the mill. Steam is raised in recovery and waste-wood boilers to drive a back-pressure steam turbine cogeneration system. If an additional design objective were to increase production of electricity for export, then improving the end-use electricity efficiency of the mill and adopting cogeneration technologies having higher electricity-to-heat ratios, like BIG/GTs, would be important. The possibilities for exporting electricity are explored here.

Hypothetical Pulp Mill Case Study. The application of BIG/GT systems to a hypothetical kraft pulp mill is explored

---

[6] While pressurization would be desirable, it may not strictly be necessary. For example, the MTCI technology produces a relatively high heating value gas (Table 3) without using oxygen and cools the gas during wet scrubbing, so that costs to compress the gas to gas turbine combustor pressures may not be prohibitive. To produce a gas with an equally high heating value using the Chemrec technology would require use of oxygen instead of air, but at the relatively large scale of most pulp mills, oxygen could probably be provided at acceptable cost. (In the future, many pulp mills will have oxygen plants on-site to supply oxygen delignification systems that reduce chlorine use for bleaching.)

[7] In cogeneration operation, the fraction of input black liquor energy converted to steam and electricity, respectively, would be an estimated 18 and 18 percent with STIG and 13 and 22 percent with ISTIG.

[8] These costs are developed from Table 2 assuming zero cost for the fuel handling, blast air, gasification plant, and gas cleanup equipment. Other equipment costs are assumed to be the same as shown in Table 2. Total costs are assumed to follow the scaling laws given in Table 1, note (f).

Table 4 Steam and electricity demands (net of powerhouse) at a modern bleached sulfate pulp mill in the Southeastern US[a]

End Use	*Steam @ 13 bar*		*Steam @ 4.4 bar*		*Total Steam*		*Electricity*
	(t/hr)	(GJ/tp)	(t/hr)	(GJ/tp)	(t/hr)	(GJ/tp)	(kWh/tp)
Black liq. evaporation	-	-	84.1	4.33	84.1	4.33	66.0
Pulp drying	69.5	3.64	5.9	0.30	75.4	3.94	153.4[b]
Digester	19.1	1.00	23.2	1.19	42.3	2.19	145.9[c]
Dearator	-	-	34.1	1.75	34.1	1.75	-
Chemicals generation	-	-	20.9	1.08	20.9	1.08	73.5[d]
Chip pre-steaming	-	-	13.6	0.70	13.6	0.70	-
Chiller/HVAC	-	-	13.6	0.70	13.6	0.70	4.6
Bleaching	-	-	10.0	0.51	10.0	0.51	88.8[e]
Fluid-bed calciner	-	-	-	-	-	-	42.5
Other	10.9	0.57	9.5	0.49	20.4	1.06	81.5[f]
TOTAL	99.5	5.21	214.9	11.05	314.4	16.26	656.2

(a) Based on measurements from a mill in the Southeastern region of the US producing 1000 tonnes of air-dried pulp per day. The mill was started up in 1981. The data here are for typical summer operation. The powerhouse requires approximately an additional 24% steam and 19% electricity over the totals shown in this table.

(b) Consists of 35.3 kWh/tp, 117.1 kWh/tp, and 0.96 kWh/tp for stock preparation, dryer, and finishing & shipping, respectively.

(c) Consists of 43.2 kWh/tp and 102.7 kWh/tp for digester and washing/screening, respectively.

(d) Consists of 10.1 kWh/tp and 63.4 kWh/tp for chemical preparation and oxygen supply to the delignification stage, respectively.

(e) Consists of 41.5 kWh/tp and 47.3 kWh/tp to the bleach plant and the oxygen delignification stage, respectively.

(f) Consists of 25 kWh/tp, 15.8 kWh/tp, 24.7 kWh/tp, 1.92 kWh/tp, and 14.1 kWh/tp to wood preparation, water supply, air supply, odor control, and miscellaneous, respectively.

Table 5 Energy use (net of powerhouse) at Swedish bleached kraft pulp mills[a]

Year ==>	*1973*	*1980*	*1984*	*1990* (*projected*)
Steam (GJ/tp)	16.8	12.2	11.0	7.8
Electricity (kWh/tp)	790	740	740	590

(a) Quantities are expressed per air-dried tonne of pulp. For 1973, the average Swedish mill (Jonsson et al., 1977). For 1980, the most efficient Swedish mill; for 1984, representing the most efficient Swedish mill; and for 1990, the technically and economically feasible level of demand in a new Swedish mill (Alsefelt, 1990).

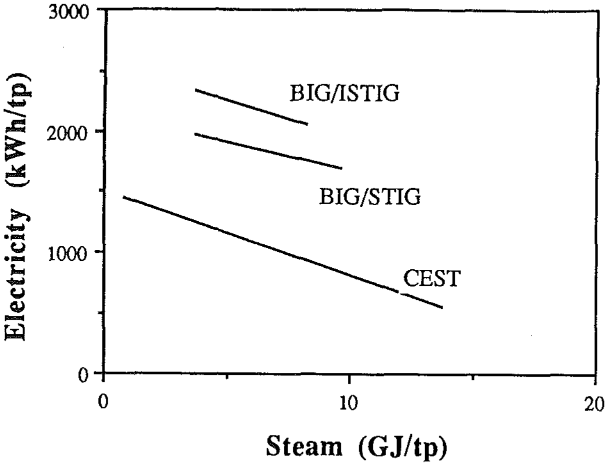

Fig. 5 Steam and electricity production (net of the cogeneration plant) with by-product fuels (7 GJ/tp hog fuel and 25.3 GJ/tp black liquor) at a hypothetical kraft pulp mill. Quantities are shown per tonne of air-dried pulp produced. For the gas turbine systems, separate gasification of the hog fuel and black liquor are assumed. Also, 3.3 GJ/tp of black liquor has been assumed to be gasified to meet the calciner energy demand (2 GJ/tp), and thus to be unavailable for steam and electricity production. The hog fuel input to the gasifier is actually 6.7 GJ/tp, which accounts for energy required for drying the fuel. For the CEST, separate hog fuel and recovery boilers are assumed. In addition, 2 GJ/tp of fuel would need to be purchased for the calciner.

based on data for a mill in the Southeastern US producing 1000 tpd of bleached sulfate pulp from loblolly pine.[9] The biomass fuels available at the real mill currently consist of black liquor (25.3 GJ per tonne of pulp produced), hog fuel (bark, sawdust, etc.) derived from logs brought into the mill (7.0 GJ/tp), and additional purchased bark (2.0 GJ/tp). The mill's energy requirements (net of the cogeneration plant) amount to 16.3 GJ/tp of process steam and 656 kWh/tp of electricity (Table 4). In addition, the calciner used to regenerate CaO from $CaCO_3$ in the chemical recovery loop of the mill requires 2 GJ/tp of fuel oil (or comparably clean fuel).

Black Liquor and Hog Fuel Use. Assuming only black liquor and hog fuel are available at the hypothetical mill (no purchased bark), CEST, BIG/STIG and BIG/ISTIG systems would cogenerate electricity and steam as shown in Fig. 5. Some reduction in mill steam use would be needed to enable any of the cogeneration systems to meet on-site steam demand.[10] On-site steam demand for the hypothetical mill would need to be 13.8 GJ/tp (15 percent less than the Southeastern US mill's demand), 9.6 GJ/tp (41 percent less), and 8.2 GJ/tp (50 percent less), respectively, for CEST, BIG/STIG, and BIG/ISTIG systems. It appears that such reductions are possible, particularly if they can be built into the design of a greenfield mill (Table 5). The corresponding electricity production levels would be 535, 1684, and 2052 kWh/tp, respectively. Some reduction in electricity demand would be needed for the CEST to be able to supply all on-site electricity needs. An electricity audit at the Southeastern US mill indicated that

---

[9] The mill is owned by a major producer that does not wish to be identified. Data we present relating to the mill are based primarily on measured values corresponding to a typical efficient summer day of operation.

[10] An alternative would be to increase steam production by augmenting the available "free" fuel supply with purchased fuel, as the case-study mill does currently. This case is not considered here.

Table 6 Wood produced as roundwood, logging residues, and other removals in the Southeastern US in 1986, and residues associated with pulpwood production from roundwood in this region

	Volume of wood produced[a] (million ft^3)			*Pulpwood prodution*[a]	*Residues produced* (tonnes per tonne of)	
	Roundwood	Logging Residues	Other Removals	(% of total)	pulpwood[d]	kraft pulp[e]
Growing Stock[b]						
Softwood	2,415	192	229	67.5	0.024	0.067
Hardwood	925	193	214	22.2	0.114	0.319
Other Sources[c]						
Softwood	111	61	29	5.1	0.809	2.27
Hardwood	276	201	156	5.2	1.297	3.63
Sub-totals						
Softwood	2,526	253	258	72.6	0.079	0.222
Hardwood	1,200	394	370	27.4	0.339	0.948
Total	3,727	648	628	100.0	0.150	0.42

(a) From (Waddell et al., 1989). The Southeastern region of the US includes the states of Florida, Georgia, North and South Carolina, and Virginia.

(b) Growing stock is defined as the main stem of live trees on timberland, between a 1-ft. (30.5 cm) stump and 4-inch (10.2 cm) diameter top (of central stem) excluding bark, or to the point where the central stem breaks into limbs. Roundwood from growing stock includes logs, bolts, and other round timber generated from harvesting trees for industrial or consumer use. Logging residues include downed and dead growing stock left on the ground after harvest. Other removals refer to unutilized wood from cut or otherwise killed growing stock during cultural operations (e.g., from precommercial thinning), or from timberland clearing.

(c) Roundwood "other sources" include salvable dead trees, rough and rotton cull trees, noncommercial tree species, trees less than 5-inches (12.7 cm) diameter at breast height, tops, and roundwood harvested from non-forest land (e.g., fence rows). Logging residues include wood other than growing stock left on the ground after harvest that is sound enough to chip, including dead and downed cull tress and tops to a 4-inch (10.2 cm) diameter (measured without bark) and excluding stumps and limbs. Other removals include wood other than growing stock left on the ground after cultural operations (e.g., precommercial thinning), or timberland clearing that is sound enough to chip (including dead and downed cull trees and tops to a 4-inch (10.2 cm) diameter—excluding bark) and excluding stumps and limbs.

(d) Estimates based on (Tansey, 1990), assuming the same specific density for residues and roundwood (38 lb/ft^3 (609 kg/m^3) for bone-dry wood). The first two numbers in this columns are weighted averages for residues from the harvest of sawtimber and poletimber trees for pulpwood, assuming that 30% of pulpwood comes from sawtimber and 70% from poletimber trees. The disaggregated residue ratios for growing stock are 0.062 t/t (softwood) and 0.220 t/t (hardwood) for sawtimber trees and 0.007 t/t (softwood) and 0.068 t/t (hardwood) for poletimber trees. [Sawtimber trees are those larger than 11 inches (27.9 cm) in diameter at breast height (dbh) for softwood and larger than 13 inches (33.0 cm) dbh for hardwood. Poletimber trees are 5 to 10.9 inches (12.7 to 27.7 cm) dbh for softwood and 5 to 12.9 inches (12.7 to 32.8 cm) dbh for hardwood.] For "other sources," the residue ratios are assumed to be the same as the average ratios calculated from the first three columns of this table. The last three numbers in the column are weighted according to the percentage of pulpwood produced.

(e) Calculated assuming that 2.8 dry tonnes of pulpwood are used to produce one tonne of kraft pulp. This is the average 1983 value for US sulphate pulp mills (American Pulpwood Association, 1989).

25 percent savings in electricity use would be cost-effective,[11] an estimate consistent with others that have been made (Larson and Nilsson, 1991), which would reduce demand from 656 to 492 kWh/tp. Reduced on-site electricity demand would permit the BIG/GT systems to produce even greater excess electricity that could be marketed off-site, e.g., sold to the local utility.

Forest Residue Use. The exportable electricity production from the hypothetical mill could be increased further if currently unutilized forest residues, produced during commercial harvest of forests, were used at the mill. Residues, as defined here, exclude roots, stumps, branches, needles and leaves. The volume of forest residues currently produced in the Southeastern US is about 1/3 the volume of harvested roundwood (Table 6). Some 0.42 tonnes of currently unutilized residues (equivalent to 8 GJ in energy terms) are associated with each tonne of kraft pulp produced. Additional residues equivalent to 21 GJ/tp are produced in forest-industry operations other than pulpwood production. Only the 8 GJ/tp of residues are considered in the analysis here, since pulp producers could reasonably be expected to be able to acquire these residues, but not necessarily the others.

It may be entirely feasible to remove all the residues in the Southeastern US without damage to long-term soil productivity (Larson, 1990), but local effects of residue removal must be well understood before beginning residue use for power. In the harvest of coniferous trees today, about 3/4 of the above-ground biomass is typically removed as merchantable wood, containing 40 to 50 percent of the tree's above-ground nitrogen, phosphorus, potassium, calcium, and magnesium (Freedman et al., 1981). Some additional nutrients would be removed with residue use, but may not necessarily result in excessive nutrient depletion (Carlisle and Methven, 1979) or degradation of soil organic matter status. Knowing the nutrient balance alone appears insufficient to predict the effects of residue removal on subsequent soil productivity, because of complex, site-specific climatologic, geologic, hydrologic, and biological considerations (Carlisle and Methven, 1979; Norton, 1976; Mann et al., 1988). It is clear, however, that forest productivity overall can be raised substantially through improved forest management and advanced genetic manipulations (Farnum et al., 1983; Wells and Jorgensen, 1978; Linder, 1989; Davey, 1989). Residue removal for power generation might be made an integral consideration of such developments. Modifications in

---

[11] This estimate is based on a 3-week on-site audit of the existing electrical system at the mill. The potential savings would come largely from trimming pump impellers to reduce inefficiencies due to oversizing and installation of variable speed drives on large pumps and fans.

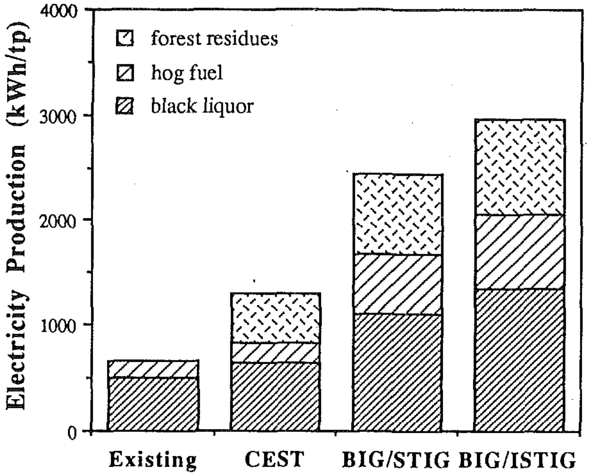

Fig. 6 Electricity production at a hypothetical 1000 tonne of pulp per day kraft mill with alternative biomass cogeneration systems. A typical existing system produces 535 kWh/tp (not enough to meet on-site needs without purchasing supplementary biofuel). For the CEST and BIG/STIG systems, the mill's process steam demand is assumed to be 9.6 GJ/tp. For the BIG/ISTIG it is assumed to be 8.2 GJ/tp. Calciner fuel demands are assumed to be met as described in the caption of Fig. 5.

forestry practices may raise unit costs of producing biomass, or resulting productivity gains could lower costs.

Assuming productivity issues relating to residue removal can be adequately addressed, utilizing the 8 GJ/tp of forest residues for electricity production at a pulp mill would lead to total electricity production from CEST, BIG/STIG, and BIG/ISTIG systems as shown in Fig. 6. The most efficient system, BIG/ISTIG, would produce nearly five times the electricity typically generated today.

Economics. The economics of producing excess electricity at the hypothetical mill will depend largely on the cost of the feedstocks. Here, hog fuel and black liquor are assigned a value essentially equivalent to their energy value today: The cogeneration facility supplies on-site steam and electricity to the mill in exchange for these fuels. All other costs of cogeneration are charged to the electricity produced in excess of on-site use. Costs for forest residues will vary locally, but would probably be in the range of \$2–\$3/GJ delivered to the mill at 50 percent moisture content, e.g., see Envirosphere (1986) and Fulkerson et al. (1989). This is roughly the cost for wood that might be grown on energy plantations (Kulp, 1990; Perlack and Ranney, 1987), which might provide a competitive alternative source of fuel. Some sizing (e.g., hogging or chipping) and drying would be required for the gas turbine systems, raising the cost of residues to \$3–\$4/GJ.[12] The CEST systems would not require the extra fuel processing.

The estimated costs of producing excess electricity at hypothetical energy-efficient pulp mills using alternative cogeneration technologies are shown in Table 7 assuming utility or private ownership. Using only hog fuel and black liquor, the busbar costs are 7.8 cents, 3.2 cents, and 2.6 cents per kWh, respectively, for the CEST, BIG/STIG, and BIG/ISTIG. Adding the forest residues, the estimated costs are 6.6–7.6 cents, 3.9–4.3 cents, and 3.2–3.5 cents per kWh.

With private ownership, the real internal rate of return before taxes and corrected for inflation (IRR) would be less than 3 percent per year for CEST, 13–16 percent per year for BIG/STIG, and 21–23 percent per year for BIG/ISTIG when excess electricity is sold for 5 cents per kWh (Table 7). Revenues from electricity sales would be up to \$124/tp. For comparison, producing bleached kraft pulp at a modern mill costs about \$400/tp.

The economic analysis here is applicable to a new mill, assuming a greenfield pulp mill incorporating energy efficiency improvements (excluding the cogeneration plant) would cost about the same as a conventional-technology greenfield mill. To assess the economics of retrofit applications to existing mills, the cost of end-use efficiency improvements would need to be estimated. This has not been done here. However, the affordable capital expenditure for retrofitting more efficient end-use equipment can be estimated. For example, for an overall IRR of 12 percent with excess electricity sold for 5 cents per kWh, the allowable capital cost for end-use retrofits at a mill installing a black-liquor/hog-fuel BIG/STIG or BIG/ISTIG would be \$37 million or \$79 million, respectively.[13]

Industry, Electric Utility, and Global Impacts. The results for the hypothetical mill can be extrapolated to provide a rough estimate of the global potential for use of BIG/GTs in the kraft pulp industry. Assuming global chemical-pulp production grows to the year 2020 at regional rates projected for the period 1980–2000 by the Food and Agriculture Organization (FAO, 1982), up to some 676 TWh of exportable electricity could be produced using black liquor, hog fuel, and forest residues as fuel (Table 8) from some 100 GW of installed BIG/ISTIG generating capacity. This electricity production is equivalent to 10 percent of the current global total from fossil fuels, or 14 percent of the total from coal.

For the US, which has the world's largest kraft pulp industry, the 1988 level of chemical pulp production would allow production of up to 111 TWh per year of excess electricity (using BIG/ISTIG) or about 7 percent of all electricity production from coal (Energy Information Administration, 1989a). The maximum associated export electricity production in 2020, assuming 1.9 percent per year growth in pulp production (FAO, 1982), would be 204 TWh per year from some 30 GW of installed capacity. This would be equivalent to 13 percent of the current electricity generation from coal. The corresponding biofuel consumption would be 3.3 billion GJ, or 7 percent of the estimated potential economically available US biomass resources (Larson, 1990).

Conclusions

The biomass-gasifier/gas turbine (BIG/GT) is a promising technology for biomass electricity generation because of expected high efficiencies and low unit capital costs at the modest scales appropriate for biomass applications and the good near-term prospects for its commercialization. Kraft black liquor gasifiers are undergoing commercial development for the recovery boiler replacement market. They may be developed for BIG/GT applications over a longer period.

Dedicated bioenergy plantations may cost-effectively provide fuel for BIG/GT applications in the long term, but initial applications are likely to be fueled with by-products of industrial processes, since large quantities are currently available

---

[12] Drying wood chips from 50 to 20 percent moisture content is estimated to cost about \$0.55/GJ, based on a commercial system, which condenses saturated 15-bar steam to provide heat and which evolves saturated 3-bar steam from the wood chips (Muenter, 1990). The 3-bar steam can then be used, e.g., in the digester, bleach plant, or evaporators at the mill. Drying 150 MW of biofuel (roughly the fuel use for an LM5000 BIG/STIG) requires 30 t/h of 15-bar steam and produces about 20 t/h of 3 bar steam, which corresponds to a net steam use of about 15 GJ/h. Electricity use is 0.75 MWh/h. Total capital cost for the dryer is estimated to be \$4.5 million. With electricity costing 5 cents/kWh and input steam valued at \$3.9/GJ_{steam} (its value if used to produce electricity selling for 5 cents/kWh), the total cost for capital, electricity, and input steam comes to \$0.80/GJ of fuel produced. Assigning to the produced 3-bar steam a value of \$1/GJ_{steam} results in a credit of \$0.25/GJ of fuel, giving a total cost of \$0.55/GJ_{fuel}.

[13] For mills where the forest residues would also be used, the affordable retrofit costs would be \$11 or \$32 million for the BIG/STIG, assuming high- or low-cost residues (Table 7), and \$71 or \$92 million for the BIG/ISTIG.

Table 7 Economics of excess electricity production at a hypothetical 1000 tpd kraft pulp mill

Fuels and Cogeneration Technologies[a]	*Utility Ownership*[b] (Busbar Cost, cents per kWh)				*Private Ownership*[c] (Internal rate of return)	*Electricity*	
	Capital[d]	O&M[e]	Fuel[f]	TOTAL		*Sales* (GWh/ year)	*Revenues* @ $0.05c/kWh ($/tp)
Black liquor							
+ *hog fuel*							
CEST	7.06	0.72	0.0	7.8	2.8	113	16
BIG/STIG	1.93	0.72	0.56	3.2	18.7	417	60
BIG/ISTIG	1.56	0.60	0.43	2.6	25.1	546	78
+ *Forest residues*							
(low-cost case)							
CEST	3.83	0.72	2.00	6.6	2.7	275	39
BIG/STIG	1.63	0.72	1.53	3.9	16.1	683	97
BIG/ISTIG	1.37	0.60	1.20	3.2	23.0	866	124
(high-cost case)							
CEST	3.83	0.72	3.00	7.6	neg.	275	39
BIG/STIG	1.63	0.72	1.92	4.3	13.5	683	97
BIG/ISTIG	1.37	0.60	1.51	3.5	20.6	866	124

(a) Steam demands met by the cogeneration systems are 9.6 GJ/tp for CEST and BIG/STIG and 8.2 GJ/tp for BIG/ISTIG. Electricity demand is 492 kWh/tp in all cases. Typical annual operating hours for a large pulping operation are assumed (8400 hours/yr).

(b) Assuming a 6.1% annual discount rate, an insurance charge equal to 0.5% of the initial capital cost per year and a 30-year life. With property and corporate taxes and existing tax preferences for renewable resource generating plants, the capital recovery factor (CRF) is 0.101 (Technology Evaluation Section, 1986).

(c) Real (inflation-corrected) internal rate of return before taxes, assuming a 25-year life, an insurance charge equal to 0.5% of the initial capital cost per year, and electricity revenues of 5 cents per kWh.

(d) Separate gasifier/gas-turbine units are assumed for black liquor and solid feedstocks. Also, a capital cost credit (equivalent to the cost of a Tomlinson recovery boiler) is assumed since the gasification system would also be serving the mill's chemical recovery requirements (see footnote 8). The capital cost for drying equipment needed with the BIG/GT units is included in the fuel cost (see footnote 12). In estimating the CEST capital cost, use of a single steam turbine is assumed, and a credit is taken equal to the cost of a Tomlinson recovery boiler.

(e) The O&M costs for the BIG/ISTIG are based on (Williams, 1989). BIG/STIG O&M costs are scaled from the ISTIG number by the ratio of STIG to ISTIG efficiency. The CEST O&M costs are assumed to be the same as for BIG/STIG.

(f) Fuel costs for CEST are assumed zero for hog fuel and black liquor. For BIG/STIG and BIG/ISTIG, $1/GJ is charged for hog fuel for drying (see footnote 12) and other pre-gasification handling. No charge for black liquor. The low and high forest-residue costs are assumed to be $3/GJ and $4/GJ charged to the gas turbine systems, respectively. CEST charges are $2/GJ and $3/GJ. The lower costs for CEST account for less required pre-processing (e.g., drying).

Table 8 Global potential for production of electricity in excess of on-site needs with BIG/ISTIG cogeneration technology in the kraft pulp industry

Region	1988			2020	
	Chemical pulp production[a] (10^6 t/yr)	*Potential electricity from pulp*[b] (TWh/yr)	*Utility fossil-fuel electricity generation*[c] (TWh/yr)	*Projected pulp production*[d] (10^6 tp/yr)	*Potential electricity from pulp*[b] (TWh/yr)
Industrialized	***95.8***	***238***	***5,231***	***204.6***	***507***
N. America	57.8	143	2,106	105.1	262
USSR	7.1	18	1,181	34.7	86
W. Europe	19.5	48	954	30.4	75
Japan	7.9	19	470	19.0	48
Oceania	0.93	3	116	11.2	27
E. Europe	2.7	7	404	3.7	9
Developing	***8.8***	***23***	***1,432***	***68.6***	***169***
Latin Am.	5.6	14	216	35.4	88
Asia	2.5	7	1,021	24.0	59
Africa	0.67	2	194	9.2	22
World	**104.7**	**261**	**6,662**	**273.1**	**676**

(a) From (FAO, 1990).

(b) Assuming 2,474 kWh/tp of electricity production in excess of process needs at efficient kraft pulp mills.

(c) From (Energy Information Adminstration, 1989b).

(d) Assuming projected production growth rates, 1980-2000 (FAO, 1982) persist till 2020. The growth rates are 1.9%/yr, North America; 5.1%/yr, USSR; 1.4%/yr, Western Europe; 2.8%/yr, Japan; 8.1%/yr Oceania; 1%/yr, Eastern Europe; 5.9%/yr, Latin America; 7.3%/yr, Asia (excluding Japan); and 8.5%/yr, Africa.

at reasonable costs. The kraft pulp industry is a major producer of biomass fuels (black liquor, hog fuel, and forest residues). BIG/GT systems using these for fuel could produce large quantities of electricity in excess of on-site needs at kraft pulp mills at total levelized busbar costs of 3.2 to 4.3 cents per kWh (assuming utility ownership) or pre-tax internal rates of return of 13 to 23 percent per year (assuming private ownership).

The large quantities of electricity that could be exported from pulp mills could reduce the need for building new utility power plants and could help offset CO_2 emissions associated with fossil-fueled plants. To achieve the high levels of excess electricity production would require some energy efficiency improvements at pulp mills and the use of forest residues associated with pulpwood production. The high expected rates of return may make large-scale biomass electricity production an interesting proposition for the pulp industry. The expertise in the industry with producing, harvesting, and processing biomass fuels and the continued market strength projected for the industry make it particularly well-positioned to undertake such an endeavor. Utilities might take an interest because the power generation would represent small increments of relatively low capital cost capacity that would be competitive at the busbar with many other new sources of utility electricity.

Acknowledgments

This research was supported by the Winrock International Institute for Agricultural Development, the Office of Energy of the US Agency for International Development, and the US Environmental Protection Agency. The author thanks Robert Williams for useful comments on draft versions of this paper and Jason Mark for assistance in the data analysis and calculations relating to energy production and use in the Southeastern US pulp mill.

References

Ahlstrom Corp. and Sydkraft, AB, 1990, "Sydkraft AB, Sweden and A. Ahlstrom, Finland Goes Ahead With Unique Gasification Process," press release, Nov. 7, Helsinki, Finland, and Malmo, Sweden.

Alsefelt, P., 1989, *Energy From the Forest Industry*, Swedish Tech. Development Board, Stockholm, Sweden.

American Pulpwood Association, 1989, *Pulpwood Statistics*, Washington, DC, Nov.

Anon., 1990, "West German Companies to Jointly Offer High Temperature Power Units," *Clean-Coal/Synfuels Letter*, McGraw-Hill, New York, June 11, p. 1.

Babu, S., 1990, Institute of Gas Technology, Chicago, Illinois, personal communication, Nov.

Carlisle, A., and Methven, I. R., 1979, "The Environmental Consequences of Intensive Forestry and the Removal of Whole Trees," *Biological and Sociological Basis for Rational Use of Forest Resources for Energy and Oganics*, US Department of Agriculture, Southeastern Forest Experiment Station, Asheville, NC, pp. 108–120.

Carpentieri, E., 1990 (Division Chief, Alternative Energy Sources, Hydroelectric Company of Sao Francisco, Brazil), "Forest Plantations for Utility Electricity in Northeast Brazil," presented at Winrock International Institute for Agricultural Development, Arlington, VA, Nov. 15.

Clark, E., 1988, "Cool Water Gasification Program: An Update," *EPRI Journal*, Electric Power Research Institute, Sept., pp. 45–48.

Corman, J. C., 1986, *Systems Analysis of Simplified IGCC Plants*, for US Department of Energy by General Electric Corp. Research Center, Schenectady, NY.

Corman, J. C., and Horner, M. W., 1986, "Hot Gas Clean-Up for a Moving Bed Gasifier," *Proc. 5th Annual Contractors' Conference on Coal Gasification* (AP-4680), Electric Power Research Institute, Palo Alto, CA, Chap. 14.

Corman, J. C., 1987, "Integrated Gasification-Steam Injected Gas Turbine (IG-STIG)," presented at the Workshop on Biomass-Gasifier Steam-Injected Gas Turbines for the Cane Sugar Industry (Arlington, VA), organized by the Center for Energy and Environmental Studies, Princeton University, Princeton, NJ.

Corman, J. C., 1989, General Electric Research and Development Center, Schenectady, NY, personal communication to R. H. Williams.

Corman, J. C., 1990, General Electric Research and Development Center, Schenectady, NY, personal communication, Aug.

Davey, C. B., 1989, "Forest Fertilization in the Americas," *Nutrition of Trees*, Marcus Wallenberg Symposia Proceedings: 6, Falun, Sweden, pp. 33–61.

de Biasi, V., 1990, "LM6000 Dubbed the 40/40 Machine Due for Full-Load Tests in Late 1991," *Gas Turbine World*, May–June, pp. 16–20.

Durai-Swamy, K., Warren, D. W., and Mansour, M. N., 1989, "Pulse-Enhanced Indirect Gasification for Black Liquor Recovery," *Proceedings, 1989 International Chemical Recovery Conference*, TAPPI, Atlanta, GA.

Elliott, P., and Booth, R. T., 1990, "Sustainable Biomass Energy," selected papers, Shell International Petroleum Company, London.

Energy Information Administration, 1989a, *Electric Power Annual 1988*, DOE/EIA-0348(88), US Dept. of Energy, Washington, DC.

Energy Information Administration, 1989b, *International Energy Annual 1988*, DOE/EIA-0219(88), US Dept. of Energy, Washington, DC.

Envirosphere, Inc., 1986, *Regional Logging Residue Supply Curve Project* (2 volumes), for the Bonneville Power Administration, Pacific Northwest and Alaska Regional Bioenergy Program, Bellevue, WA.

Evans, R. J., Knight, R. A., Onischak, M., and Babu, S. P., 1988, *Development of Biomass Gasification to Produce Substitute Fuels*, PNL-6518, Battelle Pacific NW Lab., Richland, WA.

FAO (Food and Agriculture Organization), 1982, *World Forest Products Demand and Supply 1990 and 2000*, Forestry Paper 29, United Nations, Rome.

FAO (Food and Agriculture Organization), 1990, *1988 Yearbook of Forest Products*, United Nations, Rome.

Farnum, P., Timmis, R., and Kulp, J. L., 1983, "Biotechnology of Forest Yield," *Science*, Vol. 219, Feb., pp. 694–702.

Freedman, B., Morash, R., and Hanson, A. J., 1981, "Biomass and Nutrient Removals by Conventional and Whole-Tree Clear-Cutting of a Red Spruce—Balsam Fir Stand in Central Nova Scotia," *Can. J. For. Res.*, Vol. 11, pp. 249–257.

Fulkerson, W., et al., 1989, "Energy Technology R&D: What Could Make a Difference?" ORNL-6541/V2/P2, Oak Ridge National Lab., Oak Ridge, TN, Dec., Table 2.4-3.

Grace, T. W., and Malcolm, E. W., 1989, *Pulp and Paper Manufacture, Vol. 5: Alkaline Pulping*, TAPPI, Atlanta, GA.

Hall, D. O., Mynick, H. E., and Williams, R. H., 1991, "Alternative Roles for Biomass in Coping With the Greenhouse Warming," *Science and Global Security*, Vol. 2, pp. 113–151.

Horner, M. W., 1985, "Simplified IGCC With Hot Fuel Gas Combustion," ASME Paper No. 85-JPGC-GT-13.

Hunter, W. D., 1990, Weyerhauser Co., Tacoma, WA, personal communication, Nov.

Isaksson, J., 1989, Ahlstrom Research and Development Center, Karhula, Finland, personal communication.

Jaakko Poyry Oy, 1989, *Assessment of Market Prospects for the Chemrec Black Liquor Gasification Process*, Helsinki, Finland, Mar.

Jersey Central Power & Light Co. and Sargent & Lundy, 1989, "A Comparison of Steam-Injected Gas Turbine and Combined-Cycle Power Plants: Technology Assessment," GS-6415, Electric Power Research Institute, Palo Alto, CA.

Jonsson, S. E., Nygaard, J., and Wiberg, R., 1977, *Models for Energy Use in Pulp and Paper Mills: Bleached Sulfate Pulp Mills*, Swedish Pulp and Paper Association, Stockholm, Sweden.

Kelleher, E. G., 1985, "Black Liquor Gasification and Use of the Product Gas in Combined-Cycle Cogeneration—Phase II," *Tappi Journal*, Nov., pp. 106–110.

Kignell, J. E., 1990, "Novel Concept for Chemicals and Energy Recovery From Black Liquor," *Proceedings of the EUCEPA*, SPCI, Stockholm, Sweden, May.

Kulp, J. L., 1990, "The Phytosystem as a Sink for Carbon Dioxide," EN-6786, Electric Power Research Institute, Palo Alto, CA.

Larson, E. D., and Williams, R. H., 1987, "Steam-Injected Gas Turbines," ASME JOURNAL OF ENGINEERING FOR GAS TURBINES AND POWER, Vol. 109, pp. 55–63.

Larson, E. D., Svenningsson, S., and Bjerle, I., 1989, "Biomass Gasification for Gas Turbine Power Generation," *Electricity: Efficient End-Use and New-Generation Technologies, and Their Planning Implications*, Lund University Press, Lund, Sweden, pp. 697–739.

Larson, E. D., 1990, "Biomass-Gasifier/Gas-Turbine Applications in the Pulp and Paper Industry: An Initial Strategy for Reducing Electric Utility CO_2 Emissions," *Proc. Ninth Conference of Coal Gasification Power Plants*, Electric Power Research Institute, Palo Alto, CA.

Larson, E. D., and Williams, R. H., 1990, "Biomass-Gasifier Steam-Injected Gas Turbine Cogeneration," ASME JOURNAL OF ENGINEERING FOR GAS TURBINES AND POWER, Vol. 112, pp. 157–163.

Larson, E. D., and Nilsson, L. J., 1991, "Electricity Use and Efficiency in Pumping and Air Handling Systems," *ASHRAE Transactions*, Vol. 97, Pt. 2, pp. 363–377.

Linder, S., 1989, "Nutritional Control of Forest Yield," *Nutrition of Trees*, Marcus Wallenberg Symposia Proceedings: 6, Falun, Sweden, pp. 62–89.

Mann, L. K., et al., 1988, "Effects of Whole-Tree and Stem-Only Clearcutting on Postharvest Hydrologic Losses, Nutrient Capital, and Regrowth," *Forest Science*, Vol. 34, No. 2, pp. 412–428.

MTCI (Manufacturing and Technology Conversion International, Inc.), 1990, *Testing of an Advanced Thermochemical Conversion Reactor System*, Battelle Pacific Northwest Lab., Richland, WA.

Muenter, C., 1990, Stork Friesland Scandinavia AB, Gothenberg, Sweden, personal communication, Sept.

Norton, S. A., 1976, "Nutrient Budgets of Complete Tree Harvesting Versus

Merchantable Bole Requirements," *New Horizons for the Chemical Engineer in Pulp and Paper Technology*, AIChE Symposium Series No. 157, Vol. 72, American Institute of Chemical Engineers, New York, pp. 17-23.

Ogden, J. M., Williams, R. H., and Fulmer, M. E., 1990, "Cogeneration Applications of Biomass Gasifier/Gas Turbine Technologies in the Cane Sugar and Alcohol Industries: Getting Started With Bioenergy Strategies for Reducing Greenhouse Gas Emissions," *Energy and Environment in the 21st Century*, MIT Press, Cambridge, MA, pp. 311-346.

Perlack, R. D., and Ranney, J. W., 1987, "Economics of Short-Rotation Intensive Culture for the Production of Wood Energy Feedstocks," *Energy: the International Journal*, Vol. 12, No. 12, pp. 1217-1226.

Pitrolo, A. A., and Graham, L. E., 1990, "DOE Activities Supporting IGCC Technologies," *Proc. Conf. on Integrated Gasification Combined Cycle Plants for Utility Applications*, Chap. 1a, Canadian Electrical Assoc., Montreal, Canada.

Salo, K. (Director of R&D), 1990, Tampella Corp., Helsinki, Finland, personal communication, Sept.

San Martin, R. (Deputy Assistant Secretary, Office of Utility Technologies, Division of Conservation and Renewables), 1990, "DOE Research on Biomass Power Production," presented at the conference on Biomass for Utility Applications, Tampa, FL, Oct., pp. 23-25.

Scandrett, L. A., and Clift, R., 1984, "The Thermodynamics of Alkali Removal From Coal-Derived Gases," *Journal of the Institute of Energy*, Vol. 57, Dec., pp. 391-397.

Stambler, I., 1990, "New Generation of Industrialized Aero Engines Coming for Mid-1990s Projects," *Gas Turbine World*, July-Aug., pp. 19-22.

Sterzinger, G. (Commissioner), 1990, Dept. of Public Service, State of Vermont, Montpelier, VT, personal communication, Aug.

Stigsson, L., 1989, "A New Concept for Kraft Recovery," *Proc., 1989 International Chemical Recovery Conference*, TAPPI, Atlanta, GA.

Synthetic Fuels Associates, 1983, "Coal Gasification Systems: A Guide to Status, Applications, and Economics," AP-3109, Electric Power Research Institute, Palo Alto, CA.

Tansey, J. B., 1990, Southeast Forest Experiment Station, Forest Service, US Department of Agriculture, Asheville, NC, personal communication, Aug.

Technology Evaluation Section, 1986, *TAG—Technical Assessment Guide Vol. 1: Electricity Supply—1986*, Electric Power Research Institute, Palo Alto, CA.

Waddell, K. L., Oswald, D. D., and Powell, D. S., 1989, *Forest Statistics of the United States, 1987*, Resource Bulletin PNW-RB-168, USDA Forest Service, Pacific Northwest Research Station, Portland, OR, Sept., p. 95.

Warren, D. W. (Manager of Engineering), 1990, MTCI, Sante Fe Springs, CA, personal communication, Aug.

Wells, C. G., and Jorgensen, J. R., 1978, "Nutrient Cycling in Loblolly Pine: Silvicultural Implications," *Tappi Journal*, Vol. 61, No. 1, Jan., pp. 29-32.

Williams, R. H., Larson, E. D., and Ross, M. H., 1987, "Materials, Affluence, and Industrial Energy Use," *Annual Review of Energy*, Vol. 12, pp. 99-144.

Williams, R. H., 1989, "Biomass Gasifier/Gas Turbine Power and the Greenhouse Warming," *Proc. IEA/OECD Expert Seminar on Energy Technologies for Reducing Emissions of Greenhouse Gases*, OECD, Paris, France.

Williams, R. H., and Larson, E. D., 1989, "Expanding Roles for Gas Turbines in Power Generation," *Electricity: Efficient End Use and New Generation Technologies, and Their Planning Implications*, Lund University Press, Lund, Sweden, pp. 503-553.

M. Jansen

T. Schulenberg

D. Waldinger

Siemens AG,
Muelheim,
Federal Republic of Germany

Shop Test Result of the V64.3 Gas Turbine

The V64.3 60-MW combustion turbine is the first of a new generation of high-temperature gas turbines, designed for 50 and 60 Hz simple cycle, combined cycle, and cogeneration applications. The prototype engine was tested in 1990 in the Berlin factories under the full range of operation conditions. It was equipped with various measurement systems to monitor pressures, gas and metal temperatures, clearances, strains, vibrations, and exhaust emissions. The paper describes the engine design, the test facility and instrumentation, and the engine performance. Results are given for turbine blade temperatures, compressor and turbine vibrations, exhaust gas temperature, and NO_X emissions for combustion of natural gas and fuel oil.

Introduction

As gas turbines running at 50 and 60 Hz have increased more and more in power output beyond 100 MW, Siemens/KWU is now introducing the V64.3, a medium size 60-MW gas turbine, running at 5400 rpm, for application at 50 Hz and 60 Hz electric utilities and for large industrial applications.

In particular, application of this new high-temperature gas turbine is intended for:

- electric utilities, either simple cycle for peak load power stations or combined cycle for base load plants, with a net efficiency of more than 50 percent;
- conventional fuels as natural gas or oil, as well as coal gas from integrated coal gasification plants, which are expected to be economical within the next years;
- district heating, where medium size gas turbines could be of high interest for local applications; and
- cogeneration of electric energy and process steam for industries around the plant site.

Beginning in March 1990, extensive component and load tests have been performed on the test bed in the Berlin factories. The first two units of V64.3 gas turbines have already been delivered for installation to a combined cycle power station near Helsinki. These have gone into commercial operation in autumn 1990.

Engine Description

A cross section of the new model V64.3 combustion turbine is shown in Fig. 1. It is obvious that most of the design principles of the well-approved V94.2 and V84.2 gas turbines have been adopted. Again it is a single-shaft engine with interlocking disks, stressed by an axial tiebolt to ease maintenance. It has two silo combustion chambers now arranged horizontally, again flange mounted on the gas turbine casing, a 17-stage compressor and a 4-stage turbine. Details of the design have already been described by Becker and Ziegner (1988).

Significant improvements of the thermodynamic performance were intended by increasing the pressure ratio to about 16 and by increasing the turbine inlet temperature. The first four compressor stages were equipped with adjustable guide vanes to improve performance at part-load. Profiles of compressor and turbine bladings were of new design. Due to the higher turbine inlet temperature, the transition piece between the two combustors and the turbine inlet was heat protected by shielding plates.

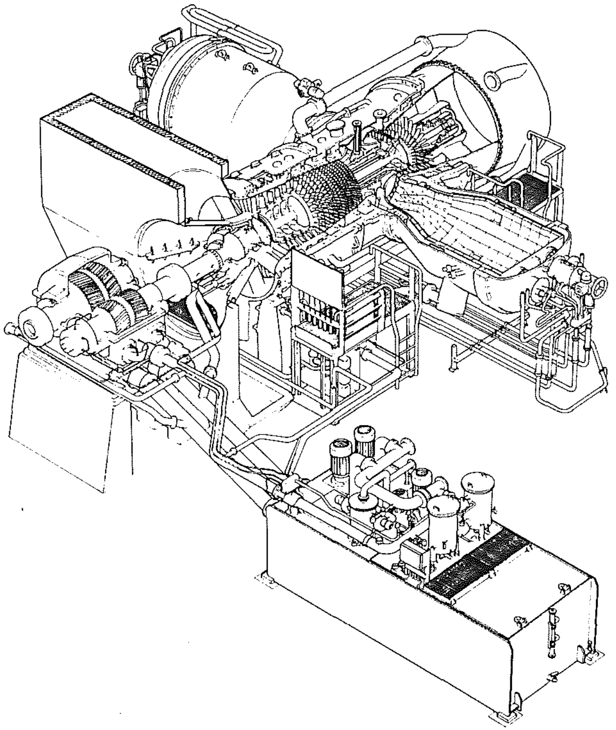

Fig. 1 V64.3 gas turbine

Contributed by the International Gas Turbine Institute and presented at the 36th International Gas Turbine and Aeroengine Congress and Exposition, Orlando, Florida, June 3-6, 1991. Manuscript received at ASME Headquarters March 4, 1991. Paper No. 91-GT-224. Associate Technical Editor: L. A. Riekert.

With the pressure ratio higher than in current machines, an intercooler was provided for more effective blade cooling in the first turbine stage. On the other hand, the combustors are almost identical to the approved V94.2 combustors, except that only three burners per combustor were required for this smaller gas turbine. The same hybrid burners as in a V94.2 were used, which enabled lowest NO_X emissions, as described by Becker et al. (1991). Ceramic tiles were used again in the combustors to protect the flame tube.

Figure 2 shows a V64.3 during assembly. In the front the mechanical drives of the four adjustable compressor guide vanes are visible. Moreover, heat shields of the transition piece can be seen in the background.

Test Facility

The test facility at the Berlin factories was designed to test heavy-duty gas turbines under full load conditions. It is described by Deblon (1978) and by Schulenberg and Bals (1987). Instead of a generator, the gas turbine was connected with a water brake, and the released energy was submitted to three cooling towers. Different from previous arrangements, a gear box was installed between water brake and gas turbine, which will also be required for electric utilities to transform the 90 Hz rotational speed to a 50 Hz or 60 Hz network. The total arrangement is shown in Fig. 3. Tests were run by supplying natural gas and fuel oil, both by using the same hybrid burners.

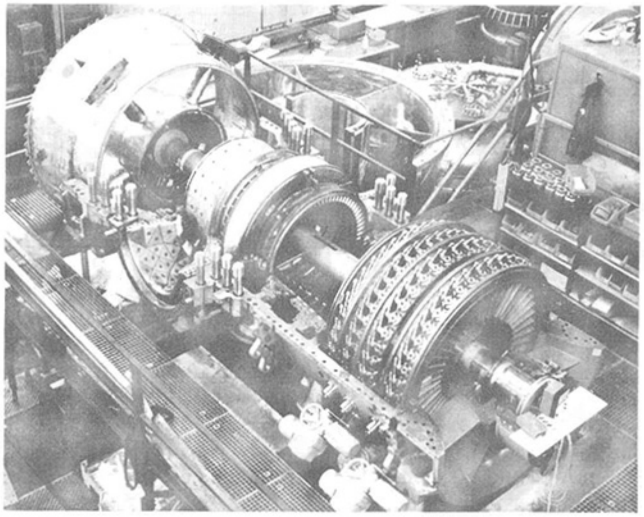

Fig. 2 Model V64.3 gas turbine during assembly

The main objectives of these tests were to validate the thermodynamic performances of compressor, combustors, and turbine, to ensure proper cooling of all components exposed to hot gas, and to determine dynamic stresses under all load conditions. Therefore several measurements were taken in addition to the standard measurements required during commissioning. They are summarized in Table 1. This list includes static pressure measurements by pressure tappings, thermocouple measurements of the gas temperature in compressor and turbine, as well as in the exhaust duct, and wall temperature measurements. The latter ones were obtained both with thermocouples and with a pyrometer, which could be inserted into each turbine stage, between the vanes, to observe the proceeding and the succeeding running blade as described by Schulenberg and Bals (1987). Blade dynamic stresses were detected with strain gages on compressor stages 1 to 4 and 9 and on all turbine stages, both on the airfoil and on the blade root. In addition, vibrations of the fourth-stage blades were observed with a laser optical system as described by Roth (1980). This additional information enables us to predict the vibratory stresses of the first mode of all blades of this stage, whereas strain gages yield complete vibration spectra of only a selected number of blades. Measurements of clearances were taken in order to minimize leakages and tip losses of compressor and turbine bladings. During the tests, emissions of NO, NO_2, CO, CO_2, and UHC could be measured continuously in the exhaust duct. All data were stored by a new data acquisition system. Thermodynamic performances were evaluated continuously during operation, so that the control center could be informed about trends and behavior already during the tests. Fast signals such as blade vibration and pyrometric temperatures were stored additionally on analogue tapes. They were digitized later on.

Table 1 Test run V64.3; measurement points

Type of measurement	Compressor	Combustor	Turbine
Pressure	28	6	27
Temperature			
Flow temperatures	12	-	93
Component temperatures			
with thermocouple	-	15	131
with radiation pyrometer	-	-	7
Cooling air mass flow	4	-	8
Blade vibration			
with strain gauge	18	-	48
with laser optic system	-	-	1
Clearances	20	-	16

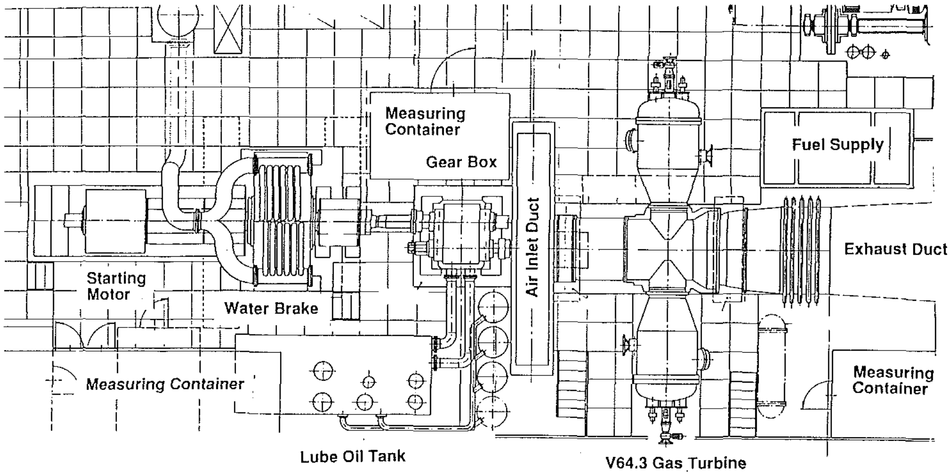

Fig. 3 Arrangement in test bed in the Berlin factories

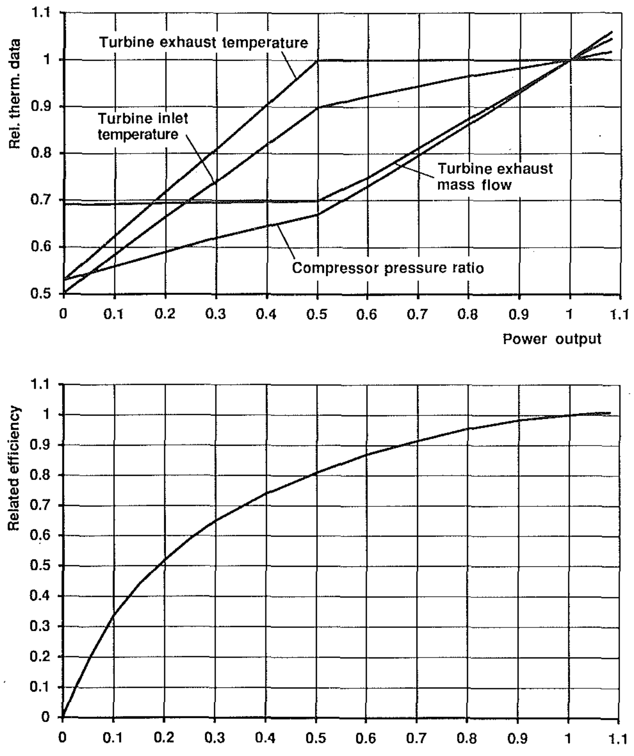

Fig. 4 Performance of V64.3, test results

Table 2 Thermodynamic data at ISO conditions

		Base Load			Peak Load		
Standard fuels			Gas	Oil		Gas	Oil
Low heat value (LHV)	kJ/kg	H_u	50056	42000	H_u	50056	42000
Turbine output at coupling	MW	$P_{K\text{-}IG}$	61.5	60.0	$P_{K\text{-}IS}$	66.7	64.9
Turbine efficiency at coupling	%	$\eta_{K\text{-}IG}$	35.8	35.4	$\eta_{K\text{-}IS}$	36.1	35.7
Compressor pressure ratio	—	$\Pi_{V\text{-}IG}$	15.6	15.5	$\Pi_{V\text{-}IS}$	15.9	15.8
Fuel mass flow	kg/s	$\dot{m}_{Br}$	3.44	4.04	$\dot{m}_{Br}$	3.69	4.33
Turbine exhaust mass flow	kg/s	$\dot{m}_{TII}$	187	187	$\dot{m}_{TII}$	187	187
Turbine exhaust temperature	°C	$\vartheta_{TII\text{-}IG}$	534	535	$\vartheta_{TII\text{-}IS}$	565	566

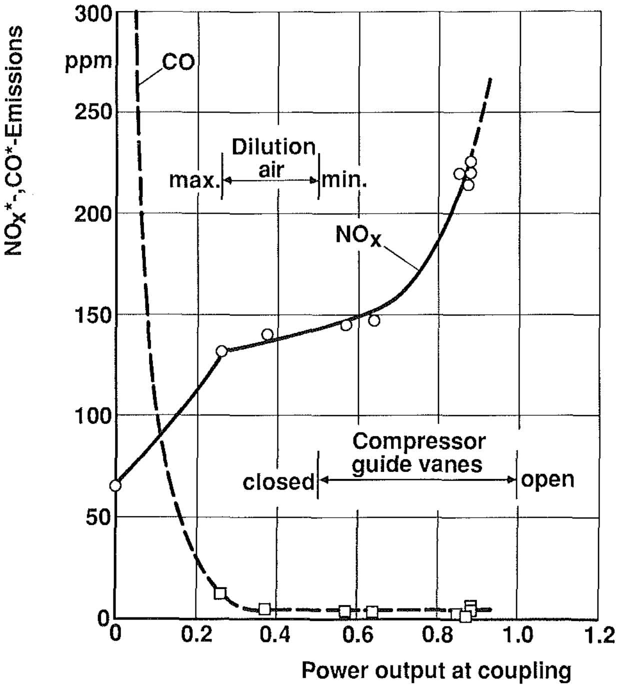

* in the dry exhaust gas with 15% O_2 by Volume

Fig. 5 Emissions of NO_X and CO, natural gas in diffusion burner mode

Test Program

After installation in the test stand, commissioning of V64.3 gas turbine was started on Feb. 28, 1990. One week later we tested ignition and acceleration of the gas turbine to operation speed. From this test the start-up curves and the lube oil system were optimized, and the control and measuring systems were checked. On Apr. 20, the gas turbine was fully loaded up to 65 MW, using natural gas in the diffusion burner mode. From this test we obtained all material temperatures measured with thermocouples, the exhaust duct temperature pattern, all vibratory amplitudes, and the engine performance. Compressor and turbine bladings performed well. Measured data were within the design limits. Some hot metal temperatures in the combustors, however, required some modifications.

A second test phase was conducted in June 1990 with modified combustors. These tests included optimization of the adjustable compressor vanes, pyrometric measurements of turbine blades, and laser optical measurements of the last-stage blades. A third test phase in July 1990 included also tests with natural gas in the premix burner mode and with fuel oil. In the following sections results of all these tests will be discussed in more detail.

Engine Performance

The first loading cycle in Apr. 1990 revealed that power and efficiency of the gas turbine were already higher than predicted. Differences in efficiency were mainly due to significantly higher turbine efficiency, whereas the compressor efficiency only slightly exceeded the predicted level. The measured gas turbine efficiency at the coupling, turbine inlet and outlet temperature, and compressor pressure ratio are shown in Fig. 4. All data have been scaled with the base load performance.

The thermodynamic data at base load and peak load, corrected to ISO conditions (i.e., 15°C ambient temperature, 1013 mbar ambient pressure, 60 percent humidity) are listed in Table 2. In these data, all measuring uncertainties and tolerances of manufacturing, as well as gear losses, are subtracted. Therefore the power and efficiency of future machines can be expected to be higher than listed.

Emissions

During the first test phase the gas turbine was run with natural gas. The hybrid burner, which has successfully been applied already to all types of Siemens gas turbines, was also installed in the V64.3. This burner can be operated with natural gas, either in a diffusion burner mode or in a premix burner mode. Details are described by Becker et al. (1990).

Emissions of NO_X and CO for the diffusion burner mode are shown in Fig. 5. At zero load the compressor guide vanes were closed, in order to obtain high turbine exhaust temperatures and low CO emissions. Adjustable dilution air holes in the combustors were open, by which combustion air was bypassed to minimize CO emissions.

With increasing load the compressor guide vanes were opened as soon as the maximum turbine exhaust temperature had been reached, i.e., at 50 percent power output as shown in Fig. 4. From 26 percent load to 50 percent load the adjustable dilution air openings were closed, giving an almost constant fuel-to-air ratio in the flame within this load range.

In this way, the NO_X emissions could be minimized over the whole load range. A further, efficient reduction of NO_X emis-

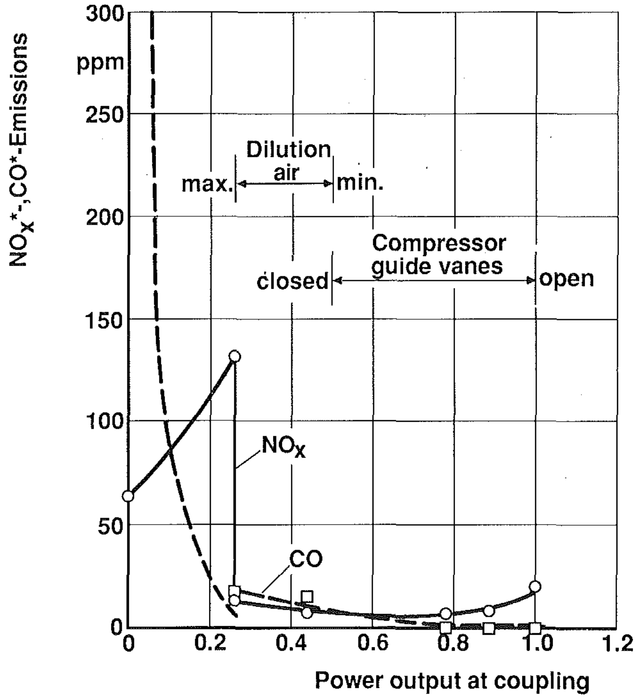

* in the dry exhaust gas with 15% O_2 by Volume

Fig. 6 Emissions of NO_X and CO, natural gas in premix burner mode

sions in the diffusion burner mode will be achieved by injection of water and steam. Tests will be performed next. At base load a NO_X reduction to about 10 percent of the dry emissions (Fig. 5) is expected.

A significantly better NO_X reduction was obtained however with the premix burner mode. By switching over at 26 percent load, as shown in Fig. 6, NO_X emissions were kept below 20 ppm, for all loads up to base load. Here again, the adjustable compressor guide vanes and the dilution air openings in the combustors were controlled such that almost a constant fuel-to-air ratio was gained. Below 26 percent load, however, the diffusion burner mode is preferable, in comparison to the premix burner mode, which causes higher CO emission in that range.

Compressor

The static pressure rise in the compressor and diffuser showed good agreement with the design calculation. The anticipated compressor efficiency was in fact exceeded during testing. Because the first four stages were fitted with adjustable vanes, the efficiency for 50 percent power output decreased to only 95 percent of the base load efficiency.

The tip clearances of the unshrouded rotor blades have been minimized to achieve maximum possible compressor efficiency. Measurements of the rotor blades in rows 1, 4, 8, 13, and 16 were performed as part of the test program to check tip clearances. Two techniques were used to measure clearances. Minimum clearances were measured in each run with four abrasion pins arranged around the circumference. In addition, the non-steady-state behavior of the tip clearances was investigated using a trace pin method developed by Siemens. Applying this method, a pin is moved step-by-step into the radial gap until it has contact with the rotating blades. By this method it is possible to determine the local tip clearances at individual times during operation.

Figure 7 shows the non-steady-state tip clearances in the first and fourth rows of rotor blades. The clearance is related to the cold gap. The associated speed curve is shown in the bottom half of Fig. 7. During start-up the clearances are reduced to 48 percent (row 4) and 35 percent (row 1) of that in the cold condition as a result of centrifugal forces. The subsequent increase in tip clearances is attributable to thermal expansion.

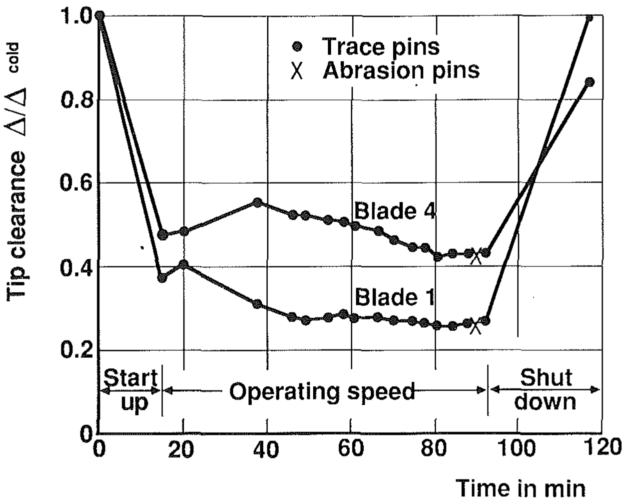

Fig. 7 Real time blade tip clearances

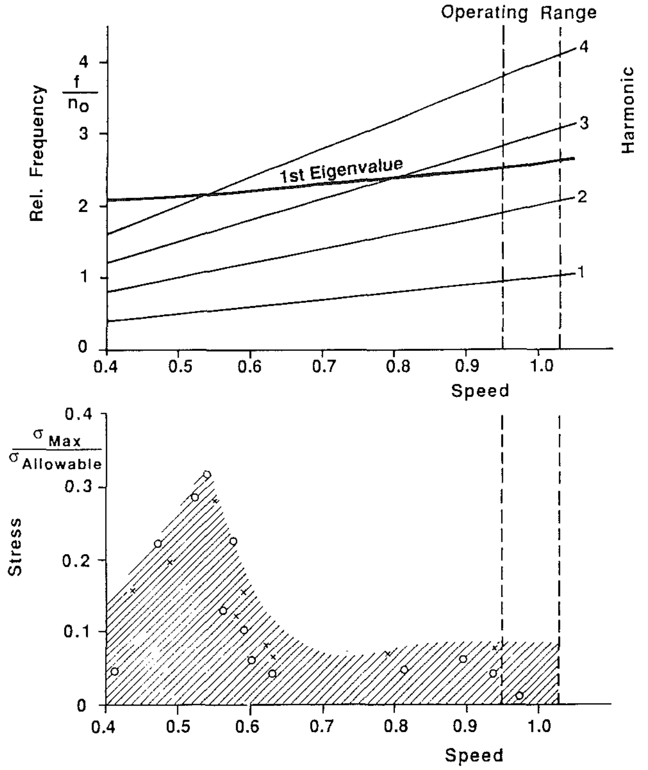

Fig. 8 First-stage compressor blade frequency and stress

Looking at the fourth row of rotor blades, the slow heat-up of the compressor disks becomes apparent only 20 minutes after rated speed is achieved. Figure 7 also shows the results obtained with abrasion pins. These results are the averages of the four measurements around the circumference. The measurements show that the Model V64.3 can be reliably operated with minimal tip clearances in favor of compressor efficiency. Vibration measurements were performed on rows 1, 2, 3, 4, and 9 to check the dynamic stresses acting on the compressor rotor blades. In each stage two blades were fitted with strain gages. The signals were monitored with the aid of a telemetric system. Figure 8 shows the result of vibration measurements

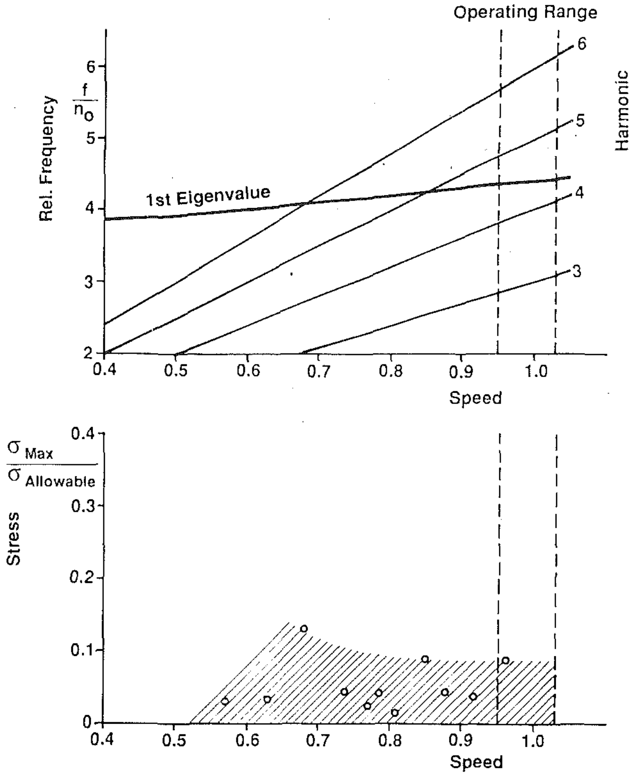

Fig. 9 Fourth-stage compressor blade frequency and stress

for the rotor blade in the first compressor stage. The upper half of the figure shows the Campbell diagram. It is apparent that the first natural frequency of the blade as required does not coincide with integral multiples of the rotor's rotational frequency (harmonic). The Campbell diagram also shows that, in the range from zero to rated speed, resonances between the natural frequency modes and speed harmonics cannot be avoided. Special attention is paid to the effect of nozzle excitation.

The alternating stressing of the blade recorded by the strain gages was converted for each eigen mode to the point of maximum blade stress. Here we reverted to the results of finite element calculations. The results of this analysis are shown in the lower half of Fig. 8. The stresses are related to the allowable strength. Maximum stresses occur during start-up as a result of nonincident flow conditions and because of resonance excitation in the first eigen mode. The stresses encountered are, however, low by comparison with allowable stresses (fatigue strength of the structure). They are within the empirical range, of our well-approved V94.2 and V84.2 gas turbines. Figure 9 shows the Campbell diagram and the cyclic stresses measured for the rotor blades in the fourth stage.

These stresses are likewise converted to the point of maximum blade stress. The maximum stresses in this stage are also low. In Table 3 the highest measured dynamic stresses of the first compressor blades are listed. They are related to the allowable stress of the blade. Most of these stresses occur only during start-up or shut-down. In the operating speed range only 14 percent of the allowable stresses have been measured.

Table 3 Maximum dynamic stress of compressor blade for whole speed range

Row	Rel. Speed	$\frac{\text{Alternating Stress}}{\text{Allowable Stress}}$
1	0.56	0.28
2	0.77	0.17
3	0.98	0.14
4	0.67	0.13

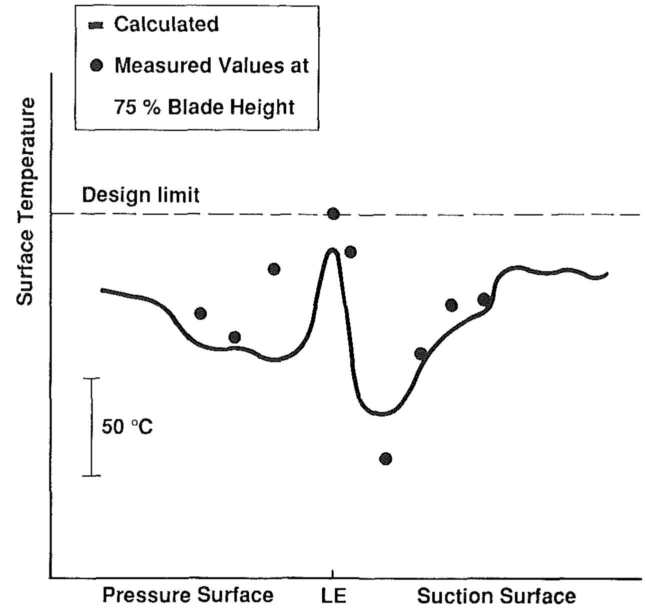

Fig. 10 Temperature profile of first turbine vane

Turbine

The first seven of the eight blade rows in the four-stage turbine are cooled. The moving blades in the first stage are shrouded in order to reduce tip losses. The proven combination of convection and impingment was selected as the cooling method. To verify the effectiveness of cooling, the surface temperature of the blades in the first stage was measured, in addition to the gas and cooling air temperatures. Several thermocouples were installed in two guide vanes in each row. The surface temperatures of the moving blades were measured with the aid of pyrometers, which were fitted between stationary vanes. They could be moved transversely across the blade height, as described by Schulenberg and Bals (1987).

Figure 10 shows the surface temperature of the stationary vane in the first stage for a section at 75 percent of the blade height. The measurement was carried out for a load of 65 MW. The temperature measured in the range of the stagnation point is higher than that calculated. Although this surface temperature is just allowable, the cooling of these vanes will be improved for future machines, to achieve a more uniform temperature distribution on the airfoil.

Figure 11 shows the calculated surface temperature curve of the moving blades in stage one at 50 percent blade height for the same turbine inlet temperature. The data recorded with the pyrometer are within the limits of design data for this operation point.

The dynamic stress of all turbine blades was investigated with the aid of strain gages. In addition, vibrations of the fourth-stage blades were observed with an optical method as shown by Roth (1980). This method covers each blade in the row under observation. The results take into account the existing scatterband in the dynamic behavior of the blades as a result of fabrication tolerances. The dynamic stress of the blades in the fourth stage is shown in Fig. 12 represented as

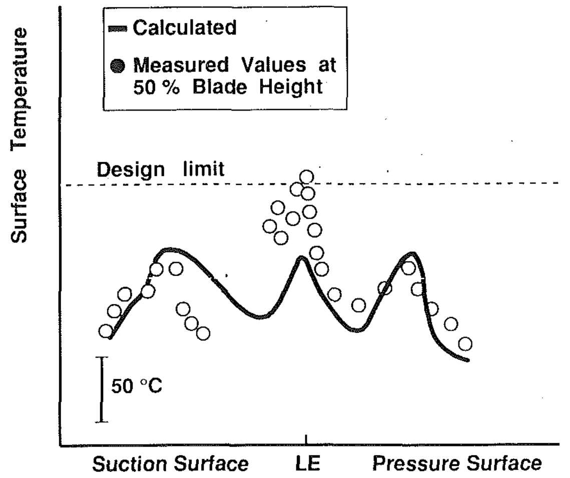

Fig. 11 Temperature profile of first turbine blade

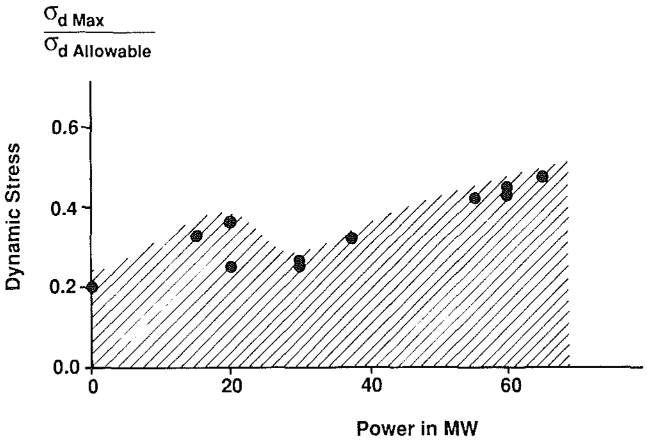

Fig. 12 Vibration stress of fourth turbine blade

a function of output. Figure 12 shows the measured maximum stress converted to the point of maximum blade loading. There is an adequately large margin to the permissible stress.

Table 4 Maximum dynamic stress of turbine blades

Row	1	2	3	4
$\frac{\sigma_d \text{ Max}}{\sigma_d \text{ Allowable}}$	0.25	0.10	0.28	0.48

In Table 4 the highest measured dynamic stresses for all turbine blade rows are listed. The dynamic stresses are far below the allowable limit.

Conclusion

- Full-load tests of the gas turbine V64.3 demonstrated that the expected performances were exceeded.
- Safe and reliable operation of the engine was proven.
- NO_X and CO emissions are extremely low using the dry low NO_X hybrid burner.
- The V64.3 is the smallest machine of a new Siemens gas turbine generation. These have been scaled in dimension and rotational speed. Therefore the performance of these future machines can also be estimated.

Acknowledgments

The authors wish to thank Mr. Brandner for the completion of the tests. This work was supported by the Bundesministers für Forschung und Technologie, Förderkennzeichen 03E6097A.

References

Becker, B., and Ziegner, M., 1988, "The New Siemens/KWU Model V64.3 Gas Turbine," *Motortechnische Zeitschrift*, Vol. 49, No. 6, pp. 233-240.

Becker, B., Bonsen, F., and Simon, G., 1990, "A Simple and Reliable Combustion System," ASME Paper No. 90-GT-173.

Becker, B., Berenbrink, P., and Schulenberg, T., 1991, "Operating Experience With Hybrid Burners," submitted for publication to 19th CIMAC Congress, Apr. 15-19.

Deblon, B., 1978, "Full Load Tests of the 80 MW Gas Turbine V93.2 Using a Water Break," ASME Paper No. 78-GT-68.

Roth, H., 1980, "Vibration Measurements on Turbomachine Rotor Blades With Optical Probes," *Proceedings of the ASME Fluids Engineering Gas Turbine Conference*, New Orleans, Mar. 10-13.

Schulenberg, T., and Bals, H., 1987, "Blade Temperature Measurements of Model V84.2, 100 MW/60 Hz Gas Turbine," ASME Paper No. 87-GT-135.

Status of Steam-Injected Gas Turbines

J. Tuzson
Gas Research Institute,
Chicago, IL 60631

The injection of exhaust-heat-generated steam into gas turbines for power augmentation has been proven to provide exceptional flexibility of operation in cogeneration applications. The chronology of development of this technology is presented, including a list of available turbines. A description is then given of the design process for converting existing gas turbines to steam injection. Finally, the water purification issue, which is perceived by some as a barrier to cost-effective implementation of such installations, is addressed. It is shown that water purification cost is of the order of 5 percent of the fuel cost and is therefore not a decisive factor.

I Introduction

Steam injection into gas turbines for power augmentation represents a combined Brayton and Clausius-Rankine cycle in which exhaust-generated steam is introduced ahead of the turbine section of the gas turbine. Conceptually, it is equivalent to a combined cycle except that the steam is expanded together with the air in the same turbine instead of in a separate steam turbine.

Combined cycles have demonstrated the highest power generation efficiencies and the lowest cost in sizes above 50 MW. With decreasing size, the steam turbine represents an increasing portion of the overall cost. Therefore, in smaller sizes steam injected gas turbines, which do not need a steam turbine, become attractive.

Steam injection can also improve part-load efficiency. Single shaft gas turbines usually have poor efficiency at reduced load. With steam injection, steam can displace fuel demand and raise the part-load efficiency.

In a cogeneration configuration the flexibility of a steam-injected gas turbine is particularly valuable. For example, at universities, or other institutional applications, or in district heating, steam is only needed in winter for heating. In summer the steam can be injected to generate more electricity for air conditioning or other uses. A flexible ratio between steam and electric power production also facilitates the matching of site demands, and the siting of installations.

Injection of steam into the gas turbine combustor is a well-accepted means to reduce NO_x emissions. Reductions down to 25 ppm at 15 percent O_2 are warranted by manufacturers and even lower values haves been measured occasionally. The relatively low carbon content of natural gas and high efficiencies minimize CO_2 emissions when compared with other fossil fuel fired plants.

These advantages make steam injection an important gas turbine technology, the status of which will be reviewed on the following pages.

II Historical Perspective

Steam injection was used by one of the first gas turbine investors, Aegidius Ellving of Norway in 1903 (Wilson, 1984). There are accounts of gas turbine field installations with steam injection from the 1950s (Stephens, 1990). An ASME paper was published (1969) by Bultzo (1969) on an installation at the Exxon, Baytown facility and another by Day and Kydd of GE on the maximum possible amount of steam that can be injected (Day and Kydd, 1972).

From 1976 on a new impetus was given to the technology by the patents and activity of D. Y. Cheng, who coined the "Cheng Cycle" designation. Cheng pursued development as president at International Power Technology (IPT) and tested steam injection in the laboratory on a small, 65 kW, Solar T 45 turbine (Farmer, 1981). By Nov. 1981 tests were in progress on a 3.5 MW Allison 501KB turbine, which is well suited because of its large surge margin. Allison Turbine Division of GM reinforced the 501 and added the steam injection equipment in cooperation with IPT (Jones et al., 1982). Performance data were published in 1984 and the turbine was designated 501KH (Messerlie and Strother, 1984). A first installation at the San Jose Campus of the University of California in 1984 (Kosla et al., 1985) was followed by two units at Sunkist Growers, Inc., in Ontario, CA (Barber, 1984). By the end of 1985 several more installations were under construction (*Gas Turbine World*, 1985). Earlier in 1984 IPT also injected Garrett's liquid-fueled IE 831, 500 hp turbine (Digumarthi and Chang, 1984). In 1987 IPT licensed Kawasaki Heavy Industries (Stambler, 1987), and their MIA-01-CC 1800 kW turbine became available in a steam-injected configuration. Since 1989 US Turbines is the exclusive licensee of the Cheng Cycle in the US, including the Allison 501KH and the 2570 kW Kawasaki MIA 13CC as well (*Cogeneration*, 1989; *Diesel & Gas Turbine Worldwide*, 1990). Most recently the Western European rights were licensed to Voest-Alpine Maschinenbau GmbH in Linz, Austria.

In a parallel development, the Turbonetics Division of Mechanical Technology, Inc., supported by the Gas Research Institute, also developed a cogeneration system around the Allison 501KH (Leibowitz and Tabb, 1984). In particular, a steam purification system was designed that was fed by conventional boiler steam. Performance and emissions were ver-

---

Contributed by the International Gas Turbine Institute and presented at the ASME Cogen-Turbo V, Budapest, Hungary, September 3-5, 1991. Manuscript received at ASME Headquarters November 1991. Associate Technical Editor: L. A. Riekert.

ified in a field installation at the Hydra-Matic plant of GM in Warren, MI, in 1988 (Rose and Ralbovsky, 1987; Cain, 1989).

General Electric investigated the merits of steam injection systems (called STIG by GE) long before 1979, when a comparison with combined cycle systems was published by the Electrical Power Research Institute (EPRI) (Brown, 1979). It found that steam injection offered greater flexibility of operation but was comparable in efficiency and cost effectiveness. The study also raised the issue of steam cleanliness and cost of feed water purification (Brown and Cohn, 1980). Around this time EPRI developed a computer program (GATE) to simulate the performance of various gas turbine systems including steam injected gas turbine cycles (Cohn, 1988). In 1984 GE executed an economic and technical analysis on behalf of Pacific Gas and Electric Co., which considered in addition to steam injection also the possibility of intercooling (ISTIG) the LM5000 for a power increase from 34 MW to 110 MW and an efficiency increase from 37 to 55 percent (Pacific Gas & Electric, 1984; Frasca et al., 1986; Cohn, 1984).

In 1986 an existing LM5000, which has operated at the Shasta plant of the Simpson Paper Co. in California since 1983, was successfully retrofitted with partial steam injection (Burnham et al., 1987; Kolp and Moeller, 1989; Moeller et al., 1987). Subsequent tests demonstrated the feasibility and benefits of steam injection: a power increase from 34 MW to 49 MW and efficiency increase from 37 to 41 percent were obtained. Reliability was 99.5 percent. Soon after orders were being taken for the factory-equipped LM2500 STIG and LM5000 STIG units. More recently a conversion of the new GE LM1600 was initiated with partial funding from the Gas Research Institute (Thames and Coleman, 1989). This project also examined in depth the water purification requirements and costs. It concluded that these costs were of the order of 5 percent of the fuel costs and, therefore, the water issue was not a barrier to widespread use of steam injection (Ayala, 1989).

A broad interest in steam injection arose in 1986. The potential of steam injection for affecting the electric power industry was examined and evaluated by Drs. Williams and Larson and Princeton University (Larson and Williams, 1987; Williams and Larson, 1986). Several papers were presented at the 1987, 1988, 1989, and 1990 ASME GOGEN - TURBO meetings on alternate steam injected cycle configurations. Mr. H. U. Frutschi and A. Plancherel of BBC made a cycle comparison in a paper at the 1988 ASME COGEN-TURBO and found that for large power plants combined cycle systems remained preferable (Frutschi and Plancherel, 1988).

Economic studies for various STIG plants were done by architect-engineering companies. A 50 MW aircraft-derivative STIG installation with a once-through boiler was found to be particularly attractive (Soroka and Kamali, 1987). A siting study and comparison with combined cycle systems was commissioned by EPRI on behalf of a major utility. It concluded that in sizes below 150 MW STIG systems were equivalent or slightly better (Van Laar et al., 1988; Cohn, 1988).

At this time approximately two dozen steam-injected gas turbine installations are in operation and the technology can be considered mature. However, only a limited number of gas turbines equipped for steam injection are available (see Table 1).

Table 1 Available steam-injected gas turbines

	Power KW	Heat Rate BTU/KW.hr KJ/KW.hr	Efficiency %
GE LM5000	51000	7900 8334	43
GE LM2500	26400	8630 9100	39.5
GE LM1600	17000	8500 8970	40
Allison 501KH	5300	8690 9170	39
Ruston TB5000	4200	11370 12000	30
Kawasaki M1A-13CC	2570	9750 10470	35
Garrett IE-831	500	13650 14400	25

III Design Guidelines

Steam injection is an optional feature on gas turbine power plants. It has been implemented in the past as a retrofitted modification of existing gas turbines. This will be the most likely approach in the near future since the development of an entirely new gas turbine is very expensive and takes a long time. The question then arises: What criteria must be observed and what procedure should be followed when an existing turbine is equipped with steam injection?

The objective of the design process is to determine the temperature, pressure, and quantity of the steam to be injected and the location of injection.

The first important requirement is that the gas turbine must operate equally well and efficiently with or without steam injection. All combinations of steam and fuel use, at full or part power, must be satisfactory. One of the major benefits of steam injection derives from such a flexibility of operation.

A second requirement is that the fewest possible modifications should be made on the gas turbine. This is important not only to minimize the expense of the modification but also to retain as much as possible the established record of reliability of the existing components. Reliability is of primary importance in power-generating equipment, which is built for a life of 20 years or more. Therefore, the incremental performance improvement must be weighed against the reliability risk of the modification.

Single-Shaft Gas Turbines. Single-shaft, smaller gas turbines warrant simple steam injection methods. Steam is premixed with the natural gas fuel and is injected through a modified fuel nozzle. Since combustors have been adapted in the past for a great variety of fuels, the technique for such an adaptation is well known. Steam is also injected ahead of the combustor and mixes with the primary and secondary air. The greater specific heat of steam will facilitate combustor liner cooling. Combustor liner durability can actually increase. The uniformity of the temperature profile at the combustor exit must be ascertained, preferably by a combustor test.

The increased mass flow through the turbine section, typically up to 15 percent, creates a back pressure on the compressor section. The surge limit of the compressor then limits the amount of steam that can be safely injected without turbine modifications. Increasing the size of the turbine section to provide a greater flow passage is not feasible. An alternative approach is to restagger or change the incidence of the vanes. This is a major modification but it is feasible. A compromise must then be found between operation with and without steam injection.

The pressure ratio of the turbine will dictate the steam pressure. Generally speaking, higher pressure ratios, as in aircraft derivative gas turbines, and higher steam pressures and temperatures favor higher thermodynamic efficiencies. Provision must be made for an additional pressure drop through the valving and fuel nozzles.

The second major limitations on steam injection is the power rating of the shaft, bearings, and mounting assemblies. While these are usually designed with ample capacity, they cannot be ignored.

It is important to consider the start-up process of the steam injection system. Condensation and liquid carryover in the steam injection lines can cause catastrophic damage and must be avoided. Purging with air or preheating of the lines and some superheating of the steam (50 to 100°F) is required.

The question also arises whether allowance should be made for some engine deterioration or fouling during the normal operating life of the engine.

Multiple Shaft Turbines. When the gas turbine has a separate shaft for the gas generator and the power turbine, and when the gas generator itself has two shafts for the low and high-pressure compressor sections, steam injection design becomes more complex. Steam can be injected at two or more pressure levels. This can result in a more efficient use of the exhaust heat. The temperature differential between exhaust gases and the steam in the boiler can be reduced and, therefore, the irreversible thermodynamic losses due to heat transfer can also be reduced. While the power turbine speed is usually fixed, the gas generator speed can be altered slightly to optimize performance.

Considering the complexity of the optimization process, a computer program will have to be prepared and calibrated on experimental data that will predict the performance of the particular gas turbine with and without steam. The program must include a multiple pressure heat recovery steam generator (HRSG). Power and efficiency must be predicted within less than one percent, because initial gas turbine rating and warranties may have to be based on calculated values. This is the first of several computational tools that will be required.

Possible locations of steam injection are: ahead of the combustor, through the fuel nozzles premixed with natural gas, ahead of the low-pressure turbine of the gas generator, and ahead of the power turbine. Adjustable parameters are the injection quantities, steam superheat, speed changes, and adjustment of the vane settings. It has also been suggested that the adjustable compressor guide vanes be used to accommodate steam injection.

When a possible arrangement has been found, several additional requirements must be met. These again must be verified by calculation:

1 Performance without steam is not impaired.
2 The cooling air flow is sufficient.
3 Turbine blade and combustor liner temperature and life are acceptable.
4 Thrust loads are not excessive.

Finally, the steam injection passages must be designed in a manner that will not significantly alter the casing and overall structure of the existing gas turbine. At the compressor section exit, a port is sometimes provided for bleed or bypass air, which can also be used for steam injection. A port between the high and low-pressure turbines of the gas generator is often very difficult to make. An injection port between the gas generator and power turbine is less constrained. But the gas stream must not be disrupted and proper mixing of hot gas and steam must be assured. This may require a longer transition passage. The internal cooling air passages may need adjustment. Finally, the routing, functioning, and start up of the external steam piping system must by properly designed, as pointed out above.

If any of the requirements are not met, an alternative trial arrangement must be found and the cycle of iteration must be repeated.

At the end of the technical design, economic issues must be considered. The added cost of modifications and the risk of reduced reliability have to be weighed against the value of the added power and operating efficiency. The cost of the incremental power in \$/kW should be considerably less than the \$/kW cost of the original turbine to make steam injection cost-effective.

IV The Water Issue

In steam-injected gas turbines, the injected steam is exhausted with the combustor gases through the stack. The boiler make-up water has to compensate for this loss of water. Usually the customary boiler water treatment is not sufficient to assure adequate steam purity and avoid damage to the turbine. Therefore, the water supply and purification issue is considered by some an obstacle to the widespread use of steam injection. It was suggested that it may be economical to condense and recovery some of the moisture in the exhaust, but this approach has not been implemented in practice to date.

Three issues must be clarified to evaluate the economic impact of the steam purity requirements: acceptable contaminant levels, appropriate water purification processes, and cost.

Contaminants affecting a steam injection system can be classed in three groups: those affecting the gas turbine, the steam system, and secondary contaminants.

The first group includes alkali metals (Li, Na, K), lead (Pb), vanadium (V), and calcium (Ca). The second consists of silica (SiO_2), copper (Cu), and iron (Fe). In the third group are sulfur (S) and chlorides (Cl).

Contaminants have the same effect on the gas turbine components regardless of whether they enter with the inlet air, the fuel, or the injected steam. When these streams are mixed, the resulting concentration levels must be adjusted according to the mass flow rates of each stream. Conversely, the permissible contaminant concentration levels in the injected steam will depend on the levels already existing in the gas stream. Because of the high air–fuel ratio in gas turbines, the contaminant levels in the fuel or steam have proportionately less effect than those in the intake air.

In gas turbines a primary mechanism of deterioration is hot corrosion of metals, alloys, and other materials by accelerated oxidation in the presence of molten salts such as alkali sulfates (Na_2SO_4 and K_2SO_4). The first group of contaminants is involved here. Heavy-duty industrial gas turbines are more tolerant and can accommodate concentrations of contaminants approximately five times higher than can aircraft-derivative gas turbines. GE recommends for the LM turbine series the concentration levels in the gas stream and the injected steam shown in Table 2 (Ayala, 1989). Similar limits are specified by other turbine manufacturers.

The concentration levels of the second group are the usual limits for steam turbines.

Sulfur in the third group is normally not a problem with sulfur-free natural gas fuel, especially when the alkali metals of the first group are properly controlled.

Total dissolved solids (TDS), which include other less harmful contaminants, can provide an easy measure of the contamination level. Conductivity is usually also specified because it can be continuously monitored and can give a fast indication of an upset condition.

The boiler feed water specification needed for reaching the required contaminant levels in the steam to be injected will depend on blowdown, mist collector efficiency, and other factors. The conservative levels shown in Table 3 (Ayala, 1989) are generally recommended. Alkali metal concentrations should be ascertained independently from total dissolved solids (TDS) because they are critical for steam injected operation.

There are two approaches for providing for purification of the steam: Smaller installations often supplement existing process steam boilers at the same location. In this case the boiler

Table 2 LM 1600 STIG system limits

Contaminant	In Total Gases (ppb)	In Steam (ppb)
Group I:		
Li + Na + K	4	18 - 30
Pb	3	10 - 24
V	2	2 - 16
Ca	7	41 - 55
Group II:		
SiO_2	20	20
Cu	5	5
Fe	20	20
Group III:		
S	11	73 - 87
Total Solids	18	128 - 141
Steam Conductivity (Total S/Cm)		< 1.0

Based on Air/Fuel = 48:1 and Steam/Fuel = 7.1
Steam pressure = 460 psia.Steam temp. $\leq$ 800 F.

Table 3 Water quality limits for STIG system, ppm

Li + Na + K,	0.4 - 0.7
Pb,	0.2 - 0.6
V	0.1 - 0.4
Ca	1.0 - 1.4
Silica	0.1
Copper	0.05
Iron	0.1
Oxygen	0.02
Total Solids	1.5 - 3.0
Hardness	0
Total Alkalinity ($CaCO_3$)	4
pH	7

Based on steam injection at pressures
below 600 psi, 0.04% carry over, 1% blowdown.

water treatment has to conform to the existing standards and practices used by the operating personnel. A purification system is then needed that eliminates liquid and solid carry-over from the steam to be injected. Certain boiler water treatment chemicals, such as amines for example, require special consideration because they are present as gases in the steam and cannot be trapped as solids or liquids. Being ionic, they register on conductivity measuring instruments and can give misleading readings. Such a steam filtration and purification system was built and tested by Turbonetics for an Allison 501KH turbine with satisfactory results (Cain, 1989).

Larger systems are likely to require a dedicated feed water purification plant. While available water quality varies widely depending on the location, it has a surprisingly small influence on overall water costs if extremes such as brackish or seal water are excluded. Two principal techniques can be used: deionization or reverse osmosis. The typical treatment plant must include several treatment steps:

1 Multimedia and carbon filters.
2 Demineralizer or acid-inhibitor.
3 Degasser.
4 Two reverse osmosis units.
5 Mixed-bed demineralizer.
6 Neutralizer of regeneration waste.

For a steam-injected turbine in the 20 MW size range, total water treatment costs including amortization, utilities, chemicals, and labor are in the range of $8.40 to $6.70 per 1000 gallons (Ayala, 1989). Of this, capital-related costs account for 35 to 45 percent. The cost of chemicals increases with increasing dissolved solids in the feed for deionization processes but remains unaffected for reverse osmosis. Therefore, selection of one or the other of these alternate processes will depend on the quality of the local water supply.

The typical operating cost of the water treatment system is calculated to be about 5 percent of the fuel cost. The capital cost of the equipment will be approximately the same proportion of the cost of the total installation.

Therefore, the expense of water treatment for steam injection is not significant and is not a barrier to the use of steam-injected gas turbine systems.

V Conclusion

A historical perspective illustrates that steam injection for power augmentation in gas turbines is an economically variable technology. Its primary advantage is the flexibility of operation in cogeneration and district heating applications by allowing more electric power generation when steam is not needed.

However, the number of steam-injected gas turbines available commercially is limited. The design process is described above, which has to be followed to convert an existing gas turbine to steam injection. It is shown that, generally, a conversion is technically and economically feasible.

Finally, the specifications for injection steam purity, the needed water purification process, and the treatment costs are reviewed. Since water costs are only of the order of 5 percent of fuel costs, the water issue is not a barrier to widespread use of steam-injected gas turbines.

References

Ayala, R. E., 1989, "Water Treatment for Steam Injected Gas Turbine Systems," GRI-89/0048, Mar.

Barber, J., 1984, "Steam Injection Seen Opening Cogen for Variable-Load Users," *Energy User News*, July 9.

Brown, D. H., 1979, "Steam Injected Gas Turbine Study," EPRI - AF - 1186, Sept.

Brown, D. H, and Cohn, A., 1981, "An Evaluation of Steam Injected Combustion Turbine Systems," ASME Journal of Engineering for Gas Turbines and Power, Vol. 103, pp. 13-19.

Bultzo, C., 1969, "Steam Injection, a Source of Incremental Power," ASME Paper No. 69-GT-68.

Burnham, J. B., Giuliani, M. H., and Moeller, D. J., 1987, "Development, Installation, and Operating Results of Steam Injection System (STIG^{TM}) in a General Electric LM5000 Gas Generator," ASME Journal of Engineering for Gas Turbines and Power, Vol. 109, pp. 257-262.

Cain, W. G., 1989, "Gas Turbine Cogeneration System With Steam Injection," GRI 89/0261, NTIS PB90-19842.

Cogeneration, 1989, "Kawasaki Develops Four Gas Turbines for Cogeneration, IPP Applications," May/June.

Cohn, A., 1984, "Gas Turbine Performance Evaluation," *EPRI Journal*, June, pp. 38-39; EPRI-AP-2871-CCM, Feb. 1983.

Cohn, A., 1988, "Steam Injected Gas Turbines Versus Combined Cycles," *EPRI J*,. Oct./Nov.

Day, W. H., and Kydd, P. H., 1972, "Maximum Steam Injection in Gas Turbines," ASME Paper No. 72-JPG/GT-1.

Diesel and Gas Turbine Worldwide, 1984, "LM2500's Potential in Cogeneration Applications," July/Aug., pp. 35-37.

Diesel and Gas Turbine Worldwide, 1990, "Advances With Steam Injected Small Gas Turbines," Jan./Feb., pp. 42-43.

Digumarthi, R., and Chang, C. N., 1984, "Cheng-Cycle Implementation on a Small Gas Turbine Engine," ASME Journal of Engineering for Gas Turbines and Power, Vol. 106, pp. 699-702.

Farmer, R., 1981, "Dual-Fluid 501K Rated 5.3 MW With 38% Efficiency," *Gas Turbine World*, Nov.

Frasca, J. D., Klumpe, H. W., and McCrank, J. M., 1986, "A Study to Determine the Cost-Effectiveness of Using Steam Injected Gas Turbines With Coal Gasification Equipment," EPRI AP-4507, Apr.

Frutschi, H. U., and Planchgerel, A., 1988, "Comparison of Combined Cycles With Steam Injection and Evaporation Cycles," *ASME Cogen-Turbo 1988*, p. 137.

Gas Turbine World, "IPT Says Cheng Cycle Cogen Units Running Over 94% Availability," Nov./Dec. 1985, p. 40.

Jones, J. L., Flynn, B. R, and Strother, J. R., 1982, "Operating Flexibility and Economic Benefits of a Dual-Fluid Cycle 501-KB Gas Turbine Engine in Cogeneration Applications," ASME Paper No. 82-GT-298.

Kolp, D. A., and Moeller, D. J., 1989, "World's First Full STIG LM500 Installed at Simpson Paper Co.," ASME JOURNAL OF ENGINEERING FOR GAS TURBINES AND POWER, Vol. 111, pp. 200-210.

Kosla, L. A., Shepherd, S. H., and Orbach, H. S., 1985, "Cogeneration Fills San Jose Needs," *ASHRAE J.*, July, pp. 30-34.

Larson, E. D., and Williams, R. H., 1987, "Steam-Injected Gas Turbines," ASME JOURNAL OF ENGINEERING FOR GAS TURBINES AND POWER, Vol. 109, pp. 55.

Leibowitz, H. U., and Tabb, E., 1984, "The Integrated Approach to a Gas Turbine Topping Cycle Cogeneration System," ASME JOURNAL OF ENGINEERING FOR GAS TURBINES AND POWER, Vol. 106, pp. 731-736.

Messerlie, R. L., and Strother, J. R., 1984, "Integration of the Brayton and Rankine Cycles to Maximum Gas Turbine Performance," ASME Paper No. 84-GT-52.

Moeller, D. J., Burnham, J., and Oganowski, G., 1987, "Steam-Injected Gas Turbine Enhance Cogeneration Plant Performance," *Pulp & Paper*, Sept.

Pacific Gas & Electric, Engineering Dept., 1984, "Scoping Study: LM5000 Steam-Injected Gas Turbine," PG&E Paper No. 84-STIG-1.

Rose, R. K., and Ralbovsky, F. S., 1977, "New Options and Design Approaches for Gas Turbine Cogeneration Plants," *Turbomachinery International*, Mar./Apr., pp. 25-30.

Soroka, G., and Kamali, K., 1987, "Modular Remotely Operated Fully Steam-Injected Plant for Utility Applications," *ASME Cogen-Turbo 1987*, p. 55.

Stambler, I., 1987, "KHI Steam Injected MIA-01 Base Rated at Over 1800 kW," *Gas Turbine World*, May/June, p. 44.

Stephens, J. O., 1990, "The Little Train to San Angelo," *Turbomachinery International*, Sept/Oct., p. 64.

Thames, J. M., and Coleman, R. P., 1989, "Preliminary Performance Estimates for a GE Steam Injected LM1600 Gas Turbine," ASME Paper 89-GT-9.

Thames, J. M., Casper, R. L., and Vincent, C. T., 1989, "Efficient, Clean Cogeneration With the GE LM1600," *ASME Cogen-Turbo 1989*.

Van Laar, J. A., Wendord, A. W., Cohn, A., Esposito, N. T., Yosh, D. F., and Foster-Pegg, R. W., "Site Assessment of STIG and Combined-Cycle Plants," ASME Paper No. 88-JPGC/Pwr-21.

Williams, R. H., and Larson, E. D., 1986, "Gas Turbines Could Meet Electricity Demand," *Wall Street J.*, Sept. 17.

Wilson, D. G., 1984, *The Design of High-Efficiency Turbomachinery*, MIT Press, p. 25.

K. Ito
Professor.
Mem. ASME

R. Yokoyama
Assistant Professor.

T. Shiba
Research Assistant.

Department of Mechanical Engineering,
College of Engineering,
Osaka Prefectural University,
Osaka 593, Japan

Optimal Operation of a Diesel Engine Cogeneration Plant Including a Heat Storage Tank

The effect of heat storage on a cogeneration plant is investigated using a mathematical programming approach. For a diesel engine plant, an optimal planning method is presented by which the operational policy of constituent equipment is determined together with the charging history of a heat storage tank so as to minimize the daily operational cost. An algorithm is designed to solve this optimization problem efficiently by combining the dynamic programming method with the mixed-integer programming one. Through a case study, it is made clear how the volume of the heat storage tank influences the daily operational policy and the long-term economy of the total plant.

Introduction

In recent years, cogeneration plants have been introduced successfully in Japan into various kinds of buildings such as hotels, offices, and hospitals. The energy demand fluctuates widely with time and season in commercial and public buildings, and the demand ratio of thermal energy to electricity changes widely through a day and a year.

Heat storage systems are in general available as buffers compensating for the mismatch between demand and supply of thermal energy. The installation of heat storage systems into cogeneration plants brings the following merits: (1) The capacity or the investment of equipment producing thermal energy can be reduced because of peak shaving; (2) the operational cost can be decreased by operating each piece of equipment at the loading level with higher thermal efficiency and during the period with lower energy price. On the other hand, the usage of heat storage systems causes the necessity of new investment and results in heat loss from the storage units.

The following questions must be considered when installing heat storage systems into cogeneration plants:

(*a*) Should the heat storage system be installed?
(*b*) What volume of the storage unit is most appropriate?
(*c*) What pattern of charging and discharging should be adopted for the storage unit?
(*d*) What operational policy should be adopted for other pieces of constituent equipment?

Thus, the planning of cogeneration plants with heat storage systems can be very complex and difficult. In fact, heat storage systems have been installed into some cogeneration plants without enough investigation of their effects on the total plants.

The purposes of this paper are to develop an optimal operational planning method for a cogeneration plant including a heat storage tank and to investigate the effect of heat storage on the total plant. For a diesel engine cogeneration plant, an optimal planning method is first presented by which the operational policy of constituent equipment is determined together with the charging history of the heat storage tank so as to minimize the daily operational cost. In order to solve this optimization problem efficiently, an algorithm is developed by combining the dynamic programming method (Angel and Bellman, 1972) with the mixed-integer linear programming one (Garfinkel and Nemhauser, 1972). Lastly, a case study is carried out for a cogeneration plant to be installed in a hotel to ascertain the effectiveness of the method. Through the study, how the volume of the heat storage tank influences the daily operational policy and the long term economy of the plant is analyzed.

Optimal Operational Planning Method

Cogeneration plants have many operational policy alternatives to satisfy the energy demand, because the supply and the demand of both electricity and thermal energy are complexly connected to each other. For several types of cogeneration plants without heat storage systems, the authors have proposed an optimal planning method by which the operational policy is determined rationally from the economical viewpoint using the mixed-integer linear programming method (Horii et al., 1987; Ito et al., 1987, 1988, 1990a, 1990b). In this case, the hourly operational policy has been determined independently for every hour on a representative day. However, for the cogeneration plant with the heat storage tank investigated here, the operational policy must be determined simultaneously throughout a period of tank usage. This is because the operational policy includes the charging history of the heat storage tank. Therefore, the optimal operational planning problem is a large-scale one with a large number of unknown variables

---

Contributed by the Advanced Energy Systems Division for publication in the JOURNAL OF ENGINEERING FOR GAS TURBINES AND POWER. Manuscript received by the Advanced Energy Systems Division November 19, 1990; revision received August 20, 1991. Associate Technical Editor: M. J. Moran.

and constraints. For example, consider an optimal operational planning problem formulated by using 50 unknown variables for the plant without the heat storage tank. If the heat storage tank is used periodically with a period of 24 hours, and the operational policy is determined for every hour, more than 1200 variables are necessary to formulate the problem for the plant with the heat storage tank. It is easy to solve linear programming problems of such scale. However, it is very difficult to solve mixed-integer linear programming problems considered here in practical computation time. Therefore, it is necessary to develop an algorithm to solve these problems efficiently. In this paper, such an algorithm is developed by combining the dynamic programming method (Angel and Bellman, 1972) with the mixed-integer linear programming method (Garfinkel and Nemhauser, 1972). The optimization procedure is described for an example plant in the following.

Plant Structure. The concept of the optimal operational planning method proposed in this paper can be applied to various types of cogeneration plants. In order to describe the method, an example of a diesel engine cogeneration plant, shown in Fig. 1, is investigated. Although only one unit is illustrated for each kind of equipment in Fig. 1, there may be several units. Solid lines, dot-dash lines, and two dots-dash lines indicate the flows of hot water, electricity, and fuel oil, respectively.

This plant meets the electricity demand by running the diesel generators and by purchase of electricity from an outside electric power company. The exhaust heat recovered from both the jacket cooling water and the exhaust gas of the diesel engines is stored in the heat storage tank, and then reused for hot water. The heat storage tank is used to compensate for the mismatch between the exhaust heat generation and the thermal energy requirement. The hot water is supplemented by oil-fired boilers.

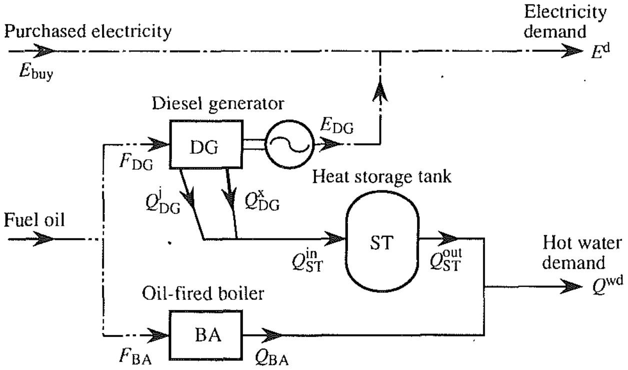

Fig. 1 Structure of a simplified diesel engine cogeneration plant

In order to describe the trunk of the optimization procedure, the structure of this plant is rather simplified. However, the structure of an actual plant is more complex for the following reasons:

(*a*) Several kinds of thermal energy such as space cooling and space heating are also demanded.
(*b*) In such a case, refrigerators should also be installed.
(*c*) Cooling towers are installed to dispose of surplus exhaust heat; electricity for driving them should be considered.
(*d*) Other kinds of auxiliary machinery such as pumps are also installed; electricity for driving them should be considered.

Nomenclature

Equipment symbols

BA = oil-fired boiler
CT = cooling tower for heat disposal
DG = diesel generator
PC, PD, PH, PT, PW = pumps
RA = oil-fired absorption refrigerator
RE = vapor compression refrigerator
RW = single effect absorption refrigerator
ST = heat storage tank

Quantities of energy

E = electric power, kW
F = fuel oil consumption, L/h
Q = heat flow rate, kW

Other miscellaneous symbols

C = specific heat of fluid for heat storage, MJ/(kg°C)
f_k = operational cost at the kth sampling time interval, Yen/h
J = objective function (daily operational cost), Yen/d
K = total number of sampling time intervals
k = index for each sampling time
N = number of equipment installed
P = initial capital cost of heat storage tank, Yen
p, q = parameters related to performance characteristics of each piece of equipment
r_k = function used for formal expression of constraints
S = surface area of heat storage tank, m^2
T = temperature of fluid for heat storage, °C
T_{amb} = ambient air temperature, °C
t_k = kth sampling time, h
Δt = sampling time interval, h
$\mathbf{u}$ = control vector
V = volume of heat storage tank, m^3
z_{K-k} = optimal cost function between sampling times k and K
α = cost coefficient of heat storage tank
δ = zero-one integer variable expressing on/off status of each piece of equipment
η = heat loss coefficient of heat storage tank, kW/(m^2°C)
ρ = mass density of fluid for heat storage, kg/m^3
φ = unit cost of purchased electricity or fuel oil, Yen/MJ or Yen/L
$\underline{(\ )}, \overline{(\ )}$ = lower and upper bounds of the corresponding quantity, respectively

Superscripts

a = electricity for auxiliary equipment
c = space cooling
d = energy demand
h = space heating
in = inlet of heat storage tank
j = jacket cooling water
out = outlet of heat storage tank
w = hot water supply
x = exhaust gas

Subscripts

buy = purchased electricity
disp = heat disposal
n = index for each piece of equipment

In the case study described later, the optimization is carried out by considering these items.

Formulation of Optimal Operational Planning Problem. We consider the optimal operational planning problem by assuming that the heat storage system is used periodically with a period of 24 hours, i.e., the operational policy of the plant is investigated for a representative day on which the energy demand is estimated. By dividing 24 hours into K identical sampling time intervals, the kth sampling time t_k is defined by

$$t_k = t_0 + k\Delta t \quad (k=0, \cdots, K), \tag{1}$$

where

$$\Delta t = 24/K. \tag{2}$$

In the following formulation, the value of a quantity X at the sampling time t_k is expressed by $X(k)$.

Performance Characteristics of Equipment. The performance characteristics of each piece of equipment are considered as constraints in this optimization problem.

(*a*) *Diesel Generator* (*DG*). At each sampling time k, the performance characteristics of diesel generators can be expressed by relationships among generated electric power, flow rate of heat recovered from both the jacket cooling water and the exhaust gas, and fuel oil consumption. A typical example of performance characteristics is shown in Fig. 2. The actual data at the rated load and part-load status are plotted, and the lines determined by the least-squares method are also drawn. This graph shows that the relationships can be approximated by the following linear equations:

$$\left.\begin{array}{l} E_{DGn}(k) = p_{DGn}F_{DGn}(k) + q_{DGn}\delta_{DGn}(k) \\ Q^j_{DGn}(k) = p^j_{DGn}F_{DGn}(k) + q^j_{DGn}\delta_{DGn}(k) \\ Q^x_{DGn}(k) = p^x_{DGn}F_{DGn}(k) + q^x_{DGn}\delta_{DGn}(k) \\ \underline{F}_{DGn}\delta_{DGn}(k) \le F_{DGn}(k) \le \overline{F}_{DGn}\delta_{DGn}(k) \\ \delta_{DGn}(k) \in \{0, 1\} \end{array}\right\} \quad (n=1, \cdots, N_{DG};\ k=0, \cdots, K-1), \tag{3}$$

where E, F, and Q denote the electric power, the fuel oil consumption, and the heat flow rate, respectively; coefficients p and q are parameters related to the performance characteristics and are determined, respectively, as slopes and intercepts of the lines shown in Fig. 2; the symbols $\underline{(\ )}$ and $\overline{(\ )}$ denote, respectively, lower and upper bounds of the corresponding quantity. The zero-one integer variable δ expresses the on ($\delta=1$)/off ($\delta=0$) status of operation. The subscript DG and n indicate that the quantity is related to the nth of N_{DG} diesel generators, and the superscripts j and x denote the relations with the jacket cooling water and the exhaust gas.

Performance characteristics of other pieces of equipment are similarly approximated by linear equations.

(*b*) *Oil-fired Boiler* (*BA*).

$$\left.\begin{array}{l} Q_{BAn}(k) = p_{BAn}F_{BAn}(k) + q_{BAn}\delta_{BAn}(k) \\ \underline{F}_{BAn}\delta_{BAn}(k) \le F_{BAn}(k) \le \overline{F}_{BAn}\delta_{BAn}(k) \\ \delta_{BAn}(k) \in \{0, 1\} \end{array}\right\} \quad (n=1, \cdots, N_{BA};\ k=0, \cdots, K-1). \tag{4}$$

Energy Balance in the Heat Storage Tank. The dynamic relationship concerning the heat balance in the heat storage tank is expressed by the following difference equation:

$$C\rho V\{T(k+1) - T(k)\}/\Delta t = Q^{in}_{ST}(k) - Q^{out}_{ST}(k) - \eta S\{T(k) - T_{\text{amb}}(k)\} \quad (k=0, \cdots, K-1), \tag{5}$$

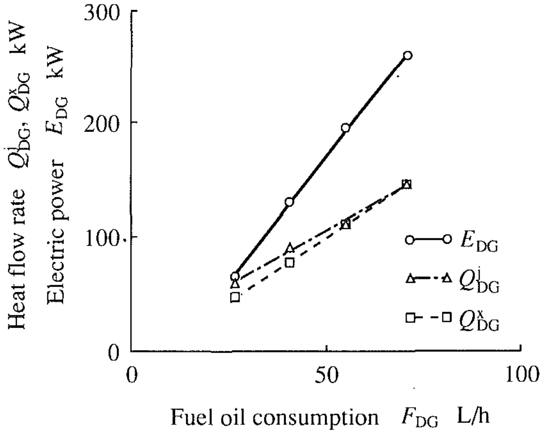

Fig. 2 Performance curves of diesel generator

with the bound condition

$$\underline{T} \le T(k) \le \overline{T} \quad (k=1, \cdots, K-1), \tag{6}$$

and both the initial and the terminal conditions

$$\left.\begin{array}{l} T(0) = T_0 \\ T(K) = T_K \end{array}\right\}, \tag{7}$$

where C, ρ, and T denote the specific heat, the mass density, and the temperature of the fluid used for heat storage (typically, water); V and S denote the volume and the surface area of the tank; Q^{in}_{ST} and Q^{out}_{ST} are the inlet and the outlet flow rate of heat; η is the heat loss coefficient of the tank; T_{amb} is the ambient air temperature.

Energy Balance and Supply-Demand Relationships. From the plant structure shown in Fig. 1, the following relationships are obtained for each energy flow. They are also considered as constraints.

(*a*) *Electricity*

$$\left.\begin{array}{l} E_{\text{buy}}(k) + E_{DG}(k) = E(k) \\ E_{DG}(k) = \sum_{n=1}^{N_{DG}} E_{DGn}(k) \\ E(k) = E^d(k) \end{array}\right\} (k=0, \cdots, K-1). \tag{8}$$

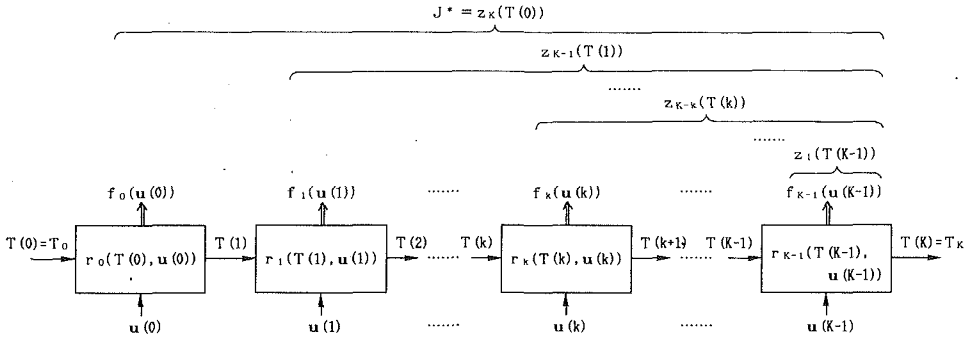

Fig. 3 Multistage decision process

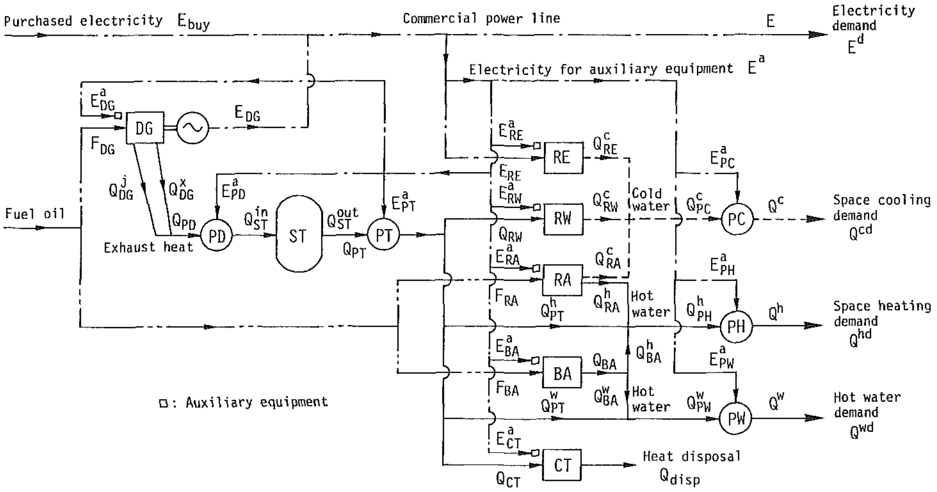

Fig. 4 Structure of a diesel engine cogeneration plant with a heat storage tank

(*b*) *Hot Water*

$$\left.\begin{aligned}
&\sum_{n=1}^{N_{DG}} Q^j_{DGn}(k)=Q^j_{DG}(k)\\
&\sum_{n=1}^{N_{DG}} Q^x_{DGn}(k)=Q^x_{DG}(k)\\
&Q^j_{DG}(k)+Q^x_{DG}(k)=Q^{in}_{ST}(k)\\
&\sum_{n=1}^{N_{BA}} Q_{BAn}(k)=Q_{BA}(k)\\
&Q^{out}_{ST}(k)+Q_{BA}(k)=Q^w(k)\\
&Q^w(k)=Q^{wd}(k)
\end{aligned}\right\}\ (k=0,\ \cdots,\ K-1). \qquad (9)$$

(*c*) *Fuel Oil*

$$\left.\begin{aligned}
F_{DG}(k)&=\sum_{n=1}^{N_{DG}} F_{DGn}(k)\\
F_{BA}(k)&=\sum_{n=1}^{N_{BA}} F_{BAn}(k)
\end{aligned}\right\}\ (k=0,\ \cdots,\ K-1). \qquad (10)$$

Objective Function. The objective function to be minimized is the daily operational cost defined by

$$J=\sum_{k=0}^{K-1}\{\varphi_{DG}F_{DG}(k)+\varphi_{BA}F_{BA}(k)+\varphi_{\text{buy}}(k)E_{\text{buy}}(k)\}\Delta t, \qquad (11)$$

where φ_{DG} and φ_{BA} are the unit costs of fuel oil used by the corresponding equipment, and φ_{buy} is the unit cost of purchased electricity.

The optimal operational planning problem results in a mixed-integer linear programming one, i.e., subject to Eqs. (3)-(10), the zero-one integer and the continuous variables expressing the daily operational policy are determined so as to minimize J in Eq. (11).

Solving Method Based on Dynamic Programming. The dynamic programming method is an approach to solve this problem efficiently; i.e., the problem is regarded as a multistage decision process where the operational policy of constituent equipment is determined sequentially together with the temperature of the heat storage tank. This approach makes it possible to divide the large-scale problem into several small-scale ones with sequential relations, which can be solved rather simply.

Multistage Decision Process. In order to describe the original problem as the multistage decision process shown in Fig. 3, Eqs. (3)-(10) are expressed formally by the following difference equation:

$$T(k+1)=r_k(T(k),\ \mathbf{u}(k)) \quad (k=0,\ \cdots,\ K-1), \qquad (12)$$

where the temperature $T(k)$ is considered as the state variable, and $\mathbf{u}(k)$ is the control vector composed of the zero-one integer and the continuous variables expressing the operational policy of constituent equipment. The function r_k is a formal expression including the equalities and the inequalities in Eqs. (3)-(10). Defining the operational cost at the sampling time interval k by

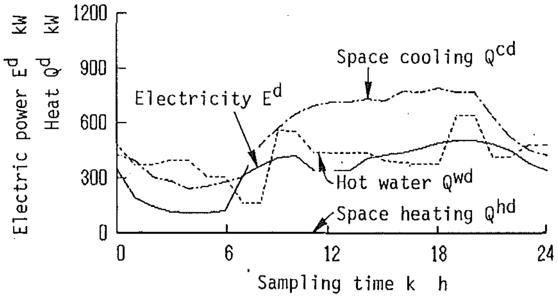

Fig. 5 Energy demand pattern on a representative day in August

Table 1 Capacities and numbers of constituent equipment

Constituent equipment		Capacity	Number
Diesel generator		$\bar{E}_{\mathrm{DG}n} = 260$ kW	$N_{\mathrm{DG}} = 3$
Single effect absorption refrigerator		$\bar{Q}^{\mathrm{c}}_{\mathrm{RW}n} = 316$ kW	$N_{\mathrm{RW}} = 1$
Electric compression refrigerator		$\bar{Q}^{\mathrm{c}}_{\mathrm{RE}n} = 598$ kW	$N_{\mathrm{RE}} = 1$
Oil-fired absorption refrigerator	Cooling	$\bar{Q}^{\mathrm{c}}_{\mathrm{RA}n} = 440$ kW	$N_{\mathrm{RA}} = 1$
	Heating	$\bar{Q}^{\mathrm{h}}_{\mathrm{RA}n} = 384$ kW	
Oil-fired boiler		$\bar{Q}_{\mathrm{BA}n} = 733$ kW	$N_{\mathrm{BA}} = 1$

Table 2 Cost of purchased electricity

Demand charge		1 638 Yen/(kW · month)
Energy charge $\varphi_{\mathrm{buy}}(k)$	July ~ Sept.	5.294 Yen/MJ
	Other months	4.813 Yen/MJ

Table 3 Annual capital cost of heat storage tank

(Unit : $\times 10^3$ Yen/y)

Cost coefficient α \ Volume V m^3	10	20	30	40
0.5	150.2	238.4	312.4	378.5
1.0	300.4	476.8	624.8	756.9

$$f_k(\mathbf{u}(k)) = \{\varphi_{DG}F_{DG}(k) + \varphi_{BA}F_{BA}(k) + \varphi_{\mathrm{buy}}(k)E_{\mathrm{buy}}(k)\}\Delta t, \quad (k=0,\cdots,K-1), \tag{13}$$

the objective function in Eq. (11) is given by

$$J = \sum_{k=0}^{K-1} f_k(\mathbf{u}(k)). \tag{14}$$

Next, introducing the function that expresses the minimum cost between sampling times k and K

$$z_{K-k}(T(k)) = \min_{\mathbf{u}(k),\,\cdots,\,\mathbf{u}(K-1)} \left\{ \sum_{k'=k}^{K-1} f_{k'}(\mathbf{u}(k')) \right\} \quad (k=0,\cdots,K-1), \tag{15}$$

with the terminal condition

$$z_0(T(K)) = z_0(T_K) = 0, \tag{16}$$

the following recurrence relation is obtained on the basis of the principle of optimality:

$$z_{K-k}(T(k)) = \min_{\mathbf{u}(k)} \{ f_k(\mathbf{u}(k)) + z_{K-k-1}(r_k(T(k),\,\mathbf{u}(k))) \} \quad (k=0,\cdots,K-1). \tag{17}$$

The recurrence relation, Eq. (17), and the terminal condition, Eq. (16), are used to yield the solution sequentially.

Numerical Method. The analytical solution cannot be obtained through the multistage decision process, because the function r_k is a very complex one, and the control vector $\mathbf{u}(k)$ includes zero-one integer variables. Thus, a numerical solution is derived using the following procedure.

On the assumption that the state variable $T(k)$ is constrained to be a member of a discrete set of values, $\{T_k^1, \cdots, T_k^l, \cdots, T_k^L\}$, the control vector changing the state variable from T_k^l to $T_{k+1}^{l'}$ is expressed by $\mathbf{u}(T_k^l, T_{k+1}^{l'})$. Thus, Eq. (12) is rewritten as follows:

$$T_{k+1}^{l'} = r_k(T_k^l,\, \mathbf{u}(T_k^l, T_{k+1}^{l'})) \quad (l,\, l'=1,\cdots,L;\ k=0,\cdots,K-1). \tag{18}$$

According to the above expression, Eq. (17) is reduced to

$$z_{K-k}(T_k^l) = \min_{\substack{T_{k+1}^{l'} \\ 1\le l'\le L}} \left\{ \min_{\mathbf{u}(T_k^l,\,T_{k+1}^{l'})} f_k(\mathbf{u}(T_k^l, T_{k+1}^{l'})) + z_{K-k-1}(T_{k+1}^{l'}) \right\} \quad (l=1,\cdots,L;\ k=0,\cdots,K-1). \tag{19}$$

This recurrence relation is solved sequentially with the terminal condition, Eq. (16), to obtain the optimal solution.

In Eq. (19), the minimization with respect to $\mathbf{u}(T_k^l, T_{k+1}^{l'})$ is necessary to select the optimal control vector from many alternatives concerning the operational policy, which changes the temperature from T_k^l to $T_{k+1}^{l'}$ for a given set $\{T_k^l, T_{k+1}^{l'}\}$. This optimization problem is defined as the one in which subject to the constraints at the sampling time k in Eqs. (3)-(5) and Eqs. (8)-(10), the control vector $\mathbf{u}(T_k^l, T_{k+1}^{l'})$ is determined so as to minimize the hourly operational cost $f_k(\mathbf{u}(T_k^l, T_{k+1}^{l'}))$. This small-scale optimization problem is solved using the mixed-integer linear programming method. A branch and bound algorithm based on the Land-Doig method (Land and Doig, 1960) is adopted for that purpose (Kuester and Mize, 1973).

The whole optimization algorithm is summarized in the following. For each sampling time k and each temperature level l, the optimal control vector $\mathbf{u}(T_k^l, T_{k+1}^{l'})$ is first determined by changing the temperature level l' from 1 to L. Next, $T_{k+1}^{l'}$ is selected from a set $\{T_k^1, \cdots, T_k^{l'}, \cdots, T_k^L\}$ so as to minimize the term enclosed with the braces in the right-hand side of Eq. (19). Thus, the values of the function $z_{K-k}(T_k^l)$ can be determined by changing the temperature level l from 1 to L. By repeating this procedure from $k=K-1$ to $k=0$, the minimum value of the objective function J^* is obtained as follows:

$$J^* = z_K(T(0)) = z_K(T_0). \tag{20}$$

Case Study

Input Data. For a diesel engine cogeneration plant to be installed in a hotel, a case study is carried out to investigate the effect of heat storage on the daily operational policy and the long-term economy of the total plant. The structure of the plant is shown in Fig. 4. Equipment symbols in Fig. 4 are explained in the nomenclature. Although only one unit is illustrated for each kind of equipment in Fig. 4, there may be several units. Solid lines, dot-dash lines, two dots-dash lines, and broken lines indicate the flows of hot water, electricity, fuel oil and cold water, respectively. In this plant, three types of refrigerator and auxiliary machinery such as pumps and cooling towers are added to the equipment of the plant in Fig. 1.

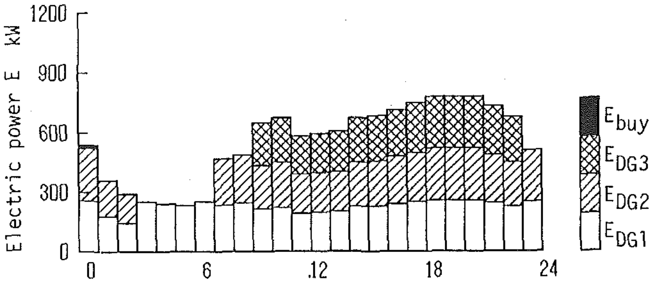

Fig. 6(*a*) Electricity supply

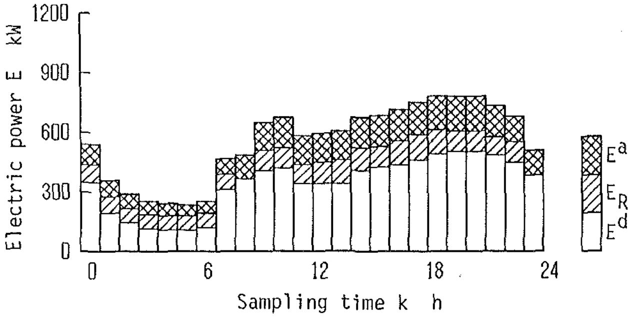

Fig. 6(*b*) Electricity consumption

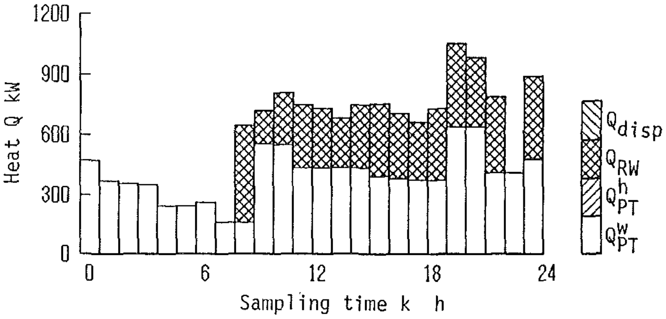

Fig. 6(*c*) Utilization of exhaust heat

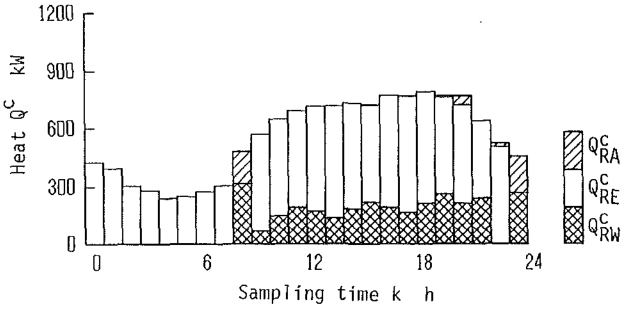

Fig. 6(*d*) Space cooling supply

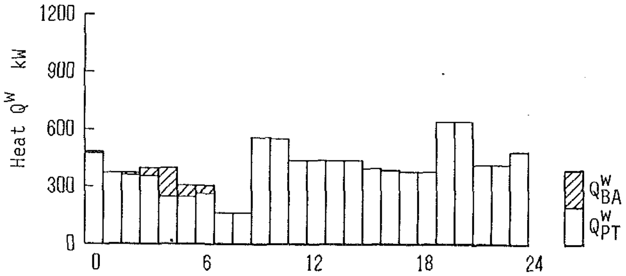

Fig. 6(*e*) Hot water supply

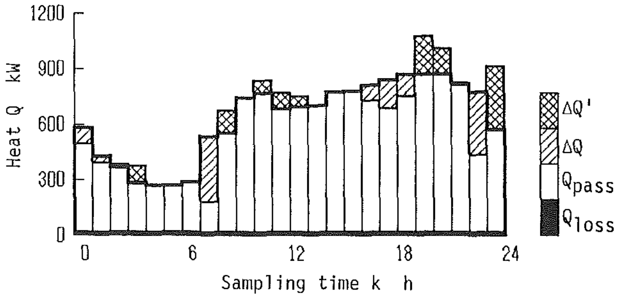

Fig. 6(*f*) Pattern of charging and discharging

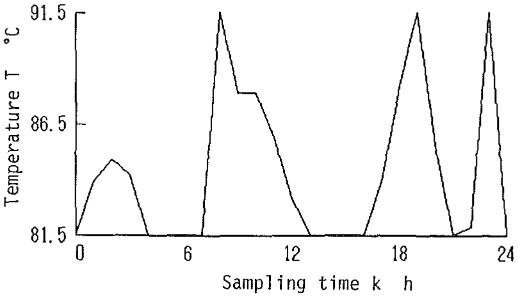

Fig. 6(*g*) Temperature fluctuation

Fig. 6 Optimal operational policy of the cogeneration plant with the heat storage tank of $V = 30$ m^3

The hourly energy demand is estimated on 12 representative days for a year. For example, Fig. 5 shows the energy demand pattern on the representative day in August. Table 1 shows the capacity and the number of each kind of equipment installed, which are determined in advance so as to meet the estimated energy demand. Table 2 gives the cost of purchased electricity adopted in this study. Concerning the unit cost of fuel oil used for diesel generators, oil-fired absorption refrigerators, and oil-fired boilers, the following four cases are investigated: $\varphi_{DG} = \varphi_{RA} = \varphi_{BA} = \varphi_{\text{oil}} = 20$, 25, 30, and 35 Yen/L (1 Yen/L = 7.14 \$/m^3).

On the assumption that the demand charge of purchased electricity and the initial capital cost of constituent equipment except the heat storage tank are constant, how the volume or the capital cost of the heat storage tank influences the long-term economy of the total plant is analyzed. The long-term economy of the plant is evaluated on the basis of the annualized costs method (Witte et al., 1988); i.e., as an evaluation criterion the annual total cost is adopted, which is composed of both the fixed and variable costs. The annual fixed cost is determined by multiplying the initial capital cost of constituent equipment by the capital recovery factor. The capital recovery factor is calculated from a life of equipment and an interest rate. The salvage value of equipment may be included in this evaluation. The annual variable cost is calculated as the sum of the operational and the maintenance costs. The proposed optimal operational planning method is used to calculate the daily operational cost due to both the energy charge of purchased electricity and the fuel oil consumption. The annual operational cost is determined by summing up the daily operational cost for each day, and by adding the demand charge of purchased electricity. The initial capital cost of the heat storage tank P is assumed to be proportional to its surface area S, or the two-thirds power of its volume V as follows:

$$P/P_0 = \alpha (V/V_0)^{2/3}, \tag{21}$$

where α is a cost coefficient, and the standard values of V and P are $V_0 = 50$ m^3 and $P_0 = 8 \times 10^6$ Yen, respectively. Table 3 shows the annual capital cost of the heat storage tank calculated for a life of 15 years, an interest rate of 7 percent, and zero

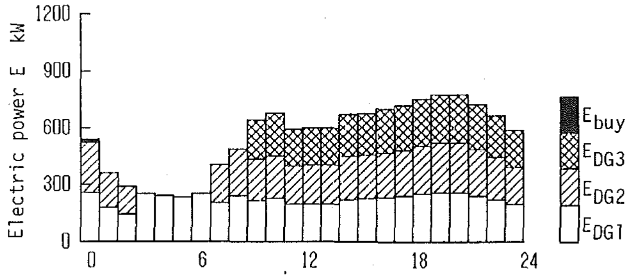

Fig. 7(*a*) Electricity supply

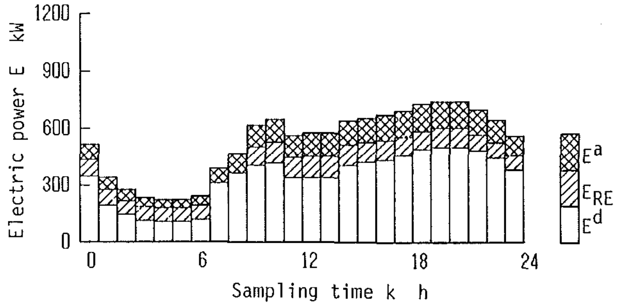

Fig. 7(*b*) Electricity consumption

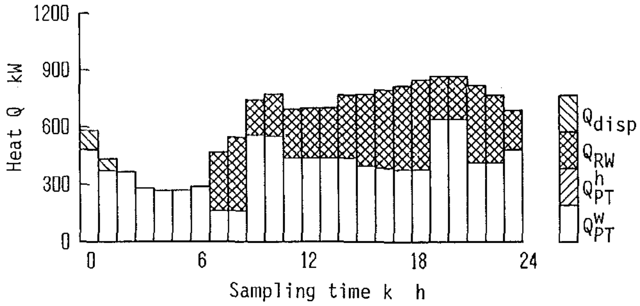

Fig. 7(*c*) Utilization of exhaust heat

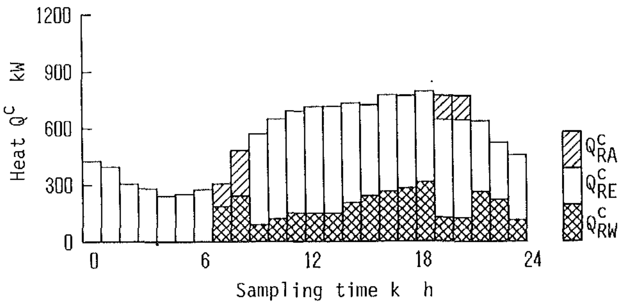

Fig. 7(*d*) Space cooling supply

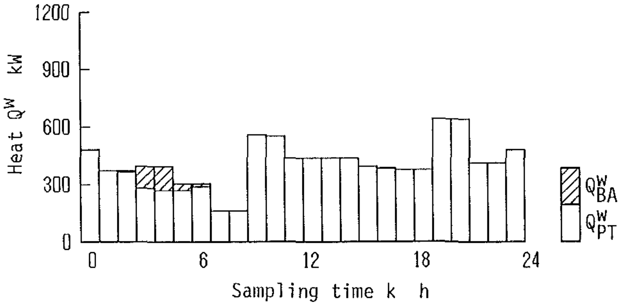

Fig. 7(*e*) Hot water supply

Fig. 7 Optimal operational policy of the cogeneration plant without heat storage tank

salvage value. As shown in Table 3, the daily operational policy is investigated for each case of $V=0$, 10, 20, 30, and 40 m^3. The long-term economy is evaluated for each case of combinations of $\alpha=0.8$, 1.0, and 1.2 with the above values of V.

The optimization calculation for the plant shown in Fig. 1 was carried out for several values of the number of temperature levels L. It was found that the approximate solution by this method approaches the true solution as L increases, and that $L=20$ is enough to approximate the true solution with a high accuracy. Therefore, $L=20$ is adopted also in this case study.

Results and Considerations

Daily Operational Policy. The result about the daily operational policy is first described in detail for the case of the unit cost of fuel oil $\varphi_{\text{oil}}=30$ Yen/L. Figures 6 and 7 show the operational patterns on the representative day in August for the plant with the heat storage tank of $V=30$ m^3 (plant A) and the plant without the tank (plant B), respectively. In Fig. 6(*f*), ΔQ is the heat charged into the heat storage tank; $\Delta Q'$ is the heat discharged from the tank; Q_{pass} is the heat passing through the tank; Q_{loss} is the heat loss from the tank surface. These operational patterns are similar to each other. However, a careful view reveals some points of difference from which the effect of heat storage can be understood. For example, plant B has the heat disposal at the sampling times $k=0$ and 1 in Fig. 7(*c*), while plant A has no heat disposal at those times in Fig. 6(*c*). In plant A, a part of the exhaust heat recovered from both the jacket cooling water and the exhaust gas is charged into the heat storage tank as noticed from Figs. 6(*f*) and 6(*g*). It is used for hot water supply at $k=4$ as seen by the comparison between Figs. 6(*e*) and 7(*e*). In plant A, the heat output of the oil-fired boiler is less than that in plant B. At the sampling time $k=7$, plant B uses a large amount of exhaust heat for driving the single effect absorption refrigerator, while plant A charges it into the tank for future usage at $k=8$ and $10\sim12$, and the vapor compression refrigerator is operated to supply cold water for space cooling. From Figs. 6(*f*) and 6(*g*), it is also seen that the heat storage tank repeats the charging and the discharging at the sampling times $k=16\sim20$ and $22\sim23$. Thus, the charging and the discharging are repeated rather frequently so as not to increase the heat loss from the tank. The installation of the heat storage tank reduces the daily operational cost by 0.48 percent in August. This reduction rate has a maximum in case of $V=30$ m^3. This means that the operational pattern of plant A is determined rationally by utilizing the heat storage tank as a buffer, and by considering the demand fluctuation and the thermal efficiency of each piece of equipment.

Long-Term Economy. Next, the investigation is made into the influence of the volume or the capital cost of the heat storage tank on the annual total cost for several values of the fuel oil price. It is assumed that the annual capital cost is only due to the installation of the heat storage tank. The result is summarized in Fig. 8. In Fig. 8(*a*), for example, the annual variable cost has a minimum in vicinity of $V=20$ m^3, which means that the annual operational cost can be reduced by the installation of the heat storage tank of an appropriate volume. However, when the tank volume is oversized, the demerit due to the heat loss from the tank surface dominates, which results in the increase of the annual operational cost. As shown in Fig. 8(*d*), the reduction of the annual operational cost increases with the fuel oil price. This is because the value of thermal energy becomes relatively high as the fuel oil price increases. In Fig. 8(*d*), the annual total cost for $\alpha=0.8$ has a minimum in the vicinity of $V=10$ m^3. In other cases, however, the demerit

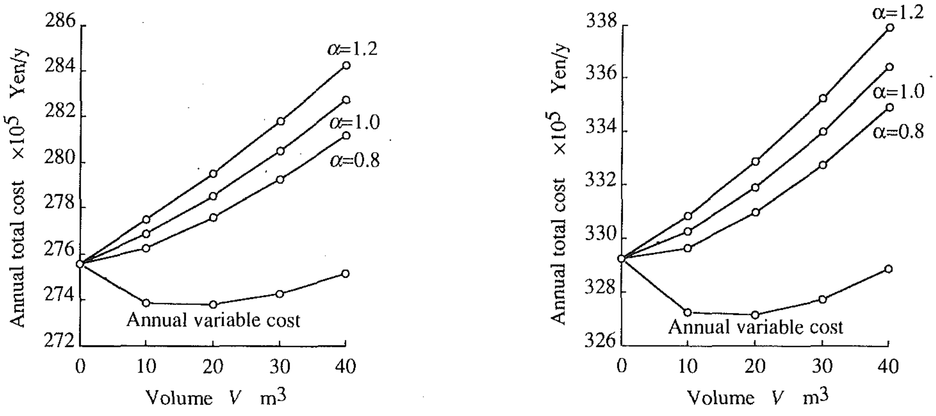

Fig. 8(*a*) $\varphi_{oil} = 20$ Yen/L

Fig. 8(*b*) $\varphi_{oil} = 25$ Yen/L

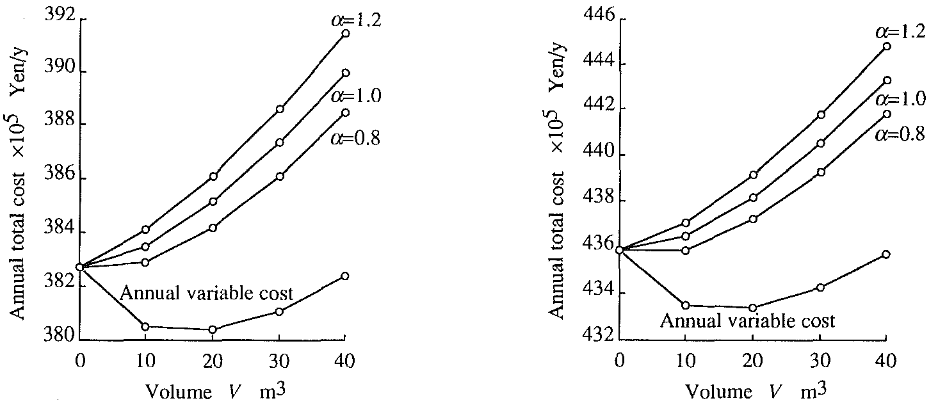

Fig. 8(*c*) $\varphi_{oil} = 30$ Yen/L

Fig. 8(*d*) $\varphi_{oil} = 35$ Yen/L

Fig. 8 Relationship between annual total cost and volume of heat storage tank

due to the investment of the tank dominates, and the plant without the tank is superior to the one with the tank in the annual total cost; i.e., the results show that thermal storage is not a desirable option in the annual total cost.

Conclusions

An optimal operational planning method has been proposed for a cogeneration plant including a heat storage tank. An effective algorithm for solving this problem has been developed on the basis of the dynamic programming method and the mixed-integer programming one. Through a case study, the effect of the heat storage on the total plant has been investigated from the viewpoint of the daily operational policy and the long-term economy. The following results have been obtained:

1 The proposed method enables easy and rational determination of the operational policy for the cogeneration plant with the heat storage tank.

2 The optimal operational policy adopts a daily pattern in which the charging and the discharging are repeated rather frequently so as not to increase the heat loss from the heat storage tank.

3 The installation of the heat storage tank and the adoption of the optimal operational policy reduce the daily and the annual operational costs of the total plant.

4 The installation of the heat storage tank does not have much effect on the annual total cost.

Although this paper has dealt with the restricted case study, the proposed optimal planning method has the flexibility for application to investigation into other cases.

References

Angel, E., and Bellman, R., 1972, *Dynamic Programming and Partial Differential Equations*, Academic Press, New York, pp. 12–14.

Garfinkel, R. S., and Nemhauser, G. L., 1972, *Integer Programming*, Wiley, New York, pp. 5–7.

Horii, S., Ito, K., and Suzuki, Y., 1987, "A Computer-Aided Planning (CAP) System for the Gas Engine Co-generation Plant," *International Journal of Energy Research*, Vol. 11, pp. 491–505.

Ito, K., Yokoyama, R., Horii, S., Matsumoto, Y., and Akagi, S., 1987, "An Optimal Operational Planning Model for Gas Turbine Cogeneration Plants," *Proceedings of the 1987 Tokyo International Gas Turbine Congress*, Vol. I, pp. 97–104.

Ito, K., Yokoyama, R., Yamaguchi, T., Matsumoto, Y., and Akagi, S., 1988, "Optimal Operational Planning of a Gas Turbine Combined Heat and Power Plant Based on the Mixed-Integer Programming," *Proceedings of the IFAC International Symposium on Power Systems, Modeling and Control Applications*, pp. 13.4.1–13.4.7.

Ito, K., Yokoyama, R., Akagi, S., and Matsumoto, Y., 1990a, "Influence of Fuel Cost on the Operation of a Gas Turbine-Waste Heat Boiler Cogeneration Plant," ASME JOURNAL OF ENGINEERING FOR GAS TURBINES AND POWER, Vol. 112, pp. 122–128.

Ito, K., Yokoyama, R., Akagi, S., and Matsumoto, Y., 1990b, "Optimal Operation of Cogeneration Plants With Steam Injected Gas Turbines," *Proceedings of the 4th International Symposium and Exposition on Gas Turbines in Cogeneration, Repowering and Peak-Load Power Generation*, pp. 93–100.

Kuester, J. L., and Mize, J. H., 1973, *Optimization Techniques With Fortran*, McGraw-Hill, New York, pp. 66–90.

Land, A. H., and Doig, A. G., 1960, "An Automatic Method of Solving Discrete Programming Problems," *Econometrica*, Vol. 28, pp. 497–520.

Witte, L. C., Schmidt, P. S., and Brown, D. R., 1988, *Industrial Energy Management and Utilization*, Hemisphere Publishing Corp., Washington, DC, pp. 68–69.

M. Nakhamkin

L. Andersson

E. Swensen

Energy Storage and
Power Consultants, Inc.,
Mountainside, NJ 07092

J. Howard

R. Meyer

Alabama Electric Cooperative, Inc.,
Andalusia, AL 36420

R. Schainker

R. Pollak

B. Mehta

Electric Power Research Institute,
Palo Alto, CA 94303

AEC 110 MW CAES Plant: Status of Project

Introduction

The 110 MW Compressed Air Energy Storage (CAES) plant being built by the Alabama Electric Cooperative, Inc. (AEC) in McIntosh, AL, is currently in the final construction and plant testing phase and is scheduled for commercial operation by June 1991. The contract to build the plant was signed in Aug. 1988.

Throughout the engineering and construction phases of the project, various problems surfaced owing to the plant being the first of its kind in the United States. As a result of these problems, valuable lessons have been learned that can be applied generically to the conceptual design, detailed engineering, scheduling, and construction of future CAES plants.

The objective of this paper is to describe major problems and their solutions and to provide information regarding the overall status of the project. After a brief description of the plant and its mode of operation, the paper is divided into sections describing engineering problems, shop testing, and construction status including recent photographs taken in Jan. 1991.

Plant Description

The McIntosh CAES plant will use relatively inexpensive off-peak energy to drive a motor to compress air, which will be stored in a solution mined underground cavity in the McIntosh salt dome. When peaking or intermediate power is needed, the stored air will be withdrawn, preheated in a recuperator, heated further by burning fuel, and expanded through reheat expansion turbines, which drive a generator. The overall plant schematic is shown in Fig. 1.

The roof of the storage cavity is approximately 1500 feet below the surface. The cavern shape is cigarlike, with a length of approximately 1000 feet, and a diameter varying from 200 feet near the cavern roof, to 180 feet in the center, and 90 feet near the bottom. Total usable volume is expected to be approximately 19,000,000 cubic feet. Air pressure within the cavern will vary from a maximum of about 1150 psia when fully charged, to a minimum of about 750 psia at cavern discharge. The maximum plant output is 110 MW and can be regulated to be a constant 100 MW during this pressure change. The minimum compressor discharge pressure for stable operation is 500 psia.

Contributed by the International Gas Turbine Institute and presented at the ASME Cogen-Turbo V, Budapest, Hungary, September 3-5, 1991. Manuscript received at ASME Headquarters October 1991. Associate Technical Editor: L. A. Riekert.

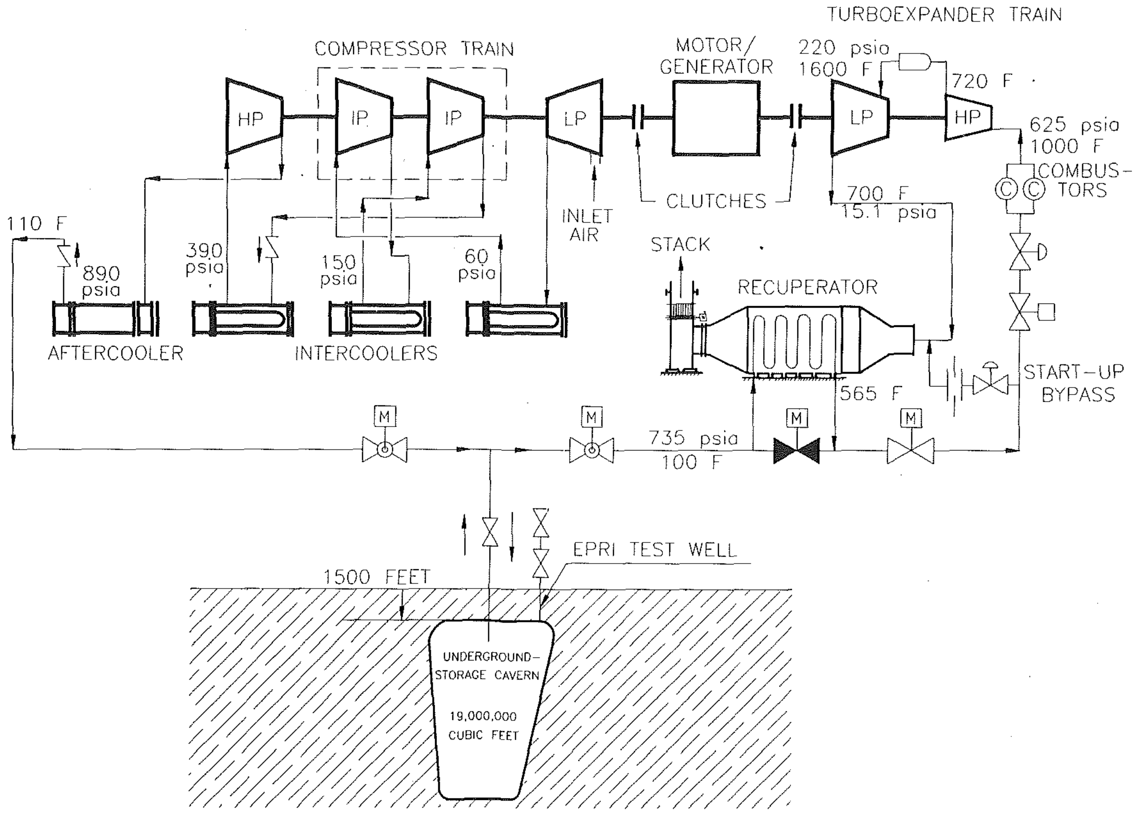

Fig. 1 CAES plant schematic

The plant is expected to operate on a weekly cycle with power generation five days per week and compression during both weeknights and the weekend. Each hour of power generation at 110 MW will require 1.6 hours of compression. The cavern is sized for 26 hours of continuous generation at 100 MW. Each kilowatt-hour (net) of energy generated to the grid is expected to require 4100 Btu of fuel consumption during power generation at peak/intermediate hours plus approximately 0.8 kWh of off-peak electrical energy consumption during the compression cycle.

Engineering Advances Related to CAES Technology

Turbomachinery. The unique characteristics of CAES systems necessitated significant development and innovative engineering efforts to provide an efficient, cost-effective, and reliable plant design. This specifically applies to the development of the turbomachinery train, supplied by Dresser-Rand, as described below:

The turbomachinery includes a three-body compressor train, a motor/generator, and two expanders. The expanders and compressors are connected to the motor/generator via clutches.

To reduce the specific air consumption, lb/kWh, and minimize compressor and air storage requirements, a reheat expander design was selected. The expander train consists of a steam turbine derivative high-pressure expander with an inlet temperature of 1000°F, and a newly developed LP expander with inlet temperature of 1600°F, direct coupled and designed to operate at 3600 rpm. The LP expander design is based upon Dresser-Rand's gas expander experience with cooling of the first-stage nozzles. The required cycling duty of the CAES plant placed limits on the temperatures to be used in this first U.S. plant.

The combustor design was developed by Lucas Aerospace, now AIT, of England for Dresser-Rand. The two HP combustors operate at approximately 625 psia and are believed to be the highest pressure currently available. For the LP expander, eight canted combustor cans are located circumferentially around the inlet. During the development of the combustors, several engineering challenges were faced. The CAES plant specification required that the combustor be free of hot spots for its operating life. After initial testing showed that hot spots did exist, AIT altered the fluid mechanics within the combustor to eliminate the hot spots rather than applying exotic coatings to minimize their effect. Another challenge was the proper atomization of fuel to provide correct ignition and proper burning over the full load range from 10 MW to 110 MW. Several modifications were made to the prototype to achieve the proper flow characteristics which were then proven in a full size rig test. To prove that emissions would meet plant guarantees, full-scale tests were conducted both with and without water injection.

The compressor train includes an axial compressor, which operates at 3600 rpm, a speed-increasing gear, a compound centrifugal compressor, and a barrel type high-pressure centrifugal compressor, both operating at 6025 rpm. To minimize power consumption during the compression cycle, three intercoolers are provided at selected stages as shown in Fig. 1. An aftercooler reduces the compressor discharge air temperature in order to minimize the cavern storage volume and to be compatible with the underground formation.

The motor/generator is a double-ended machine with one end connected to the expanders and the other to the compressors with self-synchronizing clutches.

Other innovative advancements regarding the turbomachinery included the development of investment casting techniques for flow path elements and combustor transition pieces, and new shipping methods for the large pieces of equipment.

Recuperator. Cavern air enters the recuperator at approximately 95°F and is preheated by the LP expander exhaust gas to approximately 565°F on its way to the HP combustors. The "advanced" recuperator design proposed for the McIntosh plant is one in which the potential corrosion problem due to sulfuric acid condensation is eliminated by arranging the tubes and airflow so that the tube temperatures are always above the acid dew point (Nakhamkin et al., 1986). It has been proven during the course of this project that although the theory of the advanced recuperator design is a valid one, the actual detail design of the equipment must be supported by extensive thermal and stress analyses, which consider the many modes of operation to which the recuperator will be subjected. Of particular concern are normal and emergency startups, and recuperator bypass modes.

The large surface area and accompanying mass of metal required to provide the heat transfer between the exhaust gas and compressed air from the cavern give the recuperator tremendous thermal inertia. Under an emergency start with a cold recuperator, there is a significant amount of time required to achieve steady-state metal temperatures corresponding to design conditions. During the initial phases of the project, it was assumed that the turbomachinery ramp rate would be the limiting factor on achieving full load from a cold or warm condition, not the recuperator. Consequently the turbomachinery components, mainly the combustors, were not designed with the extra capacity to overcome the thermal lag of the recuperator. Various solutions were considered, but the schedule of the project did not allow for modification of either the recuperator or the combustors. The solution selected by the designers of the plant was temporarily to increase expander inlet air pressure to permit increased mass flow through the turbine until the recuperator metal temperature starts to increase, and the combustor heat input is adequate to achieve full load. This allows a full load output to be achieved in 9 minutes. In future units with recuperators, it is recommended that the combustor design during cold startup be based upon no heat input contribution from the recuperator. This can be accomplished by an additional combustor used only for fast startup.

Thermal integrity and temperature distributions are another area of concern. Independent analyses conducted on the proposed design indicate that: (*a*) localized tube metal temperatures below the dew point may exist even under certain steady-state part-load and/or cold cavern air conditions, and (*b*) severe localized stresses on the tube joints may occur during the bypass mode when no cooling air is flowing through the tubes. An analysis is currently on-going to determine possible solutions.

The lessons learned regarding the recuperator design are generic in nature and can be directly applied to future CAES plant designs.

Motive Air System Design. The turboexpander train is designed for constant inlet pressure operation; however, cavern pressure varies over a range of approximately 400 psi. As a cost conservation measure, and to provide a relatively constant inlet pressure to the expander control values, the motive air system design includes a pressure control valve upstream of the recuperator. Several problems resulted due to the system design pressure downstream of the control valve being lower than maximum cavern pressure. Code interpretation required the installation of four large overpressure safety valves to protect the system, and the recuperator design pressure was increased to account for potential overpressure downstream of the control valves. A bypass startup valve was added to the initial design of the system to establish flow at startup and minimize these possible pressure excursions.

The difficulties associated with the installation of the safety valves and potential overpressurization can be avoided in the future by designing the entire motive air system for the maximum cavern pressure.

Cavern Temperature Transients. One of the initial concerns raised regarding the underground storage was the adequacy of the proposed volume to account for the secondary temperature effects of compression and expansion within the cavern during cavern charging and power generation, respectively. For the McIntosh plant design parameters, a potential increase in cavern air temperature of 35°F during the possible 41 hour continuous compression mode was calculated (Nakhamkin et al., 1989; Swenson et al., 1990). This temperature change increases the cavern volume requirements from an isothermal situation by as much as 30 percent. The calculations are sensitive to initial conditions, assumed cavern wall salt temperatures, and air injection temperatures. An investigation will be made to verify these calculations by comparison to data taken during actual plant operation.

The temperature transient calculations developed for this project can be used for future plants to estimate initial cavern volume requirements. However, since the cost of mining extra volume (about $1/kW for each additional hour of storage), once the solution mining plant is in place, is relatively minor compared to a potential shortage of stored energy, extra conservatism is recommended in the specification of required cavern volume.

Cavern Dewatering and Initial Cavern Pressurization. Cavern solution mining, dewatering, and initial pressurization were defined as the critical path elements on the original project schedule (due to the maximum water flow rate expected from a nearby source). As solution mining progressed, several factors contributed to extending the cavern completion schedule. In order to return the schedule to near its completion date, it was concluded that the dewatering and initial cavern pressurization scheme should be reviewed and modified. This sequence required complete cavern dewatering through the main CAES well before installation of the permanent CAES wellhead and pressurization of the cavern by portable compressors. The overall schedule from start of dewatering until the cavern has adequate air pressure for turbomachinery testing was approximately 186 days.

A test well, used for initial investigation of the salt and which intersects the main cavern, was completed with a larger casing than required. In addition to providing access to the cavern for test instrumentation, this test well could be used for dewatering. As a result of this, several additional options were considered for cavern dewatering and pressurization. Multiple options were investigated that differed by the method of water removal (pump versus air pressurization), number and location of dewatering pumps, timing and sequence of operations, and portable compressor capacity. The actual procedure used to dewater the cavern is summarized as follows:

1 Install a single dewatering pump of maximum capacity limited by the casing size in the test well.

2 Start dewatering through the test well and install the CAES production liner and permanent wellhead on the main CAES well when the cavern water level is safely below the bottom of the liner.

3 Start pressurization with portable compressors while continuing dewatering. When cavern volume and pressure are adequate to maintain minimum pressure requirements of expander train, air is withdrawn for turbomachinery starting and testing.

4 Dewatering continues through the pump in the test well. When the cavern is fully dewatered, the pump and casing is stripped out under pressuring using conventional oil/gas well methods. The main CAES compressor completes cavern pressurization to the required maximum pressure.

Utilization of this dewatering method is anticipated to save approximately 128 days off the original dewatering and pressurization plant construction schedule. If the test well were not available for dewatering, AEC's only alternative to meet the commercial operation date would have been to stop solution mining earlier and accept a smaller storage volume, or get another source for higher flow rate water.

Therefore, for future CAES units, the dewatering and initial pressurization method has important cost consequences and should be considered early in the project engineering before the overall plant construction schedule is formalized.

Turbomachinery Shop Testing

Several of the components supplied for the turbomachinery train are based on either prototype designs, conventional designs used in a new application, or scaled designs based upon existing smaller frame size machinery. As a result, an intense effort was expended, to the practical, to verify integrity and performance of the machinery, prior to shipment from the factory. A synopsis of this testing and the resulting findings is given below:

Compressor Sections. The CAES turbomachinery train includes a string of three individual, standard compressor sections. Performance and integrity testing of the complete string was not feasible in the factory; however, testing of individual components, including both the gear and the clutch, was performed.

The performance testing of the individual compressor sections, confirming the design performance assumptions for head, flow, and efficiency, followed the guidelines of the ASME PCT-10, and covered the entire operating range, from compressor choke to surge condition.

Four-hour mechanical integrity tests of all compressors, confirming correct assembly, internal fits, and clearances, was conducted in accordance with API Standard 617. Overspeed testing included operation at 110 percent of rated speed. All sections were verified for acceptable mechanical performance, having no detectable rubs, low vibrations, and first critical speeds close to predicted, well away from their operating speeds.

The first section is an axial compressor model MEGA-4015 compressor with 15 stages and 5 movable IGVs. The casing is a horizontally and vertically split, welded construction with cast iron discharge volute. This unit is directly driven by the motor generator at 3600 rpm through a SSS clutch.

Factory testing of the axial compressor was conducted in late Mar. 1990, using an open-loop test rig. The procedure followed PTC-10, for Class II testing. Because of limitations with the 20,000 hp test rig steam turbine driver, the compressor was tested with the inlet valve throttled to reduce power consumption. Five performance points for each of three IGV settings, fully open (+10 deg), fully closed (−30 deg), and design position (−1 deg) were run. All results met guarantees and acceptance standards.

The second compressor is a centrifugal compressor model 4M8-6 with six stages and intercooling between the third and fourth stages. As such, this compressor operates as two separate sections in series, each with 95°F inlet air temperature. The casing is horizontally split of cast iron construction. In the compressor string, this compressor section is located on the outer shaft end of the axial compressor and driven at 6025 rpm through a MAAG speed increasing gear.

The scheduled factory testing of this unit comprised two performance runs, one for each three-stage section, together with a mechanical integrity test of the complete unit. An initial performance test of the first section produced "camelback" characteristics, that is, a low point on the head-capacity curve, resulting in unstable operation. Modifications to improve the flow profiles entering the first and second-stage rotors were made to eliminate this unstable region in the performance envelope.

Re-testing of the modified compressor was conducted in Jan. 1991, using an open-loop test rig for a PTC-10 Class II performance test. The results were accepted although the head-capacity curve of the modified first section did not have a pronounced, continuous rise through its design operating range. The second section performance test revealed a head-capacity curve that exhibited a negative slope toward the surge region, well beyond the design operating range. These undesirable features for individual compressors were judged to be acceptable when the sections are sequential parts of a compressor string, with an axial section that sets the operating envelope for all compressors.

The third section is a vertically split centrifugal compressor model 553-8. The section has an eight-stage rotor and the casing is fabricated from a heavy wall, longitudinally welded length of pipe (ASTM A-516). The section is located on the outboard end of the entire compressor string, operating at 6025 rpm.

The formal witness test, performed in conjunction with the second compressor unit, was conducted in a closed test loop, using nitrogen as the test gas, and conforming to a PTC-10 Class III test. The performance characteristic curve was acceptable.

A relatively high vibration amplitude was recorded at the drive end of the shaft during the mechanical testing of the barrel compressor. The vibration occurred when the unit operated on slow roll, at about 500 rpm, and was almost as high as the critical speed vibration recorded for the same location. The cause was attributed to an oil film, designed to dampen radial shaft oscillations, that did not develop at slow roll rotating speeds.

Turboexpander Sections. The CAES turbomachinery includes a reheat turboexpander train. The expanders were factory tested in accordance with API standards as a single unit at full-speed, no-load conditions. However, these expanders, unlike gas turbines, are not equipped with a self-contained compressor to provide high-pressure air to the combustors. Therefore, the high-pressure and low-pressure combustion systems were tested separately on a full-scale test rig.

As described earlier, the turboexpander train includes a high-pressure expander with combustors, followed by a low-pressure expander with reheat. The test rig arrangement used the high-pressure expander as a steam turbine driver, admitting process steam at about 105 psia and 900°F through one of the combustor mounting flanges (all combustors removed for the test), and driving the low-pressure expander. To reduce the windmill losses in the low-pressure expander, especially during the overspeed sequence, the high-pressure expander exhaust was routed through the low-pressure expander (steam having a lower density than air) before discharging to the atmosphere. To simulate actual operating conditions, to the extent practical, the low-pressure expander exhaust end temperature was kept as close to 800°F as possible.

The mechanical integrity testing of the turboexpander train was conducted in Sept. 1990. The testing included a four-hour, 100 percent speed run, followed by a 120 percent overspeed test. The procedure followed API 612 for most requirements.

The test sequence was followed until thirty seconds before scheduled shutdown, at which time the machine was shut down because of excessive vibrations. Subsequent disassembly and investigation revealed a thermal growth interference in one shaft-to-diaphragm seal, causing rubbing as seal clearances diminished when steady-state temperatures were approached. An unfortunate combination of seal materials aggravated the problem, ultimately causing large pieces of metal to become dislodged from the rotating seal half.

The problem was promptly rectified by opening all shaft seal clearances and spray applying an abrasive material in the grooves on the rotating seal half, allowing any future rubs to grind the opposing seal teeth.

A second mechanical test run of the turboexpander train, following these modifications, proved its integrity.

The combustors and clutch assembly were factory tested separately with satisfactory results.

Motor/Generator The motor/generator provided for this project is a double-ended machine. One shaft is connected to the compressor string, driving this equipment in the motoring configuration. The second shaft end is connected to the turboexpander train, which drives the unit in the generation configuration. Self-synchronizing clutches are provided on each shaft end to disengage the appropriate section.

The motor/generator design is TEWAC, 13.8 kV, 3600 rpm machine with a brushless exciter. The rated generator gross output in the generating mode exceeds 110 MW. The motor power output rating is limited to 54 MW because of exciter shaft design limitations.

During high potential testing of the completed unit, a soldered joint in the stator-winding end-turn melted from an excessive temperature rise. The stator-winding end-turns are L-shaped rectangular copper bars, joined together to form a full 180 deg return bend. The failure, not found by measurements but rather through a coincidental inspection by the manufacturer immediately prior to the scheduled shipment, required a complete disassembly of the generator, including unstacking the stator. A modified end-turn design, using a brazed joint design with a compression sleeve, was developed and installed. The unit was accepted for shipment after retesting and inspection of the modified design.

Current Project Construction Status

Current construction activities are essentially complete. Remaining activities are primarily related to completion of electrical wiring, terminations, and circuit checks. Dewatering of the underground cavern is reaching the point that supports initial turbomachinery operation. The focus of the remaining site activities is changing toward the plant start-up related work, verification of DCS logics, system commissioning, equipment acceptance, and system turnover. Substantial engineering efforts are being expended in support of the start-up program, generating a detailed plant acceptance test procedure, including all supporting design information required to adjust test data to the guarantee conditions. Challenging the development of the plant test procedures are problems associated with a first-of-a-kind unit, and a very extensive contract performance test program.

The project is on schedule with first turbomachinery rotation schedule for late Feb., start of final cavern pressurization with the compressor train by early Mar., start of performance testing by May 1, and the owner's acceptance of the plant by June 1, 1991.

A major pre-operational milestone recently passed is the motive air system line blowout. This blowout consisted of repeated, high-velocity air blows of the piping between the cavern and the recuperator outlet. To maintain the same high velocities through the recuperator tubes, a temporary air/water/steam blow arrangement was used. Portable heaters were arranged to exhaust into the gas side of the unit, heating the tubes to 700°F. Water was mixed with the inlet air and heated to its steam phase as it passed through the recuperator. Target inspections showed this method to be effective.

The following photographs, when compared with Fig. 2, the overall plant plot plan, show the extent of plant construction as of late Jan. 1991.

Figure 3 is a view of the front of the turbine hall looking toward the northwest.

Figure 4 shows the entire, 140-ft-long turbomachinery train, looking north in the turbine hall. The high-pressure barrel compressor is in the foreground, followed by the centrifugal and axial compressors. The larger unit at the center of the train is the motor/generator. The expander train is in the background.

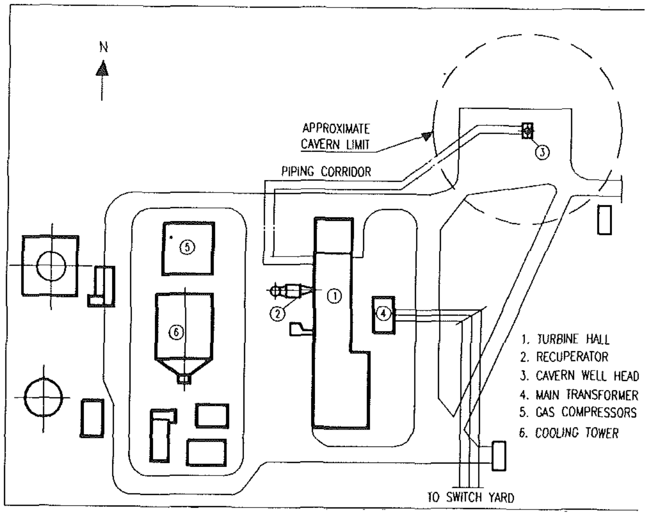

Fig. 2 AEC 110 MW CAES plant plot plan

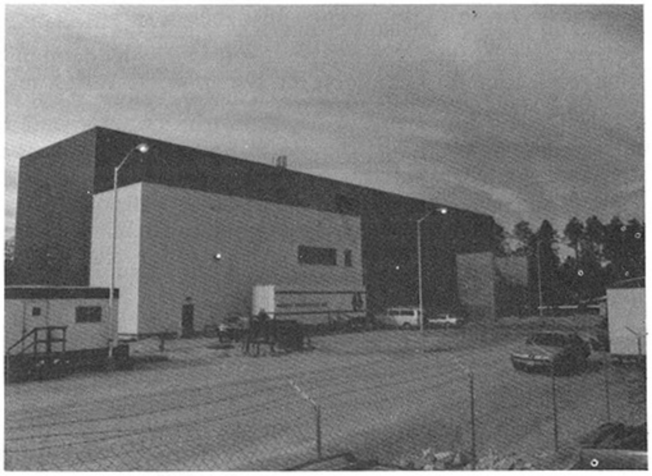

Fig. 3 View of turbine hall looking toward northwest

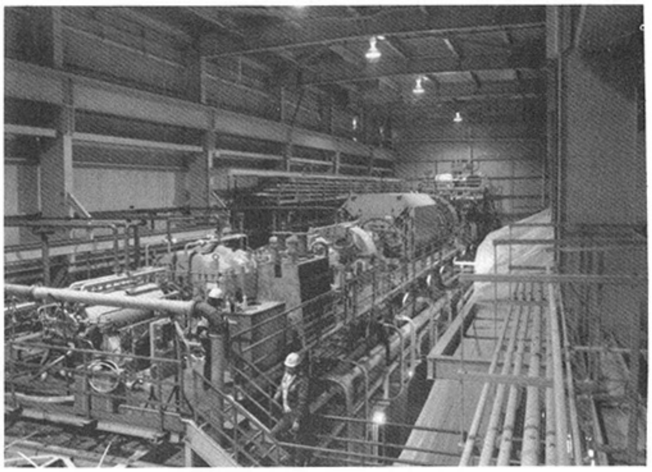

Fig. 4 View of turbomachinery train

Figure 5 is the back wall of the turbine hall looking east. The prominent, large cylindrical equipments in the center of the view are silencers for the compressor surge control blow-off valves. These valves are used to protect the compressors during compressor train start-up, shut-down, and simultaneous compression/generation during emergency conditions.

Figure 6 is a second view of the back wall of the turbine hall, immediately north of the previous picture and looking

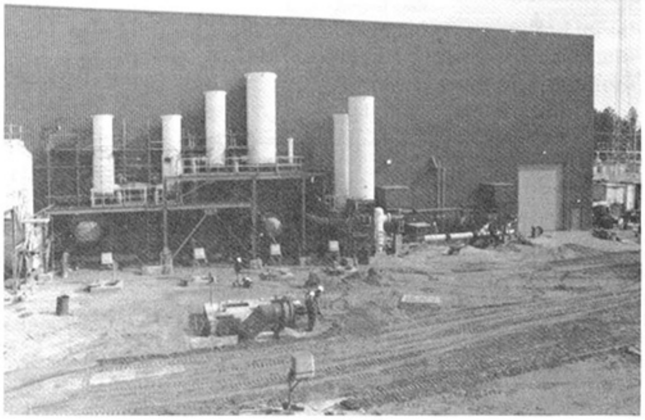

Fig. 5 View of west wall of turbine hall showing compressor blow-off valves and silencers

east. This photograph shows from right to left: the axial compressor air inlet filter, the recuperator (partially hidden), discharge silencers for the motive air system safety valves, and the plant stack.

Conclusions

At present, the project is essentially on schedule and on budget, and is proceeding toward final testing and turnover to the client for commercial operation.

There have been problems during various stages of the project, but each problem has been resolved to all participants' satisfaction. It is anticipated that any future problems will also be solved expeditiously and without any impact on schedule.

Due to the nature of CAES and this first-of-a-kind plant, there are many more major participants in this project than typically found in a conventional power plant project. The authors wish to acknowledge the efforts and the continuous coordination and cooperation of the following organizations:

Harbert International, Inc.—General Contractor
Gibbs & Hill, Inc.—Engineer
Burns & McDonnell—AEC's House Engineer
Dresser-Rand—Turbomachinery Supplier
Fenix & Scission—Solution Mining
  Engineer/Contractor
Struthers Thermo-Flood—Recuperator Supplier

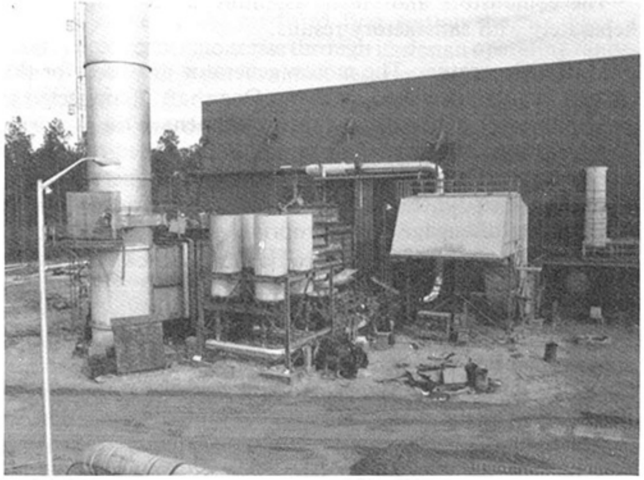

Fig. 6 View of west wall of turbine hall showing air inlet filter, recuperator, and stack

References

Nakhamkin, M., et al., 1986, "Advanced Recuperator for Compressed Air Energy Storage Plants," ASME Paper No. 86-JPGC-GT-7.

Nakhamkin, M., et al., 1989, "CAES Plant Performance and Economics as a Function of Underground Salt Dome Storage Transient Processes," ASME Paper No. 89-GT-143.

Swensen, E., Mehta, B., and Nakhamkin, M., 1990, "Analysis of Temperature Transients of Undergound Air Storage in a Salt Dome During CAES Plant Operation," presented at Solution Mining Research Institute Fall Meeting, Paris, Oct.

Author's Note

This paper was written for presentation during the final construction phases of the project in early 1991. The project started commercial operation in June 1991 and has been a successful addition to the AEC generating capability since then. For more recent detailed information, the reader is referred to the following publications:

Nakhamkin, M., Swensen, E., Andersson, L., et al., 1991, "AEC 110-MW CAES Plant Status of Project," *Proceedings of the 1991 American Power Conference*, Vol. 1, pp. 743-749.

Nakhamkin, M., Andersson, L., et al., 1992, "First US CAES Plant Initial Startup and Operation," *Proceedings of the 1992 American Power Conference*, Vol. 1, pp. 154-161.

Nakhamkin, M., Andersson, L., et al., 1992, "AEC 110 MW CAES Plant Shop Performance and Testing," presented at Second International Conference on Compressed Air Energy Storage, San Francisco, CA, July.

Considerations on the Design Principles for a Binary Mixture Heat Recovery Boiler

S. S. Stecco

U. Desideri

Department of Energy Engineering,
University of Florence,
Firenze, Italy

The use of a binary mixture as a working fluid in bottoming cycles has in recent years been recognized as a means of improving combined cycle efficiency. There is, however, quite a number of studies dealing with components of plants that employ fluids other than water, and particularly binary mixtures. Due to different specific volume, viscosity, thermal conductivity, and Prandtl number, heat recovery boilers designed to work with water require certain modifications before they can be used with binary mixtures. Since a binary mixture is able to recover more heat from the exhaust fumes than water, the temperature difference between the hot and the cold fluids is generally lower over the whole recovery boiler; this necessitates greater care in sizing the tube bundles in order to avoid an excessive heat transfer surface per unit of thermal power exchanged. The aim of this paper is to provide some general criteria for the design of a heat recovery boiler for a binary mixture, by showing the influence of various dimensional parameters on the heat surface and pressure drop both in the cold and the hot side. Heat transfer coefficients and pressure drops in the hot side were computed by means of correlations found in the literature. A particular application was studied for an ammonia-water mixture, used in the Kalina cycles, which represents one of the most interesting binary cycles proposed so far.

Introduction

Over the last five years, since the Kalina cycle was first presented (Kalina, 1984), the interest in cycles using nonconventional working fluids has increased greatly. So far, however, considerable work concentrated on showing the theoretical advantages of a binary mixture cycle compared to the previously assessed Rankine cycle (Stecco and Desideri, 1989; Radermacher, 1989). Less work, however, has been devoted to the principles that should be applied when a new fluid is used instead of water.

The advantages in using a binary mixture could be lost if turbines, pumps, and heat exchangers were not optimized for the thermodynamic and flow characteristics of the substances employed, and had a low efficiency. Parameters such as sonic velocity, viscosity, thermal conductivity, specific heat, and specific volume change so much from one compound to another that not only the dimensions of turbomachines or heat exchangers vary, but the design of blade profiles and labrinth seals in the former and the heat transfer characteristics in the latter, can also be significantly affected.

In combined cycle power plants, one of the main parts is the heat recovery boiler (HRB), and this is where most of the exergy losses are generated (Kotas, 1985). Due to the complexity of the heat transfer correlations for bundles of finned tubes, and the low overall cost of an HRB, manufacturers tend to reduce the time devoted to research of better correlations and developing new concepts to improving the performance of heat recovery boilers. In HRBs, where steam is produced, experience plays such an important role in design that manufacturers often know, almost without any mathematical computation, how large the heat transfer surface should be for a given heat duty.

The authors believe that this approach should change, not only for new HRBs employing fluids other than water, but also for traditional HRBs employing water itself. Criteria to optimize HRBs can lead to savings in costs and dimensions when the fluid is water, and are necessary to design an efficient plant when another fluid is used.

Temperature Profiles in Binary Mixture Heat Recovery Boilers

The main feature of a binary nonazeotropic mixture is that the isobar change of state from liquid to vapor is not isothermal as it is for a pure substance. The temperature differences between a hot fluid, which lowers its temperature while transferring heat to a colder fluid, and a binary mixture, which vaporizes, are smaller than between the mentioned hot fluid and a pure substance subject to the same change of state. Exergy losses from heat transfer, which are a function of temperature difference between the fluids exchanging heat, are thus smaller.

As the use of a binary mixture can reduce the temperature difference between the hot and cold fluids, the log mean temperature difference in the whole HRB can be reduced consid-

---

Contributed by the International Gas Turbine Institute and presented at the ASME Cogen-Turbo V, Budapest, Hungary, September 3-5, 1991. Manuscript received at ASME Headquarters October 1991. Associate Technical Editor: L. A. Riekert.

Table 1 Results for an HRB with working fluid composition ranging from 0 (pure water) to 1 (pure ammonia)

x	0	0.1	0.2	0.3	0.4	0.5	0.6	0.7	0.8	0.9	1	
Q	44.04	47.06	49.45	51.36	52.89	54.07	55.07	55.92	56.64	57.29	57.70	MW
ΔT_{ec}	53.79	46.61	40.62	35.55	31.26	27.75	24.63	21.80	19.23	16.71	15.83	K
ΔT_{bo}	72.52	71.73	71.32	70.92	70.48	70.08	69.58	68.93	68.29	67.90	71.86	K
ΔT_{sh}	79.34	78.51	78.06	77.64	77.17	76.75	76.22	75.51	74.84	74.41	76.14	K
τ_{ec}	0.238	0.266	0.285	0.295	0.298	0.300	0.302	0.309	0.332	0.382	0.413	MW/K
τ_{bo}	0.314	0.352	0.386	0.415	0.441	0.456	0.465	0.466	0.452	0.416	0.288	MW/K
τ_{sh}	0.107	0.120	0.133	0.147	0.162	0.179	0.200	0.226	0.259	0.304	0.400	MW/K
τ/τ_{0ec}	1	1.118	1.198	1.240	1.252	1.261	1.269	1.298	1.395	1.605	1.735	
τ/τ_{0bo}	1	1.121	1.229	1.322	1.405	1.452	1.481	1.484	1.440	1.325	0.917	
τ/τ_{0sh}	1	1.122	1.243	1.374	1.514	1.673	1.869	2.112	2.421	2.841	3.738	

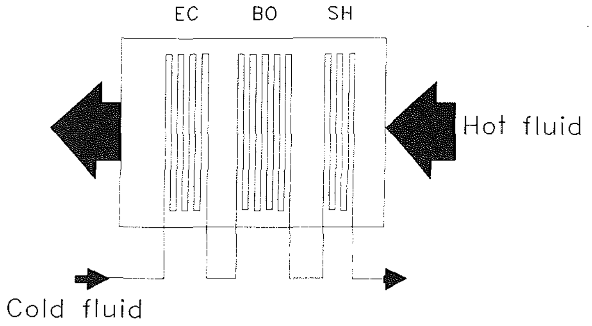

Fig. 1 Heat recovery boiler

erably. This might lead to such an increase in the heat transfer surface that the cost of an HRB, with a binary mixture as cold fluid, could become so much grater than for a steam HRB as to influence negatively the eventual economic advantage of a binary mixture plant.

The temperature profiles presented in this paper, even though they are valid for most of the binary nonazeotropic mixtures, were computed for the ammonia-water mixture. The reasons for this choice are the following:

- The Kalina cycle, which seems to be the most promising binary mixture cycle, uses an ammonia-water mixture as the working fluid.
- The authors have experience with this mixture, for which a computerized system that allows the calculation of the thermodynamic properties was implemented on a personal computer and applied in previous works (Stecco and Desideri, 1989, Olsson et al., 1991; Desideri et al., 1991).

The HRB was computed for ammonia mass fraction ranging from 0 to 1, i.e., from pure water to pure ammonia, and with the same assumptions for all the cases. The heat source is a gas, with a temperature of 797 K, a flow rate of 100 kg/s, and a known specific heat linearly dependent on temperature. Pinch point and approach temperature differences are 15 and 20 K, respectively; the temperature of the cold fluid entering the economizer is 298 K, and its pressure is 4000 kPa. The HRB consists of an economizer, a boiler, and a superheater, arranged in series as shown in Fig. 1.

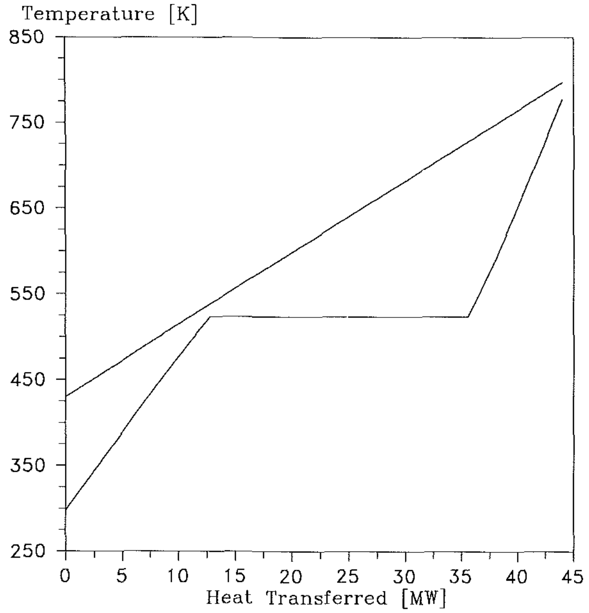

Fig. 2 Temperature profile for a HRB using water as the working fluid

The only variable starting datum is the ammonia mass fraction; the HRB is thus optimized for the given set of parameters, and the cold fluid flow rate and exhaust gas stack temperature are different in each case. The cold fluid flow rate is computed from the heat balance in the boiler and the superheater; the stack temperature is computed from the heat balance in the economizer. Table 1 shows some of the results concerning the heat exchanged and the log mean temperature differences.

Two temperature-heat exchanged diagrams are plotted in Figs. 2 and 3. In the first, water at 4000 kPa is heated, evap-

Nomenclature

c = specific heat
d = diameter
Dh = hydraulic diameter
Δp = pressure drop
ΔT = temperature difference
f = friction factor
h = heat transfer coefficient
k = thermal conductivity
L = length of tubes
Nu = Nusselt number
Pr = Prandtl number
Q = heat
R = thermal resistance of materials
Re = Reynolds number
S = exchange surface
u = velocity
U = overall heat transfer coefficient
v = specific volume
x = ammonia mass fraction
ϵ = efficiency of fins
μ = viscosity
τ = heat transfer ratio

Subscripts

b = bubble
bo = boiler
d = dew
ec = economizer
f = fin
in = inside
ml = log mean
out = outside
p = constant pressure
sh = superheater

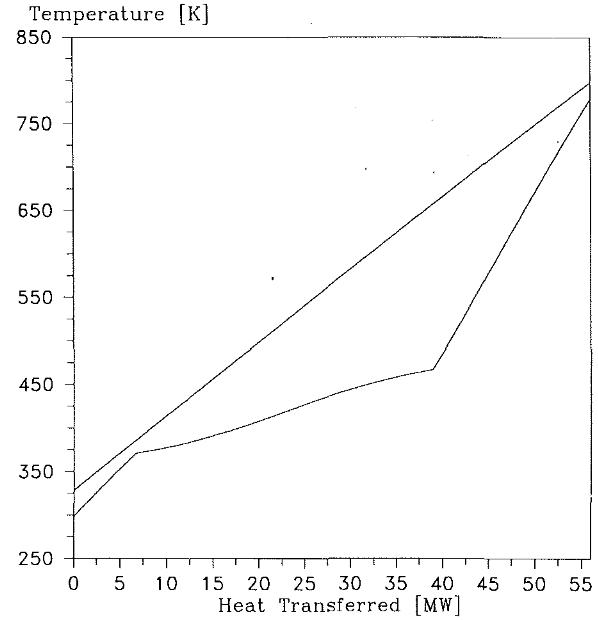

Fig. 3 Temperature profile for a HRB using a 70 percent NH_3/H_2O mixture

orated, and superheated from 298 to 777 K by exchanging 44 MW heat with the gas, which is cooled from 797 to 430 K. In Fig. 3, the hot gas exchanges 56 MW heat with a mixture of water and ammonia, with an ammonia mass fraction of 0.70, and exits to the stack at 329 K.

It is important to notice that not only is the shape of the cold curve changed, when a binary mixture is used, but the amounts of heat transferred in the three sections of the HRB are also different.

The HRB with water as the cold fluid exchanges 12.8 MW heat in the economizer, 23 MW in the boiler, and 8.5 MW in the superheater, with log mean temperature differences of 53.8, 72.5, and 79.3 K, respectively. The HRB with the 70 percent ammonia-water mixture, instead, exchanges 6.7 MW heat in the economizer, 32 MW in the boiler, and 17 MW in the superheater, with log mean temperature differences of 21.8, 68.9, and 75.5 K, respectively. The greatest decrease in the log mean temperature difference is found in the economizer, but if the amount of heat transferred in the other sections is considered, then a decrease of only 4 K might lead to a considerable increase in the exchange surface.

As the heat transfer rate is proportional to the log mean temperature difference by means of the product of the heat transfer surface and the overall heat transfer coefficient, a good parameter to evaluate the importance of the increase in the amount of heat transferred and the reduction of the log mean temperature difference is the ratio:

$$\tau = Q/\Delta T_{ml} = US$$

The τ ratio increases about 29.8 percent in the economizer, 48.4 percent in the boiler, and 11 percent in the superheater when a 70 percent ammonia-water mixture is used instead of water as cold fluid in a HRB, with the same constraints on minimum temperature differences and with the same hot fluid.

The change in the cold fluid affects not only the τ ratio, but also the overall heat transfer coefficient U, for which an expression is the following:

$$U=\left(\frac{1}{h_{\text{out}}\epsilon_f}+\frac{S_{\text{out}}}{h_{in}S_{in}}+\sum_i \frac{S_{in}R_i}{S_i}\right)^{-1}$$

where the only parameter dependent on the properties of the cold fluid is h_{in}.

Cold Side Heat Transfer and Pressure Drop

The cold side heat transfer coefficient h_{in} is contained in the Nusselt number, Nu, which is correlated to the Reynolds and Prandtl numbers:

$$\text{Nu} = h_{in}d/k = C\text{Re}^a\text{Pr}^b$$

where C, a, and b are constants that are dependent mainly on the flow conditions and on the thermodynamic state of the fluid flowing inside the tubes. Reynolds and Prandtl numbers are a function of the fluid, its velocity and the dimensions of the tubes:

$$\text{Re} = uDh/(V\mu)$$

$$\text{Pr} = c_p\mu/k$$

As viscosity, specific heat, and thermal conductivity of different substances can be quite different, the variations in the Nusselt, Reynolds, and Prandtl numbers can be fairly high when another fluid is employed instead of water.

In the cases described above, the variation in density during the transformations from the liquid to the superheated vapor state, for pure water and for a 70 percent ammonia-water mixture are as follows:

		H_2O	70 percent NH_3-H_2O	
Economizer	In	1000	770	[kg/m^3]
	Out	770	625	”
Boiler	Out	19.6	20.5	”
Superheater	Out	11.4	10.9	”

A significant decrease in density can be observed in the economizer if a mixture is used. As ammonia and water are substances with similar molecular weight, and with a polar molecule of quite the same structure, the differences in their properties are not so great as the differences in the properties of other fluids that could be suitable as a binary mixture component, such as ethanol or some CFCs, even if their utilization is going to be strongly limited in the future.

Various expressions can be used to compute properties, such as viscosity and thermal conductivity, for a binary mixture. They are functions of the properties of the pure substances and of the mass fractions of the components, but they often require the knowledge of some functions that take into account the interaction factors, especially for the liquid state. A general review of many theoretical works on this subject is reported by Reid et al. (1987), and some expressions were used by El-Sayed (1988). As available data on binary mixtures are scarce, it is impossible to compare experimental and computed data for a wide range of temperature and pressures such as those encountered in HRBs for combined cycles.

For the ammonia-water mixture, the authors followed the indications given by Reid et al. (1987), who suggest the use of Lucas' correlation for the viscosity of the pure components' vapor state, a modification of Vogel's equation for the viscosity of the pure components in the liquid state, Miller's equation for the thermal conductivity in the vapor and liquid states. For the viscosity of the mixture in the vapor state, Chung's theory is considered to give acceptable results, while the Teja-Rice correlation is more suitable for the viscosity of the liquid. Thermal conductivities for the vapor and liquid states are computed by means of the Chapman-Enskog and Jamieson correlations, respectively.

The mixture's specific heat is computed as the ration of the enthalpy change due to a temperature variation of 0.01 K and the temperature variation itself. Values for the enthalpy of the mixture as a function of pressure and temperature are computed as explained by Stecco and Desideri (1989).

Results obtained with this approach were compared with data presented by El-Sayed (1988), and showed a good agreement with them. The authors, however, believe that more theoretical and experimental work is necessary for the computation of binary mixture thermodynamic and mass transfer properties, in order to design a binary mixture power plant or one of its parts with a high degree of accuracy.

The comparison between a pure water and a 70 percent ammonia-water mixture HRB revealed a great difference both in liquid state viscosity and in vapor state thermal conductivity. The viscosity of the mixture in the liquid state is much higher than that of pure water, while thermal conductivity of the mixture in the vapor state is about half as much as steam thermal conductivity. No computations were performed during the change of state, because the internal heat transfer coefficient is not usually calculated from fluid properties, but fixed at some reasonable value, as it does not influence the overall heat transfer coefficient very much, when the hot fluid is a gas.

Properties such as fluid viscosity and density affect another important design parameter, i.e., the pressure drop in the cold side. Computation of the pressure drop is necessary to avoid an excessive increase in the fluid velocity inside the tubes, which is a positive factor for augmenting the transferred heat. Pressure drops in the cold side of a HRB can be computed with the following expression:

$$\Delta p = \frac{fL}{d} \frac{1}{v} \frac{u^2}{2}$$

where the friction factor f is a function of the Reynolds number and of the roughness of the tube.

Hot Side Heat Transfer and Pressure Drop

On the hot side, computation of heat transfer and pressure drop is complicated by the use of finned tubes, which enhance the heat transfer when one of the two fluids in the heat exchanger is a gas. Finned tubes have a complex exchange surface for which appropriate correlations must be provided. The only reasonable way to obtain these data is to correlate experimental results, which on the other hand are limited as far as the range of dimensional and operational parameters is concerned.

Some of the correlations for heat transfer and pressure drops in bundles of finned tubes are reported by Kröger (1986), Vampola (1965), and Rohsenow et al. (1985). The authors used some of these correlations (Kröger, 1986; Vampola, 1965) to determine the hot side heat transfer coefficient and pressure drops in a HRB.

The heat transfer coefficient, in this case, is a function not only of Reynolds and Prandtl numbers, but also of the geometric characteristics of both the finned tubes and their layout. In particular, the most important parameters are the diameter of the tube, the number of fins per meter, the transverse and longitudinal distances, and the thickness and height of the fins.

It is important to note that the overall heat transfer coefficient is dependent mainly on the gas side heat transfer coefficient and that, for this reason, the variation in the τ ratio, is much more important than the variations in the overall heat transfer coefficient.

Therefore, even if an accurate design of a HRB for a power cycle employing a binary mixture requires the exact determination of the overall heat transfer coefficient and of the mixture's properties, the change in the heat exchange surface is mainly due to the different τ ratio.

Other Features of an HRB for a Binary Mixture

When a binary mixture changes its state from liquid to vapor, a separation of the two components occurs, so that, at temperatures between the bubble and the dew points, the vapor is richer in the lower boiling component and the liquid is richer with the higher boiling component. Figure 4 shows the dew and bubble lines for the ammonia-water mixture at the same pressure. If a mixture in the liquid state at a given concentration and temperature T_1 is heated, as soon as it reaches the bubble point, T_b, a vapor, which is rich in the low-boiling component, x_{db}, is formed. As the temperature increases, T_2, the vapor becomes richer in the high boiling component, x_{d2}, while the liquid becomes poorer in the low boiling component, x_{b2}. When the temperature, T_3, is higher than the dew temperature, T_d, the vapor has the same composition as the liquid from which the process was started.

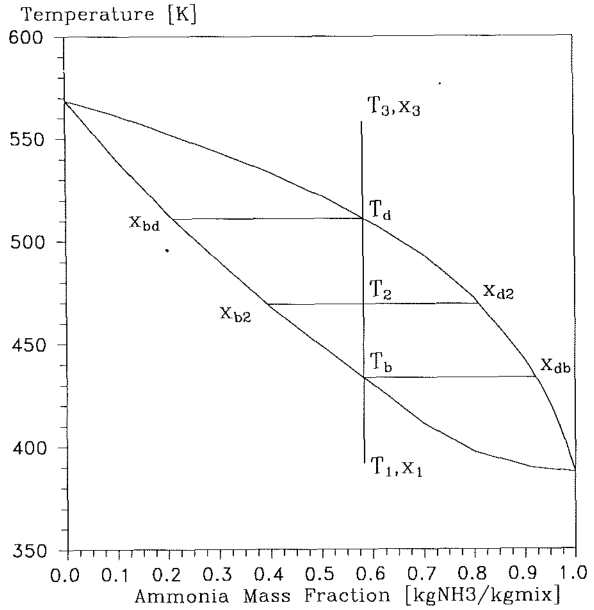

Fig. 4 Dew and bubble lines for a water-ammonia mixture at 8000 kPa

A consequence of this behavior is that the boiler section must not have any drum, to avoid the separation of the low boiling component from the mixture, and the enrichment of the mixture contained in the drum with the high boiling component. The HRB for a binary mixture must then be a once-through heat exchanger where the pressurized mixture passes through all the sections only once.

If one or both the mixture components are hazardous to health, safety devices can increase the complexity of the HRB, and maintenance costs. If, for example, the toxicity of a substance is proportional to the concentration, relief valves should be designed to discharge the fluid at the highest velocity possible to increase the mixing effect with the surrounding air. Moreover, sensors to detect the presence of such substances inside or in the vicinity of the HRB should be located in different places and connected to some alarm devices. In addition, appropriate emergency procedure must be available.

When dissociation at high temperatures can occur, sensors should be used to detect the presence of such substances. Dissociation of ammonia into hydrogen and nitrogen not only causes the presence of incondensables in the working fluid, but may also enhance the phenomenon of nitrogen deposition on steel tubes and can create an explosive mixture if oxygen is present.

Elimination of incondensables from a binary mixture power cycle is also a problem for two important reasons:

- If the components are hazardous, there must be no deaerator in the plant to avoid discharge of the substances in the atmosphere.
- The cost and the availability of some substances discourages a continuous loss in the atmosphere, as in deaerators.

Table 2 Results for a HRB with a 70 percent NH_3/H_2O mixture as the working fluid

```
THERMODYNAMIC PROPERTIES
  p        T        h      s        v        M
 kPa       K      kJ/kg  J/kgK    m3/kg     kg/s
 4076.  298.15   -75.7   238.    .0013    19.12
 4000.  371.39   276.7  1292.    .0016    19.12
 3832.  465.25  1956.1  5336.    .0510    19.12
 3777.  777.15  2847.8  6809.    .0972    19.12
  101.  328.59    64.2   214.    .8373   100.00
  101.  386.39   131.6   402.    .9818   100.00
  102.  656.79   452.8  1030.   1.6598   100.00
  103.  797.15   623.4  1263.   1.9976   100.00
HEAT TRANSFER RESULTS
Heat exchanged with gas          =   55.9 MW
 Heat exch. in economiser        =    6.7 MW
 Heat exch. in boiler            =   32.1 MW
 Heat exch. in superheater       =   17.1 MW
Pinch Point Temp. difference     =   15.0 K
 Economizer Temp. differences    =   30.4 -  15.0 K
 Boiler Temp. differences        =   15.0 - 191.5 K
 Superheater Temp. differences   =  191.5 -  20.0 K
Heat transfer coeff. in EC       =   26.8 W/m2K
Heat transfer coeff. in BO       =   35.9 W/m2K
Heat transfer coeff. in SU       =   15.5 W/m2K
         Econ.   Boiler   Super.
h_in     2606.   10000.    460.    W/m2K
h_t     15109.   14349.   12639.   W/m2K
h_out     34.9     40.7     47.3   W/m2K
 Heat transfer surface in EC     =  11530. m2
 Heat transfer surface in BO     =  12901. m2
 Heat transfer surface in SU     =  14479. m2
Total heat transfer surface      =  38910. m2
PRESSURE DROPS
 Press. drop in EC cold side     =  76809. Pa
 Press. drop in EV cold side     = 167915. Pa
 Press. drop in SU cold side     =  54773. Pa
Press. drop in HRB cold side     = 299497. Pa
 Press. drop in EC hot  side     =    293. Pa
 Press. drop in EV hot  side     =    552. Pa
 Press. drop in SU hot  side     =    864. Pa
Press. drop in HRB hot  side     =   1709. Pa
EXERGETIC ANALYSIS
Exergy from gas                  =   25.7 MW
Exergy to mixture                =   19.7 MW
 Exergy loss in economiser       =     .4 MW
 Exergy loss in boiler           =    4.2 MW
 Exergy loss in superheater      =    1.4 MW
 Exergy loss in exhaust          =     .3 MW
Boiler exergy loss               =    6.2 MW
Boiler exergetic efficiency      =   76.0 %
```

The absence of a deareator is then another important feature of a binary mixture HRB.

Results for an Ammonia-Water Mixture HRB

An application has been studied, for the case of the 70 percent ammonia-water mixture with a pressure of 4000 kPa. The starting data are the same as these described above, with the constraints on the minimum pinch-point temperature difference, on the approach temperature difference, and with given inlet gas and mixture temperatures. The mixture flow rate is computed from the enthalpy balance in the boiler and superheater.

Pressure drops inside the tubes are calculated on both the hot and the cold sides, and the input value of 4000 kPa is the pressure at the outlet of the economizer. Pressures before and after the mentioned point are computed from pressure drops in the HRB sections. On the hot side, pressure at the outlet of the boiler is known, being the atmospheric pressure, and the pressures at the other sections are also computed from pressure drops.

Both pressure drops and heat transfer coefficients are computed following Vampola's correlations (1965), because they are the ones giving the nearest values to the average of all the others (Kröger, 1986). Characteristics of the finned tubes are the following:

- Diameter = 40.64 mm (1.6 in.)
- Fins per meter = 236 (6 fins/in.)
- Fin height = 20 mm
- Fin thickness = 1.5 mm
- Staggered layout
- Material: steel

Transverse and longitudinal distances between the rows are set to 100 and 90 mm, respectively. Direction of the hot gas is horizontal, while the cold tubes are vertical, so that the heat exchange can be considered to be identical to a crossflow arrangement.

Lower limits on the velocity of the cold and hot flows are imposed, in order to avoid an excessive reduction of speed with the aim of decreasing pressure drops. In fact, stability and safety considerations do not allow the liquid velocity to be lower than 1 m/s, and heat transfer considerations require the vapor velocity to be higher than 10 m/s. The heat transfer coefficient for the boiling mixture is set at 10 kW/m^2K, and is supposed to be constant.

With all these starting data, the results computed are shown in Table 2. The sum of all the pressure drops on the cold side is about 7.5 percent of the maximum pressure, and half of it is found to be in the boiler. Heat transfer surfaces are equally distributed among the three sections: 11,530, 12,901, and 14,478 m^2 in the economizer, in the boiler, and in the superheater, respectively. The heat exchange surface in the economizer is strongly influenced by the very low log mean temperature difference, while the high heat exchange surface in the superheater is mainly due to the low heat transfer coefficient.

A comparison with a similar HRB, whose cold fluid is water, was made, by using the same constraints as the ones for the mixture HRB. The only differences are the tube dimensions, which were reduced not to violate the constraints on cold fluid velocities. The diameter for the economizer and boiler tube bundles is 1.25 in. and the transverse and longitudinal distances between rows are 90 and 80 mm, respectively. The computed cold flow rate is 13.13 kg/s.

Table 3 shows the results for the HRB employing water. It can be observed that the global exchange surface is about half that required for the ammonia-water mixture. This is due either to a reduction in the heat transferred to the cold fluid, or to the increase in the log mean temperature differences. The increase in the heat transfer coefficients is another factor that influences the reduction in the exchange surface.

Lower pressure drops on the cold side are the consequence of the reduction in the cold flow rate, and only partly the consequence of the change of the fluid. Instead, pressure drops on the hot side are almost the same.

An exergy analysis of the HRBs in Tables 2 and 3 is also presented. The exergy losses in the three sections of the HRBs take into account not only those due to the heat exchange but also those caused by the pressure losses.

The global exergy losses in the HRB using water are higher than in the HRB using the water-ammonia mixture, but the distribution of the losses in the three sections of the recovery boiler is different for the two fluids. The water-ammonia mixture has higher exergy losses in the boiler and the superheater because in those sections most of the total heat is exchanged, and their relative importance is much bigger than for the same sections in the water HRB. If the water-ammonia mixture were richer in water, the exergy losses in the boiler and superheater would be smaller but the global exergy loss would be bigger.

Table 3 Results for a HRB with water as the working fluid

```
THERMODYNAMIC PROPERTIES
   p       T        h       s       v        M
  kPa      K      kJ/kg   J/kgK   m3/kg    kg/s
 4053.  298.15    108.6    369.   .0010    13.13
 4000.  523.38   1083.3   2792.   .0013    13.13
 3893.  521.76   2816.9   6114.   .0525    13.13
 3854.  777.15   3462.8   7132.   .0909    13.13
  101.  430.20    183.0    529.  1.0962   100.00
  102.  538.38    311.0    794.  1.3687   100.00
  102.  727.62    538.6   1155.  1.8426   100.00
  102.  797.15    623.4   1265.  2.0127   100.00
HEAT TRANSFER RESULTS
Heat exchanged with gas          =   44.0 MW
 Heat exch. in economiser        =   12.8 MW
 Heat exch. in boiler            =   22.8 MW
 Heat exch. in superheater       =    8.5 MW
Pinch Point Temp. difference     =   15.0 K
 Economiser Temp. differences    =  132.0 -   15.0 K
 Boiler Temp. differences        =   15.0 - 205.9 K
 Superheater Temp. differences   =  205.9 -   20.0 K
Heat transfer coeff. in EC       =   31.4 W/m2K
Heat transfer coeff. in BO       =   39.7 W/m2K
Heat transfer coeff. in SU       =   25.8 W/m2K
          Econ.   Boiler  Super.
h_in      7403.   10000.   1022.    W/m2K
h_t      14976.   13978.  12397.    W/m2K
h_out      36.7     46.9    54.5    W/m2K
 Heat transfer surface in EC     =    7562. m2
 Heat transfer surface in BO     =    7860. m2
 Heat transfer surface in SU     =    4115. m2
Total heat transfer surface      =   19538. m2
PRESSURE DROPS
 Press. drop in EC cold side     =   52930. Pa
 Press. drop in EV cold side     =  106901. Pa
 Press. drop in SU cold side     =   38945. Pa
Press. drop in HRB cold side     =  198776. Pa
 Press. drop in EC hot  side     =     240. Pa
 Press. drop in EV hot  side     =     396. Pa
 Press. drop in SU hot  side     =     300. Pa
Press. drop in HRB hot  side     =     936. Pa
EXERGETIC ANALYSIS
Exergy from gas                  =   22.8 MW
Exergy to mixture                =   18.5 MW
 Exergy loss in economiser       =    1.5 MW
 Exergy loss in boiler           =    2.2 MW
 Exergy loss in superheater      =     .7 MW
 Exergy loss in exhaust          =    3.1 MW
Boiler exergy loss               =    7.4 MW
Boiler exergetic efficiency      =   71.3 %
```

Conclusions

The use of nontraditional working fluids for power cycles requires an accurate examination of all the differences existing between the chosen fluid and water, which is the most widely used and best known fluid. Power plant components designed to work with water at acceptable performance levels might give negative results if used with another fluid.

In order to design an efficient power plant using a binary mixture as the working fluid, knowledge of all the properties of the mixture is necessary. A greater effort from researchers and HRB manufacturers for more experimental and theoretical work in this field is desirable, at least for all the substances and mixtures that offer an improvement in cycle performance if used instead of water.

When comparing HRBs using an ammonia-water mixture and pure water, the disadvantages of the former must be weighed against the better thermodynamic performance that it offers. A 25 percent increase of the heat recovered and a higher exergetic efficiency of the HRB using the ammonia-water mixture must not be overlooked when considering the economic advantages.

Acknowledgments

This study was made possible thanks to the financial support of the MURST. Its contribution is gratefully acknowledged.

References

Desideri, U., Olsson, E., Stecco, S. S., and Svedberg, G., 1991, "The Ammonia-Water Mixture Rankine Cycle: Considerations on Its Applicability as Bottoming Cycle," presented at the 26th IECEC, Boston, MA.

El-Sayed, Y., 1988, "On Energy and Surface Requirements for Heat Transfer Processes Involving Binary Mixtures," *Proceedings, ASME Winter Annual Meeting*, Chicago, IL.

Kalina, A., 1984, "Combined Cycle System With Novel Bottoming Cycle," ASME JOURNAL OF ENGINEERING FOR GAS TURBINES AND POWER, Vol. 106, pp. 737–742.

Kotas, T. J., 1985, *The Exergy Method of Thermal Plant Analysis*, Butterworths, London.

Kröger, D. G., 1986, "Performance Characteristics of Industrial Finned Tubes Presented in Dimensional Form," *International Journal of Heat and Mass Transfer*, Vol. 29, No. 8, pp. 1119–1125.

Olsson, E., Desideri, U., Stecco, S. S., and Svedberg, G., 1991, "An Integrated Gas Turbine-Kalina Cycle for Cogeneration," ASME Paper No. 91-GT-202.

Radermacher, R., 1989, "Thermodynamic and Heat Transfer Implications of Working Fluid Mixtures in Rankine Cycles," *International Journal of Heat and Fluid Flow*, Vol. 10, No. 2, pp. 295–305.

Reid, R., Prausnitz, J., and Poling, B., 1987, *The Properties of Gases and Liquids*, 4th ed., McGraw-Hill, New York.

Rohsenow, W. M., Hartnett, J. P., and Ganic, E. N., 1985, *Handbook of Heat Transfer Applications*, 2nd ed., McGraw-Hill, New York.

Stecco, S. S., and Desideri, U., 1989, "A Thermodynamic Analysis of the Kalina Cycles: Comparisons, Problems, Perspectives," ASME Paper No. 89-GT-149.

Vampola, I., 1965, "Generalization of Heat Transfer and Pressure Drop Relationships for Gas Flow Across a Bundle of Finned Tubes," *Heat and Mass Transfer*, Vol. 1, pp. 295–305.

Optimal Synthesis and Operation of Thermal Systems by the Thermoeconomic Functional Approach

C. A. Frangopoulos
Department of Naval Architecture
and Marine Engineering,
National Technical University of Athens,
Zografou, Greece

Methods developed for optimization of thermal systems usually work on a predetermined configuration of the system. Consequently, in order to select the best system, it is necessary to apply the method separately for each possible configuration and compare the results. The designer's work would be significantly facilitated, if the optimization method could synthesize the optimal configuration of the system automatically. Such a method is presented here, based on the Thermoeconomic Functional Approach (TFA). TFA is a method developed for optimal design or improvement of complex thermal systems. It combines thermodynamic concepts with economic considerations in a systems approach. A thermal system is considered as a set of interrelated units; each unit has one particular function (purpose, or product). The documented determination of the function of the system as a whole and of each unit individually is achieved by functional analysis. The problem is mathematically formulated (objective function, constraints) at two levels: (A) optimization of operation, (B) optimization of the configuration and the design of the system. The solution is obtained by a two-level algorithm. As an example, the method is used to optimize a cogeneration system supplying a process plant with heat and electricity, which are known functions of time.

1 Introduction

The problem of thermal system optimization is usually studied at either the operation level or the design level, while the configuration (structure) of the system is predetermined. The final decision is based on a comparison among several system configurations. Only a few attempts have been made to synthesize the optimal system configuration and the procedures developed are usually appropriate for a particular kind of system. For example Pinch Technology has been very successful in optimal synthesis of heat exchanger networks. An application of the method for optimization of a power plant has been published recently (Linnhoff and Alanis, 1989), but again from the point of view of heat exchangers (e.g., feedwater heaters). A different approach, which is not restricted to systems of a particular kind, is described in the following.

The complete optimization problem may be stated in the form of questions interwoven with each other: Which are the configuration (set of interrelated equipment) of the system, the design characteristics of the components, and the operating strategy that lead to an overall optimum? The degree of freedom increases when the task of the system is not completely specified, but it has to be decided (e.g., optimal production rates); and this is more so in case of a multiproduct system. Time-dependent operation adds one more dimension making the problem more complicated.

A new formulation of the Thermoeconomic Functional Approach (TFA) is presented here, which can be used in order to solve problems of this type in a systematic way. Earlier work on thermoeconomics (Tribus and Evans, 1962; El-Sayed and Evans, 1970; Evans, 1980; Evans et al., 1983) led to the development of TFA for the analysis and optimization of complex thermal systems (Frangopoulos, 1983). In preceding forms of the method (Frangopoulos, 1984, 1987a), it has been considered that the system has a given fixed structure and operates under steady-state conditions. In the new formulation of TFA presented in the following, the type of the system is considered known (e.g., a steam plant, a diesel-engine plant, etc.), but the system configuration, the design characteristics of the components, and the point of operation at any instant of time, which lead to an overall optimum, are determined by the solution of an appropriately formulated problem. Also, a numerical example is presented, which serves to clarify the method and the application procedure further.

2 Thermoeconomic Functional Analysis

2.1 Concepts and Definitions. In TFA, thermodynamic concepts are combined with economic considerations in a systems approach. A thermal system (thermal power plant, re-

---

Contributed by the Advanced Energy Systems Division for publication in the JOURNAL OF ENGINEERING FOR GAS TURBINES AND POWER. Manuscript received by the Advanced Energy Systems Division January 10, 1991; revision received July 2, 1991. Associate Technical Editor: M. J. Moran.

frigeration plant, chemical plant, propulsion plant, etc.) is considered as a set of interrelated units (Kramer and Smit, 1977). Each unit has one particular function (purpose or product). Consequently, "Functional Analysis" does not imply that particular branch of mathematics, but it is the formal and documented determination of the function of the system as a whole and of each unit individually (Dickerson and Robertshaw, 1975; Frangopoulos, 1983).

2.2 The Functional Diagram of a System. The system is depicted by the "Functional Diagram," which is composed of small geometric figures representing the units and a network of lines representing the distribution of the unit functions. Junctions (where the functions of two or more units merge) and branching points (where the function of a unit is distributed to more than one unit) are considered as fictitious units, unless they correspond to real components of the plant.

3 Thermoeconomic Functional Optimization Under Time-Dependent Operating Conditions

3.1 Mathematical Formulation of the Problem. Several objectives may be considered in economic optimization: maximize the return on investment, minimize the payback period, maximize the life cycle savings, minimize the life cycle cost, etc. The objective function selected here and written for time-dependent operating conditions is

$$\min F=\sum_{r=1}^{\sigma} Z_r+\sum_{r=1}^{R}\sum_{j=1}^{J_r}\left[\int_t \dot{\Gamma}_{0j.r}dt\right]-\sum_{r=1}^{R}\left[\int_t \dot{\Gamma}_{r,0}dt\right] \qquad (1)$$

where

Z_r = annualized capital cost of unit r
$\dot{\Gamma}_{0j.r}$ = cost per unit time for the function $y_{0j.r}$ supplied by the environment to the unit r
$\dot{\Gamma}_{r,0}$ = revenue per unit time from selling the function (product) $y_{r,0}$ to the outside world

The quality of each product is known (e.g., electricity, steam at (P, T), hot water, etc.), but the production rate is not necessarily predetermined. If the revenues $\dot{\Gamma}_{r,0}$ of all the system products are included in Eq. (1), then F is the negative of the system profit. However, if the production rate of a product is predetermined, the corresponding revenue $\dot{\Gamma}_{r,0}$ is fixed and there is no need to include it in Eq. (1), since addition of a constant to the objective function does not change the optimum point. If the quantity of a product is not predetermined, then the corresponding revenue function $\dot{\Gamma}_{r,0}(\dot{y}_{r,0})$ must be included in Eq. (1) in order to determine the optimum production rate $\dot{y}_{r,0}$.

The time period t of integration in Eq. (1) is one year. It is often practical to replace integrals with summations over K time intervals each of length Δt_k. In each time interval the system is considered to be operating under steady-state conditions. Then, the objective function takes the form

$$\min F=\sum_{r=1}^{\sigma} Z_r+\sum_{k=1}^{K}\left[\sum_{r=1}^{R}\sum_{j=1}^{J_r}\dot{\Gamma}_{0j.r}-\sum_{r=1}^{R}\dot{\Gamma}_{r,0}\right]_k \Delta t_k \qquad (2)$$

The number K of time intervals is such that the result obtained by Eq. (2) approximates the one of Eq. (1) closely enough. Since the exact configuration of the system is not known at the beginning, σ is the total number of units that might be required. If the solution of the optimization problem shows that there is no need of unit r, then it is set $Z_r=0$ and the interconnections between units are readjusted automatically.

The following functional relations are valid:

$$Z_r=Z_r(\mathbf{x}_r) \qquad (3a)$$

$$\dot{\Gamma}=\Gamma(\dot{y}), \quad \dot{y}=y(\mathbf{x}, \mathbf{z}) \qquad (3b)$$

$$F=F(\mathbf{x}, \mathbf{z}, \mathbf{y}) \qquad (4)$$

where

$\mathbf{x}$ = set of design decision (independent) variables, e.g., specification of equipment
$\mathbf{z}$ = set of operation decision (independent) variables
$\mathbf{y}$ = set of all the functions y (see also Eqs. (5) and (6))

In each time interval, the following equality constraints must be satisfied:

$$y_{0j,r}=Y_{0j,r}(\mathbf{x}_r, \mathbf{z}_r, \mathbf{y}_r)\equiv Y_{0j,r}, \quad j=1, 2, \ldots, J_r \qquad (5a)$$

$$y_{r,r'}=Y_{r,r'}(\mathbf{x}_{r'}, \mathbf{z}_{r'}, \mathbf{y}_{r'})\equiv Y_{r,r'}, \quad \begin{matrix} r,r'=1, 2, \ldots, R \\ r\neq r' \end{matrix} \qquad (5b)$$

Nomenclature

C = annual fixed charge rate
c_e = unit price of electricity purchased
c_F = unit price of fuel
c_{ri} = cost coefficient (constant)
F = objective function
g = amplifier gain
$\mathbf{g}$ = set of inequality constraint functions
h = specific enthalpy
J_r = number of inputs to unit r from the environment
K = number of time intervals per year
L = Lagrangian
$\dot{m}$ = mass flow rate
P = pressure
p_e = unit price of electricity sold
$\dot{Q}_s$ = heat flow rate in the form of steam (plant requirement)
$\dot{Q}_w$ = heat flow rate in the form of hot water (plant requirement)
R = number of units and junctions
T = temperature
t = time
$\dot{W}$ = electric power (plant requirement)
$\dot{W}_s$ = electric power sold to the grid
$\dot{W}_p$ = electric power purchased from the grid
x = quality of wet steam
$\mathbf{x}$ = set of design decision variables
Y = constraint function
$\dot{Y}_r$ = rated output of unit r
$\mathbf{y}$ = set of all functions (products)
Z_r = annualized capital cost of unit r
$\mathbf{z}$ = set of operation decision variables
$\dot{\Gamma}_{0j.r}$ = cost rate of the jth function entering unit r from the environment
η = efficiency
μ = operation Lagrange multiplier
σ = number of units
Φ = operation objective function
φ_r = maintenance factor
$\chi_{r,r'}$ = $y_{r',r}/y_r$ = contribution of unit r' to the product of unit r
Ψ_{rk} = as defined by Eq. (13)

Subscripts

AB = auxiliary boiler
B = main boiler
FA = function amplifier
G = generator
$0j$ = the jth input to a unit from the environment
k = the kth time interval
r = the rth unit ($r=0$: environment)
r, r' = function going from unit r to r'
wp = hot water to process plant
wr = hot water from process plant

Superscript

$*$ = optimum value

Overmarks

$\cdot$ = per unit time
— = reference quantity (constant)
ˆ = fixed value of an otherwise variable quantity

$$y_{0j.r} = y_{0j,r} \tag{6a}$$

$$y_r = \sum_{r'=0}^{R} y_{r,r'} \tag{6b}$$

The constraints (5) give the inputs to a unit as functions of the output and the decision variables of the unit. The constraints (6) represent interconnections between units or between a unit and the environment, which are revealed by the functional diagram of the system.

In addition to the equality constraints, inequality constraints written in a general form

$$\mathbf{g}(\mathbf{x}, \mathbf{z}, \mathbf{y}) \leq 0 \tag{7}$$

may be imposed by the operability of the system, state regulations, etc.

3.2 Optimization of the System Operation. In the overall objective, Eq. (1) or (2), maintenance and operating expenses other than cost of commodities purchased by the system are included in the Z_r's. If it can be assumed that these expenses do not depend on (or they are very weak functions of) the operating mode of the system, then the capital cost including these expenses may be considered sunk for operation optimization. On the other hand it can be assumed that, in general, the operation mode of a time interval does not affect the mode of another time interval. Then, the operation optimization problem of each time interval is stated by the objective function

$$\underset{\mathbf{z},\ \mathbf{y}}{\mathrm{mim}}\ \Phi_k = \left[\sum_{r=1}^{R} \sum_{j=1}^{J_r} \Gamma_{0j.r} - \sum_{r=1}^{R} \Gamma_{r,0} \right]_k \tag{8}$$

subject to the constraints given by Eqs. (5), (6). In Eq. (8), the symbol $\Gamma = \dot{\Gamma} \cdot \Delta t$ is used.

For reasons explained elsewhere (Frangopoulos, 1983, 1984), the method of Lagrange multipliers is selected to solve the optimization problem. In order not to obscure the basic principles of the method, inequality constraints, Eq. (7), are not introduced in the analytical formulation. However, they are taken into consideration during the development of the algorithm for the numerical solution of the problem. The Lagrangian is

$$\begin{aligned} L_k = & \left[\sum_{r=1}^{R} \sum_{j=1}^{J_r} \Gamma_{0j.r} - \sum_{r=1}^{R} \Gamma_{r,0} \right]_k \\ & + \sum_{r=1}^{R} \left[\sum_{j=1}^{J_r} \mu_{0j,r} (Y_{0j,r} - y_{0j,r}) + \sum_{r'=1}^{R} \mu_{r,r'} (Y_{r,r'} - y_{r,r'}) \right]_k \\ & + \sum_{r=1}^{R} \left[\sum_{j=1}^{J_r} \mu_{0j.r} (y_{0j,r} - y_{0j.r}) + \mu_r \left(\sum_{r'=0}^{R} y_{r,r'} - y_r \right) \right]_k \end{aligned} \tag{9}$$

The first-order necessary conditions for an extremum are

$$\nabla_{\mathbf{z}} L_k(\mathbf{z}, \mathbf{y}, \boldsymbol{\mu}) = 0 \tag{10a}$$

$$\nabla_{\mathbf{y}} L_k(\mathbf{z}, \mathbf{y}, \boldsymbol{\mu}) = 0 \tag{10b}$$

$$\nabla_{\boldsymbol{\mu}} L_k(\mathbf{z}, \mathbf{y}, \boldsymbol{\mu}) = 0 \tag{10c}$$

The conditions (10*b*) lead to the equalities

$$(\mu_{0j,r})_k = (\mu_{0j.r})_k, \quad (\mu_{r,r'})_k = \mu_{rk} \tag{11}$$

i.e., the Lagrange multiplier associated with an input function to a unit is equal to the Lagrange multiplier associated with that output function, which supplies the input. Then, it can be proved that the Lagrangian takes the simplified form

$$\begin{aligned} L_k = & \sum_{r=1}^{R} (\Psi_r - \mu_r y_r)_k \\ & + \sum_{r=1}^{R} \left[\sum_{j=1}^{J_r} (\Gamma_{0j.r} - \mu_{0j.r} y_{0j.r})_k - (\Gamma_{r,0} - \mu_r y_{r,0})_k \right] \end{aligned} \tag{12}$$

where

$$\Psi_{rk} \equiv \sum_{j=1}^{J_r} (\mu_{0j,r} Y_{0j,r})_k + \sum_{r'=1}^{R} (\mu_{r',r} Y_{r',r})_k \tag{13}$$

Conditions (10*a*) lead to

$$\frac{\partial}{\partial z_{ri}} \left(\sum_{r=1}^{R} \Psi_{rk} \right) = 0, \quad \begin{matrix} r = 1, 2, \ldots, R \\ i = 1, 2, \ldots, I_r \end{matrix} \tag{14}$$

Conditions (10*c*) give a restatement of the constraints, Eqs. (5), (6). Conditions (10*b*) lead to Eq. (11) and the following equalities:

$$\mu_{rk} = \frac{\partial \Psi_{rk}}{\partial y_{rk}} \quad r = 1, 2, \ldots, R \tag{15}$$

$$(\mu_{0j.r})_k = \left(\frac{\partial \Gamma_{0j.r}}{\partial y_{0j.r}} \right)_k \quad \begin{matrix} r = 1, 2, \ldots, R \\ j = 1, 2, \ldots, J_r \end{matrix} \tag{16}$$

$$\left(\frac{\partial \Gamma_{r,0}}{\partial y_{r,0}} \right)_k = \mu_{rk} \quad r = 1, 2, \ldots, R \tag{17}$$

Equations (13)–(17) lead to the interpretation of each Lagrange multiplier μ_{rk} as the marginal operation cost for producing y_{rk}. Capital cost is not included in μ_{rk}. Each Ψ_{rk} may be interpreted as the operating cost of unit r during the time interval Δt_k (keeping in mind that such an interpretation is not very accurate when marginal costs are not equal to unit costs of the functions). Hence, Eq. (14) shows that the optimum value of an operation decision variable z_{ri} is the one that minimizes the operating cost of those units whose cost Ψ_{rk} is an explicit function of z_{ri}.

Since Ψ_{rk} and $(\Gamma_{0j.r})_k$ are known functions of y_{rk} and $(y_{0j.r})_k$, respectively, Eqs. (15), (16) are used to determine μ_{rk} and $(\mu_{0j.r})_k$. If a product $y_{r,0}$ of the system is not predetermined quantitatively but the related revenue is a known function $\Gamma_{r,0}$ of the production rate $\dot{y}_{r,0}$, then the value of μ_{rk} determined by Eq. (15) is used in Eq. (17), which is solved for $\dot{y}_{r,0}$. The value of $(\dot{y}^*_{r,0})_k$ thus obtained is the optimal production rate of the product $(r,0)$ during the kth time interval. A case with no product quantitatively specified has been called "total optimization" (Frangopoulos, 1983, 1987a).

If a production rate is fixed,

$$(\dot{y}_{r,0})_k = (\hat{\dot{y}}_{r,0})_k \tag{18}$$

then the corresponding income function $(\Gamma_{r,0})_k$ does not appear in the preceding equations and consequently there is no need for $\Gamma_{r,0}$ to be known. In Eq. (12), $y_{r,0}$ is replaced by $\hat{y}_{r,0}$. The marginal operation cost of such a product is equal again to the corresponding μ_r. A case with all products quantitatively specified has been called "fixed-product optimization."

3.3 Procedure for Solving the Complete Optimization Problem. The optimal solution is obtained when the configuration of the system (set of interconnected units), the design characteristics of the components, and the operation mode in each time interval are determined, which satisfy the overall objective, Eq. (1) or (2). The complete optimization problem is solved by a two-level algorithm. The optimal operation mode is determined at the level A. The optimal configuration is synthesized by the level B algorithm, which also determines the optimal design characteristics of the components. The steps are the following (the letter in front of the number indicates the level):

B1 Select an initial set of values $\mathbf{x}^0$ for the design decision variables.

B2 Solve the operation optimization problem in each time interval. For the first time interval ($k = 1$):

  A1 Select an initial set of values $\mathbf{z}^0$ for the operation decision variables.

  - A2 Solve Eqs. (5) and (6) for the dependent variables $\mathbf{y}$.
  - A3 Calculate the Lagrange multipliers μ by Eqs. (11), (15), and (16).
  - A4 Solve Eqs. (17) for y_{r0} to obtain the optimum production rates $\dot{y}^*_{r0}$ of those functions (system products) which are not predetermined quantitatively.
  - A5 Check Eqs. (14); if they are satisfied to an acceptable degree of approximation, then stop. Otherwise, select a new set of values for $\mathbf{z}$ and go to step A2.

  Repeat steps A1-A5 for each time interval ($k=2$, 3, ..., K).

- B3 Calculate the overall objective F by Eq. (2).
- B4 Search for the optimum set $\mathbf{x}^*$ (i.e., the set of $\mathbf{x}$ that minimizes the objective function F) by making use of any appropriate nonlinear programming algorithm (Himmelblau, 1972; Kuester and Mize, 1973; Reklaitis et al., 1983).

The nominal value of the function of a unit (e.g., rated power output) may be among the independent or dependent variables. If the level B algorithm gives zero for the nominal value of a function, then there is no need of the corresponding unit; appropriate statements in the computer program readjust the interconnections between the remaining units. Thus, the optimal system configurations is synthesized.

3.4 Special Forms of TFA. When the number of components increases significantly, it may not be convenient (if at all possible) to solve the optimization problem for the system as a whole. Special forms of TFA (the functional decomposition and functional isolation) presented in earlier work (Frangopoulos and Evans, 1984; Frangopoulos, 1988a) can also be used with the present formulation of the method in order to decompose the system into subsystems and solve the optimization problem.

4 Application Example: Synthesis and Operation Optimization of a Cogeneration System

4.1 System Description and Main Assumptions. TFA is applied here for the optimization of a steam-cycle cogeneration system, which supplies a process plant with electricity and heat in the form of steam as well as hot water. Figure 1 depicts the system in a simplified form, consisting of the main components only. Electricity and heat produced by the subsystem of main boiler-turbine generator and related equipment may not match the plant requirements $\dot{W}(t)$, $\dot{Q}_s(t)$, and $\dot{Q}_w(t)$. For this reason, an auxiliary boiler (for supplementary heat) and grid connections (for absorbing extra electricity produced or supplying the plant with supplementary electricity required) are considered as components of the system to be studied. In addition, a water heater is included in case the heat supplied by the condenser is less than $\dot{Q}_w(t)$ or there is no condenser at all.

Figure 1 is a generic scheme of the system. It contains all the main components envisaged in this example, even if some of those may not appear in the optimal configuration of the system, which will be synthesized by the solution of the optimization problem for each particular case.

The quality of steam, return condensate and the hot water temperatures (states 2, R, wp, wr) are specified by the process plant. In order to avoid undue complication here, the following assumptions are made: states $2B$, $2T$, $2C$, $2A$ are the same as state 2; the components are well insulated; losses through the pipes connecting the components are negligible; there is no need of make-up water ($\dot{m}_2=\dot{m}_R$, $\dot{m}_{wp}=\dot{m}_{wr}\rightarrow\dot{m}_w=0$). Also for simplicity, power consumed by the auxiliary equipment is not taken into consideration here, although it may not be negligible.

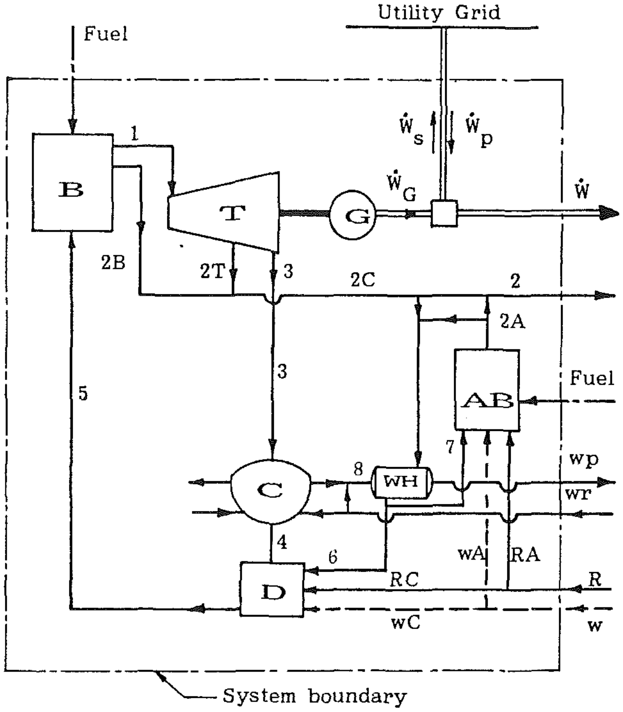

Fig. 1 Flow diagram of the cogeneration system: (B) main boiler; (T) turbine; (G) generator; (C) condenser; (D) deaerator; (WH) water heater; (AB) auxiliary boiler

4.2 The Functional Diagram of the System. The procedure described in earlier publications (Frangopoulos, 1983, 1984, 1987a) has been followed to identify the function of each unit (Appendix A) and to construct the functional diagram of the system (Fig. 2). The units of the system are the following: (1) main boiler including the deaerator; (2, 3) high and low-pressure turbine-generator; (4) condenser with auxiliary equipment; (5) auxiliary boiler; (6) water heater; (7, 8) connection of units 2, 3 to the grid; (9, 10, 11) junctions of functions related to electricity, steam, and hot water, respectively.

In the aforementioned publications, the functions of the units have been quantified by using second-law quantities (essergy, entropy, negentropy). It is evident from the TFA formulation presented in the preceding sections that no restriction is placed on the quantification basis of each function. This fact makes TFA applicable also when function quantification is based on first-law analysis, as is the case with this example. If the objective function and the constraints are the same, the optimization results obtained by a first-law approach are expected to be the same as those of a second-law approach. However, when the problem is not one of optimization but, e.g., of product costing, the results obtained by a first-law approach are, in general, different from those of a second-law approach (Frangopoulos, 1988b).

A distinction should be drawn here between a unit and a component; for example, a turbine or a generator are components in themselves. However, in this example they are not considered as separate units but, combined with the related auxiliary equipment, as one unit having one function. The number of units in a system in not unique; it depends on the available information and the requested results. The designer may select a high resolution level (many units) or a low one (a few units) depending on his/her objectives.

It is clarified that an arrow pointing toward a unit does not necessarily represent a stream (of mass, energy, essergy, etc.) entering the unit. For example, exhaust gases of a boiler form a stream exiting the boiler; however, the service of getting rid

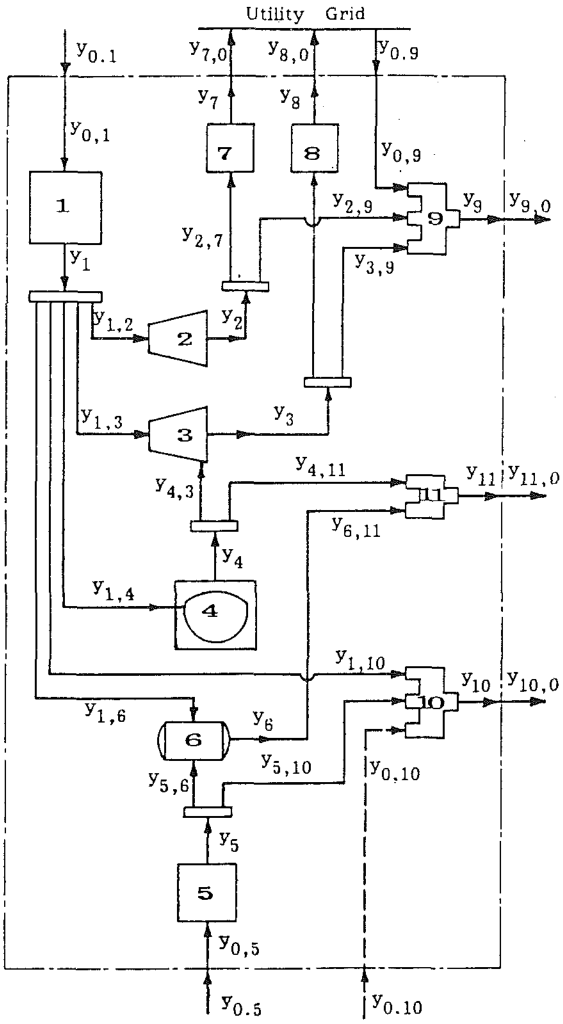

Fig. 2 Functional diagram of the cogeneration system

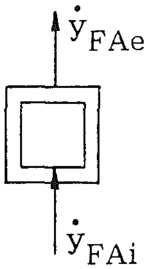

Fig. 3 *Function amplifier*

of exhaust gases is provided to the boiler by some other unit (although not shown separately in Fig. 2, because of the resolution level selected). Similarly, if the boiler is to be penalized for environmental pollution, then the corresponding expenditure will depend on an appropriate measure of pollution, to be represented by an arrow pointing toward the unit.

In earlier work (Frangopoulos, 1983, 1984, 1987a), the function of the condenser has been quantified by the negentropy it supplies to the rest of the system. In the present example, the condenser provides service not only to the low-pressure turbine, but also to the hot water needs of the plant. The condenser utilizes a function $\dot{y}_{1,4}$ (coming from the boiler) to produce a function of higher quantity than the one utilized:

$$\dot{y}_4 = \dot{y}_{4,3} + \dot{y}_{4,11} = \dot{y}_{1,4} + \dot{y}_{4,11} \geq \dot{y}_{1,4} \qquad (19)$$

In order to handle situations of this type conveniently during the analysis and optimization procedure, we introduce here the concept of "Function Amplifier." The "amplifier gain" is defined by

Table 1 Plant A requirements and electricity tariffs

k	$\dot{W}$	$\dot{m}_2$	$\dot{m}_{wp}$	$\dot{Q}_s$	$\dot{Q}_w$	Δt	c_e	p_e
	kW	kg/s	kg/s	kW	kW	h	\$/kWh	\$/kWh
1	25000	40.0	120.0	111628	15049	1000	0.06	0.05
2	20000	35.0	100.0	97675	12541	1000	0.06	0.05
3	20000	35.0	100.0	97675	12541	3000	0.05	0.04
4	15000	30.0	80.0	83721	10033	1000	0.05	0.04
5	10000	30.0	80.0	83721	10033	1000	0.04	0.03

$$g_{FA} = \frac{\dot{y}_{FAe} - \dot{y}_{FAi}}{\dot{y}_{FAi}} \qquad (20)$$

For example, the gain of the condenser in Fig. 2 as a function amplifier is $g_4 = \dot{y}_{4,11}/\dot{y}_{1,4}$.

4.3 Optimization of the System. The objective function, Eq. (2), is written in this case

$$\min_{x,y,z} F = \sum_{r=1}^{8} Z_r + \sum_{k=1}^{5} [\dot{\Gamma}_{0.1} + \dot{\Gamma}_{0.5} + \dot{\Gamma}_{0.9} - \dot{\Gamma}_{7,0} - \dot{\Gamma}_{8,0}]_k \Delta t_k \qquad (21)$$

Analytic expressions for the Z_r's and $\dot{\Gamma}$'s are given in Appendix C. The sets of independent decision variables are selected to be

$$\mathbf{x} = (\dot{Y}_2, \dot{Y}_3, \dot{Y}_5, \dot{Y}_6, \dot{Y}_7, \dot{Y}_8)$$

$$\mathbf{z} = (T_3, \chi_{6.1}, \chi_{9.2}, \chi_{9.3}, \chi_{10.1}, \chi_{11.4}, \dot{y}_{7,0}, \dot{y}_{8,0})$$

The rest of the quantities involved are either dependent variables or parameters. The solution of the optimization problem will give the optimum value $\dot{Y}_r^*$ for the rated power of each unit as well as the optimum operating power output $\dot{y}_{rk}^*$ of each unit in each time interval. Zero value for a $\dot{Y}_r^*$ means that unit r is not required. It is noted that the system products $\dot{y}_{9,0}$, $\dot{y}_{10,0}$, $\dot{y}_{11,0}$ are fixed by the plant requirements for electricity, steam, and hot water, respectively, while the products $\dot{y}_{7,0}$, $\dot{y}_{8,0}$ (electricity sold to the grid) will be determined by the solution of the optimization problem.

Four Lagrange multipliers (marginal costs), in addition to those obtained by Eq. (15), have been very helpful in determining the optimal operation mode. They are derived in Appendix B.

As numerical examples, let two plants be considered: plant A with requirements given in Table 1 and plant B with similar requirements except that it does not need hot water ($\dot{m}_{wp} = 0$, $k = 1$-5). The values selected for state properties and equipment efficiencies are the following:

$P_1 = 80$ bar $\quad P_R = 1.0$ bar $\quad \eta_B = 0.90$

$T_1 = 490°\text{C} \quad T_R = 40°\text{C} \quad \eta_{AB} = 0.88$

$P_2 = 12.0$ bar $\quad P_{wp} = 2$ bar $\quad \eta_G = 0.92$

$T_2 = 260°\text{C} \quad T_{wp} = 60°\text{C} \quad T_{wr} = 30°\text{C}$

When condensing heat is not utilized for heating the water, it is assumed $P_3 = 0.05$ bar, $x_3 = 0.85$ ($T_3 = 32.9°\text{C}$); otherwise the inequality constraint $T_3 \geq T_{wp} + 10$ K is imposed in order for the temperature difference between condensing steam and cooling water (hot water to process) not to be unacceptably low. Also, it is assumed that, for example due to state regulations, the rated power of the installed generators cannot exceed the maximum anticipated plant load:

$$(\dot{Y}_2 + \dot{Y}_3)_{\max} \leq \dot{W}_{\max}$$

The results of optimization for several values of fuel cost are summarized in Tables 2-5; values of those operation Lagrange multipliers that help interpret the results are given in the tables.

4.4 Discussion of Results. Since the efficiency of the aux-

Table 2 Optimization results for plant A with $c_F=3.75\times10^{-6}$ \$/kJ

Synthesis and design	$\dot{Y}_1^*$	$\dot{Y}_2^*$	$\dot{Y}_3^*$	$\dot{Y}_4^*$	$\dot{Y}_5^*$	$\dot{Y}_6^*$	$\dot{Y}_7^*$	$\dot{Y}_8^*$
	kW	kW	kW	kW	kW	kW	kW	kW
	150,023	15,309	6170	30,094	0	0	5595	0

Operation	k	T_3^*	$\chi_{6.1}^*$	$\chi_{9.2}^*$	$\chi_{9.3}^*$	$\chi_{10.1}^*$	$\chi_{11.4}^*$	g_4^*	$\dot{y}_{7,0}^*$	$\dot{y}_{8,0}^*$	$\dot{y}_2^*$	$\dot{y}_3^*$	$\dot{y}_{0,9}^*$
		°C	—	—	—	—	—	—	kW	kW	kW	kW	kW
	1	70	1.0	0.6124	0.2468	1.0	1.0	1.0	0	0	15309	6170	3521
	2	70	1.0	0.6698	0.3085	1.0	1.0	0.8334	0	0	13396	6170	434
	3	70	1.0	0.6698	0.2571	1.0	1.0	1.0	0	0	13396	5142	1462
	4	70	1.0	0.7258	0.2742	1.0	1.0	1.0	595	0	11482	4113	0
	5	70	1.0	0.5887	0.4113	1.0	1.0	1.0	5595	0	11482	4113	0
	μ_{rk} (\$/kWh) $k=1\div5$			$\mu_1=0.0150$ $\mu_2=0.0163$				$\mu_{3c}=0.0346$ $\mu_{3g}=0.0529$			$\mu_{4c}=0.0075$ $\mu_{4,3g}=0.0150$		

Table 3 Optimization results for plant A with $c_F=5.0\times10^{-6}$ \$/kJ

Synthesis and design	$\dot{Y}_1^*$	$\dot{Y}_2^*$	$\dot{Y}_3^*$	$\dot{Y}_4^*$	$\dot{Y}_5^*$	$\dot{Y}_6^*$	$\dot{Y}_7^*$	$\dot{Y}_8^*$
	kW	kW	kW	kW	kW	kW	kW	kW
	146,826	13,396	5142	25,081	0	2508	5595	0

Operation	k	T_3^*	$\chi_{6.1}^*$	$\chi_{9.2}^*$	$\chi_{9.3}^*$	$\chi_{10.1}^*$	$\chi_{11.4}^*$	g_4^*	$\dot{y}_{7,0}^*$	$\dot{y}_{8,0}^*$	$\dot{y}_2^*$	$\dot{y}_3^*$	$\dot{y}_{0,9}^*$
		°C	—	—	—	—	—	—	kW	kW	kW	kW	kW
	1	70	1.0	0.5358	0.2057	1.0	0.833	1.0	0	0	13396	5142	6462
	2	70	1.0	0.6698	0.2571	1.0	1.0	1.0	0	0	13396	5142	1462
	3	70	1.0	0.6698	0.2571	1.0	1.0	1.0	0	0	13396	5142	1462
	4	70	1.0	0.7258	0.2742	1.0	1.0	1.0	595	0	11482	4113	0
	5	70	1.0	0.5887	0.4113	1.0	1.0	1.0	5595	0	11482	4113	0
	μ_{rk} (\$/kWh) $k=1\div5$			$\mu_1=0.0200$ $\mu_2=0.0217$				$\mu_{3c}=0.0461$ $\mu_{3g}=0.0705$			$\mu_{4c}=0.010$ $\mu_{4,3g}=0.020$		

Table 4 Optimization results for plant B with $c_F=3.75\times10^{-6}$ \$/kJ

Synthesis and design	$\dot{Y}_1^*$	$\dot{Y}_2^*$	$\dot{Y}_3^*$	$\dot{Y}_4^*$	$\dot{Y}_5^*$	$\dot{Y}_6^*$	$\dot{Y}_7^*$	$\dot{Y}_8^*$
	kW	kW	kW	kW	kW	kW	kW	kW
	128,269	15,309	0	0	0	≠	1482	0

Operation	k	T_3^*	$\chi_{6.1}^*$	$\chi_{9.2}^*$	$\chi_{9.3}^*$	$\chi_{10.1}^*$	$\chi_{11.4}^*$	g_4^*	$\dot{y}_{7,0}^*$	$\dot{y}_{8,0}^*$	$\dot{y}_2^*$	$\dot{y}_3^*$	$\dot{y}_{0,9}^*$
		°C	—	—	—	—	—	—	kW	kW	kW	kW	kW
	1	†	≠	0.6124	0	1.0	≠	0	0	0	15309	0	9691
	2	†	≠	0.6698	0	1.0	≠	0	0	0	13396	0	6604
	3	†	≠	0.6698	0	1.0	≠	0	0	0	13396	0	6604
	4	†	≠	0.7655	0	1.0	≠	0	0	0	11482	0	3518
	5	†	≠	1.0	0	1.0	≠	0	1482	0	11482	0	0
	μ_{rk} (\$/kWh) $k=1\div5$				$\mu_1=0.0150$ $\mu_2=0.0163$					$\mu_3=\mu_{3g}=0.00486$ $\mu_4=\mu_{4,3g}=0.0150$			

† irrelevant since $\dot{y}_3^*=0$ ≠ irrelevant to this plant

iliary boiler is lower than the main boiler efficiency ($\eta_5<\eta_1$), the operation Lagrange multiplier (marginal cost) of the auxiliary boiler function is higher than the operation Lagrange multiplier of the main boiler function ($\mu_5>\mu_1$) for any fuel cost, c_F. Consequently, it is not justified economically to install and operate an auxiliary boiler under the given conditions (unless it utilizes a much cheaper fuel).

The values of the Lagrange multipliers change, in general, from one time interval to the other. The multipliers appearing in Tables 2-5 remain constant for all time intervals, because they depend either on parameters that are considered constant here (e.g., price of fuel, equipment efficiencies, etc.) or on the condensing temperature T_3, whose optimum value, T_3^*, turns out to be the same for all time intervals. When heat of condensation is used to heat the water, T_3^* obtains the minimum permissible value ($T_{wp}+10\text{ K}=70°\text{C}$). When heat of condensation is rejected to the environment, T_3^* is equal to the saturation temperature at 0.05 bar (32.9°C).

A more general and detailed discussion on the stability of Lagrange multipliers and how it facilitates the solution of the problem is given elsewhere (Frangopoulos, 1983, 1984; Frangopoulos and Evans, 1984). Because of space limitations, the discussion is not repeated here.

In the following, some comments are made on the results appearing in Tables 2-5.

Plant A With $c_F=3.75\times10^{-6}$ \$/kJ (*Table 2*). The operation Lagrange multiplier (marginal cost) of the function of unit 2 is lower than the selling price as well as the purchase unit cost of electricity in all time intervals ($\mu_2<p_e<c_e$ for every k). Therefore, unit 2 operates at the maximum possible power with an upper limit being imposed either by the steam flow rate to the plant or by the rated power of unit 2. The optimum value $\dot{Y}_2^*$ determined by the level B algorithm is the power generated at the peak load ($k=1$). Excess electricity is sold to the grid during the fourth and fifth time intervals.

Regarding unit 3 of plant A, two operation Lagrange multipliers are defined for its function (Appendix B): μ_{3c} for electricity generated with the corresponding heat of condensation fully utilized for heating the water, and μ_{3g} for electricity generated with the corresponding heat of condensation rejected to the environment. Since $\mu_{3c}<c_e$ for $k=1$-4 and $p_e<\mu_{3c}<c_e$

Table 5 Optimization results for plant B with $c_F = 2.5 \times 10^{-6}$ \$/kJ

Synthesis and design	$\dot{Y}_1^*$	$\dot{Y}_2^*$	$\dot{Y}_3^*$	$\dot{Y}_4^*$	$\dot{Y}_5^*$	$\dot{Y}_6^*$	$\dot{Y}_7^*$	$\dot{Y}_8^*$
	kW	kW	kW	kW	kW	kW	kW	kW
	151,555	15,309	9691	18,449	0	≠	11,173	0

Operation	k	T_3^*	$\chi_{6.1}^*$	$\chi_{9.2}^*$	$\chi_{9.3}^*$	$\chi_{10.1}^*$	$\chi_{11.4}^*$	g_4^*	$\dot{y}_{7,0}^*$	$\dot{y}_{8,0}^*$	$\dot{y}_2^*$	$\dot{y}_3^*$	$\dot{y}_{0,9}^*$
		°C	—	—	—	—	—	—	kW	kW	kW	kW	kW
	1	32.9	≠	0.6124	0.3876	1.0	≠	0	0	0	15309	9691	0
	2	32.9	≠	0.5155	0.4845	1.0	≠	0	3087	0	13396	9691	0
	3	32.9	≠	0.5155	0.4845	1.0	≠	0	3087	0	13396	9691	0
	4	32.9	≠	0.3540	0.6460	1.0	≠	0	6173	0	11482	9691	0
	5	†	≠	0.0310	0.9690	1.0	≠	0	11173	0	11482	9691	0
	μ_{rk} (\$/kWh) $k = 1 \div 5$	$\mu_1 = 0.0100$ $\mu_2 = 0.0109$							$\mu_3 = \mu_{3g} = 0.0300$ $\mu_4 = \mu_{4,3g} = 0.0100$				
	† irrelevant since $\dot{y}_3^* = 0$										≠ irrelevant to this plant		

for $k = 5$, unit 3 produces electricity economically, when the corresponding heat of condensation is fully utilized for heating the water. This is really the optimum mode of operation, as is shown by the value $\chi_{11.4}^* = 1.0$ for $k = 1$-5. Any additional quantity of electricity with the corresponding heat of condensation rejected to the environment is justified only when $\mu_{3g} < c_e$. This inequality is satisfied during the first and second time intervals. The value of g_4^* indicates that in the second interval there is electricity production with part of the heat rejected to the environment. Although the fact that $\mu_{3g} < c_e$ for $k = 1$, 2 would allow unit 3 to cover the plant needs, the result for $\dot{Y}_3^*$ produced by the level B algorithm shows that the extra investment is not justified. All the hot water required is produced by the condensing heat; hence there is no need to install unit 6.

Plant A With $c_F = 5.0 \times 10^{-6}$ \$/kJ (Table 3). Regarding unit 2, comments similar to those in the previous case are valid, except that the optimum size $\dot{Y}_2^*$ of the unit is the power generated by the base load steam requirements of the process plant.

For $k = 1$-5, it is $\mu_{3g} > c_e > p_e$ and for $k = 1$-4, it is $\mu_{3c} < c_e$. Therefore, it is not economically justified for unit 3 to operate unless all the condensing heat is utilized for heating the water. This is verified by the results: $g_4^* = 1.0$ for $k = 1$-5. The size of unit 3 is smaller than the one in the previous case and the heat of condensation during the first time interval is not enough to cover the hot water requirements ($\chi_{11.4}^* < 1$ for $k = 1$). Therefore, there is need of unit 6, which operates during the peak load period only.

Plant B With $c_F = 3.75 \times 10^{-6}$ \$/kJ (Table 4). Unit 2 is sized and operated at the maximum power that the required steam can produce. In the case of plant B, there is no need of hot water; therefore any heat of condensation is rejected to the environment and only one Lagrange multiplier, μ_3, is defined for unit 3. Although the fact that $\mu_3 < c_e$ for $k = 1$-4 would allow unit 3 to produce electricity for the plant needs and the fact that $\mu_3 < p_e$ for $k = 1$, 2 would allow unit 3 to sell electricity during the first two time intervals, the level B algorithm shows that investing in unit 3 is not justified economically ($\dot{Y}_3^* = 0$).

Plant B With $c_F = 2.5 \times 10^{-6}$ \$/kJ (Table 5). Unit 2 is sized and operated again at the maximum power produced by the steam. The low value of μ_3 in this case justifies the investment in unit 3, which is sized at the maximum load requirements of the plant. Unit 3 operates at its rated power in all time intervals in order to cover the plant needs. Excess electricity generated by unit 2 is sold to the grid in all time intervals except the first one.

The preceding results demonstrate that TFA gives not only the optimal size and operating mode of each component, but also the optimal configuration of the system. Three different configurations have been obtained automatically for the four cases examined: (*i*) a condensing steam turbine with no water heater for the first and fourth cases, (*ii*) a condensing steam turbine with water heater for the second case, and (*iii*) an extraction steam turbine with neither condenser nor water heater for the third case.

5 Closure

The capabilities of Thermoeconomic Functional Analysis have been enhanced and the method has become appropriate for determining the synthesis, design, and operation mode of thermal systems in such a way that an overall optimum is achieved. As an application example of TFA in its new formulation, a multiproduct cogeneration system, not of a predetermined configuration, has been optimized. The numerical example presented serves to clarify the methodology only; the obtained results are valid under the assumptions made in this example with no claim of general applicability. Different sets of data (process plant requirements, cost parameters, etc.) lead to different optimum system configurations and operation modes. Therefore, those data should be based on the most accurate information possible, if a real-world system is to be optimized.

TFA is still at an evolutionary stage. Several assumptions made in order to solve the optimization problem (section 3) have to be relaxed in order to increase the applicability of the method further.

Acknowledgment

The authors expresses his sincere gratitude to Dr. R. B. Evans for his advice and encouragement throughout the graduate studies, when TFA was given its first formulation. Support provided by the National Technical University of Athens for further development of TFA as presented above is gratefully acknowledged.

References

Dickerson, S. L., and Robertshaw, J. E., 1975, *Planning and Design*, Lexington Books, Lexington, MA.

El-Sayed, Y. M., and Evans, R. B., 1970, "Thermoeconomics and the Design of Heat Systems," ASME JOURNAL OF ENGINEERING FOR POWER, Vol. 92, pp. 27-35.

Evans, R. B., 1980, "Thermo-economic Isolation and Essergy Analysis," *Energy*, Vol. 5, Nos. 8-9, pp. 805-821.

Evans, R. B., Hendrix, W. A., and Kadaba, P. V., 1983, "Essergetic Functional Analysis for Process Design and Synthesis," *Efficiency and Costing: Second Law Analysis of Processes*, R. A. Gaggioli, ed., ACS Symposium Series No. 235, pp. 239-261.

Frangopoulos, C. A., 1983, "Thermoeconomic Functional Analysis: A Method for Optimal Design or Improvement of Complex Thermal Systems," Ph.D. Thesis, Georgia Institute of Technology, Atlanta, GA.

Frangopoulos, C. A., 1984, "Thermoeconomic Functional Analysis: An Innovative Approach to Optimal Design of Thermal Systems," *Second Law Aspects of Thermal Design*, A. Bejan and R. L. Reid, eds., ASME HTD-Vol. 33.

Frangopoulos, C. A., and Evans, R. B., 1984, "Thermoeconomic Isolation and the Optimization of Thermal System Components," *Second Law Aspects of Thermal Design*, A. Bejan and R. L. Reid, eds., ASME HTD-Vol. 33.

Frangopoulos, C. A., 1987a, "Thermoeconomic Functional Analysis and Optimization," *Energy*, Vol. 12, No. 7, pp. 563–571.

Frangopoulos, C. A., 1987b, "Thermoeconomic Functional Optimization of a Cogeneration System," *International Symposium on Turbomachinery, Combined-Cycle Technologies and Cogeneration*, G. K. Serovy, ed., ASME IGTI-Vol. 1, pp. 323–329.

Frangopoulos, C. A., 1988a, "Functional Decomposition for Optimal Design of Complex Thermal Systems," *Energy*, Vol. 13, No. 3, pp. 239–244.

Frangopoulos, C. A., 1988b, "Costing of Heat and Electricity From a Cogeneration System," *2nd International Symposium on Turbomachinery, Combined-Cycle Technologies and Cogeneration*, G. K. Serovy and T. H. Fransson, eds., ASME IGTI-Vol. 3, pp. 349–356.

Garceau, R. M., 1982, "Thermoeconomic Optimization of a Rankine Cycle Cogeneration System," M.S. Thesis, Georgia Institute of Technology, Atlanta, GA.

Himmelblau, D. M., 1972, *Applied Nonlinear Programming*, McGraw-Hill, New York.

Kramer, N. J. T. A., and Smit, J., 1977, *Systems Thinking: Concepts and Notions*, Martinus Nijoff Social Sciences Division, Leiden.

Kuester, J. L., and Mize, J. H., 1973, *Optimization Techniques With Fortran*, McGraw-Hill, New York.

Linnhoff, B., and Alanis, F. G., 1989, "A System's Approach Based on Pinch Technology to Commercial Power Station Design," presented at the ASME Winter Annual Meeting, San Francisco, CA.

OTA, 1983, "Industrial and Commercial Cogeneration," Technical Report, U.S. Government Printing Office, Washington, DC.

Reklaitis, G. V., Ravindran, A., and Ragsdell, K. M., 1983, *Engineering Optimization*, Wiley, New York.

Tribus, M., and Evans, R. B., 1962, "A Contribution to the Theory of Thermoeconomics," UCLA Report No. 62-36, University of California at Los Angeles, Los Angeles, CA.

APPENDIX A

Functions of the Units of Fig. 2

$$\dot{y}_1 = \dot{m}_1 h_1 + \dot{m}_{2B} h_2 - \dot{m}_5 h_5$$

(Assumption: no heat losses in the deaerator.)

$$\dot{y}_2 = \dot{m}_{2T}(h_1 - h_2)\eta_{G2}$$

$$\dot{y}_3 = \dot{m}_3(h_1 - h_3)\eta_{G3}$$

$$\dot{y}_4 = \dot{m}_3(h_3 - h_4)(1 + g_4)$$

$$\dot{y}_5 = \dot{m}_{2A} h_2 - (\dot{m}_7 h_7 + \dot{m}_{wA} h_w + \dot{m}_{RA} h_R)$$

$$\dot{y}_6 = \dot{m}_{wp}(h_{wp} - h_8) = (1 - \chi_{11.4})\dot{Q}_w$$

$$\dot{y}_7 = \dot{y}_{7,0}$$

$$\dot{y}_8 = \dot{y}_{8,0} \quad (\dot{y}_{7,0} + \dot{y}_{8,0} = \dot{W}_s)$$

$$\dot{y}_9 = \dot{W}$$

$$\dot{y}_{10} = \dot{Q}_s$$

$$\dot{y}_{11} = \dot{Q}_w$$

The functions of units 7 and 8 are the electric power supplied to the grid by units 2 and 3, respectively. Units 7 and 8 represent the equipment necessary for connection to the grid.

APPENDIX B

Lagrange Multipliers

The Lagrange multipliers (marginal costs) are obtained by Eqs. (11) and (15)–(17). In addition, four more marginal costs have been proved very helpful in identifying the optimal operation mode and they are derived as follows.

Let y_{4c} be the part of the condenser function y_4, which serves both electricity and hot water production, and $y_{4,3g}$ the part of y_4 serving electricity production only:

$$\dot{y}_4 = \dot{y}_{4c} + \dot{y}_{4,3g}$$

Then, it can be proved that

$$\Psi_4 = \mu_1 \dot{y}_{1,4} = \mu_1 \left(\frac{\dot{y}_{4c}}{2} + \dot{y}_{4,3g} \right)$$

Since $\dot{y}_{4c}$ and $\dot{y}_{4,3g}$ are independent of each other, two marginal costs can be defined:

$$\mu_{4c} = \frac{\partial \Psi_4}{\partial y_{4c}} = \frac{\mu_1}{2}, \quad \mu_{4,3g} = \frac{\partial \Psi_4}{\partial y_{4,3g}} = \mu_1$$

Respectively, two marginal costs can be derived for the electricity produced by unit 3

$$\mu_{3c} = \frac{\mu_1}{\eta_{G3}} \left(1 + \frac{1}{2} \cdot \frac{h_3 - h_4}{h_1 - h_3} \right)$$

$$\mu_{3g} = \frac{\mu_1}{\eta_{G3}} \left(1 + \frac{h_3 - h_4}{h_1 - h_3} \right)$$

with the following interpretation: Electricity generated by unit 3, with the corresponding heat in the condenser fully utilized for heating the water, is produced with marginal cost μ_{3c}; any additional quantity of electricity, with the corresponding heat in the condenser rejected to the environment, is produced with marginal cost μ_{3g}, which is higher than μ_{3c}.

APPENDIX C

Cost Functions

Information from several sources (Garceau, 1982; Frangopoulos, 1983; OTA Report, 1983) has been used to derive the following functions:

$$Z_1 = a_{11} \dot{Y}_1^{c_{12}} g_{1\eta} g_{1T} g_{1P}$$

$$Z_r = a_{r1} \dot{Y}_r^{c_{r2}} g_{r\eta} g_{rT} \qquad r = 2, 3$$

$$Z_r = a_{r1} \dot{Y}_r^{c_{r2}} \qquad r = 4, 6, 7, 8$$

$$Z_5 = a_{51} \dot{Y}_5^{c_{52}} g_{5\eta}$$

$$\Gamma_{0.r} = c_{0r} y_{0.r} \qquad r = 1, 5, 9, 10$$

$$\Gamma_{r,0} = c_{r0} y_{r,0} \qquad r = 7, 8$$

where

$$a_{r1} = C\varphi_r c_{r1} \qquad r = 1, 2, \ldots, 8$$

$$g_{r\eta} = 1 + \left(\frac{1 - \overline{\eta}_r}{1 - \eta_r} \right)^{c_{r3}} \qquad r = 1, 2, 3, 5$$

$$g_{rT} = 1 + c_{r4} \exp\left(\frac{T_1 - \overline{T}_1}{c_{r5}} \right) \qquad r = 1, 2, 3$$

$$g_{1P} = \exp\left(\frac{P_1 - \overline{P}_1}{c_{16}} \right)$$

Values of the parameters appearing in the preceding equations are given in Table C1.

Table C1 Values of capital cost parameters

	σ_{ri}					
r \ i	1	2	3	4	5	6
1	360 $/kW$^{0.8}$	0.8	7	5	10.42 K	150 bar
2	3000 $/kW$^{0.7}$	0.7	3	5	10.42 K	
3	3000 $/kW$^{0.7}$	0.7	3	5	10.42 K	
4	12 $/kW	1.0		C = 0.182, φ = 1.06 $\bar{\eta}_1 = \bar{\eta}_5 = 0.90$ $\bar{\eta}_2 = \bar{\eta}_3 = 0.95$ $\bar{T}_1 = \bar{T}_2 = \bar{T}_3 = 866$ K $\bar{P}_1 = 28$ bar		
5	560 $/kW$^{0.8}$	0.8	7			
6	10.4 $/kW	1.0				
7	1000 $/kW$^{0.6}$	0.6				
8	1000 $/kW$^{0.6}$	0.6				

Thermodynamic Analysis of Four Magnetic Heat-Pump Cycles

F. C. Chen
Mem. ASME

R. W. Murphy

V. C. Mei
Mem. ASME

G. L. Chen

Oak Ridge National Laboratory,
Oak Ridge, TN 37831

Magnetic heat pumps have been successfully used for refrigeration applications at near absolute-zero-degree temperatures. In these applications, a temperature lift of a few degrees in a cryogenic environment is sufficient and can be easily achieved by a simple magnetic heat-pump cycle. To extend magnetic heat pumping to other temperature ranges and other types of application in which the temperature lift is more than just a few degrees requires more involved cycle processes. The possible cycle applications include cooling of superconducting transmission lines, space conditioning, and industrial heating. This paper investigates the characteristics of a few better-known thermomagnetic heat-pump cycles (Carnot, Ericsson, Stirling, and regenerative) in extended ranges of temperature lift. The regenerative cycle is the most efficient one. Cycle analyses were done for gadolinium operating between 0 and 7 Tesla, and with a heat-rejection temperature of 320 K. The analysis results predicted a 42 percent reduction in coefficient of performance at 260 K cooling temperature and a 15 percent reduction in capacity at 232 K cooling temperature for the magnetic Ericsson cycle as compared with the ideal regenerative cycle. Such substantial penalties indicate that the potential irreversibilities from this one source may adversely affect the viability of certain proposed MHP concepts if the relevant loss mechanisms are not adequately addressed.

Introduction

The concept of a magnetic heat pump (MHP) is based on the principle of the magnetocaloric effect of materials, in which entropy can change, when a material is magnetized or demagnetized. When a magnetic working material is in its natural (i.e., zero magnetic field) state, the magnetic dipoles in the material are in a relatively disordered state; if a magnetic field is imposed upon the material, the dipoles align with the field and are transformed into an ordered state, and a decrease in entropy (due to the work done on system) occurs. Conversely, if a magnetic material is suddenly demagnetized by being removed from a magnetic field, an increase in entropy will occur. If the magnetic material in a magnetic field is isolated from the surroundings, then a decrease and an increase in entropy will result in an increase and a decrease in the working material's temperature, respectively.

The origin of the concept of magnetic cooling can be traced back more than half a century when researchers wanted to produce refrigeration at ultralow temperatures. In 1933, Giauque and MacDougall achieved a cooling temperature of 0.5 K down from 3.5 K by using the magnetocaloric effect [1]. Their method was to cool a paramagnetic salt to 3.5 K in a magnetic field and then to demagnetize it adiabatically to achieve 0.5 K. This adiabatic demagnetization method is a one-shot or single-step refrigeration process that does not provide continuous cooling. It is still being used in low-temperature physics experiments to create temperatures extremely close to absolute zero, and its progress can be found elsewhere [2].

The possibility of constructing a heat pump using the magnetocaloric effect to produce continuous cooling was apparently first suggested in 1949 by Daunt and Heer [3], who combined two isothermal and two adiabatic magnetization and demagnetization processes to form a "magnetic" Carnot cycle that is capable of providing sustained cooling. However, the laboratory experimentation on this concept was not performed until 1975, when Brown [4] built and tested a reciprocating MHP assembly using gadolinium as the working medium. Brown's study of MHP was aimed primarily toward room-temperature space-conditioning applications. Several experimental and analytical studies have been done since then for applications ranging from liquid helium production at 4 K [5] to low-pressure steam production at 400 K [6] for industrial process heating.

The needs for developing non-ozone-depleting, no-greenhouse-effect heat pump systems and for exploring the potential of new high-temperature superconducting materials have prompted renewed interest in MHP technology. The new materials can provide the high magnetic field that an effective superconducting MHP requires, and MHPs do not use freon as working fluids.

In ultralow temperature applications, a temperature lift of a few degrees in a cryogenic environment is often sufficient and can be easily achieved by a simple MHP cycle. To extend magnetic heat pumping to other temperature ranges and other types of applications in which the temperature lift is more than

---

Contributed by the Advanced Energy Systems Division for publication in the Journal of Engineering for Gas Turbines and Power. Manuscript received by the Advanced Energy Systems Division November 6, 1990; revision received September 12, 1991. Associate Technical Editor: M. J. Moran.

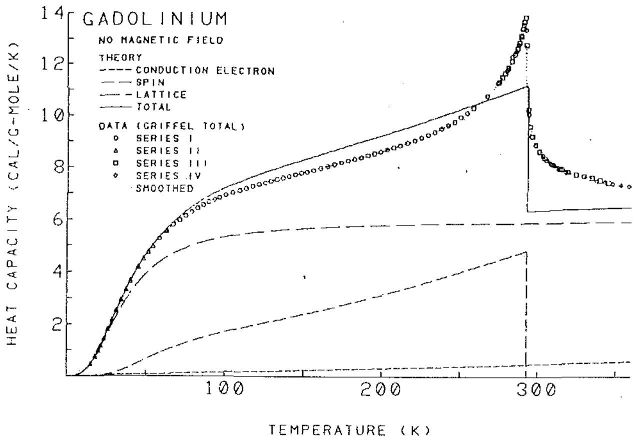

Fig. 1 Measured and computed components of heat capacity at zero field

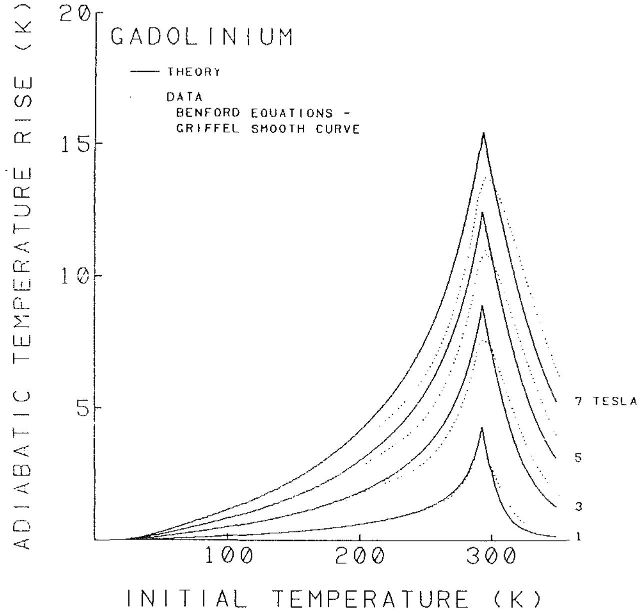

Fig. 2 Measured and computed adiabatic temperature rise

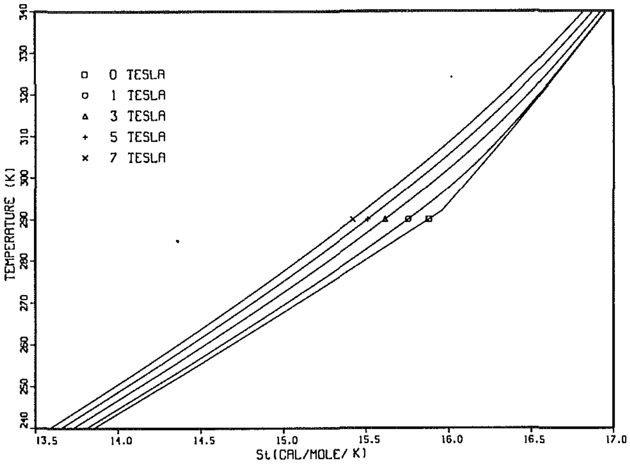

Fig. 3 Computed total entropy of Gd

just a few degrees requires more involved cycle processes. The behavior of these magnetic cycle processes is not clear. This paper analytically investigates the attributes of four heat pump cycles, viz., the magnetic equivalent of Carnot, Stirling, and Ericsson, and ideal regenerative cycles in extended ranges of temperature lift, using gadolinium as the working medium.

Entropy of Gadolinium

In order to analyze MHP cycles, one needs to know the entropy change produced in a magnetic material when it is subjected to changes in magnetic field and temperature. The total entropy of a magnetocaloric material is assumed to have three independent additive components: lattice, conduction electron, and magnetic spin [4]. The first two components are functions of temperature only (Debye dependence in the first case, proportional dependence in the second) and the last one is a function of temperature and applied magnetic field [7]. Assuming that a magnetic material is homogeneous and isotropic and obeys an ideal equation of state, such as the Curie Law, *the total entropy can be computed by theory* [8]. Gadolinium (Gd) approximately fits the assumptions [4] and a computer model was developed [9] to predict the magnetization, specific heat, and entropy of Gd.

The entropy of Gd can also be derived from experimentally measured adiabatic temperature rise at a given initial material temperature [10] and heat capacity of Gd at zero field [11]. A comparison of measured and model predicted heat capacity of Gd is shown in Fig. 1. The discontinuity in the figure that occurs at the Curie temperature (293 K for Gd) is due to the change of material property, which is ferromagnetic below the Curie temperature and paramagnetic above it. A comparison of the Benford and Brown [10] and Griffel [11] date of adiabatic temperature rise and the model prediction is shown in Fig. 2. The computed total entropy shown in Fig. 3 was used in the cycle analysis.

Magnetocaloric Cycles

In an MHP, magnetic field work is to be combined with changes in heat and internal energy to create thermodynamic cycles of practical use. In place of the pressure and volume variables employed in a closed cycle for mechanical work, the equivalent-state variables here are applied magnetic field and magnetization. As usual, the MHP cycles can be plotted on the temperature-entropy (T-s) diagrams for the working material. To simplify the cycle analysis, boundary work (work from a close cycle) will be the only form of work considered.

Boundary Work Cycles. When work is defined on the system boundary and in the absence of magnetocaloric effect, the traditional form of the energy equation for a working medium is

$$du = Tds - pdv, \qquad (1)$$

Let us assume that the working medium obeys the ideal gas equation of state; then u will be a function of T only. It implies

Nomenclature

H = applied magnetic field
M = magnetization of the material
p = pressure
s = entropy
Δs_h = cycle entropy change at the high-temperature limit
Δs_l = cycle entropy change at the low-temperature limit
T = absolute temperature
T_h = high-temperature limit
T_l = low-temperature limit
u = internal energy of the work material
v = specific volume

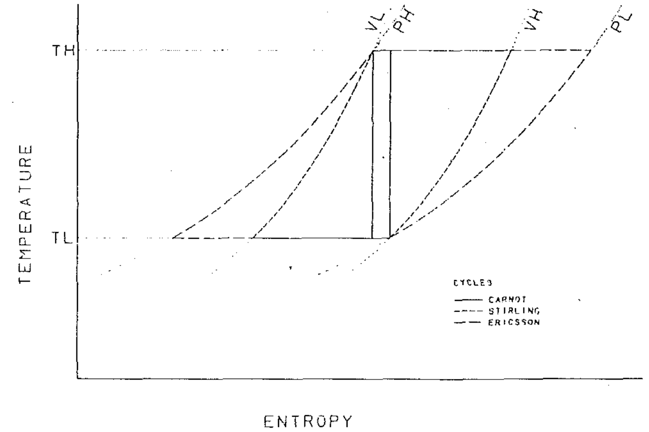

Fig. 4 Carnot, Stirling, and Ericsson gas cycles

that the horizontal distance (entropy difference) between any two constant volume lines on the *T-s* diagram is independent of temperature. In addition, the horizontal distance between any two constant *pressure* lines on the *T-s* diagram is also independent of temperature. These relationships are illustrated in Fig. 4.

Referring to a graphic representation of these relationships on the *T-s* diagram in Fig. 4, some of the ideal gas refrigeration cycles within specified temperature and pressure limits are shown. For each cycle, the heat rejection is given by

$$Q_h = T_h \Delta s_h, \tag{2}$$

the cooling capacity by

$$Q_c = T_1 \Delta s_1, \tag{3}$$

the work input by

$$W = Q_h - Q_c, \tag{4}$$

and the cooling coefficient of performance (COP_c) by

$$\text{COP}_c = \frac{Q_c}{W}. \tag{5}$$

The Carnot cycle consisting of two isothermal and two isentropic processes will have the maximum thermodynamic efficiency and COP, but it may be severely limited in cycle capacity for given heat source and sink temperatures and allowable variations in pressure and volume. One way to increase cycle capacity is to employ regenerative processes (storing and recovering heat) on the nonisothermal part of the cycle. Ideal regeneration requires reversible storage and recovery of heat with no net entropy generation, which, in turn, implies a fixed horizontal distance between the regenerative process lines on the *T-s* diagram. An ideal regenerative cycle will have thermodynamic efficiency equivalent to that of Carnot.

The commonly known regenerative cycles include Stirling and Ericsson cycles. The regenerative processes are kept at constant volume in a Stirling cycle, and at constant pressure in an Ericsson cycle. From Fig. 4, it is obvious that, within fixed temperature and pressure constraints, the Stirling cycle can substantially increase cycle cooling capacity while maintaining a COP equal to that of Carnot. However, this may require the regenerator to store and furnish significant amounts of heat during the cycle. The figure shows that within the same limits even greater capacity is achievable (and even greater energy storage is required) with the Ericsson cycle.

Magnetic Work Cycles. In magnetic work cycles, a solid material will be employed as the working medium, which is assumed to be incompressible, and we have

$$du = Tds + HdM, \tag{6}$$

If we follow the previous line of reasoning and postulate that the solid material obeys the ideal magnetic equation of state, i.e., the Curie Law,

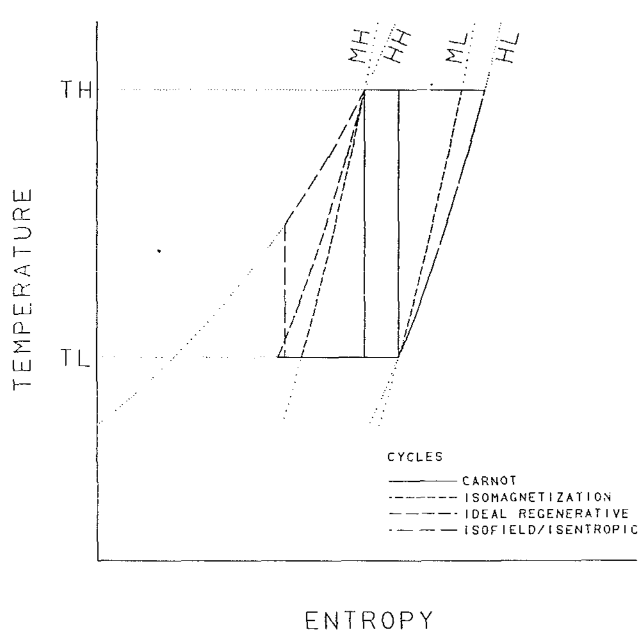

Fig. 5 Magnetic Carnot, Stirling, Ericsson, and ideal regenerative cycles

$$M = \frac{CH}{T}, \tag{7}$$

where C is the Curie constant. Once again, u will be a function of T only. The horizontal distance (entropy difference) between any two constant magnetization lines on the *T-s* diagram of a solid working medium is independent of *T*. However, the horizontal distance between any two constant *applied field* lines on the *T-s* diagram is no longer independent of *T*, and we have

$$ds = \frac{CH}{T^2} \cdot dH \tag{8}$$

These relationships are illustrated in Fig. 5.

The magnetic equivalent of a Stirling cycle, composed of two isothermal and two isomagnetization processes, is an ideal regenerative cycle (as shown in Fig. 5). In principle, such a cycle will have Carnot COP with capacities greater than Carnot. On the other hand, the magnetic equivalent of an Ericsson cycle, composed of two isothermal and two isofield process, is no longer an ideal regenerative cycle. The heat exchange is not balanced between the two isofield processes. The magnetic Ericsson cycle cannot even sustain steady-state cycle operation without some additional heat source. To balance the heat released and absorbed between the two isofield processes (which is done in a regenerator) in Fig. 5, one way is to terminate the high-field process before the minimum temperature is reached and replace it with a segment of isentropic demagnetization. It is denoted as a pseudo-constant-field cycle.

When compared to the constant magnetization (magnetic Stirling) cycle described above, the pseudo-constant-field cycle shows (1) the same amount of heat rejection at the maximum temperature, (2) the same amount of heat stored in and recovered from the regenerator, (3) a smaller amount of heat absorbed from the refrigeration load, and (4) a greater amount of work input to the system. Because the last two results require a reduction in the cooling coefficient of performance, the net effect of going from the ideal regenerative cycle to this cycle is a reduction in both refrigeration figures of merit: capacity and coefficient of performance. In turn, for the present example, these reductions are caused solely by irreversibilities associated with imperfect regeneration inherent to this thermodynamic cycle.

In addition to constant magnetization, there are other nonisothermal processes that offer ideal regeneration [for example, the low-isofield process combined with a varying higher-field process such that the horizontal distance (entropy difference) remains constant through the temperature range], but the isofield-line pairs are not in the group.

At this point we must discuss two real-world factors that affect how we extend the examination of magnetic refrigeration cycles. First, even the best currently available magnetic materials operating within the maximum realistic field ranges do not show isentropic temperature rises sufficient to accommodate typical temperature lifts required for room-temperature range applications, i.e., at present, it will require the use of regenerative cycles. Second, the best available materials are those that show ferromagnetic characteristics and have Curie temperatures in the operating-temperature range, i.e., they do not obey the Curie Law in the range of interest.

Accordingly, our approach is (1) to implement a model that, while still simple, simulates the important features of realistic material, and (2) to use the model to investigate the behavior of magnetic refrigeration cycles.

Cycle Analysis

For ease of comparison, MHP cycles with isothermal heat exchange with the surroundings are selected that include (1) a Carnot cycle, (2) a constant magnetization cycle, (3) an ideal regenerative cycle, and (4) a pseudoconstant field cycle. In the analysis, Gd is the working medium, the heat rejection temperature is fixed at 320 K, and the magnetic field limits are 0–7 Tesla (easily achievable by superconducting magnets).

Carnot Cycle. In the case of the Carnot cycle, if the cooling temperature (*TL*) initially equals the heat rejection temperature (*TH* = 320 K), the cycle is a horizontal line extending between the low-field (0 Tesla) and the high-field (7 Tesla) on the *T–s* diagram (cf. Fig. 5). In this case, the temperature lift and the work input are zero and the COP is infinity. As the *TL* starts to drop, the shape of the rectangle on the *T–s* diagram will be elongated and the available isothermal entropy change (the horizontal difference between the entropy of the low-temperature, low-field corner and that of the high-temperature, high-field corner of the cycle) decreases rapidly, implying a corresponding decrease in heat rejection and in cooling capacity, and an increase in work input. At *TL* = 314 K, work input reaches a maximum, while both cooling capacity and heat rejection continue to decrease [9]. Eventually, the rectangle collapses into a vertical line indicating the minimum cooling temperature (308 K) that can be achieved by the Carnot cycle with zero cooling capacity. The maximum attainable temperature lift of a Carnot cycle in this case is 12 K.

Constant Magnetization Cycle. Since the heat rejection temperature (*TH* = 320 K) is higher than the Curie point of Gd (*Tc* = 293 K), as the cooling temperature drops from the heat rejection temperature toward the Curie point, the available isothermal entropy change does not vary because we have made the low-field limit zero. This is a direct consequence of the fact that the zero magnetization line coincides with the zero field line above the Curie point. As a result, the heat rejection remains fixed, the cooling capacity falls linearly, and the work rises linearly [9]. As the cooling temperature drops below the Curie point, the available isothermal entropy change of Gd starts to decrease (limited by the now nonzero magnetization of the low-temperature, low-field "corner" of the cycle). In this range, the heat rejection begins to decrease, the cooling capacity decreases more rapidly, and the work input decreases from its maximum until the cooling temperature reaches a value for which the magnetization of the low-temperature, low-field corner equals that of the high-temperature, high-field corner. At this point (*TL* = 278 K) the "cycle" has collapsed to a single constant magnetization curve that has no cooling capacity, no heat rejection, and no work input.

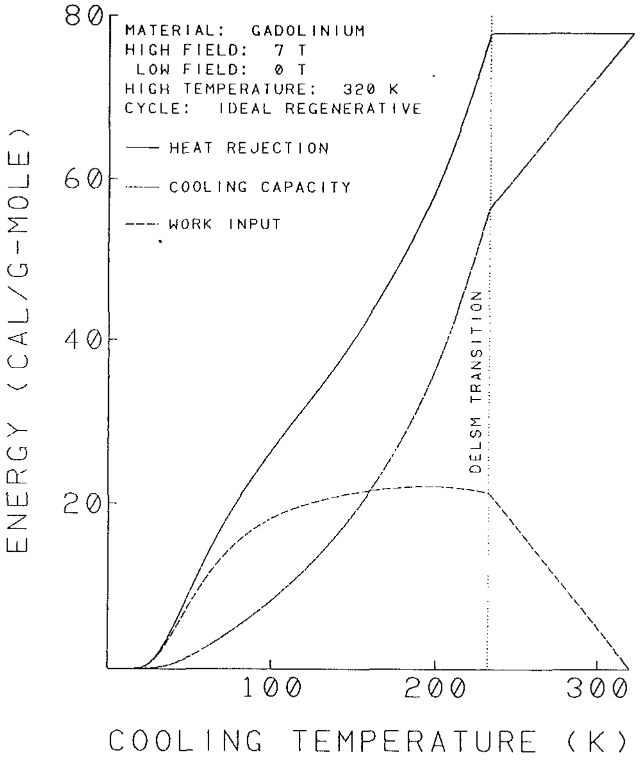

Fig. 6 Performance of an ideal regenerative cycle

In comparison with the Carnot cycle, available cooling capacity and temperature lift of this cycle have been increased without compromising the COP_c. However, some reversible provision must be made for the storage and removal of energy during the constant magnetization processes. Although capacities have been increased substantially over those of Carnot, the maximum available temperature lift (at zero cooling capacity) of this cycle is still only about 42 K.

Ideal Regenerative Cycle. To take full advantage of the operating region bounded by the established temperature and field limits, it is clear that a different cycle, denoted "ideal regenerative," is required. For convenience in illustration, we have let the nonisothermal processes of the ideal regenerative cycle be comprised of a constant low-field (actually zero here) storage path and a varying high-field recovery path that maintains a fixed horizontal separation on the *T–s* diagram. As the cooling temperature drops from the heat rejection temperature toward the Curie point, because we have let the low-field limit be zero, the ideal regenerative cycle coincides with the constant magnetization cycle; thus, the respective energy flows and performances are identical. As shown in Fig. 6, in contrast to the constant magnetization cycle, both the cooling capacity and the work input remain linear functions of the cooling temperature until it falls far enough below the Curie point that the corresponding isothermal entropy change between the high- and low-field limits equals that of the heat rejection temperature. As cooling temperature decreases further, the entropy change follows the (decreasing) low-temperature value, the heat rejection begins to decrease, the cooling capacity falls faster, and the work input increases more slowly. At some lower temperature, the work input reaches a maximum, and, from this point on, all three energy quantities decrease toward zero as the cooling temperature approaches absolute zero.

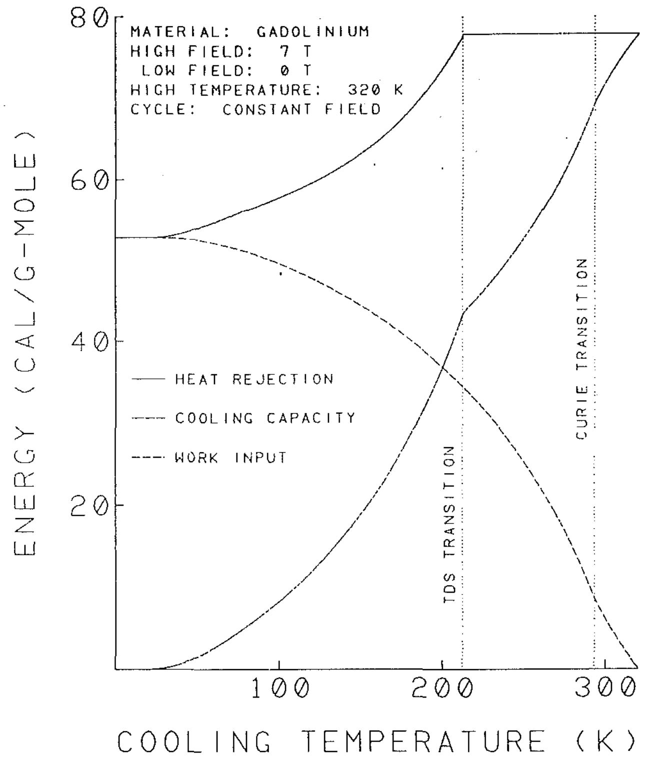

Fig. 7 Performance of a pseudoconstant field cycle

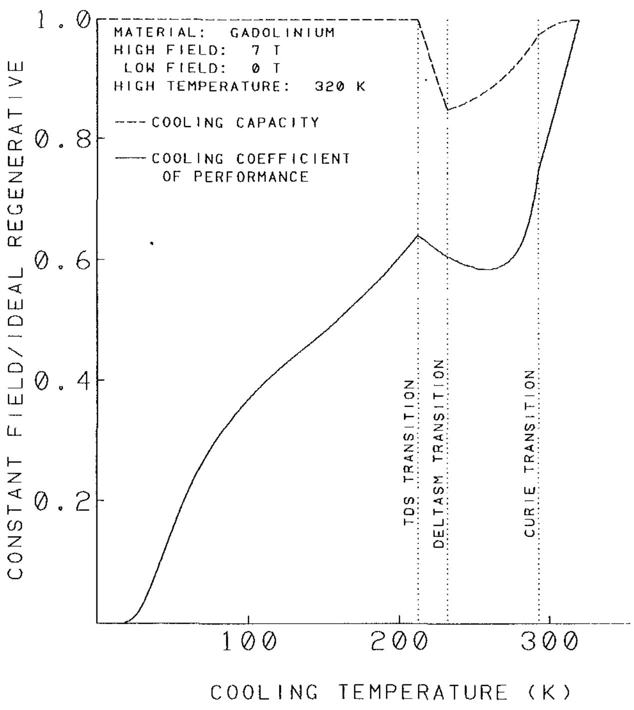

Fig. 8 Relative cycle performance

Thus, in principle, the ideal regenerative cycle can extend the minimum cooling temperature toward absolute zero, and, for our example, can give cooling capacities equal to those of the constant magnetization cycle for cooling temperatures above the Curie point, and greater than those of the constant magnetization cycle for cooling temperatures below the Curie point. These potential improvements have come while the COP_c was maintained at the "Carnot" value. As before, some reversible provision must be made for the storage and removal of energy during the execution of the nonisothermal processes of the cycle.

Pseudoconstant Field Cycle. In this (magnetic Ericsson) cycle, as the cooling temperature drops from the heat rejection temperature toward the Curie point, the heat rejection again remains fixed while the cooling capacity falls, the work input rises, and the COP_c decreases as shown in Fig. 7. However, for this cycle, as was demonstrated earlier for a Curie Law magnetic material, the changes are more rapid than those of the ideal regenerative cycle because of irreversibilities introduced in the regeneration processes. Because an energy balance on the regenerator cannot be maintained by following the high-field line all the way from the heat rejection temperature to the cooling temperature, the process must be terminated and replaced with a segment of adiabatic demagnetization before the cooling temperature is reached.

As the cooling temperature passes through the Curie point, the shapes, but not the trends, of the curves change. From the previous discussion it should be recalled that, according to the model employed here, the zero-field specific heat undergoes a step increase as the Curie point is reached from above. At this temperature the value changes from one smaller than the high-field value to one greater than the high-field value. In other words, below the Curie point the material at zero field can absorb more heat over a given temperature interval than can the material at high field. The reverse is true above the Curie point. A consequence of this is that, below the Curie point, as the cooling temperature decreases, the portion of high constant-field line that must be replaced by the adiabatic demagnetization leg is progressively reduced until some lower temperature is reached where no adiabatic demagnetization portion is required. At this point and for all lower temperatures, the cooling capacity of the constant-field cycle equals that of the ideal regenerative cycle. However, for lower temperatures the regenerator energy balance requirement leads to termination of the low-field (zero) line below the heat rejection temperature and to insertion of an adiabatic magnetization process to complete the cycle (cf. Fig. 7). A direct result of the insertion of an adiabatic magnetization process is a decrease in heat rejection.

As shown previously, when compared with the ideal regeneration cycle described above, this cycle results in (1) a smaller entropy change during the isothermal process at the cooling temperature, (2) a reduced cooling capacity, (3) a greater amount of work input to the cycle, and (4) a smaller COP_c.

Discussion

For the example here the pseudoconstant field cycle also extends the minimum cooling temperature toward zero, but, when compared with the ideal regenerative example, it does so with reduced refrigeration capacity within some of the range and with reduced COP_c in the entire range. These trends are illustrated in Fig. 8, which shows, for example, a 42 percent reduction in COP at 260 K cooling temperature and a 15 percent reduction in capacity at 232 K cooling temperature for the constant-field cycle as compared with the ideal regenerative cycle. The comparative cycles for these two conditions are presented on the *T-s* diagrams in Fig. 9 and 10.

In thermal engineering studies, the effectiveness of energy equipment may be judged by its performance relative to that of a corresponding Carnot cycle machine (frequently expressed in terms of a percentage of the Carnot efficiency). It serves as a simple indicator to show how efficient an energy conversion device is. In the study of the magnetic heat pumps, a magnetic Carnot cycle cannot exist beyond a certain temperature lift. The effectiveness of a thermomagnetic energy conversion device can be judged with respect to that of a corresponding

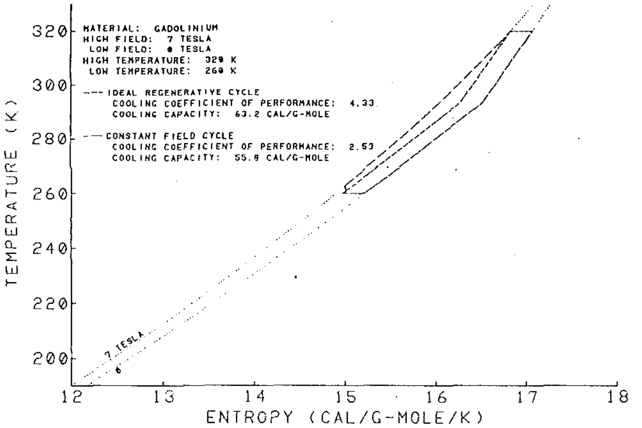

Fig. 9 Ideal regenerative and pseudoconstant field cycles for $TL = 260$ K

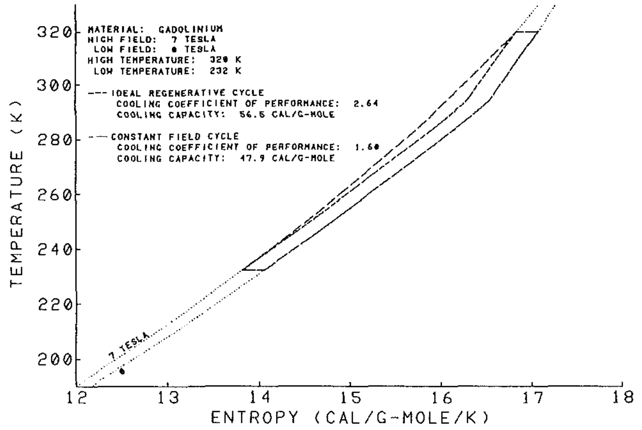

Fig. 10 Ideal regenerative and pseudoconstant field cycles for $TL = 232$ K

ideal regenerative cycle and the simple energy efficiency indicator will still be meaningful. We have shown its usefulness in the analysis of the pseudo-constant field cycle.

Experimental magnetic heat pumping devices including reciprocating [4, 5] and rotary [5, 12] concepts have been built and tested. They cover a wide range of practical applications, which include providing cooling for superconducting electric power transmission lines [5], space conditioning [13], and industrial heating [6]. Many of these devices are based on magnetic Ericsson or Brayton cycles [5, 12] because of the relative simplicity for achieving constant field processes. In any real device, many other loss mechanisms can affect cooling performance, such as heat transfer and flow friction losses, etc. These thermal, mechanical, and electrical losses have been analyzed by many investigators [5, 9, 14]. However, to date none of the experimental heat pump devices had performances near expectation. In our analysis, we showed that a machine operating on a pseudoconstant field cycle could suffer a substantial penalty due to the nonperfect regeneration resulting from the heat imbalance between the isofield cycle processes. The potential irreversibilities from this one source alone may adversely affect the viability of certain proposed MHP concepts if the relevant loss mechanisms are not adequately mitigated.

Acknowledgments

This work was a part of the Thermal Sciences Research Program performed at the Oak Ridge National Laboratory for the Advanced Industrial Processes Division, U.S. Department of Energy, under contract DE-AC05-84OR21400 with Martin Marietta Energy Systems, Inc. The authors appreciate the support of Messrs. M. Gunn and D. Knoebel during the study and of Ms. P. Gillis and D. Penland for technical editing.

References

1 Giauque, F., and MacDougall, D. P., "Attainment of Temperatures Below 1 Degree Absolute by Demagnetization of $Gd_2(SO_4)_3 \cdot 8H_2O$," *Phys. Rev.*, Vol. 43, 1933, p. 768.

2 Fast, R. W., ed., *Advances in Cryogenic Engineering*, Vol. 35B, Plenum Press, New York, 1989, pp. 1087–1190.

3 Daunt, J. G., and Heer, C. V., "Heat Flow in Metals Below 1 K and New Method for Magnetic Cooling," *Phys. Rev.*, Vol. 76, 1949, p. 854.

4 Brown, G. V., "Magnetic Heat Pumping Near Room Temperature," *J. Appl. Phys.*, Vol. 47, No. 8, 1976, p. 3674.

5 Barclay, J. A., and Steyert, W. A., *Magnetic Refrigerator Development*, EL-1757, Electric Power Research Institute, 1981.

6 Mills, J. I., and Kirol, L. D., "Magnetic Heat Pump Cycles for Industrial Waste Heat Recovery," *Proceedings of the 19th IECEC*, 1984, p. 1369.

7 Carlin, R. L., and Duyneveldt, A. J., *Magnetic Properties of Transient Metal Compounds*, Springer-Verlag, New York, 1977.

8 Barron, R., *Cryogenic Systems*, McGraw-Hill, Toronto, 1966.

9 Chen, F. C., et al., *Loss Analysis of the Thermodynamic Cycle of Magnetic Heat Pumps*, ORNL/TM-11608, Oak Ridge Natl. Lab., Martin Marietta Energy Systems, Inc., Oak Ridge, TN, 1991.

10 Benford, S. M., and Brown, G. V., "*T-s* Diagram for Gadolinium Near the Curie Temperature," *J. Appl. Phys.*, Vol. 52, No. 3, 1981, pp. 2110–2112.

11 Griffel, M., Skochdopole, R. E., and Spedding, F. H., "The Heat Capacity of Gadolinium From 50 to 355 K," *Phys. Rev.*, Vol. 93, 1954, p. 657.

12 Barclay, J. A., Steyert, W. A., and Zrudsky, D. R., *The Design and Performance of a Magnetic Refrigerator and Heat Engine*, LA-UR-79-662, Los Alamos Scientific Laboratory, Los Alamos, NM, 1979.

13 Brown, G. V., "Basic Principles and Possible Configurations of Magnetic Heat Pumps," *ASHRAE Trans.*, Vol. 87, No. 2, 1981, pp. 783–793.

14 Kirol, L. D., et al., *Magnetic Heat Pump Feasibility Assessment*, EGG-2343, Idaho Natl. Eng. Lab., EG&G, Inc., Idaho Falls, ID, 1984.

Mission Design Drivers for Closed Brayton Cycle Space Power Conversion Configuration

W. G. Baggenstoss

T. L. Ashe

Allied-Signal Aerospace Company,
Garrett Fluid Systems Division,
Tempe, AZ 85285

Future space power requirements will vary from the subkilowatt range for deep space probes, to the hundreds of kilowatts range for a lunar base, to the multimegawatt range for interplanetary propulsion systems. Closed Brayton cycle (CBC) power conversion has the flexibility to be used in all these power ranges and with a variety of heat source options such as isotope, solar, and nuclear. Each of these types of heat sources has different characteristics that make it more appropriate for particular mission profiles and power output ranges. Heat source characteristics can also be major design drivers in the closed Brayton cycle design optimization process. This paper explores heat source selection and the resulting CBC system designs, and discusses optimization methods as a function of the main design drivers. Such power system requirements as power level, man-rated radiation shielding, fuel costs, eclipse/darkness duration, system mass, radiator area, reliability/mission duration, and insolation level are evaluated through several CBC parametric case studies. These cases include: (1) a 500 We power system for deep space probes; (2) a 50 kWe solar dynamic system for earth orbit and other applications; (3) a 100 kWe man-rated lunar/Mars stationary/rover power system; (4) a 200 to 825 kWe power system for the lunar outpost; and (5) 3300 kWe modules for interplanetary propulsions.

Introduction

Space missions being planned for the 21st century range from small, deep space probes to large, extraterrestrial manned bases and the interplanetary vehicles required to establish these bases. Power requirements will vary accordingly. Proposed heat sources for power conversion systems include radioisotopes, solar collectors, and nuclear reactors, each with characteristics to make it more suitable for particular mission profiles and power output levels. Closed Brayton cycle (CBC) power conversion has advantages over other conversion systems for space power applications. It is more efficient that static conversion systems (Harper et al., 1990) and more flexible than other dynamic conversion systems such as organic Rankine (English, 1986). CBC has the flexibility to be used in all the anticipated power classes, with any of the possible heat sources.

In addition, CBC space power systems can be tailored to account for the design drivers of a particular heat source and application.

Case studies presented show that CBC can provide:

1 High conversion efficiency required of low power level isotope systems.
2 Energy storage and high efficiency required of moderate power level solar dynamic systems.
3 High efficiency required of man-rated nuclear applications.
4 Low mass, modularity, and easily implemented redundancy of high power, fixed base nuclear systems.
5 High power capability and efficiency required of multimegawatt nuclear propulsion power systems.

Closed Brayton Cycle Power Systems Flexibility

The flexibility of the CBC conversion system is a key feature of the power generation system. The most important aspects of this flexibility are:

(*a*) Heat source options
(*b*) Freedom in selecting cycle pressures and temperatures
(*c*) Design adaptability to mission-specific criteria
(*d*) Excellent off-design performance
(*e*) High reliability through easily implemented redundancy

The design flexibility possible with CBC power conversion systems allows specific tailoring to a given set of mission requirements. A CBC system design can be optimized relative to any parameter that is key to a particular mission. Thus, systems can be designed for minimum mass, minimum radiator area, high efficiency, or any combination of these. Closed Brayton cycle technology, when tailored to a specific requirement, yields a low-mass, compact power conversion system.

Individual component technologies will change in different

Contributed by the International Gas Turbine Institute and presented at the 36th International Gas Turbine and Aeroengine Congress and Exposition, Orlando, Florida, June 3-6, 1991. Manuscript received at ASME Headquarters February 20, 1991. Paper No. 91-GT-139. Associate Technical Editor: L. A. Riekert.

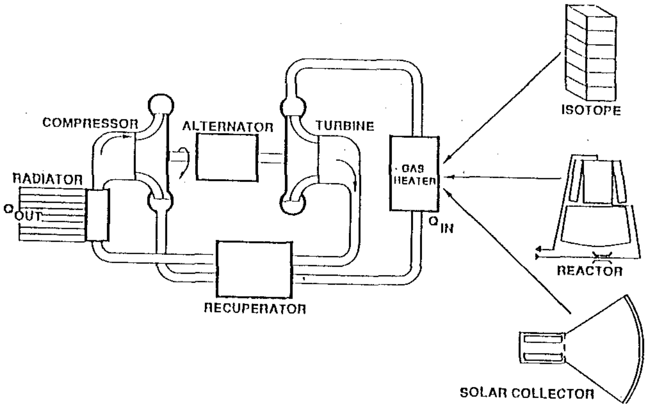

Fig. 1 Closed Brayton Cycle schematic diagram

power ranges, but the basic system configuration shown in Fig. 1 is applicable to designs from the subkilowatt to several hundred kilowatt range. CBC conversion systems commonly use an inert gas working fluid. This fluid places no restrictions on operating temperatures, pressures, or selection of construction materials.

In addition to its design flexibility, the CBC power conversion system has good operational flexibility. Its broad off-design performance capability yields near constant conversion efficiency over a wide range of user load or environmental conditions. The operating speed, turbine inlet temperature, and working fluid inventory level can all be adjusted to vary the output power level.

Heat Source Alternatives. An isotope heat source is appropriate for CBC power conversion systems at power outputs from less than 0.5 kWe to about 15 kWe. Above 15 kWe the cost of the isotope fuel tends to make such systems uncompetitive. A solar dynamic heat source makes sense for CBC systems from about 2 kWe to about 100 kWe. Below 2 kWe the size of the solar concentrator/supporting structure is excessive when compared to an isotope system. Above about 100 kWe the mass of the thermal storage subsystem tends to make a nuclear heat source more attractive. Nuclear reactor heat sources are competitive for any system above about 15 kWe. Below this the fixed mass (reactor structure, controls, etc.) usually makes the nuclear heat source too heavy compared to the other options.

CBC System Design and Optimization Process

The first step in power conversion system optimization is to determine what system characteristic is to be optimized. As mentioned above, system mass, radiator area, and conversion efficiency are the most common characteristics evaluated. It is often the case that optimization of these three characteristics is in conflict and a compromise is necessary. In this case an objective function to be minimized of the form

$$\text{Mass} + m \times \text{radiator area} + n \div \text{conversion efficiency}$$

is used, where m and n reflect the relative importance of radiator area and conversion efficiency to system mass for the system designer.

The independent variables used in the optimization process are:

(*a*) Turbine inlet temperatures
(*b*) Compressor inlet temperatures
(*c*) Level of recuperation used in the cycle
(*d*) Pressure drops in the system
(*e*) Compressor pressure ratio
(*f*) Compressor specific speed
(*g*) Rotor speed
(*h*) Working fluid molecular weight

A basic design program takes the values for these variables and matches empirical turbine and compressor performance data to the thermodynamics of the Brayton cycle and defines the complete state points throughout the closed loop. The analysis includes alternator, bearing, windage, and thermal losses, cooling flows, and the variation in working fluid transport properties with temperature. Component size and mass estimates are based on empirical data from production heat exchangers, alternators, and aerodynamic components. System ducting is sized to be consistent with the pressure drops assumed in the thermodynamic analysis.

From an initial feasible solution, the optimization routine varies the independent variables sequentially, in small steps, and evaluates the objective function. The independent variables are constrained by mission requirements and/or physical limitations. After all of the independent variables have been varied in sequence, the process is begun again. When further variation of the independent variables provides no further improvement in the objective function, an optimum solution has been reached.

Design Drivers

Different heat source characteristics and mission requirements act as design drivers in the optimization of CBC power conversion systems.

Isotope Heat Source. A radioisotope heat source drives the power conversion design in several ways. First, due to the high cost of the isotope and the importance of this limited resource to national energy policy, a key design driver is to minimize the amount of isotope required to meet a given power requirement. This means, of course, that high cycle conversion efficiency is desired. Second, the isotope heat source is usually of a modular design and changes in heat input are possible only in discrete, incremental steps. Therefore, the power conversion system design must provide the required output power with an integer number of isotope heat source modules. Finally, since the isotope thermal output decays over time, the conversion system design, particularly the control system, must be able to compensate for the decrease in heat input.

Solar Dynamic Heat Source. The main design driver for solar heat source systems is the energy storage for eclipse periods. As discussed by Pietsch and Brandes (1989), if continuous power generation is required during eclipse periods, some sort of energy storage is necessary to continue operation of the turbine. Harper et al. (1990) noted that the use of thermal energy storage in the form of a eutectic salt mixture, phase-change material is appropriate for CBC systems due to its high heat of fusion and melting temperatures appropriate for high efficiency CBC systems. In comparing thermal energy storage systems, Gintz (1976) reported phase-change material as having far higher energy storage density than sensible heat systems and as being far more technically mature than thermochemical concepts. Phase-change material thermal energy storage is assumed in this study.

Since the phase-change material is a large percentage of the power system mass, solar dynamic heat sources drive the power system design to high conversion efficiency. The longer the eclipse period, the stronger this design driver becomes.

Nuclear Heat Source. The main design driver for nuclear CBC power conversion systems is a function of the reactor shielding requirement. For missions where the shielding requirements are minimal (e.g., remote fixed base power or unmanned propulsion power), the reactor subsystem is a moderate fraction of the total power system mass and does not dominate the system design. However, for manrated power systems where high reactor shielding is required, the shielding mass is a very large fraction of the system mass (as much as 75 percent). This drives the power system design to very high efficiency levels to minimize the amount of shielding required.

Mission Design-Drivers. Two of the mission-related design drivers have been discussed above. Long eclipse time drives solar dynamic systems to high-efficiency designs. For missions with very long eclipse times, such as lunar or Mars surface applications, solar dynamic systems are probably rendered impractical by the excessive thermal energy storage that would be required. As mentioned above, nuclear CBC systems for man-rated missions are driven to very high efficiency designs by the reactor shielding requirement.

The effective sink temperature for the power conversion system on a particular mission affects the system design. For a deep space probe, the effective sink temperature will be very low, thus improving radiator performance and cycle efficiency. For a lunar base application, during the lunar day the effective sink temperature will be relatively high, requiring a higher heat rejection temperature and making radiator orientation important to minimize the view factor of the high temperature lunar surface.

Very long-term missions and/or man-rated missions will have particularly high reliability requirements. This can drive the system component designs. For example, higher strength advanced materials may be required to increase system life. Similarly, the system configuration may be altered by adding more power conversion units to increase redundancy and system reliability.

Certain missions, where spacecraft drag is a significant factor, will require minimum radiator area. Low earth orbit applications or interplanetary transportation missions, will place importance on minimum drag and, hence, mission radiator area. This drives the power conversion system design to higher heat rejection temperatures.

Minimum mass will be a more important consideration for missions where boost cost is a major factor and deployed system volume is less critical. A lunar or Mars base power application would likely fall into this category.

Design Driver Case Studies

The following case studies demonstrate how different heat sources and mission requirements act as design drivers for CBC power systems.

Low Power System With Isotope Heat Source. A 500 kWe version of the Dynamic Isotope Power Subsystem (DIPS) power conversion system using the CBC has been studied for potential use on a deep-space probe mission.

This power system uses the general purpose heat source (GPHS) isotope modules designed by Rocketdyne, as part of the DIPS program. The CBC turboalternator-compressor (TAC) is completely gas cooled by the working fluid and a direct gas-coupled radiator is used. Two turbine inlet temperatures, 1100 K (1520°F) and 1300 K (1880°F), were examined.

The proprietary computer optimization program discussed above was used to generate feasible CBC system designs. By varying the relative importance of system mass and radiator area in the optimization parameter, a curve of minimum mass versus radiator was generated. By adding system efficiency to the optimization parameter, curves of feasible designs with an integer number of GPHS isotope modules at various efficiency levels were generated. The results for the 1300 K (1880°F) turbine inlet temperature are shown in Fig. 2.

These results show the flexibility of the CBC power conversion system for use with an isotope heat source. The CBC system provides the high conversion efficiency (from 26 percent to 32 percent or higher) desired for isotope systems with relatively small penalties in weight and radiator area as efficiency increases. The mission designer also has the ability to determine the appropriate trade between system mass and radiator area for specific mission requirements.

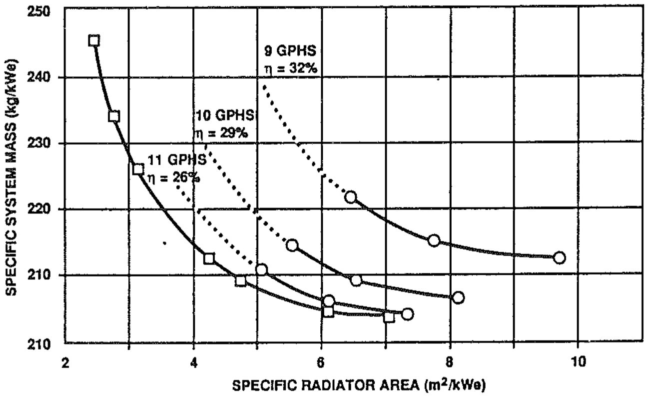

Fig. 2 500 We isotope/CBC system optimization trends

Table 1 50 kWe solar/CBC system optimization results

50 kW, Solar Heat Source			
	km Orbit		
	2,000	10,378	35,817
Orbital Period, hr	2.12	6.00	24.00
Light Time, hr	1.49	5.25	22.80
Maximum Eclipse Time, hr	0.63	0.75	1.20
Comp Inlet Temp, K (°F)	302 (84)	301 (82)	298 (76)
Turb Inlet Temp, K (°F)	1000 (1340)	1000 (1340)	1000 (1340)
Rotor Speed, rmp	34,261	34,855	34,524
Recup Effect	0.96	0.96	0.97
Pressure Drop, Beta	0.94	0.94	0.94
Cycle Efficiency	34.6	35.1	36.1

50 kWe Solar Dynamic System. A 50 kWe solar dynamic CBC system was studied for use on an earth orbiter mission. Possible applications include an earth observation satellite for the Mission to Planet Earth programs, a space-based radar satellite, or a direct broadcast television satellite.

This power conversion system uses a Newtonian solar collector and a receiver with thermal energy storage. A pumped loop radiator is used, with a turbine inlet temperature of 1000 K (1340°F).

An optimization parameter with an equal emphasis on system mass and radiator area was used in the study and the characteristics of the system at different orbits were examined. Table 1 and Fig. 3 show the results. As the orbit altitude increases, the percentage of time in the sun increases, which allows a smaller, lighter solar collector to be used. But the eclipse duration also increases, which increases the size of the receiver and thermal energy storage required. As can be seen from the data, this later effect dominates and the system mass increases at higher orbits. In order to minimize this trend, the CBC system optimizes at higher conversion efficiency at higher orbits to lessen the amount of thermal energy storage required.

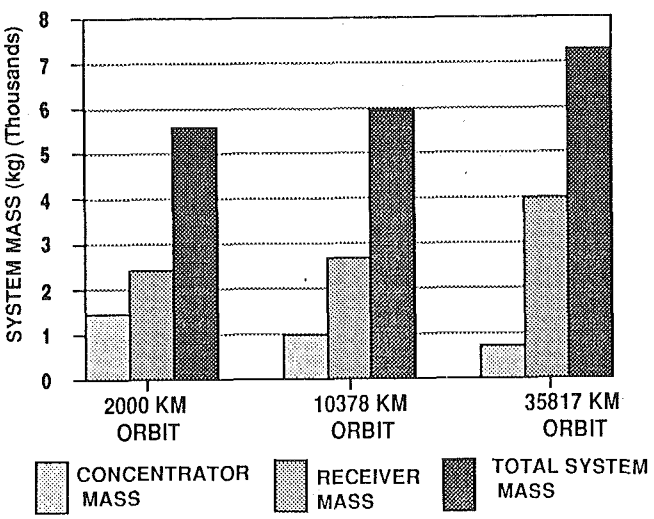

Fig. 3 50 kWe solar/CBC heat source and system mass trends

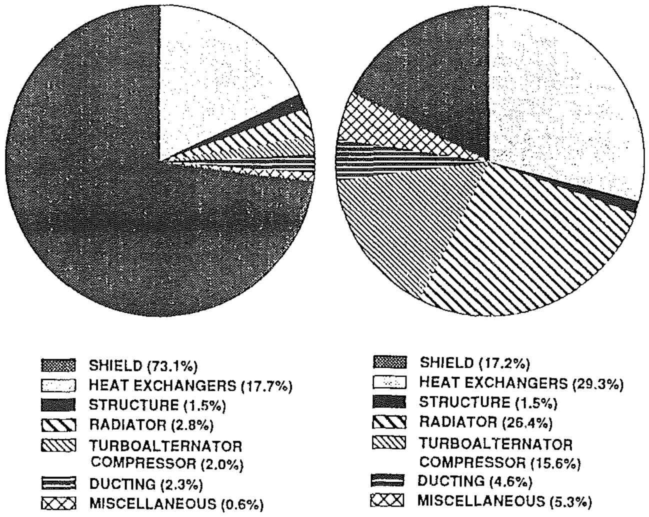

Fig. 4 100 kWe nuclear CBC mass comparison for instrument-rated shielding and man-rated shielding systems

Table 2 100 kWe nuclear CBS system optimization results

	Case	
	1	2
Sink temperature, K	194	194
Radiation dose	Man	Inst
Total mass, kg	18,116	2,256
Shield mass, kg	13,173	391
Radiator area, m^2	100.0	174.9
Compressor inlet temperature, K	383	401
Efficiency	0.374	0.227
Recuperator effectiveness	0.969	0.750
Pressure loss ratio	0.970	0.940
Compressor pressure ratio	1.71	2.03
Rotor speed, rpm	26,662	28,207

CBC solar heat source power systems can provide the energy storage required to operate continuously during periods of solar eclipse. Such systems operate at high conversion efficiencies to minimize the weight of the energy storage system required.

100 kWe System With Nuclear Reactor Heat Source. Extraterrestrial exploration and development missions of the next century will require reliable, low-mass power generation modules of 100 kWe and more. In the 100-kWe power range, these modules will be required to support both fixed base needs (such as the emplacement phase lunar base) and manned rover/explorer power requirements. Low insolation levels at and beyond Mars and long periods of darkness on the moon make solar conversion less desirable for surface missions. For these missions, a closed Brayton cycle energy conversion system coupled with an SP100 or gas-cooled type reactor heat source is a very attractive approach.

The system studied by Ashe and Baggenstoss (1990) uses an SP100 type liquid-metal reactor configuration with a turbine inlet temperature of 1250 K (1790°F). (The use of an SP100 type reactor is simply assumed in this study and yields valid trend results, although it is not necessarily the optimum configuration.) Man-rated shielding is used for the rover mission, while the fixed base uses instrument rated shielding. A pumped loop radiator configuration is used. The radiator is limited to a single-sided, 100 m^2 (1076 ft^2) unit for the rover mission. A two-sided radiator with no area limit is used for the fixed base. One hundred percent redundancy of the CBC loop components is used to ensure high reliability.

The results of the minimum mass optimization for the rover and fixed base systems are shown in Table 2. The way the shielding requirement drives the system design is clear if the rover and fixed base system configurations are compared. With the man-rated shielding requirement, the rover power system is driven to a very high conversion efficiency of 37 percent. The instrument rated shielding of the fixed base system leads to a moderate 23 percent efficiency and a much lower system mass. Figure 4 shows the dramatic difference in the mass breakdown of the power systems for the two different mission applications.

Heat source and mission-related design drivers led to a dramatic difference in the configurations of two systems at the same power level, using the same power conversion technology. CBC power conversion can provide the high conversion efficiency required for man-rated nuclear power systems or the low system mass of fixed base power systems.

200 kWe to 825 kWe Systems With Fixed SP100 Reactor Heat Source. Power system requirements are being defined for the NASA Space Exploration Initiative lunar outpost. These power systems must support the housing, transportation, and construction activities necessary for exploration of the moon. The lunar outpost mission will be accomplished in phases with fixed base power requirements growing from 200 to 600 kWe in the consolidation phase to 825 kWe in the utilization phase. Closed Brayton cycle power conversion systems, coupled to one or more SP100 nuclear reactors, could meet this entire range of output power requirements.

The fixed, 2400 kW SP100 reactor with a turbine inlet temperature of 1250 K (1790°F) is used in the study by Ashe and Baggenstoss (1991). The reactor configuration was not part of the system optimization; the SP100 reactor was chosen due to the desirability of using an existing reactor design, capable of thermal output to meet the entire power range of interest. A pumped loop, two-sided radiator is used. To ensure high system

Table 3 200 to 825 kWe nuclear CBC system mass and radiator area trends

Parameter	Case Number				
	1	2	3	4	5
Conversion Efficiency	0.100	0.150	0.199	0.231	0.344
Module Power Level, kWe	79.9	120.3	159.5	184.5	206.3
Number of Modules	3	3	3	3	3
System Power Level, kWe	239.6	360.9	478.6	553.5	825.2
Compressor Inlet Temp, K	497	472	436	411	356
Compressor Pressure Ratio	1.67	1.73	1.82	1.99	1.78
Recuperator Effectiveness	0.349	0.622	0.740	0.775	0.918
Pressure Loss Ratio (Beta)	0.953	0.951	0.942	0.945	0.962
Rotating Speed, rpm	31,464	25,851	22,339	20,834	19,714
System Radiator Area, m^2	402	546	771	938	1,946
Total System Mass, kg	6,298	8,330	10,565	12,116	22,636
Specific Radiator Area, m^2/kWe	1.68	1.51	1.61	1.70	2.36
Specific Mass Area, kg/kWe	26.3	23.1	22.1	22.0	27.4

reliability, 100 percent redundancy of the CBC loop components is also assumed.

The variation in the characteristics of a CBC power conversion system mated to a single SP100 reactor was examined over the entire range of power requirements. This was done by optimizing for minimum system mass while varying the required system efficiency, and hence power output. The results are shown in Table 3 and Fig. 5. As the required efficiency of the system increased, the heat rejection temperature dropped, and the recuperation level and radiator area increased. The minimum specific mass level occurs at approximately 550 kWe output and the minimum specific radiator area is at approximately 350 kWe output. The single reactor, 825 kWe CBC SP100 system has an estimated mass of 22,470 kg (case 5). From the curve of Fig. 5, a 412.5 kWe system has a specific mass of approximately 22.2 kg/kWe. Therefore, two 412.5 kWe systems would have a total mass of approximately 22.2 × 425 × 2 = 18,900 kg or almost 4000 kg less than a single reactor system.

CBC power conversion can be used over the entire power output range envisioned for the lunar outpost with a single heat source. A CBC system can be optimized for use with a single reactor with very low specific mass anywhere in the 400 to 600 kWe range. A single reactor system capable of the full 825 kWe power goal is also possible, or a lighter, two reactor CBC system could be used. The low mass, modularity, and easily implemented redundancy of the CBC system make it well suited to the lunar base power application.

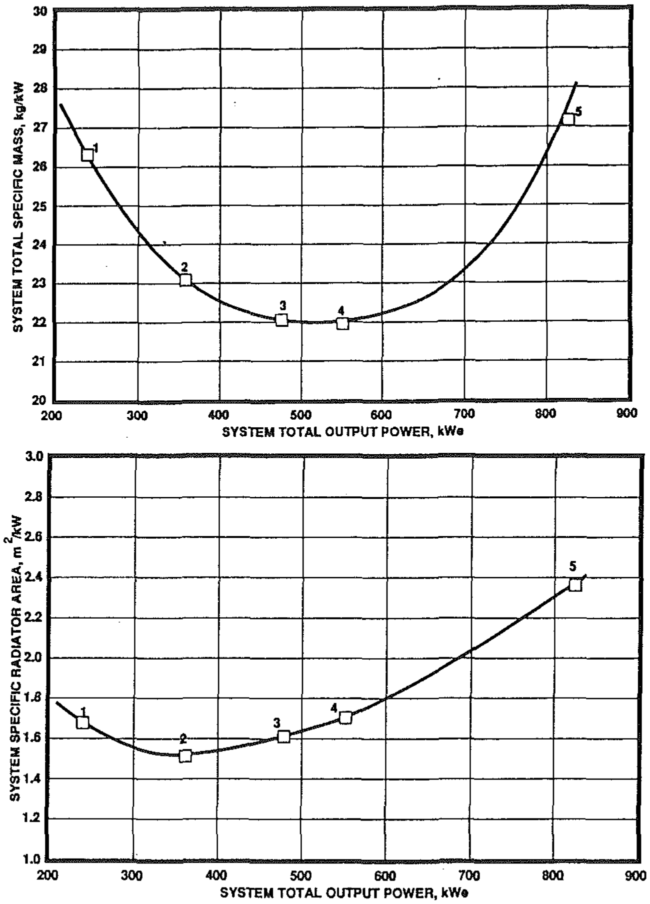

Fig. 5 200 to 825 kWe nuclear CBC system mass and radiator area trends

Multimegawatt Nuclear Electric Propulsion System. Several propulsion systems are under consideration for propelling unmanned cargo and manned exploratory vehicles to Mars and return. One of these systems uses nuclear electric propulsion (NEP). In this concept, a relatively high level of electrical power is generated by a nuclear power conversion system (PCS) to provide the energy for electric thrusters that propel the vehicle. This system is attractive because of the potentially high specific impulse characteristic of electric thrusters and low specific mass of the overall system. Since it can be readily scaled to the multimegawatt power range (English, 1986), the closed Brayton cycle represents a low specific mass power conversion system ideally suited for the NEP application.

Dramatic improvements can be attained in power systems specific mass and specific radiator area by increasing turbine inlet temperature from current levels of approximately 1150 K (1610°F) to 2000 K (3140°F) as discussed by Harper et al. (1989). Recent developments in gas turbine technology in high-temperature metallics, ceramics, and composite materials provide the capability of increasing the operating temperature of the closed Brayton cycle to this range. Since the power conversion system represents a large fraction of the overall NEP vehicle mass, any reduction in its specific mass pays large dividends.

A gas-cooled, particle bed nuclear reactor/CBC system of 3.3 mWe was examined by Brandes (1991). Turbine inlet temperature was varied from 1150 K (1610°F) to 2000 K (3140°F). Recuperated and nonrecuperated configurations were examined. A pumped loop radiator was assumed in all cases.

An optimization parameter with an equal emphasis on system mass and radiator area was used in the study and the

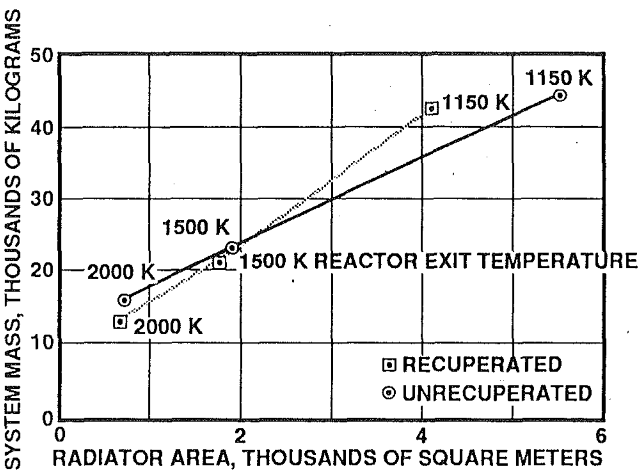

Fig. 6 3.3 mWe CBC NEP system mass and radiator area reduction with increased reactor exit temperature

characteristics of the system at different turbine inlet temperatures were examined. A plot of system specific mass versus specific radiator area for the resulting designs is given in Fig. 6. The 1150 K (1610°F) design represents demonstrated superalloy metals technology. The observed dramatic improvements in system mass and area approach diminishing returns as turbine inlet temperature exceeds 2000 K (3140°F), where material considerations for the radiator heat exchanger become problematic. Recuperation at 2000 K (3140°F) provides marginal gains and would require recuperators constructed from ceramic or carbon-carbon material systems.

The CBC power conversion system can provide multimegawatt power requirements for NEP missions. Recent provements in materials technology will allow increases in turbine inlet temperature over the current state-of-the-art and provide dramatic improvement in system specific mass and specific radiator area. These improvements are highly desirable for the multimegawatt NEP missions.

Conclusions

Future space power requirements will vary from the subkilowatt range to the multimegawatt range. The closed Brayton cycle can be used in all these power ranges to generate electrical power using an isotope, solar, or nuclear heat source. Due to a variety of performance and cost considerations, particular heat sources are appropriate for different power ranges and applications. Each heat source has its own characteristics, which drive power conversion designs. Not only can CBC be used with all of the potential heat sources, but its flexibility also allows it to be tailored to account for the design drivers of a particular heat source and application.

Case studies presented show how CBC systems can provide:

1 High conversion efficiency required of low power level isotope systems.
2 Energy storage and high efficiency required of moderate power level solar dynamic systems.
3 High efficiency required of man-rated nuclear applications.
4 Low mass, modularity, and easily implemented redundancy of high power, fixed base nuclear systems.
5 High power capability and efficiency required of multimegawatt nuclear propulsion power systems.

Acknowledgments

The low-power DIPS study was conducted under subcontract to Rockwell International, Rocketdyne Division, Canoga Park, CA, under Department of Energy Contract DEAC03-88-NE32129. The 50 kWe solar dynamic work was performed under subcontract to Martin-Marietta Corporation, Denver, CO, under Air Force Contract F33615-88-C-2843. The other studies reported in this paper were sponsored by Garrett Fluid Systems Division with internal funding.

References

Ashe, T. L., and Baggenstoss, W. G., 1990, "Nuclear Reactor Closed Brayton Cycle Power Conversion System Optimization Trends for Extra-Terrestrial Applications," *Proceedings, 25th Intersociety Energy Conversion Engineering Conference* (*IECEC*), Reno, NV.

Ashe, T. L., and Baggenstoss, W. G., 1991, "SP100/Closed Brayton Cycle Options for the Lunar Outpost Consolidation and Utilization Phase Stationary Powerplants," *Proceedings, 8th Symposium on Space Nuclear Power Systems*, Albuquerque, NM.

Brandes, D. J., 1991, "High Temperature Nuclear CBC Power Conversion System for the Space Exploration Initiative," *Proceedings, 8th Symposium on Space Nuclear Power Systems*, Albuquerque, NM.

English, R. E., 1986, "Technology for Brayton-Cycle Space Powerplants Using Solar and Nuclear Energy," NASA Technical Paper 2558, Cleveland, OH.

Gintz, J. R., 1976, "Advanced Thermal-Energy-Storage Concept-Definition Study for Solar Brayton Power Plants," Final Technical Report to Energy Research and Development Administration from the Boeing Company, Seattle, WA.

Harper, W. B., Boyle, R. V., and Kudija, C. T., 1990, "Solar Dynamic CBC Power for Space Station Freedom," ASME Paper No. 90-GT-XX.

Harper, W. B., Pietsch, A., and Baggenstoss, W. G., 1989, "The Future of Closed Brayton Cycle Space Power Systems," IAF-ICOSP89-5-4, International Astronautical Federation Space Power Conference, Cleveland, OH.

Pietsch, A., and Brandes, D. J., 1989, "Advanced Solar Brayton Space Power Systems," *Proceedings, 24th Intersociety Energy Conversion Engineering Conference* (*IECEC*), Crystal City, VA.

Design Stage Acoustic Analysis of Natural Gas Piping Systems in Centrifugal Compressor Stations

L. E. Rogers
NOVA Corporation of Alberta,
Calgary, Alberta, Canada

This paper presents design stage methods to analyze centrifugal compressor station piping acoustically. The methods have been successfully applied to the design of 26 stations since 1988. Full details of the calculation procedures are given, as well as guidelines for interpreting predicted results. Finally, the relationships between acoustic and mechanical response are described.

Introduction

Traditionally, the occurrence of flow-generated pulsation problems in centrifugal compressor piping was not extensive and could be addressed by post-design remedial action. A trend toward increased flow rates in the late 1980s has led to generally higher gas velocities and more complex piping configurations. These conditions in turn have led to flow-generated pulsation that is stronger and occurs over wider ranges of frequency. Such pulsation excites acoustic resonances of the piping and results in excessive vibration and other pulsation related problems. The key objective of design stage acoustic analysis is to eliminate predicted pulsation-driven problems.

Unlike reciprocating compressor piping, where the primary source of pulsation is the compressor itself, centrifugal compressor piping is driven by pulsation generated from within the piping. Flow-generated pulsation develops at all locations where the flow separates from the pipe wall. However, flow separation past tee branches and downstream of control valves is the only source of acoustic excitation that needs to be considered for steady-state compressor operation.

In response to NOVA's need to analyze piping systems acoustically, NOVA Husky Research Corp. (NHRC), a subsidiary of NOVA Corporation of Alberta, performed extensive research to quantify flow-generated pulsation characteristics. A digital computer program that incorporated the research results (PULS) was then developed to simulate piping acoustic response.

Design Engineering, a department within NOVA's Alberta Gas Transmission Division (AGTD), further enhanced PULS with the addition of auxiliary, pre- and postprocessing programs. Design approaches to deal with flow-generated pulsation effectively were also developed and form the primary content of this paper.

Analysis Scope

Only steady-state operating modes are considered during acoustic analysis. These include operating conditions anywhere on the head-flow curve of the compressor performance map. Quasi-steady operating modes when a control valve is open to prevent compressor surge are also considered.

To clarify further the boundaries of steady-state operation, the following are examples of related analysis situations that are not considered during acoustic analysis: unit startup and shutdown, relief and blowdown events, and transitions between online and offline operation. The above are considered transient operating modes and are dealt with by other methods.

Acoustic analysis fits in the design schedule after the preliminary static stress analysis of the piping is complete. At this stage the piping layout and operating conditions are well defined and further changes to the layout are very unlikely. In fact, changes requiring additional fittings are particularly unwelcome.

Both acoustic and mechanical response of the piping system are considered. Pulsation and acoustic shaking force[1] guidelines are used to determine whether acoustic response is acceptable, or whether acoustic modification and/or structural modeling is required. Acceptable mechanical response is ensured by the use of natural frequency, vibration and stress guidelines. The final solution is the result of iterating between acoustic and mechanical analysis.

Acoustic Source Descriptions

Tee Sources. A shear layer (flow separation) develops over the branch connection of tees that do not have mean flow in their sidebranch piping. Shear layer oscillation at the mouth of these sidebranches is reinforced when the frequency of shear layer oscillation matches the acoustic quarter wave resonant frequencies of the sidebranch. Strong shear layer oscillation and corresponding high pulsation can occur at these coincident frequencies.

Control Valve Sources. Unlike tees that produce discrete

Contributed by the International Gas Turbine Institute and presented at the 36th International Gas Turbine and Aeroengine Congress and Exposition, Orlando, Florida, June 3-6, 1991. Manuscript received at ASME Headquarters March 4, 1991. Paper No. 91-GT-238. Associate Technical Editor: L. A. Riekert.

[1] Acoustic shaking forces develop when pulsation acts on unbalanced areas within the piping. Unbalanced areas occur at changes in piping direction and changes in section. Examples include elbows, reducers, end caps, and orifice plates.

pulsation frequencies, control valves generate broadband pulsation. Flow rate and pressure drop are the key factors contributing to pulsation amplitude, and maximum pulsation usually occurs at the highest flow through the valve.

Acoustic Source Interactions

Multiple flow-generated pulsation sources are always present concurrently in centrifugal compressor piping systems. However, each source is modeled alone. The reason for this is the phase relationship between flow-generated pulsation sources can only be determined by measurement, and measurement is not possible at the design stage.

Special Modeling Considerations

Modeling techniques and approaches traditionally used in the analysis of reciprocating compressors are equally applicable in the analysis of centrifugal compressors with two distinctions:

1 As described above, the sources of pulsation are located in the piping itself and are flow generated in nature; and

2 pulsation generated in the suction system can transmit through the compressor into the discharge system and vice versa. Therefore, the entire station must be included for each source model. The compressor itself is dealt with as an integral part of the system and is modeled via a specialized transfer matrix similar to that of Sparks [9]. In fact, a centrifugal compressor can amplify or attenuate pulsation transmitted through it, depending on the operating conditions.

Results Interpretation

Various analysis guidelines are possible, ranging from emphasizing strict control of acoustic response to emphasizing strict control of mechanical response. In cases where piping cannot be satisfactorily supported, acoustic shaking forces must be kept very low. In cases where acoustic response is difficult to reduce, mechanical response must be carefully evaluated. The optimum mix between acoustic and mechanical modification will vary from station to station and even within the same station.

Initially the design approach is to ensure mechanical resonance of the piping occurs at frequencies well above dominant excitation force. This ensures the piping response is stiffness-controlled[2] in the frequency range of dominant excitation. Higher predicted problem frequencies are then resolved on a case-by-case basis.

There are two basic criteria that lead to corrective recommendations:

1 Predicted damage to piping or equipment
2 Predicted impairment of equipment operation

Guidelines for stress, vibration, and pulsation are used to define when the above criteria for correction are met.

A straightforward example of predicted damage is vibration that results in piping stress greater than the endurance limit.

---

[2] Stiffness-controlled refers to mechanical response that is dominated by the stiffness of the structure rather than by its mass or by its damping.

Nomenclature

A = pressure amplitude, Pa
$\bar{A}$ = normalized pressure amplitude ratio = $2A/\rho U^2$
A, B, C, D = pressure loss transfer matrix components
c = speed of sound, m/s
d = branch internal diameter, m
$\bar{d}$ = normalized branch diameter = d/D_p
d_o = orifice diameter
D_p = main pipe internal diameter, m
f = frequency, Hz
$f_{n/4}$ = nth quarter wave response frequency of tee sidebranch, Hz
F_p = piping acoustic shaking force guideline, N pk
f_s = Strouhal excitation frequency, Hz
i = square root of -1
ID = pipe inner diameter, m
k = wave number = $2\pi f/c$
l_o = acoustic equivalent length, m
L = tee branch length, m
L_a = acoustic length parameter for the globe valve, m
L_b = acoustic length parameter for the globe valve, m
L_G = length of ball valve interior, m
M = Mach number = U/c
n = nth quarter wave of tee sidebranch
NPS = nominal pipe size
P = absolute static pressure, kPa
P_1 = absolute static inlet pressure to control valve, kPa
ΔP = unrecovered pressure drop, kPa
Q = actual mean flow rate, m^3/s
r = branch edge radius, m
$\bar{r}$ = normalized branch edge radius, m
Re = Reynolds number = $\rho UD/\mu$
S = pipe cross-sectional area, m^2
SPL = sound pressure level (dBA ref 0.0002 microbars)
SR = split ratio
St = Strouhal number = $f_s d/U$
St_m = Strouhal number for maximum tone amplitude (i.e., first mode excitation of first quarter wave resonance)
STP = standard temperature and pressure (101.325 kPa, 15°C)
St_2 = Strouhal number for second mode excitation
t = time
$[T]$ = transfer matrix
$[T_a]$ = pure acoustic transfer matrix
$[T_d]$ = downstream transfer matrix
$[T_p]$ = transfer matrix resulting from unrecovered pressure drop
$[T_u]$ = upstream transfer matrix
U = mean flow velocity in the main pipe, m/s
V = amplitude of fluctuating volume velocity, m^3/s pk
V_s = source acoustic volume velocity, m^3/s rms
α = ball valve opening, deg
β = orifice-to-pipe diameter ratio = d_o/D_p
γ = ratio of specific heats = C_p/C_v
λ = acoustic wavelength, m
μ = dynamic viscosity kg/m·s
ρ = gas density, kg/m^3
ϕ = phase angle, deg

Subscripts

u = upstream
d = downstream
o = orifice
s = source

Another straightforward example, demonstrating impairment of equipment operation, is pulsation that causes incorrect gas flow measurement. Piping vibration that causes excessive vibration of equipment mounted on the piping is also an example where correction is necessary. This latter example is less straightforward, however, because excessive equipment vibration may lead to either equipment damage, impairment, or both.

Guidelines for vibration, mechanical natural frequency, and acoustic shaking forces are also used as indicators of when the above criteria may be met. The mechanical natural frequency and shaking force guidelines, demonstrated below in the sample analysis, are experience based and specific to the mechanical design philosophy described in this paper.

Acoustic Solutions

The most effective approach to solving acoustically driven problems in centrifugal compressor piping is to alter the source of pulsation directly. This is in contrast to reciprocating compressor piping, where effective solutions involve decoupling the source from the piping because the source of pulsation is largely unalterable by the analyst.

Problem Tee Source Solutions. Two solutions that alter tee source pulsations are possible: first, piping modifications that change the sidebranch length, and, second, insertion of a vortex spoiler[3] into the sidebranch. A suitable change in sidebranch length eliminates coincidence of excitation and response frequencies, while the vortex spoiler interferes with and effectively eliminates shear layer oscillation. Both solutions thereby remove the tee as a source of pulsation. The first solution is preferred when it is workable. Unfortunately the first solution is not always feasible, and many situations are encountered where the second method must be used.

Problem Control Valve Solutions. Reduced pulsation levels from control valves can be obtained directly in two ways. One way includes various types of modifications, including silencers and noise-reducing trims, that stage the pressure drop across the valve. Splitting the flow between two or more valves in parallel is another way to reduce pulsation. Usually the simplest, and preferred, solution is to install noise-reducing trims.

Sample Analysis

A small to medium sized (NPS 24 yard piping) single unit centrifugal compressor station is taken for the sample analysis. Valve source (V1) and tee sources (T1, T2, T3, T4) are shown in Fig. 1. Nodes relevant to the following discussion are also shown.

The compressor is driven by a 5 MW gas turbine and the operating conditions are as follows:

	Minimum	Maximum
Suction pressure, kPa abs	6450	7550
Suction temperature, °C	0	35
Flow rate, m^3/s STP	85	265
Discharge pressure, kPa abs	8150	9400
Discharge temperature, °C	5	65

The dimensions of T2 (the tee discussed in the following sample) are:

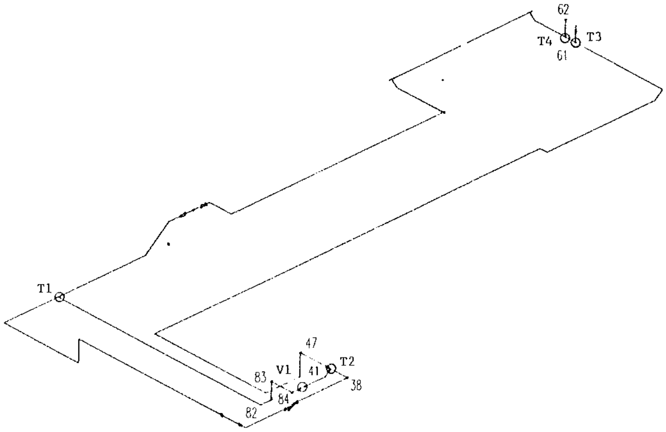

Fig. 1 Centrifugal compressor station isometric

Tee run inner diameter, D_p	476 mm
Tee branch inner diameter, d	375 mm
Branch edge radius, r	37.5 mm

Tee Sources. Tee source analysis proceeds in two steps. First, tees throughout the piping are examined for coincidence of shear layer oscillation frequencies and sidebranch quarter wave resonant frequencies. The first step is a screening step meant to eliminate detailed analysis of tees that obviously will not have problems. Tees that have a potential for problems (indicated by overlap in excitation and response frequencies) are modeled as the second step in the analysis procedure.

The first step in tee source analysis indicated that all four tees (T1, T2, T3, T4) required detailed acoustic analysis. However, only T2 analysis results will be described. The recycle and discharge piping tee (T2) is a common problem area, and in this case provides the opportunity to present extensions to the original research results summarized in Appendices A1 and A2.

Frequency of Tee Sources. Figure 2 shows an interference diagram for T2 where the overlapping (shaded) regions indicate flow and frequency ranges of potential pulsation problems. The diagram is constructed by plotting excitation frequency ranges versus flow past the tee, then quarter wave response frequencies that overlap are added.

Excitation frequencies are calculated by first determining the Strouhal number for the first mode. Two modes[4] of flow/acoustic interaction have been identified, and the second mode occurs at frequencies roughly twice the frequency of maximum source strength for the first mode.

A simplified formula (Eq. (1)) for St_m is used when the Reynolds number of the flow past the sidebranch is greater than 16×10^6.[5]

$$St_m = 0.413(\bar{d})^{0.316} \pm 13 \text{ percent} \qquad (1)$$

$$\text{for T2, } St_m = 0.413\ (0.788)^{0.316} \pm 13 \text{ percent}$$
$$= 0.33 \text{ to } 0.43$$

The Strouhal numbers for the first harmonic of the second mode and for the third harmonic of the first mode are calculated as shown in Appendix A1.

---

[3] Vortex spoilers referred to here are patented devices specifically designed for tee source pulsation suppression (Patent numbers: US(89)4,867,190; CDN(90)1,269,023).

[4] Mode refers to the number of vortices in the sidebranch when viewed in the plane of the tee. Mode 1 has one vortex while mode 2 has two vortices. See Jungowski [1] for further details.

[5] Good agreement has been found with measurements for operating compressor stations with Reynolds number up to 110×10^6.

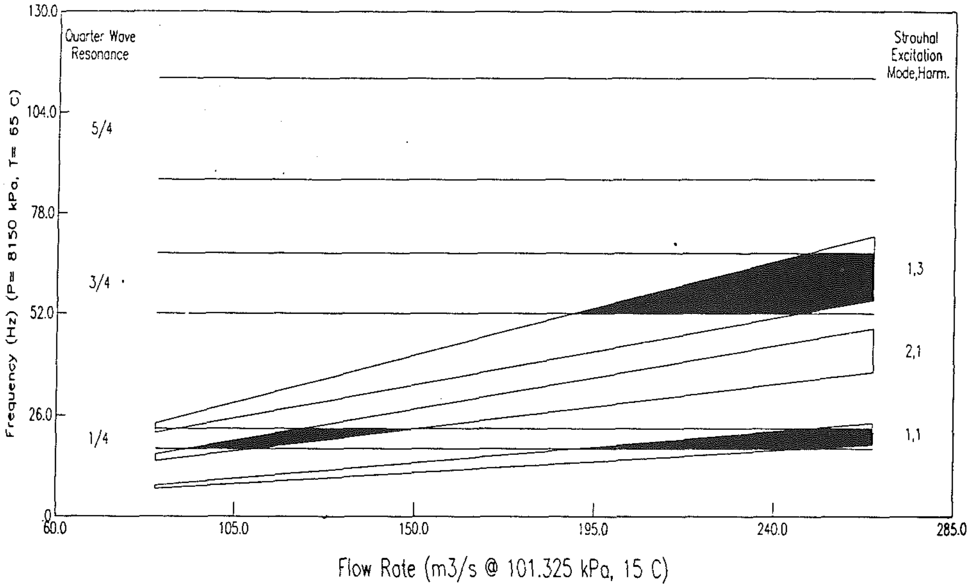

Fig. 2 Tee source interference diagram; recycle valve from discharge side (T2)

Table 1 T2 excitation frequency regions

Flow Rate (m^3/s @ STP)		85	265
Strouhal Number		Strouhal Frequency (Hz)	
St_m	(0.33) (0.43)	6.0 7.8	18.6 24.3
St_2	(0.67) (0.87)	12.1 15.8	37.9 49.2
$St_{1,3}$	(1.0) (1.3)	18.1 23.6	56.5 73.5

$$\text{for T2, } St_2 = 2\ (St_m) = 0.67 \text{ to } 0.87 \tag{2}$$

$$St_{1,3} = 3\ (St_m) = 1.0 \text{ to } 1.3 \tag{3}$$

Once the Strouhal numbers are determined for both modes, the excitation frequency ranges are calculated from the definition for Strouhal number as shown in Appendix A1. For the range of flow past T2 the extreme flow/frequency points given in Table 1 outline the excitation frequency regions shown in Fig. 2.

Acoustic resonance of the tee sidebranch occurs approximately at odd integer multiples of the quarter wavelength as expected from acoustic theory. The actual maximum response may not occur at an exact multiple of the quarter wavelength frequency for two reasons. First, in the absence of other effects, experimental measurements [1] indicate the effective length of the sidebranch is 1-12 percent longer than the actual length. Second, resonances in the piping system can interact with the sidebranch resonance to shift its frequency [1]. Appendix A1 details how to determine the quarter wave response frequencies.

For T2,

$$f_{1/4} = (0.88\text{-}1.0)1(430 \text{ m/s} \pm 1.8 \text{ percent})/4(5.1 \text{ m} \pm 5 \text{ percent}) = 17.3\text{-}22.6 \text{ Hz} \tag{4}$$

$$f_{3/4} = (0.88\text{-}1.0)3(430 \text{ m/s} \pm 1.8 \text{ percent})/4(5.1 \text{ m} \pm 5 \text{ percent}) = 52.0\text{-}67.7 \text{ hz} \tag{5}$$

$$f_{5/4} = (0.88\text{-}1.0)5(430 \text{ m/s} \pm 1.8 \text{ percent})/4(5.1 \text{ m} \pm 5 \text{ percent}) = 86.7\text{-}112.9 \text{ Hz} \tag{6}$$

To compensate for shifts caused by system resonances, the analysis range is centered about the sidebranch resonant frequency predicted by detailed acoustic modeling of the entire piping system. Centering the analysis range also compensates for uncertainties in the calculation of Strouhal number.

The center of the first quarter wave resonant frequency range for T2 from Eq. (4) above is 19.9 Hz. As described below, detailed acoustic modeling predicted 21.9 Hz for the first quarter wave resonance. Therefore, the range from Eq. (4), 17.3-22.6 Hz, was shifted up 2.0 Hz for detailed acoustic analysis.

Tee Modeling Method. The tee source is modeled as a hypothetical piston located in the branch next to the mouth of the sidebranch. An idealized sketch of the source model for T2 is given in Fig. 3.

The sidebranch resonant frequency of 21.9 Hz was predicted by detailed acoustic modeling with the above source model for T2 included in the piping system. Note the resonant frequency can usually be determined by observing a dip in both the sidebranch and source impedances as shown in Fig. 4.

Once the analysis frequency range is established, the correct source strength must be determined for each frequency within the range. The correct source strength occurs when the source volume velocity of the hypothetical piston is adjusted until predicted pulsation at the closed branch end matches the calculated value from below.

Tee Source Strength. All calculated source strengths are related to the source strength predicted when the first mode excites the first quarter wave resonance of the sidebranch. First, the normalized branch end amplitude ratio ($\bar{A}$) is determined. Next, pulsation at the closed branch end is calculated as the product of normalized pressure amplitude ratio and dynamic pressure of the flow past the sidebranch.

The Reynolds number of the flow past T2 is beyond the original research data [1]. Therefore, the normalized pressure amplitude ratio is assumed to equal 10 based on measurements from operating compressor stations with similar Reynolds number flows.[5]

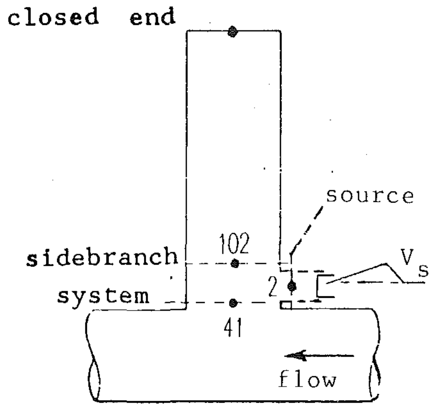

Fig. 3 T2 source model

For T2

$$\bar{A}_B = 10 \tag{7}$$

$$A_{B1,1} = 10(51.4\ \text{kg/m}^3)(19.5\ \text{m/s})^2/2 \tag{8}$$

$$= 97.7\ \text{kPa pk}$$

To obtain closed-end pulsation amplitudes for second mode excitation, and for excitation of third and higher quarter wave resonances, the *amplitude for first-mode excitation of the first* quarter wave resonance is attenuated as shown in Appendix A2.

Although conservative for most situations, predicted results may be unconservative when there are a number of sidebranches in series, as documented by Jungowski [1] and Bruggeman [2]. This typically occurs at large stations where more than one relief and/or blowdown stack is required.

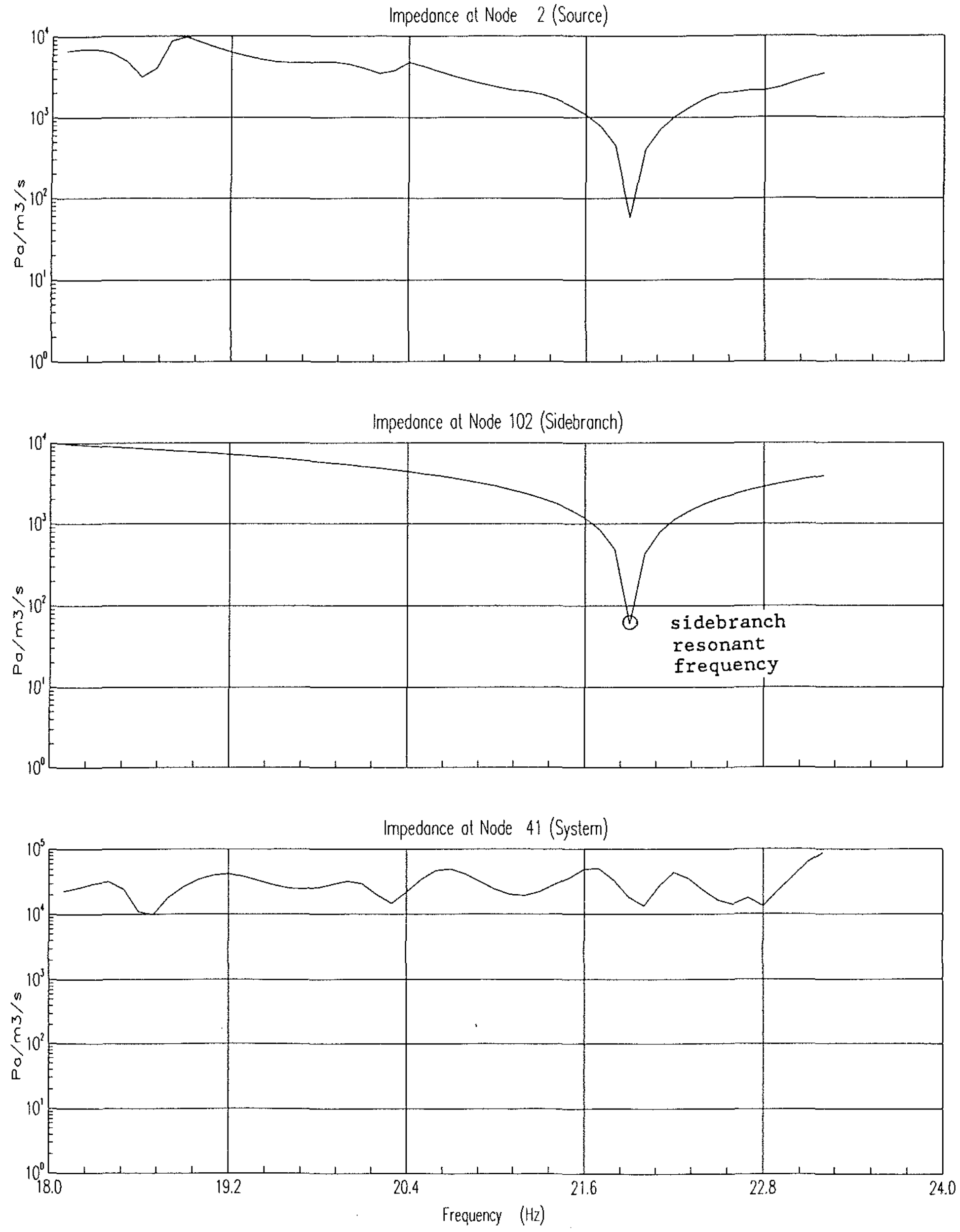

Fig. 4 Predicted acoustic results for pulsation source—T2; mode 1, harmonic 1 excitation of 1/4 wave resonance

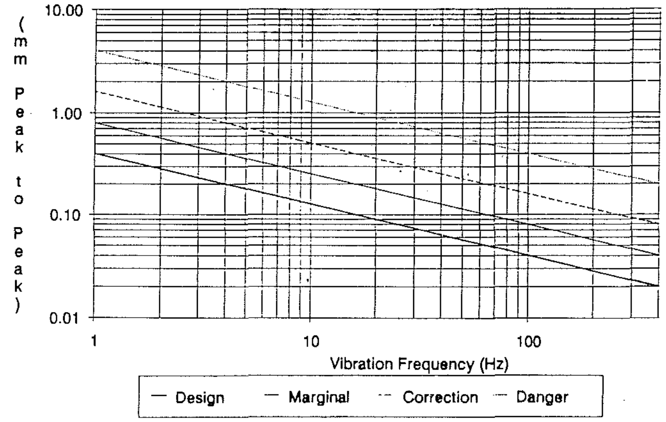

Fig. 5 Allowable piping vibration levels [8]

T2 Results. The following acoustic shaking force guideline has been developed in concert with the minimum mechanical natural frequency guideline.

$$F_p = 7874(ID)/\sqrt{(f/30)} \tag{9}$$

Notes:

(*a*) If f is less than 30 Hz, then use 30 Hz.

(*b*) If ID is greater than 0.255 m, then use 0.255 m.

Typical band clamp support stiffness for correctly placed supports will have acceptable piping vibration levels at low frequencies[6] when shaking force amplitudes are not greater than 2000 N pk. Therefore, the guideline for acoustic shaking forces results in a maximum amplitude of 2000 N pk. The constant 30 in the equation is related to the use of 30 Hz for the minimum mechanical natural frequency.

---

[6] Low frequencies refer to frequencies where mechanical response is stiffness-controlled.

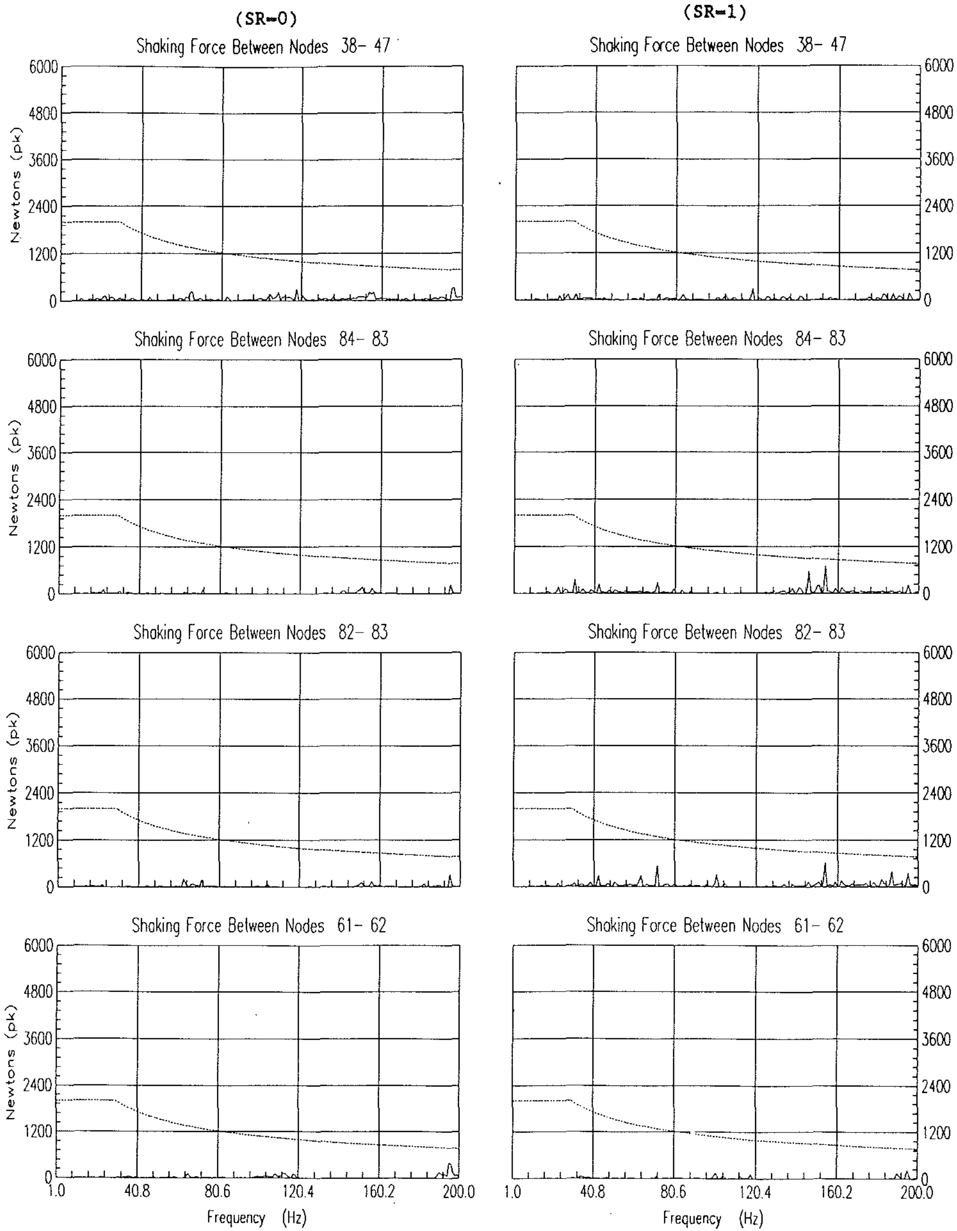

Fig. 6 Predicted acoustic results for pulsation source—V1

The maximum acoustic shaking force of 16.8 kN pk occurs between nodes 41 to 84 at 21.9 Hz. This clearly exceeds the above shaking force guideline; therefore, finite element forced response analysis was performed to evaluate vibration levels. Before calculating forced response of the piping, supports were located to ensure the lowest piping mechanical natural frequency was not less than 30 Hz.

Maximum predicted piping vibration in the direction from node 41 to 84 (see Fig. 1) is 0.6 mm p-p (23 mils p-p). Cyclic piping stress for the predicted vibration levels is well below the piping endurance limit. However, the piping vibration will provide base motion excitation to the control valve actuator that may impair control valve operation or damage the actuator. To help judge the acceptability of the above vibration, Fig. 5 may be used. Predicted piping vibration levels should meet the "Design" guideline given in Fig. 5. Note the vibration guidelines are statistical [8] and therefore require judgment when applied to various piping situations.

The "Design" guideline vibration from Fig. 5 for 22 Hz is 0.09 mm p-p. Therefore, the piping vibration predicted above (0.6 mm p-p) should be reduced to eliminate the possibility of damaging the valve actuator.

T2 Solution. The sidebranch could not be shortened. To reduce the predicted vibration to negligible levels, insertion of a vortex spoiler was the recommended solution.

Control Valve Sources. Flow rate and pressure drop are the key factors contributing to pulstaion amplitude generated by control valves. The sound pressure level (SPL) is checked for the worst combination of flow and pressure drop to determine whether detailed acoustic modeling is required. Experience has shown that valves with maximum SPL below 95 dBA will not result in excessive vibration for properly supported piping.

The control valve (V1) is a plug and cage style valve with noise-reducing trim. The maximum predicted SPL is 90 dBA; therefore detailed acoustic analysis is not required. For demonstration purposes, however, predicted results for V1 are given.

Analysis Frequency Range. Acoustic analysis is restricted to frequencies below 200 Hz. Experience indicates beam[7] modes of piping vibration are not significantly excited at frequencies above 200 Hz. Significant response frequencies for equipment sensitive to pulsation (for example metering devices and relief valves) have also been found to occur below 200 Hz.

Control Valve Source Strength. Investigation by NHRC has quantified pulsation source strength for two types of valves:

1 Ball valves [4, 6, 7]
2 Globe (plug only) valves [7]

The pulsation source strength of other valve types that are commonly used in compressor stations can be approximated by either of the above. Other valve types include V-ball valves and cage-plug valves. The source strength for V-ball valves is conservatively estimated by assuming the same source strength as a ball valve, and cage-plug valve source strength is assumed the same as a globe valve. Appendix A3 depicts each valve type and shows how to determine valve source strength.

The effect of noise-reducing trims on source strength is assumed to be the same as their effect on noise. That is, source strength is attenuated by the same amount that predicted noise is attenuated.

Control Valve Modeling Method. Pulsation transmission characteristics of ball and globe valve types can be modeled as shown in Appendix A4.

When other valve types are to be analyzed, for which transmission characteristics are unknown, two analysis runs are required. For the first run, the full source strength is applied to the upstream node of the valve model and a zero source strength applied to the downstream node ($SR = 0$). For the second run the sources are reversed ($SR = 1$). The run with the highest predicted amplitude for a particular acoustic variable corresponds to the worst case for that variable.

The two-run approach is quite conservative and should only be used as a last resort. Acoustic designers are further encouraged to develop a database that contains source strength constants, characteristic acoustic transmission variables, and pressure loss split ratios for different valve types.

V1 Modeling Method. V1 is a cage-plug valve as shown in Appendix A3. The source strength is calculated as follows:

$$\begin{aligned} V_s &= cS(0.00245)(\mathrm{M})(\Delta P/P_1)^{0.4363} \\ &= (427\ \mathrm{m/s})(0.0236\ \mathrm{m}^2)(0.00245)(0.19)(2310/8450)^{0.4363} \\ &= 0.00267\ \mathrm{m}^3/\mathrm{s\ rms} \end{aligned} \tag{10}$$

V_s is further attenuated 11 dB to 0.000753 m^3/s rms to account for the noise-reducing effect of a Whisper I trim versus a standard trim.

Transfer matrix characteristics are not known to the author for cage-plug valve types; therefore, the two-run approach described above is used. Figure 6 shows the predicted shaking forces of four areas of the piping. The maximum predicted shaking force between nodes 83 to 84 was the highest throughout the piping (840 N pk at 154 Hz). As expected the predicted shaking forces are well below guideline throughout the analysis frequency range.

Concluding Remarks

While there are similarities, there are also basic differences between acoustic analysis of centrifugal and reciprocating compressor piping. The fundamental approach of avoiding coincidence between excitation and resonant response is common to both types of piping systems. Pulsation sources, however, are treated very differently. The role of the centrifugal compressor in acoustic analysis is also very different from the role of the reciprocating compressor. For example, centrifugal compressors are modeled as specialized elements that connect the suction and discharge piping systems.

Pulsation sources in centrifugal compressor piping are flow generated and occur at all locations where the flow separates

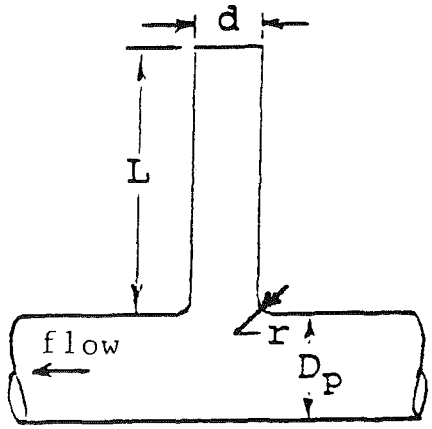

Fig. 7 Schematic of tee dimensions

---

[7] Beam modes refer to lateral vibration of the piping and do not include modes where pipe wall vibration varies around the circumference.

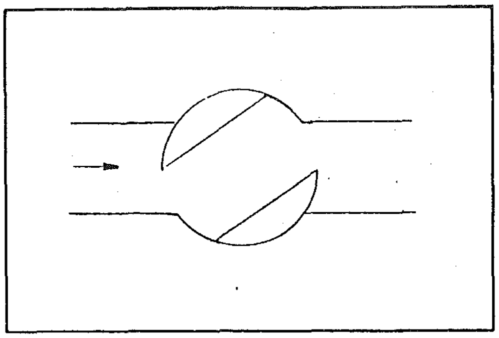

a) **Ball Valve**

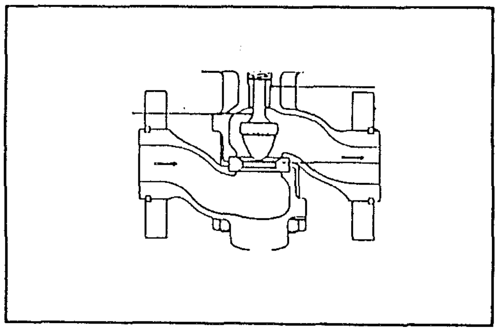

b) **Globe Valve (plug only)**

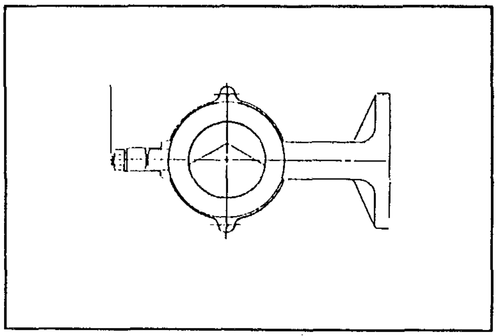

c) **V-ball Valve**

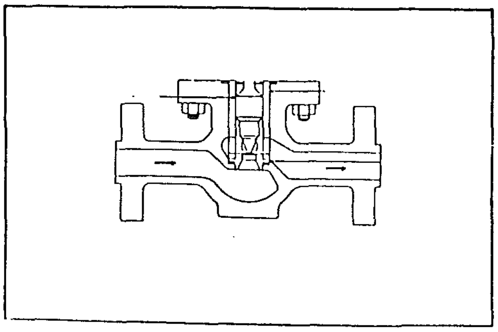

d) **Cage-plug Valve**

Fig. 8 Valve type diagrams

from the pipe wall. In practice, only tees and control valves generate significant pulsation. Flow-generated sources occur simultaneously; however, for design stage analysis each source is modeled individually. Further, and in contrast to reciprocating compressor piping, effective solutions to flow-generated pulsation deal directly with the pulsation source.

The source modeling methods described in this paper have been presented as manual calculation procedures so they may be used by all designers who have access to an acoustic simulator. To simplify and reduce design effort, each of the methods described has been incorporated into PULS, the acoustic simulator developed by NHRC and AGTD.

Finally, the influence of mechanical response on acoustic design, and vice versa, is very important. This is clearly demonstrated by the use of closely linked mechanical and acoustical guidelines. For example, the minimum mechanical natural frequency guideline and the acoustic shaking force guideline were developed in unison for design stage analysis based on designers' field and office experience.

Acknowledgments

The work presented here is typical of the acoustic analysis approach utilized by NOVA Corporation of Alberta when centrifugal compressor stations are designed and permission to publish is hereby acknowledged. The use of figures from references [1, 4–7] is greatly appreciated and permission to reproduce them is also hereby acknowledged.

References

1 Jungowski, W. M., Botros, K. K., and Studzinski, W., "Cylindrical Sidebranch as Tone Generator," *Journal of Sound and Vibration*, Vol. 131, 1989, pp. 265–285.

2 Bruggeman, X. X., "Flow-Induced Pulsations in Piping Systems," Doctoral Dissertation, Technische Universiteit Eindhoven, The Netherlands, 1987.

3 Botros, K. K., et al., "Pressure Pulsations at Orifice Plates and General Pipeline Flow—Acoustic Simulator," *1986 International Gas Research Conference*, 1986, pp. 243–256.

4 Jungowski, W. M., Botros, K. K., and Studzinski, W., "Generation and Transmission of Pressure Pulsations at the Ball Valve," *Noise-Con 87*, 1987, pp. 65–70.

5 Botros, K. K., Jungowski, W. M., and Studzinski W., "On the Transfer Matrix of Orifice Plate With Flow," *Noise-Con 88*, 1988, pp. 475–480.

6 Jungowski, W. M., et al., "Measuring the Transmission Characteristics of Pulsating Flows Through Orifice Plates and a Ball Valve," *Measuring and Metering of Unsteady Flows*, ASME FED-Vol. 40, pp. 21–32.

7 Botros, K. K., et al., "Influence of Flow in Pulsation Simulation of Gas Pipeline Installations," *IMEChE Seminar: Gas and Liquid Pulsations in Piping Systems Prediction and Control*, Dec. 1988, pp. 89–96.

8 *SGA-PCRC Seminar on Controlling the Effects of Pulsations and Fluid Transients in Industrial Plants*, presented by Southwest Research Institute, Oct. 1983, pp. 6–12.

9 Sparks, C. R., "Compressor Dynamic Response Theory for Pulsation and Surge in Centrifugal Compressors," Report No. 84-4, Southern Gas Association, Feb. 1984.

APPENDIX A1

Tee Source Frequency Calculation Procedure

Excitation Frequency Calculations. The Strouhal number when the first mode excites the first quarter wave resonant frequency of the sidebranch is calculated from the following formula:

$$St_m = 0.399(1-\bar{r})^{0.622}(\bar{d})^{0.316}(M)^{-0.083}(Re/10^6)^{-0.065} \quad \pm 5.35 \text{ percent} \qquad (11)$$

NHRC determined the empirical constants in the above equation by a least-squares fit of their test data [1].

The Strouhal number range for the second mode is calculated from the Strouhal number for the first mode as follows:

$$St_2 = 2\ (St_m) \qquad (12)$$

Harmonics of the first mode were also found to be present. The Strouhal number range for the third harmonic of the first mode is calculated as follows:

$$St_{1,3} = 3\ (St_m) \qquad (13)$$

The excitation frequency ranges are now determined from the definition for Strouhal number and the Strouhal numbers calculated above:

$$f_s = \text{St}\ U/d \tag{14}$$

Response Frequency Calculations. Uncertainty in the actual operating conditions in the sidebranch and in sidebranch length are compensated for by calculating a range in sidebranch response frequency corresponding to ± 10°C temperature and ± 5 percent length variation. A range in response frequency is calculated by taking the extremes obtained from varying temperature and sidebranch length in the following formula:

$$f_{n/4} = (0.88 \text{ to } 1)nc/4L \qquad n = 1, 3, 5 \ldots \tag{15}$$

APPENDIX A2

Tee Source Strength Calculation Procedure

The normalized branch end amplitude ratio $\overline{A}_B$), when the first mode excites the first quarter wave resonance of the sidebranch, is calculated from one of the following formulae:

$$\overline{A}_B = 0 < \text{Re} < 10^5 \tag{16}$$

$$\overline{A}_B = 0.412(1-\bar{r})^{2.272}(\bar{d})^{-2.113}(\text{M})^{0.922}(\text{Re}/10^6)^{0.629} \tag{17}$$

$$10^5 < \text{Re} < 16 \times 10^6$$

$$\overline{A}_B = 10\ \text{Re} < 16 \times 10^6 \tag{18}$$

As with the equation for St_m, the constants of Eq. (17) were determined by least-squares fit to measurement data [1]. Equation (17) should not be applied when any of the variables are outside the test data ranges[8]; Eq. (18) should be used instead to provide a generally conservative estimate for $\overline{A}_B$. The peak pulsation amplitude at the closed end of the sidebranch for first-mode excitation of the first quarter wave resonance is:

$$A_{B1,1} = \overline{A}_B \rho U^2/2 \tag{19}$$

Closed-end pulsation when the sidebranch third and higher quarter wavelength resonances are excited by the first mode is attenuated relative to $A_{B1,1}$ as follows:

$$A_{B1,n} = A_{B1,1} - (3\ \text{dB} \times (n-1)/2) \qquad n = 3, 5, 7 \ldots \tag{20}$$

Source strength for second mode excitation can vary from equalling to being reduced 30 dB when compared to first-mode excitation source strength. The experimental data available [1] for the second mode lead to the following conservative estimates for pulsation at the closed end of the sidebranch:

$$A_{B2,1} = A_{B1,1} \qquad \text{Re} < 16 \times 10^6;\ d = 1 \tag{21}$$

$$A_{B2,1} = A_{B1,1} - 20\ \text{dB} \qquad \text{Re} < 16 \times 10^6;\ d < 1 \tag{22}$$

APPENDIX A3

Control Valve Source Strength Calculation Procedure

Source strength is calculated from the following empirical formula:

$$V_s/(cS) = k_1 \text{M}(\Delta P/P_1)^{k_2} \tag{23}$$

The constants k_1 and k_2 for different valve types are:

Valve type	k_1	k_2
Ball, V-ball	0.04000	0.9768
Globe, cage plug	0.00245	0.4363

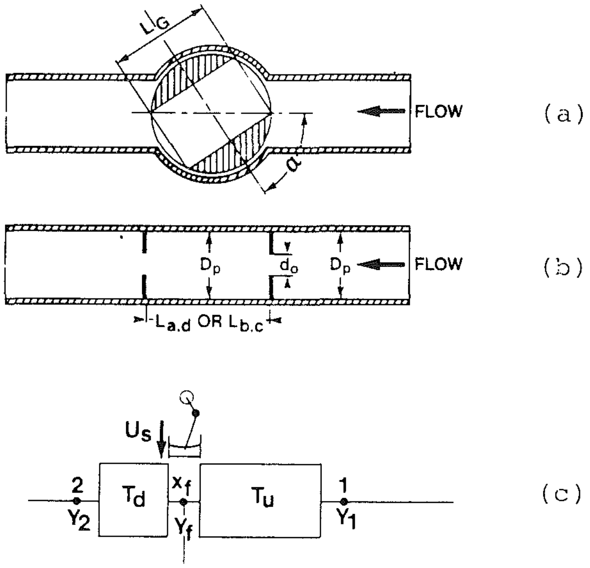

Fig. 9 Flow-acoustic model for ball valve [4]

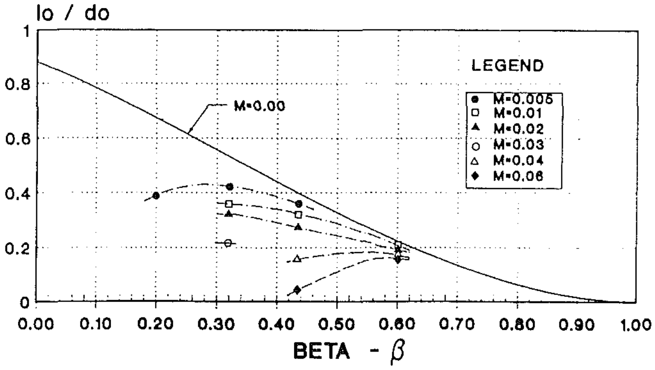

Fig. 10 Dimensionless acoustic equivalent length for orifice plate with flow [5]

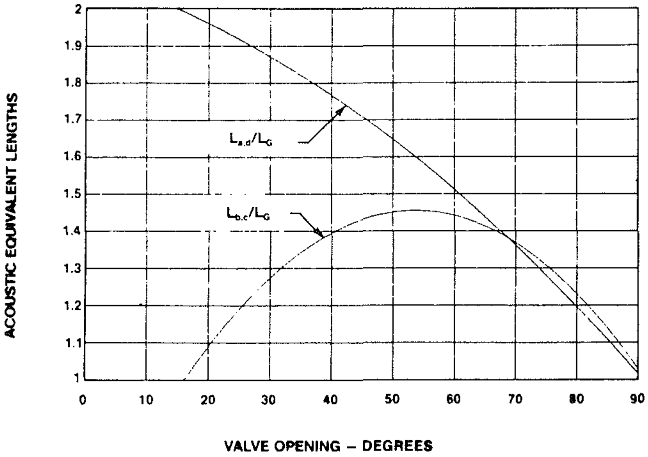

Fig. 11 Dimensionless acoustic equivalent lengths for the ball valve interior [6]

APPENDIX A4

Control Valve Source Modeling

Ball Valve Source Model. Figure 9 shows the ball valve (*a*), its equivalent acoustic representation using orifice and pipe models (*b*), and a schematic of the treatment of its source (*c*).

---

[8] Test data ranges include: $\bar{r} < 0.6$; $0.136 < \bar{d} < 1$; $\text{M} < 0.2$; $10^5 < \text{Re} < 16 \times 10^6$.

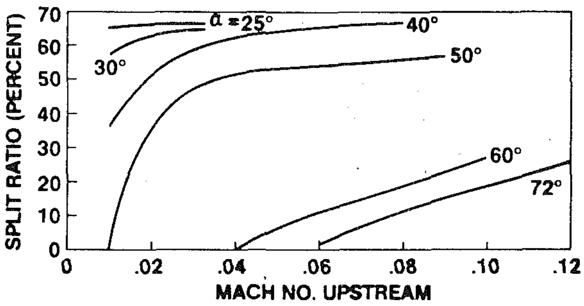

Fig. 12 Split ratio for various ball valve openings [4]

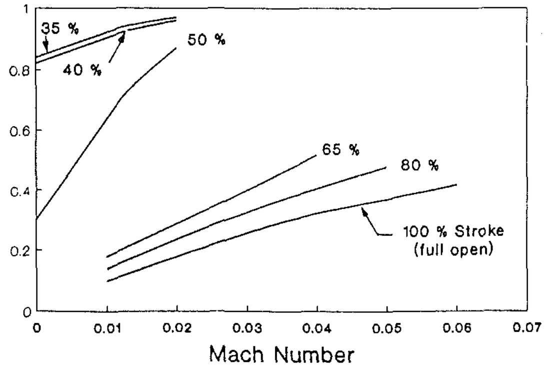

Fig. 13 Split ratio for various globe valve openings

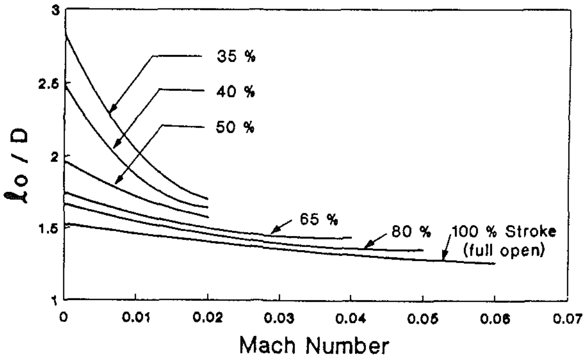

Fig. 14 Dimensionless acoustic equivalent length for globe valve with flow [7]

The overall transfer matrix is assembled by multiplying the transfer matrices for pipe, orifice, and pressure loss elements. To obtain the correct source distribution, the pressure loss components of the overall transfer matrix must be split into upstream[9] and downstream components. The upstream matrix also contains the equivalent pure acoustic transfer matrix of the ball valve.

The pure acoustic transfer matrix is composed of three pipe matrices as follows:

$$[Ta]=\begin{bmatrix} a_o & b_o \\ c_o & d_o \end{bmatrix}_1 \begin{bmatrix} a_{a,d} & b_{b,c} \\ c_{b,c} & d_{a,d} \end{bmatrix}_2 \begin{bmatrix} a_o & b_o \\ c_o & d_o \end{bmatrix}_3 \tag{24}$$

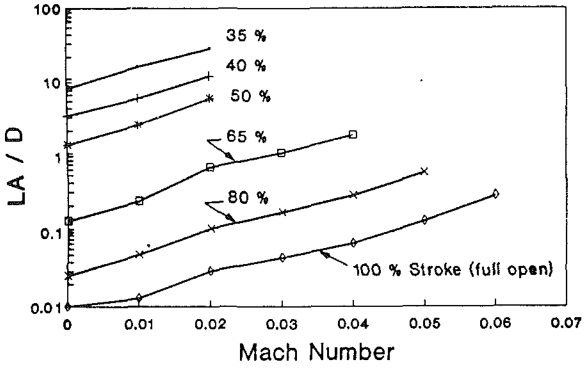

Fig. 15 Dimensionless acoustic parameter L_A for globe valve [7]

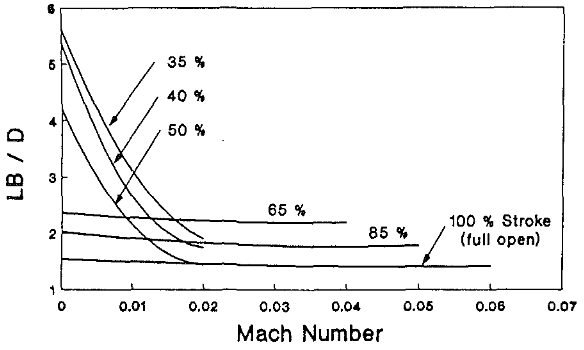

Fig. 16 Dimensionless acoustic parameter L_B for globe valve [7]

The equivalent pipe length for matrices 1 and 3 is obtained from Fig. 10 with $B = \sqrt{(A_c/A_p)}$ where A_c is the restricted valve area and A_p is the pipe cross-sectional area. Two equivalent pipe lengths $L_{a,d}$ and $L_{b,c}$ are obtained from Fig. 11 to make up the four poles of matrix 2 as shown in Eq. (24).

Upstream and downstream pressure loss matrices are proportioned according to the split ratio from Fig. 12.

The total upstream transfer matrix is obtained by multiplying the upstream pressure loss and pure acoustic transfer matrices. The multiplication order of the matrices depends on whether other sources are modeled upstream of the ball valve.

$$[T_u]=[T_p]_u[T_a] \text{ for downstream or no other sources} \tag{25}$$

$$[T_u]=[T_a][T_p]_u \text{ for upstream sources} \tag{26}$$

Globe Valve Source Model. The globe valve source must be inserted between upstream and downstream transfer matrices the same as shown for the ball valve in Fig. 9(*c*). However, the complicated geometry of the globe valve does not permit separation of the pure acoustic and pressure loss transfer matrices as can be done for the ball valve. Instead upstream and downstream transfer matrices have the same form, as follows:

$$[T]=\begin{bmatrix} A\cos(kl_o)+ikL_a & B+ikL_bZ_c \\ iD\sin(kl_o) & D\cos(kl_o)+ikL_a \\ Zc & \end{bmatrix} \tag{27}$$

The pressure loss components A, B, D in Eq. (27) are calculated with different pressure drops for the upstream versus downstream transfer matrices according to the split ratio from Fig. 13. Figures 14–16 give the equivalent lengths l_o, L_a, L_b, respectively.

---

[9] Upstream and downstream refer to the transfer matrix location in the direction of flow with respect to the valve source location.

M. Schneider
Werner Genest und Partner,
Ludwigshafen, Federal Republic of Germany

J. Mann
G&H Montage GmbH,
Ludwigshafen, Federal Republic of Germany

Noise Control Technology With Reference to Natural Gas Compressor Stations Under the Aspect of Investment Costs

For the conveyance and storage of natural gas, compressor stations are required where the installed power output varies mostly between 1 MW and 20 MW. The noise control measures involved to meet the environmental noise emission regulations in Europe will be presented. The most economical noise control techniques are described particularly for the intake and exhaust systems of gas turbines, the housing of such engines, and peripheral sound sources like gas coolers, oil coolers, and aboveground piping.

Description of Actual Situation

For natural gas distribution, basically two types of compressor station are required: one for conveyance of gas and another for underground storage.

In the majority of cases, gas turbines are used as drive units, with the aid of which the actual compressor (rotary compressor) is powered. A typical pressure relationship between the intake and discharge sides of the compressor is 40/60 bar. However, for the MEGAL pipeline, the relationship is approximately 60/80 bar.

For the storage of natural gas in natural underground reservoirs or artificially created caverns, a pressure of approximately 180 to 220 bar is necessary. To generate such a high pressure, piston compressors are required. As drive units for the piston compressors, low-speed gas engines are used.

These two different drive systems have had a decisive influence on noise control techniques, as gas engines and piston compressors emit sound primarily in the middle frequency ranges, whereas gas turbines and centrifugal compressors produce their maximum sound emission in the high-frequency range (see Fig. 1).

For sound insulation of the engine houses, two types of building construction are now favored: the solid concrete type and the prefabricated lightweight approach. Both types of engine house provide enough space to allow maintenance work to be carried out inside the building, thus affording protection against inclement weather (Fig. 2 and Fig. 3). The solid mode of construction is preferred when a high degree of sound insulation is required in the low-frequency range (e.g., for gas engines). Here, approximately 17.5 to 24-cm-thick walls composed of sand-lime brickwork, or approximately 18-cm-thick concrete walls with an airborne sound insulation index of >55 dB are used. Equivalent to the solid construction, a prefabricated modular double-shell lightweight construction with a TL greater than 50 dB can be chosen.

If a lightweight mode of construction is sufficient, sheet steel panels with sound absorption material on the inside are used. The insertion loss of such a structure can vary between 30 dB and 40 dB.

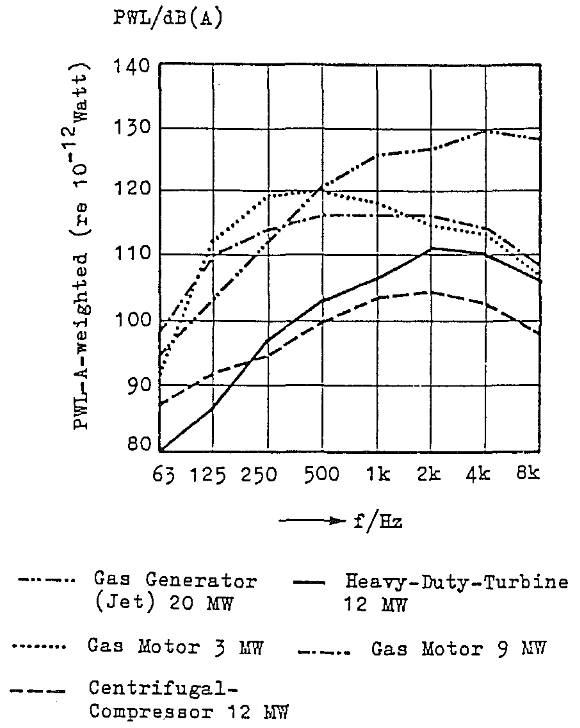

Fig. 1

Contributed by the International Gas Turbine Institute and presented at the 36th International Gas Turbine and Aeroengine Congress and Exposition, Orlando, Florida, June 3–6, 1991. Manuscript received at ASME Headquarters March 4, 1991. Paper No. 91-GT-237. Associate Technical Editor: L. A. Riekert.

Fig. 2 Engine house in solid construction

Fig. 3 Engine house in lightweight construction

The requirement of 40 dB (A), frequently set by authorities in the Federal Republic of Germany as a reference value of night-time emission at the site of the nearest adjacent property (with a typical distance between compressor station and point of emission of 400 m), can only be realized if all sound sources are optimally balanced against each other. To achieve this, the issue of a proper sound level balance in the planning stage of the station is indispensable (Fig. 4).

The economy of the noise control measures is then given if all peripheral sound sources, such as engine coolers, natural gas coolers, and piping, which must all necessarily be located in the open, are designed in such a way that standard products can be used as far as possible (Fig. 5).

According to VDI 3734 regulation (equivalent to ASME), a sound power of 82–84 dB (A) is achievable by standard coolers of the low-noise type with a drive power of 35 kW per fan (diameter approximately 4 m). Quieter types are only possible if secondary noise control measures are incorporated, e.g., acoustic enclosures.

The high sound power (see Fig. 6) generated by an untreated gas turbine or gas engine on the exhaust side or air-intake side must be reduced by means of silencers. Admittedly, it is technically possible to achieve extraordinarily high sound attenuation by incorporating appropriate equipment design features, but this involves substantial pressure losses, which adversely affect performance characteristics and lead to increased fuel costs.

Conclusions

The following emission sound power levels have been found to be technically and economically favorable:

Exhaust opening: PWL = 90 dB (A)

Intake side: PWL = 85 dB (A)

This results in a necessary insertion loss for the turbine silencers of approximately 45–55 dB for the exhaust and intake side.

This means that silencer lengths of 3–4 m are necessary on the intake side and 5–6 m on the exhaust side, at which dimensions the flow velocity at the silencer outlet may amount to approximately 30 m/s. In the intake silencer, values of about 20 m/s are sensible. The pressure loss for such silencers amounts to approximately 200 to 300 Pa.

As far as a forecast of the emission values at a point situated approximately 400 m away is concerned, this means that the

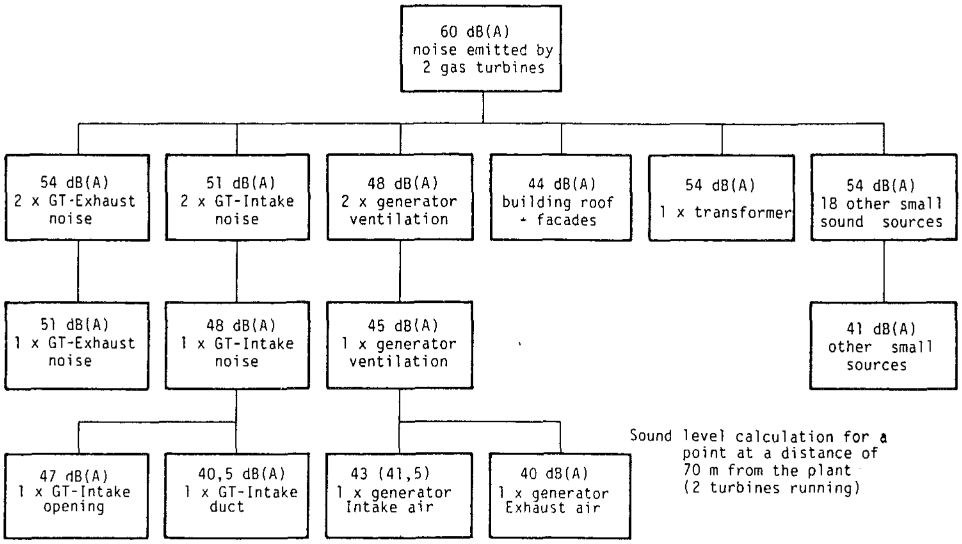

Fig. 4 Typical sound emission analysis for a gas turbine plant with two 60 MW turbines

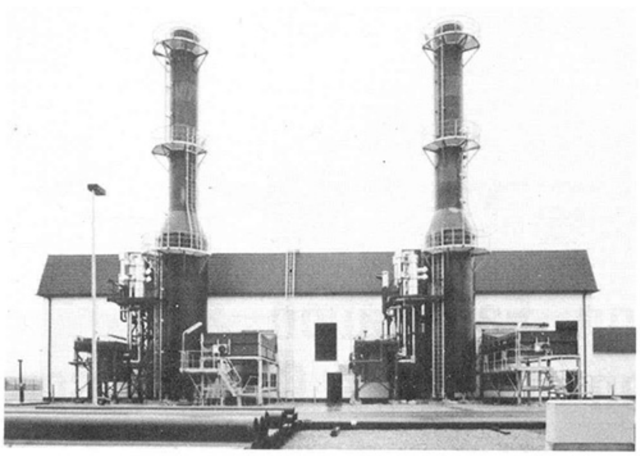

Fig. 5 Gas compressor station with peripheral sound sources in the open

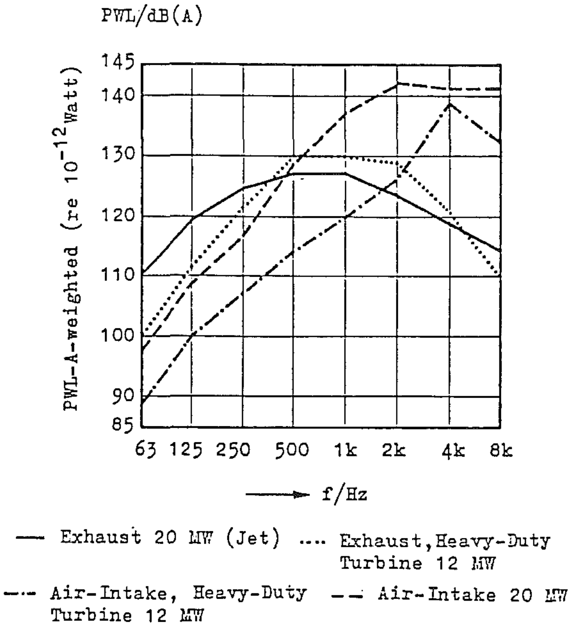

Fig. 6

sound power of the previously mentioned emitters (e.g., air coolers, gas coolers, aboveground piping, and silencer openings of 90 or 85 dB (A)) is to be regarded as given, and to calculate the overall level one must concentrate on the remaining emitters. These are, however, only the machine houses with their sound-insulated structural components: walls, roof, doors, and ventilation openings.

Finally, reference is made to the following statement of overall sound power, worked out for a typical compressor station. The statement was prepared in accordance with the VDI-regulation 2714. The station comprises, in its present state of development, two compressor units, each of 20 MW, and is designed for an extension up to four operational engines and one reserve unit.

Table 1

Structural component	Emission PWL/dB(A) Alt.1/Alt.2		Propagation loss $\Sigma\Delta L$/dB	Emission SPL/dB(A) Alt.1/Alt.2	
Engine house 1	80	92	60	20	32
Engine house 2	80	92	60	20	32
Engine house 3	80	92	60	20	32
Engine house 4	80	92	60	20	32
Exhaust opening 1	90	80	65	25	15
Exhaust opening 2	90	80	65	25	15
Exhaust opening 3	90	80	65	25	15
Exhaust opening 4	90	80	65	25	15
Filter house					
Intake opening 1	85	75	61	24	14
Intake opening 2	85	75	61	24	14
Intake opening 3	85	75	61	24	14
Intake opening 4	85	75	61	24	14
Engine coolers 1	88	78	62	26	16
Engine coolers 2	88	78	62	26	16
Engine coolers 3	88	78	62	26	16
Engine coolers 4	88	78	62	26	16
Gas coolers (32 fans)	103	88	67	36	21
Piping (acoustically insulated)	90	90	56	34	34
Total emission level:				39.9	39.7
				≤40 dB(A)	

Table 2 Cost comparison for noise control measures per unit

	Alt. 1	Alt. 2
Exhaust silencer (approximately 5 m for Alt. 1 and 10 m for Alt. 2)	US $ 115,000	250,000
Intake silencer (3 m or 6 m long)	US $ 50,000	100,000
Engine house (solid construction or lightweight construction, approximately TL 50 dB)	US $ 600,000	- - - -
Engine house (lightweight construction approximately TL 38 dB)	US $ - - - -	360,000
Gas cooler with additional silencer	US $ - - - -	20,000
	US $ 765,000	1,190,000

Under Alternative 1 (Table 1) the solution is listed with reasonable silencer lengths and no secondary noise control measures on other sound sources. Alternative 2 shows the solution with the cheap lightweight engine house but necessary additional acoustical treatments from other sources.

As can be seen in Table 1, the noises radiated by the engine houses are virtually insignificant for Alternative 1 when compared with the group exhaust gas, intake system, gas coolers, engine coolers, and piping.

Summary

The work reported shows that the most economical method of noise control on gas compressor stations is to erect the engine house in a solid concrete or masonry construction or to choose the highly efficient lightweight construction with an attenuation of ≥50 dB.

This allows the user to select for the remaining sound sources the available standard products such as air coolers, oil coolers, etc., and one does not need to spend extra money for secondary noise control measures on those. Only the turbine intake and exhaust must be provided with silencers of suitable length.

E. Humphries
Manager, Facilities Design.

D. Schulz
Senior Engineer, Pipeline Services,
Stone and Webster Engineering Co.
Boston, MA 02107

J. Binek
President,
SPL Control, Inc.,
Cambridge, Ontario, Canada

The Design, Fabrication, and Installation of a Quiet Compressor Station

Stringent environmental constraints are usually associated with or applied to the siting and installation of new pipeline facilities. This has resulted in the dedication of a significant portion of the design effort and ultimate cost of the facility to the mitigation of these environmental concerns. This paper describes how a compressor station can be designed and built such that stringent silencing requirements can be satisfied. The paper also references specific aspects of design that were successfully applied to the Parkway Compressor Station, Canada.

Introduction

The hydraulic design of oil and gas transmission systems determines the locations at which compression facilities need to be sited in order to ensure that design objectives are satisfied in a cost-effective manner. Although it is in the best interests of pipeline companies and the general public at large to avoid each other as much as possible, it is inevitable that occasionally compression facilities must be located close to existing populated regions or at locations in which urban development will eventually occur.

One of the issues that invariably causes heated debate concerns the subject of noise generated by the proposed compression facility. People can easily relate to this and most want their voices to be heard. Ironically, this is one issue over which the pipeline company has a great deal of control. Compression facilities can be designed and constructed to meet very stringent silencing requirements. While the costs of comparative silence may be high initially, the investment is invariably worthwhile to foster good community relations from the outset.

Types of Noise

The types of noise generated by compression facilities can generally be divided into the four groups listed below. Each type of noise source may require different treatments in order to be attenuated to levels acceptable to the local community.

Continuous Audible Noise Source. This will consist of noise at frequencies above the lower threshold of hearing, as shown in Fig. 1. Such noise sources will typically be generated by turbomachinery, pumps, fans, valves, and piping. Some of these noise sources will be more dominant than others; however, all need to be considered during the overall station analysis.

Continuous Subaudible Noise Source. This consists of noise at frequencies below the lower threshold of hearing, also shown as Fig. 1 [1]. While subaudible noise, as its name implies, cannot be heard directly, the indirect effects can be profoundly disturbing to occupants of residences in the vicinity of a low-frequency subaudible noise source. Low-frequency noise, unless attenuated at the source, will propagate over a wide area and will manifest itself by causing structures such as residential houses to vibrate. This in turn causes windows and pictures to rattle and light objects such as crockery, cutlery, and ornaments to be set vibrating.

Occasional Audible Noise Sources. Such noise sources will be associated with auxiliary equipment such as emergency power generation units. These will be gas engine or gas turbine driven units, which will start automatically when utility power fails. They will also typically be started and operated once per month as a reliability check. Other noise sources will be air compressors and maintenance equipment used at the station.

Impulsive Noise Source. Such noise sources are very loud but occur infrequently and are of short duration. They are

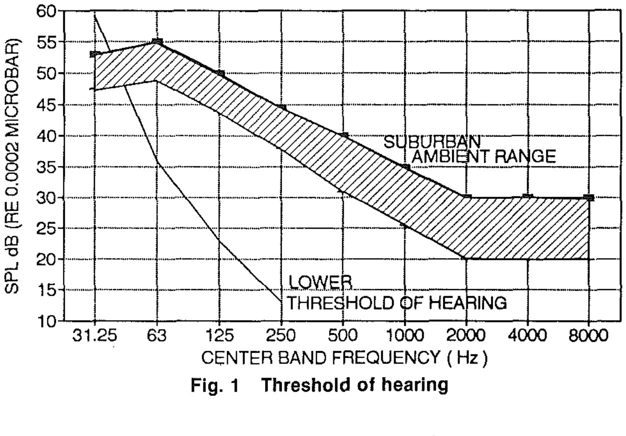

Fig. 1 Threshold of hearing

Contributed by the International Gas Turbine Institute and presented at the 36th International Gas Turbine and Aeroengine Congress and Exposition, Orlando, Florida, June 3-6, 1991. Manuscript received at ASME Headquarters March 4, 1991. Paper No. 91-GT-239. Associate Technical Editor: L. A. Riekert.

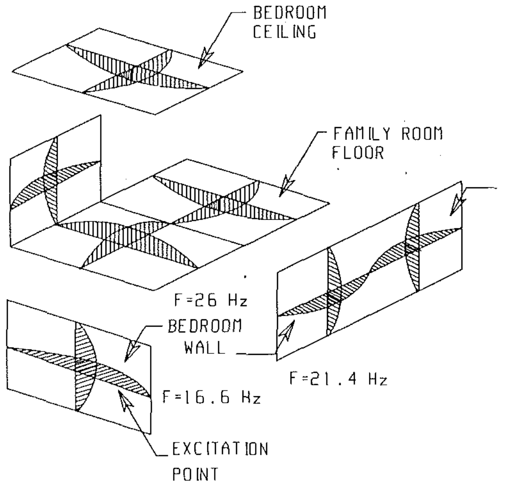

Fig. 2 Low-frequency mode shapes

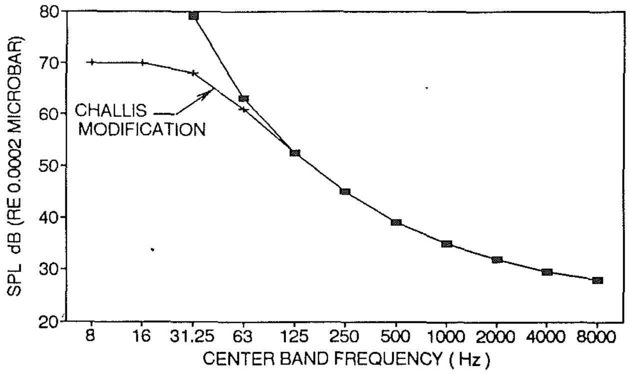

Fig. 3 ISO NR35 plus challis modification

caused by venting pressurized piping to atmosphere. This may involve venting of small volumes of gas such as from unit piping or relatively large volumes from station piping. The duration is usually less than two minutes. This will result from manual venting to allow repair or modifications to be carried out, accidental venting as a result of instrumentation malfunction, or deliberate venting as a safety precaution to protect the installation from overpressure due to an equipment or control system malfunction.

Design Criteria

The design criteria established for the acoustic design of a compressor station will depend on a number of factors. The most important limits are the requirements set by the Department of the Environment, which has jurisdiction in the area. This may take the form of a fenceline noise level, of more commonly, the noise level at the closest residence. Typically this may be "ambient levels or 40 dBA, whichever is greater." The ability of a facility to meet this goal will depend upon the nature of the noise sources and distance from the noise sources to the nearest residence. It will also be influenced by terrain, vegetation, and prevailing winds.

Consideration of Low-Frequency Noise. One aspect of noise control, which is overlooked by many regulatory authorities, can result in the degradation of the quality of life of local residents, even though the design requirements of 40 dBA may have been achieved. This concerns the generation of low-frequency noise present in some types of gas turbine. This needs to be recognized by the station designer and dealt with as necessary. In general, this type of problem will require design criteria more stringent than those based upon DOE requirements alone. The risk associated with ignoring such an unfortunate machinery characteristic has led, in the past, to expensive and disruptive retrofits being installed some time after the facility has been in operation.

Since residential structures have many components that are readily excited by noise and that can be coupled, they respond as complex vibrating systems. A person inside the house can sense the impingement of low-frequency noise on the external surface of the house by means of the following phenomena: vibrations of the primary components of the building such as the floors, walls, and windows; the rattling of objects such as dishes, ornaments, and shelves, which are set in motion by the vibration of the primary components and in the extreme case; damage to the secondary structure such as plaster and tile and/or furnishings.

The problem occurs due to the physical size and shape of walls and floor joists in residences. Figure 2 shows sample mode shapes and resonant frequencies of a single-story test house obtained by carrying out a frequency sweep while imposing a constant input vibratory force at a single point on the structure [2]. Note that the resonant frequencies of various parts of the structure range from 16.6 to 26 Hz, which lie well below the threshold of hearing, as shown in Fig. 1.

Discussion of Criteria. The design criteria for the recently constructed Parkway Compressor Station [3] were initially established as an NR35 curve at 100 m from the compressor building. However, because of the proximity of existing houses and plans for future residential development, the curve was modified by reducing the maximum permitted sound pressure levels at frequencies below 125 Hz; see Fig. 3. This modification was suggested by Challis [4] in 1978 and was adopted following an intensive literature search of cases where residents in the vicinity of gas turbine driven equipment had complained about housing vibration. Some of these residents lived over 1 km away from the low-frequency noise source. In most instances the owner of the equipment eventually carried out modifications aimed at reducing the level of low-frequency noise from the plant.

Hoover [5] investigated the sound levels of seven gas turbines, four of which had noise complaints, and three of which did not. This study indicated a maximum allowable sound level of 68 dB in the 31.5 Hz band, to avoid complaints from the nearest neighbor.

Other investigators have reached similar conclusions. Hessler [6] recommends a maximum sound level of 65 dB at 31.5 Hz. He also presents a curve of probability of complaints that increases linearly from zero percent at 60 dB, 20 percent at 65 dB, to 100 percent at 80 dB.

The lowest criterion used is that reported by Newman [7] of British Gas of 60 dB at 31.5 Hz. This criterion was arrived at as a result of their own experiences with compressor stations in rural areas.

Recommendations. A summary of gas turbine noise criteria proposed by the various investigators is given in Table 1. The recommended levels for "no complaints" range from 60 to 68 dBA at the nearest residence. As a result of these studies, the low-frequency modification to the NR-35 curve recommended by Challis, shown in Fig. 3, was selected for the purchase of the gas turbine. By specifying 68 dB at 31.5 Hz at 100 m, the resulting sound pressure level at the nearest planned residence, approximately 260 m NE of the compressor building, would be 60 dB. This level is compatible with the low-frequency criteria suggested by Hessler and Newman for zero complaints. It also provides a design margin for future station expansion.

Impulsive Noise. Because of the short duration and infre-

Table 1 Comparison of low-frequency sound level criteria: recommendations for gas turbines

REFERENCE	CRITERIA AT RESIDENCE		COMMENTS
	16 Hz	31.5 Hz	
Challis	70 dBA	68 dBA	
Hoover		65 dBA	
Hessler		65 dBA	60 dBA for zero complaints
Newman		60 dBA	

Table 2 Community noise measurement; octave band center frequencies in Hz

dBA	31	63	125	250	500	1K	2K	4K	8K
36	56	48	42	36	34	26	18	15	14

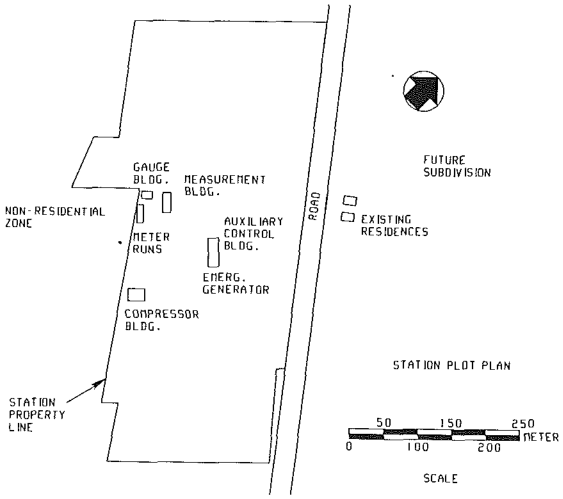

Fig. 4 Compressor station plot plan

quent occurrence of impulsive noise, the allowable pressure levels were set at 85 dB(A) at the property line.

Establishing the Baseline

In order to evaluate the level of noise reduction required for the facility accurately, it was important to establish the background noise levels that existed at the site prior to compressor station construction and operation. Because the ambient noise levels may vary during the year, two separate noise surveys were performed at the Parkway Station site, one in early fall and one during the winter.

The survey identified a representative set of sound receptor locations inside the station property and other potentially sensitive areas outside the property. At each location a set of sound pressure levels was sampled using a calibrated precision octave band analyzer for octave bands ranging from 31.5 Hz through 8000 Hz. The area experiences some carryover noise from nearby aircraft and vehicular traffic and therefore sound pressure levels were measured only when such foreign noise sources were absent. An "A" weighting was applied to the spectrum data and the resulting ambient noise level in dBA was established. The ambient air temperature, wind speed, and direction were noted during each survey. Table 2 presents a typical result of the survey taken at the perimeter of the station property line, adjacent to an existing residence.

Station Layout

The station layout will directly affect the acoustic design of the overall facility. To a certain extent the deployment of equipment will be determined by the location of the mainline piping, station boundaries, future expansion considerations, spacing between facilities, safety, and access for construction and operation. Wherever possible it is prudent to separate the sources of continuous noise from the residences by as great a distance as possible. In addition appropriate orientation of equipment within the compressor building will result in reduced far field noise levels due to the effects of building screening; see Fig. 4.

Sources of Noise

There are many sources of noise in a compressor station. The major noise sources of gas turbine intake and exhaust will always require attenuation. The level of attenuation will depend on the overall station design criteria and thus the noise level can be controlled to the desired values through the use of individual equipment specifications. The gas turbine casing noise is quite often attenuated through the use of an acoustic enclosure. This is usually large enough for personnel to enter and work on the unit. It also contains ancillary equipment such as enclosure cooling, fire and gas detection, fire protection equipment, etc.

Other equipment is not usually fitted with acoustic treatment by the vendor but their level can be significant. Typically the compressor casing, compressor and gas turbine lube oil consoles, oil cooler fans, building ventilation system, recycle control valves, and exposed gas piping will all contribute to the noise level experienced within the compressor building. In the quiet station all such sources of noise must be considered and this is usually resolved by making a simple choice. Either all noise sources are treated individually or they are treated collectively through the use of the effects of building attenuation.

With the exception of acoustic wrapping of exposed piping, the problem associated with individual acoustic treatment is threefold; (*a*) It hinders routine maintenance, (*b*) inhibits ventilation, and (*c*) introduces safety-related problems. One advantage of this approach is that the compressor building need not receive special attention and can be regarded as being acoustically transparent.

The approach more commonly taken is to treat all such noise sources collectively by acoustically treating the compressor building. However, such treatment is expensive and it also introduces a significant design problem that in turn must be solved. This design problem concerns the ability of the building design to satisfy the requirements of NFPA 68A-Guide for Explosion Venting, and is dealt with later in this paper.

Figures 5, 6, and 7 show vendor data for the aeroderivative gas turbine proposed for the Parkway installation. Note that vendor data shown in Fig. 6 for the gas turbine exhaust are cut off at 31.5 Hz. Figure 8 shows data measured at two separate compressor stations of gas compressors similar to the units installed at Parkway. Measurements were taken 1 m from the casing.

Station Yard Equipment. Station yard equipment will all be treated individually by specification and consideration during equipment selection. Major noise sources are blowdown vents, regulator valves, meter runs, and gas aftercoolers.

Piping blowdown vent silencing is selected from a wide range of standard units available from several manufacturers.

Gas aftercoolers will be customized to meet the process and noise requirements. In addition, a stringent acoustic specifi-

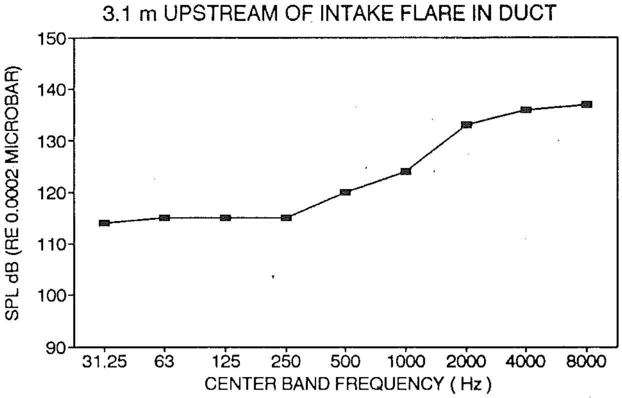

Fig. 5 Gas generator inlet

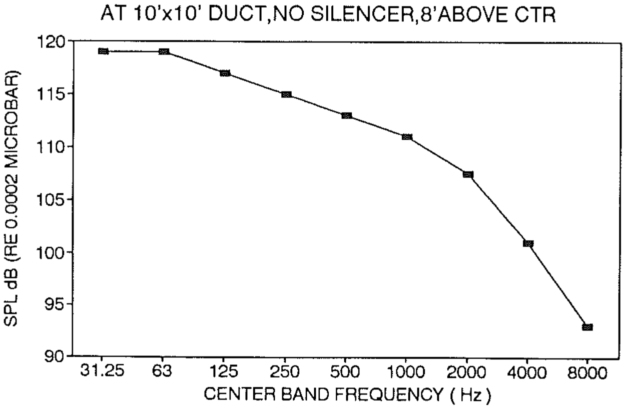

Fig. 6 Gas turbine exhaust

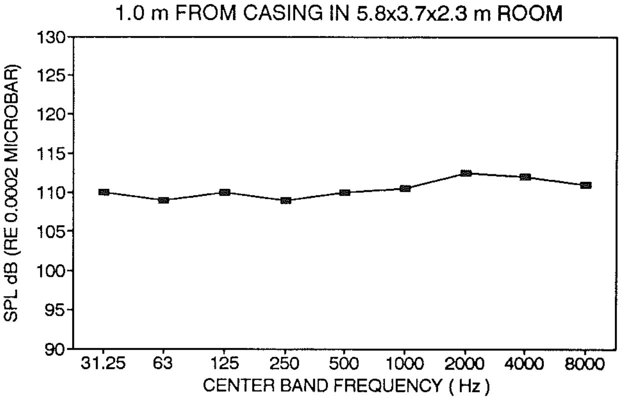

Fig. 7 Gas generator casing

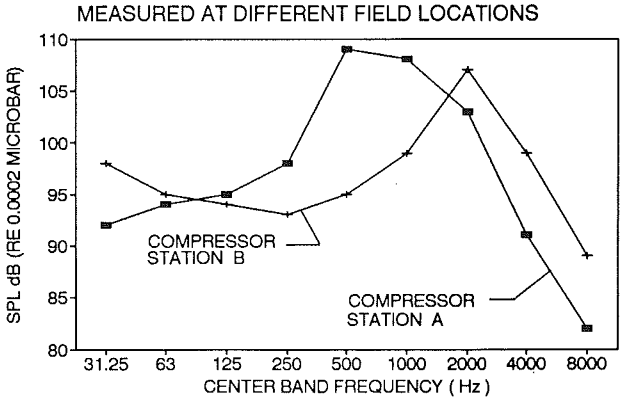

Fig. 8 Typical compressor noise

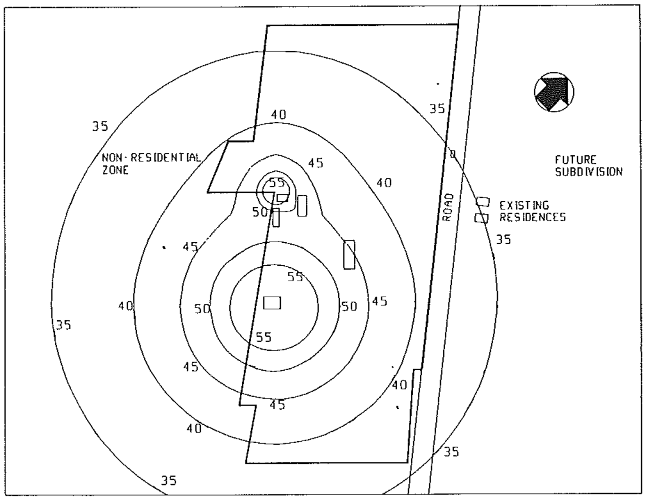

Fig. 9 SPL contour plot

cation will require the use of low-speed fans. These would be fitted with the maximum practical number of blades and would be designed with a good aerodynamic profile. Two-speed or variable-speed motors may also be considered to take full advantage of low ambient temperatures in order to reduce fan speeds to the minimum values possible while satisfying the process requirement.

Yard piping will be buried, but meter runs may have to be housed in an enclosure or treated with acoustic wrapping.

Calculation of Noise Level at Receptors

Once the design criteria have been established, it is possible to calculate the steady-state noise level that would be experienced at the existing and proposed residences. This should be carried out for both audible and subaudible frequencies. It should be recognized that several factors need to be taken into account during the calculations. These include consideration of the prevailing wind direction, effect of future additions at the station site, expected accuracy of calculations, background noise levels, and degree of conservatism required. The results of the calculations will verify that the criterion selected is appropriate or will indicate that further modification to the criterion is required.

Audible Noise Levels at Receptors. These are calculated by summing the effects of all significant individual noise sources at a specific location. In general, attenuation from the noise source to the receptor is calculated using hemispherical spreading and the effect of air absorption. However, noise sources originating inside the compressor building require special treatment.

It is first necessary to calculate the resultant sound pressure level at the inside surface of the building wall. The equivalent sound pressure level outside the building wall can then be calculated by deducting the attenuation due to the transmission loss through the wall section. Once this value has been established, the noise level at the receptors can be determined. The results can be presented either in a tabular form at specific locations or in the form of a contour plot; see Fig. 9.

Subaudible Low-Frequency Noise at Receptors. If the gas turbine selected for a particular project is suspected of producing low-frequency noise, or exhaust rumble as it is sometimes called, it is essential to obtain accurate data in order that a successful attenuation design may be carried out. One method of obtaining these data is to take field measurements at a similar gas turbine driven compressor station, if such a facility exists.

Measurements were carried out during design of the Parkway

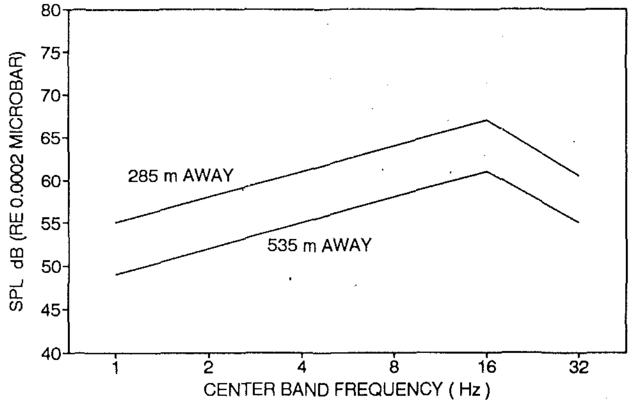

Fig. 10 Far field SPL—Low Frequency

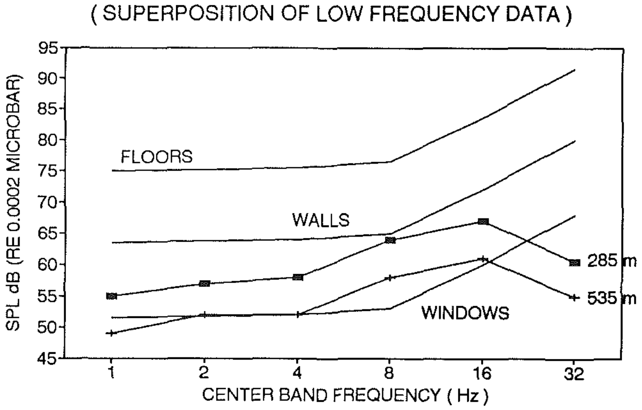

Fig. 11 House element response

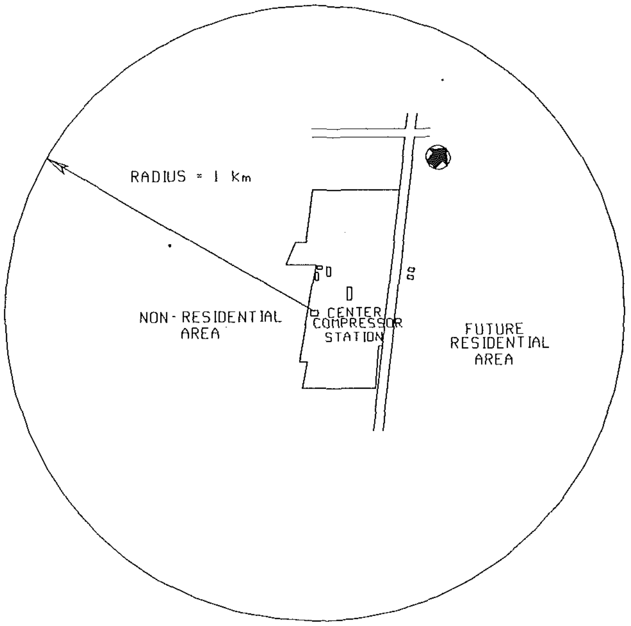

Fig. 12 Residential noise impact plan

project where low-frequency noise was anticipated. The exhaust silencer installed at the measured station was of a conventional style attenuating middle and high frequencies, and was judged to be of limited effect at very low frequencies.

Measurements were taken at 285 and 535 m away using 1/3 octave filters. The low-frequency results are shown in Fig. 10. Note high levels at the frequency band centered at 16 Hz. Using the hemispherical dispersion assumption, it was calculated that 78 dB at 100 m distance at the 16 Hz band could be expected. This level exceeded the design criterion selected for the Parkway Compressor Station by 10 dB.

In order to understand the significance of these observations, the results have been superimposed on to the house element response curves shown in Fig. 11. These response curves labeled "floors," "walls," and "windows" show the outside sound pressure levels required to produce perceptible vibrations over a range of frequencies. They were obtained from both measured and observed data [8].

From the interaction of the observed data with the response curves, the affected area of residences that would potentially be impacted if low-frequency attenuation was not incorporated into the design philosophy is shown in Fig. 12. It is estimated that this could be as high as 1000 dwellings within a 1 km radius of the compressor building. It was apparent from these results that considerable low-frequency attenuation would definitely be required. This was calculated to be 24 dB at 31.5 Hz.

Compressor Building Construction

Design of the compressor building presents many challenges as it must simultaneously address many requirements. The most important requirement is a high acoustic transmission loss across the walls and roof. The building also features ventilation openings, man doors, and equipment doors, which need to be carefully considered. High sound attenuation is obtained by adding mass to the building walls and roof. Construction materials that would readily accomplish this are concrete and masonry, however, the use of such materials in North America creates a conflict with the intent of NFPA 68A, "Guide for Explosion Venting." The requirement of NFPA 68A is to construct a building such that automatic venting would occur in the event of an internal explosion. The intent of this is to limit the pressure rise within the building such that the support structure would not collapse. A practical way to achieve this is to attach the wall panels to the building structure with hinges such that the panels would swing outward in the event of an explosion within the building.

Reverberation Effects

The propagation of noise produced outdoors may easily be determined through the use of distance attenuation calculations. However, noise produced indoors must consider the absorption and reflection of acoustic energy off surfaces such as floors, walls, and ceilings. When this occurs, the reflected noise reinforces itself as it bounces around and continuously crosses its own path. This effect is called reverberation, and the resulting noise levels cannot be treated in the same manner as far field noise propagation.

Sound absorption occurs when acoustic pressure waves get trapped within the porous surface of a material and are unable fully to escape. Generally the denser the material and the more porous the surface of the material, the greater the sound absorption. Inner reflective building surfaces will result in higher overall far field noise levels as a result of reverberation, when compared to far field noise from a similar unenclosed source radiating outdoors.

In order to calculate the effect of reverberation indoors, the individual absorption of each surface component must first be identified. Absorption properties are determined at each center band frequency and are represented by a coefficient (alpha) having a value between 0 (no absorption) and 1.0 (complete absorption). After collecting the data for each inner surface, they are then combined into an average sound absorption coefficient by summing the product of each surfaces' alpha by its area and then dividing by the total surface area of the room.

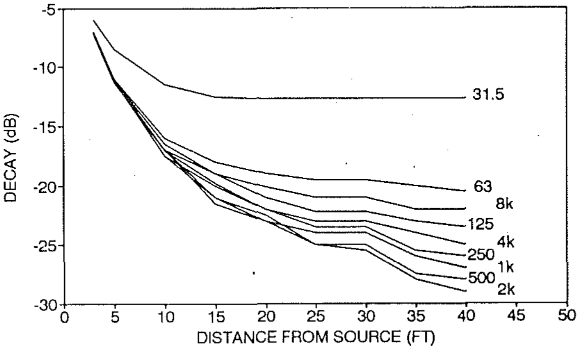

Fig. 13 Sound reverberation effects

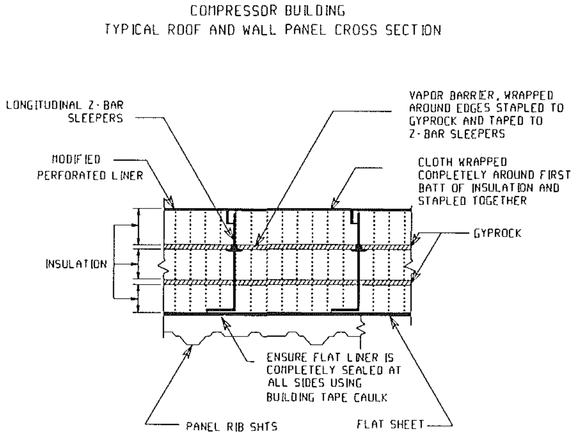

Fig. 14 Typical panel cross section

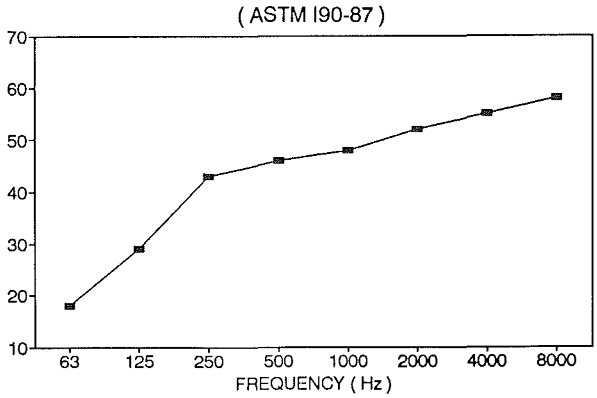

Fig. 15 Transmission loss test: ASTM I90-87

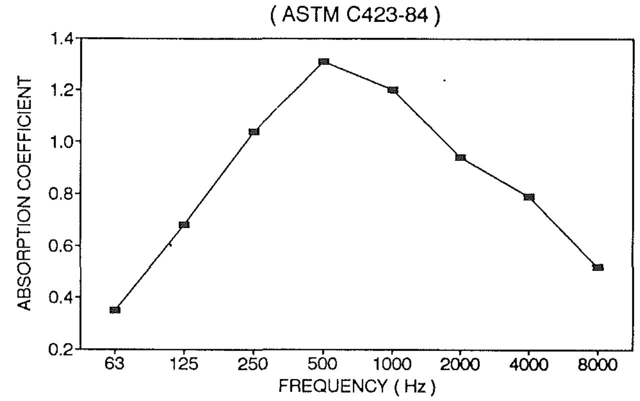

Fig. 16 Sound absorption test, ASTM C423-84

The average sound absorption for the room is then used to calculate the room constant *R*, which may be used directly to determine the sound pressure level at the inner surface of the building walls. Figure 13 shows the effect of sound attenuation with distance within a compressor building that features good absorption characteristics.

Building Wall Design and Construction

In order to achieve a high acoustic transmission loss at the Parkway Station, a special wall section was designed using a multiple layer approach. This takes advantage of the impedance mismatch offered to the sound propagating across various density media. The wall consists of three fiberglass layers separated by gyprock sheets. The inside surface of the wall consists of a perforated steel plate, allowing for absorption as well as adding the surface weight of the wall. The average surface weight is 73 kg/m^2; see Fig. 14. The acoustic performance of a section of wall was tested at the National Research Council Canada.

The sound transmission test was conducted in accordance with the requirements of ASTM E90-87, "Standard Method for Laboratory Measurement of Airborne Sound Transmission Loss of Building Partitions," and of ISO 140/III 1978(E), "Laboratory Measurement of Airborne Sound Insulation of Building Elements." The results are shown in Fig. 15.

The sound absorption test was conducted in accordance with the requirements of ASTM C423-84. The results are shown in Fig. 16. The entire building at Parkway, including the roof, utilized the test panel configuration. A special method of erection was developed and consisted of the following steps:

(*a*) Erection of the structural skeleton including horizontal girts.
(*b*) Erection of the various layers starting with perforated plates.
(*c*) Erection of the last layer, which consists of a decorative cladding.

Throughout construction, the presence of an acoustical engineer was required to resolve interface problems. Meticulous care and attention were given to proper caulking of all the joints and to ensure that penetrating items were not mechanically connected to the walls.

Due to the pressure relief requirement, most of the vertical walls consist of hinged welded frames. These frames are hinged in a vertical plane, and will swing open under overpressure conditions. To facilitate this action, teflon runners are installed at the bottom part of each frame. The frames are double gasketed against the building structure and are constructed using tested panel configurations. The panels are secured in place with specially designed latches, which will release at a specified internal building pressure.

Acoustic Protection of the Building Openings

All access and building ventilation openings were acoustically protected so as not to degrade the acoustic integrity of the building walls significantly.

Building Ventilation The ventilation exhaust system consists of two vane axial fans mounted inside the building, close to the roof. The fans collect air via circular ducts, also located under the roof. The discharge is through a silencer and acoustically lined weather hoods; see Fig. 17. The inlet ventilation air is admitted to the building through specially designed silencers in the form of a long folded passage containing two right angle bends; see Fig. 18.

Equipment Access Door. Conventional equipment access doors are of the overhead roll-up type, large enough to allow

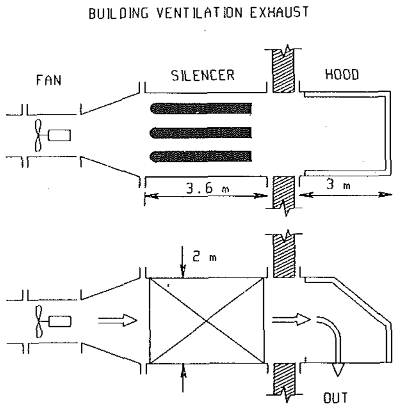

Fig. 17 Building ventilation exhaust

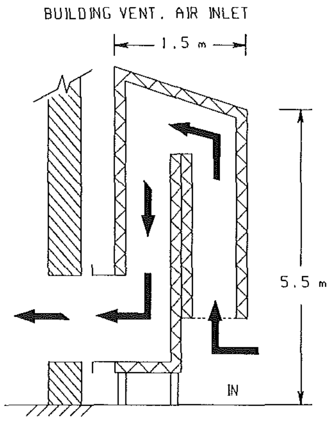

Fig. 18 Building ventilation inlet

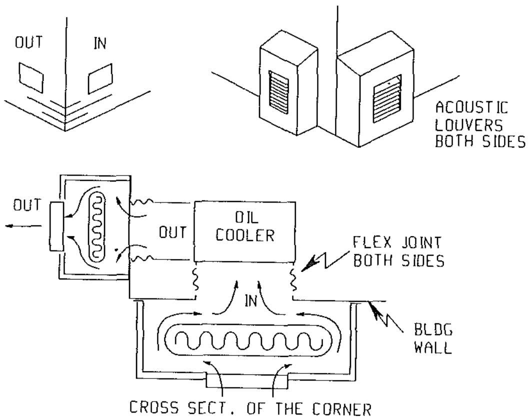

Fig. 19 Silencer configuration

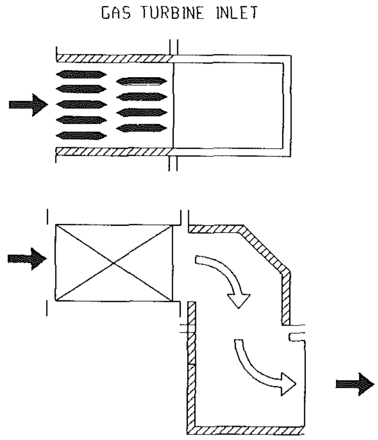

Fig. 20 Gas turbine inlet

passage of heavy maintenance vehicles. This type of door is virtually acoustically transparent and would not be appropriate for a quiet station. At Parkway the equipment access doors were purchased from a manufacturer of acoustically rated doors. The doors are rated at STC 51, which is close to the rating of the building walls and roof.

Man Access Doors. The man doors also feature high acoustic transmission loss and were manufactured from 5 mm steel plate lined with acoustic media protected with perforated plates. The man doors were supplied with double-gasketed steel frames, which were then fitted to the building support structure.

Lube Oil Cooler. The lube oil cooler consists of an oil-to-air heat exchanger and propeller fan driven by a variable speed electric motor. The heat exchanger is located at one of the corners of the building. The inlet and exhaust openings were acoustically protected with specially designed silencers featuring high attenuation and low pressure drop. The configuration of these silencers is shown in Fig. 19.

Acoustic Design of Gas Turbine Package

Gas Turbine Inlet. The acoustic energy radiated from a typical gas turbine inlet is concentrated in the last three octave bands; see Fig. 5. The noise spectrum consists of a dominant blade passing frequency and its harmonics. The attenuation of noise due to the inlet is achieved by means of an acoustically lined plenum chamber, and a specially designed silencer. The silencer consists of a series of parallel baffles arranged in two rows. The spacing between the baffles is dictated by the blade passing frequency. The two rows of baffles are staggered, preventing "line of sight" across the silencer. The configuration of this system is shown in Fig. 20.

Gas Turbine Casing. The acoustic energy radiated by the gas turbine casing is evenly distributed in all octave bands; see Fig. 7. The attenuation of this noise is by means of an airtight enclosure. The enclosure walls consist of specially designed acoustic panels, bolted together along gasketed flanges. Two man doors on each side of the enclosure provide access. The doors are sealed with double gaskets, and are equipped with the panic hardware to allow rapid egress under emergency conditions. The maintenance access to the casing is by means of a removable roof section.

The heat rejected by the gas turbine casing is carried away by the ventilation system. The ventilation system consists of two vane axial fans, pressurizing the enclosure spaces with filtered outside air. Inlet and exhaust sides of the ventilation system have silencers consisting of acoustically lined multiple right angle bends.

A typical cross section of the enclosure wall is shown in Fig. 21.

Gas Turbine Exhaust. The attenuation of the noise due to the exhaust provided a significant design challenge. To avoid possible problems associated with low-frequency excitation, and to ensure that there would be no complaints from the adjacent residences, the acoustic specification limits noise to 68 dB at 31.5 octave at 100 m. To meet this requirement an attenuation of 20 dB in the lowest octave is required.

The conventional design approach used in the absorptive type silencer would require a very tall stack 30 m high. Such

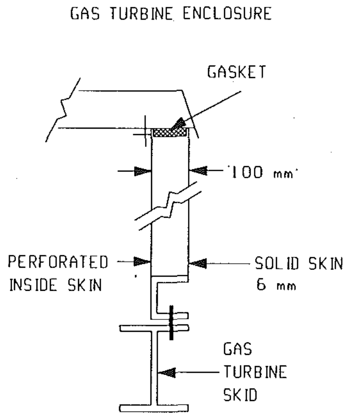

Fig. 21 Gas turbine enclosure

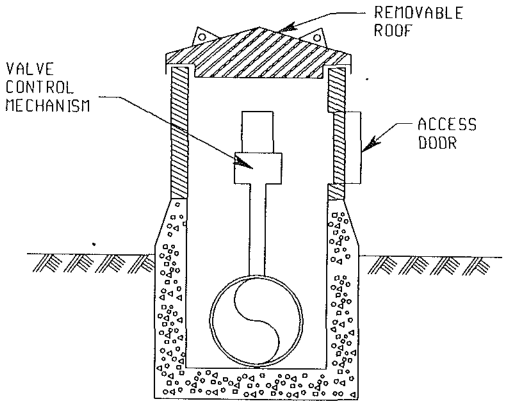

Fig. 23 Control valve enclosure

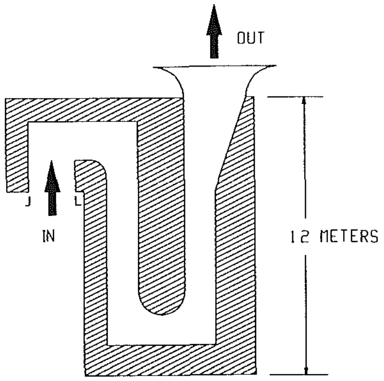

Fig. 22 Folded channel acoustic silencer

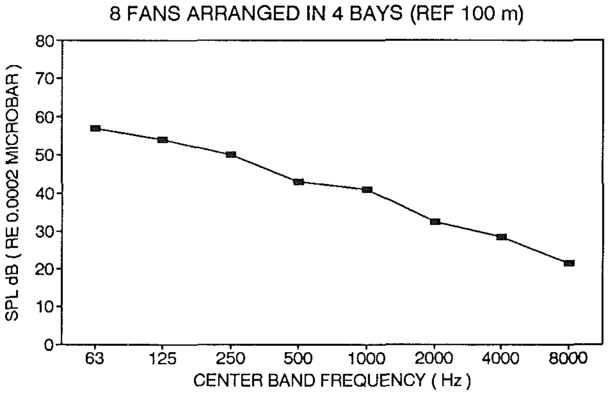

Fig. 24 Guaranteed cooler noise spectrum

a stack would be a very dominant structure in the vicinity and would require aviation warning lights. A new and unconventional approach was devised. The new design uses a "folded channel" passage concept. This not only provides an acoustic length equal to the wavelength at low frequency but also results in a very compact silencer only 12 m high. The exit velocity of the exhaust gas was kept below 30 m/s to prevent regeneration of sound above the silencer. The exit lip was fitted with a special aerodynamic fairing to prevent the possibility of generation of edge tones under strong side wind conditions. The configuration of the silencer is shown in Fig. 22.

Other Special Silencing

Yard Valves. Wherever possible the station piping was buried underground. However, it was not possible to bury all the control valves. These generate noise especially when throttling. To prevent noise radiation from the valves, acoustically lined enclosures were fitted around these valves. The enclosures were mounted on concrete curbs and feature access doors and removable roof to allow maintenance. The configuration of this enclosure is shown in Fig. 23.

Station Piping. High-pressure piping was treated in three different ways. All piping that could be buried was buried. Unit piping outside of the compressor building was installed in concrete vaults located on either side of the compressor building. Because the compressor was scheduled to be converted to a tandem unit in the future, the vault arrangement would greatly facilitate this activity. Unit piping inside the compressor building was treated with acoustic wrap. This was considered to be necessary because of the large surface area of pipe, which radiates noise into the compressor building. This would be particularly noisy during recycle operations if not treated.

Gas Aftercoolers. The gas aftercoolers at Parkway were specified to meet NR35 at 100 m. The successful bidder quoted a cooler arranged in four bays with two fans per bay. Each fan contains nine blades and runs at a conservative 1607 m/min tip speed. This enabled the manufacturer to offer guaranteed and predicted noise levels, as shown in Fig. 24. Operation of the gas aftercoolers is seasonal and only on rare occasions do all eight fans operate simultaneously. Therefore the small margin by which the guaranteed level exceeds the NR 35 curve was considered acceptable.

Summary

The design approach described above was successfully applied during the design and construction of the Parkway Compressor Station. This approach resulted in a very quiet compressor station, which will coexist comfortably with the large subdivision adjacent to the property line. Several attempts were made to measure the station noise level without success. At the point on the road closest to the compressor building the station noise was no higher than ambient background levels, reaching a total of 39 dBA.

During 1990, Union Gas accepted an award from the Canadian Hearing Society, which recognized the significant acoustic design achieved at the Parkway Compressor Station.

References

1 Hoover, R. M., "Beware Low Frequency Gas Turbine Noise," *Power Magazine*, May 1973.

2 Carden, H. D., and Maves, W. H., "Measured Vibration Response Characteristics of Four Residential Structures Excited by Mechanical and Acoustical Loadings," NASA TN D-5776, 1970.

3 Pappas, G. P., "Natural Gas Compressor Station Noise Abatement Systems," ASME Paper No. 90-GT-292, 1990.

4 Challis, L. A., and Challis, A. M., "Low Frequency Noise Problems From Gas Turbine Power Stations," *Proceedings of Inter-Noise 78*, 1978, p. 475.

5 Hoover, R. M., *Gas Turbine Installation for Tampa Electric Company*, 1972.

6 Hessler, G. F., "Gas Turbine Silencing—Then and Now," *International Electric Power Industry Noise Abatement Engineering Workshop*, EEI and BBN, 1986, p. 21.

7 Newman, J. R., and McEwan, K. I., *Operational Problems Associated With Gas Turbine Exhaust Silencers*, 1979.

8 Hubbard, H. H., "Noise Induced House Vibrations and Human Perception," *Noise Control Engineering Journal*, Sept./Oct. 1982, pp. 49–55.

C. A. Skira
U.S. Air Force,
Aero Propulsion and Power Laboratory,
Wright-Patterson AFB, OH 45433

M. Agnello
U.S. Navy,
Naval Air Propulsion Center,
Trenton, NJ 08628

Control Systems for the Next Century's Fighter Engines

The paper describes a conceptual control system design based on advanced technologies currently in the exploratory development phase, and, in some cases, emerging into the advanced development phase. It explores future propulsion control systems that focus on improvements in three areas: (1) significantly reducing control system weight; (2) enhancing engine performance (thrust, sfc, etc.); and (3) improving control system reliability and tolerance to high-threat environments (temperature, vibration, EMI, EMP, etc.). The factors that will influence the design and hardware configuration of future propulsion control systems are described. Design goals for future systems, based on the DOD/NASA IHPTET Initiative, and projections of emerging technology capability (and availability) form the basis for future propulsion control system design requirements and for estimating future hardware configurations.

Introduction

The future direction of propulsion control system development will be within the guidelines and objectives of the DOD/NASA IHPTET Initiative. The broad goal of the IHPTET Initiative is to demonstrate technology by the turn of the century that will double propulsion capability for a wide range of potential military and missile applications. Using the current technology state of the art as a basis, specific IHPTET goals include:

1 A 100 percent increase in thrust/weight ratio and a 40 percent reduction in fuel consumption for fighter/attack engines.
2 A 120 percent increase in power/weight ratio and a 40 percent decrease in fuel consumption for rotorcraft engines.
3 A 40 percent reduction in fuel consumption for strategic missile engines and a 100 percent increase in thrust/airflow for tactical missiles engines.
4 A 30 percent decrease in fuel consumption for subsonic transport/patrol engines. These goals are to be achieved without compromises in engine life, reliability, or maintainability.

From these broad engine guidelines, requirements have been defined for future gas turbine engine control systems for all of the above engine classes as shown in Fig. 1. Notice that these goals are generally identical for all man-rated propulsion systems, i.e., fighter/attack, rotorcraft, and transport/patrol aircraft. Missile engine control systems tend to be entirely different. This paper will address only the control system issues for man-rated fighter/attack aircraft engines—the low bypass ratio, afterburning turbofan.

This paper presents a conceptual control system design for the fighter aircraft engine of the future. It is based on the requirements established in the DOD/NASA IHPTET Initiative and on the advanced technologies currently in the exploratory development and advanced development phases. It explores a future propulsion control system that focuses on improvements in these three areas: (1) systems that significantly reduce control system weight through the application of advanced, lightweight materials and through systems integration; (2) systems that increase engine system performance through the development of advanced engine control modes and logic; and (3) systems that maintain or enhance the basic control system reliability and tolerance to environmental effects (temperature, vibration, EMI, EMP, etc.). All three of these areas are so closely related that advancements in one area will impact (favorably or unfavorably) the other two to varying degrees as will be discussed throughout the paper.

Control 2000$^+$

The final design and hardware implementation of an engine control system is a function of many variables. The availability and maturity level of component technology, aircraft mission requirements, propulsion system complexity, and engine performance requirements are just a few of the many factors that must be considered before an acceptable design is achieved. This paper will concentrate on the component technologies that, at this time, show the most promise of satisfying the IHPTET propulsion controls system goals for a Mach 2.5 class air superiority fighter.

A comparison of a conventional propulsion control system with a candidate control for the future is shown in Fig. 2.

Today's state-of-the-art engine controls are characterized by a centralized, redundant full authority digital electronic control (FADEC) processor. All control law processing, redundancy management, and input/output signal conditioning is done in

---

Contributed by the International Gas Turbine Institute and presented at the 36th International Gas Turbine and Aeroengine Congress and Exposition, Orlando, Florida, June 3-6, 1991. Manuscript received at ASME Headquarters March 4, 1991. Paper No. 91-GT-278. Associate Technical Editor: L. A. Riekert.

ENGINE GOALS

	TF/TJ		EXP		TS/TP	
	FN/WT	FUEL BURN	FN/WA	COST	HP/WT	SFC
BASE	-	-	-	-	-	-
PHASE I	30%	-23%	35%	-30%	40%	-20%
PHASE II	60%	-32%	70%	-45%	80%	-30%
PHASE III	100%	-38%	100%	-60%	120%	-40%

CONTROLS SYSTEM GOALS

	TF/TJ			EXP			TS/TP		
	WT	PERF (SFC/FN)	ENV (°F)	WT	COST	ENV (°F)	WT	PERF (SFC/HP)	ENV (°F)
BASE	15%	-	-	-	-	-	-	-	-
PHASE I	-20%	-2%/3%	+ 100	-20%	-30%	+ 200	-20%	-2%SFC/3%HP	+ 50
PHASE II	-35%	-3%/5%	+ 250	-35%	-50%	+ 400	-35%	-3%SFC/5%HP	+ 150
PHASE III	-50%	-5%/10%	+ 400	-50%	-60%	+ 600	-50%	-5%SFC/10%HP	+ 200

Fig. 1 IHPTET engine and control system goals

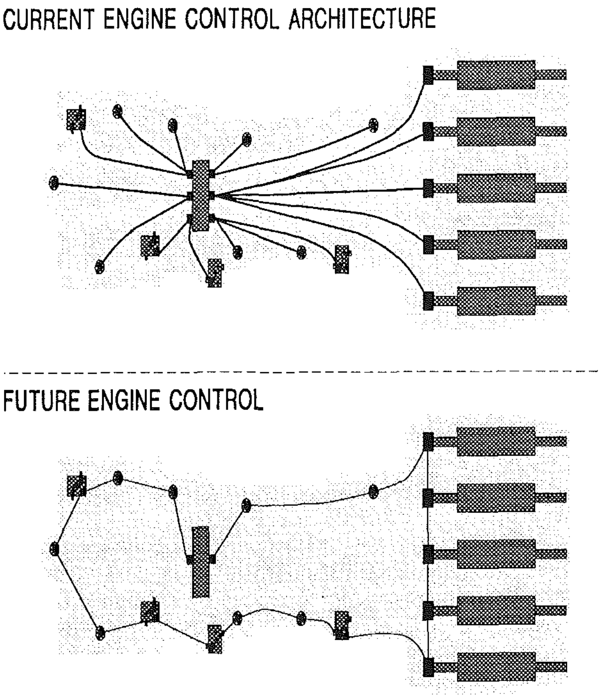

Fig. 2

the FADEC. As a result, one of the heaviest components for today's controls is the harnesses and connectors.

Tomorrow's controls will be highly distributed, characterized by a multiredundant digital processor, which functions as the interface to the aircraft and main propulsion system controller. This unit may not be engine mounted, as is today's practice, depending on the application and system requirements. The controller will utilize engine-mounted smart sensors and actuators, which communicate to the propulsion system controller through a redundant, high-speed optic data bus. In order to minimize heat rise and power consumption, variable speed, flow on demand fuel pumps will be used. The engine control will share electrical and hydraulic power with the aircraft. Both have the requirements of being prime reliable. Recent studies have shown that this approach results in a minimal weight system with higher reliability than today's engines.

A distributed control system results in reduced control system complexity, improving both maintainability and reliability. This approach would permit the FADEC to be a common processing module that could be standardized for a family of engines, resulting in a significant cost savings. Significant weight reductions are possible.

In order for this approach to become a reality, advancements in several key technologies must be made. The remainder of this paper will address the expected advancements required for the major components of the distributed propulsion control system. These are: the fuel handling system; the sensors and actuators; the electronic processor; the control modes/logic;

Nomenclature

ATF = Advanced Tactical Fighter
BIT = Built-In Test
DARPA = Defense Advanced Research Projects Agency
EMA = Electromechanical Actuation
EHA = Electrohydrostatic Actuation
EMI = Electromagnetic Interference
EMP = Electromagnetic Pulse
FADEC = Full Authority Digital Electronic Control
GaAs = Gallium arsenide
IHPTET = Integrated High Performance Turbine Engine Technologies
HIDEC = Highly Integrated Digital Engine Control
MIPS = Millions of instructions per second
MMC = Metal Matrix Composite
NASA = National Aeronautics and Space Administration
OEC = Opto Electronic Control
OMC = Organic Matrix Composite
SiC = silicon carbide
Si = silicon
SFC = Specific fuel consumption (lbm of fuel per hour per lbf of engine thrust)
STOVL = Short Take-Off, Vertical Landing
TALIF = Thermally Assisted Laser Induced Fluorescence

and an increasingly important factor, the integration with the other aircraft subsystems.

Fuel Handling

Various options remain as viable candidates for a fuel handling system, which is defined as the main and afterburner fuel pumps and metering system. Simplicity, low weight, low heat rise (the amount of heat added to the fuel due to the inefficiency of the pumps), and high reliability are desired. With the exception of a gear pump, positive displacement fuel pumps tend to be very complicated, requiring an equally complex fuel metering system. Recent activity has been aimed toward the development of lightweight centrifugal pumps as the main engine fuel pump. Centrifugal pumps are inherently simple, in both design and control, requiring a simple throttling valve. Their performance at low flow conditions, however, is very poor. This is particularly evident during engine starting. A common solution is to provide a separate starting pump, usually a retractable vane pump.

A simpler, lighter approach would be to utilize a variable speed, variable flow gear pump for the main engine. The proven reliability of gear pumps makes them an attractive candidate for future engines. Centrifugal pumps could be used for afterburner fuel flow.

Electric motors will supply the variable speed, provided improvements in electric motor weight, volume, and reliability can be made. Since the electric motor size increases with the horsepower rating, it is critical that the power density (horsepower per pound) of electrical motors be improved. Upward of 300 hp can be required to drive the main and afterburner fuel pumps.

The final fuel handling approach will be based on several factors. Whatever the configuration, it's a certainty that the fuel system will be much lighter. Current efforts are focused on applying lightweight composite materials as a replacement for stainless steel. Organic matrix composites (OMCs), such as graphite epoxies and plastics, would seem to offer the greatest weight savings potential over metals (metal matrix composites and metal alloys). The biggest challenge facing component vendors is learning to design pumps and other control components with these new materials. OMCs are not metals. Fracture mechanics, not fatigue, govern OMCs. They will require different design approaches. Manufacturers will need to build their experience base with these new materials before successful designs become a reality.

Engine control components will not be made entirely of OMCs. Metallic liners, bolt attachments, threaded inserts, and other metallic interfaces are required. Bonding with metals is a problem, especially where high temperatures can cause stress fractures and ultimately failure of the OMC to metallic bond due to a mismatch of the thermal coefficients of expansion.

To be practical, high-temperature OMCs are required. Current materials are limited to temperature environments of 400°F or less. Research is under way to develop newer, high-temperature (up to 750°F) OMCs.

Unless the temperature capability and bonding problems are solved, the best overall solution may lie in the development of high-temperature, lightweight metals, even though they are higher in density. High-temperature (750 to 900°F) aluminum alloys are already under development for aircraft and engine component applications. Metal matrix composites, because they are continuous, alleviate the thermal stress problems associated with the OMCs. Because they are better understood, MMCs might offer the most lightweight and cost effective solution.

Sensors/Actuators

Today's high-performance turbine engines can have as many as fifteen sensed inputs and seven controlled variables. This will increase for future engines. The requirement for high reliability and low mission abort rates has necessitated the use of redundant sensors and actuators. This leads to many undesirable features. A typical dual-element electrical sensor requires the use of five copper wires. A direct drive servovalve requires fourteen individual wires. Electrical cables must also be shielded to protect against the upset currents and surges caused by electromagnetic environmental effects. These factors contribute greatly to the cable and engine harness weight, which for some large commercial engines already exceeds one hundred pounds. As shown in Fig. 3, sensors and actuators account for a major percentage of the engine control system's weight.

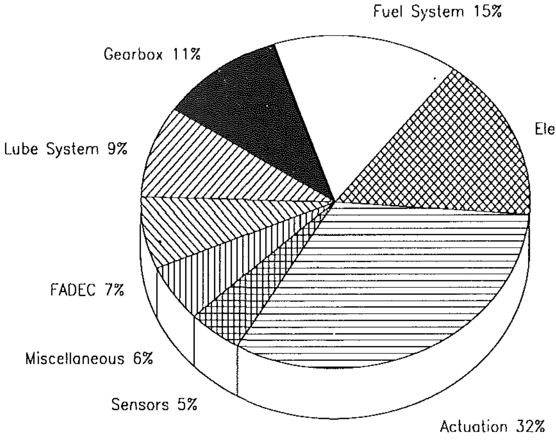

Fig. 3 Weight distribution

All sensors and actuators require some form of compensation, i.e., their own control systems. Currently, sensor compensation and actuator loop closures are accomplished by the engine's FADEC. Not only does this attribute to enormous cable and harness weights, but it consumes a significant portion of the FADEC's processing time. In the propulsion control systems of the future, sensors and actuators will be co-packaged with electronic modules that will provide for signal compensation directly at the source. Functionally, these "smart" sensors and actuators will:

1 Actively compensate for known environmental conditions, such as temperature effects.
2 Perform all appropriate signal conditioning and conversion.
3 Diagnose faults, perform limit checks and built-in-test functions.
4 Advise the FADEC of its operational status.
5 Provide for automatic scaling and self-calibration.
6 Perform closed-loop control of commanded actuator position.
7 Provide for simple communication/interface with the FADEC.

When interfaced to the FADEC by a redundant, high-speed optic data bus (50 Megabit/s or greater), the smart sensors and actuators can, in effect, operate independently of the FADEC's clock cycle. In fact, a virtual memory concept could be employed whereby data are continually being updated, refreshed, and sent to a data register to be accessed by the FADEC. Optic cable harnesses with composite connectors result in a significant weight savings over shielded, copper wire. Multiplexing the optic signals will result in further weight savings.

Two key supporting technologies are critical to the successful development of smart sensors and actuators. They are fiber optic sensors and high-temperature electronics.

Current state-of-the-art fiber optic sensors are passive devices designed as direct substitutes for existing electrical sensors. Compared to thermocouples, LVDTs, RVDTs, and turbine type flow meters, they offer reduced weight, higher temperature capability, and immunity to Electromagnetic Environmental Effects (E3). Development work is proceeding under government and industry sponsorship in the following areas:

1 Low to medium temperature probes to cover the range from −65°F to 350°F. Competing design approaches include fluorescent decay and Fabry-Perot sensors. The former are simpler to implement but the Fabry-Perot approach offers the ability to measure temperature and pressure with one probe. This is desirable from the standpoint of minimizing the number of intrusive sensors in an engine's gas path. These designs are suited for total inlet, compressor inlet, fuel, oil, and lube temperatures.

2 Low and high-temperature pressure sensors. Competing design approaches include the previously mentioned Fabry-Perot type and reflective diaphragm types. The latter requires simpler electronics but it is not presently suited for high-temperature applications such as main burner pressure. The development of optic pressure sensors is particularly desirable because they will eliminate the practice of mounting the sensor in the FADEC and running pressure lines to it.

3 High-temperature probes to cover the range from 800°F to 4000°F. Competing approaches fall into two categories, intrusive and nonintrusive. Intrusive sensor designs are based on blackbody radiation measurement and nonintrusive designs are based on the TALIF technique. Blackbody probes are more mature at this point and packaging techniques for their electronics are progressing rapidly. These probes are necessary for measuring turbine inlet temperature on advanced high-performance engines.

4 Rotational speed sensors. The predominant technique is based on magneto-optic materials, which have varying light transmission properties in proportion to the strength of an applied magnetic field. When mounted close to a gear or compressor, the passage of light through the sensor is attenuated by each passing tooth or blade.

5 Rotational and linear position sensors. Competing techniques are based on wavelength division multiplexing (WDM), time division multiplexing (TDM), diffraction gratings, and variable polarizers. Currently, there is no clear winner among these designs. WDM and variable polarizers offer the desirable attribute of field replacement without the need for recalibration.

6 Fuel mass flow sensors. Competing designs are based on vortex shedding principles and opto-fluidic oscillators. These sensors will simplify fuel metering devices because when combined with optic position sensors for the fuel valve, they eliminate the need for P regulators.

All of these designs rely on processing opto-electronics in the controller for signal conditioning. Their great advantage is the elimination of heavy shielded cables to connect them to the controller. The key technical issues in implementing optic sensors are reliable low-loss connectors, which can live in the engine environment, and reliable high-output sources to improve the optical power budget. Currently, there are restrictive limits to the number of sensors that can be multiplexed due to losses through the connectors and sensors. Higher output light sources will alleviate this problem.

Implementing these designs in smart sensors is a logical evolutionary step. The problem of a restrictive optical power budget is minimized when they are communicating on a digital optic bus. Attenuation of digital optic signals is not damaging to the signal content as long as the ones and zeroes are still identifiable. Attenuation of analog optic signals is a serious problem that affects calibration and measurement accuracy. The primary technical challenge confronting optic implementation of smart sensors is the development of high-temperature semiconductors with desirable opto-electronic properties. The current contenders are GaAs and SiC.

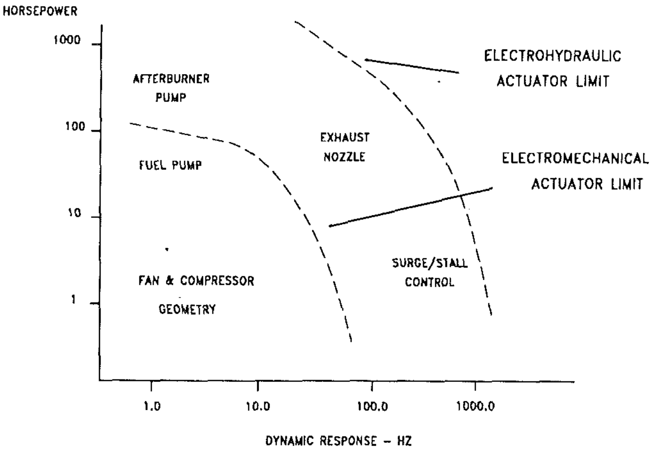

Fig. 4 Actuator comparison

Recent advancements in silicon carbide (SiC) wafer technology have revived interest in this unique semiconductor material [2]. Because of its wide energy bandgap, SiC can yield superior performance over Si and GaAs in a high-stress (temperature, field, radiation, and power) environment. This makes it an ideal candidate for high-performance aircraft and engine applications. For smart sensors and actuators, electronic circuits need to be rugged and as simple as possible. It is hoped that SiC devices and circuits will offer the solution.

Electric actuation for flight and engine controls is being considered, based on recent developments in power electronic devices, particularly in the application of MOS-controlled thyristor technology. Recent advancements in electric motor technology are making electromechanical actuation (EMA) an attractive alternative to the fuel-hydraulic engine actuators used today.

As shown in Fig. 4, for low-horsepower applications, such as fan and compressor variable geometry, EMAs are a viable technology. For higher horsepower systems, such as the engine's exhaust nozzle, fluid power amplification might be used unless advances in electric motor technology are made. An electrohydrostatic actuator (EHA) could be a viable option. By far, the largest horsepower requirement associated with the engine is from the main and afterburner fuel pumps. Electric motor driven fuel pumps are currently under development for test and evaluation.

Processors/Data Communication

Advanced propulsion control systems will require a significantly higher throughput processing capability than available today. Fortunately, the propulsion control community can take advantage of the advancements being made in the highly competitive electronics industry. Future processors may utilize GaAs integrated circuitry, currently being developed under DARPA sponsorship. GaAs chips offer speeds up to six times that of silicon-based chips [3]. Another approach to achieving higher throughput is parallel processing. Estimates of available throughput for future technology processors are in the 100 MIPS range. With the added increases offered by parallel processing, achieving the necessary throughput requirements would appear feasible.

In order to satisfy flight safety and mission abort requirements, triplex or quad redundant systems will be utilized. Fault-tolerant electrical power will be provided by the aircraft. Emergency power, if any, will be a systems driven issue. Besides the basic engine control function, the FADEC's role may be expanded to include power conditioning and control as the use of electric motors broadens.

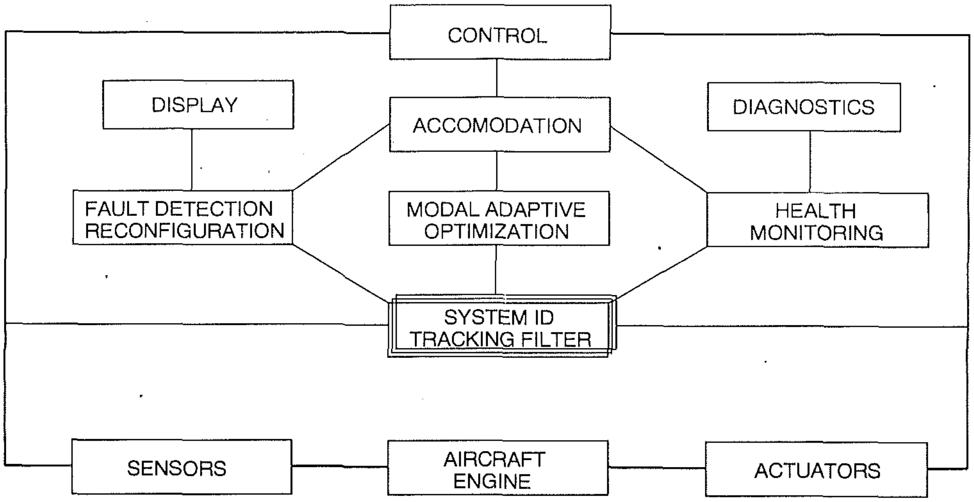

Fig. 5 Generation 7 control logic

By using a multiplexed, fiber optic data bus and distributed controls (smart sensors and actuators) instead of shielded, point-to-point copper wiring, the engine harness weight will be greatly reduced, perhaps to the point where it may be practical to consider mounting the propulsion control unit off of the engine to a more benign environment. Off-engine mounting would have obvious benefits in increased life and reliability for the controller. Eliminating the hardware associated with fuel cooling the propulsion control unit would also reduce weight. Despite the benefits, removing the FADEC from the engine may not be a wise decision for all applications. Generally, engines are purchased independently from the aircraft they are to power. Ease of removal, maintainability, and accountability factors must also be taken into account.

The FADEC will, by necessity, contain opto-electronic interface circuit cards in order to communicate with the optic sensors and actuators. Actuators may even use optical switching as part of their control scheme; however, the prime power medium will either be hydraulic, fluidic, or electrical. The NASA/NAVY FOCSI-II (Fiber Optic Control System Integration) Program and the NAVY's OEC (Full Authority Digital Opto Electronic Control) programs are currently developing prototype opto-electronic interface hardware for engine and flight control applications. Several issues remain to be resolved through test and evaluation. One of the more critical issues is the optic multiplexing scheme, as it will influence the interface hardware design. One major drawback is the lack of appropriate specifications and standards for optic technologies.

Control Modes and Logic

Despite the digital control systems revolution that aircraft gas turbine engines have undergone over the past decade and a half, the control modes used in today's high-performance engines haven't changed significantly since the days of the hydromechanical control systems. Analytical studies have shown the potential for significant performance improvements. Through NASA's HIDEC program, some of these improvements are now being demonstrated in flight tests on a modified F-15 aircraft [4].

Future fighter engines will employ advanced control modes, which will automatically adjust the engine's operating point to optimize performance (thrust, SFC, life, or observability) throughout the flight envelope. Because the performance requirements change as a function of the aircraft's mission requirements, engine performance may be optimized for each mission segment—a notion termed "modal adaptive control." A functional schematic of an advanced engine control system is shown in Fig. 5. This figure is intended to illustrate the control logic features of tomorrow's fighter engines.

As shown in the figure, the basic engine controller has been augmented to include three enhancement functions: (1) failure accommodation and reconfiguration; (2) diagnostics and health monitoring; and (3) mission or modal adaptive performance optimization. These three functional elements will be managed by an accommodation logic function and the appropriate adjustments will be made to the engine control system.

Failure accommodation, in the context of this paper, means accommodating for those system failures with absolutely no loss of propulsive or aircraft system performance. An example would be a failed sensor whose output is replaced by a redundant sensor or by a value computed from an analytical model. Reconfiguration, on the other hand, is associated with a system failure that, unless otherwise compensated for, results in the loss of performance. The reconfiguration logic will assess the severity of the performance loss and attempt to recover as much performance as safely possible through adjustments to the engine control. An example of such a failure might be a jammed or inoperative actuator, or damage to the turbomachinery itself. Recovery of full mission capability will be the first priority of the reconfigurable control with minimal, get-home capability being the final option. Having identified the impact of the damage to the performance capability of the engine, information can be displayed to the pilot to advise him/her of the status of the engine and provide an assessment of the various mission options available.

The control system logic will have knowledge of the current performance capability of the engine, i.e., the engine's current health. Through its ability to perform failure detection, isolation and accommodation, the engine diagnostic information would be available to guide postflight maintenance of the engine and for engine performance trending. The engine diagnostic information would be fed directly to the aircraft onboard central diagnostics unit.

Modal adaptive optimization would be performed to maximize engine performance for a given mission segment. In combat, an engine control that maximizes engine thrust and thrust response would be required. For steady-state cruise, minimum fuel burn control modes would be employed. Control modes that reduce engine observables, such as infrared, contrail, or acoustic signatures, might be used during ingress and egress to a target zone.

The heart of this advanced control logic approach is a real-time engine model. The engine mode is used by all three logic elements. Using an engine model offers several advantages. Analytical models offer full engine observability, i.e., every engine parameter is available, as opposed to the actual engine where sensed instrumentation is limited due to weight and cost considerations. Also, an engine model is much better suited for optimization analysis. Perturbing an actual engine in flight in order to search for an optimum set point is both inefficient and disturbing to the pilot.

The engine model may be derived with a minimal engine sensor compliment. The on-board engine model will be continuously updated to match the engine's installed performance. More detail on the derivation of these types of models can be found in [5-7].

Ultimately, the performance improvements gained through the use of these advanced control modes may lead to fundamental changes in the way engines are designed and built. For example, an increased performance control mode that can safely, precisely, and consistently operate the fan or compressor at reduced stall margins, can lead to the design of compression systems with equivalent performance with either fewer blades per stage, fewer stages, or both—a direct and dramatic system weight savings.

Summary

This paper describes a conceptual control system for future fighter aircraft engines, as our community strives toward the goals of IHPTET. Many factors will influence the ultimate design. However, future systems will be significantly lighter and will enable improved propulsion and aircraft system performance, reliability, maintainability, and flight safety. These goals will be met by the application of new, lightweight materials, and through the development of emerging technologies, such as fiber optics, high-temperature electronics, advanced digital processors, and electric actuation.

Although the focus of this paper has been on the propulsion control system, it must be recognized that the design of the engine control cannot occur in isolation. Future aircraft designs will be highly integrated in order affordably to reach an optimal blend of performance, weight, and maintainability.

The propulsion control will be functionally integrated with the aircraft flight control [8, 9] to provide superior aircraft performance throughout the flight envelope. The flight and propulsion control will also be part of the aircraft's vehicle management system (VMS) [10, 11], which will integrate the flight vehicle with the other aircraft systems, such as the weapons, and guidance and navigation systems. For optimized performance, future aircraft will rely more heavily on the ability of advanced controls to harness the power of individual component technologies.

References

1 Sobey, A. J., and Suggs, A. M., *Control of Aircraft and Missile Powerplants*, Wiley, New York, 1963.

2 Przybylko, S. J., "High Temperature Electronics for Aircraft Engines," Paper No. AIAA-90-2035, 1990.

3 Danca, "DARPA Invests in GaAs Firm, Can Keep Profit," *Federal Computer Week*, Vol. 4, No. 15, Apr. 16, 1990, p. 28.

4 Putnam, T., and Christiansen R., "Integrated Controls Payoffs," Paper No. AIAA-89-2704, 1989.

5 Luppold, R., and Roman, J., "Estimating In-Flight Engine Performance Variations Using Kalman Filter Concepts," Paper No. AIAA-89-2584, 1989.

6 Shaw, P. D., Foxgrover, J., Berg, D. F., Swan, J. A., Adibhatla, S., and Skira, C. A., "A Design Approach to a Performance Seeking Control," Paper No. AIAA-86-1674, 1986.

7 Tich, E. J., Shaw, P. D., Berg, D. F., Adibhatla, S., and Skira, C. A., "Performance Seeking Control for Cruise Optimization in Fighter Aircraft," Paper No. AIAA-87-1929, 1987.

8 Clifton, J. V., Smith, K. L., Lehtomaki, N. A., and Langton, R., "Design Methods for Integrated Control Systems," AIAA Paper No. AIII-83-2562, 1983.

9 Shaw, P. D., Haiges, K.R., and Skira, C. A., "Validation of an Integrated Flight and Propulsion Control Design for Fighter Aircraft," Paper No. AIAA-87-1928, 1987.

10 Mattes, B., and Yonke, B., "The Evolution: IFPC to VMS," Paper No. AIAA-89-2705, 1989.

11 Benson, J. M., "Secondary Power: Benefits of Digital Control and Vehicle Management Systems Integration," SAE Paper No. 881498, 1988.

Integrated Flight/Propulsion Control for Flight Critical Applications: A Propulsion System Perspective

K. D. Tillman
Project Engineer.

T. J. Ikeler
Senior Engineer.

Pratt & Whitney,
Government Engine Business,
West Palm Beach, FL 33405

The Pratt & Whitney and Northrop companies together, under the Air Force Wright Research and Development Center (WRDC) sponsored Integrated Reliable Fault-Tolerant Control for Large Engines (INTERFACE II) Program [1, 2], designed and demonstrated an advanced real-time Integrated Flight and Propulsion Control (IFPC) system. This IFPC system was based upon the development of physically distinctive, functionally integrated, flight and propulsion controls that managed the Northrop twin engine, statically unstable, P700 airplane. Digital flight control and digital engine control hardware were combined with cockpit control hardware and computer simulations of the airplane and engines to provide a real-time, closed-loop, piloted IFPC system. As part of a follow-on effort, lessons learned during the INTERFACE II program are being applied to the design of a flight critical propulsion control system. This paper will present both the results of the INTERFACE II IFPC program and approaches toward definition and development of an integrated propulsion control system for flight critical applications.

Introduction

Aircraft system performance and maneuverability improvements have been realized through control integration concepts added to present-day demonstrator aircraft in programs such as the Air Force STOL Maneuvering Technology Demonstrator (S/MTD) Program. Future aircraft designs will, from the start, take full advantage of aircraft control integration. The increasing level of integration will significantly influence the flight criticality of the integrated flight and propulsion control system.

The benefits of expanded levels of digital flight and propulsion control integration are constantly evolving. The control power of vectoring and reversing nozzles in combination with aerodynamic aircraft surfaces will provide enhanced aircraft performance and agility during takeoff, cruise, combat, and landing. Once integrated for these purposes, a natural follow-on will be the use of vectored thrust in reconfiguration schemes to compensate for flight control surface failures or battle damage. Advanced Short Take-Off and Vertical Landing (STOVL) aircraft will require a very high level of flight critical control integration.

The goal of the INTERFACE II program was to validate and demonstrate high-risk, high-payback technologies for future development program application. A major element of the INTERFACE II program was to demonstrate successful integration of dissimilar redundant flight and propulsion controls in a pilot-in-the-loop aircraft simulator environment.

During INTERFACE II the Pratt & Whitney and Northrop companies designed and demonstrated a highly integrated flight and propulsion control system, Fig. 1. This design incorporated advanced aircraft and multifunction thrust vectoring nozzle technologies in order to exploit the supermaneuverability potential made possible by highly integrated aircraft control.

The INTERFACE II system design utilized redundant effectors in order to achieve performance and robustness improvements. An effector is simply propulsive thrust or any aerodynamic surface that has control power to affect the air-

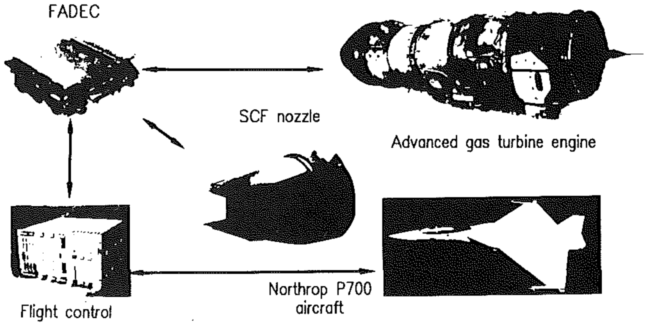

Fig. 1 INTERFACE II IFPC system overview

Contributed by the International Gas Turbine Institute and presented at the 36th International Gas Turbine and Aeroengine Congress and Exposition, Orlando, Florida, June 3-6, 1991. Manuscript received at ASME Headquarters March 4, 1991. Paper No. 91-GT-284. Associate Technical Editor: L. A. Riekert.

craft's attitude or spatial position. By this definition, symmetric trailing edge flap deflection and pitch thrust vectoring are seen to be redundant pitch axis effectors. If a control can be configured to take full advantage of redundant effectors, it can realize performance benefits through the advent of more control power. Similarly, the degree of robustness to faults is increased due to the fact that the loss of one effector does not mean that control of that function is lost. This fault tolerance was accomplished in the INTERFACE II program without an active control reconfiguration system.

System performance and fault tolerance testing during INTERFACE II validated and demonstrated that redundant flight and propulsion controls can be successfully integrated in the digital world while maintaining fault detection and isolation capabilities. Additionally, testing showed that functional control integration of thrust vectoring nozzles with aircraft aerodynamic surfaces can be effectively and advantageously accomplished with suitable dynamics for application in statically unstable fighter aircraft. The real-time demonstration tests revealed the agility expected from a highly integrated aircraft with nozzle pitch vectoring, yaw vectoring, and reverse thrust capability. Pilots favored the enhanced maneuverability, calling it "a distinct tactical advantage," and were especially impressed with system performance and fault tolerance during extremely high Angle of Attack (AOA = 70–90 deg) maneuvers.

Vectored propulsive forces and control integration will be key elements in future aircraft designs as well. The propulsion system's role in enhancing aircraft performance and maneuverability will continue to expand and will drive requirements for flight critical propulsion system control. As reliability requirements increase and the demands placed upon a thrust vectoring propulsion system escalate (i.e., STOVL applications), the flight criticality of the propulsion effectors becomes a key design criterion for any IFPC system. Although the design considerations for propulsion control system performance are numerous, mission requirements, reliability, weight, technology availability, and cost must all be considered. The incorporation of multiple redundant engine controls, distributed architectures, and advanced engine control modes may all be utilized to benefit total vehicle performance.

This paper will present both the results of the INTERFACE II IFPC program and design considerations for the development of a flight critical integrated propulsion system.

Interface II Demonstration

System Overview. Quadruple digital flight control and dual engine control hardware were combined with cockpit control hardware and simulations of the airplane and engines to provide a real-time, closed-loop, piloted IFPC system demonstration. The airplane model was implemented using aerodynamic data established from wind tunnel tests under previous programs. The gas turbine engine model was derived from PW1120 engine characteristics and included a pitch, yaw, and reverse thrust vectoring nozzle model, which represented the Pratt & Whitney Spherical Convergent Flap (SCF) advanced multifunction nozzle.

Integrated control laws were developed to provide optimal blending of vectored thrust and aerodynamic control surfaces under all flight conditions and to modulate forward/reverse thrust operation. The control mode selector and blending logic were executed in the flight control while vectored thrust execution logic was performed in the engine control. MIL-STD-1553B and high-speed optic token passing data busses were used for integrated control communication and simulation feedback information.

The task of integrating the flight and propulsion controls in the INTERFACE II program was simplified by dividing the control system into functional groups. This control partitioning is displayed pictorially in Fig. 2. The highest level in this control philosophy was the aircraft's Stability and Command Augmentation System (SCAS). The SCAS received pilot commands and sensor feedback information, which it used to produce generalized actuator commands for aircraft movement.

The next level in the control configuration was the control selector. This element performed the integration of the aerodynamic and propulsive effectors. The control selector [3] received the generalized actuator commands from the SCAS and produced the commands that were sent to each effector. These commands became the actual actuator commands for the aerodynamic effectors. However, as Fig. 2 shows, the propulsive commands were treated as vectoring and reversing angle requests; the propulsion control system was responsible for commanding the propulsive actuators.

The control selector performed the actual control integration by optimizing control power from the aircraft's redundant effectors, Table 1. The control selector had knowledge of how

Nomenclature

AOA = Angle of Attack
ASSIST = Abstract Semi-Markov Specification Interface to the SURE Tool
DMICS = Design Methods for Integrated Control Systems
EMI = ElectroMagnetic Interference
FADEC = Full Authority Digital Engine Control
FCC = Flight Control Computer
IFPC = Integrated Flight and Propulsion Control
IFSD = In Flight Shutdown
INTERFACE II = Integrated Reliable Fault Tolerant Control for Large Engines
I/O = Input/Output
LPLC = Lift Plus Lift Cruise
MA = Mission Abort
MFVT = Mixed Flow Vectored Thrust
MHz = megahertz
MIPS = Million Instructions Per Second
MVC = Multi-Variable Control
N1 = low rotor speed
N2 = high rotor speed
RCS = Reaction Control System
SCAS = Stability and Command Augmentation System
SCF = Spherical Convergent Flap
SFC = Specific Fuel Consumption
S/MTD = STOL Maneuvering Technology Demonstrator Program
STEM = Scaled Taylor Exponential Model
STOL = Short Takeoff and Landing
STOVL = Short Takeoff and Vertical Landing
SURE = Semi-Markov Range Evaluator
SVM = State Variable Model
VMS = Vehicle Management System
WRDC = Wright Research and Development Center

Table 1 Redundant effectors

Pitch	Roll	Yaw
Symmetric Ailerons	Asymmetric Ailerons	Rudder
Symmetric Flaperons	Asymmetric Flaperons	Yaw Thrust Vectoring
Symmetric Thrust Vectoring	Rudder	Yaw Thrust Reversing
Symmetric Thrust Reversing	Asymmetric Thrust Vectoring	Differential Reversing
	Asymmetric Thrust Reversing	

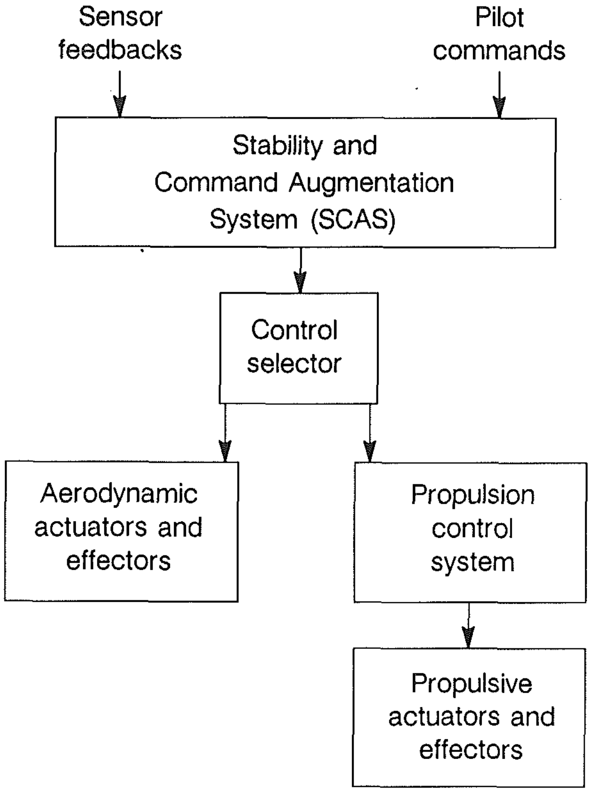

Fig. 2 Control system functional overview

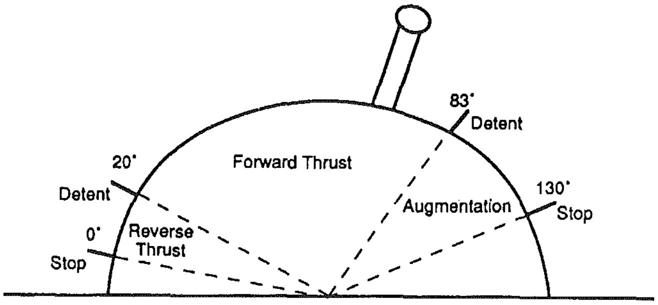

Fig. 3 Integrated throttle thrust reverser control

powerful each effector was at producing pitch, roll, and yaw moments as a function of flight condition and thrust level. With this information, the control selector used a combination of all effectors to achieve the aircraft movement that was commanded by the SCAS. The solution employed the most productive effectors to achieve the commanded accelerations in each axis and cancel the cross-coupling between axes. This approach minimized the total effector deflection, which was needed to satisfy the SCAS commands. No distinction between propulsive and aerodynamic effectors was made in the control selector. In high dynamic pressure flight conditions, aircraft movement was mostly controlled by aerodynamic effectors. At low dynamic pressure flight conditions, the propulsive effectors were the most significant. As the aircraft transitioned between these extremes, the control selector varied the solution to reflect the change in effectiveness. Utilizing the effectors in this way increased the degree of integration between the flight and propulsion systems, thus making the goals of INTERFACE II more ambitious.

Subsystem Control Elements. The aerodynamic subsystem consisted of the aerodynamic actuators of the P700 aircraft. The P700 aircraft is a twin engine, low aspect ratio configuration with a single vertical fin and no horizontal tail. This advanced aerodynamic configuration was designed to be statically unstable (nominally -10 deg mean aerodynamic chord static margin) to maximize performance. Aerodynamic surfaces for this airplane consisted of leading edge flap as well as left and right aileron, flaperon, and rudder.

The propulsive subsystem consisted of dual channel Full Authority Digital Engine Controls (FADECs), which controlled the PW1120 based engine and SCF nozzle. The dual channel FADEC provided for maximum engine performance from start to augmentation throughout the flight envelope and was responsible for achieving nozzle vector and reverse requests issued by the control selector.

The SCF nozzle provided ± 20 deg of pitch vectoring, ± 20 deg of yaw vectoring, and vectored reverse capability. In reverse mode, four independent reverser port door angles could be commanded to achieve any combination of pitching, rolling, and yawing moments. Any in-range combination of pitch and yaw vectoring angles could be achieved while "in" or "out" of reverse mode.

An integrated throttle thrust reverser concept was utilized in the IFPC system as well. The integrated throttle/thrust reverser operated in two modes, which were controlled by a two-position switch on the throttle. With the reverser discrete in the "off" position, the throttle behaved conventionally by commanding an engine power level. When the reverser discrete was in the "on" position, the engine was placed at intermediate power and the position of the throttle then determined the magnitude and direction of the net (forward minus reverse) thrust. The integrated throttle/thrust reverser control was designed so that above the idle detent the net thrust produced was independent of the reverser discrete. This required the propulsion subsystem control to regulate the transition into and out of reverse mode. After a "smooth" transition into reverse mode, reverse thrust was obtained by simply pulling the throttle through the idle detent toward what would normally be the engine shut-off stop. In this way, the relationship between throttle movement and aircraft response remained conventional, i.e., moving the throttle forward accelerated the aircraft and moving the throttle aft decelerated it. Figure 3 demonstrates the throttle's functionality while in the reverse mode.

Smooth reverse transitions were achieved by including the use of thrust estimates in the FADEC with a "closed-loop" feature on net thrust. When reverse mode was engaged, the FADEC commanded the engine to spool up to maximum dry power and opened the reverse area in order to maintain the

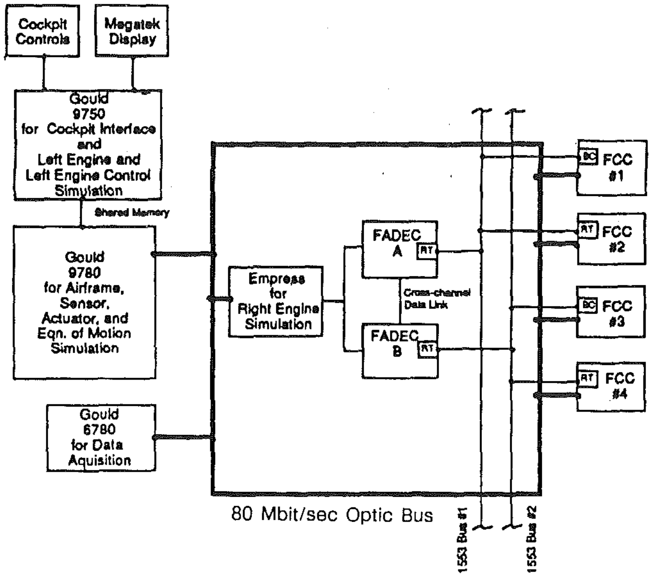

Fig. 4 INTERFACE II IFPC system functional block diagram

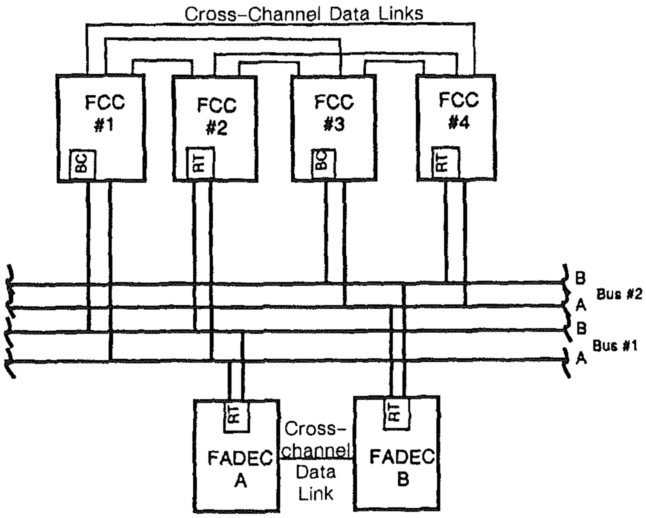

Fig. 5 MIL-STD-1553B bus configuration

same net thrust as would normally be achieved at the current throttle setting.

System Architecture. The INTERFACE II real-time closed-loop IFPC system was comprised of numerous hardware controls, simulation models and communication media, Fig. 4. A description of each system element is included below.

The quad-redundant flight control system consisted of off-the-shelf VME hardware. The processor was a Motorola 68020 with a 68881 floating point coprocessor operating at 20 MHz. While this system was not flight hardware, it was configured to be functionally equivalent to the actual aircraft system. Flight control software was written in Ada.

Engine control was provided by a dual channel FADEC, which scheduled actuators, solenoids, and relays as a function of flight control inputs and engine sensors to control engine performance and nozzle vectoring response. Each FADEC communicated to the flight control computers via a MIL-STD-1553B data bus and to each other over a dual 1 Mbit/s manchester cross channel data link. Each FADEC executed identical control laws that were written in the MIL-STD-1815 Ada programming language and designed to service all FCC requests optimally including changes in throttle, pitch vector angle, yaw vector angle, and reverse mode engagement.

Table 2 Flight conditions

Condition	Altitude Feet	Mach Number
Air to Air Combat	36,000	0.8
Supermaneuverability	20,000	0.4
Landing	500	0.2

The P700 aircraft model was a high fidelity, six degree-of-freedom model based on the nonlinear aerodynamic database established for this vehicle from a number of wind tunnel test programs. Linear interpolation techniques were applied to the nonlinear database to "build up" aircraft forces and moments. These forces and moments were accurate up to 90 deg angle of attack due to the extreme fidelity of the database.

State Variable Modeling (SVM) was used to develop a nonlinear dynamic engine model, which was accurate throughout the entire operating range and capable of running real time. The engine model was a piecewise linear representation of engine thermodynamic processes based on partial derivatives of engine states about fixed operating points. The operating points were selected so that the transient engine model had the capability to accommodate the complete power range from idle to full military power.

The SCF nozzle model was developed by formulating kinematic equations that described the relationship of nozzle exit area and pitch vector angle with actuator strokes. Coefficients of discharge effects and flow turning losses were accounted for in the SCF simulation.

One of the keys to a successful integrated flight/propulsion control system is the communication system used to link the system computers. To ensure that this communication network fulfills the system requirements, it must be reliable, efficient, and fault tolerant. The dual redundant MIL-STD-1533B bus configuration, Fig. 5, was chosen for FCC to FADEC communication.

An 80 megabit per second fiber optic data link served as the common laboratory bus for the integration test bench. Specifically, the optic bus provided communication: (1) of physical information between the engine and aircraft simulations, (2) between the FCCs and the aircraft simulation, (3) for all subsystems on the optic data bus and the data acquisition system, (4) between the FCCs as a cross-channel data link. Use of this high throughput data link avoided any potential bus overloading problems that could occur in time critical, high bus traffic environments.

System Demonstration. The purpose of the INTERFACE II IFPC testing was to demonstrate the functionality, fault-tolerance, and robustness of a highly integrated flight and propulsion control system. The system needed to be operational throughout the aircraft's flight envelope, but three specific flight conditions were of particular interest. These flight conditions are defined in Table 2. The air-to-air combat flight condition was chosen to demonstrate the system's performance in an aerodynamically dominated regime. Similarly, the landing condition was chosen to demonstrate performance in a propulsively dominate regime. The supermaneuvering condition was chosen as a regime where aerodynamic and propulsive forces were balanced. This condition was also used to demonstrate maneuvering performance benefits of integrating the flight and propulsion systems.

The IFPC demonstration progressed in three phases. The majority of the effort was spent validating the system. In this phase, all communication and simulation issues needed to be addressed. Once the system was validated, nonpiloted testing commenced. This phase was necessary to demonstrate the functionality of the "fail-op," "fail-op," "fail-safe" integrated control system. The conclusion of the demonstration was the piloted testing phase in which Northrop and Pratt & Whitney pilots helped to assess the fault tolerance and robustness of the system and provided a qualitative appraisal of system performance.

The approach to validating the demonstration test bench was to create a non-real-time simulation of the entire aircraft, including aircraft, engine, and nozzle models as well as flight and propulsion control systems and to use this simulation to generate test cases. These test cases were then used to validate the real-time test bench as it was pieced together. The test cases were considered to be ideal cases because the simulation that generated them did not contain the noise and latency that could be present in the real-time system. By comparing the real-time results to these ideal test cases, not only could the system be validated, but some insight into the sensitivity of the system to noise and latency could be obtained. The test bench validation was divided into three categories. The first two categories occurred concurrently and validated the propulsion system in the absence of the aircraft system and vice versa. Once both systems were validated, the complete demonstration test bench was assembled.

Nonpiloted Testing. The purpose of nonpiloted testing was to demonstrate the functionality of the integrated control system. The control system should maintain proper aircraft motion in the presence of failures. For system reliability and adherence to military specifications a "fail-op," "fail-op," "fail-safe" fault tolerance strategy was adopted. This required that the control system be able to accommodate two like failures of any of its components without significant performance degradation. During nonpiloted testing, the aircraft performed maneuvers in the presence of failures that identically matched the ideal test cases discussed earlier. Nonpiloted testing showed that the control system could transparently accommodate like failures of sensors, MIL-STD-1553B busses, and FCC channels. Even failures of both FADEC channels, which caused one engine to shut down, were shown not to degrade aircraft controllability severely.

Piloted Testing. The purpose of piloted testing was to assess the robustness of the integrated control system in the presence of actuator failures and to assess the performance gains resulting from integration of the flight and propulsion control systems. During nonpiloted testing, results were compared to the ideal test cases. When the match was identical, it was easy to declare that the system had passed the particular test. However, the match was not identical during actuator failures. Actuator failures could not be accommodated by voting, nor was there any complex active reconfiguration system that could handle the loss of an actuator. Therefore, when an actuator failed, it effectively lowered the loop gain of that control loop. It also caused cross coupling between the aircraft's longitudinal and lateral/directional control axes. Simply stated, an actuator failure reduced the robustness of the control system. During piloted testing, the demonstration test bench was subjected to actuator failures and the pilots were asked to comment on the resultant performance degradation.

Three types of actuator failures were simulated. The failure types were reduced actuator time constant, floating actuator, and an unresponsive actuator. Physically, these failures correspond to a loss of hydraulic pressure, a battle-damaged actuator or an actuator with a broken stroke arm, and the loss of communication, respectively. When these failures were injected into a single aileron, flaperon, rudder, or vectoring actuator, pilot comments suggested that performance was not significantly degraded. Piloted evaluation further determined that the system performed favorably during most combinations of two actuator failures. The only combination of two failures that was found to be deficient was a failed flaperon and any other actuator. An active reconfiguration scheme could have accommodated these failures; however, this condition was too extreme for the INTERFACE II passive reconfiguration scheme.

It should be noted that all of these actuator failures could happen concurrent with multiple channel and sensor failures in the integrated control system, as these failures would be automatically accommodated by the redundancy management logic in the system. The result of multiple failure accommodation would be the ability of a severely damaged aircraft to display minimal performance degradation.

Performance Gains. Piloted testing showed that the integrated system performed exceptionally well. The extra control power that was gained through integrating the flight and propulsion control systems resulted in an envelope expansion that turned the P700 into a supermaneuvering aircraft. The pitch, roll, and yaw control power, and thus maneuvering capability, that this aircraft exhibited at 70 deg angle of attack was comparable to that which would be expected of most aircraft at 35 deg. This capability was described by one pilot as a "distinct tactical advantage." The reversing capability, as implemented in this system, was also looked upon favorably by the pilots. They thought the rapid thrust response and increased low-speed control power available in reverse mode were very advantageous. Overall, the INTERFACE II vehicle was consistent with the engagement philosophy of several test pilots. This philosophy requires an aircraft to cruise at high speed into an engagement arena and then decelerate rapidly in order to perform a series of low-speed, low-*g*, "point and shoot" maneuvers that provide a tactical advantage over the enemy. The engagement is then terminated by a rapid acceleration for a high-speed egress.

Flight Critical Integrated Control Development

The successes of integrated control and vectored propulsive forces that were demonstrated in the INTERFACE II program have set the stage for development of highly integrated, high-performance aircraft of the future. Such advanced vehicles must be affordable and maintainable while providing the increased performance and maneuverability required for multimission roles. New technologies must be developed for propulsion and airframe systems and these technologies must be integrated into the overall air vehicle design. For example, realization of maximum benefits from multiaxis, multifunction nozzles requires highly integrated flight and propulsion control along with optimization of airframe inlets for high alpha/beta flight. The merits and penalties associated with each technology or integration concept must be assessed to assure a balance of performance, reliability, cost, weight, complexity, maintainability, supportability, and technical risk. The remainder of this paper will address these considerations from a propulsion system perspective, for development of a flight critical propulsion control system.

As the role of the propulsion system grows from solely providing thrust to actively playing a part in aircraft stability, the flight criticality of the propulsion control system will increase dramatically. To assess the degree of this criticality, examine the implementation requirements of an advanced Short Takeoff and Vertical Landing (STOVL) vehicle. Here, the emphasis is placed upon a single-engine STOVL aircraft because the demands placed upon the propulsion control system are indeed high, especially during vertical landing modes of flight. For several STOVL propulsion concepts, Mixed Flow Vectored Thrust (MFVT), Lift Plus Lift Cruise (LPLC), etc., Fig. 6, not only must a primary pitch and yaw vectoring multifunction nozzle be controlled, but several auxiliary lift nozzles must also be modulated to control both thrust level and vector

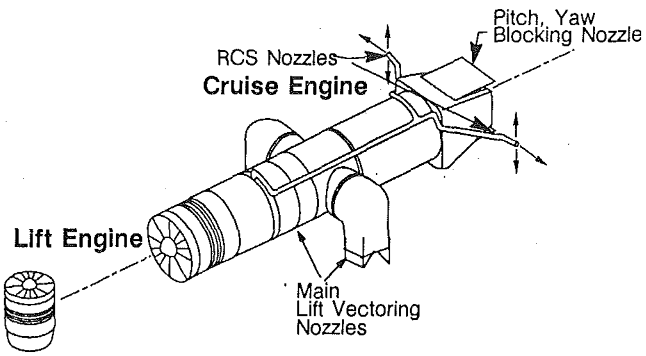

Fig. 6 Lift plus lift/cruise propulsion concept

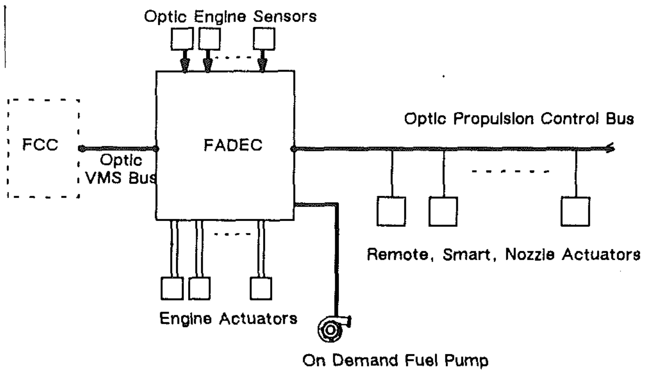

*Single channel shown

Fig. 8 Candidate high-level hybrid propulsion control system

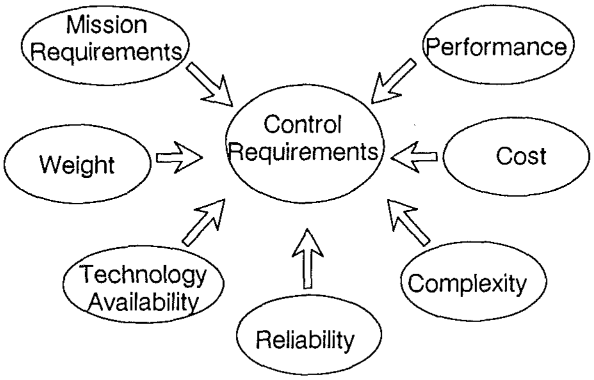

Fig. 7 Control requirements definition

angle. Effective utilization of each of these nozzles will be heavily dependent upon a well-designed IFPC system and, at the same time, will place additional flight critical control requirements on the propulsion control system.

Design Considerations. The final design and hardware implementation of the integrated flight/propulsion control system will be a function of many variables. Considerations such as mission requirements, technology availability, complexity, performance, reliability, weight, and cost [4] must all blend to yield a set of consensus requirements for both the flight and propulsion control systems, Fig. 7. With these design considerations in mind, one of the leading issues that must be resolved is the logically partioned architecture of the IFPC system. This partitioning must be established prior to the actual design of the propulsion or flight control systems in order to define the technologies needed for each system and to establish hardware implementation requirements. The partitioning study will determine which actuators or sensors will be controlled by the flight and/or propulsion control system. Applying analysis techniques to the partitioning problem (i.e., modal analysis, controllability analysis, observability analysis, etc.) will yield a functionally partitioned baseline system. However, engineering intuitive knowledge must also play a part in this important decision. This intuitive aspect will ensure that the analytical results do not place an undesirable burden, or overly increase complexity, on either the flight or propulsion control system. For the STOVL example, the functional partitioning results may show that the propulsion control system should control all engine and nozzle functions, to maintain engine pressure ratio control, while the flight control will have direct authority over all aerodynamic effectors. In this manner, the propulsion "subsystem" will be responsible for achieving flight control vectored force requests while providing for the desired overall engine operation.

Candidate Architecture. Once the high-level system partitioning decisions are made, a detailed design of the propulsion control system may begin. A prime consideration will be determination of an architecture that will satisfy reliability requirements.

To define a suitable control configuration adequately, several architectures capable of providing control for the propulsion system, but that have varying levels of electrical and mechanical redundancy, must be designed in considerable detail. For instance, electrical redundancy of the FADECs may be varied from single to quadruple with each of the defined systems having several different actuator, electrical, hydraulic, and fuel pumping configurations. One candidate architecture for the flight critical propulsion system is shown in Fig. 8.

For the purposes of this paper, the propulsion controller is envisioned to be engine mounted and multiple redundant. This architecture, Fig. 8, represents a hybrid concept where engine sensors and actuators located in close proximity to the redundant FADECs are connected via point-to-point optic fiber or electrical wiring. Remote sensors and actuators, such as those required for the primary pitch and yaw multifunction nozzle and auxiliary lift nozzles, are considered to be smart devices and are connected via a redundant high-speed optic propulsion control bus. These "smart" devices will have the capability to:

1 Provide their own environmental/temperature compensation.
2 Utilize built-in test features to assess their own health.
3 Compute any necessary engineering units conversions.
4 Perform minor loop closure.
5 Resolve position requests from redundant FADECs.

Use of these smart devices will eliminate the need for point-to-point wiring for actuators located at extended distances from the redundant FADECs and will, in turn, result in greatly reduced engine harness weight. The use of smart actuators is currently limited by the availability of mature high-temperature electronic components that can withstand the engine operating environment. However, as this technology develops, smart devices will increasingly appear in engine applications.

Another developing technology is the use of flow on-demand fuel pumps. These variable speed electric motor-driven fuel pumps show promise for simplifying fuel metering and also minimizing fuel system heat rise. Advanced on-demand fuel pumps will also incorporate composite material technologies in order to reduce control system weight further.

Although some of the FADEC's computational burdens can be relieved through the use of smart components, the need for increased control throughput will continue to grow. How these

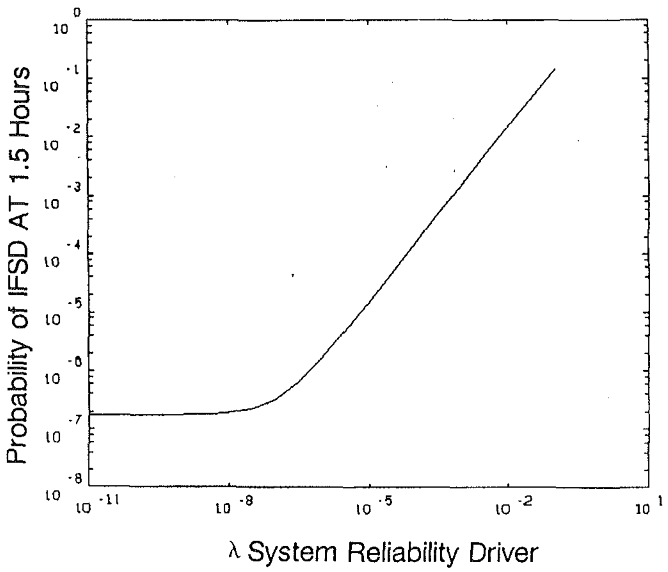

Fig. 9 Sensitivity analysis

required gains in control throughput will be achieved will be greatly dependent upon technology availability. For instance, a 100 MIP throughput requirement could today only be met by the use of a parallel processing controller architecture. However, in the future, it is conceivable that such a high throughput may be achieved by a single microprocessor. In either case, the throughput requirements for the FADEC must be carefully considered so that the appropriate microprocessor architecture may be selected.

Whether engine mounted or remotely located, the FADECs will also contain interfaces for optic technology. These optic interfaces will be used not only to communicate with the control system's smart actuators, but may also be used for VMS communication over a high-speed optic bus and additionally to provide communication with engine mounted optic sensors (i.e., N1, N2, etc.). In this manner, the optic sensor signals will be interfaced directly to the engine controllers to provide for a light weight, EMI immune, sensor interface environment.

Reliability Study. In order to perform the actual control system reliability analysis, failure rate and coverage information for the candidate control system's components must be collected. These data are essential in order to perform a detailed Markov analysis. Markov analysis tools, such as Abstract Semi-Markov Specification Interface to SURE Tool (ASSIST) [5], and Scaled Taylor Exponential Model (STEM), which aid in producing and solving the Markov model, are essential in determining Mission Abort (MA) and In-Flight Shutdown (IFSD) rates for systems that contain many components. Additionally, these tools offer the flexibility to evaluate and construct the appropriate Markov model for several separate propulsion control configurations quickly and easily. Given the rules of operation/failure of the system, ASSIST will generate the Markov model. Since the model is generated automatically, the Markov model may include a greater number of states than a more traditional, error-prone, "hand drawn" model. STEM will then solve the model to yield the desired information, i.e., IFSD and MA rates.

The propulsion control system reliability assessment should evaluate various levels of electrical and mechanical redundancy and also include the IFPC bus interface in order to get a true picture of system reliability. Additionally, with these analyses, the components of the system that may be forcing the system reliability to be lower than expected (the least reliable component) may also be identified. Through the use of sensitivity analysis, the low-reliability component can have its failure rate decreased until total system reliability shows no increase, Fig. 9. At this point, another system component will be driving the results. The same sensitivity analysis may be repeated for other components until the desired system reliability is achieved. Afterward, any improvement made in component reliabilities will have to be implemented through engineering change or redesign.

Integrated Control Modes. Mission adaptive integrated control modes and logic will play an essential role in the development of a flight critical propulsion control system. These adaptive control modes will optimize engine performance and enhance engine operation during each segment of the mission. For instance, a quick thrust response engine operating mode may be desirable during vertical landing modes of flight while optimization of Specific Fuel Consumption (SFC) may be included during a cruise leg of the mission. In either case, the propulsion control will have the ability to adapt to the various requirements of different mission segments and produce an output that is optimized to the mission segment requirements.

On-board engine models (real-time engine model that executes in each FADEC) will play a key role in engine performance optimization and will also provide thrust information to both the engine and flight control systems. The on-board model will have observability into engine states that are not measured by engine control sensors. This observability allows extremely accurate thrust "estimates" to be computed. These estimates, when properly applied, will allow an enhanced IFPC system to be designed that may carefully coordinate all aircraft effectors, propulsive and aerodynamic, to yield enhanced maneuverability. Individual thrust(s) from each nozzle(s) can then be directly commanded to the propulsion control system by the flight controllers to yield precise aircraft control. Through propulsion control computation of thrust estimates, the flight control will be provided the necessary intelligence for commanding a blending of available aerodynamic and propulsive effectors. This dynamic blending of the aerodynamic and propulsive forces by the IFPC system will provide highly agile aircraft performance.

The flight critical propulsion control will also require advanced fault accommodation logic. Through increased redundancy levels, failures of individual sensors or FADECs may easily be isolated and accommodated. Voting algorithms have been successfully demonstrated in the past in numerous programs that mask sensor failures. However, a new challenge will be active reconfiguration by the propulsion control system for propulsion subsystem failures. For instance, these reconfiguration modes will provide, as a minimum, get home safe capability for stuck/frozen actuator failures or battle damage. Reconfiguration may require a change in engine control mode, i.e., the high-response Multivariable Control (MVC) may be reduced to a single input single output mode, but the payoff will be increased mission reliability. Active control reconfiguration may also be extended to the IFPC system. A well-designed IFPC system will be capable of utilizing nozzle thrust vectoring to compensate for failures of aerodynamic surfaces. Active reconfiguration schemes utilizing redundant aerodynamic and vectored propulsion control power will accommodate failures that may have resulted in degraded aircraft performance, by allowing these failures to be accommodated transparent to the pilot.

Conclusions

The INTERFACE II IFPC system demonstrated that a high degree of flight and propulsion control integration is both beneficial and practical today. Functional control integration of thrust vectoring/reversing nozzles and aerodynamic control surfaces can be effectively accomplished with suitable dynamics to provide supermaneuverable aircraft operation. During INTERFACE II IFPC testing, aircraft control was maintained while executing low-speed, high-AOA maneuvers. The use of pitch vectoring, yaw vectoring, and reversing nozzles as primary control effectors at low air speeds in combination with robust control laws and a control selector yielded greatly enhanced aircraft agility throughout the entire flight envelope. Pilots were very impressed with the performance benefits of the closed-loop system. During system testing, fault accommodation experiments also verified that vectoring nozzles can be integrated into flight critical redundancy schemes when prior emphasis on control integration and mode selection is applied.

Future aircraft designs will benefit through extension and enhancement of these integration concepts. Designs integrated from the start, and application of rapidly emerging component technologies such as high-temperature electronics, fiber optics, electric actuation, high-performance digital processors, and new lightweight composite materials, will all contribute to improved propulsion and aircraft system performance at an affordable cost and weight. Multiaxis thrust vectoring nozzles, when integrated with adaptive, performance optimizing control modes and active reconfiguration algorithms, will further enhance future aircraft by providing for highly increased maneuverability and survivability.

Fault-tolerant digital electronic propulsion system controls have proven performance and reliability through millions of flight hours in commercial and military service over the past decade. As the role of the propulsion system expands to effect aircraft stability in highly integrated aircraft design, the propulsion control will become one of the most critical elements. Evolution of the propulsion control to meet these new flight critical performance and reliability demands offers an exciting engineering challenge for the future.

References

1 "Integrated, Reliable, Fault Tolerant Control for Large Engines (INTERFACE II)," Final Report, Contract F33657-85-C-2130, WRDC-TR-90-2040, Nov. 1989.

2 Tillman, K., Ikeler, T., and Purtell, R., "The Pursuit of Integrated Control: A Realtime Aircraft System Demonstration," Paper No. AIAA-89-2701, July 1989.

3 "Design Methods for Integrated Control Systems: Final Report," Contract F33615-82-C-2214, AFWAL-TR-88-2061, June 1988.

4 Skira, C., and Agnello, M., "Aircraft Propulsion Control Systems for the Next Century," Paper No. AIAA 90-2034, July 1990.

5 Butler, R., "An Abstract Language for Specifying Markov Reliability Models," *IEEE Trans. Rel.*, Vol. R-35, No. 5, Dec. 1986, pp. 595–601.

Optimal State-Space Control of a Gas Turbine Engine

J. W. Watts

T. E. Dwan

C. G. Brockus

Weapons and Systems
Engineering Department,
U.S. Naval Academy,
Annapolis, MD 21402

An analog fuel control for a gas turbine engine was compared with several state-space derived fuel controls. A single-spool, simple cycle gas turbine engine was modeled using ACSL (high level simulation language based on FORTRAN). The model included an analog fuel control representative of existing commercial fuel controls. The ACSL model was stripped of nonessential states to produce an eight-state linear state-space model of the engine. The A, B, and C matrices, derived from rated operating conditions, were used to obtain feedback control gains by the following methods: (1) state feedback; (2) LQR theory; (3) Bellman method; and (4) polygonal search. An off-load transient followed by an on-load transient was run for each of these fuel controls. The transient curves obtained were used to compare the state-space fuel controls with the analog fuel control. The state-space fuel controls did better than the analog control.

1.0 Introduction and Model Description

The development of a state-space fuel control on a single-shaft, simple cycle gas turbine engine is the subject of this paper. A model of this simple engine with analog fuel control was available. The load transients of this model have been compared with actual load transients and found to be accurate. This verified model becomes a tool for developing multimode state-space controllers for more complicated engines. For example, a possible future high-efficiency engine for powering naval ships is an intercooled, regenerated (ICR) gas turbine engine [1]. The control for this future engine will involve monitoring several outputs and will have three to five inputs. The number of inputs will vary with the mode of operation. A computer in the control loop will allow for many sophisticated modes and, also, allow for improvements in control strategy after initial development and even after installation. Fuel controls for future engines will be developed and verified with this simpler engine model as a tool.

A simple cycle single-shaft gas turbine engine was modeled using ACSL (Advanced Continuous Simulation Language) [2]. Figure 1 shows the engine components and the three control volumes used for modeling the dynamic behavior. For each control volume a mass balance and an energy balance produced two first-order differential equations [3]. For example, the compressor control volume V3 equations are:

Mass balance:

$$DW3 = WA2 - WA3 - WBL \qquad (1.1)$$

where:

DW3 is change in mass in V3 per unit time

WA2 is mass rate into V3

WA3 is mass rate out of V3

WBL is all bleed flow rates from V3

Energy balance:

$$DT3 = ((WA2^{*}(H3P - H3))/CV3 + T3^{*}DW3^{*}(GM3 - 1)/W3 \qquad (1.2)$$

where:

DT3 is the time derivative of exit temperature

H3 is enthalpy at exit of V3 without considering the volume storage of V3

H3P is enthalpy at exit considering storage

CV3 is the heat capacity (const. vol.) at exit

T3 is the temperature at the exit of V3

GM3 is the ratio of the heat capacities at the exit

W3 is the mass in the control volume V3

There are three control volumes in this model. A mass balance and an energy balance on each one yields six first-order dif-

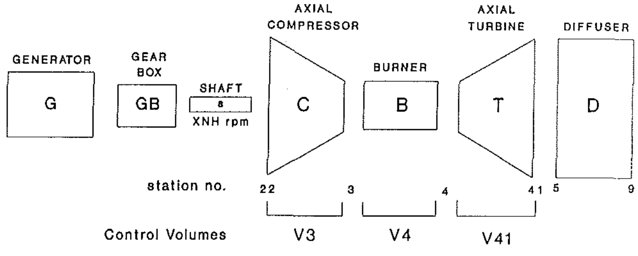

V3 = flow spaces of compressor

V4 = flow spaces of burner

V41 = flow spaces of turbine

Fig. 1 Engine components and control volumes

Contributed by the International Gas Turbine Institute and presented at the 36th International Gas Turbine and Aeroengine Congress and Exposition, Orlando, Florida, June 3-6, 1991. Manuscript received at ASME Headquarters March 4, 1991. Paper No. 91-GT-219. Associate Technical Editor: L. A. Riekert.

ferential equations of the type shown above. A seventh differential equation is needed to define an energy balance on the rotating group. A torque imbalance (torque input from the turbine and torque output to the compressor and to the load) will produce an acceleration of the rotating group.

In addition the model has sensor delays, actuator delays, and lead-lag elements in the fuel control. A total of 11 states are present in the unaltered model. For purposes of devising a state-space fuel control, the number of states is reduced to eight. These are the control volume states and the shaft speed for a total of seven states. It is convenient to add an eighth state, integral of speed, so that the error in speed can be driven to zero. A ninth state, derivative of speed, provides anticipatory control at the expense of being sensitive to noise. This ninth state was obtained from the eight-state model by taking the dot product of the first row of the A matrix with the state vector. Only the polygonal search method used a control gain on this ninth state. The states in the state-space model are:

1 WGG shaft speed, rad/s
2 WGGINT integral of WGG, rad
3 T41 exit temperature from the turbine, R
4 W41 mass in the turbine control volume, lb
5 T4 inlet temperature to the turbine, R
6 W4 mass in the burner control volume, lb
7 T3 exit temperature from the compressor, R
8 W3 mass in the compressor control volume, lb
9 DWGG shaft acceleration, rad/s^2

The state-space fuel control gains (up to nine in number) were gains on each of these nine states.

2.0 Analysis

A good introduction to state-space methods and optimal control can be found in numerous texts, for example, Phillips and Harbor [4]. A fundamental knowledge of state-space methods is assumed in the rest of this development. With the analog model resident in ACSL, it is possible through ACTION and PROCED statements to look at various load set points and obtain perturbation models of the form [4]:

$$\delta\dot{\mathbf{x}} = A\delta\mathbf{x} + B\delta\mathbf{u} \tag{2.1}$$

where the A matrix is $(n \times n)$ and is the standard Jacobian array of the form

$$A = \begin{bmatrix} \dfrac{\partial f_1}{\partial x_1} & \dfrac{\partial f_1}{\partial x_2} & \cdots & \\ \vdots & & & \\ \dfrac{\partial f_n}{\partial x_1} & \cdots & & \dfrac{\partial f_n}{\partial x_n} \end{bmatrix}_{\mathbf{x}^0,\ \mathbf{u}^0} \tag{2.2}$$

and

$$B = \begin{bmatrix} \dfrac{\partial f_1}{\partial u_1} & \dfrac{\partial f_1}{\partial u_2} & \cdots & \\ \vdots & & & \\ \dfrac{\partial f_n}{\partial u_1} & \cdots & & \dfrac{\partial f_n}{\partial u_m} \end{bmatrix}_{\mathbf{x}^0,\ \mathbf{u}^0} \tag{2.3}$$

and the dimension of B is $(n \times m)$. The $\mathbf{x}^0$ and $\mathbf{u}^0$ vectors represent the selected operating point nominal values where

$$\mathbf{x} = \mathbf{x}^0 + \delta\mathbf{x} \tag{2.4}$$

and

$$\mathbf{u} = \mathbf{u}^0 + \delta\mathbf{u} \tag{2.5}$$

The output matrix, C, is also available and matrix D is null for these models. Varying the load, several operating points were established. The A, B, and C arrays were identified at each of these operating points using the ASCL JACOB command and routed directly into MATLAB [5], a high-level programming tool available for systems analysis.

2.1 Scaling. The A matrices identified using this Jacobian procedure are, of course, very poorly conditioned arrays. Following Brockus [6], for a set of state equations given in the form

$$\dot{\mathbf{x}} = A\mathbf{x} + B\mathbf{u} \tag{2.6}$$

Let the normalizing constant (scale factor) for variable x_i be denoted X_i, and let the scaled variable z be related to the state variables by the linear transformation

$$\mathbf{x} = T\mathbf{z} \text{ in which } x_i = X_i z_i \tag{2.7}$$

The T matrix so defined is diagonal with the scale factors constituting the diagonal elements. Its inverse is equally simple, being diagonal with the inverse scale factors on the diagonal. Thus the completed transform

$$\dot{\mathbf{x}} = T^{-1}A\,T\mathbf{z} + T^{-1}B\,u$$

or

$$\mathbf{z} = A_s\mathbf{z} + B_s u \tag{2.8}$$

is a very simple one in which it is apparent that the scaled A matrix is formed by dividing row i of the system matrix by scale factor i, and by multiplying column j of the system matrix by scale factor j. Therefore if

$$A = [a_{ij}]$$

then

$$A_s = [R_{ij}a_{ij}]$$

in which

$$R_{ij} = X_j/X_i \tag{2.9}$$

Thus the actual ratios of scale factors are of predominant importance for scaling the system matrix, and the scaling problem centers around the selection of that set of ratios. Assigning scaling factors as outlined by Brockus, we present a typical A and A_s (scaled) in Table 1. The conditioning of these two arrays is significantly different with A_s several orders of magnitude better than the original unscaled array A. The B matrix was also scaled to B_s with a "1" for the single input element, fuel flow, and a "0" for all others.

2.2 State Feedback Control. To implement a full-state feedback law of the form [7]

$$u = -g^T\mathbf{x} \tag{2.10}$$

where g is $(n \times l)$, the "place" command in MATLAB using Ackerman's formula was exercised. Fuel flow, u, is the single input for this system.

Three operating points (100, 50, and 0 percent load) were examined in detail. Eigenvalues of the identified A matrices from ACSL each had one right half-plane pole. We arbitrarily elected to move the poles to stable points in the s plane, solve for the q_i's and then do a linear system simulation about the designated operating point. Further, to perturb the system the speed (XNH) was varied by 5 percent for each operating point. Table 2 contains a typical set of eigenvalues for A_s and $A_s - Bg^T$.

Once the feedback gains have been obtained, a simulation over a 10 second interval using the load transient depicted in Fig. 2 was run in ACSL and the results are shown in Fig. 3. There are, of course, an infinite number of possibilities for the selection of the eigenvalues.

2.3 Linear Quadratic Regulator (LQR) Control. The solution of the LQR control problem [7] amounts to calculating the optimal feedback gain matrix K such that the feedback law

$$u = -K\mathbf{x} \tag{2.11}$$

Table 1

A:

$$\begin{bmatrix}
-8.1e-1 & 0 & -2.9e-1 & -1.4e4 & 6.9e-1 & 2.6e3 & -9.9e-2 & -2.1e2 \\
1 & 0 & 0 & 0 & 0 & 0 & 0 & 0 \\
-2.8e1 & 0 & -3.8e3 & -1.4e8 & 1.05e3 & 7.1e5 & -2.8e2 & -6.3e5 \\
-3.1e-4 & 0 & -1.4e-1 & -8.3e3 & 8.1e-3 & 8.0e1 & -2.7e-3 & -5.5 \\
1.9 & 0 & 6.0e-1 & 1.1e4 & 2.1e2 & 1.9e6 & -6.2e2 & -1.5e6 \\
1.05e-3 & 0 & 3.4e-4 & 6.2 & -1.7e-1 & -9.6e2 & 3.6e-1 & 7.9e2 \\
4.5e1 & 0 & 0 & 0 & 1.3e2 & 7.1e5 & -3.6e2 & -6.0e5 \\
3.9e-2 & 0 & 0 & 0 & 1.6e-1 & 8.8e2 & -3.6e-1 & -7.9e2
\end{bmatrix}$$

A_S:

$$\begin{bmatrix}
-8.1e-1 & 0 & -2.9e1 & -4.3e1 & 2.2 & 2.6 & -1.4e-1 & -2.2e-1 \\
1.1 & 0 & 0 & 0 & 0 & 0 & 0 & 0 \\
-2.8e-1 & 0 & -3.8e3 & -4.4e3 & 3.4e1 & 6.9 & -3.7 & -6.5 \\
-9.8e-2 & 0 & -4.4e3 & -8.3e3 & 8.3 & 2.5e1 & -1.1 & -1.8 \\
5.8e-1 & 0 & 1.9e1 & 1.1e1 & 2.1e2 & 5.7e2 & -2.6e2 & -5.0e2 \\
1.1 & 0 & 3.5e1 & 2.0e1 & -5.5e2 & -9.6e2 & 5.0e2 & 8.4e2 \\
3.3e1 & 0 & 0 & 0 & 3.0e2 & 5.1e2 & -3.6e2 & -4.5e2 \\
3.8e1 & 0 & 0 & 0 & 4.9e2 & 8.3e2 & -4.8e2 & -7.9e2
\end{bmatrix}$$

Table 2 Eigenvalues

A_S	$A_S - Bg^T$
-1.0976e+04	-1.0976e+04
-1.6660e+03	-1.6660e+03
-1.1471e+03	-1.1471e+03
-1.2181e+02	-1.2181e+02
4.8941e-01	-7.2998e+01
-7.2998e+01	-5.0000e-01
-4.0995e+01	-4.0995e+01

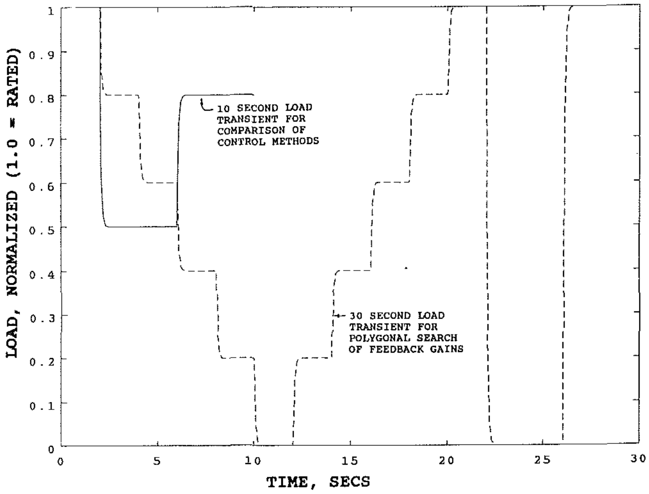

Fig. 2 Load transients

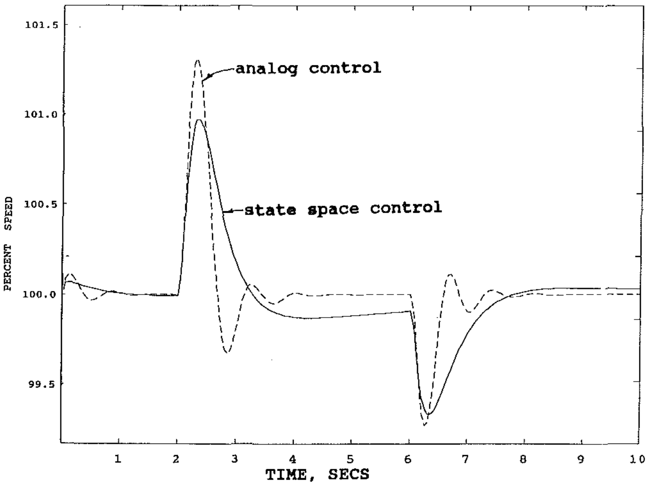

Fig. 3 Comparison of state feedback controller with analog controller

minimizes the cost function

$$J=\int_0^{tf}(\mathbf{x}\,Q\mathbf{x}+\mathbf{u}\,R\mathbf{u})dt \tag{2.12}$$

subject to the constraint equation

$$\mathbf{x}=A\mathbf{x}+B\mathbf{u} \tag{2.13}$$

Assuming the A and B arrays identified in ACSL for the different operating points are correct, then the main difficulty is selecting Q and R subject to the further constraints that Q be symmetric and positive semidefinite and the R be symmetric and positive definite.

Since only one input (fuel flow) is in the model, R may be any positive number. Once again, the choices and possibilities are endless. So for the purpose of getting started Q was chosen to be the $(n\times n)$ identity array and R was chosen to be "1" for the first case. The gains K were found using MATLAB at all three operating points and a simulation using one of these results was done over the standard load transient shown in Fig. 2. The results, shown in Fig. 4, show the LQR determined controller to compare favorably with the commercial analog controller.

2.4 Bellman Solution for Optimization. Given a homogeneous state equation

$$\dot{\mathbf{x}}=A\mathbf{x} \tag{2.14}$$

with quadratic cost function of the form

$$J=\int_0^{\infty}\mathbf{x}R\mathbf{x}\,dt \tag{2.15}$$

then the Bellman solution uses the Lyapunov function

$$R=A^TF+FA \tag{2.16}$$

with F a symmetric matrix. Find F to minimize the cost function

$$J=-\mathbf{x}^T(0)F\mathbf{x}(0) \tag{2.17}$$

Our linearized control system with control law $u=-k\mathbf{x}$ is just the form for the Bellman optimization. The gains K are perturbed to minimize the cost function (Eq. (2.17)). Simulation results for this optimization scheme are given in Fig. 5. Figure

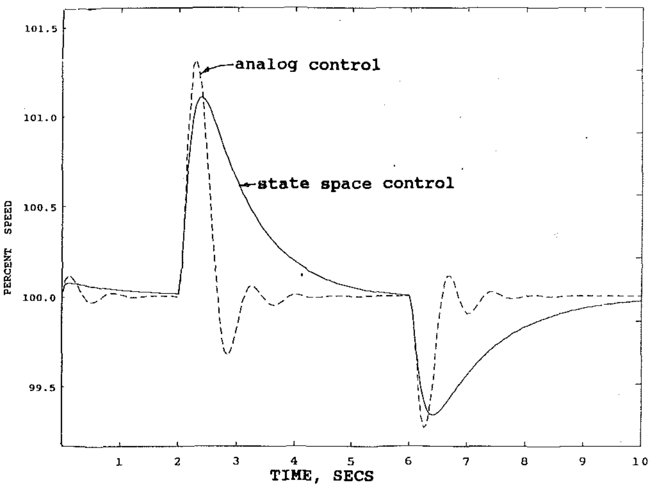

Fig. 4 Comparison of LQR feedback controller with analog controller

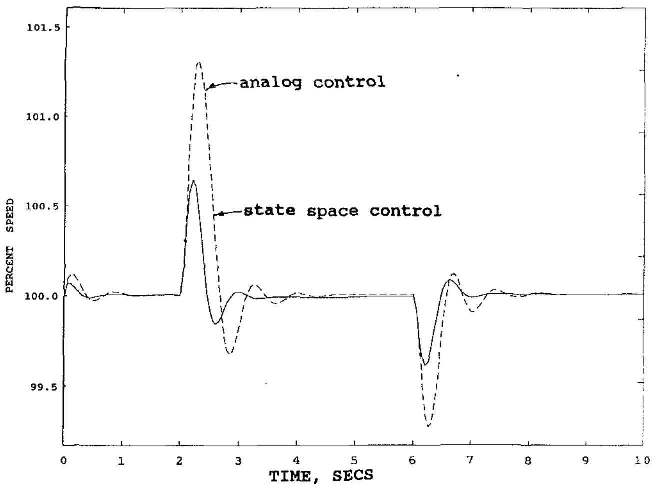

Fig. 6 Comparison of Bellman feedback controller with analog controller (with presetting)

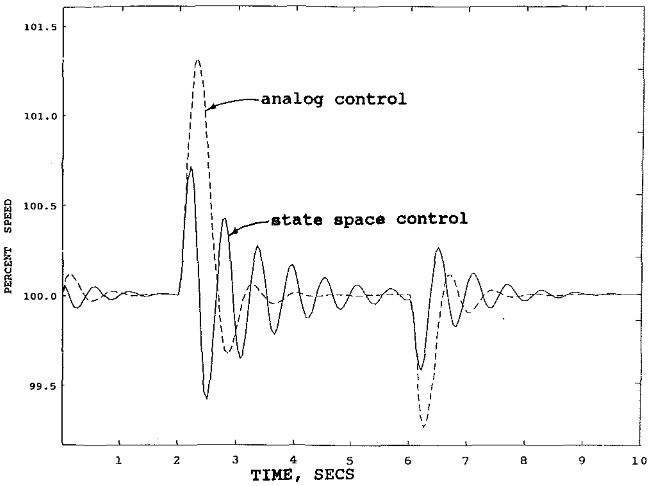

Fig. 5 Comparison of Bellman feedback controller with analog controller (no presetting)

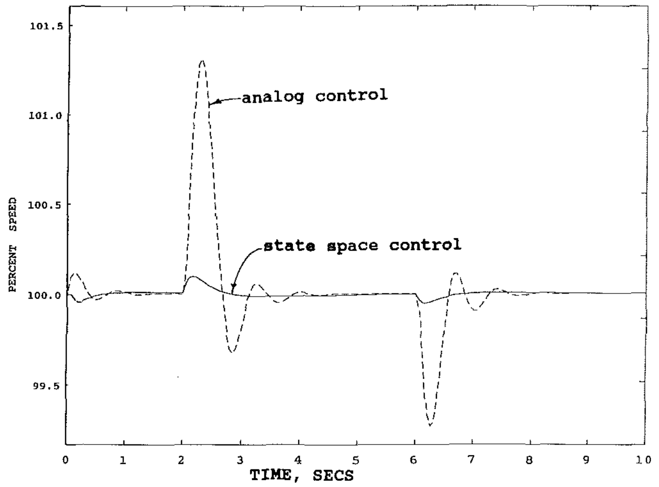

Fig. 7 Comparison of polygonal search feedback controller with analog controller (no speed sensing delay)

6 is an improvement over the results shown in Fig. 5 and required presetting some of the eigenvalues.

2.5 Polygonal Search. One method of obtaining fuel control feedback gains is through a search optimization technique as follows:

1 The parameters in the search are the feedback gains.
2 The cost function is the integral of the speed error over some arbitrary load transient.
3 The "optimal" gains are obtained by repeated runs of the simulation over the arbitrary load transient.

A flexible polygonal search [8] works well in this case. The parameters (up to nine in number) create a search polygon in nine space that becomes oblong in the direction of cost function improvement as the search progresses. Figure 2 shows the somewhat extravagant 30 second load transient that was used for this method. A lot of computer time is required for this method so batch run were made overnight. The various sets of feedback gains and the resultant eigenvalues are shown in Table 3. Figure 7 is a comparison of the fuel control using gains obtained by the polygonal search versus the analog fuel control where it is noted that the state feedback gains control extremely well. Part of this is because the delay in speed sensing was removed for this initial search. When the sensing delay was put back into the model the transient curve shown in Fig. 8 was obtained. It still does much better than the analog control, but a lead circuit (anticipatory) can be applied to the speed sensing and reduce the effect of the sensing delay. Figure 9 shows the transient with this lead circuit present. An interesting result is shown in Fig. 10. The feedback gains for this control are also presented in Table 3 where it can be noted that only three states were used in the control. The polygonal search was thus only a search in three space. The extremely tight control is probably not realizable in practice because of the very high gain on the derivative of speed, which as noted before, is too subject to noise to be practical.

3.0 Summary and Conclusions

Several different schemes for arriving at controllers for a gas turbine engine have been investigated. An analog model programmed in ACSL was used to develop a linearized state-space representation for use in MATLAB. The different approaches for obtaining feedback gains and the results from each set of gains are presented. The approaches are: state feedback, LQR, Bellman, and polygonal search.

The state-space approach to developing controllers is a viable one for simulations of this size and larger. In particular, multi-input, multimode fuel controllers are readily adaptable to this approach.

No comparison has been attempted to analyze which of these state-space approaches is the "best" other than a graphical

Table 3 Feedback gains and eigenvalues

Feedback Gains:

Fig 3	Fig 4	Fig 5	Fig 6	Fig 7	Fig 8	Fig 9	Fig10
-7.442	-3.497	-60.36	-41.26	-61.10	-61.25	-62.37	-3945.
-1.924	-.0470	-1.398	-4.683	-159.4	-157.3	-156.9	143.9
.00025	.00012	.00026	0	56.40	58.34	58.54	0
7.920	3.991	6.248	0	16.00	18.87	20.46	0
.0255	-.0130	-.6e-6	0	-14.00	-9.464	-2.180	0
-278.2	-141.0	-9016.	0	-150.0	-146.6	-139.8	0
-.0257	-.0129	-.0124	0	-340.7	-336.9	-336.9	0
-207.7	-105.4	-37.36	0	-430.0	-428.9	-427.1	0
Derivative of Speed feedback gain:							
0	0	0	0	-100.0	-97.93	-97.56	-3436.

Eigenvalues (of A+B*K):

Fig 3	Fig 4	Fig 5	Fig 6	Fig 7	Fig 8	Fig 9	Fig10
-10976	-10976	-10976.	-10976	-11938	-11872	-11799	-18576
-1667.	-1666.	-1737.6	-1666.	-5723.	-5363.	-4909.	-10366
-1147.	-1147.	-1146.8	-1147.	-2123.	-2140.	-2151.	-1370.
-116.4	-121.9	-23.6+j35.4	-101.5	-615.2	-559.9	-492.4	-1051.
-73.51	-72.97	-23.6-j35.4	-80.86	-33.39	-31.16	-26.10	-1.182
-.4730	-40.99	-72.66	-10.52	-.9627	-.7840	-5.360	-354.2
-1.098	-.4191	-44.04	-.1204	-1.958	-54.94	-.6863	-37.74
-41.03	-.0291	-.0219	-42.69	-56.41	-3.053	-52.93	-65.29

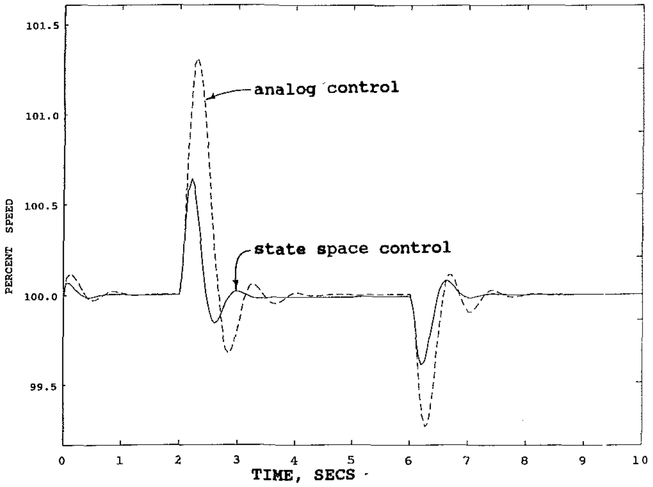

Fig. 8 Comparison of polygonal search feedback controller with analog controller (with speed sensing delay)

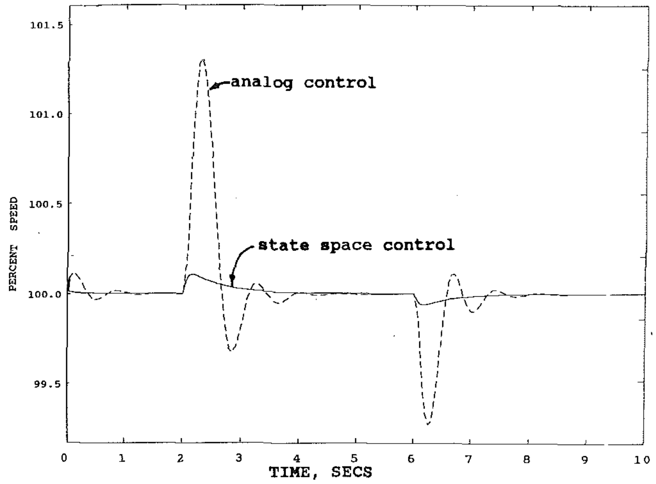

Fig. 9 Comparison of polygonal search feedback controller with analog controller (with lead filter)

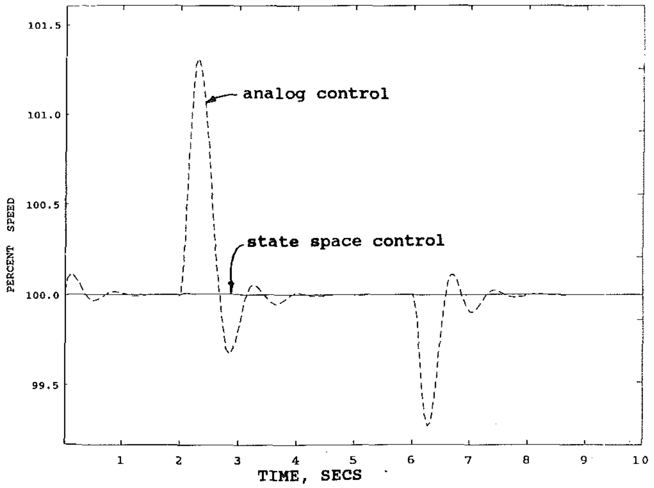

Fig. 10 Comparison of polygonal search (three states) feedback controller with analog controller

comparison of the controller in action. Much research of the seemingly endless variations in these methods needs to be conducted.

References

1 Harmon, R. A., "Marine Gas Turbines: A New Generation," *Mechanical Engineering*, May 1990, pp. 48-51.

2 Mitchell and Gathier Associates, *Advanced Continuous Simulation Language Reference Manual*, 1986.

3 Daniels, C. J., et al., "Digital Computer Program for Generating Dynamic Turbofan Engine Models (DIGTEM)," NASA Technical Memorandum 83446, Sept. 1983.

4 Phillips, C. L., and Harbor, R. D., *Feedback Control Systems*, Prentice-Hall, 1988.

5 *PRO-MATLAB*, the Mathworks, 1987.

6 Brockus, C. G., "Scaling the Equations for Polynomial Least Mean Squares Curve Fitting," *Proceedings of the 19th Annual Pittsburgh Modeling and Simulation Conference*, Vol. 19, Part 5, pp. 2077-2081.

7 D'Azzo, J. J., and Houpis, C. H., *Linear Control System Analysis and Design*, 3rd ed., McGraw-Hill, New York, 1988.

8 Himmelblau, D. M., *Applied Nonlinear Programming*, McGraw-Hill, New York, 1972.

Influence of a Shroud on Swirler Flow Fields

H. Eroglu

N. Chigier

Department of Mechanical Engineering,
Carnegie Mellon University,
Pittsburgh, PA 15213

The flow fields for swirlers with and without a shroud were measured using a two-component laser-Doppler velocimeter (LDV) system. The primary goal of this study is to investigate the effect of shrouds on swirler flow fields, in order to provide useful design information for the manufacture of gas turbine fuel nozzles, and to supply benchmark data for comparison with numerical predictions. As a result of the measurements, the radial distributions of three mean velocity components, turbulence intensity, and shear stresses were obtained at five locations ($x/d = 0.1, 1, 2, 4,$ and 8) along the axis of the swirlers. The LDV system was operated in the 20 deg off-axis forward scatter mode with beam expanders and Bragg cell frequency shifting on both components. The flow was seeded by 1 μm mean diameter atomized particles of glycerol and water (50/50) mixture. Comparison of flow with and without the shroud showed that the jet diameter was much smaller, and the flow deceleration in the downstream direction was faster, due to the influence of the shroud, at the same supply pressure (750 mm H_2O). As a result of the significant reduction in the swirl number due to the addition of the shroud, the recirculation zone disappeared. In addition to its influence on recirculation, the shroud caused a radially inward shift of the maximum mean and turbulence parameters at all axial locations. The anisotropy of turbulence increased as compared to the values for the swirler without the shroud.

Introduction

Swirlers are used in modern gas turbine burners for controlling the spray angle and generating recirculation to provide proper fuel placement and for improving atomization. A shroud is very often added downstream of the swirler, in order to protect the nozzle from overheating by the flame, and to prevent the deposition of coke, by directing the flow radially inward across the nozzle face. The shroud also enhances atomization. However, it influences the flow field significantly, often reducing the swirl number, with a subsequent adverse effect on the flame stability.

Vane type swirlers are the most common swirl generators used with airblast atomizers in gas turbines and other combustion systems (Martin, 1987). They are made of either straight or curved vanes. Curved vanes have higher aerodynamic efficiencies, but straight vanes are also used for reasons of ease and economy of manufacture. Measurements of swirling flow fields have been made for various geometries. In the earliest experimental studies, flow velocity was measured by five-hole impact probes; later studies used hot-wire anemometers and some results have been reported on measurements performed by laser velocimetry. The results of these studies are reviewed in the books by Beer and Chigier (1972) and Gupta et al. (1984). Many problems encountered while using pressure probes and hot-wire anemometers in complex turbulent isothermal and combusting flow fields were overcome by the advent of laser-Doppler velocimetry (LDV), which is a linear nonintrusive measurement technique. The results of some of the recent LDV measurements in turbulent, swirling, isothermal and combusting flows are reported by Fujii et al. (1981), Gupta et al. (1984), and Kihm et al. (1990). Fujii et al. (1981) presented the three mean velocity and all six turbulent stress tensor components in an unconfined swirling jet under isothermal and combusting flow conditions, as a result of the first attempt of using LDV technique in such flow fields. The results indicate that the turbulence and its anisotropy increase as a consequence of combustion. Ramos and Sommer (1985) investigated the flow fields of co- and counterswirling jets in a cylindrical combustor. A two-component LDV was used simultaneously to measure axial and circumferential velocity components. Measurements results are reported of axial and circumferential mean and fluctuating velocity components and one turbulent shear stress component. In addition, numerical calculations are presented for the same geometry and inlet flow conditions. The experimental and numerical results are compared to the results of hot-wire anemometer measurements for a similar geometry. The experimental data obtained using LDV agree satisfactorily with the numerical results, but do not agree with the other experimental data acquired using hot-wire anemometry under coswirl flow conditions. Sislian and Cusworth (1986) present the results of LDV measurements of the three mean velocity and six turbulent stress tensor components in a free isothermal swirling jet. The results provide a detailed data base for the numerical procedures using various turbulence models. Kihm et al. (1990) report LDV measurement results for straight

---

Contributed by the International Gas Turbine Institute and presented at the 35th International Gas Turbine and Aeroengine Congress and Exposition, Brussels, Belgium, June 11-14, 1990. Manuscript received by the International Gas Turbine Institute December 23, 1989. Paper No. 90-GT-31.

vaned swirlers at two different supply pressures (750 mm and 1500 mm H_2O). Three mean velocity and five turbulent shear stress components are presented for three different swirl angles (20, 40, and 60 deg). The results demonstrate that there is similarity between the normalized velocity profiles at the different supply pressures, and the turbulence is locally isotropic except near the nozzle exit. The swirler with the 40 deg vane angle was found, surprisingly, to generate higher swirl velocities than the 60 deg swirler.

This paper presents the LDV measurement results for a 40 deg vane angle swirler with and without a shroud. Three mean velocity and five turbulent stress distributions were obtained at five axial locations with x/d: 0.1, 1, 2, 4, and 8, by measuring two orthogonal velocity components simultaneously at each point. In particular, the effect of the shroud on the swirler flow field was investigated, by comparing the results for the swirlers, with and without a shroud, at the same supply pressure, and vane geometry. The primary objectives of this study were to provide useful design information for the manufacture of gas turbine fuel nozzles and to supply benchmark data for comparison with numerical predictions.

Experimental Setup

The experimental setup is shown schematically in Fig. 1. It consists of the air swirler, the seeding particle atomizer, and the laser-Doppler velocimetry (LDV) system.

Test Rig. The high-pressure supply air (maximum 100 psig) passes through a valve, a filter, and a pressure regulator before entering the air swirler, as shown in Fig. 1. Mass flow rate can be varied by using the valve and the pressure regulator. The air swirler setup contains a honeycomb and a settling chamber upstream of the vanes. The flow is seeded, and the inlet pressure to the swirler is measured with a U-tube manometer, which has an accuracy of 0.1 in. (2.54 mm) in the settling chamber. Figure 2 shows the configuration of the shrouded swirler used in this study. It was manufactured by modifying the air swirler without the shroud in order to study the effect of shroud on the flow field. This swirler has twelve vanes made of flat plates with the shroud section following the vanes. The annular gap width for the vaned section is 7 mm, and the hub and tip diameters are 12 mm and 23 mm, respectively. The vane angle is 40 deg with respect to the axis of the swirler. The shroud directs the air radially inward, and its walls have an angle of 35 deg measured from the axis of the swirler. The swirling air is discharged to atmosphere through the 10-mm-dia exit area of the shroud section.

The swirler is installed to the frame of a three-dimensional traversing mechanism controlled via d-c stepping motors. Positioning accuracy is 0.25 mm in all three directions.

Flow Seeding. A TSI model 9306 six-jet atomizer was used to seed the flow with particles of 50/50 glycerol and water mixture. The atomizer was connected to the settling chamber of the test rig through a 12.7-mm (0.5 in.) diameter and 915-mm (36 in.) length flexible tube as shown in Fig. 1. The average maximum range of particle densities was found to be on the order of 6×10^{12} particles/m^3. Although the maximum particle diameter at the atomizer outlet reaches 8 μm, fewer than 1 percent of the particles have diameters more than 7 μm according to the TSI model 9306 six-jet atomizer instruction manual. The size distributions were measured repeatedly using the Aerometrics phase Doppler particle size analyzer (PDPA). The mean diameter at the exit of the atomizer was 2 μm. However, the arithmetic mean particle diameter was less than 1 μm at the exit of the air swirler. The maximum particle diameter was found to be about 4 μm. The change in particle size was due to the condensation of larger drops on the flexible tube walls and the swirler vanes.

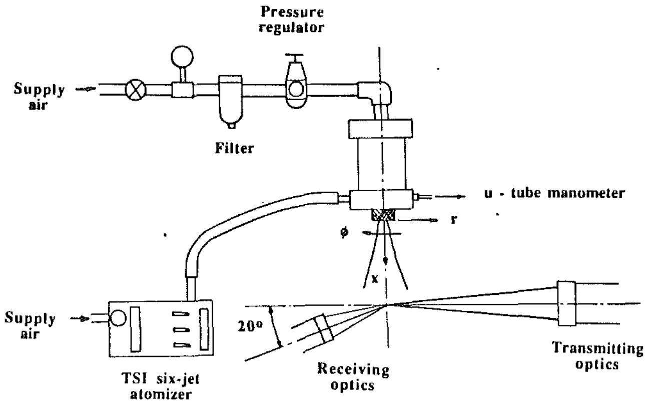

Fig. 1 Experimental setup

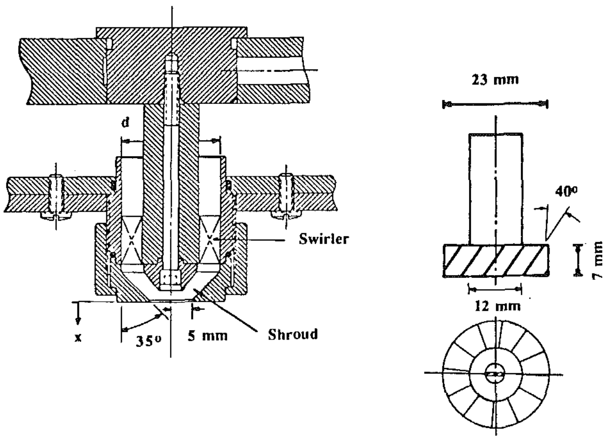

Fig. 2 Schematic of the air swirler configuration

LDV System. A two-color, two-component LDV system was used in the 20 deg off-axis, forward scatter mode. The

Nomenclature

d = vane tip diameter
k = turbulent kinetic energy
m_e = entrainment mass flow rate
m_o = swirler exit mass flow rate
N = sample size
r = radial direction
rms = root mean square
S = swirl number
s_v = standard deviation of velocity components
u, v, w = axial, radial, and circumferential velocity components
Δv = uncertainty of velocity component v
$\overline{u}, \overline{v}, \overline{w}$ = axial, radial, and circumferential mean velocity components
u', v', w' = axial, radial, and circumferential fluctuating velocity components
$\overline{u'v'}, \overline{u'w'}$ = turbulent shear stress components
x = axial distance measured from nozzle exit
τ_v = transit time
ϕ = circumferential direction

LDV system consists of a 4 W argon-ion Lexel model 95 laser, TSI optics, counters and data acquisition system. An IBM PC/AT computer is connected to the LDV system for data processing.

The optical components separate the laser beam into two components with green and blue colors of wavelengths 0.5145 μm and 0.488 μm, respectively. Each component is split into two equal intensity beams on two orthogonal planes after being polarized. The two beam pairs are focused into one common measuring volume to create two orthogonal interference fringe patterns. A beam expander provides a 3.75-fold decrease in the measuring volume diameter with a 50 fold increase in the signal-to-noise ratio (SNR). The focal lengths are 762 mm and 242 mm for the transmitting and receiving lenses, respectively. The present optical arrangement, with the 20 deg off-axis forward scatter mode, generates an effective measurement volume of length 0.71 mm, and diameters 102.3 μm and 97.12 μm for the vertical (green) and horizontal (blue) components, respectively. The corresponding fringe spacings are 4.76 μm and 4.51 μm for the green and the blue beam pairs. Each component contains 21 fringes. Bragg cell frequency shifters with the downmixers enable frequency shifts of 1 to 10 MHz applied on both channels in order to determine the velocity directions and reduce the directional bias. On-line data acquisition is achieved through the TSI interface boards. These boards between the counters and the computer can set a coincidence window between the two channels, to ensure the simultaneous measurement of two orthogonal velocity components. The optical components of the LDV system were carefully aligned, calibrated, and rigidly mounted on massive optical tables.

Measurement Technique. The experiments were performed at five locations along the axis of the swirler. These locations have the normalized distances x/d = 0.1, 1.0, 2.0, 4.0, and 8.0, where x is the distance from the exit of the swirler, and d is the vane tip diameter.

Providing uniform seeding particle concentrations inside and outside the swirling jet was practically impossible for the present experimental setup. During the experiments, average data rates were 5000/s in the central flow and about 100/s at the edges of the swirling jet. Although the surrounding air was not seeded, laser sheet flow visualization studies showed that there are considerable numbers of particles suspended in the surrounding air. Therefore, it was possible to observe visually the surrounding air entrainment into the jet. The suspended particles in the surroundings allowed LDV measurements of the entrained air; however, because of the significantly low seeding density, the accuracy of these latter measurements was less. The velocity bias due to the spatial variations of particle concentration is reduced by means of the sampling and data averaging technique used in this investigation according to Durst et al. (1981). This technique is explained in a later paragraph. Similarly, a low seeding density region was observed at the center of the swirling jet, extending from the exit of the swirler to a distance between 1 and 2 diameters downstream. Typical data rates were about 100/s in this region.

The LDV counters were operated in the N-cycle mode. Eight cycles were used for the measurement of Doppler frequencies, with 7 percent comparison for the validation of each data. The number of cycles timed was selected according to a rule given in the TSI model 1980B counter type signal processor instruction manual. This rule states that the number of cycles timed should be less than half of the number of fringes across the center of the measuring volume. Eight cycles is the maximum possible setting with the present optical arrangement. Seven percent comparison was selected in order to keep the data acquisition time within reasonable limits. A lower setting would improve the accuracy; however, this improvement is not significant since the amplitude discriminators of the counters used during the experiments effectively eliminate all Doppler signals of low signal-to-noise ratio, and reduce the influence of time comparisons according to Durst et al. (1981). This was also confirmed by the measurements performed at several locations with different time comparisons. The effect of this parameter on the accuracy was negligible as compared to that of other error sources. The use of frequency shifts reduced the directional bias considerably. The filter settings were carefully selected with repeated trials in order not to collect samples very close to the cutoff frequencies, since strong signal biasing has been shown to occur near the band edges (Oberle and Seasholtz, 1985). Band widths were kept as small as possible to block the noise off from the regions out of the Doppler frequency range. For the simultaneous measurement of the velocity components, coincidence window of 10 to 100 μs were tested. The Reynolds shear stress values were found to be strongly dependent on the coincidence window setting, and the data rate as also mentioned by Edwards (1987). As a result, a 10 μs coincidence window, which is the minimum possible setting with the TSI model 1998 interface, was selected for the simultaneity of the measurements.

The axisymmetry of the jet and the repeatability of the measurements were checked during the initial phase of the experimental work. Figure 3 shows the axial velocity component variation with radius as a result of the measurements along a complete longitudinal traverse through the center of the jet at x/d = 1.0. The symmetry on both sides of the jet is satisfactory except that there is a kink at the peak of the velocity distribution on the left side. Similarly, the distributions shown in Fig. 4 as a result of the longitudinal and transverse traverses at x/d = 2.0 show good agreement. The longitudinal traverse of Fig. 3 was repeated at one side of the jet center, in order to check the repeatability of the measurements. The

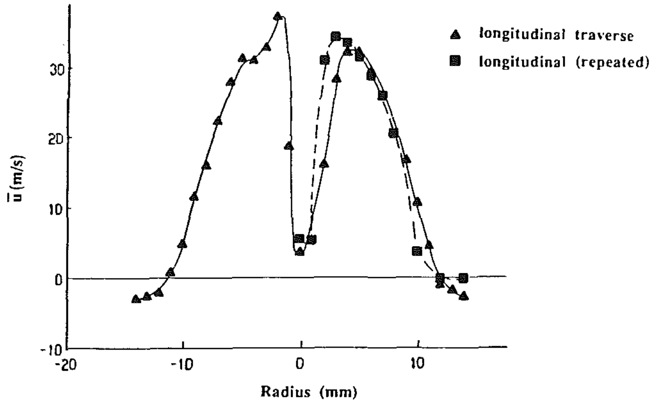

Fig. 3 Axial mean velocity profiles at x/d = 1.0

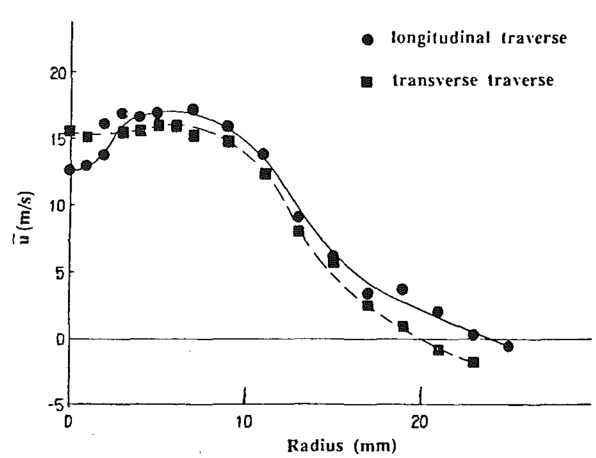

Fig. 4 Axial mean velocity profiles at x/d = 2.0

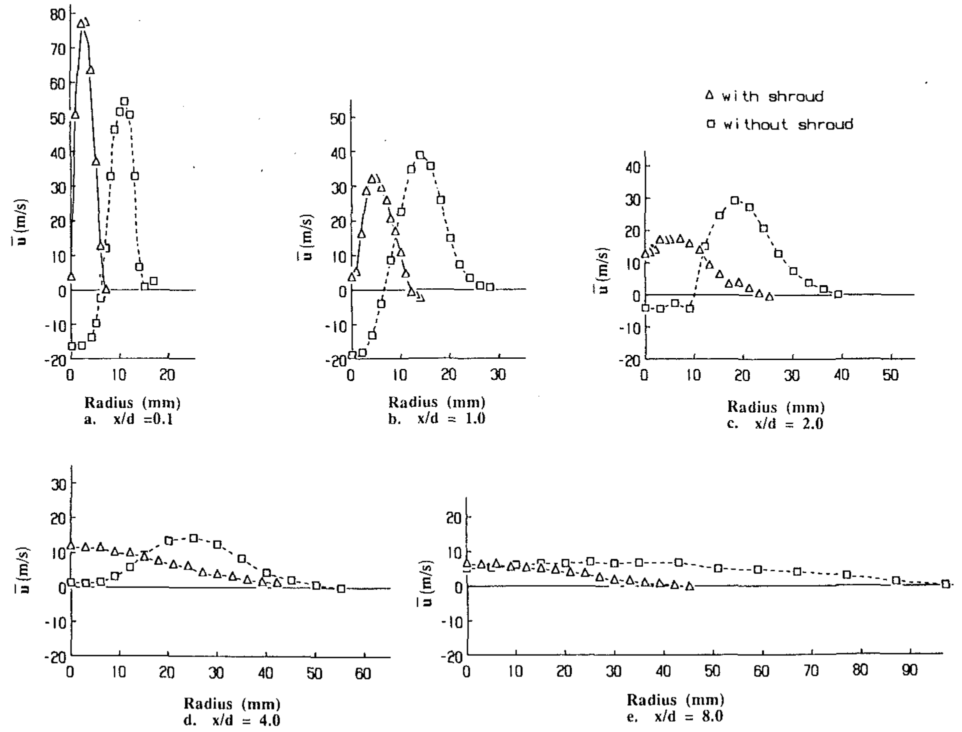

a. x/d = 0.1
b. x/d = 1.0
c. x/d = 2.0
d. x/d = 4.0
e. x/d = 8.0

Fig. 5 Axial mean velocity profiles

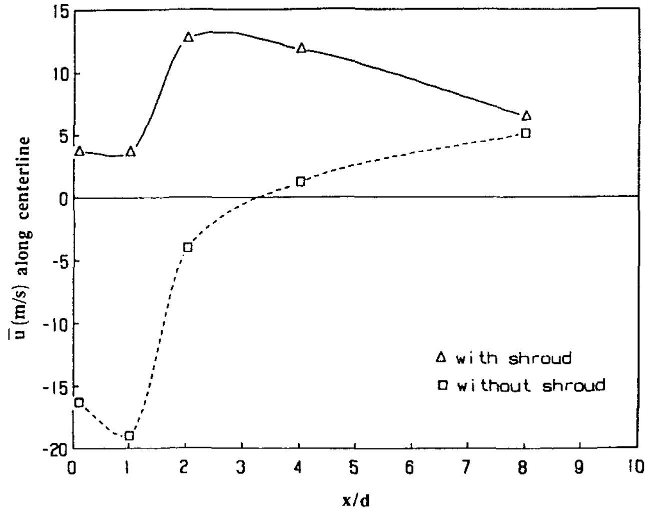

Fig. 6 Axial mean velocity measured along the centerline

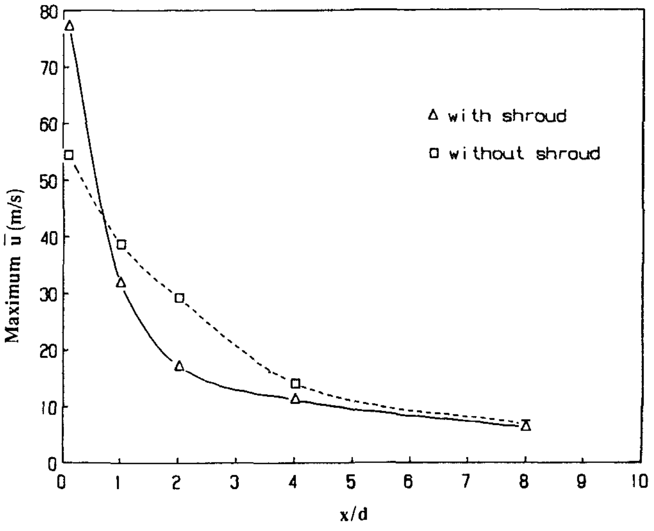

Fig. 7 Decay of maximum axial mean velocity

measured mean velocities were found to change less than 5 percent except at the center and the edge of the jet, where the data rates are much lower.

For each data point, 5000 samples were averaged. Since different data densities were encountered in the jet, a transit time-weighted averaging was used in the statistical calculations as suggested by Oberle and Seasholtz (1985), and implemented in the TSI data acquisition software. For instance, the mean velocity was obtained from

$$\bar{u}=\frac{\Sigma u\tau_u}{\Sigma\tau_u} \qquad (1)$$

where u is the instantaneous velocity, and τ_u is the transit time of a particle in the measurement volume. In this way, the velocity bias error was corrected for the different operation modes of LDV.

During the experiments, the orientation of the ellipsoidal measurement volume was such that the minor axis where the diameter is about 100 μm coincided with the radial direction of the swirler for the radial (v) and circumferential (w) velocity component measurements. The axial component was simultaneously measured with these two components at two times. One of these allowed the minor axis of the ellipsoid to be in the radial direction with better spatial resolution, since the maximum gradients are in this direction. The maximum velocity gradients were observed in the exit plane where x/d = 0.1. The maximum variation of the mean velocity inside the measurement volume was found to be 6.5 percent of the maximum velocity in this plane. In the downstream flow direction, the gradients and consequently the error due to spatial resolution gradually decreased.

The uncertainty of the measured mean velocities was determined using the techniques described by Snyder et al. (1981,

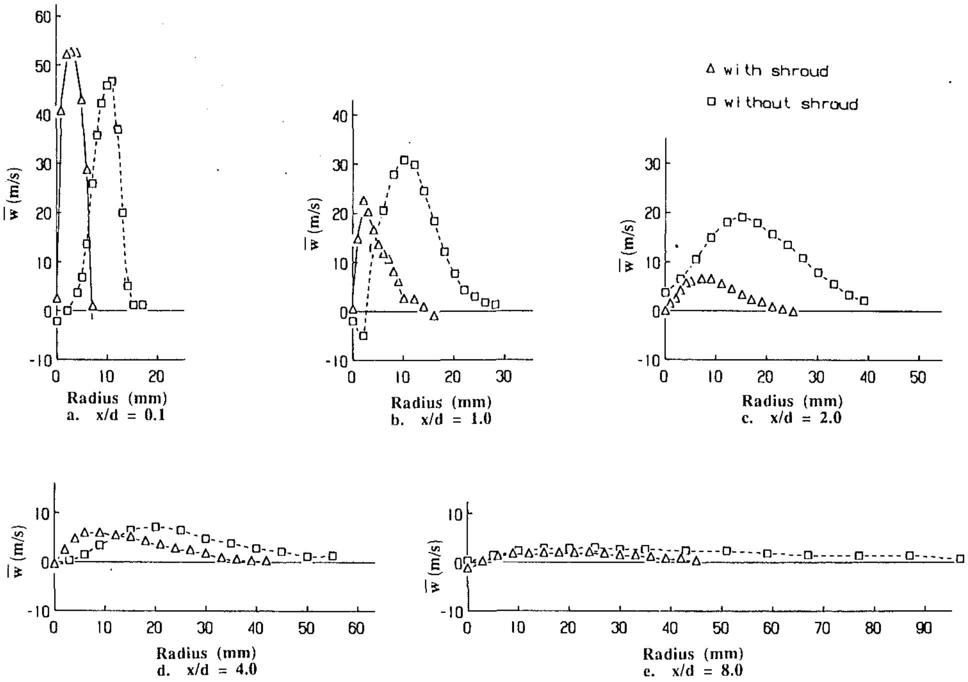

Fig. 8 Circumferential (swirl) mean velocity profiles

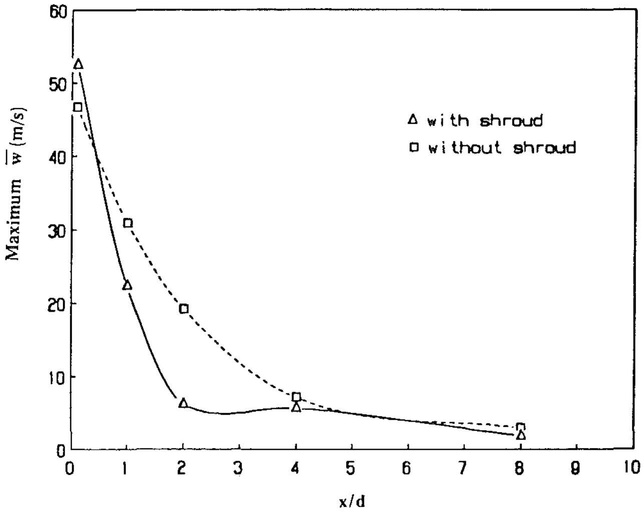

Fig. 9 Decay of maximum circumferential (swirl) mean velocity

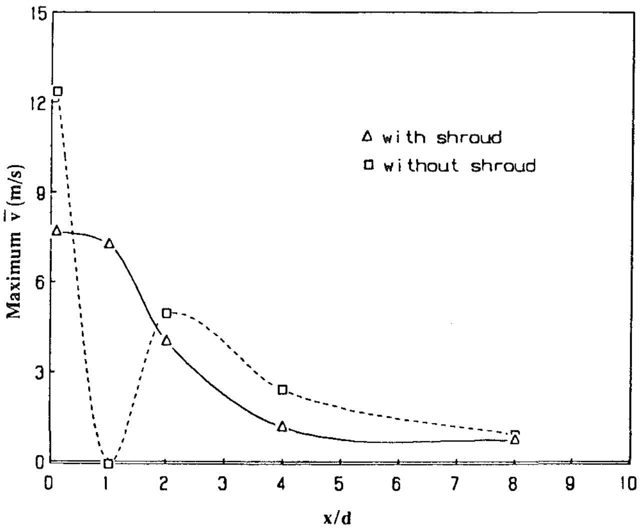

Fig. 10 Decay of maximum radial mean velocity

1984) and Orloff and Snyder (1982). These references related the measurement uncertainty interval to the sample size through the relation

$$\Delta U = \pm \frac{1.96 s_u}{\sqrt{N}} \qquad (2)$$

for 95 percent confidence level; s_u is an estimator for the true standard deviation and N is the sample size. The constant 1.96 is used for 95 percent confidence level. Using Eq. (2), the maximum uncertainties of the mean quantities due to random errors were found to be 0.9, 0.8, and 4 percent of their respective maximum axial, circumferential, and radial velocity components. The overall uncertainties of the mean velocity and turbulent stresses are estimated as 3 and 7 percent respectively.

Results and Discussion

Measurements of mean velocity, turbulent intensities, and shear stresses were made at the axial distances x/d: 0.1, 1, 2, 4 and 8 for the 40 deg vane angle swirler with and without a shroud, at 750 mm water column supply pressure.

The radial distributions of mean axial velocity component are shown in Figs. 5(*a-e*) for the five axial measurement stations. The distributions for the swirlers with and without shroud are compared in these figures. Unlike for the swirler without the shroud, the axial component profiles for the shrouded swirler do not show any reverse flow in the central region. As shown in the centerline axial velocity versus x/d plot of Fig. 6, the recirculation zone completely disappeared due to the existence of the shroud. The swirl numbers determined using the definition of Beer and Chigier (1972) and integrated velocity measurements at the different axial stations gave the range of values 0.3 to 0.46 for the shrouded swirler, with the higher values at the exit station (x/d = 0.1). These numbers are below the critical swirl number, which is about 0.6, as compared to the range of swirl numbers, 0.7 to 1.2 for the swirler without the shroud. The velocity profiles are at smaller radii for the swirler with the shroud at all axial stations denoting a decrease in the jet diameter. This radial inward shift is more pronounced at the upstream stations. The radial distance of the axial velocity maximum increases with distance downstream. The shroud reduces the flow area at the exit at the swirler. The blockage of the flow by this area reduction caused the mass flow to decrease significantly, although the inlet pressures for the swirlers with and without the shroud were the same. This is evidenced by the integration of the axial velocity profiles of Figs. 5 (*a–e*), since density variation is not important for Mach No. < 0.3. Although the peak velocity for the shrouded swirler is higher at $x/d = 0.1$ (Fig. 5*a*), the mass flow rate for the swirler without the shroud has in general higher values (Figs. 5*a–e*), because of the larger flow areas at greater radii. Figure 7 shows the decay of the maximum axial mean velocity with respect to the axial distance x/d. The jet leaving the shrouded swirler decelerates much faster up to $x/d = 2$, then continues its deceleration more gradually as compared to the jet from the swirler without the shroud. It is interesting to note that the maximum velocities at $x/d = 8$ for both swirlers reach almost the same value. This vaue is about 10 percent of the exit maximum axial velocity for the shrouded swirler.

Figures 8 (*a–e*) display the radial distributions of the mean swirl velocity component at the five axial measurement stations. These distributions have the general form of a Rankine vortex with a solid-body rotation core and a free vortex in the outer region of the jet for both swirlers. The profile shapes are similar to those of Fujii et al. (1981), Sislian and Cusworth (1986), and Kihm et al. (1990). The radial distance of the swirl velocity maximum increases with distance downstream. Similar to the distributions in Figs. 5 (*a–e*), the swirl velocity profiles for the shrouded swirler are at smaller radii, as compared to the profiles for the swirler without the shroud, as shown in Fig. 8 (*a–e*). The decay of maximum swirl velocity along the downstream axial direction is shown in Fig. 9 for the swirlers with and without the shroud. Similar to the decay of axial velocity maximum in Fig. 7, the maximum swirl velocity component decreases rapidly up to $x/d = 2$, then it continues to decrease at a much slower rate. Unlike the axial velocity component (Fig. 7), the swirl velocity component for the shrouded swirler has a lower magnitude than for the swirler without the shroud at $x/d = 8$.

Figure 10 shows the decay of the mean radial velocity component for the swirlers with and without the shroud in the downstream axial direction. The maximum radial velocities are higher for the swirler without the shroud at all axial locations except at $x/d = 1.0$. This is consistent with the radial distributions of mean axial and circumferential velocity components in Figs. 5 and 8, since the jet diameter and divergence are smaller for the shrouded swirler. The decay of the radial velocity component in the downstream axial direction is very rapid, especially between $x/d = 1$ and 4 for both swirlers; however, it is gradual for the shrouded swirler between $x/d = 0.1$ and 1.

The mass entrainment rate was calculated by integrating the velocity profiles and by subtracting the mass flow rate at the exit of the shrouded swirler at each axial location. Its value was found to be 3.24 at $x/d = 4.0$. The entrainment rate was also calculated using the following equation (Eq. (5.23) of Beer and Chigier, 1972):

$$\frac{m_e}{m_o} = (0.32 + 0.8S)\,\frac{x}{d} \qquad (3)$$

where S is the swirl number; m_e and m_o are the entrainment and swirler exit mass flow rates. Equation (3) shows the influence of swirl number on the entrainment rate. It was found to be 2.774 at $x/d = 4.0$ using this equation where the swirl number S was obtained from the experimental results at the swirler exit ($x/d = 0.1$).

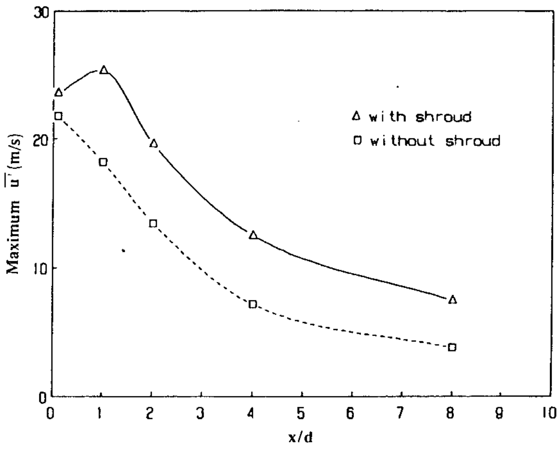

Fig. 11 Decay of maximum axial fluctuating (rms) velocity

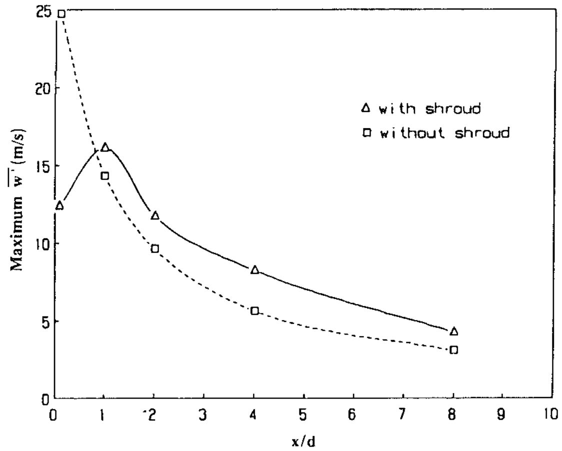

Fig. 12 Decay of maximum circumferential (swirl), fluctuating (rms) velocity

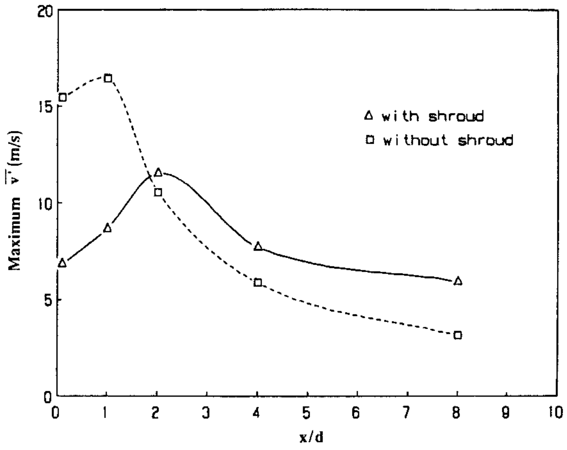

Fig. 13 Decay of maximum radial fluctuating (rms) velocity

The maxima of the rms (fluctuating) velocity components $\overline{u'}$, $\overline{w'}$, $\overline{v'}$ are plotted against the axial distance x/d for the swirlers with and without the shroud in Figs. 11, 12, and 13. The maxima of the rms (fluctuating) velocity components are in general higher for the shrouded swirler except at the exit station ($x/d = 0.1$). Figures 11 and 12 show that the maxima of the rms velocities $\overline{u'}$ and $\overline{w'}$ first increase up to $x/d = 1$,

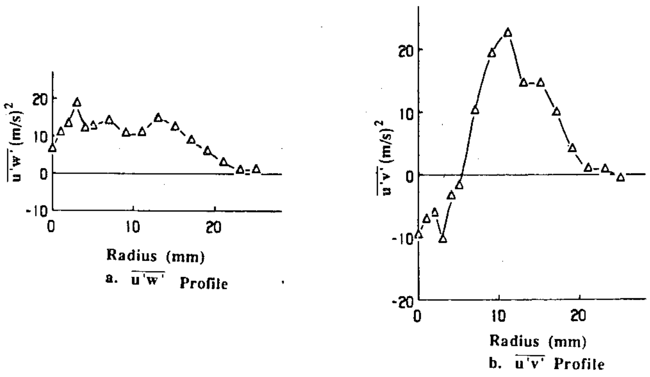

a. $\overline{u'w'}$ Profile

b. $\overline{u'v'}$ Profile

Fig. 14 Turbulent shear stress profiles at x/d = 2.0

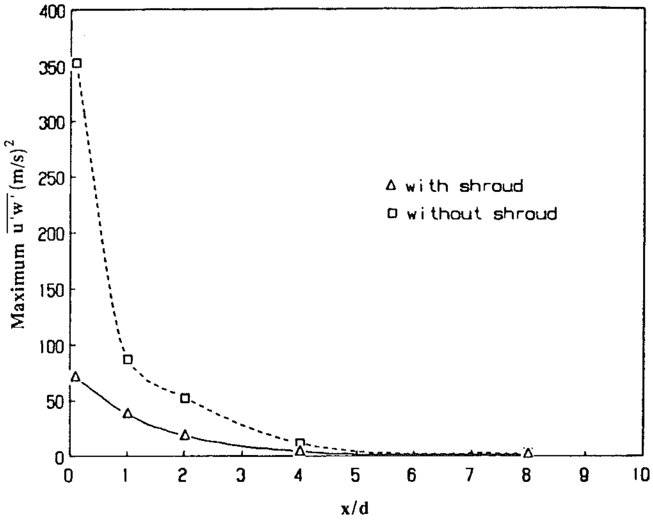

Fig. 15 Decay of maximum turbulent shear stress component $\overline{u'w'}$

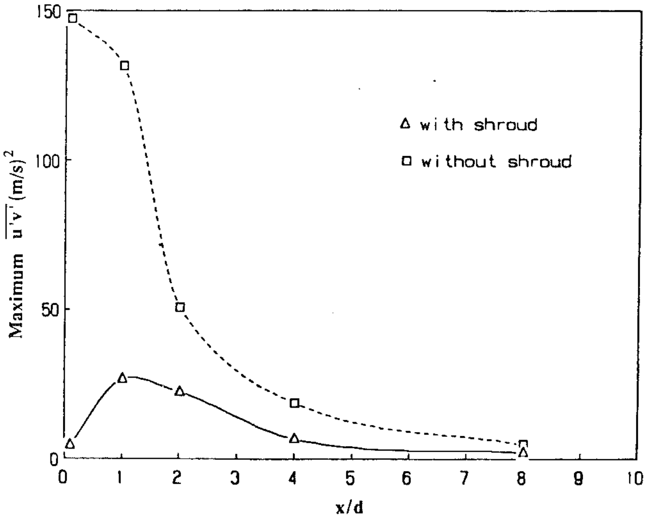

Fig. 16 Decay of maximum turbulent shear stress component, $\overline{u'v'}$

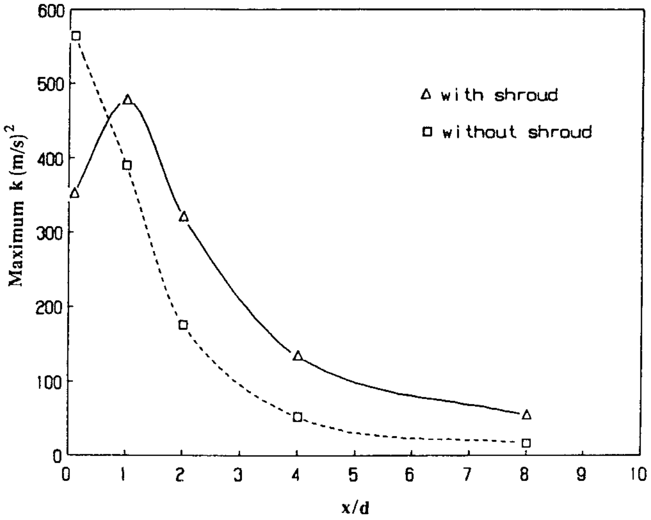

Fig. 17 Decay of maximum turbulent kinetic energy

then start decaying for the shrouded swirler. However, the axial position where the decaying starts is at about $x/d = 2$ for the rms velocity component $\overline{v'}$, as shown in Fig. 13. The lower values of the rms velocity components in the upstream locations are probably due to the better guidance of the flow by the shroud at the exit of the swirler, and due to the lack of a recirculation zone. Comparisons of the three fluctuating velocity components at each experimental point reveal that the turbulence is locally anisotropic.

Double peak values of turbulent shear stresses were observed in the measurements for the shrouded swirler. Similar double peak values were also reported by Fujii et al. (1981) and Sislian and Cusworth (1986). These peaks are produced in the regions of high mean velocity gradients. Figure 14(*a*) displays the Reynolds shear stress $\overline{u'w'}$ profile at $x/d = 2$ for the shrouded swirler. The double peaks appear quite clearly in this plot. However, unlike the higher peaks of Fujii et al., (1981) and Sislian and Cusworth (1986), the peak values at the smaller radii are less pronounced due to the lack of a recirculation zone. The turbulent shear stress $\overline{u'v'}$ profile also shows double peaks for the shrouded swirler as shown in Fig. 4(*b*) as in Sislian and Cusworth (1986). These peaks are in the opposite direction of the peaks of the $\overline{u'w'}$ profile. In general, the maximum values of $\overline{u'w'}$ are higher than $\overline{u'v'}$ values in the first three upstream measurement stations. The maximum $\overline{u'w'}$ versus x/d plot of Fig. 15 indicates a rapid decay between the swirler exit and $x/d = 4$ due to the drag from the surrounding air. The decay is much slower farther downstream because of the lower velocities. Much lower shear stress values were observed with the shrouded swirler, as compared to the shear stress values for the swirler without the shroud. The maximum $\overline{u'v'}$ values first increase up to $x/d = 1$, then steeply decrease up to $x/d = 4$, and continue to decrease more gradually, farther downstream for the shrouded swirler (Fig. 16). For the swirler without the shroud, the maximum turbulent shear stresses are much higher, and they decrease continuously after the exit. This decrease is more gradual up to $x/d = 1$, and relatively steep between $x/d = 1$ and 4, with a much more gradual decrease between $x/d = 4$ and 9. The overall turbulent kinetic energies were found to be higher for the shrouded swirler except at the exit station ($x/d = 0.1$) as manifested in Fig. 17. This is consistent with the results of Figs. 11, 12, and 13, and can be attributed to the better guidance of the flow at the exit station, and the influence of higher velocity gradients for the shrouded swirler.

Conclusions

Using a laser-Doppler velocimeter, detailed measurements of the mean velocity components and the turbulence values were made for a 40 deg vane angle swirler with and without a shroud at 750 mm H_2O inlet pressure. In particular, the effect of a shroud was investigated by comparing the results of the swirler with the shroud to that of the swirler without the shroud, but with the same geometry for the rest of the test rig, and the same inlet pressure.

The shroud reduced the flow area at the exit of the swirler. The blockage of the flow by this area reduction caused the mass flow to decrease significantly, although the inlet pressures for the swirlers with and without the shroud were the same. The maximum axial velocity at the exit of the shrouded swirler was higher than that without the shroud, despite the lower mass flow rate. The jet diameter was much smaller, and the flow deceleration was faster in the downstream direction. The measured mean velocity distributions showed that the relative magnitude of the tangential momentum was reduced with respect to the axial momentum of the flow, as a result of the swirler exit flow area reduction, and the increased friction with the shroud. As a consequence of the significant reduction in the swirl number with the addition of the shroud, the recirculation zone disappeared. Since recirculation is a requirement for stable combustion, but also the cause of deposition on the injector, a balance between these two effects should be established in the design of swirlers. In addition to its influence on recirculation, the shroud caused a radially inward shift of the maximum mean and turbulence parameters at all axial locations. The anisotropy of turbulence increased, and, in general, lower values of shear stress were obtained as compared to that for the swirler without the shroud.

Acknowledgments

The authors gratefully acknowledge the financial assistance and encouragement of this research by Parker Hannifin Corporation.

References

Béer, J. M., and Chigier, N. A., 1972, *Combustion Aerodynamics*, Applied Science Publishers Ltd., London.

Durst, F., Melling, A., and Whitelaw, J. H., 1981, *Principles and Practice of Laser-Doppler Anemometry*, Academic Press, London.

Edwards, R. V., 1987, "Report of the Special Panel on Statistical Particle Bias Problems in Laser Anemometry," ASME *Journal of Fluids Engineering*, Vol. 109, pp. 89-93.

Fujii, S., Eguchi, K., and Gomi, M., 1981, "Swirling Jets With and Without Combustion," *AIAA Journal*, Vol. 19, 1981, pp. 1438-1442.

Gupta, A. K., Lilley, D. G,. and Syred, N., 1984, *Swirl Flows*, Abacus Press, Kent.

Kihm, K. D., Chigier, N., and Sun, F., 1990, "Laser Doppler Velocimetry Investigation of Swirler Flow Fields," *AIAA Journal of Propulsion and Power*, Vol. 28.

Martin, C. A., 1987, "Aspects of the Design of Swirlers as Used in Fuel Injectors for Gas Turbine Combustors," ASME Paper No. 87-GT-139.

Oberle, L. A., and Seasholtz, R. G., 1985, "Filter Induced Errors in Laser Anemometry Using Counter-processor," *International Symposium on Laser Anemometry*, ASME, Miami Beam, FL, Nov. 17-22, pp. 221-230.

Orloff, K. L., and Snyder, P. K., 1982, "Laser Doppler Anemometer Measurements Using Nonorthogonal Velocity Components: Error Estimates," *Applied Optics*, Vol. 21, pp. 339-344.

Ramos, J. I., and Sommer, H. T., 1985, "Swirling Flow in a Research Combustor," *AIAA Journal*, Vol. 23, No. 2, pp. 241-248.

Sislian, J. P., and Cusworth, R. A., 1986, "Measurements of Mean Velocity and Turbulent Intensities in a Free Isothermal Swirling Jet," *AIAA Journal*, Vol. 24, No. 2, pp. 303-309.

Snyder, P. K., Orloff, K. L., and Aoyagi, K., 1981, "Performance and Analysis of a Three-Dimensional Nonorthogonal Laser Doppler Anemometer," NASA TM-81283.

Snyder, P. K., Orloff, K. L., and Reinath, M. S., 1984, "Reduction of Flow Measurement Uncertainties in Laser Velocimeters With Nonorthogonal Channels," *AIAA Journal*, Vol. 22, No. 8, pp. 1115-1123.

M. R. Baxter
Graduate Student.

A. H. Lefebvre
Reilly Professor of Combustion Engineering.

Thermal Sciences and Propulsion Center,
School of Mechanical Engineering,
Purdue University,
West Lafayette, IN 47907

Weak Extinction Limits of Large-Scale Flameholders

Weak extinction data obtained from an experimental apparatus designed to simulate the characteristics of practical afterburner combustion systems are presented. The apparatus supplies mixtures of varied composition (equivalence ratio and degree of vitiation), temperature and velocity to Vee-gutter flame holders of various widths and shapes similar to those found in jet engine systems. The fuel employed is a liquid hydrocarbon whose chemical composition and physical properties correspond to those of aviation kerosine, JP5. An equation for predicting weak extinction limits which accounts for upstream vitiation and the chemical characteristics of the fuel is derived from stirred reactor theory. The correlation between the predictions and experimental results indicates that the stirred reactor approach can provide a framework for predicting the lean blowout limits of practical flameholders over wide ranges of engine operating conditions.

Introduction

One of the main problems encountered in jet engine afterburners is that of maintaining a stable flame in a fast flowing stream where the Mach number can attain values approaching 0.3. A widely used method of stabilizing flames in combustible mixtures flowing at such high velocities is by the insertion of bluff objects such as cones or "Vee"-gutters, which produce in their wake a sheltered region in which stable combustion can proceed at low velocities although surrounded by a stream of high velocity gas.

The practical importance of the bluff-body stabilization process has given rise to a large number of theoretical and experimental studies. Much of our present understanding of the flame stabilization process is due to the pioneering studies carried out in the 1950's by Longwell et al. (1949, 1953), Zukowski and Marble (1955), Williams et al. (1949), Barrère and Mestre (1954), De Zubay (1950), and Spalding (1955). More recent studies include those of Ballal and Lefebvre (1979, 1980) and Rao and Lefebvre (1982) whose work led to the development of equations for predicting stability limits in terms of bluff-body dimensions, blockage ratio, and the pressure, temperature, velocity, turbulence properties, and equivalence ratio of the incoming fresh mixture. Plee and Mellor (1979) have correlated successfully lean blowout data for bluff-body stabilized flames, using a characteristic time model.

The present study attempts to remedy a perceived deficiency in previous experimental studies on bluff-body flame stabilization. It employs large-scale flameholders, of the size and shape that are widely used in practical afterburner and ramjet systems, in conjunction with a preheat combustor and heat exchanger to vary the oxygen concentration in the high-temperature gases approaching the flameholder. The analytical objective of this study is to ascertain if an approximation of the wake region as a well-stirred reactor can satisfactorily model the stability characteristics of large-scale practical flameholders operating at realistic conditions of velocity, temperature, and degree of vitiation.

Experimental

A schematic diagram of the test facility used in the present investigation is shown in Fig. 1. The basic system consists of an air supply at essentially atmospheric pressure, an in-line preheater, a duct which contains all the components needed to produce a uniform mixture of vaporized fuel and air at the desired levels of velocity, temperature and equivalence ratio and, finally, a test section in which the flameholder is located. In normal operation, the flameholder is mounted horizontally, spanning the 0.15 m width of the test section.

The preheat combustor is a modified tubular gas turbine combustor approximately 0.46 m in length and 0.27 m in diameter. Since the flow capacity of this combustor is much larger than was required for this program, both the combustor and the fuel injector were modified to achieve the desired liner pressure drop for good mixing and good atomization over the entire range of combustor operating conditions. A series of detailed exit temperature profile measurements were performed at various preheat fuel/air ratios and air mass flow rate to establish a preheat combustor efficiency correlation. This correlation was then used to calculate the preheat com-

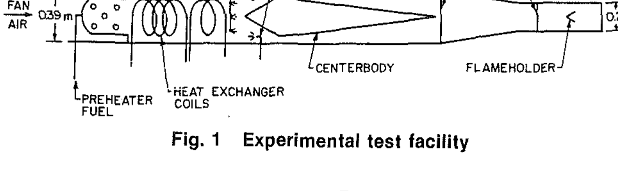

Fig. 1 Experimental test facility

Contributed by the International Gas Turbine Institute and presented at the 36th International Gas Turbine and Aeroengine Congress and Exposition, Orlando, Florida, June 3-6, 1991. Manuscript received at ASME Headquarters March 4, 1991. Paper No. 91-GT-234. Associate Editor: L. A. Riekert.

bustor's efficiency and equivalence ratio, ϕ_1, during extinction testing. Unburnt fuel, arising from preheater inefficiency, is assumed to enrich the mixture reaching the test section.

Several alternative methods of duct fuel injection were investigated in attempting to achieve a perfectly uniform fuel distribution in the mixture flowing into the test section. The fuel-injection system finally adopted consists of a converging-diverging duct (see Fig. 1) in conjunction with six pressure-swirl atomizers. The flow number of the atomizers was selected to insure that atomization quality is always satisfactory at the point of flame extinction. Two perforated plates are located downstream of the diverging section and adequate length is provided to fully prevaporize the fuel and completely mix the fuel vapor with air upstream of the test section. Uniformity of distribution is assessed by injecting water through the fuel injectors into a hot gas stream and carrying out temperature traverses in the plane of the flameholder.

A heat exchanger was constructed to allow the level of inlet air vitiation and, consequently, inlet oxygen concentration, to be varied while maintaining a specified test section inlet temperature. It is a simple tube-in-shell design, with four sets of tubular coils, each set consisting of two coils. The eight coils were fabricated from 12.7 mm stainless steel tubing and employ water as a coolant. This internal cooling is supplemented by an array of nozzles mounted above the ducting which spray water downward over its external surface. The water flow from these nozzles is such that a film of water always covers the ducting.

Pressure loss considerations limited the size of the heat exchanger that could be fitted into the duct. To extend the range of attainable vitiation levels for a specified inlet temperature, water is injected in a finely atomized form from eight equispaced pressure-swirl nozzles directly into the vitiated airstream upstream of the fuel injectors. As the water droplets evaporate, they simultaneously lower the mixture temperature and decrease the oxygen concentration, thereby simulating a more highly vitiated airstream.

The flow conditions over which weak extinction data have been obtained are listed next along with details of the various test section geometries employed in the study.

Mainstream Mach number:	0.18 to 0.26
Inlet temperature:	650 to 850 K
Preheater equivalence ratio:	0.15 to 0.6
Flameholder width:	25.4 to 65.1 mm
Flameholder angle:	45, 60 and 90 deg
Flameholder geometric blockage:	0.125 to 0.32

The lowest values of Mach number, inlet temperature and preheater equivalence ratio are set by the combustion performance of the preheater which deteriorates at extremely low air and fuel flow rates. Another controlling factor is the requirement that the duct stream be hot enough to fully vaporize the injected fuel and water droplets. The maximum attainable approach Mach number is dictated by the capacity of the air blower, while the maximum inlet gas temperature is limited by the onset of flashback or autoignition upstream of the flameholder. As the test section area is fixed, any increase in flameholder width creates a corresponding increase in flameholder blockage.

The test procedure for acquiring lean blowout data is quite simple. For any given flameholder, the inlet conditions are established, and an oxygen-propane torch is used to ignite a flame in the wake region of the gutter. The duct fuel flow is then gradually decreased until flame extinction occurs. At extinction, all pertinent mass flow rates and auxiliary raw data are recorded. These raw data are then fed into a data reduction routine, which processes the data into its final form.

Results

The results shown in Figs. 2-6 are typical of those obtained during this investigation. They have been selected to illustrate the effects of various inlet parameters and flameholder geometry on weak extinction characteristics. The data, shown in Fig. 6, were obtained with the heat exchanger coils *in situ*. For the data presented in Figs. 2-5, these coils were removed to minimize the pressure drop through the system.

A flow parameter of importance to weak extinction limits is the velocity of the combustible mixture as it approaches the flameholder. Generally, it is found that any increase in approach stream velocity invariably has an adverse effect on flame stability by reducing the residence time of the reactants in the wake region. This effect is evident in Fig. 2, which also shows that stability is improved by an increase in gutter width due to the additional residence time provided by a larger wake region. Figure 2 also serves to demonstrate that for a flameholder located in a duct, which is the usual practical situation, an additional parameter affecting stability characteristics is the *blockage ratio*, B_g, which is defined as the ratio of the projected area of the flameholder to the cross-sectional area of the duct. All stability theories show that stability limits are widened as the characteristic flameholder dimension increases. In a ducted system, however, the rigid walls restrict the free movement of air over the body and, in consequence, the axial velocity in its vicinity is higher than it would be if the body were located in

Nomenclature

B_a = flameholder aerodynamic blockage
B_g = flameholder geometric blockage
C = constant in Eqs. (14) and (15)
C_1 = constant in Eq. (13)
C_D = flameholder drag coefficient
C_F = reaction rate constant
E = activation energy, kcal/kg mole
Kw = water/fuel ratio by mass
L = flameholder length perpendicular to flow, m
m = fuel mole fraction exponent in rate equation
$\dot{m}$ = inlet mixture mass flow rate, kg/s
$\dot{m}_e$ = mass entrainment rate, kg/s
$\dot{m}_D$ = duct mass flow rate, kg/s
M = Mach number
MW_f = molecular weight of fuel, kg/kg mole
$\dot{N}_{O_2}$ = inlet molar flow rate of oxygen, kg mole/s
n = global reaction order
P = pressure, atm
R = universal gas constant = 1.986 kcal/kg mole K
T = reaction temperature, K
T_0 = test section inlet mixture temperature, K
U = mainstream velocity, m/s
V = reaction volume, m^3
w = flameholder geometric width, m
w_a = flameholder aerodynamic width, m
x = fuel carbon molar content
x_f = fuel mole fraction
x_0 = oxygen mole fraction
y = fuel hydrogen molar content
y_{O_2} = inlet stream oxygen mass fraction
β = fraction of fuel burned
ϵ = flameholder shape factor
ϕ_1 = preheater equivalence ratio
ϕ_2 = overall equivalence ratio
ϕ_D = duct equivalence ratio $= \phi_2 - \phi_1$
ϕ_{WE} = duct weak extinction equivalence ratio
ρ = density, kg/m^3
Θ = flameholder total included angle

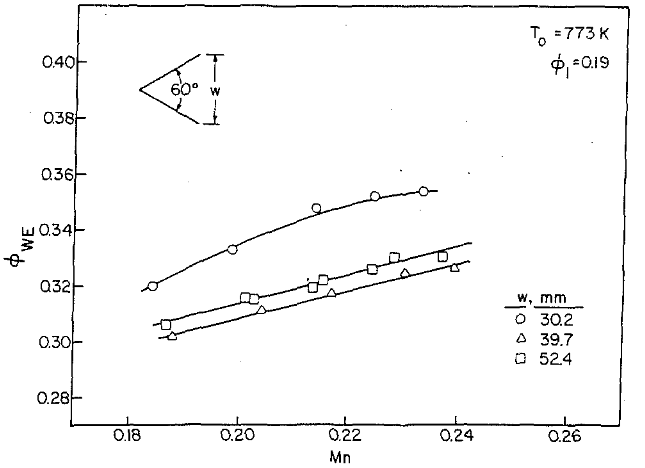

Fig. 2 Influence of approach stream Mach number and flameholder width on weak extinction limits

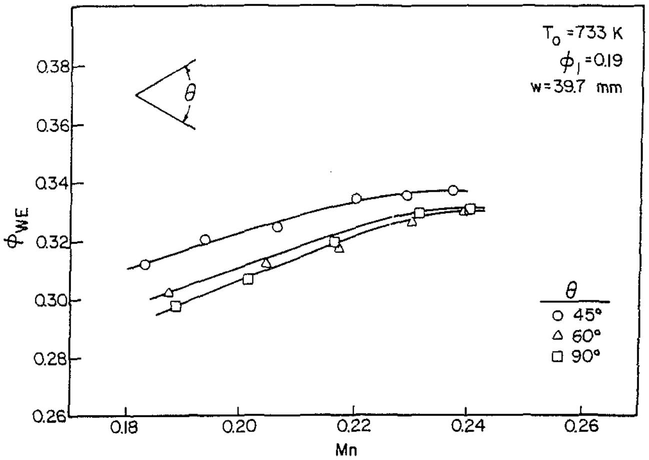

Fig. 3 Influence of approach stream Mach number and flameholder shape on weak extinction limits

an unlimited stream. One effect of this high axial velocity is a reduction in the width of the recirculation zone. Thus, for a fixed flameholder width, any increase in geometric blockage—obtained, for example, by decreasing the duct size—will reduce the size of the recirculation zone and thereby impair flame stability. The influence of blockage on weak extinction limits is illustrated in Fig. 2. The figure shows that an increase in gutter width from 30.2-39.7 mm reduces ϕ_{WE}, i.e., improves stability, but a further increase in w from 39.7-52.4 mm has an adverse effect on stability due to the blockage effect discussed previously.

The shape of a bluff-body flameholder affects its stability characteristics through its influence on the size and shape of the wake region. The effect of shape is illustrated in Fig. 3, which shows weak extinction data for three gutters having different included angles but the same projected width. These data confirm the results of Barrère and Mestre (1954) in showing that the characteristic dimension of a bluff-body flameholder should be not its geometric width, w, but rather the maximum width of the wake created behind it, w_a. The ratio w_a/w increases with increase in gutter included angle, thereby improving stability performance by enlarging the recirculation-zone volume.

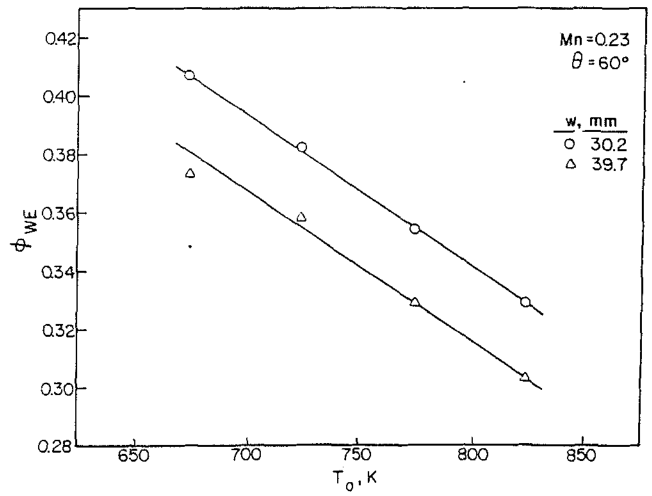

Fig. 4 Influence of inlet temperature at constant Mach number on weak extinction limits

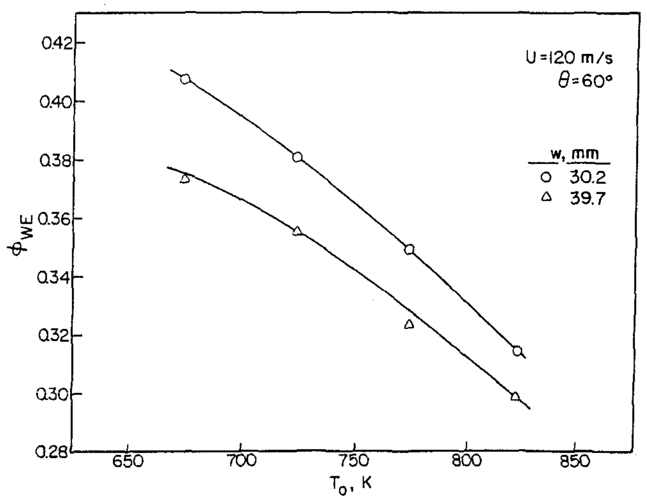

Fig. 5 Influence of inlet temperature at constant velocity on weak extinction limits

The influence of inlet mixture temperature on weak extinction limits is illustrated in Figs. 4 and 5. Both figures are based on data obtained from two Vee-gutters of the same included angle (60 deg), but having different widths of 30.2 and 39.7 mm. In view of the well-known exponential dependence of chemical reaction rates on reaction temperature, it would be expected that an increase in inlet mixture temperature should lead to a widening of the stability limits and a reduction in ϕ_{WE}. This expectation is fully borne out by the results shown in Fig. 4 for a constant approach stream Mach number of 0.23, and in Fig. 5 for a constant approach stream velocity of 120 m/s.

It should be noted that, for the data shown in Figs. 4 and 5, an increase in temperature is always accompanied by an increase in inlet-air vitiation. The effects of vitiation on flame stability are shown more directly in Fig. 6. The data contained in this figure for the higher equivalence ratios (>0.3) were obtained with water injection, and an analytical approach, as described next, was used to calculate the effective values of ϕ_I. An interesting feature of Fig. 6 is that the slopes of the lines drawn through the data points become quite steep at the highest values of ϕ_I. This would appear to suggest that the stability loops are attaining their peak values, an event which, for unvitiated combustile mixtures, is normally associated with near-stoichiometric fuel/air ratios. However, it should be borne in mind that, due to the exceptionally high levels of inlet-air vitiation encountered in these experiments, effective fuel/oxygen ratios at these high ϕ_I conditions are very close to the stoichiometric values. The fact that inlet-air vitiation has a strong adverse effect on weak extinction limits, as illustrated

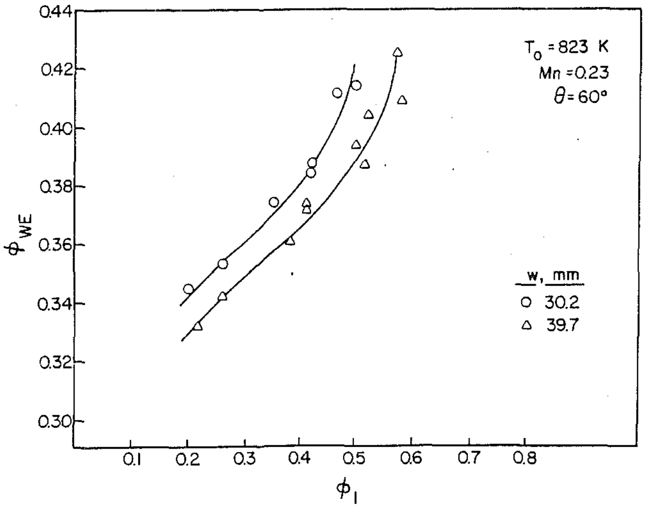

Fig. 6 Influence of upstream vitiation level on weak extinction limits

in Fig. 6, is clearly of practical importance to the designers of advanced afterburner systems.

Inspection of all the data contained in Figs. 2–6 indicates that weak extinction limits are governed mainly by inlet mixture temperature and, to a lesser extent, by mixture velocity and the degree of upstream vitiation. Over the range of conditions examined, increases in inlet mixture temperature tend to lower weak extinction limits, while increases in velocity or vitiation levels tend to raise the weak extinction limits. Increases in flameholder width serve to lower extinction limits until a critical blockage ratio is reached. Further increases in flameholder width beyond this critical point raise the weak extinction limits.

Analysis

In the analysis described next, weak extinction is postulated to occur when the amount of energy required to ignite the fresh mixture being entrained into the flameholder's wake region just exceeds the energy being liberated by combustion in that region. Following Longwell et al. (1953), the wake reaction zone is considered to approximate a well-stirred reactor. This premise leads to the following material balance equation, which equates the molar consumption rate of oxygen to the rate of reaction for weak mixtures ($\phi < 1$) of fuel and air

$$\beta\phi\dot{N}_{O_2} = C_F V T^{0.5} \exp(-E/RT)\left(\frac{P}{RT}\right)^n x_f^m x_0^{n-m} \tag{1}$$

For weak mixtures of a hydrocarbon fuel and air

$$\begin{aligned}\phi C_xH_y + (x+y/4)O_2 + 3.76(x+y/4)N_2 &\rightarrow x\beta\phi CO_2 \\ &+ (y/2)\beta\phi H_2O + (x+y/4)(1-\beta\phi)O_2 \\ &+ 3.76(x+y/4)N_2 + \phi(1-\beta)C_xH_y \end{aligned} \tag{2}$$

In turbojet afterburner systems the reactant mixture consists of fuel and air that is vitiated by combustion products issuing from the main engine combustion chamber. If the preheater is assumed to burn with 100 percent combustion efficiency at an equivalence ratio of ϕ_1, and one allows for water dilution, the reaction rate equation becomes

$$\begin{aligned}&(\phi_2-\phi_1)C_xH_y + (x+y/4)(1-\phi_1)O_2 + 3.76(x+y/4)N_2 \\ &\quad + \left[(y/2)\phi_1 + \mathrm{Kw}\,\frac{\mathrm{MW}_f}{18}(\phi_2-\phi_1)\right]H_2O + x\phi_1 CO_2 \rightarrow x[\phi_1 \\ &\quad + \beta(\phi_2-\phi_1)]CO_2 + \left\{(y/2)[\phi_1+\beta(\phi_2-\phi_1)] + \mathrm{Kw}\,\frac{\mathrm{MW}_f}{18}(\phi_2 \right. \\ &\quad \left. -\phi_1)\right\}H_2O + (x+y/4)[1-\phi_1-\beta(\phi_2-\phi_1)]O_2 + 3.76(x \\ &\qquad + y/4)N_2 + (1-\beta)(\phi_2-\phi_1)C_xH_y \end{aligned} \tag{3}$$

where ϕ_2 is the overall equivalence ratio. Defining the duct equivalence ratio ϕ_D as $\phi_2 - \phi_1$ yields the following expressions for the product mole fractions

$$x_f = \frac{(1-\beta)\phi_D}{(x+y/2)(\phi_1+\beta\phi_D) + \left[(1-\beta) + \mathrm{Kw}\,\frac{\mathrm{MW}_f}{18}\right]\phi_D + (x+y/4)(4.76-\phi_1-\beta\phi_D)} \tag{4}$$

and

$$x_0 = \frac{(x+y/4)(1-\phi_1-\beta\phi_D)}{(x+y/2)(\phi_1+\beta\phi_D) + \left[(1-\beta) + \mathrm{Kw}\,\frac{\mathrm{MW}_f}{18}\right]\phi_D + (x+y/4)(4.76-\phi_1-\beta\phi_D)} \tag{5}$$

If y_{O_2} is the mass fraction of oxygen in the inlet mixture stream, $\dot{m}$, then clearly

$$\dot{N}_{O_2} = \frac{y_{O_2}\dot{m}}{32} \tag{6}$$

Substituting this expression for the molar influx of oxygen and the oxygen and fuel mole fraction relations into Eq. (1) yields Eq. (7).

$$\frac{\dot{m}}{VP^n} = \frac{C_F \exp\left(\frac{-E}{RT}\right)}{R^n T^{n-0.5}}\,\frac{32}{y_{O_2}\beta\phi_D^{1-m}}\,\frac{(1-\beta)^m\{(x+y/4)(1-\phi_1-\beta\phi_D)\}^{n-m}}{\left\{(x+y/2)(\phi_1+\beta\phi_D) + \left[(1-\beta)+\mathrm{Kw}\,\frac{\mathrm{MW}_f}{18}\right]\phi_D + (x+y/4)(4.76-\phi_1-\beta\phi_D)\right\}^n} \tag{7}$$

Lefebvre (1985) noted that lean blowout data from a number of practical combustion systems conformed to an apparent overall reaction order, n, of 1.3 when operating near lean blowout, while Longwell and Weiss (1955) found that a value of $n = 1.8$ provided the best correlation of their complete stability loop data (both lean and rich) from their spherical reactor experiments. Clarke et al. (1965), in a set of similar spherical reactor studies, correlated peak blowout data with values of $n = 2$ and $m = 1$. Since the present study concerns lean blowout, the peak blowout value of $n = 2$ is inappropriate. However, as is shown in Fig. 6, the stability loops obtained at high vitiation levels exhibit the characteristic curvature which occurs as the peak blowout point is approached. Consequently, an intermediate value of $n = 1.75$ was chosen for the analysis. The value of m was maintained at unity, since it is considered that the fuel concentration should be no less rate-determining at weak extinction than at peak blowout conditions. It is perhaps worthy of mention that an attempt was made to correlate the weak extinction data using a lower value of n of 1.3. This was found to give a very satisfactory fit to the data acquired under conditions of low air vitiation, and is fully consistent with the values of 1.25 and 1.3 obtained by Ballal and Lefebvre (1979) and Lefebvre (1985) for unvitiated inlet air mixtures. However, the data fit was much less satisfactory when a value for n of 1.3 was applied to the highly vitiated inlet mixtures selected for this study due to their relevance to advanced afterburner systems.

The utilization of kerosine as the fuel presents the dilemma of attempting to chemically model a combustion reaction which has no precise chemical formula. According to Sutton et al. (1984), a mean chemical formula for the type of fuel employed is $C_{14.3}H_{26.0}$, and this composition was used in the formulation of Eq. (7) along with an activation energy of 54,000 kcal/kg mole as recommended by Ballal and Lefebvre (1979).

The reaction temperature T for Eq. (7) is readily calculated using heat balance methods for any stipulated values of β, ϕ_D, ϕ_1, Kw and inlet mixture temperature T_0. Substitution of corresponding values of T, β, ϕ_D, ϕ_1, and Kw into Eq. (7) allows plots of $(\dot{m}/VP^{1.75})$ versus β to be generated for various inlet conditions, as shown in Fig. 7. Attention is focused on the peak of each curve since it represents the highest possible heat release rate for the given inlet conditions.

Values of $(\dot{m}/VP^{1.75})_{\max}$ were calculated for various combinations of inlet conditions. The inlet conditions examined were ϕ_1 from 0–0.9, ϕ_2 from 0.2–0.9, T_0 from 300–1000 K, and Kw from 0–2. For these ranges of inlet conditions a least-squares analysis yields the following correlation for $(\dot{m}/VP^{1.75})_{\max}$

$$\left(\frac{\dot{m}}{VP^{1.75}}\right)_{\max} \alpha \frac{(1-\phi_1)^{1.36}\phi_D^{6.18}\exp(T_0/125)}{(1+\mathrm{Kw})^{0.8}} \qquad (8)$$

or

$$\dot{m}_{\max}\alpha \frac{VP^{1.75}(1-\phi_1)^{1.36}\phi_D^{6.18}\exp(T_0/125)}{(1+\mathrm{Kw})^{0.8}} \qquad (9)$$

In the previous expression, $\dot{m}_{\max}$ represents the maximum mixture flow rate the combustion zone can tolerate before extinction. Clearly, at the point of flame blowout, it must equal the entrainment rate of fresh mixture into the wake region. The methods adopted for estimating the entrainment rate and the volume of the wake region are described next.

A relatively large amount of data exists concerning the aerodynamic structure of the flowfield in the wake of a bluff body. Much of the data, unfortunately, are from axisymmetric flameholders, taken under cold flow conditions, making their translation to the present two-dimensional geometry and hot flow conditions difficult. However, some two-dimensional studies on conventional Vee-gutters exist and provide a basis for estimating the entrainment rate and recirculation-zone volume.

The volume of the recirculation region per unit length of flameholder may be considered proportional to the region's aerodynamic width, w_a, and length, L_a. According to Lefebvre (1965), the relationship between the aerodynamic blockage of a bluff-body flameholder and its corresponding geometric blockage is given by

$$\left[\frac{1}{(1-B_a)^2}-1\right]=3.7C_D\frac{B_g}{(1-B_g)^2} \qquad (10)$$

In the foregoing equation, the drag coefficient, C_D, is determined mainly by the forebody shape of the flameholders. Rizk and Lefebvre (1986), in an aerodynamic study using the present test section geometry, developed for double-sided Vee-gutters the following expression for C_D

$$C_D=2\sin(\theta/2) \qquad (11)$$

where θ is the total included angle of the gutter.

For any given geometric gutter width, Eqs. (10) and (11) allow the aerodynamic width to be estimated. The other parameter needed to estimate the volume of the wake region is its length, which corresponds to the furthest distance downstream of the flameholder where reverse flow exists. Wright (1959) performed a number of measurements on flames stabilized by flat plates in a ducted stream. He found that recirculation length varied in proportion to aerodynamic width (i.e., $L_a \; \alpha \; w_a$). Thus, for straight Vee-gutters, it is reasonable to assume that the volume per unit length of gutter is proportional to w_a^2.

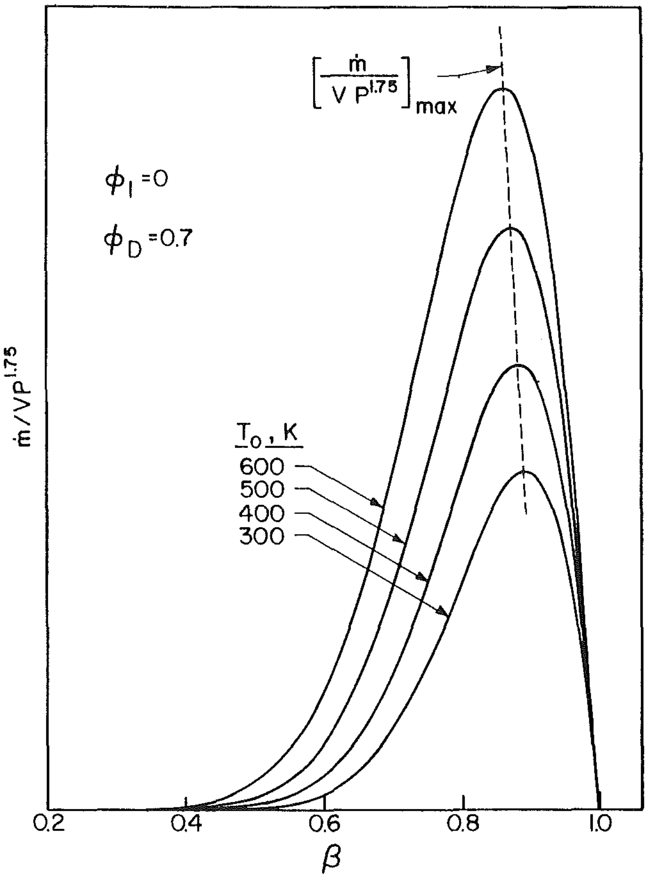

Fig. 7 Reaction rate curves for various values of inlet mixture temperature

Zhang (1980) developed the following correlation for estimating the gas entrainment rates of Vee-gutter flameholders

$$\frac{\dot{m}_e}{\dot{m}_D}=\left[0.155+0.08\left(\frac{\theta}{30}-1.0\right)\right]\left(\frac{B_g}{1-B_g}\right) \qquad (12)$$

The foregoing correlation stems from an experimental study performed under cold flow conditions at a single velocity. If it is expanded to include the effects of stream velocity and temperature on entrainment fraction, as determined experimentally by Lefebvre et al. (1960), then Eq. (12) may be rewritten as

$$\frac{\dot{m}_e}{\dot{m}_D}=C_1Z \qquad (13)$$

where

$$Z=\left[0.155+0.08\left(\frac{\theta}{30}-1\right)\right]\left(\frac{B_g}{1-B_g}\right)\left(\frac{U}{T_0^{0.75}}\right)$$

Equating at lean blowout the mixture mass entrainment rate from Eq. (13) to the maximum sustainable loading from Eq. (9), and noting that the wake region volume per unit length is proportional to w_a^2, yields the following correlation for ϕ_{WE}

$$\phi_{\mathrm{WE}}=C\left[\frac{\dot{m}_DZ(1+\mathrm{Kw})^{0.8}}{P^{0.75}\exp(T_0/125)(1-\phi_1)^{1.36}w_a^2}\right]^{0.16} \qquad (14)$$

The aforementioned equation includes a term Kw to account for the injected water used to extend the range of attainable

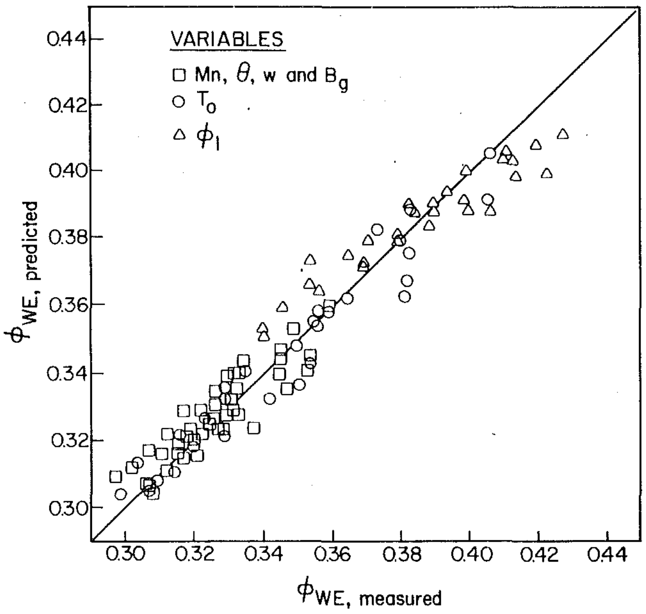

Fig. 8 Comparison of measured and predicted values of weak extinction limits

vitiation levels for a specified test section inlet temperature. As water injection is seldom used in practical combustion systems, it may be simplified to

$$\phi_{WE} = C\left[\frac{\dot{m}_D Z}{P^{0.75}\exp(T_0/125)(1-\phi_1)^{1.36}w_a^2}\right]^{0.16} \qquad (15)$$

The constant C in Eqs. (14) and (15) embodies the constant C_1 from Eq. (13). Its value depends on the turbulence properties of the duct flow and on acoustic interactions that are combustor unique and are not modeled in the present analysis.

Comparison With Experiment

Figure 8 shows the values of ϕ_{WE} obtained experimentally for various values of w, ϕ, B_g, T_0, ϕ_1, and M plotted against the corresponding values calculated from Eq. (15) using a value for C of 0.52. The level of agreement demonstrated in Fig. 8 is generally good and may be regarded as support for the validity of the assumptions employed in the analytical derivation of Eq. (15). The minor discrepancies between theory and experiment observed in Fig. 8 may be due to a combination of several factors. For example, the analysis takes no account of the blockage created by the boundary layers on the duct walls. These boundary layers decrease slightly the effective cross-sectional area of the duct, thereby increasing the aerodynamic blockage of the flameholder. This could explain why the optimum value for the aerodynamic blockage of a two-dimensional flameholder, as determined experimentally, was slightly less (0.40–0.45) than the value of 0.50 predicted by the analysis.

Another factor influencing the experimental data is the aspect ratio, i.e., the ratio of gutter length to gutter width. For the larger gutters, their low aspect ratio of less than 3 most likely precludes a true two-dimensional comparison. Heat loss from the recirculation zone at the ends of the flameholder to the test section walls also is more significant for the wider flameholders. These flameholders are characterized by larger flames which increase the area for heat loss to the walls. This effect also may contribute to the bias toward a lower optimum gutter width, as discussed previously, since near the lean blowout limit small variations in the amount of heat loss can significantly affect the sustainable loading.

In any case, the measurements indicate that an optimum blockage ratio exists beyond which any further increase in gutter width is detrimental. The analysis confirms this expectation but predicts a slightly higher optimum blockage ratio. If consideration is given to the need to minimize pressure losses in any afterburner design, the optimum blockage ratio is probably close to that observed experimentally. Also worthy of note is that, as the optimum blockage ratio is approached, any stability improvements achieved by further increases in gutter width tend to be minor and unattractive when considered alongside the concurrent increase in flow pressure loss.

Conclusions

From an analysis based on simplifying assumptions for the rates of heat liberation and heat loss in the wake region of a baffle-stabilized flame, it is concluded that the influence of operating conditions, inlet-air vitiation, and flameholder dimensions on weak extinction limits is adequately described by the relationship

$$\phi_{WE} = C\left[\frac{\dot{m}_D Z}{P^{0.75}\exp(T_0/125)(1-\phi_1)^{1.365}w_a^2}\right]^{0.16}$$

The value of C in the aforementioned equation is dependent on the geometrical and flow factors that govern the acoustic and turbulence properties of the system, and must be determined experimentally. The results of the present study show that weak extinction limits are governed mainly by inlet mixture temperature and to a lesser extent by mixture velocity and upstream vitiation level. Also, for a constant duct cross-sectional area, weak extinction limits are extended by an increase in flameholder width up to a critical value after which blockage effects start to outweigh and eventually override the beneficial effect of the increased flameholder width.

References

Ballal, D. R., and Lefebvre, A. H., 1979, "Weak Extinction Limits of Turbulent Flowing Mixtures," ASME JOURNAL OF ENGINEERING FOR POWER, Vol. 101, No. 3, pp. 343–348.

Ballal, D. R., and Lefebvre, A. H., 1980, "Weak Extinction Limits of Turbulent Heterogeneous Fuel/Air Mixtures," ASME JOURNAL OF ENGINEERING FOR POWER, Vol. 102, No. 2, pp. 416–421.

Barrère, M., and Mestre, A., 1954, "Stabilisation des Flammes par des Obstacles," *Selected Combustion Problems: Fundamentals and Aeronautical Applications*, Butterworths, London, pp. 426–446.

Clarke, A. E., Odgers, J., Stringer, F. W., and Harrison, A. J., 1965, "Combustion Processes in a Spherical Combustor," *Tenth Symposium (International) on Combustion*, pp. 1151–1166.

DeZubay, E. A., 1950, "Characteristics of Disk-Controlled Flames," *Aero Digest*, Vol. 61, No. 1, pp. 54–56, 102–104.

Herbert, M. V., 1960, "Aerodynamic Influences on Flame Stability," *Progress in Combustion Science and Technology*, Vol. 1, J. Ducarme, M. Gerstein, and A. H. Lefebvre, eds., New York, Permagon Press, pp. 61–109.

Lefebvre, A. H., 1985, *Influence of Fuel Properties on Gas Turbine Combustion Performance*, AFWAL Report No. TR-84-2104.

Lefebvre, A. H., 1965, "A Method of Predicting the Aerodynamic Blockage of Bluff Bodies in a Ducted Air Stream," CoA Report Aero. No. 188, College of Aeronautics, Cranfield, Bedford, United Kingdom.

Lefebvre, A. H., Ibrahim, A. R. A. F., Benson, B. C., 1966, "Factors Affecting Fresh Mixture Entrainment in Bluff-Body Stabilized Flames," *Combustion and Flame*, Vol. 10, pp. 231–239.

Longwell, J. P., Chenevey, J. E., Clark, W. W., and Frost, E. E., 1949, "Flame Stabilization by Baffles in a High Velocity Gas Stream," *Third Symposium on Combustion, Flame and Explosion Phenomena*, Williams and Wilkins, pp. 40–44.

Longwell, J. P., Frost, E. E., and Weiss, M. A., 1953, "Flame Stability in Bluff-Body Recirculation Zones," *Industrial Engineering Chemistry*, Vol. 45, p. 1629.

Longwell, J. P., and Weiss, M. A., 1955, "High Temperature Reaction Rates in Hydrocarbon Combustion," *Industrial and Engineering Chemistry*, Vol. 47, pp. 1634–1643.

Plee, S. L., and Mellor, A. M., 1979, "Characteristic Time Correlation for Lean Blowoff of Bluff-Body Stabilized Flames," *Combustion and Flame*, Vol. 35, pp. 61–80.

Rao, K. V. L., and Lefebvre, A. H., 1982, "Flame Blowoff Studies Using Large-Scale Flameholders," ASME JOURNAL OF ENGINEERING FOR POWER, Vol. 104, pp. 853–857.

Rizk, N. K., and Lefebvre, A. H., 1986, "The Relationship Between Flame Stability and Drag of Bluff-Body Flameholders, *AIAA Journal of Propulsion and Power*, Vol. 2, No. 4, pp. 361–365.

Spalding, D. B., 1955, *Some Fundamentals of Combustion*, Academic Press, New York.

Sutton, R. D., Troth, D. L., and Miles, G. A., 1984, *Analytical Fuel Property Effects—Small Combustors*, NASA CR-174738.

Williams, G. C., Hottell, H. C., and Scurlock, A. C., 1949, "Flame Stabilization and Propagation in High Velocity Gas Streams," *Third Symposium on Combustion, Flame and Explosion Phenomena*, Williams and Wilkins, pp. 21–40.

Wright, F. H., 1959, "Bluff-Body Flame Stabilization: Blockage Effects," *Combustion and Flame*, Vol. 3, p. 314.

Zhang, Quingfang, "An Investigation on Recirculation Flow With a Two-Dimensional Flame Stabilizer," 1980, Scientific Report No. 698, Nanjing Institute of Aeronautics and Astronautics, PRC.

Zukowski, E. E., and Marble, F. E., 1955, "The Role of Wake Transition in the Process of Flame Stabilization on Bluff Bodies," *AGARD Combustion Researches and Reviews*, Butterworths, London, pp. 167–180.

Aerodynamics of Bluff-Body Stabilized Confined Turbulent Premixed Flames

J. C. Pan

M. D. Vangsness

D. R. Ballal
Fellow ASME

University of Dayton,
Dayton, OH 45469

Detailed information on the influence of geometric and flow parameters on the structure and properties of recirculation zone in confined combusting flows is not available. In this paper, recirculation zone structure and turbulence properties of methane-air mixtures downstream of several conical flameholders were measured using LDA. These tests employed different blockage ratios (13 and 25 percent), cone angles (30, 45, 60, and 90 deg), equivalence ratios (0.56, 0.65, 0.8, and 0.9), mean annular velocities (10, 15, and 20 m/s), and approach turbulence levels (2, 17, and 22 percent). It was found that increasing the blockage ratio and cone angle affected the recirculation zone size and shape only slightly. Also, these parameters increased the shear stress and turbulent kinetic energy (TKE) moderately. Increasing the equivalence ratio or approach turbulence intensity produced a recirculation zone shape very similar to that found in the cold flow. TKE decreased due to turbulent dilatation produced by increased heat release. These observations are discussed from the viewpoint of their importance to practical design and combustion modeling.

Introduction

Bluff-body flameholders are used in ramjet engines, afterburners, and many other combustion systems to maintain a steady flame in a high-speed turbulent combustible mixture. The flame is stabilized by the recirculation zone formed in the wake of the bluff body. This recirculation zone provides long residence time and continuous ignition source for flame propagation into the incoming fresh mixture. Thus the size, shape, and turbulence characteristics of the recirculation zone are crucial for flame stabilization.

The combustion performance of the afterburner depends upon the geometry and mixture characteristics of the flow. Flameholders, such as a cone or a vee gutter, introduce an area blockage in the afterburner pipe which creates pressure drop and recirculatory flow in the wake of the bluff body. The apex angle of the bluff body causes parallel streamlines of the incoming flow to curve and increase the aerodynamic width of the recirculation zone. Thus, blockage ratio (BR) and apex angle (θ) affect flameholding. Also, incoming mixture velocity (U) and turbulence intensity (I) influence flameholding by entraining the combustion zone with fresh mixture. Finally, a combination of air loading parameter (ALP) and mixture equivalence ratio (ϕ) determines the width of the combustion stability limits. In this manner, the five parameters BR, θ, U, I and ϕ play an important role in the design and performance of practical afterburner flameholders.

Detailed information on the influence of geometric and flow parameters on the structure and properties of recirculation zone in confined combusting flows is scanty. Winterfeld (1965) studied combustion behind flameholders, but did not measure any turbulence properties, Rizk and Lefebvre (1986) investigated the influence of BR and θ, but only for isothermal flows. Heitor et al. (1988) examined velocity and scalar characteristics but mostly for a confined *disk-stabilized* flame, and Fujii and Eguchi (1981) provide a comparison of cold and reacting flow turbulence properties, also for a single flameholder only. As pointed out by Moreau et al. (1987), the available data provide only limited information about bluff-body flame stabilization.

In a previous paper, Pan et al. (1992) examined the turbulence properties of confined conical stabilizers in a combusting flow. Measurements of turbulent velocity fluctuations such as mean and rms values, skewness and flatness factors, Reynolds shear stresses, and axial mean pressure gradients were reported and data interpreted to elucidate recirculation zone structure, effects of flow confinement, and the role of combustion-generated turbulence. The objectives of this work were: (*i*) to investigate the influence of geometric parameters BR and θ, and flow parameters U, I, and ϕ on the recirculation zone structure and the turbulence properties within and surrounding this zone, and (*ii*) to provide benchmark quality data set for evaluating and refining computer models used for the design of bluff-body flameholders in practical afterburners. The present work fills a long-overdue need for detailed information on the influence of parametric variations on recirculation zone structure and turbulence properties.

Experimental Work

1 Test Rig. Figure 1 shows the test rig employed for these experiments. Several stainless steel conical flame stabilizers were manufactured including two base diameters, d = 4.44

Contributed by the International Gas Turbine Institute and presented at the 36th International Gas Turbine and Aeroengine Congress and Exposition, Orlando, Florida, June 3-6, 1991. Manuscript received at ASME Headquarters March 4, 1991. Paper No. 91-GT-218. Associate Editor: L. A. Riekert.

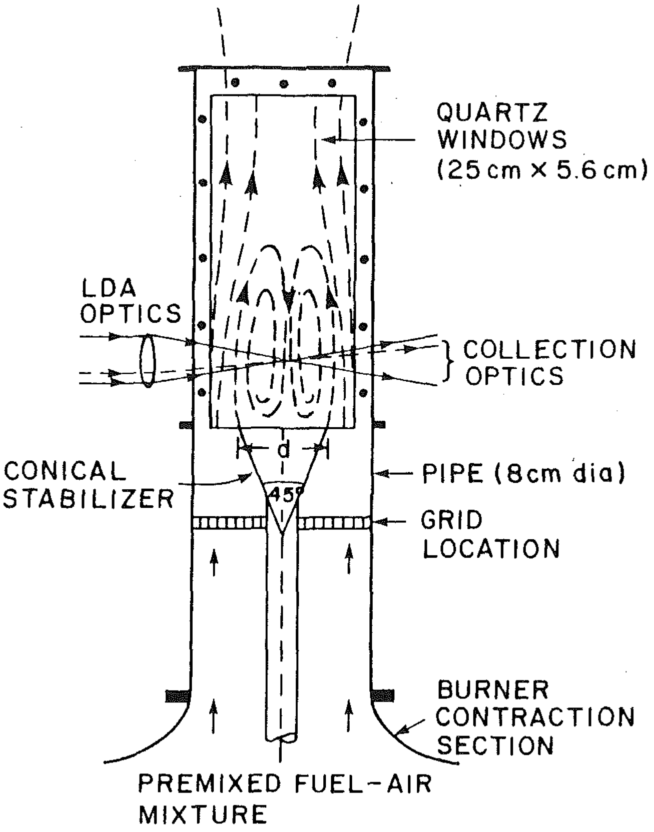

Fig. 1 Schematic diagram of the confined flame stabilizer test facility

cm and 3.18 cm, corresponding to the blockage ratio BR = 25 percent and 13 percent, respectively, and four apex angles, θ = 30, 45, 60 and 90 deg. Each stabilizer was mounted coaxially inside a 8 cm × 8 cm × 28.4 cm test section with rounded corners which has four 5.64 cm × 25.4 cm cutouts for quartz windows. This test section was mounted on a vertical combustion tunnel with a three-axis traversing mechanism described by Ballal et al. (1987). Different turbulence grids could be inserted at 5.8 cm upstream of the base of the conical bluff body. Measurements of turbulence quantities and mean wall-static pressure were performed downstream of the confined conical flame stabilizer by using a two-component laser-Doppler anemometer (LDA) and a precision micromanometer, respectively.

2 Flow Condition. In these experiments, premixed methane-air flames were studied. The mean annular velocities were 10, 15, and 20 m/s which covered a range of Reynolds number from Re = 3×10^4 to 6×10^4. Zukoski and Marble (1955) have pointed out that the bluff-body wake region becomes fully turbulent when Re = $U_a d/\nu \geq 10^4$. Four different equivalence ratios, 0.56, 0.65, 0.8, 0.9 were tested, corresponding to adiabatic flame temperatures of 1590 K, 1755 K, 1990 K, and 2130 K, respectively. The inlet turbulence intensity level was varied from 2–22 percent by using different grids.

Table 1 2-component LDA system parameters

15 W argon-ion laser wavelength	514.5 nm
Laser beam e^{-2} size	1.58 mm
Input lens focal length	350 mm
Beam intersection half-angle	2.88 deg
Fringe spacing	5.106 μm
LDA measuring spot size	175 μm × 1500 μm
Signal collection angle	9.5 deg forward
Collection lens focal length	400 mm
PMT pinhole aperture	200 μm
Net frequency shift	5 MHz
Seed particles	ZrO_2
Seed particle size	97 percent < 1 μm

3 LDA Instrumentation. A two-component LDA system was used for all velocity measurements. Essentially, this instrument uses polarization separation of the two channels and is an upgraded and refined version of the LDA system used by Ballal et al. (1989). The LDA system parameters are listed in Table 1.

Principally, this instrument incorporates Bragg cell frequency shifting for measurements in a recirculatory flow, a unique coincidence circuit for rapid acquisition of valid data, software to filter spurious signals, for example, due to seed agglomeration, and a correction subroutine to account for the LDA signal biasing effect in combusting flows. A fluidized bed seeder was used to inject submicron sized ZrO_2 seed particles into the flowing combustible mixture. Scattered signals were detected by TSI Counter Processors (CP) and processed by our custom-designed software which calculates intensity, shear stresses, higher moments (skewness and kurtosis), and pdfs. Typical sampling rates for LDA measurements exceeded 1 kHz for both isothermal and combusting flows.

4 Error Analysis. Both the fuel flow and airflow were monitored by separate electronic flow control units to ±0.5 and ±1.5 percent, respectively. The combined error produced an uncertainty of ±1.5 percent in equivalence ratio. The primary source of error in LDA measurement is the statistical bias of the final measured velocity toward higher mass flux (velocity × density) when number-weighted averages are used to calculate stationary statistics. Chen and Lightman (1985) and Glass and Bilger (1978) have discussed bias correction schemes. After allowing for this bias, we estimated that for the single-stream seeding and relatively high-sampling rates of our experiments, the uncertainty in the measurement of mean velocity was 1 percent and for rms velocity 5 percent. Near the flame front, where intermittency would be much higher, the uncertainty in rms velocity could be greater than 7 percent.

Nomenclature

BR = blockage ratio
C_p = pressure coefficient ($\Delta p/0.5\, \rho U_a^2$)
d = base diameter of conical stabilizer
I = approach axial turbulence intensity
l = turbulence integral scale
L_r = length of the recirculation zone
p = static pressure
q = turbulent kinetic energy (TKE)
r = radial direction
S = flame burning velocity
T = temperature
U, V = mean velocities in axial and radial directions
u, v = fluctuating velocities in axial and radial directions
$\overline{uv}$ = Reynolds shear stress
x = axial direction
δ = flame-front thickness
ν = kinematic viscosity
θ = cone apex angle
ρ = density
τ = heat release parameter ($T_f - T_u/T_u$)
ϕ = equivalence ratio

Superscript

$\overline{}$ = mean value
$'$ = rms value
$''$ = density-weighted value

Subscripts

a = annular flow
f = flame
l = laminar
u = unburned
t = total, turbulent

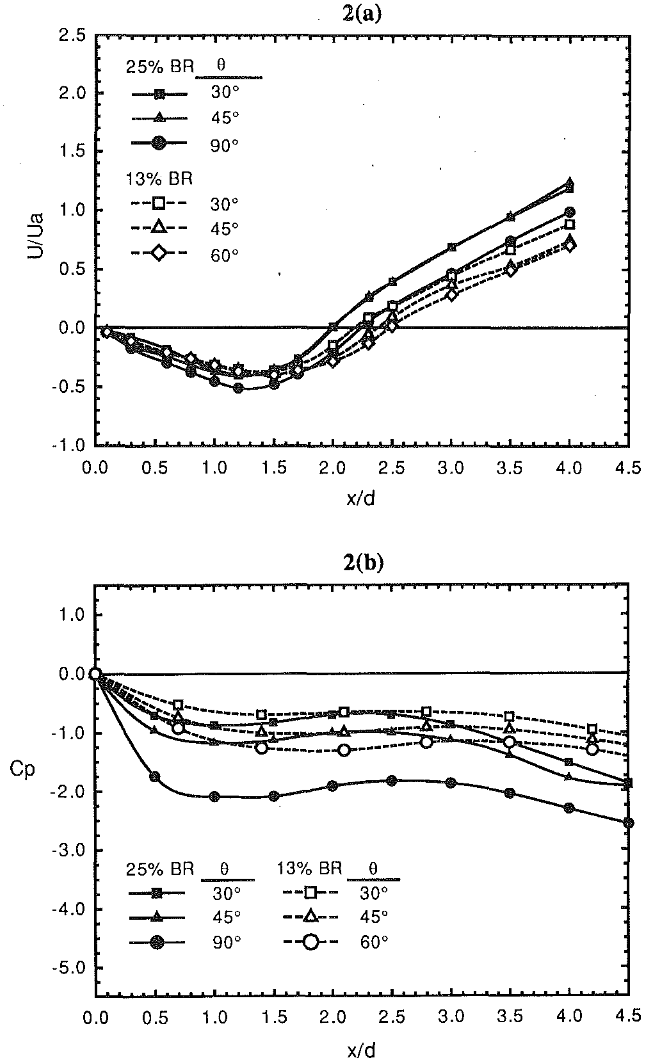

Fig. 2 **Velocity and pressure coefficient characteristics plotted to illustrate the influence of blockage ratio and cone angle on mean flowfield. All measurements are in a confined combusting flow (ϕ = 0.65, U_a = 15 m/s): 2(*a*) Centerline mean velocity; 2(*b*) Axial pressure coefficient.**

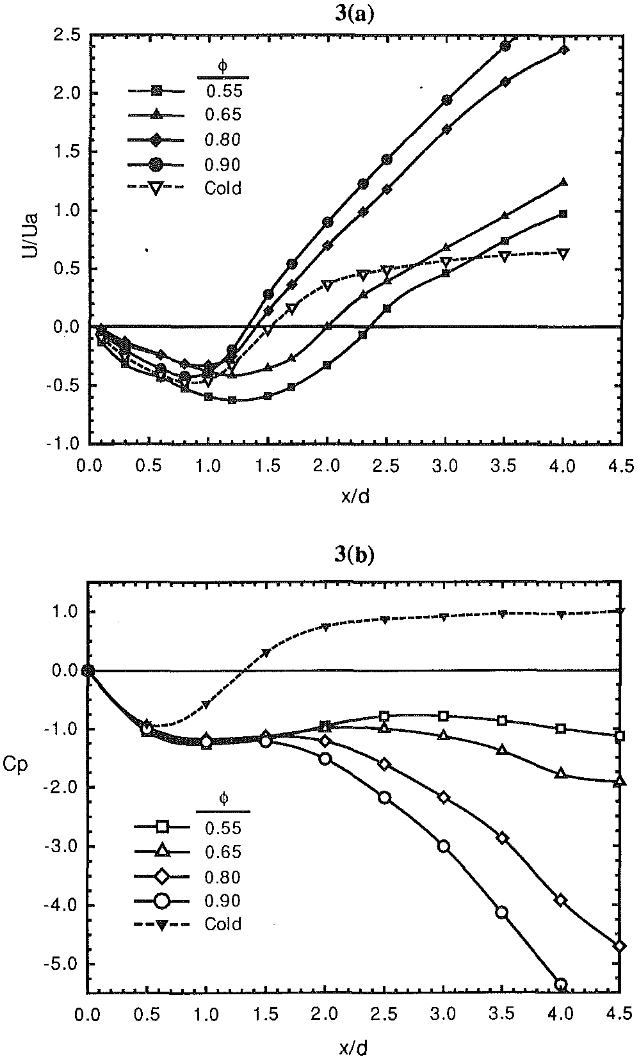

Fig. 3 **Velocity and pressure coefficient characteristics plotted to illustrate the influence of equivalence ratio on mean flowfield. All measurements, except one, are in a confined combusting flow (BR = 25 percent, θ = 45 deg, U_a = 15 m/s): 3(*a*) Centerline mean velocity; 3(*b*) Axial pressure coefficient.**

The long-term repeatability of measurements was found to be within 5 percent for turbulence quantities.

Results and Discussion

Our turbulence measurements encompassed a large test matrix. All these data, which may be used for evaluating and refining models of turbulent combusting recirculatory flows, are available in a separate report (Pan and Ballal, 1991). Lack of space precludes us from presenting all our data (for example, increasing mean velocity above 15 m/s did not reveal any significant changes in the recirculation zone and hence these results are not shown here). Therefore, only selected data that illustrate the influence of parametric variation on mean flowfield and turbulence properties are presented and discussed next.

1 Mean Flowfield. Figures 2–4 show mean velocity and axial pressure coefficient for all the conical stabilizers tested. In general, the mean axial velocity characteristics of Figs. 2(*a*)–4(*a*) reveal the magnitude of maximum reverse velocity, length of the recirculation zone, and acceleration of products due to combustion downstream of the rear stagnation point. Likewise, the pressure coefficients plotted in Figs. 2(*b*)–4(*b*) show a minimum associated with the maximum width of the recirculation zone, a favorable pressure gradient corresponding to the acceleration of products, and cold-flow pressure recovery, Figs. 3(*b*)–4(*b*), downstream of the recirculation zone. These trends for both combusting and cold flows are broadly in agreement with the past work of Ballal et al. (1989), Pan et al. (1992), and Heitor et al. (1988). However, these data reveal important influences of blockage ratio, cone angle, equivalence ratio, mean annular velocity, and incoming turbulence level on the mean flowfield. A discussion of these effects is facilitated by identifying three regions; (*i*) Region 1 spans the axial distance between the base of the bluff body and the location of maximum recirculation zone width, (*ii*) Region 2 covers the axial distance downstream up to rear stagnation point, and (*iii*) Region 3 is downstream of the rare stagnation point.

(*a*) *Blockage Ratio.* Figures 2(*a*, *b*) show the influence of approximately doubling the blockage ratio, BR, on axial mean velocity and pressure coefficient in a combusting flow. In Region 1, increase in BR decreases the pressure coefficient. For Region 2, we observe a slight decrease in the recirculation zone length with increasing BR, an observation in line with the results of Winterfeld (1965) and Wright (1959). Finally, in Region 3, the acceleration of the flow is relatively greater with higher BR. This occurs, presumably, because of an increase in the dilatation due to a larger amount of heat released in this region.

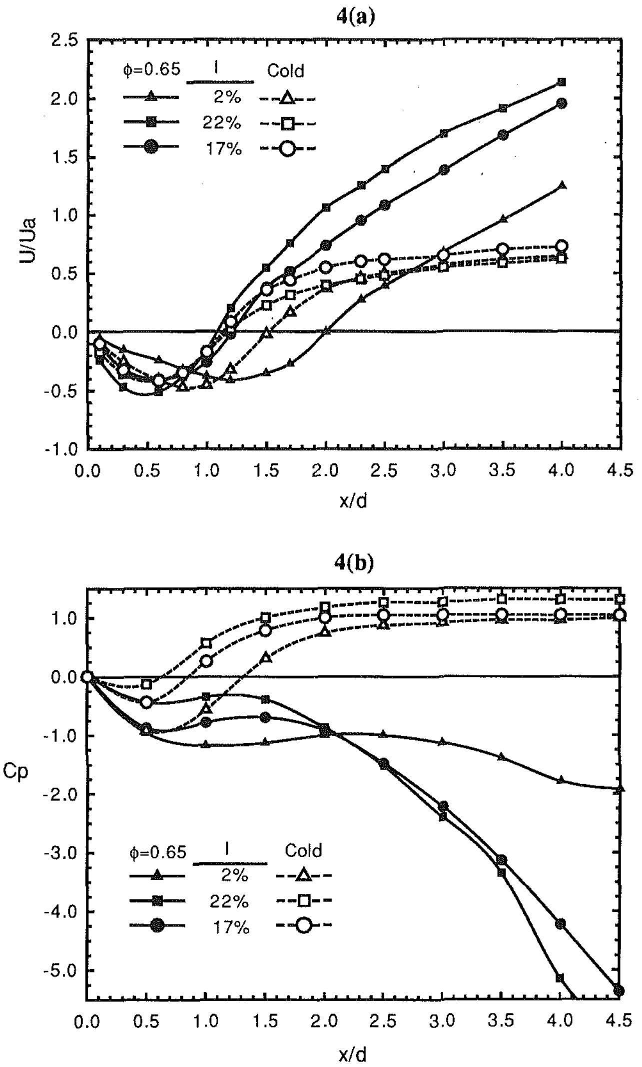

Fig. 4 Velocity and pressure coefficient characteristics plotted to illustrate the effects of approach turbulence intensity on mean flowfield. Comparisons between combusting (ϕ = 0.65) and cold flows are shown (BR = 25 percent, θ = 45 deg, U_a = 15 m/s): 4(*a*) Centerline mean velocity; 4(*b*) Axial pressure coefficient.

(*b*) *Cone Angle.* The effects of cone angle on mean velocity and pressure coefficient also are demonstrated in Figs. 2(*a*, *b*). Increasing the cone angle increases the deflection of the mean separation streamline from the trailing edge of the bluff body. As Lefebvre (1983) has shown, in cold flow, this increases the aerodynamic blockage and hence the recirculation zone width. In Region 1 of the confined combusting flow, recirculation zone width increases due to increased streamline curvature. Also, in Region 2, recirculation zone is elongated because wall confinement decreases streamline curvature. The net effect of these two changes is to produce a slightly larger recirculation zone volume and widen the flame stability limits. However, in confined flows, rigid walls accelerate the axial velocity in the vicinity of the flame and this may adversely affect flame stabilization with further increases in cone angle.

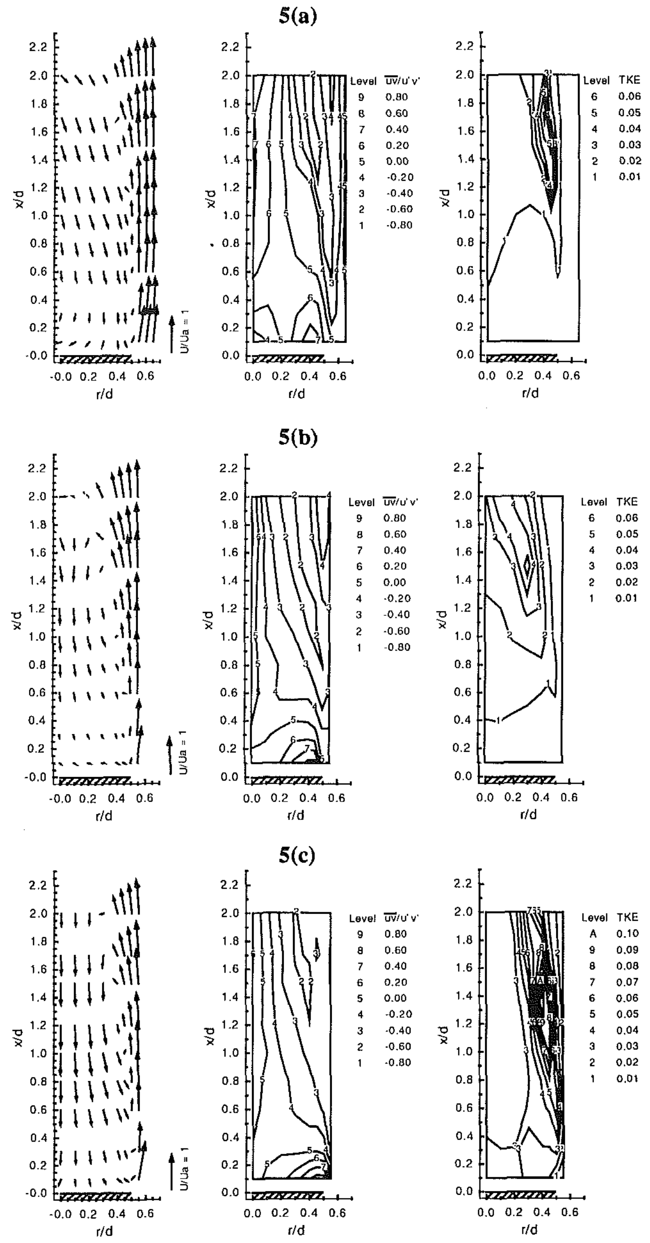

Fig. 5 Mean flow structure, Reynolds shear stresses, and turbulent kinetic energy plotted to illustrate the effects of blockage ratio and cone angle on turbulence flowfield. All measurements are in a confined combusting flow (ϕ = 0.65, U_a = 15 m/s): 5(*a*) BR = 13 percent, θ = 30 deg; 5(*b*) BR = 25 percent, θ = 30 deg; 5(*c*) BR = 25 percent, θ = 90 deg.

(*c*) *Equivalence Ratio.* Figures 3(*a*, *b*) show the effects of equivalence ratio of the incoming fresh mixture, ϕ, on mean velocity and pressure coefficient. An increase in ϕ from 0.56 to 0.90 decreases the recirculation zone length dramatically from x/d = 2.35 to 1.32, i.e., slightly shorter than that found in the cold flow (x/d = 1.52). It also accelerates axial velocities in Region 3 as clearly seen in Fig. 3(*b*). Both these effects are a result of increasing heat release rates and higher turbulent flame propagation speed (fast chemistry) brought about by increasing the equivalence ratio toward stoichiometry. This result clearly shows how compact the primary zone of a gas turbine combustor can be, provided it operates at or near stoichiometric equivalence ratios. It also demonstrates that for $\phi \leq 0.75$, combustion is kinetically controlled and requires recirculation zone of size larger than that for cold flow to stabilize a flame.

(*d*) *Approach Turbulence Intensity.* Figures 4(*a*, *b*) demonstrate the influence of increasing the approach mixture turbulence intensity, u'/U_a from 2 percent (no grid) to 17 percent (grid 7), to 22 percent (grid 3). In Region 1, increase in turbulence shifts the location of maximum recirculation width upstream from $x/d \approx 0.8$ to 0.4. It also shortens the length of Region 2 from $x/d \approx 2$ to 1.1, a value close to that for cold flow. This dramatic change in the structure of the

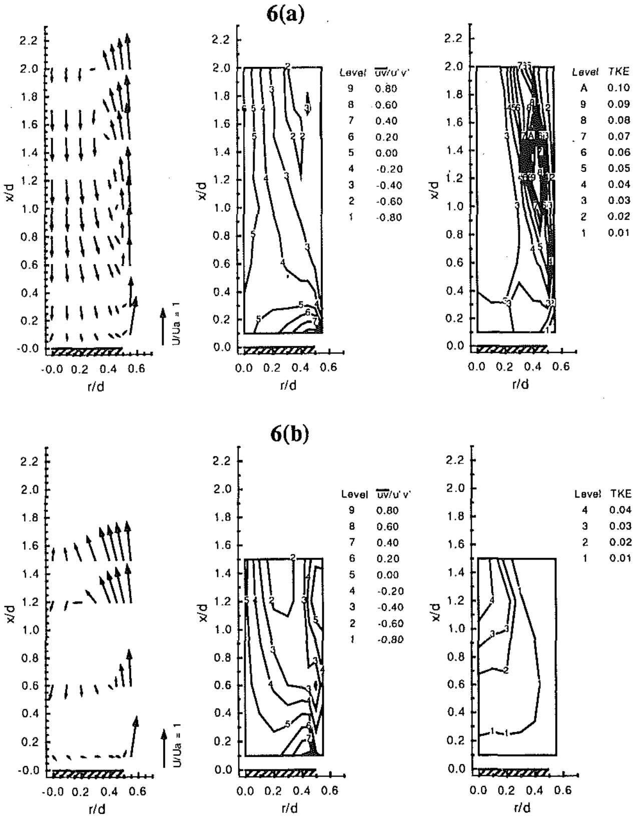

Fig. 6 Mean flow structure, Reynolds shear stresses, and turbulent kinetic energy plotted to illustrate the effects of equivalence ratio on turbulence flowfield. All measurements are in a confined combusting flow (BR = 25 percent, θ = 45 deg, U_a = 15 m/s): 6(*a*) Lean extinction limit, ϕ = 0.56, 6(*b*) Near-stoichiometric combustion, ϕ = 0.90.

recirculation zone can be explained by recognizing that the turbulent burning velocity of the flame increases with an increase in the turbulence intensity; for example, Lefebvre (1983) gives $S_T/S_L = [1+(u'/S_L)^2]^{0.5} \approx u'/S_L$ for large values of u'/S_L. Thus a five or six fold increase in turbulent burning velocity dramatically reduces the size of the recirculation zone. In Region 3, acceleration of products downstream of the recirculation zone continues. Similarities between the effects of increasing equivalence ratio and increasing turbulence intensity are very evident in Figs. 3 and 4.

2 Turbulence Flowfield. Figures 5-7 illustrate the turbulent combusting flowfield in and around recirculation zones, produced by different bluff bodies confined in the test section. Each figure has three parts:

(*i*) The recirculation zone structure sketched by the mean flow streamlines shows not only the width and length, but also the reverse velocity flowfield. The location of zero velocity (eye) region also is evident.

(*ii*) The contours of Reynolds shear stress ($\overline{uv}/u'v'$) illustrate regions of maximum shear stress and locations where the shear stress changes sign.

(*iii*) The TKE contours provide information on turbulence production due to normal stresses.

In general, strong turbulence activity is present around the periphery of the recirculation zone. This is because, in confined flames, the production of TKE is by the interaction of Reynolds stress and shear strain, i.e., by way of the term $\overline{uv}(\partial U/\partial r)$, and therefore generally restricted to the shear layer surrounding the maximum width of the recirculation zone. This observation is in agreement with the results of Pan et al. (1992).

It also is found that in these confined combusting flows, the locations of zero stress lines do not coincide with those of zero mean velocity gradient. This suggests that not only shear stresses (production term) but also normal stresses [dilatation term of the form $u'^2(\partial U/\partial r)$] play an important role in modifying the turbulence flowfield. The influence of blockage ratio, cone angle, equivalence ratio, and inlet turbulence intensity on turbulence flowfield is now discussed.

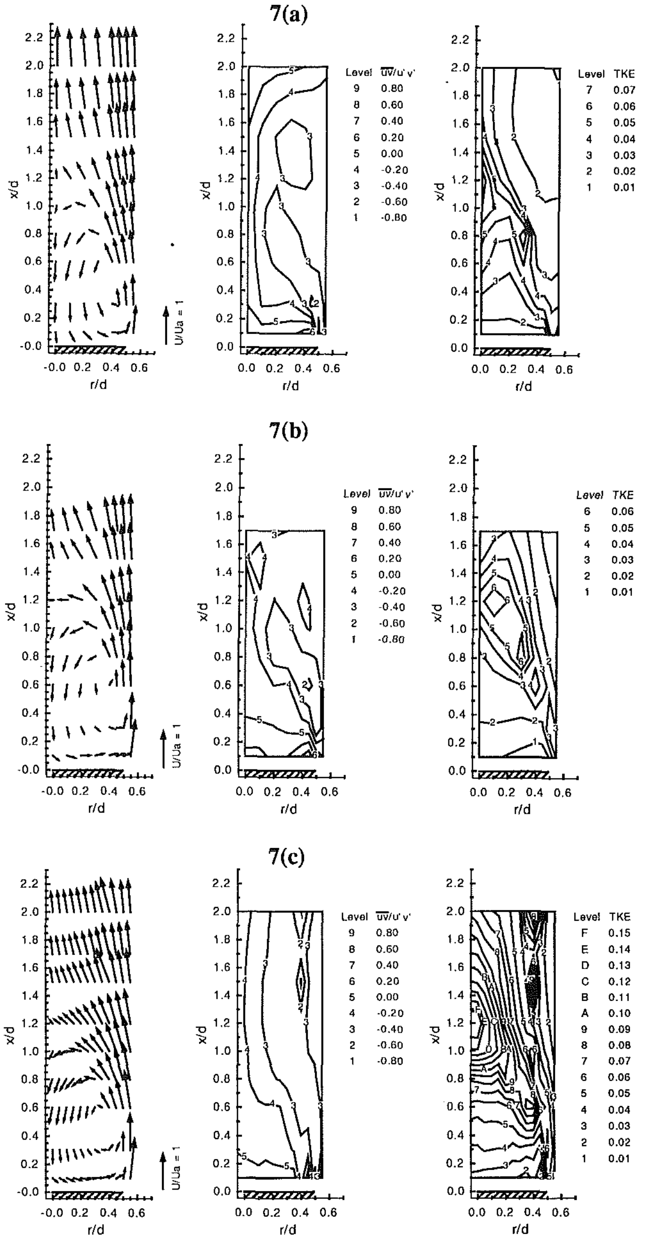

Fig. 7 Mean flow structure, Reynolds shear stresses, and turbulent kinetic energy plotted to illustrate the effects of approach turbulence intensity on turbulence flowfield. All measurements, except 7(*c*), are in a confined combusting flow (BR = 25 percent, θ = 45 deg, ϕ = 0.65, U_a = 15 m/s): 7(*a*) Approach turbulence intensity, I = 22 percent; 7(*b*) Approach turbulence intensity, I = 17 percent; 7(*c*) Confined cold flow, I = 17 percent.

(*a*) *Blockage Ratio.* A comparison between Figs. 5(*a*, *b*) reveals the effect of almost doubling the blockage ratio (but maintaining the same value of U_a = 15 m/s) on the recirculation zone structure and the surrounding flowfield. High blockage ratio narrows the width of the annular gaseous jet surrounding the bluff body. Thus the incoming fresh mixture behaves more as a *thin* annular jet than as a *thick* jet spreading into a dump combustor. As a consequence, in Fig. 5(*b*), streamlines around the recirculation zone are crowded and mean velocity gradient increased, particularly in the narrow $r/d = 0.45$–0.55 region. Also, acceleration of gases produces a relatively thin flame at the trailing edge of the bluff body. However, further downstream, i.e., $x/d > 1$ (Region 2), rapid entrainment leads to a thickened flame front.

The measurements of Reynolds shear stresses and TKE in Figs. 5(*a*, *b*) show that for a high value of blockage ratio, both shear stresses and TKE are spread throughout the recirculation zone, (Fig. 5(*b*)), rather than being confined to a narrow region surrounding it, Fig. 5(*a*). This may be a consequence of high spreading rate (0.14) of the boundary of thin annular jet as compared to 0.09 for the thick jet (see Ribeiro and Whitelaw, 1980).

(*b*) *Cone Angle.* A comparison between the results plotted in Figs. 5(*b*, *c*) demonstrates the influence of increasing the cone angle from 30–90 deg. A larger cone angle produces a radially outward deflection of the separation streamline at the trailing edge of the bluff body, effectively increasing its aerodynamic blockage. This causes pinching of the annular gaseous jet at the axial location of maximum recirculation zone width ($x/d \approx 1$). Upstream of this location, no significant effects of cone angle on shear stresses or TKE can be detected, because the shearing action is decreased. However, further downstream (i.e., in Region 2), the TKE appears to be concentrated around the periphery of the recirculation zone. This is presumably because the slight elongation of the recirculation zone in this region shifts turbulence production radially outward, in the vicinity of the flame zone.

(*c*) *Equivalence Ratio.* Figures 6(*a*, *b*) show measurements of turbulence flowfield at $\phi = 0.56$ ($T_f = 1590$ K, $\tau = 4.5$) corresponding to lean extinction limit and at $\phi = 0.9$ ($T_f = 2130$ K, $\tau = 6.3$) close to stoichiometric combustion, respectively. Dramatic changes in the mean flow structure of the recirculation zone are clearly evident, principally a decrease in the recirculation zone length to its cold flow value. Due to increased heat release rates and wall confinement of the flame, streamline curvature is smaller. Therefore, turbulent dilatation and *not* turbulent shear production is the dominant process in these experiments. Thus TKE is significantly decreased at high equivalence ratios as evident in Fig. 6(*b*).

Another effect of increasing the equivalence ratio is that it decreases chemical reaction time (S_L/δ_L) or increases the Damkohler number, $D = (lS_L/u'\delta_L)$. As Bray (1980) has stated and McDannel et al. (1982) have found, premixed flames of large Damkohler number produce strong scalar (temperature or density) fluctuations. Thus, bearing in mind that the dilatation term dominates, Reynolds shear stresses are not altered significantly.

(*d*) *Approach Turbulence Intensity.* Figures 5(*b*), 7(*a*), and 7(*b*) illustrate the effect of increasing the approach turbulence intensity on the turbulence flowfield. As the approach turbulence intensity increases from 2 percent, Fig. 5(*b*), to 17 percent, Fig. 7(*b*), the recirculation zone length decreases dramatically from $x/d = 2$ to $x/d = 1.2$. But, further increase in turbulence intensity to 22 percent, Figure 7(*a*), has an insignificant effect as compared to Fig. 7(*b*). This dramatic shortening of the recirculation zone length shifts regions with strong concentration of both shear stress and TKE from the outer periphery of the recirculation zone to radially inward location around $r/d = 0.2$. The magnitude of shear stresses is about the same but the TKE appears to be slightly higher for the high turbulence case Fig. 7(*a*).

Since the size of the combusting recirculation zone in Fig. 7(*b*) resembled that of the cold flow (see Ballal et al., 1989), measurements of cold turbulence flowfield were performed for grid 7. These are plotted in Fig. 7(*c*) for comparison with Fig. 7(*b*). Although the mean recirculation zone structure, and to some extent the shear stresses, are identical, magnitude of TKE in cold flow is much higher than in combusting flow.

The foregoing observations can be explained by recognizing that increasing approach turbulence affects the flame and the recirculation zone structure in two different ways. First, higher turbulence in the fresh mixture augments turbulent burning velocity. This increases heat release rates and hence the turbulence dilatation which suppresses TKE in combusting flows. Second, higher turbulence decreases mixing time, increases entrainment between the fresh mixture and the flame, i.e., the flame loading is increased and the flame front is thickened. Thus combustion shifts from a mixing-controlled to a reaction-controlled process. As Bray (1980) has pointed out, scalar thermodynamic variables of temperature, density, and composition do not fluctuate relatively strongly in this type of thick flame.

Further Comments

Here, we briefly discuss recirculation zone structure and turbulence properties from the viewpoint of their importance to practical design and combustion modeling.

(*i*) *Recirculation-Zone Structure.* In these experiments, we have observed that, in turbulent confined combusting flows, increasing the blockage ratio or approach flow turbulence and, in the limit of fast chemistry, the recirculation-zone size decreases to its value for fully developed, cold turbulent flow wake. Thus, in the limit of high Reynolds number, *mixing-controlled* combustion, the recirculation-zone size can be predicted from the nonreactive turbulence modeling codes. In contrast, for *reaction-controlled* combustion, the recirculation zone is highly elongated. Intermediate between these two extremes, recirculation-zone size and shape may vary with geometric (BR, θ), chemical (ϕ), and flow (U_a, I) parameters. Therefore, numerous past observations on the recirculation-zone size and shape can be reconciled by developing a criteria for mixing- or reaction-controlled combustion in that particular experiment.

For the present, we observe that only ϕ and I have a strong effect on the recirculation-zone structure in combusting flows. Although geometric (hardware) parameters, BR and θ undoubtedly influence cold flow results (see Heitor et al., 1988, and Rizk and Lefebvre, 1986) and indeed have an important practical role in the flameholder design (pressure loss, heat transfer, fuel-injection considerations) they appear to be less important in defining the recirculation-zone structure in combusting flows.

(*ii*) *Turbulence Properties.* We have noted that the geometric parameters BR and θ produce a moderate increase in the shear stress and TKE in either the interior or at the periphery of recirculation zone, respectively. Increasing ϕ or I increases heat release and presumably this increases magnitude of both the shear-generated turbulence and the turbulence dilatation terms. However, dilatation predominates in the presence of wall confinement and small streamline curvature and the net result is a decrease in TKE in this combusting flow. Thus, in practical gas turbine combustors, combustion may actually suppress TKE.

In the context of combustion modeling, another term of importance in *a confined combusting turbulent flow* is the source term $-u_i''(\partial P/\partial x_i)$ from the conservation equation of turbulence stresses. The magnitude of this term would be important in regions where both u_i'' and $(\partial P/\partial x_i)$ are large. Although no local measurements of $(\partial P/\partial x_i)$ in the combusting flow were possible, it is easy to visualize at least two distinct regions where the streamline curvature is high and the term $u_i''(\partial P/\partial x_i)$ could become important. First, the stretched flame region surrounding the recirculation zone at the location of its maximum width would provide a source of turbulence. Second, the highly curved region in the vicinity of the rear stagnation point represents yet another region of turbulence production.

Conclusions

Detailed measurements of the mean and turbulence combusting flowfield were performed in the wake and downstream region of several conical flameholders confined in a test section. The following conclusions were drawn on the influence of blockage ratio, cone angle, equivalence ratio, and approach turbulence intensity on recirculation-zone structure and turbulence properties in and surrounding flowfield.

1 Increasing the blockage ratio slightly decreases the recirculation-zone length and produces a moderate increase in the shear stress and TKE in either the interior or at the periphery of recirculation zone, respectively.

2 Increasing the cone angle produces a slightly larger recirculation-zone volume and moderately augments TKE production, downstream of the axial plane of maximum recirculation-zone width.

3 Increasing the equivalence ratio from its lean extinction limit to near-stoichiometry decreases the recirculation-zone length to one-half its original value and very close to its value in the cold flow. TKE is drastically decreased due to suppression of turbulence by dilatation.

4 Increasing the approach turbulence intensity drastically shortens the recirculation-zone length close to its value in the cold flow. The distribution of both shear stresses and TKE shifts from the outer periphery of the recirculation zone to radially inward locations.

Finally, recirculation-zone structure and turbulence properties of the flow are discussed from the viewpoint of their importance to practical design and combustion modeling.

Acknowledgments

This work was supported by the U.S. Air Force, Wright Research and Development Center, Aero Propulsion and Power Laboratories, Ohio, under Contract No. F33615-87-C-2767. The authors are grateful to Dr. W. M. Roquemore, the Air Force Technical Monitor, for his interest and helpful discussions during the course of this work.

References

Ballal, D. R., 1986, "Studies of Turbulent Flow-Flame Interaction," *AIAA Journal*, Vol. 24, pp. 1148–1154.

Ballal, D. R., Chen, T. H., and Schmoll, W. J., 1989, "Fluid Dynamics of a Conical Flame Stabilizer," ASME JOURNAL OF ENGINEERING FOR GAS TURBINES AND POWER, Vol. 111, pp. 97–102.

Ballal, D. R., Lightman, A. J., and Yaney, P. P., 1987, "Development of Test Facility and Optical Instrumentation for Turbulent Combustion Research," *AIAA Journal of Propulsion and Power*, Vol. 3, pp. 97–104.

Bray, K. N. C., 1980, "Turbulent Flows With Premixed Reactants," in: *Turbulent Reacting Flows*, P.A. Libby and F. A. Williams, eds., Springer Verlag, New York, NY, pp. 115–183.

Chen, T. H., and Lightman, A. J., 1985, "Effects of Particle Arrival Statistics on Laser Anemometer Measurements," ASME FED-Vol. 33, pp. 172–176.

Fujii, S., and Eguchi, K., 1981, "A Comparison of Cold and Reacting Flows Around a Bluff-Body Flame Stabilizer," ASME *Journal of Fluids Engineering*, Vol. 103, pp. 328–334.

Glass, M., and Bilger, R. W., 1978, "The Turbulent Jet Diffusion Flame in Coflowing Stream—Some Velocity Measurements," *Combustion Science and Technology*, Vol. 18, pp. 165–177.

Heitor, M. V., Taylor, A. M. K. P., and Whitelaw, J. H., 1988, "Velocity and Scalar Characteristics of Turbulent Premixed Flames Stabilized on Confined Axisymmetric Baffles," *Combustion Science and Technology*, Vol. 62, pp. 97–126.

Lefebvre, A. H., 1983, *Gas Turbine Combustion*, Hemisphere Publishing, New York, NY, pp. 179–220.

McDannel, M. D., Peterson, P. R., and Samuelsen, G. S., 1982, "Species Concentration and Temperature Measurements in a Lean Premixed Flow Stabilized by a Reverse Jet," *Combustion Science and Technology*, Vol. 28, pp. 211–220.

Moreau, P., Labbe, J., Dupoirieux, F., and Borghi, R., 1987, "Experimental and Numerical Study of a Turbulent Recirculation Zone With Combustion," *Turbulent Shear Flows*, Vol. 5, Springer Verlag, New York, pp. 337–346.

Pan, J. C., and Ballal, D. R., 1991, "Turbulent Combustion Properties of Premixed Flames Stabilized Behind a Conical Bluff Body-Data Sets," Rept. No. UDR-TR-91-102, University of Dayton, Dayton, OH, July.

Pan, J. C., Schmoll, W. J., and Ballal, D. R., 1992, "Turbulent Combustion Properties Behind a Confined Conical Stabilizer," ASME JOURNAL OF ENGINEERING FOR GAS TURBINES AND POWER, Vol. 114, pp. 33–38.

Ribeiro, M. M., and Whitelaw, J. H., 1980, "The Structure of Turbulent Jets," *Proceedings of the Royal Society*, London, Vol. A370, pp. 769–775.

Rizk, N. K., and Lefebvre, A. H., 1986, "The Relationship Between Flame Stability and Drag of Bluff-Body Flameholders," *AIAA Journal of Propulsion*, Vol. 2, pp. 361–365.

Winterfeld, G., 1965, "On Processes of Turbulent Exchange Behind Flameholders," *Tenth Symposium (International) on Combustion*, The Combustion Institute, Pittsburgh, PA, pp. 1265–1275.

Wright, F. H., 1959, "Bluff-Body Flame Stabilization—The Blockage Effects," *Combustion and Flame*, Vol. 26, pp. 319–328.

Zukoski, E. E., and Marble, F. E., 1955, "The Role of Wake Transition in the Process of Flame Stabilization on Bluff Bodies," AGARD *Combustion Researchers and Reviews*, A. H. Lefebvre et al., eds., Butterworths Publishing Co., London, pp. 167–180.

Wave Engine Aerothermodynamic Design

H. E. Weber
Professor Emeritus,
Pennsylvania State University;
President, Flow Energy Engineering,
San Diego, CA 92115

A method for aerothermodynamic preliminary design of a wave engine is presented. The engine has a centrifugal precompressor for the wave rotor, which feeds high and low-pressure turbines. Three specific wave engine designs are presented. Wave rotor blades are naturally cooled by the ingested air; thus combustion temperatures can be as high as 1900 K. Engine pressure ratios of over 25 are obtained in compact designs. It is shown that placing no nozzles at the end of the rotor blade passages yields the highest cycle efficiencies, which can be over 50 percent. Rotor blades are straight and easily milled, cast, or fabricated.

Introduction

Principles of shock compression in time-dependent flow have been applied for over half a century. Some applications are the buzz bomb, shock tubes and tunnels, and wave rotors. On a wave rotor the time variable for an observer rotating with the blades is the peripheral distance divided by the peripheral speed. The observer or blades are exposed to different conditions at various times as stator ports and end walls are passed.

Brown Boveri began development of a wave rotor or pressure exchanger (Seippel, 1946, and later Keller, 1984). It is currently used for supercharging IC engines. Pearson (1985), Coleman and Weber (1974), Weber (1978, 1986), and Coleman (1984) at General Power Corporation (GPC) have invented, designed, and constructed wave engines. Others who have contributed to development of wave machines are: Weatherston and Hertzberg (1967), Azoury (1965), Berchtold and Lutz (1974), Thayer et al. (1981), Taussig et al. (1983), Taussig and Hertzberg (1984), and Jenny and Bulaty (1973). Many developments in wave machines are discussed in a volume edited by Shreeve and Mathur (1985). However, unsteady flow machines have received little attention even though shock compression is very efficient; e.g., single shock pressure ratios of up to 2.5 are over 90 percent efficient when compared to isentropic compression (Weber, 1986).

Wave machines are naturally cooled by air ingested by the rotor. This air is often referred to as scavenge air, because it scavenges the hot gases from the rotor after expansion. Blades on the rotor pass through cool air and hot combustion gas flow in each revolution. Therefore, the blade temperatures are an average of the hot combustion gas and the cool air temperatures. Heating of the air and cooling of the gas by the blades is negligible at wave rotor speeds. A typical wave rotor or gas generator is shown in Figs. 1 and 2. The vertical or Y direction of Fig. 2 also represents the time variable; an observer on the rotor passes the ports as time, Y/Vw, progresses. Thus, Fig. 2 is the conventional x–t diagram of time-dependent flow.

Wave engines behave like the Brayton cycle when viewed from the stator, i.e., adiabatic compression, constant pressure combustion, and adiabatic expansion. Wave engines can develop large pressure ratios. With high pressure and combustion inlet temperatures of 1900 K cycle efficiencies of over 50 percent may be attained.

Possibly an even greater advantage over steady flow turbomachinery is the considerably lighter weight of the wave machines. This light weight is due to two factors:

1 Shock compression occurs in much smaller distances than does conventional steady flow compression.

2 Compression pressure ratio across a single shock is much

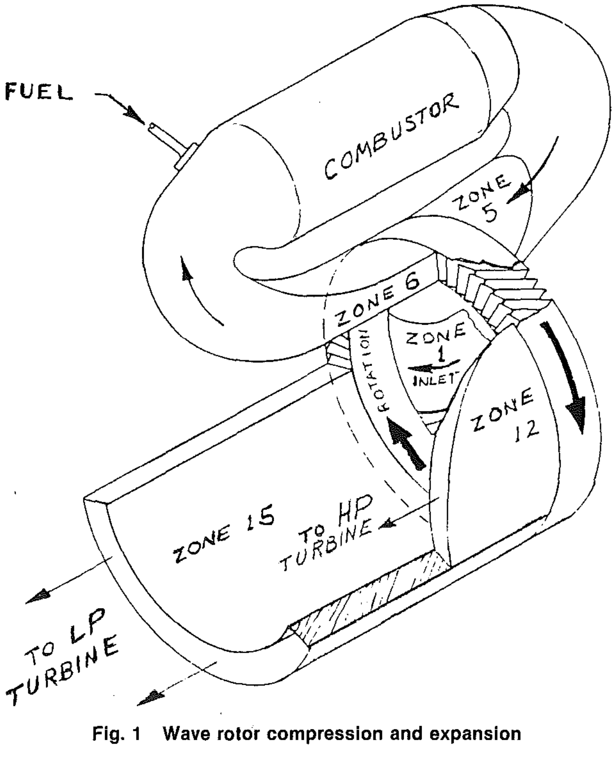

Fig. 1 Wave rotor compression and expansion

Contributed by the International Gas Turbine Institute and presented at the 36th International Gas Turbine and Aeroengine Congress and Exposition, Orlando, Florida, June 3–6, 1991. Manuscript received at ASME Headquarters January 18, 1991. Paper No. 91-GT-4. Associate Technical Editor: L. A. Riekert.

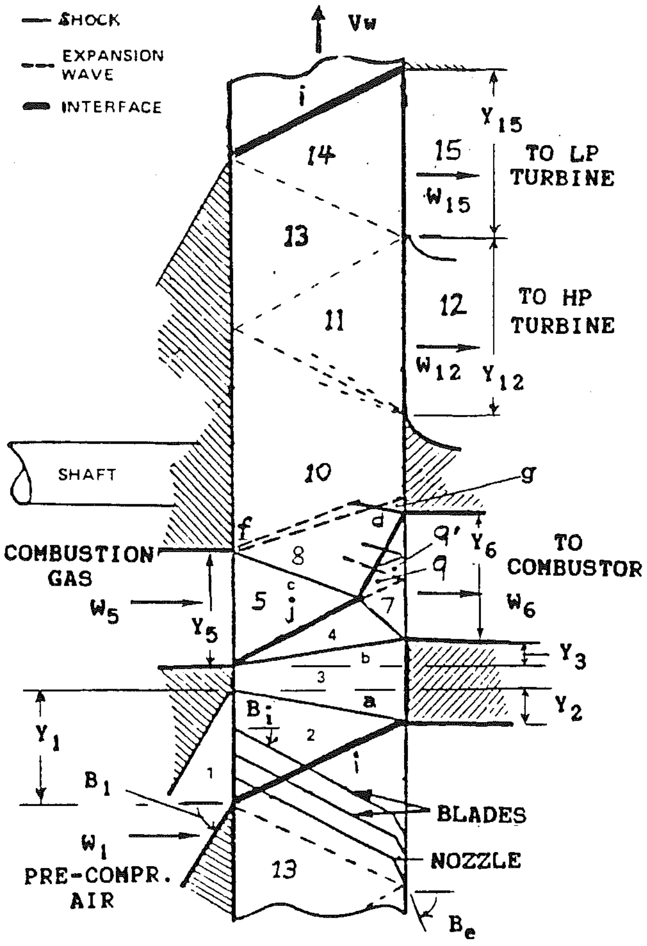

Fig. 2 Looking down on periphery of wave rotor

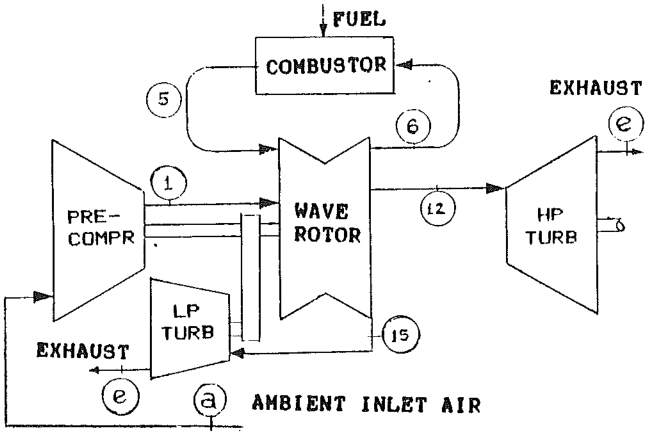

Fig. 3 Wave engine schematic

greater than in a steady flow diffuser for the same change in subsonic velocities. A shock wave travels with supersonic speed relative to the flow into which it propagates. However, the flow on both sides of the shock in this paper is subsonic.

High-speed rotation results in short axial length rotors and compact machines. Short rotors permit close control over total axial expansion and leakage between rotor and stator end walls. With the small surface area, frictional effects are less important, and wave machines retain their high efficiency as size is reduced. In addition wave rotors are not subject to surge as are conventional rotating compressors.

Wave machines have simple blade shapes and only one rotor for much of the compression and expansion. Precompression pressure ratios of 2 to 3, and final expansion are accomplished on a separate compressor and high and low-pressure turbines. This configuration is shown in Fig. 3.

Wave Engine Operation

The wave engine considered in this paper is shown in Figs. 1, 2, and 3. The wave rotor is operated at nearly constant speed, because port sizes are determined by arrival of shock waves or interfaces between hot and cold gases. Off-speed operation results in degradation of performance, because the shock waves and interfaces no longer coincide with the location of the stator port edges. The free-power turbine may operate at any speed dictated by the application. Pressure rise in the wave rotor is accomplished with a four-shock system shown in Fig. 2. These shocks are as follows:

Nomenclature

A = flow area
a = $p_4/p_6 = p_5/p_6 = a = 0.95$ (in this paper)
B = blade and port angles measured from axial direction
Cpr = compressor
c = velocity of sound
cp, cv = specific heats at constant pressure and constant volume
D = effective rotor blade passage width $= s \cdot \cos(B_i) - t$
H = blade height
HPTb = high-pressure turbine
k = specific heat ratio $= cp/cv = 1.4$
L = blade length
Lx = blade length projected on axial direction (rotor axial length)
Lb = distance from blade inlet to intersection of reflected shock with hot gas, cool air interface
Lf = distance from blade inlet to intersection of waves emanating from downstream edges of ports 5 and 6
LPTb = low-pressure turbine
M = flow Mach number (relative to rotor if state is on rotor)
Mx = shock Mach number relative to flow
P = power
p = pressure
p_0 = stagnation pressure
R = specific gas constant
Rtr = wave rotor
s = blade pitch in peripheral direction
t = blade thickness or time
T = absolute temperature
T_o = absolute stagnation temperature
U = flow velocity (relative to rotor if state is on rotor)
Vw = rotor pitch-line speed
W = mass flow rate
Y = peripheral distance at pitchline
Y_n = width of port n in peripheral direction at pitch line
η = cycle efficiency
η_{sc} = compressor polytropic efficiency
η_t = turbine efficiency
ρ = density

Subscripts

a = ambient state, absolute
c = blade passage
e = exit of blade or rotor
i = inlet of blade or rotor
1, 2, ..., n = state or region number

1 Shock "a" is generated by stopping the scavenge air flow at state 2 by the blade passages rotating past the stator end wall.

2 Shock "b" is generated by opening the blade passages to the hot gas flow at state 5.

3 Shock "c" is reflected by opening the blade passages to back pressure at state 6.

4 Shock "d" is generated by stopping the air flow from the rotor into port 6 by the blade passages rotating past the end wall. This shock is intersected and weakened by expansion waves that result when the flow is stopped by the blades rotating past the downstream edge of port 5.

Aerothermodynamic Design

Calculation Procedures and Assumptions. Leakage from the wave rotor is neglected. The rotor axial length is short compared to earlier machines. Thus rotor clearances are easily controlled as the materials expand thermally.

Nozzles are formed by bending the blades near their downstream ends as shown in Figs. 1 and 2. Nozzle length is assumed negligible compared with the blade length. It is shown in this paper that straight blades without nozzles yield the highest cycle efficiency and the most compact rotor in the range of useful combustion temperatures. Then this assumption is not needed.

A single wave is used to represent an expansion fan or waves between states 7 and 10. It is assumed that the single wave propagates at the arithmetic average of the speeds of sound before and after the expansion fan. This approximation is satisfactory, because these waves are weak. Flow balances between states 3, 5, and 6 assure that the calculated location of the interface "j" is correct. The downstream end of the interface is the location of the downstream edge of the high pressure air port 6. The aerothermodynamic conditions at which $W_5 = W_6$ also result in W_5 and W_6 calculated within 0.4 percent of W_3, the flow carried into the second-stage compression by the rotor.

Single wave representation of the expansion fans between states 10 and 14 is used to determine the separation of the outlet flow to the high and low-pressure turbines. A flow balance from state 10 to states 12 and 15 assures that the wave and interface geometry and aerothermodynamic properties are consistent. Because the pressure ratios between states 10–11, 11–13, and 13–14 are larger than those between 7–8 and 8–10, the calculated total flow into ports 12 and 15 is up to 2.5 percent larger than the flow carried by the rotor at states 3 or 10. However, the simplicity afforded by single wave representation more than compensates for these small errors.

Compression waves generated by non-instantaneous opening of a blade passage are assumed to coalesce immediately to a shock. This phenomenon is discussed later.

The polytropic precompression efficiency is taken as 0.85. Expansion from the wave rotor is isentropic. The power turbines following this expansion are taken as isentropic, because the turbines do not affect the compression process.

First-Stage Compression. Large changes in velocity result in large shock pressure ratios. However, mechanical simplicity and low losses dictate that the engine be designed for subsonic velocities in rotor and stator.

The velocity at state 2 relative to the rotor, which generates the first shock, is limited by either choked flow of hot gas leaving the blade nozzles, $M_{14e} = 1$, or sonic velocity of the flow at state 2, $M_2 = 1$. $M_{14e} = 1$ determines M_{14} upstream of the nozzle exit through the nozzle area ratio A_e/A_c, Eq. (A-8). M_2 is then obtained from

$$M_2 = M_{14} \cdot (c_{14}/c_2) \tag{1}$$

If blade end nozzles are unchoked, $M_2 = 1$ is taken at design point operation. Then

$$M_{14} = c_2/c_{14} \tag{2}$$

Once M_2 is known, state 3 is obtained by the shock Eqs. (A-12) to (A-14), Appendix, noting that $M_3 = 0$. In either case c_{14}/c_2 must be determined by the rotor compression process through states 2, 3, 5, and 10 and isentropic expansion to state 14, $p_{14} = p_2 = p_1$. This procedure is described in the next two sections.

Second-Stage Compression. The second-stage compression results from heat addition in the combustor to flow from the high-pressure air port 6. This heated flow then re-enters the rotor at port 5. Above a minimum pressure p_5 and rotor speed Vw the rate of increase of W_5 with p_5 is greater than the rate of increase of W_6 with $p_6 = p_5/a$. The fractional pressure drop in the combustor loop is $1-a$. At low pressure p_6 the flow off the rotor is larger than the flow onto the rotor. Because W_6 flows through the combustor and becomes W_5 the pressures p_5 and p_6 increase until at steady state the flows onto and off the rotor become equal. Flow W_5 increases more rapidly with pressure p_5 because the flow per unit area is greater at lower Mach numbers; $M_5 < M_{e7}$ or M_{e9}, because of the temperature rise in the combustor. The tangential momentum of flows off the rotor accelerates the rotor, as does the inflow of tangential momentum at port 1.

The largest velocity U_5 relative to the blades yields the largest shock pressure ratio, p_4/p_3 $(p_4 = p_5)$. This relative velocity is obtained from the minimum absolute velocity U_{5a}, when U_{5a} is axial. Thus the velocity in port 5 is set axial. For zero angle of attack to the blades of the relative velocity U_5, the rotor pitch line speed Vw is set equal in magnitude to the tangential component of the relative velocity, $U_5 \sin(B_i)$. Later the blade inlet angle B_i is set and the stator inlet angle B_1 at state 1 is calculated for zero angle of attack for U_2.

First, for each value of c_3/c_5 selected the procedure for second-stage compression solution is as outlined below for each A_e/A_c:

1 Select a value of M_4.

2 Calculate c_4/c_3 and p_4/p_3 with wave Eqs. (A-12) to (A-14).

3 Vary p_7/p_4 until A_e/A_c becomes the value selected. Note that $p_6/p_5 = p_6/p_4 = 1/a$ where $1-a = (p_6 - p_5)/p_6$ is the fractional pressure drop in the combustor loop. For the nozzle flow $p_o/p_6 = (p_o/p_7)\ (p_7/p_4)\ (p_4/p_6) = (p_0/p_7)\,(p_7/p_4)a$.

4 Vary p_8/p_5 until M_9 is the same when calculated from states 8-5-4-7-9 as when calculated from states 8-9. The wave Eqs. (A-9) to (A-14) are used.

5 Calculate state 9′ by noting that the nozzle exit pressure from state 9′ is the same as that of the nozzle exit pressure from state 7, or $p_{e9'} = p_{e7} = p_6$.

6 Locate points where shocks "c" and interface "j" reach the upstream and downstream ends of the blade passages, respectively. Also locate the point where shock "b" reaches the downstream end of the blades. These points relative to the leading edge of port 5 are used to locate port edges and determine the flow of gas onto and off the rotor at ports 5 and 6. Waves downstream of state 9′ are weak; thus, changes in pressure between state 9′ and the trailing edge of the exit port 6 are neglected.

7 Vary the selection of M_4 in Step 1 above until the flows W_5 and W_6 become equal.

Port Sizes and Locations. To determine port widths note that in the time that it takes waves and/or interfaces to travel down and back up the blade passages the rotor pitch line travels a distance $Y = tVw$. For example, to locate the width of the inlet air port 1

$$t_1 = Y_1/Vw = t_w = L/U_2 + L/(\mathrm{Mx}_2 \cdot c_2 - U_2) \tag{3}$$

or for the width of port 5

$$t_5 = Y_5/Vw = Lb/U_5 + Lb/(\mathrm{Mx}_5 \cdot c_5 - U_5) \tag{4}$$

Table 1 Effect of A_e/A_c on cycle efficiency and power density

	Ae/Ac	0.5000	0.6000	0.7000	0.8000	0.9000	1.0000
c3/c5=0.5	M4	0.7460	0.7350	0.7260	0.7140	0.7000	0.6885
p4=p5	Mx3	1.6716	1.6574	1.6447	1.6309	1.6164	1.6023
p5/p6=.95	p4/p3	3.0932	3.0380	2.9893	2.9364	2.8816	2.8287
	c4/c3	1.1990	1.1950	1.1900	1.1878	1.1878	1.1840
	p7/p4	1.7439	1.5780	1.4300	1.2905	1.1641	1.0526
	Mx4	1.2797	1.2229	1.1699	1.1176	1.0680	1.0223
	c7/c4	1.0854	1.0688	1.0531	1.0374	1.0220	1.0074
	M7	0.3048	0.3718	0.4401	0.5093	0.5775	0.6470
	M5	0.4472	0.4392	0.4320	0.4240	0.4157	0.4076
	p8/p5	1.5240	1.4110	1.3080	1.2105	1.1202	1.0388
	Mx5	1.2038	1.1629	1.1243	1.0865	1.0503	1.0165
	c8/c5	1.0632	1.0510	1.0394	1.0278	1.0164	1.0055
	M8	0.1282	0.1776	0.2273	0.2779	0.3286	0.3783
	pf/p8	0.8337	0.7763	0.7220	0.6701	0.6214	0.5766
	Lb/L	0.8061	0.8125	0.8199	0.8267	0.8327	0.8396
	p9/p7	0.8739	0.8942	0.9147	0.9380	0.9623	0.9869
	M9	0.2136	0.2971	0.3819	0.4679	0.5533	0.6390
	Me7	0.9397	0.8766	0.8178	0.7580	0.6994	0.6470
	Ae7/A*	1.0031	1.0137	1.0313	1.0580	1.0948	1.1385
	A7/A*	2.0067	1.6892	1.4738	1.3224	1.2162	1.1385
	Y3*c3/VwL	0.5982	0.6034	0.6080	0.6132	0.6187	0.6241
	Y5*c3/VwL	1.4340	1.4863	1.5411	1.5987	1.6576	1.7194
	Y7*c3/VwL	0.4028	0.4183	0.4336	0.4503	0.4678	0.4868
	Y9'c3/VwL	0.6117	0.4053	0.2888	0.2146	0.1655	0.1300
	W5/W3	0.9919	0.9915	0.9950	0.9953	0.9929	0.9912
	W6/W3	0.9910	0.9945	0.9992	0.9977	0.9914	0.9912
	cg/c8	1.0150	1.0208	1.0266	1.0326	1.0386	1.0445
	pg/p8	1.1095	1.1544	1.2010	1.2501	1.3010	1.3525
	Lf/L	0.7199	0.4869	0.3502	0.2624	0.2035	0.1599
	T10/T3	4.4106	4.3983	4.3862	4.3683	4.3456	4.3218
	M2	0.5221	0.6470	0.7880	0.9600	1.0000	1.0000
	Mx2	1.3612	1.4609	1.5789	1.7300	1.7662	1.7662
	c3/c2	1.1089	1.1377	1.1720	1.2166	1.2274	1.2274
	p3/p2	1.9949	2.3233	2.7419	3.3252	3.4727	3.4727
	M14	0.3059	0.3779	0.4580	0.5534	0.5759	0.5771
	A14/A*	2.0003	1.6662	1.4293	1.2500	1.2183	1.2168
	A14e/A*	0.9999	0.9999	1.0001	1.0001	1.0967	1.2168
	M14e	1.0000	1.0000	1.0000	1.0000	0.6969	0.5771
	1/(1+W9'/W7)	0.4251	0.5316	0.6186	0.6891	0.7450	0.7912
	1/(1+W7/w9')	0.5749	0.4684	0.3814	0.3109	0.2550	0.2088
	Vw/c3	0.5923	0.6862	0.7297	0.7494	0.7560	0.7558
	p01/pa	3.0000	3.0000	3.0000	3.0000	3.0000	3.0000
	T1/Ta	1.3778	1.3807	1.3873	1.3894	1.3982	1.4072
	p1/pa	2.5293	2.5480	2.5908	2.6046	2.6623	2.7230
	p5/pa	15.6079	17.9837	21.2355	25.4307	26.6412	26.7480
	T6/T5	0.3666	0.3633	0.3597	0.3581	0.3579	0.3556
	T15s/T10	0.4121	0.3940	0.3743	0.3541	0.3481	0.3464
P/(HLpacasinBi·cosBi)		26.6382	33.1259	42.6038	55.2920	59.3282	60.4252
CycleEfficiency		0.5155	0.5392	0.5638	0.5869	0.5958	0.6021

$$Y_5 \cdot c_3/(LVw) = c_3/c_5 \cdot Lb/L \cdot [1/\mathrm{M}_5 + 1/(\mathrm{Mx}_5 - \mathrm{M}_5)] \quad (5)$$

Lb/L, $Y_6 \cdot c_3/(LVw)$, and other nondimensional port widths are obtained in a similar manner. The angle of the blades B_i has no effect on the width of a port, because the relative velocities are in the same direction as the blade lengths, L and Lb. After all port sizes are calculated as if the blades were in the axial direction, the entire exit stator with its ports is rotated a distance $L \cdot \sin(B_i)$ opposite to the direction of rotation, designated as Y_o or offset in Table 2.

Flow and Flow Continuity. Flow W_5 may be less than, equal to, or greater than W_3 depending upon whether ports 5 and 6 are shorter or longer than the wave and interface geometry of Fig. 2. If the port width Y_6 is shorter, interface "j," and cool air enters region 10 decreasing the final compression temperature T_{10}, and p_{10}. In this case W_5 becomes less than W_3. Net work decreases faster than the heat added; the cycle efficiency decreases. If ports 5 and 6 are longer than shown in Fig. 2, W_5 becomes greater than W_3. Hot gas flows into port 6, mixes with high pressure air, and undergoes a pressure loss in the combustor loop. Therefore, maximum cycle efficiency results when $W_5 = W_3$, which is selected as a design condition.

To calculate the flow from port 6 and the flow onto the rotor in port 5, the continuity equations are written as

$$W_5 = \rho_5 \cdot U_5 \cdot \cos(B_i) \cdot Y_5 \cdot H = W_6 \quad (6)$$

$$W_6 = \rho_7 \cdot U_7 \cdot \cos(B_i) \cdot Y_7 \cdot H + \rho_{9'} \cdot U_{9'} \cdot \cos(B_i) \cdot Y_{9'} \cdot H \quad (7)$$

where $\rho_{9'} \cdot U_{9'}$ is assumed nearly constant until the interface reaches the downstream end of the blade passages, because waves in this region are weak. After the expansion fan emanating at the closing of port 5 and the shock emanating at the closing of port 6 intersect, the final mixed state 10 temperature is calculated with the energy equation. Weber (1978) shows that the state 10 temperature is also given by

$$T_{10} = T_3 + k \cdot (T_{o5} - T_{o6}) \quad (8)$$

Flow at states 3 and 10 is trapped between stator end walls. Because flow $W_5 = W_6$, flow $W_{10} = W_3$. Specific volumes at states 3 and 10 must be equal, because W_{10} and W_3 are carried in the same area at the same velocity. Because the gases are assumed perfect, $p_3/p_{10} = T_3/T_{10}$. This process may be considered the equivalent of constant volume combustion.

Expansion. After the flow has been trapped between end walls at state 10, expansion from the rotor occurs. To determine the width of ports 12 and 15, the single wave approximation

Table 2 Engines ($pa=1$ atm, $T_a=294$ K, 500 hp, $H=1.588$ cm, $t=0.051$ cm)

	Design 1			Design 2			Design 3
T5/Ta	4.55	5.54	6.53	4.50	5.50	6.49	5.56
p4,5/pa	18.087	20.219	22.272	17.899	20.207	22.400	14.106
M5abs	0.259	0.269	0.277	0.318	0.330	0.339	0.339
T1/Ta	1.397	1.404	1.408	1.382	1.393	1.400	1.198
p1,2/pa	2.556	2.601	2.630	2.530	2.599	2.645	1.666
M1	0.746	0.728	0.716	0.579	0.543	0.518	0.518
T3/Ta	2.104	2.115	2.121	2.082	2.098	2.108	1.805
p3/pa	8.877	9.032	9.133	8.785	9.027	9.186	5.784
T4/Ta	2.602	2.701	2.791	2.574	2.679	2.774	2.375
M4	0.485	0.545	0.600	0.485	0.545	0.600	0.600
M5	0.367	0.381	0.392	0.367	0.381	0.392	0.392
T6/Ta	2.642	2.740	2.832	2.614	2.719	2.815	2.409
p6/pa	19.039	21.283	23.445	18.841	21.270	23.578	14.848
M6axial	0.313	0.355	0.393	0.221	0.251	0.278	0.278
T10/Ta	4.776	6.037	7.297	4.725	5.989	7.253	6.209
p10/pa	20.148	25.786	31.419	19.940	25.770	31.599	19.899
T12/Ta	4.129	5.026	5.898	4.085	4.987	5.862	5.018
p12/pa	12.105	13.583	14.911	11.979	13.574	14.996	9.443
M12abs	0.267	0.343	0.410	0.189	0.249	0.308	0.308
T15/Ta	2.568	3.019	3.445	2.541	2.996	3.424	2.931
p15/pa	2.556	2.601	2.630	2.530	2.599	2.645	1.666
M15abs	0.552	0.498	0.459	0.431	0.373	0.334	0.334
Vw/ca	0.553	0.634	0.708	0.674	0.773	0.865	0.800
W1(kg/s)	1.418	0.886	0.637	1.430	0.890	0.638	0.836
W12(kg/s)	0.761	0.557	0.440	0.768	0.560	0.441	0.577
W15(kg/s)	0.657	0.329	0.197	0.662	0.330	0.198	0.259
B1	18.688	13.700	8.868	30.365	22.891	15.122	15.122
Bi,Be	45.000	45.000	45.000	60.000	60.000	60.000	60.000
Y1 (cm)	14.164	8.721	6.209	20.300	12.349	8.725	16.791
Y2 (cm)	7.605	5.484	4.285	10.899	7.765	6.021	11.587
Y3 (cm)	3.642	2.147	1.469	5.220	3.040	2.064	3.971
Y5 (cm)	11.127	6.608	4.546	16.837	9.879	6.744	12.980
Y6 (cm)	5.924	2.971	1.780	8.490	4.207	2.501	4.813
Y12 (cm)	7.373	4.192	2.802	10.567	5.935	3.937	7.578
Y15 (cm)	12.434	7.240	4.944	17.821	10.252	6.946	13.368
Yo,offset	9.285	5.003	3.192	13.307	7.084	4.484	8.630
L (cm)	13.131	7.075	4.514	15.366	8.180	5.178	9.966
Lx (cm)	9.285	5.003	3.192	7.683	4.090	2.589	4.983
RotrD(cm)	16.867	11.503	9.079	27.342	17.256	12.857	21.325
CprP(HP)	-311	-194	-139	-269	-168	-120	-87
HPTbP(HP)	652	609	587	640	595	571	566
LPTbP(HP)	204	117	79	185	109	74	49
RtrP(HP)	-45	-32	-27	-56	-36	-25	-28

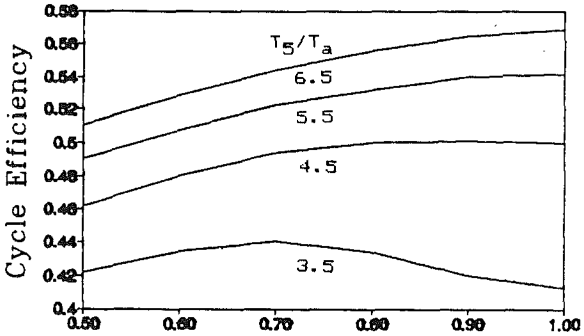

Fig. 4 Cycle efficiency: precompression stag pressure ratio 3

of an expansion fan is used as shown in Fig. 2. Wave Eqs. (A-9) to (A-11) are used to obtain a relation for $p_{10}/p_2=p_{10}/p_{14}$ expansion. Mach number M_{11} is varied until $(p_{10}/p_2)_{\exp}=(p_{10}/p_2)_{\text{compr}}$; i.e., this procedure yields the M_{11} for which the rotor expansion pressure ratio equals the rotor compression pressure ratio. Equations (A-9) to (A-11) also yield the pressures p_{11}/p_{10}, the temperatures T_{12}/T_{10} and T_{15}/T_{10} or T_{15}/T_a. Smaller A_e/A_c and lower combustion temperatures result in choking of the nozzle from state 14. Larger A_e/A_c and higher combustion temperatures result in $M_2=1$. Rotor inlet temperature is calculated, depending upon precompression, from

$$T_5/T_a=(c_5/c_3)^2\cdot(c_3/c_1)^2\cdot(T_1/T_a) \tag{9}$$

Cycle Efficiency, Power and Rotor Size. Cycle efficiency is obtained by evaluating $\eta=$net work/heat added. The net power may be written as

$$P=W_1\cdot cp\cdot(T_5-T_6)\cdot\eta \tag{10}$$

$$W_1=W_3=\rho_3\cdot Vw\cdot H\cdot L\cdot\cos(B_i) \tag{11}$$

With the equation of state the power density becomes

$$P/(HLp_a\cdot c_a)=k/(k-1)\cdot p_1/p_a\cdot p_3/p_2\cdot c_a/c_1$$
$$\cdot c_2/c_3\cdot c_4/c_3\cdot M_4\cdot\cos(B_i)\cdot\sin(B_i)\cdot T_5/T_a\cdot(1-T_6/T_5)\cdot\eta \tag{12}$$

If the precompression pressure and temperature ratios and the combustion temperature are constant, the only variable is the blade angle B_i. Thus the power density is a maximum at $B_i=45$ deg.

A sample calculation leading to the last equations is shown in Table 1 for $c_3/c_5=0.5$. Other values of c_3/c_5 yield the results plotted in Figs. 4 and 5.

Design speed $Vw/c_3=M_4\cdot c_4/c_3\cdot\sin(B_i)$. After all nondimensional port widths and power density are calculated, power and B_i are selected. Blade height, H, pitch, s, and thickness, t, are selected so that the blades are rigid and the free flow area is relatively large (84 percent for designs 2 and 3 of Table 2). With an 0.079-cm-thick shroud around the blades the entire structure is very rigid. No critical speed should exist between zero and design speed. The two end wall widths between ports 1 and 5 and ports 6 and 12 are arbitrarily taken as $4\cdot s$.

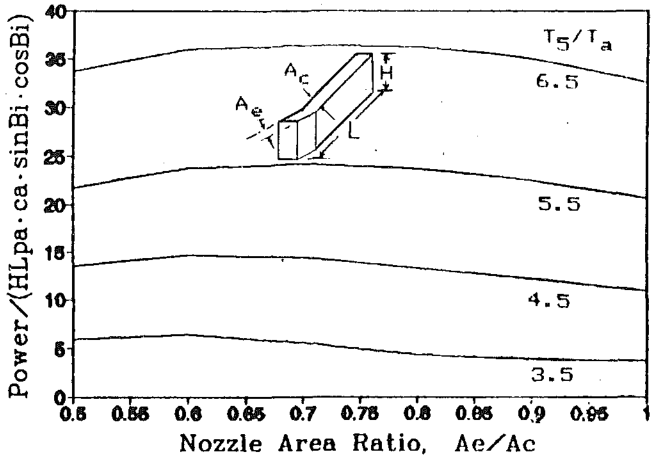

Fig. 5 Net power density

Discussion

It is found that extremely long rotor periphery is required for the smaller A_e/A_c considered. This is due to the fact that the nozzle acts as a flow restriction. Also area ratio $A_e/A_c = 1$ is selected for rotor design, because it yields maximum cycle efficiency for the combustion temperatures of interest as shown in Fig. 4. Power density decreases slightly at the larger values of A_e/A_c in Fig. 5, but it is near its maximum value at $A_e/A_c = 1$, and results in short blade lengths. Straight blades without bends for nozzles are easily fabricated or cast.

Table 2 presents three designs for a 500 hp net engine. The first has maximum power density and smallest rotor volume at blade angle $B_i = 45$ deg. This design results in an axial rotor length $Lx = 3.19$ cm for the highest temperature ratio $T_5/T_a = 6.5$. It requires a precompression stagnation pressure ratio of 3.7, although only the static pressure ratio of 2.63 must be produced. The second design has $B_i = 60$ deg. This design has a smaller power density and larger rotor volume. However, it has a shorter axial length $Lx = 2.59$ cm. It requires a precompression stagnation pressure ratio of only 3.18 with the same static pressure ratio as the first design. The first design has a wave rotor inlet Mach number $M_1 = 0.72$ whereas the second design has $M_1 = 0.52$.

A third design is shown in Table 2. It also has a blade angle of 60 deg but has a precompression static pressure ratio of only 1.67 with $M_1 = 0.52$. The rotor diameter is 23 percent larger and the axial length 22 percent larger than that of the second design.

The prototype wave engine built by GPC (Weber, 1978; Coleman, 1984) had a rotor blade area ratio $A_e/A_c = 0.5$ and a $B_i = 48$ deg. At low combustion temperature this flow restriction resulted in the expansion waves from closing of flow from port 5 intersecting the interface "j" before it reached the downstream ends of the blades. Flows W_5 and W_6 became less than W_3 for temperature ratios $T_5/T_a < 3.55$ for $A_e/A_c = 0.5$. The GPC engine was operated at $T_5 = 1123$ K or $T_5/T_a = 3.74$. The pitchline speed was 108 m/s, which was 56 percent of the design speed of 194 m/s. The flow ratio W_5/W_1 was 0.52. The overscavenging flow was not reported. However, the temperature ratio T_5/T_a was large enough to permit the flow W_5 or W_6 to be equal to W_3. The pitchline speed of operation was too low, so that the shock wave system fell inside ports 5 and 6. Thus, there was no flow onto the rotor downstream of the point where shock "c" reached the hot gas port 5. The calculations of this paper are consistent with the measured W_5/W_1.

Losses. Shock losses are included in the shock equations of the Appendix. Fractional pressure loss $1 - p_5/p_6$ is taken as 0.05 in the combustor loop for re-entry of high-pressure air as hot gas.

Because blade passages do not open instantaneously, initial compression waves may not coalesce to a shock between blade inlet and exit. For rotor speeds of Table 2 the opening time of a blade passage varies from 20 to 30 μs. The ratio of opening time to wave travel time down the passage length is 0.09 to 0.18. The GPC rotor (Weber, 1978; Coleman, 1984) had a blade length to passage width, L/D, of 5.6. Designs of Table 2 have L/D of 8 to 16. It is not certain how far the time of wave coalescence requires the location of port 6 to be moved in the direction of rotation. Measurements on the GPC rotor indicated that shock "b" of Fig. 2 impinged on the downstream end wall almost one pitch beyond predictions using instantaneous opening. Data of A. Kantrowitz at Cornell Aeronautical Labs indicate similar results with $L/D = 6$. Thus port 6 should have been moved downstream about one pitch length. The longer L/D of Table 2 designs should require smaller shifts in port 6. The required shift of port 6 can be measured.

The largest loss can result from end wall and peripheral leakage from the rotor. Leakage is minimized by small end wall and peripheral clearances. Short axial length and small diameter rotors permit designs of small clearance, because expansion is less for a given temperature rise of the rotor. The short axial length rotors are a direct result of high-speed rotation ($Vw = 190$ to 275 m/s). For high-speed rotation the peripheral width of a port increases, and more flow enters the rotor before shocks "b" and "c" return to the port inlet. This result is shown in Table 1 where the dimensionless parameters are $Y_n \cdot c_3/(VwL)$. These parameters result from the shock and flow equations of the Appendix.

Mixing at the gas-air interfaces increases the temperature of the air being compressed and decreases the temperature of the expanding gas. However, in a private communication Berchtold, consultant to Brown Boveri, stated that this effect is insignificant in the pressure produced by the wave rotor. Measurements by Thayer et al. (1981) indicated that the width of the mixing region was about 1.2 times the rotor passage width. This result suggests that much of the mixing is caused by the vortex, which is rolled up by the flow jetting into a blade passage as it begins to open. The vortex resulting from this gradual opening is expected to be about one passage width in diameter.

Entry and exit losses from the blades are not included. Exact information on the pressure loss in the combustor reentry loop is not available. Consequently, this pressure drop (taken as 5 percent in this paper) can be adjusted to include rotor inlet and exit losses.

Flow rates in ports 1, 5, 6, 12, and 15 may be calculated from a modified Eq. (6) and the information in Table 2 or, e.g.,

$$W_6 = k \cdot M_6 \cdot p_6/p_a \cdot c_a/c_6 \cdot Y_6 \cdot H \cdot p_a/c_a \tag{13}$$

Conclusions

Wave rotor designs presented in Table 2 represent extremely compact, high pressure ratio, high temperature ratio engines. The advantages of wave rotors discussed in this paper are incorporated in the wave rotor designs presented. The wave rotor is coupled with a centrifugal precompressor and two radial flow turbines. Design temperature ratios of most interest are $T_5/T_a = 5.5$ to 6.5 or combustion temperatures of 1600 to 1900 K. Rotor axial lengths are small; end wall clearances can also be small, resulting in better control of leakage. Rotor blades are straight without bends for outlet nozzles. Therefore, rotors are easily fabricated, milled, or cast even with a peripheral shroud around the blade tips.

All designs presented require the precompressor and wave rotor to be powered by the low-pressure turbine and a small fraction of the high-pressure turbine. Slightly below design speed the rotor will produce power because the momentum outflow from the rotor and inflow to the rotor produces thrust in the direction of rotation.

References

Azoury, P. H., 1965, "An Introduction to the Dynamic Pressure Exchanger," *Proc. IMechE*, Vol. 180, Part 1, No. 18.

Berchtold, M., and Lutz, T. W., 1974, "A New Small Power Output Gas Turbine Concept," ASME Paper No. 74-GT-111.

Coleman, R. C., and Weber, H. E., 1974, "Integral Turbo-Compressor Wave Engine," U.S. Patent No. 3,811,796.

Coleman, R. C., 1984, "Wave Engine Technology Development," final report prepared by General Power Corporation for AFWAL (Contract No. AFWAL-TR-83-2095).

Jenny, E., and Bulaty, T., 1973, "Die Druck wellen-Maschine Comprex als Oberstufe einer Gasturbine," *MTZ Motortechische Zeitschrift*, Vol. 34, No. 10, pp. 329–335, and Part 2, Vol. 34, No. 12, pp. 421–425.

Keller, J. J., 1984, "Some Fundamentals of the Supercharger Comprex," *Machinery for Direct Fluid-Fluid Energy Exchange*, J. F. Sladky, Jr., ed., ASME.

Pearson, R., 1985, "Pressure Exchangers and Pressure Exchange Engines," Ch. 16, *Thermodynamics and Gas Dynamics of IC Engines*, D. E. Winterbone and S. C. Low, eds., Oxford University Press, United Kingdom.

Seippel, C., 1946, "Pressure Exchanger," U.S. Patent No. 2,399,394.

Shreeve, R. P., and Mathur, A., eds., 1985, *Proceedings of the 1985 ONR/NAVAIR Wave Rotor Research and Technology Workshop*, NPS-67-85-008, ONR, Washington, DC.

Taussig, R., et al., 1983, "Investigation of Wave Rotor Turbofans for Cruise Missile Engines," final report submitted by MSNW to DARPA (Contract No. N00140-82-C-9729).

Taussig, R., and Hertzberg, A., 1984, "Wave Rotors for Turbomachinery," *Machinery Direct Fluid-Fluid Energy Exchange*, J. F. Sladky, Jr., ed., ASME.

Thayer, W. J., et al., 1981, "Energy Exchanger Performance and Power Cycle Evaluation: Experiments and Analysis," final report MSNW to DOE.

Weatherston, R. C., and Hertzberg, A., 1967, "The Energy Exchanger, a New Concept for High Efficiency Gas Turbine Cycles," ASME JOURNAL OF ENGINEERING FOR POWER, Vol. 89, pp. 217–228.

Weber, H. E., 1978, "High Efficiency Wave Engine," *Fluids Engineering in Advanced Energy Systems*, C. H. Marston, ed., ASME.

Weber, H. E., 1986, "Shock-Expansion Wave Engines—New Directions for Power Production," ASME Paper No. 86-GT-62.

APPENDIX

Summary of Commonly Used Gas Dynamic Equations

Equations referred to in this paper are summarized below. In addition to the equation of state for a perfect gas,

$$p = \rho RT \qquad \text{(A-1)}$$

the specific heats may be written

$$cp = dh/dT \qquad \text{(A-2)}$$

$$cp - cv = R \qquad \text{(A-3)}$$

$$k = cp/cv \qquad \text{(A-4)}$$

Specific heats are assumed constant. The speed of sound is

$$c^2 = kRT \qquad \text{(A-5)}$$

The following adiabatic and/or isentropic, one-dimensional, steady flow equations are used between waves to calculate states in regions of Fig. 2 where no waves are crossed:

$$T_o/T = 1 + (k-1)/2 \cdot \mathrm{M}^2 \qquad \text{(A-6)}$$

$$p_o/p = (T_o/T)^{k/(k-1)} \qquad \text{(A-7)}$$

$$A/A^* = 1/\mathrm{M} \cdot [2/(k+1) \cdot \{1 + (k-1)/2 \cdot \mathrm{M}^2\}]^{(k+1)/2(k-1)} \qquad \text{(A-8)}$$

The following isentropic, one-dimensional wave equations are used in calculation of states when expansion waves are crossed between regions of Fig. 2. Numbers 1 and 2 indicate states before and after the wave.

$$c_2/c_1 = 1 \pm (k-1)/2(U_2 - U_1)/c_1 \qquad \text{(A-9)}$$

$$T_2/T_1 = (c_2/c_1)^2 \qquad \text{(A-10)}$$

$$p_2/p_1 = (c_2/c_1)^{2k/(k-1)} \qquad \text{(A-11)}$$

The + or − sign is taken dependent upon the wave direction, noting that the speeds of sound, temperature, and pressure decrease after passage of an expansion wave.

The following one-dimensional flow equations are used in calculation of states when shock waves are crossed between regions of Fig. 2. Numbers 1 and 2 indicate states before and after the wave, respectively.

$$T_2/T_1 = 1 + 2(k-1)/(k+1)^2 \cdot [k \cdot \mathrm{Mx}^2 - 1/\mathrm{Mx}^2 + 1 - k] \qquad \text{(A-12)}$$

$$(U_2 - U_1)/c_1 = \pm 2/(k+1) \cdot [\mathrm{Mx} - 1/\mathrm{Mx}] \qquad \text{(A-13)}$$

$$p_2/p_1 = 1 + 2k/(k+1) \cdot [\mathrm{Mx}^2 - 1] \qquad \text{(A-14)}$$

R. L. Vogt
Textron Lycoming,
Stratford, CT 06497-7593

Future Trends in Turboshaft Engines up to the 5000 Horsepower Class

Advanced technology now being demonstrated in the test cell will provide growth in existing engine ratings in the near term and substantially improve new technology engines early in the twenty-first century. The benefits these advancements provide, to the engines, to the salient characteristics important to users and designers, and to the vehicles they will power, are discussed.

Introduction

The evolution of the gas turbine engine has enabled major flight vehicle performance, payload, and range improvements continuously since the late 1930s. Prior to that time turbine engines were not practical flight vehicle power plants due to their low power-to-weight ratios and high specific fuel consumption. The turboshaft configuration of the gas turbine engine has progressed over the past fifty years to the point where currently operating turboshaft engines in the 1000 to 2000 shaft horsepower (shp) class deliver 4 hp/lb of engine weight [1], and turboshaft engines in the 4000 to 6000 shp class deliver 6 hp/lb. Within the next decade, technology will have been demonstrated to double these power to weight ratios.

Similar improvements will occur in specific power, enabling the required vehicle power to be supplied by flowing only half the airflow at the inlets and exhausts.

A more important measure of merit than power-to-weight or power-to-airflow in turboshaft engine performance, perhaps the most important measure, is specific fuel consumption (SFC). The SFC of currently operating 1000–2000 shp class turboshaft engines is 0.46 lb of fuel burned for each shaft horsepower-hour delivered and 0.43 for the 4000–6000 shp class [2–8]. Within the next decade these SFC values will be reduced by one-third. To emphasize the importance of this large SFC reduction, note that future turboshaft engines will require only two thousand pounds of fuel to operate for the same time interval, delivering the same level of power, as today's engine consuming three thousand pounds of fuel.

The benefits to the new engines are considerable. The benefits to new flight vehicles are even greater than the engine benefits alone. A flight vehicle designed to move a certain payload through a given distance will be smaller and lighter due to both the reduction in engine and fuel weight, and to the additional reduction in empty vehicle weight resulting from the smaller fuel and installed engine load to be carried.

Drivers

Technology is available today that enables the development of advanced turboshaft engines. The advantages these engines offer motivates the need for them. They are needed to preclude falling behind an enemy threat capability or a commercial competitor who adopts them. Commercial applications will capture the benefits of one-third less fuel consumption from those engine suppliers able to offer them. Military missions will fully utilize these same fuel benefits as well as other advantages in order to preclude the possibility of a hostile threat possessing better technology and, therefore, superiority in battle.

In both cases the advanced engine will allow a greater payload to be carried over longer ranges than current engines. The fuel savings will reduce specific mission cost. Civil transports will have greater range and military deployment will be possible from remote bases over nonrefueled distances not possible today.

Engine Cycle Selection

The simple Brayton cycle is in common use today. It has been modified to operate with variable flow capacity in the compressor and turbine and with regenerative heating as in recuperated engines. Future variable cycles have similar advantages (and disadvantages) in advanced turboshaft engines as today. The choice is mission dependent. A mission where operation is required for a high percentage of total mission time at both high power and low power favors variable capacity. However, the improvement in SFC in future turboshafts will diminish these advantages.

Missions with ultralong range favor a recuperated cycle. The reduced exhaust enthalpy, infrared signature, and SFC can more than compensate for the added engine weight and cost.

Nevertheless, the majority of future missions will employ the simple cycle. The simple cycle is versatile. A turboshaft core engine can be effectively adapted to turboprop engine applications as well as high bypass turbofans and low bypass augmented turbofans. Development and qualification or certification costs can be shared over an engine family. Due to

---

Contributed by the International Gas Turbine Institute and presented at the 36th International Gas Turbine and Aeroengine Congress and Exposition, Orlando, Florida, June 3–6, 1991. Manuscript received at ASME Headquarters February 12, 1991. Paper No. 91-GT-74. Associate Technical Editor: L. A. Riekert.

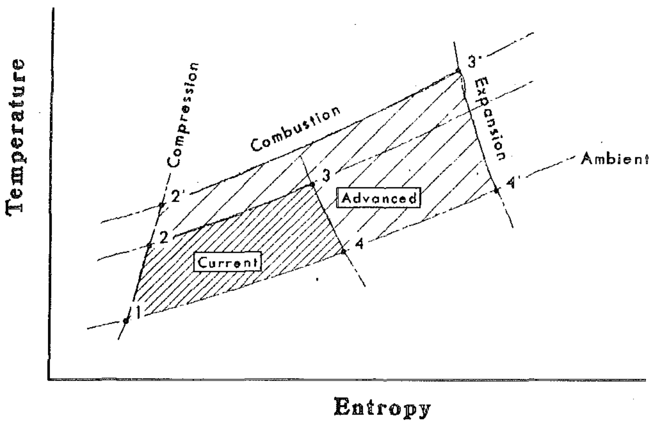

Fig. 1 *T-S* cycle diagram

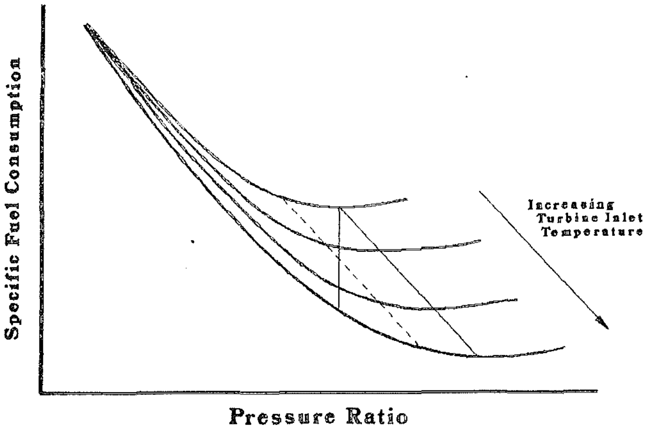

Fig. 2 SFC minimization

its versatility the simple Brayton cycle is the most widely used gas turbine engine configuration today.

The Brayton cycle is shown on the temperature–entropy diagram in Fig. 1. Current technology is shown with dense cross-hatching. Advanced technology is shown with light cross-hatching. The main differences are that future engines will operate with higher pressure ratios, points 1-2 compared to 1-2′. In conjunction with the higher pressure ratios, the turbine inlet temperature will be substantially increased, from 3 to 3′. As a result, the temperature rise required in the combustor will increase, 2-3 grows to 2′-3′, requiring greater fuel flow per unit airflow. However, the net work deliverable by the engine increases at a faster rate than the fuel energy consumed and provides greater output power. The total cycle work increase can be seen by comparing the areas enclosed by the current cycle 1-2-3-4 to the advanced cycle 1-2′-3′-4′. The dense cross-hatched area of the current cycle is small compared to the light cross-hatched area (more total work) of the advanced engine cycle. The net work produced in the cycle, which is proportional to delivered engine power, actually increases more rapidly than total cycle work because the work consumed by the compressor is two-thirds of the current engine total work per cycle but is only one-half of the total work in the advanced engine cycle. Net work and, therefore, delivered power is higher.

Thermodynamics teaches that higher source temperatures (turbine inlet in the engine) allows higher thermal efficiency.

The motivation to increase engine pressure ratio along with turbine inlet temperature is provided by the advantage of minimizing SFC. Minimizing SFC maximizes thermal efficiency. Figure 2 depicts SFC minimization on a plot of SFC versus pressure ratio with an array of constant turbine inlet temperature lines on the field. The lower the turbine inlet isotherm is located on the figure, the higher the turbine inlet temperature. The locus of SFC minimums is the zero slope of each of these isotherms. These have been connected by a solid line crossing the isotherms from above left to lower right. The vertical solid line indicates the more limited reduction in SFC achieved by maintaining constant pressure ratio while increasing turbine inlet temperature. Compare that SFC reduction to that achieved by simultaneously increasing the pressure ratio and turbine inlet temperature. Consequently, higher thermal efficiencies require higher turbine inlet temperatures and, therefore, higher pressure ratios.

Due to the shallow slope of the turbine inlet isotherm near the point of minimum SFC, it is cost effective to select a pressure ratio somewhat less than thermodynamically optimum. For example, for typical turboshaft missions for which rotorcraft are employed, numerous trade studies have shown that a reduction in an optimum pressure ratio of 25 (turbine inlet temperature dependent) to a pressure ratio of 22 increases SFC less than one percent while it reduces engine acquisition cost more than 10 percent. Life cycle cost is lowest with greater than minimum SFC. In addition, a cycle pressure ratio less than that which produces minimum SFC actually produces greater net work and horsepower than at the point of minimum SFC. The specific SFC trade varies with engine operating lifetime and fuel cost over that time. The dashed line in Fig. 2 represents the minimum life cycle cost just described.

As cycle pressure ratio is increased, the basic turboshaft engine configuration requires fundamental changes above a certain pressure ratio. That value of pressure ratio is influenced by core engine flow capacity. Achieving continually lower specific fuel consumption requires an even higher turbine inlet temperature. Increasing component efficiencies offsets some of the required temperature increase but are difficult to achieve considering the advanced state of compressor and turbine efficiencies employed today. As turbine inlet temperature increase is required, the increase in pressure ratio follows. Reducing SFC values by one-third, as will occur early in the twenty-first century, requires turboshaft engine cycle pressure ratios of 45 to 60 depending on efficiencies and the required levels of secondary leakage and cooling flows.

Pressure ratios above about 25 present considerable challenge in single spool engine configurations. Even with variable stators in the compressor axial stages a 25 pressure ratio single spool engine may not start with acceptable reliability. The flow area at the exit of the highest pressure compressor stage, likely a centrifugal in the power ranges discussed here, must be small compared to the first-stage inlet. The high exit pressure causes a low volumetric flow compared to the inlet volumetric flow. Each rotation of the compressor must sweep out a much larger volume in the first stage than in the last. High compressor polytrophic efficiency at normal engine operating power levels demands proper flow area matching.

The problem results at starting rpm, which is in the range of 20 to 30 percent of the normal power rating rpm. At low speed the last compressor stage still sweeps out a small volume compared to the first stage. However, the low pressure ratio that the compressor develops at low rpm means the volumetric flow at the exit is only slightly less than the inlet. This much higher volumetric flow cannot flow through the last compressor stage because the area is too small. Variable geometry helps, but above a pressure ratio of approximately 25 the flow mismatch at starting speed is too great.

Therefore, in future turboshaft engines with pressure ratios above 30, or more importantly in the range of 45 to 60, the engines will be two spool. A low-pressure compressor will be driven by a low-pressure turbine and a high-pressure compressor will be driven by a high-pressure turbine. Each of these spools is free to rotate at different rpm with the high-pressure spool having the fastest rotation. The rotational speed will

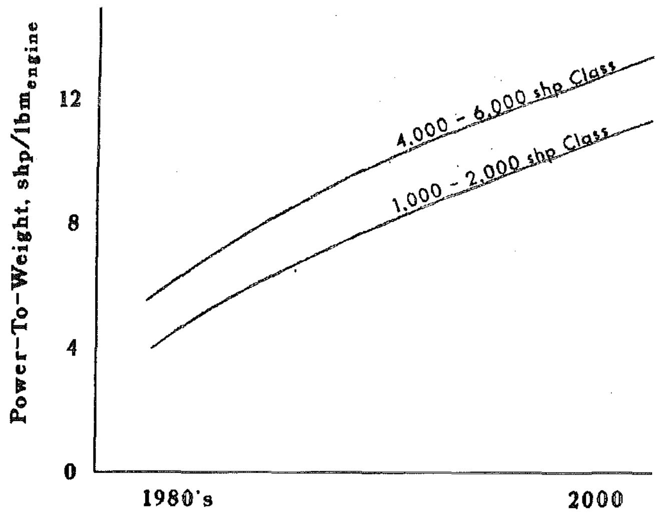

Fig. 3 Turboshaft/turboprop power-to-weight

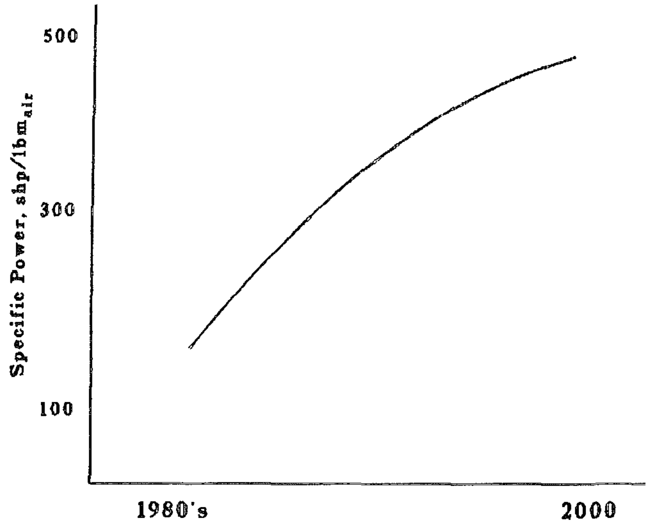

Fig. 4 Turboshaft/turboprop specific power

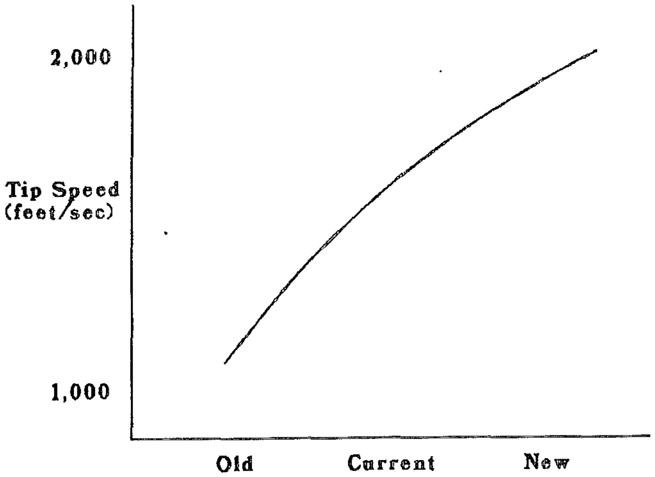

Fig. 5 Rotor tip speeds

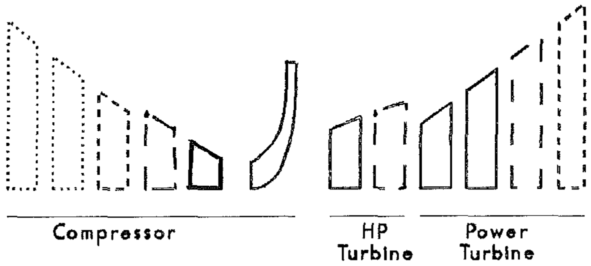

Fig. 6 Single spool rotor arrangement

vary from starting to rated power operation. The difference in rotational speed will be small at starting speed and larger at rated power operation. The starting problem is therefore solved. For simplicity in quantifying the starting benefit, compare the minimum combination of pressure ratios (which is the square root of the overall, two spool engine pressure ratio) to the maximum pressure ratio of a single spool engine which is easy to start. That pressure ratio average is approximately seven for each spool of the two spool engine with an overall pressure of 45 to 60, as mentioned earlier. A pressure ratio of 7 will have a much smaller flow mismatch at starting than the single pressure ratio of 25 on one shaft. The lower pressure ratio is able to be started with ease.

The two spools can be arranged concentrically as is common today. Or, they can be eccentric. The latter has many possibilities. Conceptually the eccentric spools can be imagined as a low-pressure spool arranged as the single spool turboshaft engine and the high-pressure spool as a turbocharger mounted beside the low-pressure spool engine. Ducted scrolls connect the flows.

Core engine flow capacity will determine the preferred configuration [9]. The 1000–2000 shp engine will have a core flow of only 3–5 lb/s. Physical space limitations in the high-pressure turbine disk and concomitantly the compressor disks to pass the high-pressure spool shaft, the low-pressure spool shaft, and the power shaft require either an eccentric arrangement to accommodate conventional superalloy disk stress limitations, or improved disk materials and designs such as nickel aluminides (NiAl), ceramic composites, or fiber-reinforced rings with diffusion bonded single crystal blades (blisks).

In the 4000–6000 shp engines the conventional concentric, two spool arrangement is desired because of the larger core flow required (10–12 lb/s). The limiting disk, which is the high-pressure turbine disk, has adequate strength using conventional super alloys to accommodate the two spool shafts and the power shaft. Larger engine power ratings will present even less challenge to the disk bore requirements.

Trends

Trends in the advanced turboshaft engines under discussion herein, which are of interest to engine users and airframe vehicle designers, are shown in Figs. 3–8. A description of these salient features will allow preliminary sizing of future vehicles to be obtained for each mission.

Figure 3 shows the improvement in engine shaft power delivered divided by engine weight. By the first decade of the twenty-first century, power per pound of engine weight will be double that which was available in the mid-1980s. The vehicle designer determines the required power to achieve the mission. The doubling of power-to-weight ratio means the required power will be provided by the engine but with only half the engine weight to be carried by the vehicle it powers.

Figure 4 is the companion to Fig. 3 and shows the trend of specific power, power divided by core air flow, over the same time period. In the 1000–2000 shp class, specific power will double from below 200 to above 400 shp per pound per second of airflow.

Figure 5 shows the increase in rotor tip speed required to achieve these high power densities and lightweight engines. The low end is typical of much of the nonflight rated turbo-

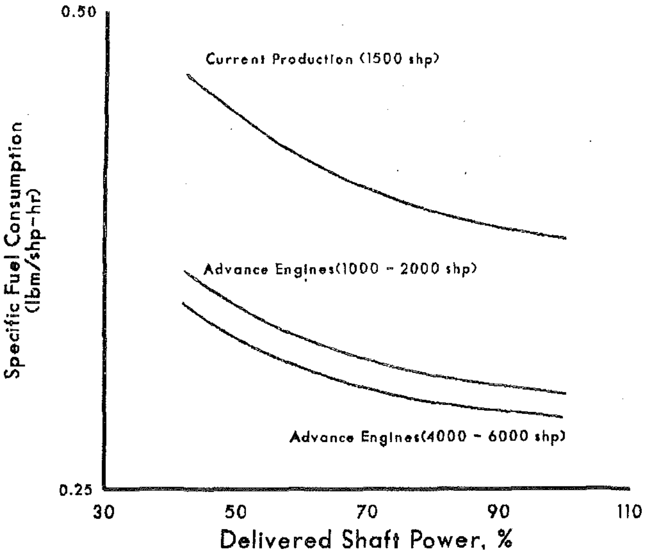

Fig. 7 Performance improvement over current production engines

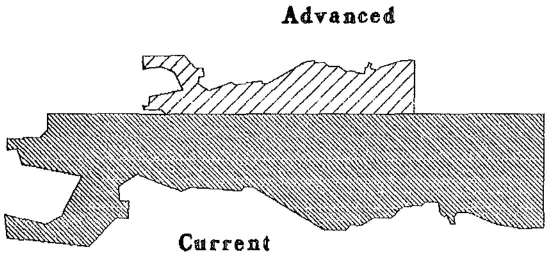

Fig. 8 Turboshaft engine size for equal power

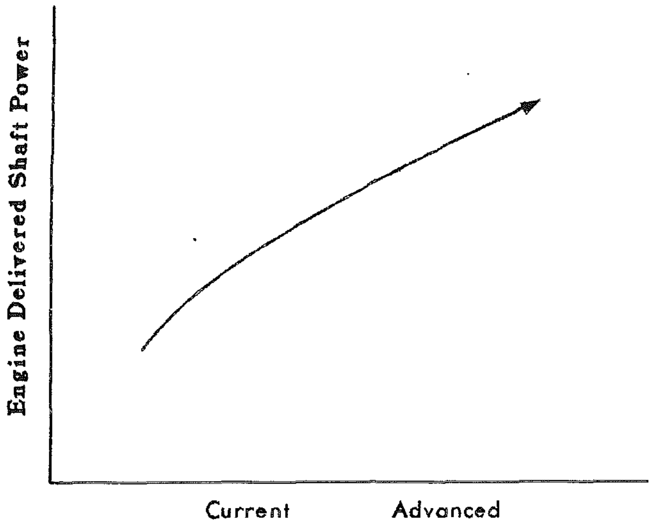

Fig. 9 Constant engine airflow

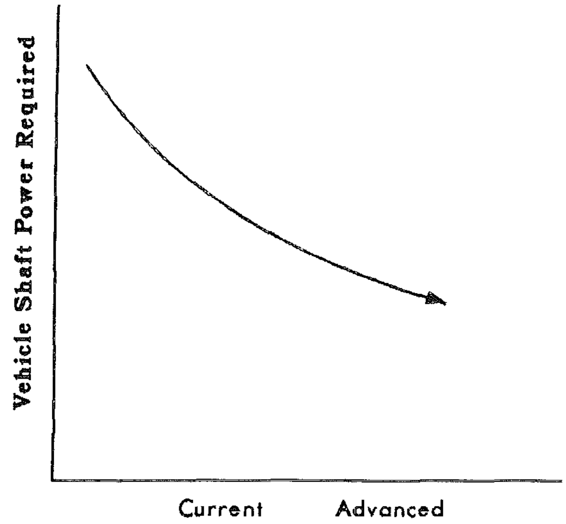

Fig. 10 Constant mission range and payload

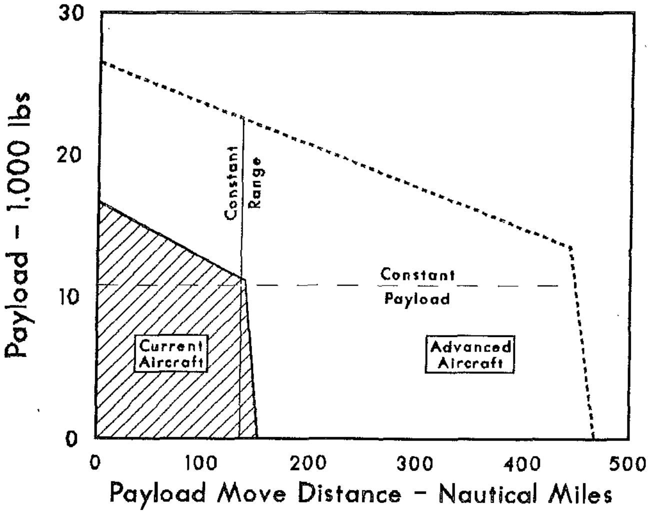

Fig. 11 Payload move range

machinery today. The high end, above 2000 feet per second, will be standard in turboshaft engines for the twenty-first century. These high tip speeds have been made possible by the recently developed high-strength, lightweight materials.

Figure 6 is the rotor stage arrangement of single spool turboshaft engines. The collection of dotted, dashed, and solid blades represents the current stage count in operational engines in the small flow class of turboshafts. Advanced engines reduce this stage count even with increased overall cycle pressure ratio, first by deleting the dotted stages and then the dashed stages as well. The high tip speed and high work per stage enable this reduction in stage count. The few remaining stages embody advanced technology in aerodynamics and in high tip speeds, which require high strength materials and high efficiencies of both the components and the cooling and leakage circuits.

Figure 7 compares SFC of current to advanced engines by flow class over the full engine speed range. An important observation is that the one-third reduction in SFC occurs not only at full power but all the way down to idle as well.

Figure 8 graphically compares the reduction in engine size for equal power output. The current engine cross section is shown below the centerline and the advanced engine is shown above. The advanced engine of the twenty-first century will be less than 50 percent of the length and diameter of current 1980s turboshaft engines at the same power rating.

These advanced turboshaft engines will have a one-third reduction in SFC, half the physical size, require half the airflow, and weigh half as much as the 1980s engines they will replace.

Mission Benefits

Figures 9, 10, and 11 characterize the benefits these advanced technology turboshaft engines will have in the vehicles and missions they perform.

Figure 9 shows the increase in power output provided by the engine. The reduced fuel consumption and engine weight will substantially reduce the vehicle power needs.

Figure 10 shows the reduction in power required by a given vehicle performing the same mission in the early twenty-first century compared to today. The power required decreases because the vehicle takeoff gross weight decreases as it hauls less fuel and engine weight. The lighter fuel and engine load require a lighter airframe to carry the same payload.

Figure 11 is the flight system overall benefit. Payload, which is typically many thousands of pounds in a turboshaft engine powered vehicle, is plotted versus move distance in nautical miles and is typically hundreds of nautical miles. The benefit can be used in various ways. Two of them are shown on the diagram. The dashed, horizontal line shows the advanced turboshaft engine allowing the same payload to be moved more than twice the current distance with the same fuel load. The vertical line shows the engines moving twice the payload over the same distance consuming the same fuel.

Conclusion

The advanced turboshaft engines that will be available during the first decade of the twenty-first century will operate on only two-thirds of the fuel required today. For the same engine power they will have only 50 percent the size, airflow, and weight. The benefits will be in moving twice the payload over equal distances or the same payload over twice the distance as is possible today. Civil transports will operate these engines moving twice the passengers over the same distance as today with the same fuel consumption. The military will be able to accomplish self deployment of Special Operations Forces [10] carrying payloads over twice the range achievable today.

Acknowledgments

Textron Lycoming has underway the advanced technology test program to demonstrate the SFC and other parameters cited above. Textron Lycoming is financially assisted under contract with the U.S. Army DAAJ02-89-C-0035, the U.S. Navy N00019-89-C-0352, and the U.S. Air Force F33657-89-C-2017. This joint program is titled Joint Turbine Advanced Gas Generator (JTAGG).

References

1 "Special Report: Rotorcraft Technology Update," *Aviation Week & Space Technology*, Jan. 19, 1987, pp. 74–75.

2 Dix, D. M., and Petty, J. S., "Aircraft Engine Technology Gets a Second Wind," *Aerospace America*, July 1990, pp. 36–39.

3 Zoccoli, M. J., and Klassen, D. D., "A Modern Technology Powerplant," ASME Paper No. 90-GT-242, 1990.

4 Schrader, J. W., and Schneider, W. F., "Aerodynamic Components for Small Turboshaft Engines," AGARD-CP-302, May 1981.

5 Kaehler, H., and Schneider, W., "Small Engine Technology Payoffs for Future Commuter Aircraft," AIAA-86-1544, July 1986.

6 Coons, L., "IHPTET Technology Mission Payoffs at the Component Level—A Look at Phase II Technologies," Paper No. AIAA-90-2404, 1990.

7 Glassman, A. J., Snyder, C. A., and Knip, G., Jr., "Advanced Core Technology: Key to Subsonic Propulsion Benefits," ASME Paper No. 89-GT-241, 1989.

8 Klassen, D. D., "Configuration Selection and Technology Transition in 5000 HP Class Engines," Paper No. AIAA-83-1411, 1983.

9 Bettner, J., "Component Arrangement Studies for an 8000 SHP Turboshaft High Technology Core," Paper No. AIAA-90-2398, 1990.

10 Lake, E. A., "Focusing Propulsion and Lift System Development for an Evolving Special Operations Forces Aircraft," Paper No. AIAA-90-2277, 1990.

J. E. McCall
Pratt and Whitney,
East Hartford, CT 06108

P. Tracksdorf

K. Heinig

Motoren- und Turbinen-Union,
Munich, Federal Republic of Germany

Advanced Ducted Engine Nacelle Aerodynamics and Integration Testing

Future aircraft engine development may lead to Advanced Ducted Engines (ADE), which have a bypass ratio significantly higher than present turbofans. The increases in bypass ratio will dictate larger diameter nacelles and an increasing importance of the nacelle aerodynamics and wing integration aerodynamics. A series of isolated wind tunnel tests was therefore designed and conducted by PWA and MTU to investigate inlet, nozzle, and reverser aerodynamics. Additional installed testing was done in cooperation with MBB and BAe. Key features of the tests are noted and significant results are discussed.

Introduction

Since the advent of the Turbofan Engine, numerous studies have been conducted by engine manufacturers to determine the "optimum" bypass ratio. The optimum is defined as the bypass ratio that demonstrates the lowest specific fuel consumption. Figure 1 shows the specific fuel consumption losses associated with an uninstalled engine relative to a current generation turbofan and how the various nacelle losses change in importance as the bypass ratio is increased. This figure demonstrates that the fan cowl drag and bypass duct pressure loss are the two loss items that become the major influencing factors forcing the optimum bypass ratio to a value less than infinity. Additional detailed information to define these losses better in the indicated optimum bypass range was necessary since relatively simplistic analytic assumptions were used to define Fig. 1.

Since little previous testing had been conducted by PWA or MTU in this BPR range, and little detailed information was available in the literature, investigations of some basic as well as more advanced nacelle designs were of interest. Nacelle geometric variations also had to be broad enough to allow significant variation in gas generator layout. A series of isolated tests were planned that investigated inlet, nozzle, and reverser designs. Installation tests were also conducted to define the interference drag characteristics.

Tests and Facilities

Isolated inlet tests were conducted in Calspan Corporation's 8 ft transonic tunnel to determine cruise and windmill (engine-out) characteristics. The same inlet hardware was also tested in the United Technology Research Center large subsonic wind tunnel 10×15 ft test section to determine inlet recovery and distortion characteristics at take off and crosswind conditions.

Isolated nozzle tests were conducted at Fluidyne Corporation to determine both thrust and flow coefficients of the fan and primary streams. Testing was first conducted in a static stand before moving into the 5.5 ft transonic tunnel.

Modifications were made to the inlet hardware to allow a series of reverse flow tests to be conducted in the large subsonic wind tunnel of DLR at Braunschweig, Germany. Both the core and fan streams were simulated with an emphasis on determining the distortion $(Pt_{local} - Pt_{average})/(Pt_{average})$ and recovery $(Pt_{average\ fan\ face})/(Pt_{free\ stream})$ characteristics of each at the reverse flow condition.

Installed flow-through nacelle tests were also conducted to determine the interference drag characteristics of the ADE nacelle/wing combination. This testing was conducted in cooperation with MBB and BAe with cruise conditions being tested using a half airplane model in the Aircraft Research Association Transonic Tunnel at Bedford. The low-speed flight

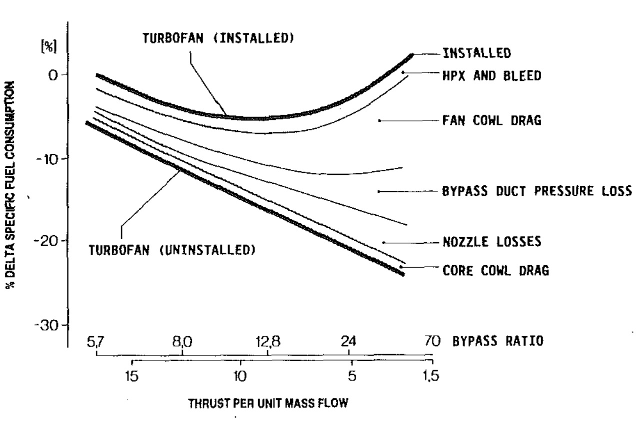

Fig. 1 SFC versus bypass ratio

Contributed by the International Gas Turbine Institute and presented at the 36th International Gas Turbine and Aeroengine Congress and Exposition, Orlando, Florida, June 3-6, 1991. Manuscript received at ASME Headquarters February 20, 1991. Paper No. 91-GT-136. Associate Technical Editor: L. A. Riekert.

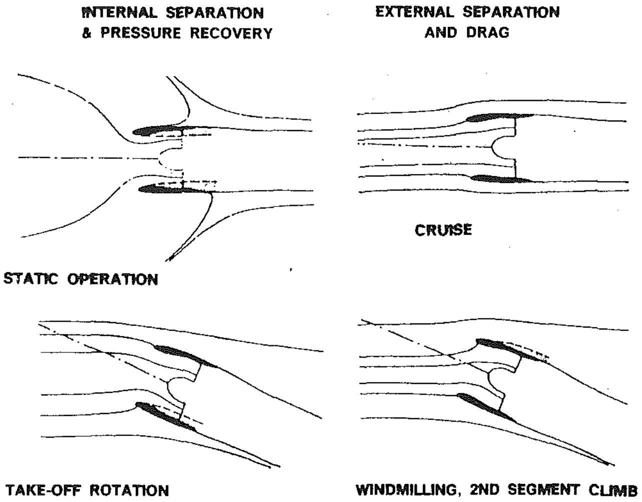

Fig. 2 Flow conditions being investigated

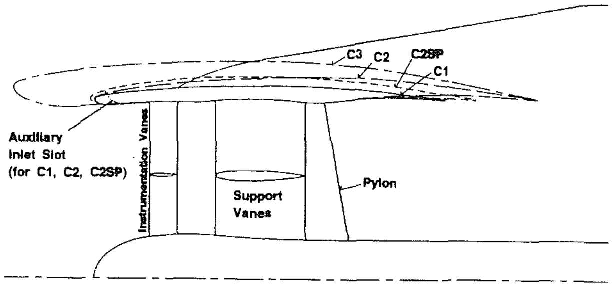

Fig. 3 Flow-through inlet configurations

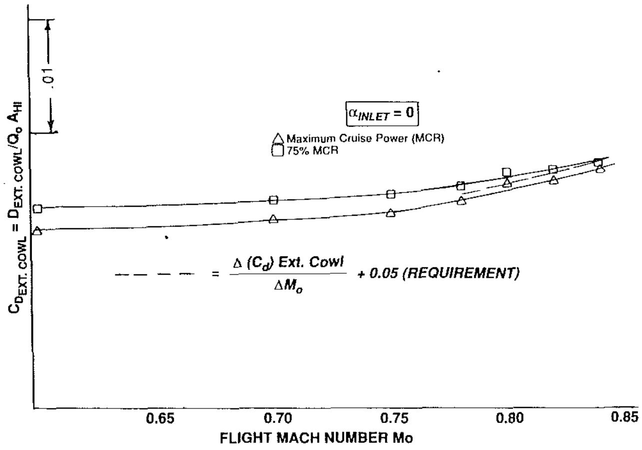

Fig. 4 Drag divergence—configuration C2SP

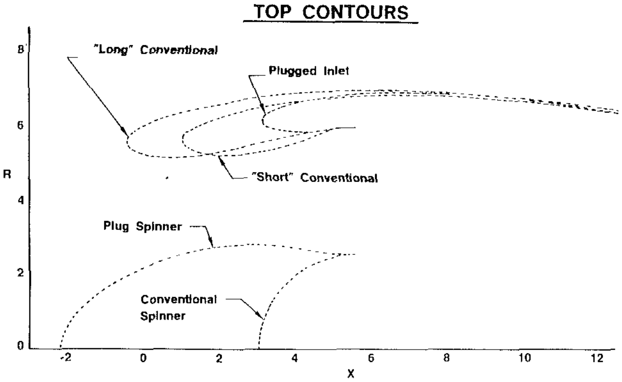

Fig. 5 Asymmetric inlets

idle and windmill interference testing was conducted with a similar model at the Messerschmitt-Bolkow-Blohm low-speed tunnel at Bremen.

Discussion

Inlet/Fan Cowl Aerodynamics. Inlet/fan cowl losses play the most important roll in optimizing the engine cycle for a minimum installed SFC (Fig. 1). In addition to the requirement for low cruise drag, the inlet/fan cowl must be contoured to maintain a low drag and/or unseparated external or internal flow at a number of off-design conditions such as engine-out windmill and takeoff rotation such as engine-out windmill and takeoff rotation (Fig. 2). The off-design conditions invariably force design changes that compromise cruise performance.

Since nacelle weight and friction drag are directly proportional to size, reducing the inlet and fan cowl boattail length will directly improve these nacelle performance related characteristics. In addition, if the nacelle maximum diameter relative to the fan tip diameter is held to a minimum (slim line nacelle) it follows that this too would benefit both nacelle weight and friction drag goals. Figure 3 shows a number of NACA 1 series slim-line designs that demonstrated good cruise performance characteristics. Figure 4 shows the drag versus Mach number characteristics for configuration C2SP at maximum and 75 percent cruise power conditions.

The off-design performance was, however, not good enough to recommend the slim-line designs as viable candidate inlets. Separation on the upper lip at engine out windmill and on the lower lip at the take-off prevented these candidates from meeting normal airplane flight envelope requirements. Figure 5 shows three advanced inlet contours that were generated using analytical techniques similar to those described by Steiner (1990).

Emphasis for these designs was placed on obtaining zero wave drag at cruise conditions while still adhering to the low flow engine-out windmill and high flow take-off airframe requirements. Each of the basic geometries were quite successful in achieving these goals and served to demonstrate the variation in the individual merits to each basic concept. Some results for these configurations are discussed later in the paper (see Figs. 9 and 11). Additional analytic and test development would of course be necessary to optimize all for any specific application.

The test technique used to obtain external cowl drag involved

Nomenclature

A = area
C_D = nacelle drag coefficient, including skin friction, pressure, and shock losses
C_L = airplane lift coefficient
D = diameter
F = thrust
H = height
L = length
M_0 = free-stream Mach number
P = pressure

Subscripts

AMB = ambient
T = total
0 = free-stream

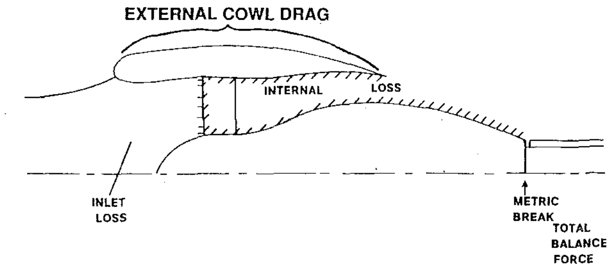

COWL DRAG = TOTAL BALANCE FORCE - INTERNAL LOSS - INLET LOSS

Fig. 6 Flow through nacelle model

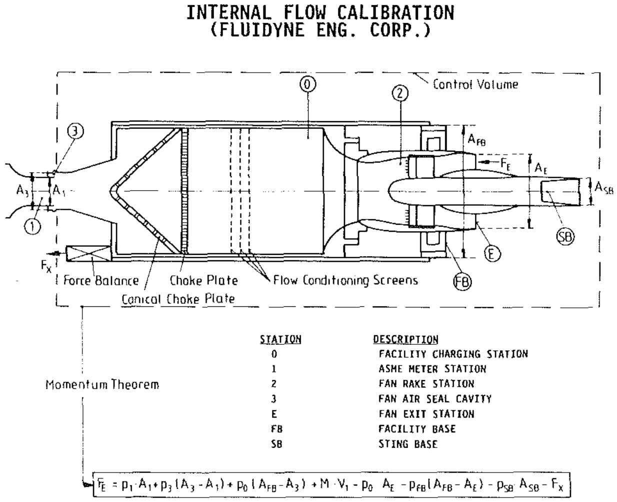

STATION	DESCRIPTION
0	FACILITY CHARGING STATION
1	ASME METER STATION
2	FAN RAKE STATION
3	FAN AIR SEAL CAVITY
E	FAN EXIT STATION
FB	FACILITY BASE
SB	STING BASE

$$\boxed{F_E = p_1 \cdot A_1 + p_3 (A_3 - A_1) + p_0 (A_{FB} - A_3) + M \cdot V_1 - p_0 \; A_E - p_{FB} (A_{FB} - A_E) - p_{SB} \cdot A_{SB} - F_x}$$

Fig. 7 Internal flow calibration (Fluidyne Engineering Corp.)

the use of flow through inlet models for which the internal loss had been previously calibrated. Figure 6 schematically describes the flow through test setup and the individual breakdown of the various forces. The internal loss was obtained by running the model statically at Fluidyne in the configuration described in Fig. 7.

The internal losses are obtained by computing the difference between the measured nacelle system thrust and the ideal system thrust based upon the flow conditions as measured at Station 2. These tests also provided the necessary inlet mass flow calibration. The inlet loss may be obtained directly from measurements made during the flow-through testing. Figure 8 is a picture of one of the flow-through models installed in the Calspan 8 ft transonic tunnel. In addition to cruise performance, engine-out (windmill) tests were also conducted at Calspan to determine the angle at which the various inlets would incur flow separation. This testing was conducted at 3 atm tunnel total pressure to simulate full-scale Reynolds number more closely and utilized static pressures and force balance measurements to determine the onset of separation. The separation characteristics of the plug inlet configuration are shown compared to a typical airplane requirement in Fig. 9.

The extra margin is a result of the higher than normal mass-flow ratio characteristic of the high bypass ratio nacelle at windmilling conditions. In an optimized design, this margin will be traded for lower cruise drag by reducing the large upper lip thickness, which had been created to improve the windmill separation characteristics. This added inlet thickness in the highlight region is necessary to offset effectively the low mass flow ratio created by the loss of engine power. Shifting the inlet streamlines effectively to increase the inlet mass flow ratio affects the same result as added lip thickness.

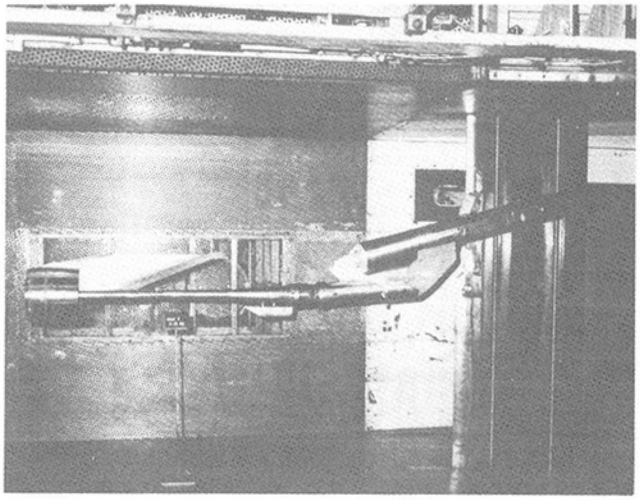

Fig. 8 Isolated inlet flow through testing at calspan

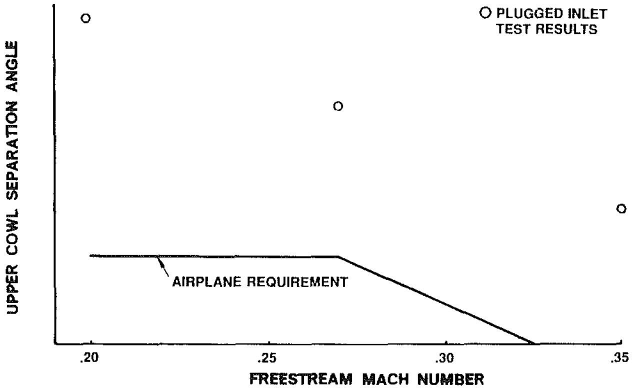

Fig. 9 Windmill separation results: airplane spec versus model results

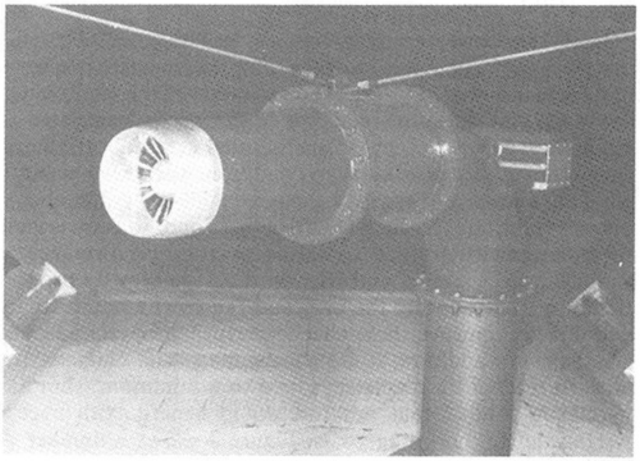

Fig. 10

The inlet models were also tested in the United Technologies Research Center large subsonic wind tunnel 10×15 ft test section to determine inlet recovery and distortion characteristics at takeoff and crosswind conditions. In this case, the model is mounted in a suck-through configuration, as may be seen in Fig. 10. The takeoff separation angle of the plugged inlet configuration is shown in Fig. 11 compared to an airplane requirement for full take-off power. In the case of the lower Mach number range where the inlet will be separated, the

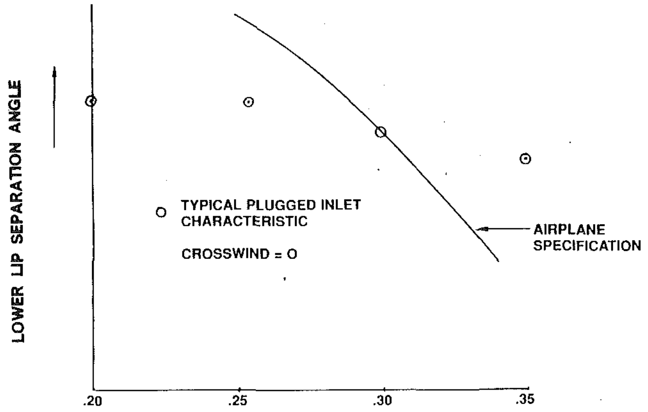

Fig. 11 Takeoff separation angle characteristics

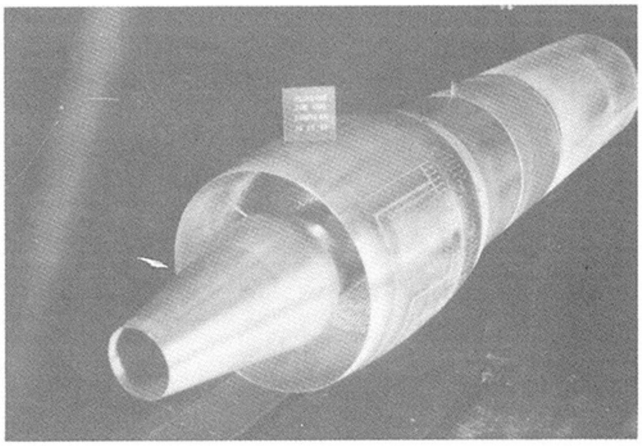

Fig. 12

engine must still be able to provide takeoff power with a flow field that could contain a significant amount of distortion. This should be an easier task with a typical ADP/CRISP engine as this bypass ratio machine is not typically thrust limited at takeoff conditions. Additional inlet development work to reduce the distortion is also a possibility. As is the case with any high-technology device today, any inherent cushion found in a specific parameter such as fan surge margin is soon traded for additional efficiency as soon as the magnitude of the margin and a trade factor are identified.

Nozzle Performance Characteristics. As was indicated by Fig. 1, fan nozzle performance also has a large impact on installation loss. A large variety of fan and primary nozzle geometries were investigated both statically and with external flow at Fluidyne. Figure 12 shows a typical nozzle configuration installed in the 5.5×5.5 ft Fluidyne Transonic tunnel.

Fan nozzle/core cowl geometric variables studied included: core cowl length/angle, core cowl shape, fan duct inner wall curvature, and engine mount/pylon variations. The range of variables tested was great enough to allow first-pass performance to be generated for front to aft mounted fans. Individual stream flow coefficients and combined thrust coefficients were generated both statically and with external flow. No configuration was typical. Figures 13 and 14 illustrate the overall thrust and fan flow coefficient characteristics of three core cowl angle/length study configurations. Some of the shorter steeper core cowl models, such as configurations 7J and 7K, had significant separation problems, as is indicated by the sudden drop in thrust coefficient. These geometries helped define the limits of good and reasonable configurations.

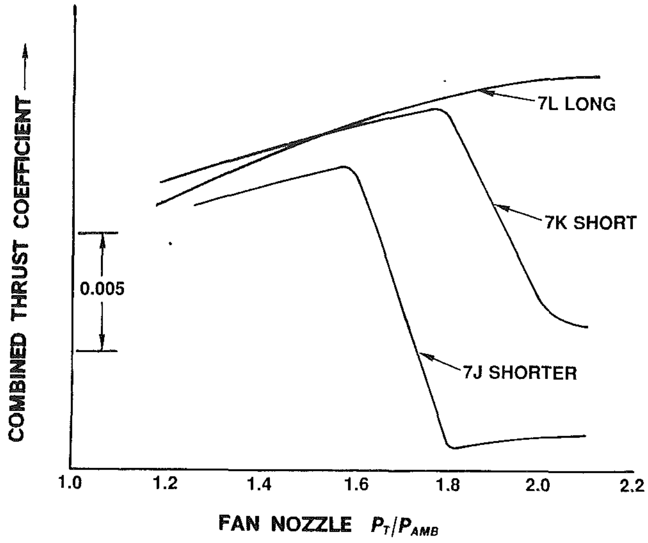

Fig. 13 Blown nozzle test; M = O; core cowl angle/length study

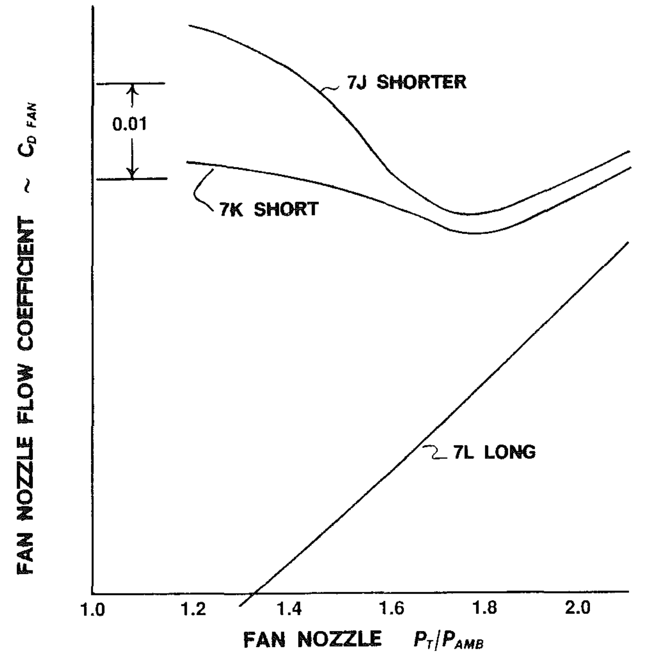

Fig. 14 ADP blown nozzle test; FEC CHN 14 M = 0; afterbody angle/length study

Reverse Thrust Performance. Assuming that advanced ducted engines may employ a variable blade pitch, which can be used to generate reverse thrust, a test was designed to sample the distortion characteristics at the entrance to the fan and low compressor in the reverse flow condition. This was done to assess better the capability of the engine to produce reverse thrust, since the degree of distortion approaching both the fan and low compressor could have significant effect on that capability. Figure 15 illustrates the basic flow separation problems associated with a counter-rotating ADE configuration that doesn't have fan exit guide vanes, while Fig. 16 illustrates the test rig and the added complexity for a single rotation ADE configuration that has fan exit guide vanes.

This test rig was run in the large subsonic wind tunnel of DLR at Braunschweig, as shown in Fig. 17. Both reversed fan and core flows were simulated by suction (see Fig. 16) with

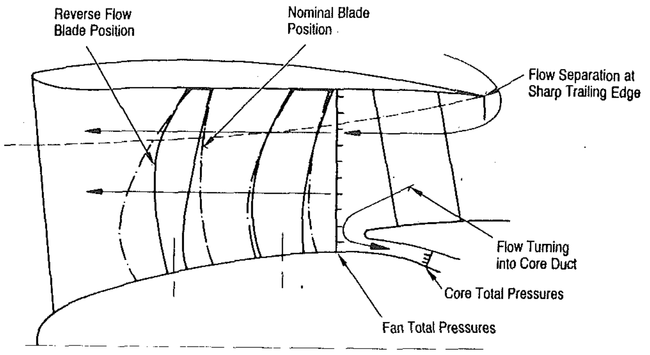

Fig. 15 Reverse flow

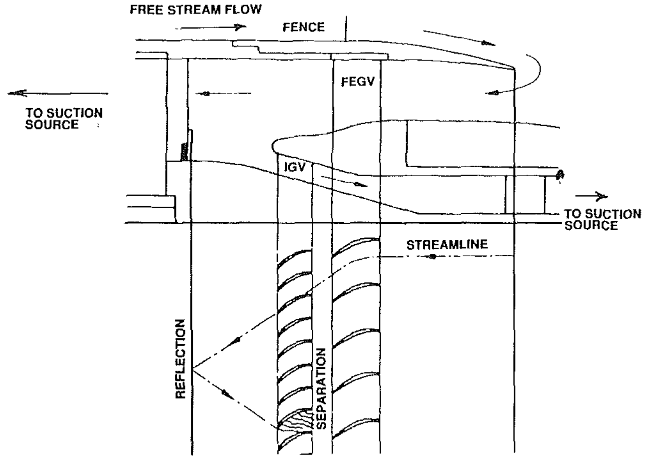

Fig. 16 Flow separation behind ADP guide vanes in reverse

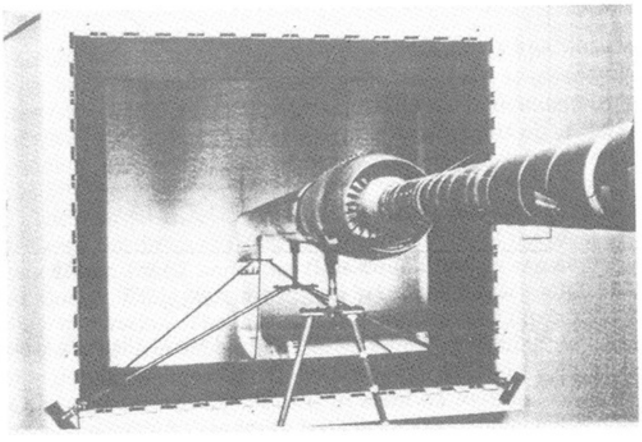

Fig. 17 ADP model with fan exit guide vanes fitted

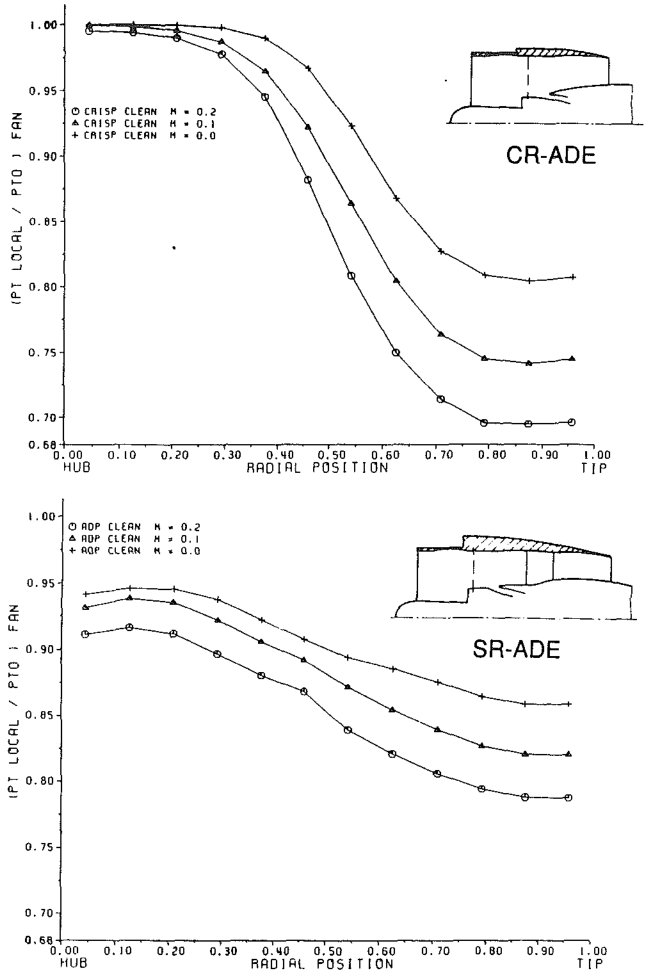

Fig. 18 Fan inlet pressure distribution for counter and single rotation ADE (typical take-off power)

numerous variations made to the fan cowl trailing edge and core entrance (such as radius of curvature, slots, etc.), to gain a better understanding of the geometry variables controlling the fan and core entrance total pressure profiles. Simulation of the large separation/reattachment zone on the inlet and fan cowl was accomplished by a fence placed near the cowl maximum diameter. A sample of the fan entrance total pressure profiles for both a counterrotation and a single rotation ADE is illustrated in Fig. 18. The difference in level of distortion is attributed to the longer fan duct length and existence of the fan exit guide vanes in the single rotation configuration. The total pressure profiles entering the core are illustrated in Fig. 19.

The difference in degree of distortion and level of recovery here is attributed to the fan exit guide van, which, in the case of the single rotation machine, causes separation to occur on the core inlet guide vanes. It should be noted that all of these profiles were generated with the normal forward flight nozzle geometries (i.e., no variations to the standard nozzle geometry were made to improve the flow entering the nozzle).

Nacelle/Wing Interference. Generally, the interference between the nacelle and aircraft causes a drag, which, for commercial aircraft, may amount to several percent of total aircraft drag. To a large extent this interference drag will be determined by nacelle diameter, distance between nacelle and wing, shape of the nacelle and pylon, as well as the flight conditions (Mach number, angle of attack, etc.). To determine this drag, wind tunnel tests were conducted with appropriate nacelle/wing-models on a scale of 1:13 in the MBB-UT low speed wind tunnel at Bremen and in the 9×8 ft ARA transonic tunnel at Bedford. For these tests a half-model of an advanced 150 seat aircraft was used in combination with through-flow nacelles simulating the ADEs.

The flow-through nacelles were first calibrated for internal losses using a suck-through system. They were then mounted on a pylon with a sting and total isolated nacelle drag determined. A fuselage and wing-alone test was also conducted prior to the fuselage, wing, pylon, and flow-through nacelle being combined. This technique allows interference drag to be obtained without any analytical calculations.

The tested configurations were different with regard to the

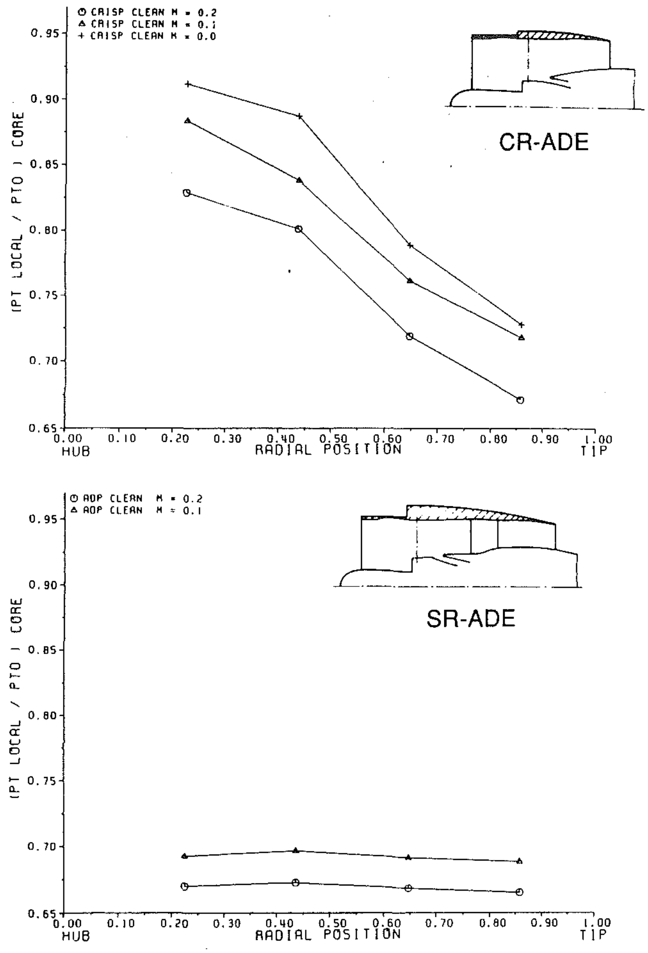

Fig. 19 Core inlet pressure distribution for counter and single rotation ADE (typical take-off power)

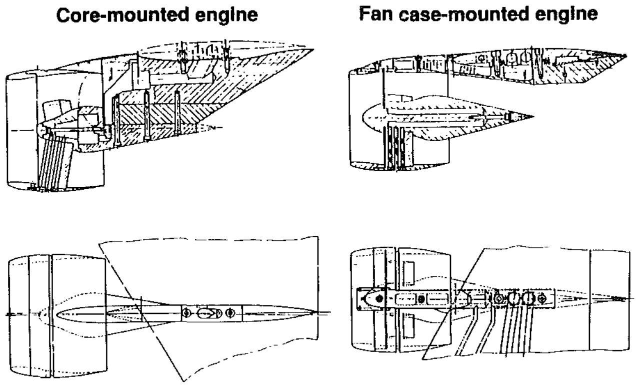

Fig. 20 Nacelle/wing models

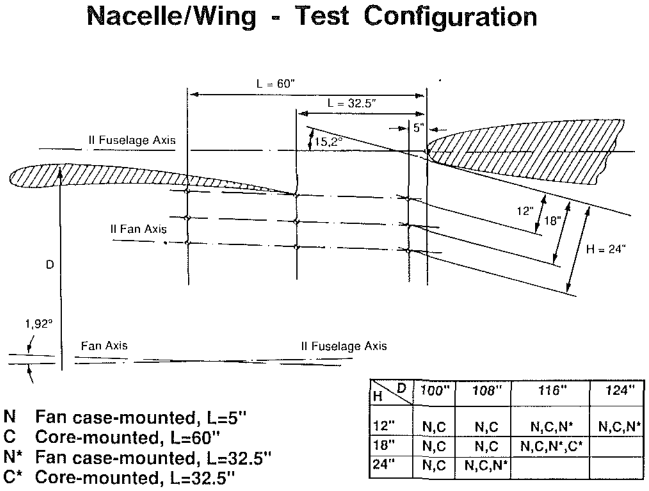

H \ D	100"	108"	116"	124"
12"	N,C	N,C	N,C,N*	N,C,N*
18"	N,C	N,C	N,C,N*,C*	
24"	N,C	N,C,N*		

Fig. 21 Nacelle/wing test configuration

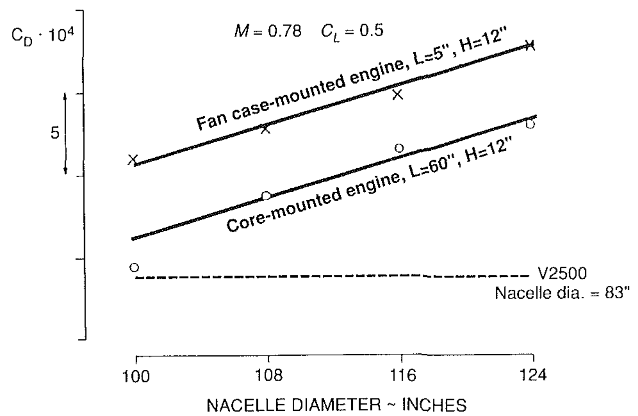

Fig. 22 Variation of installation drag with nacelle diameter

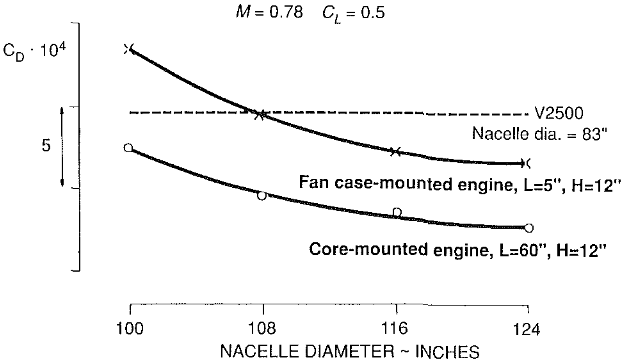

Fig. 23 Variation of interference drag with nacelle diameter

mounting (pylon) of the engine, the nacelle diameter, and the position of the nacelle relative to the wing. Figure 20 shows the two engine mountings tested in this investigation. The core-mounted configurations result in large distances between nacelle and wing. The fan case-mounted configurations allow smaller distances between nacelle and wing.

The models tested at cruise conditions are listed in Fig. 21. Tests at take-off and approach flight speeds were carried out with some of these configurations. The most important results from the high-speed tests showed that the installation drag (drag of nacelle and pylon + interference drag) of the ADE models is larger than that of a comparable advanced turbofan model denoted as V2500 (Fig. 22). The drag, however, was lower than expected because the interference drag, instead of being greater than the base turbofan, is actually less (see Fig. 23). The interference drag of the ADEs also decreases with increasing nacelle diameter (Fig. 23). This is also an unexpected result, beneficial to the ADE installation concept.

Finally, tests with the wing configured for take-off and approach flight conditions indicated that the horizontal position of the nacelle, as well as the type of pylon, have only a very slight effect on the drag polar and lift curve of the simulated aircraft. Also, at take-off conditions, the total aircraft drag will be slightly higher with ADEs than the conventional turbofan installation.

Concluding Remarks

The broad range of inlet, nozzle, reverse, and installation models tested will serve as a base of information for future test and analytical investigations. A large amount of valuable detailed information was acquired and many limits of design geometry were defined. Additional testing will have be done to develop designs for specific applications but the groundwork has been laid and prospects for satisfactory solutions to the anticipated problems associated with advanced duct engines appear good.

Acknowledgments

All test work reported on this program except for the installation testing was carried out as part of joint Pratt & Whitney and MTU IR&D efforts. The authors wish to thank Mr. R. G. Williams and J. H. Parker of British Aerospace, A. E. Harris of Aircraft Research Associates, H. W. Burgsmuller of MBB (Bremen), and Don Eiler of Pratt & Whitney for their assistance in planning and conducting the installation tests.

Reference

Steiner, A. L., 1990, "Design and Analysis of a Large Plug Inlet ADP Nacelle and Pylon," AIAA Paper No. 90-2015.

A. M. Ingraldi
NASA Langley Research Center,
Hampton, VA 23681

T. T. Kariya
Vigyan Research Associates, Inc.,
Hampton, VA 23666

R. J. Re

O. C. Pendergraft, Jr.

NASA Langley Research Center,
Hampton, VA 23681

Interference Effects of Very High Bypass Ratio Nacelle Installations on a Low-Wing Transport

A twin-engine, low-wing transport model, with a supercritical wing designed for a cruise Mach number of 0.77 and a lift coefficient of 0.55, was tested in the 16-Foot Transonic Tunnel at NASA Langley Research Center. The purpose of this test was to compare the wing/nacelle interference effects of superfans (very high bypass ratio turbofans, BPR ≈ 18) with the interference effects of advanced turbofans (BPR ≈ 6). Flow-through nacelles were used in this study. Forces and moments on the complete model were measured using a strain gage balance and extensive surface static pressure measuements (383 orifice locations) were made on the model's wing, nacelles, and pylons. Data were taken at Mach numbers from 0.50 to 0.80 and model angle-of-attack was varied from −4 to +8 deg. Results of the investigation indicate that superfan nacelles can be installed with approximately the same drag penalty as conventional turbofan nacelles.

Introduction

Current trends for commercial aircraft are toward high turbofan bypass ratios and high wing aspect ratios due to the premium placed on fuel efficiency. As a result, nacelle sizes have grown larger with respect to the wing chord. This relative nacelle growth could result in large nacelle-wing induced interference effects for low-wing transports with conventional undercarriage layouts. Additionally, the larger nacelles may need to be mounted farther outboard on the wing to reduce nacelle-fuselage flow interference.

The Propulsion Aerodynamics Branch at the NASA Langley Research Center has had an ongoing research program since the early 1980s involving problems related to the installation of twin turbofan nacelles on transport type aircraft with supercritical airfoil wings. This paper will discuss the results of a wind tunnel test during which flow-through current technology turbofans and very high bypass ratio turbofan nacelles were installed on a low-wing transport model. The discussion will be split between force data and wing pressure data. Additional force data from the investigation, as well as a more detailed description of the wind tunnel model, are given in [1].

Model and Instrumentation

The wind tunnel model, Fig. 1(*a*), is a 1/17-scale representation of a 150-passenger, twin-engine transport. It incorporates a supercritical wing designed for a lift coefficient of 0.55 at a cruise Mach number of 0.77. The wing quarter chord sweep angle is 21 deg and the wing aspect ratio is 10.795. The wing design incorporates recontoured airfoil shapes inboard of the 34 percent semispan station to counteract typical adverse interference effects due to nacelles installed at that location.

Tail surfaces are not represented on the model. Instead, a simple afterbody is used to fair into the base surrounding the model support sting. A six-component strain gage balance located on the fuselage centerline near the quarter chord of the wing mean aerodynamic chord was used to measure aerodynamic forces and moments on the model. A total of 303 wing surface static pressure orifices are located on the left wing, Fig. 1(*b*).

The wing hardware was designed to accommodate nacelle installations at two spanwise locations. The inboard location is at 34 percent of the wing semispan and the outboard location is at 40 percent of the wing semispan. Wing pressure instrumentation is most dense on the lower surface in the vicinity of the pylon/nacelle mounting locations, Fig. 1(*b*), so that local flow phenomena around the pylons and nacelles could be studied in detail. The pylon-to-wing mounts permitted setting nacelle toe-in from 0 to 3 deg and nacelle incidence relative to the fuselage centerline from −3 (nacelle tilted nose down) to +4 deg. Incidence and toe-in rotations were made about the pivot point for each nacelle (see Figs. 2–4).

Figure 2 shows a sketch of the flow-through advanced turbofan (ATF) nacelle, which represents the nacelle geometry for an engine with a bypass ratio of about 6. This configuration served as the baseline for the investigation. Figure 3 shows a sketch of one representative superfan (BPR ≈ 18) nacelle, designated SF-1 in this paper. Figure 4 shows a sketch of another representative flow-through superfan (BPR ≈ 18) nacelle designated SF-2. All three nacelle configurations incorporated approximately 20 surface static pressure orifices on the right-hand pylon and approximately 60 orifices on the right-hand fan cowls, core cowls, and centerbodies.

As can be seen in Figs. 2–4, the pylon geometries for the three nacelles have some significant differences. The pylons

---

Contributed by the International Gas Turbine Institute and presented at the 36th International Gas Turbine and Aeroengine Congress and Exposition, Orlando, Florida, June 3–6, 1991. Manuscript received at ASME Headquarters March 4, 1991. Paper No. 91-GT-241. Associate Technical Editor: L. A. Riekert.

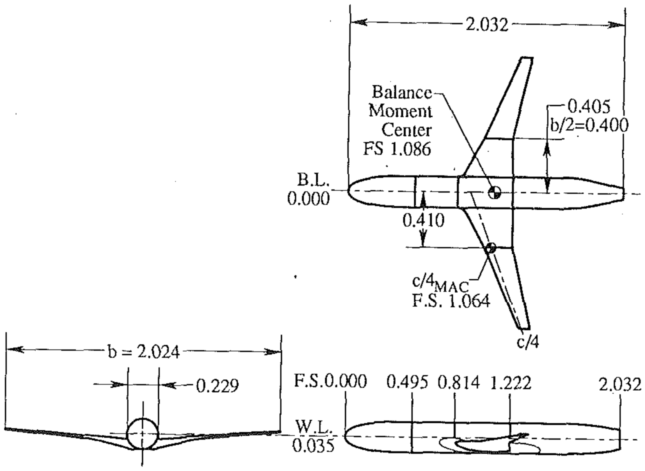

Fig. 1(*a*) Sketch of 1/17th scale low-wing transport model; dimensions shown in m.

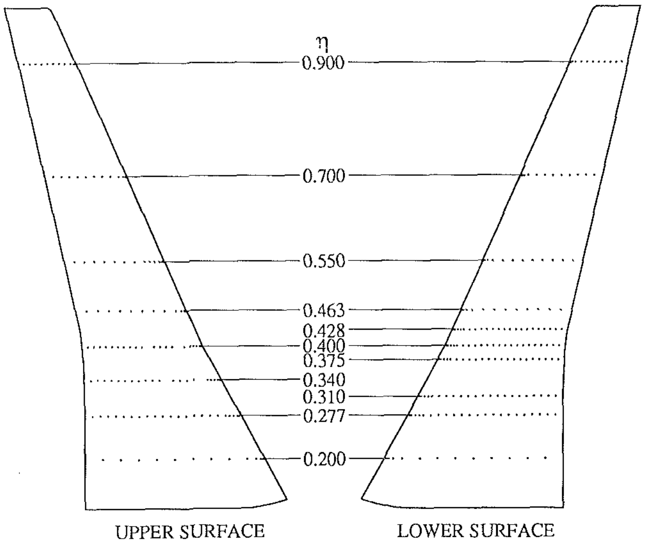

Fig. 1(*b*) Sketch of pressure orifice locations on instrumented wing

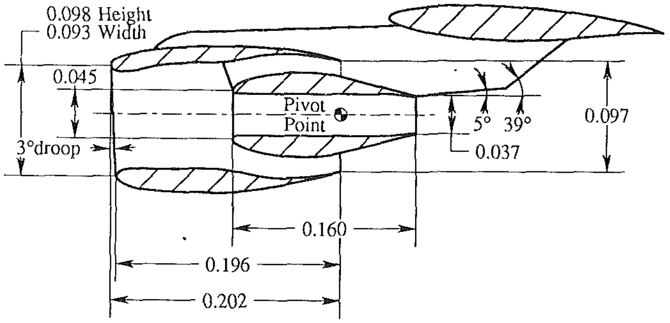

Fig. 2 Sketch of advanced technology turbofan configuration (ATF); dimensions shown in m

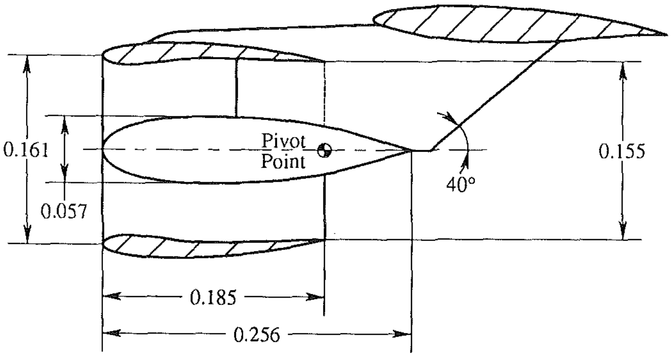

Fig. 3 Sketch of superfan configuration number 1 (SF-1); dimensions shown in m

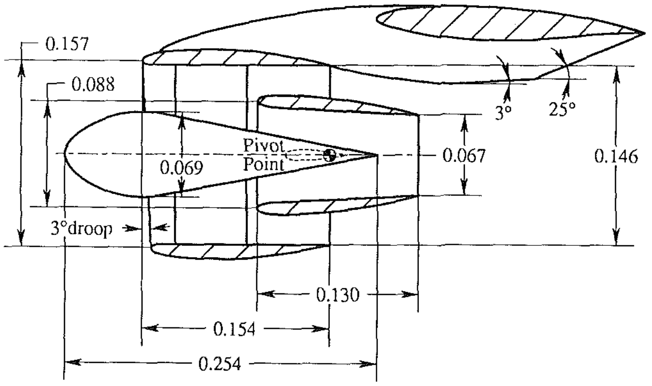

Fig. 4 Sketch of superfan configuration number 2 (SF-2); dimensions shown in m

for the ATF and SF-1 nacelles have leading edges that intersect the wing at a point on the wing lower surface and the pylons extend from the lower surface of the wing to the surface of the nacelle core or center body at the rear of the nacelle. Additionally, they have approximately the same trailing edge sweep (about 40 deg) and their trailing edges meet the wing on the lower surface at about the 75 percent chord location. The SF-2 pylon wraps over the leading edge of the wing; it follows the shape of the fan plume aft of the cowl trailing edge [2]; its trailing edge sweep is 25 deg; and it closes at the wing trailing edge. Finally, the ATF and SF-1 pylons are flat-sided while the SF-2 pylon is cambered (not shown in the figures).

Nomenclature

ATF = advanced turbofan nacelle configuration (current technology)
BPR = bypass ratio (ratio of fan mass flow to primary, or core mass flow)
B.L. = model buttline, m (distance from model centerline on planform)
c = local chord, m
C_D = drag coefficient
ΔC_D = drag increment due to nacelle/pylon installation $= (C_{D,\text{nac. on}} - C_{D,\text{nac. off}})$
C_L = lift coefficient
C_p = static pressure coefficient
F.S. = fuselage station, m
I_{nac} = nacelle incidence relative to fuselage centerline in pitch, deg (positive for nacelle nose up)
LE = leading edge
M_∞ = free-stream Mach number
MAC = mean aerodynamic chord, m
Re = Reynolds number based on mean aerodynamic chord
SF-1 = superfan (very high bypass ratio) configuration 1
SF-2 = superfan (very high bypass ratio) configuration 2
Toe-in = nacelle angle relative to fuselage centerline in yaw, deg (positive for nacelle nose toward fuselage)
x = distance along wing chord, m
η = fraction of wing semispan

Wind Tunnel and Tests

The Langley 16-Foot Transonic Tunnel is an atmospheric, single-return tunnel with continuous air exchange capable of operation at Mach numbers from 0.2 to 1.30. Mach number for the current test was varied from 0.50 to 0.80 and angle of attack was varied from -4 deg up to a maximum $+8$ deg depending on balance load limits and maximum lift coefficient desired. Mach number was varied in increments of 0.01 near the design cruise point ($M_\infty = 0.77$), and angle of attack was varied in 0.25 deg increments around the design cruise lift point ($C_L = 0.55$). Boundary layer transition on the model was fixed on all but the wing surfaces with the grit transition-strip procedure of [3]. Photographic images of fluorescent oil flow showing natural transition from laminar to turbulent flow were used to position the grit transition strips on the upper and lower wing surfaces in order to obtain transition as far aft as possible and still fix it in one location for all test conditions. Reynolds number based on the mean aerodynamic chord of the wing varied from 2.0×10^6 to 2.7×10^6 depending on Mach number and free-stream temperature. The ATF nacelle was tested at both the 34 percent and the 40 percent semispan locations. The SF-1 and SF-2 nacelles were tested only at the 40 percent location.

Axial force was corrected for the base pressures acting on the sting cavity at the base of the fuselage and angle of attack of the model was corrected for tunnel upflow angle. These standard correction procedures are given in [4]. The drag data were corrected for the internal drag of the nacelles, which was computed based on measured internal nacelle static pressures and external core cowl or center body static pressures [5]. The internal drag correction method of [5] was developed for single-flow nacelles. However, this method has also been applied to separate flow nacelles, as reported in [6].

Results

Figures 5–8 present drag polar data for the optimum incidence and toe-in angles for each configuration. These settings for a given configuration were determined by comparing drag polars for all incidence and toe angles tested and selecting the settings that resulted in the lowest drag at $M_\infty = 0.77$ and $C_L = 0.55$. Preliminary flow-field analysis using three-dimensional panel methods indicated that a toe-in angle of about 1

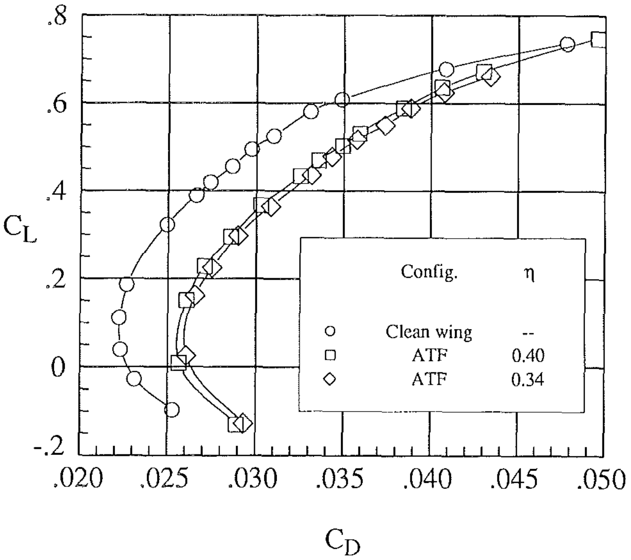

Fig. 5 Effect of ATF nacelle installed at two locations ($M_\infty = 0.77$, $Re = 2.6 \times 10^6$)

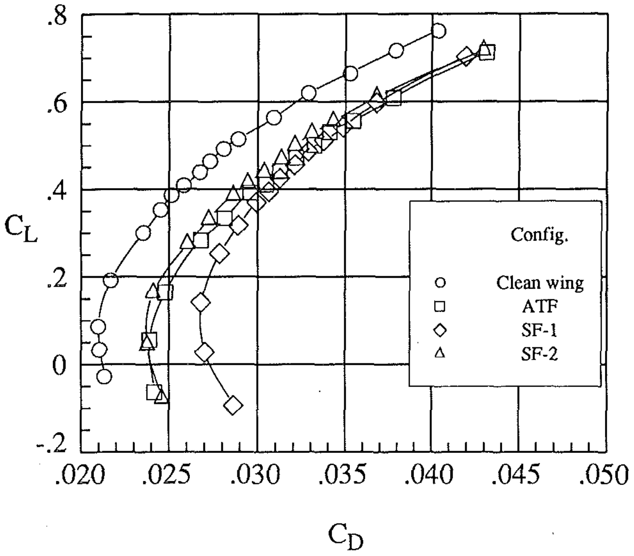

Fig. 6 Effect of nacelles installed at $\eta = 0.40$ ($M_\infty = 0.50$, $Re = 2.1 \times 10^6$)

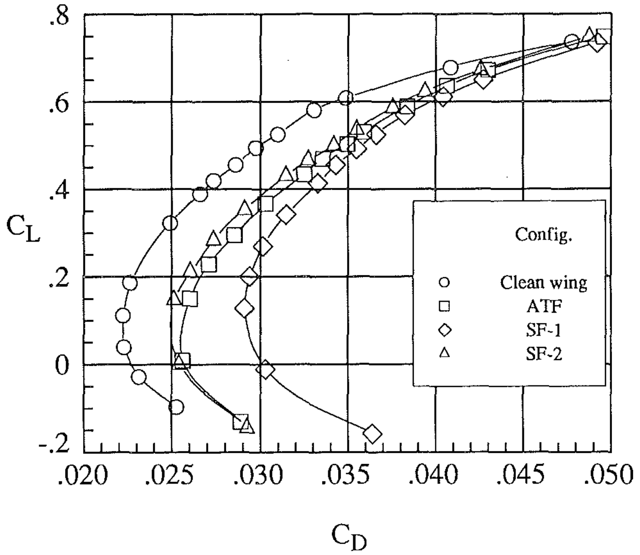

Fig. 7 Effect of nacelles installed at $\eta = 0.40$ ($M_\infty = 0.77$, $Re = 2.6 \times 10^6$)

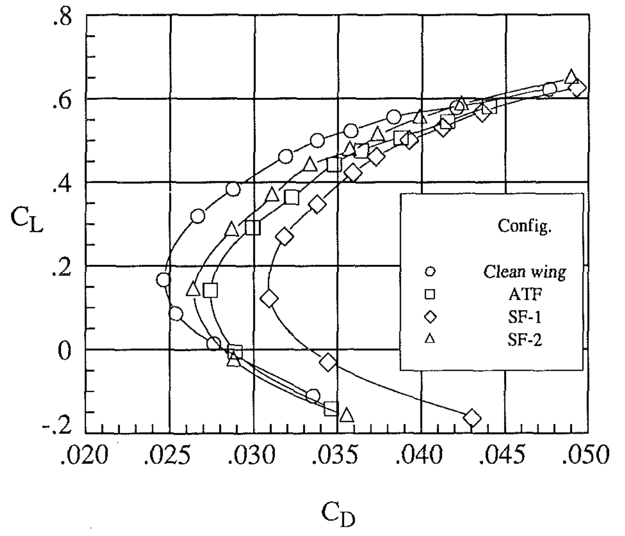

Fig. 8 Effect of nacelles installed at $\eta = 0.40$ ($M_\infty = 0.80$, $Re = 2.6 \times 10^6$)

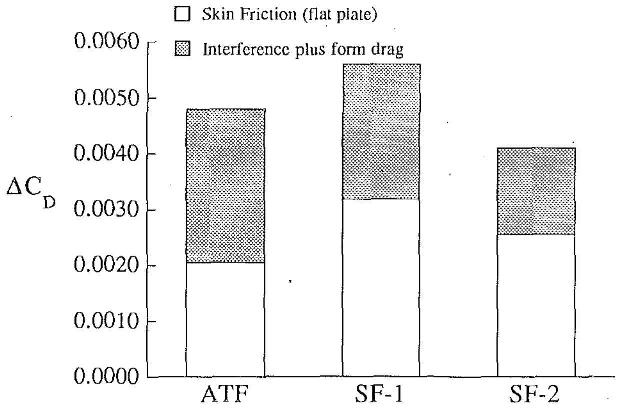

Fig. 9 Pylon/nacelle interference and skin friction drag with nacelles installed at $\eta = 0.40$ ($M_\infty = 0.77$, $Re = 2.6 \times 10^6$, $C_L = 0.55$)

deg is needed for optimum performance. Test results are in agreement with this prediction for all nacelle configurations. The experimentally determined optimum incidence angles are −3.0 and +3.0 deg for the SF-1 and SF-2 nacelles, respectively. The negative sign on the SF-1 nacelle incidence angle occurs because the inlet is not dropped on that nacelle configuration (compare Figs. 3 and 4). The optimum incidence angle for the ATF nacelle installed at the 34 percent semispan location was +3 deg while at the 40 percent semispan location the ATF nacelle had lowest drag when the incidence angle was +4 deg.

Figure 5 shows a comparison of the drag polars for the clean wing (nacelle and pylon removed) and with the ATF nacelle installed at both semispan locations for the design cruise Mach number (note: symbol sizes are not indicative of the measurement resolution). The installation of the ATF nacelle at the 40 percent semispan location resulted in lower drag than the 34 percent semispan installation even though the wing undersurface was tailored for nacelle installation at the 34 percent semispan location. This is typical of results obtained over the Mach range tested and is possibly due to stronger nacelle-pylon-fuselage interactions at the inboard location ($\eta = 0.34$). The remainder of the discussion compares data with the ATF nacelle at the 40 percent semispan location with the superfan nacelles at the same location.

Figures 6, 7, and 8 show drag polar comparisons for Mach 0.50, 0.77, and 0.80, respectively. Over the entire Mach range tested, the SF-2 nacelle installation exhibited the lowest drag at the cruise lift coefficient as well as over the majority of the lift range explored. This is an encouraging but unexpected result since the SF-2 nacelle is much larger than the ATF nacelle, which would lead one to expect more interference. Much of the improved performance with the SF-2 nacelle must be attributed to its pylon geometry. Unfortunately, there are several differences between the SF-2 and ATF pylons, thus making it difficult to determine which change produced the beneficial drag performance. The SF-1 nacelle installation had the highest drag of the configurations tested. Comparison of the SF-1 and the ATF nacelle installations isolates the effect of the increased nacelle size since the ATF and SF-1 pylon geometries are as close as their respective nacelles allow.

Figure 9 shows a comparison of the installation drag increments at the design cruise point for the three nacelle configurations tested. While the total drag increment with the SF-1 nacelle was greater than that with the ATF nacelle, Fig. 9 indicates that the interference drag for SF-1 installation was in fact lower than the interference drag with the ATF installation and the increased total drag increment results from higher skin friction drag. This is probably due to the close coupling of the wing lower surface with the core cowl of the ATF nacelle. As can be seen in Figs. 2-4, the ATF nacelle core is closer to the wing undersurface than the SF-1 nacelle centerbody or the SF-2 nacelle core cowl. The SF-2 nacelle installation produced the lowest total drag increment and the lowest interference drag.

The remaining figures (Figs. 10-16) show surface static pressures on the wing for the three different nacelle installations. These data are taken from the test points that most closely matched the design lift coefficient. Table 1 shows the actual lift coefficient for the test points presented in the Figs. 10-16. Although the pressure data are not taken from precisely the same lift conditions for all configurations, one can still compare the wing lower surface pressure distributions, since the lower surface pressure fields were found to be fairly insensitive to small increments in C_L at a given Mach number.

Figure 10 shows comparisons of wing lower surface pressure coefficients at $M_\infty = 0.5$ for the two pressure orifice rows

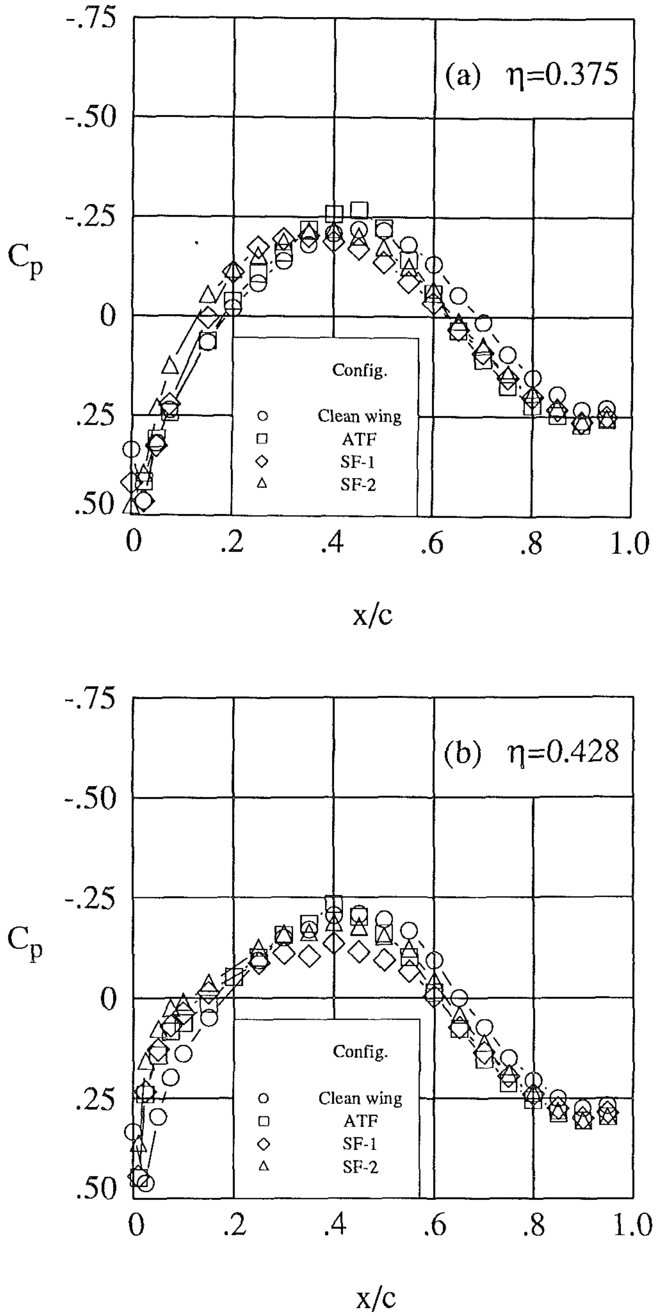

Fig. 10 Lower surface pressure coefficients for the clean wing and with nacelles installed at $\eta = 0.40$ ($M_\infty = 0.50$, $Re = 2.1 \times 10^6$, $C_L \approx 0.55$)

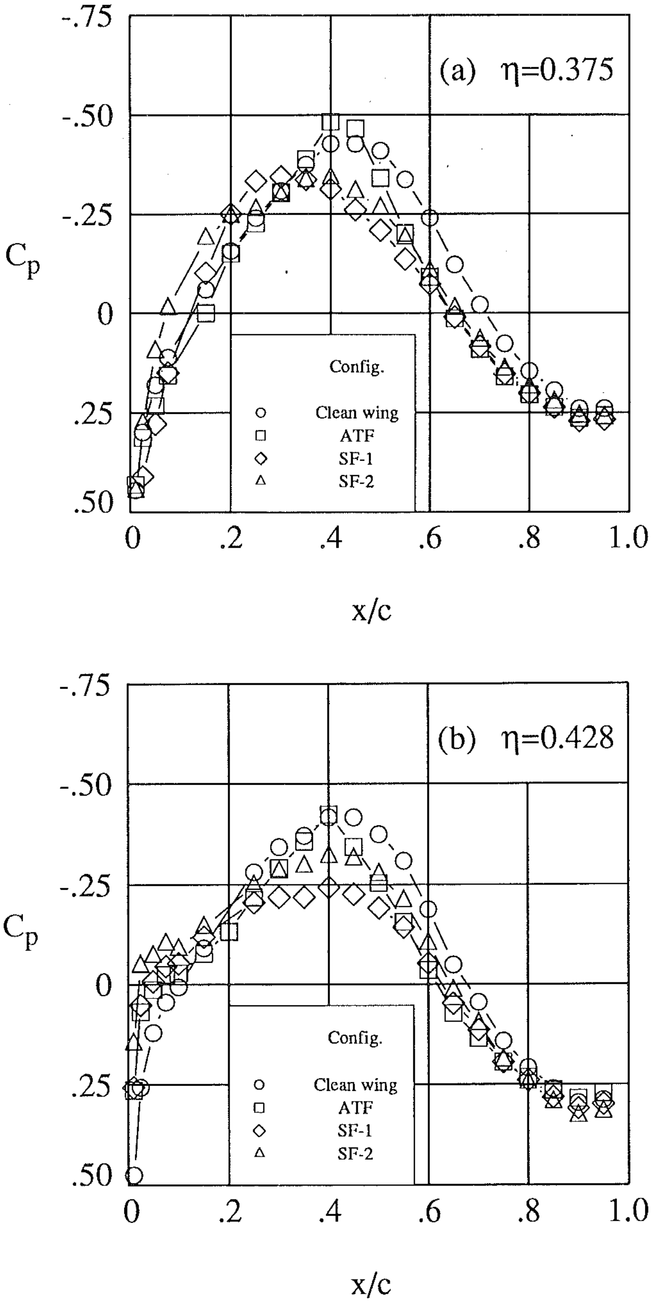

Fig. 11 Lower surface pressure coefficients for the clean wing and with nacelles installed at $\eta = 0.40$ ($M_\infty = 0.77$, Re $= 2.6 \times 10^6$, $C_L \approx 0.55$)

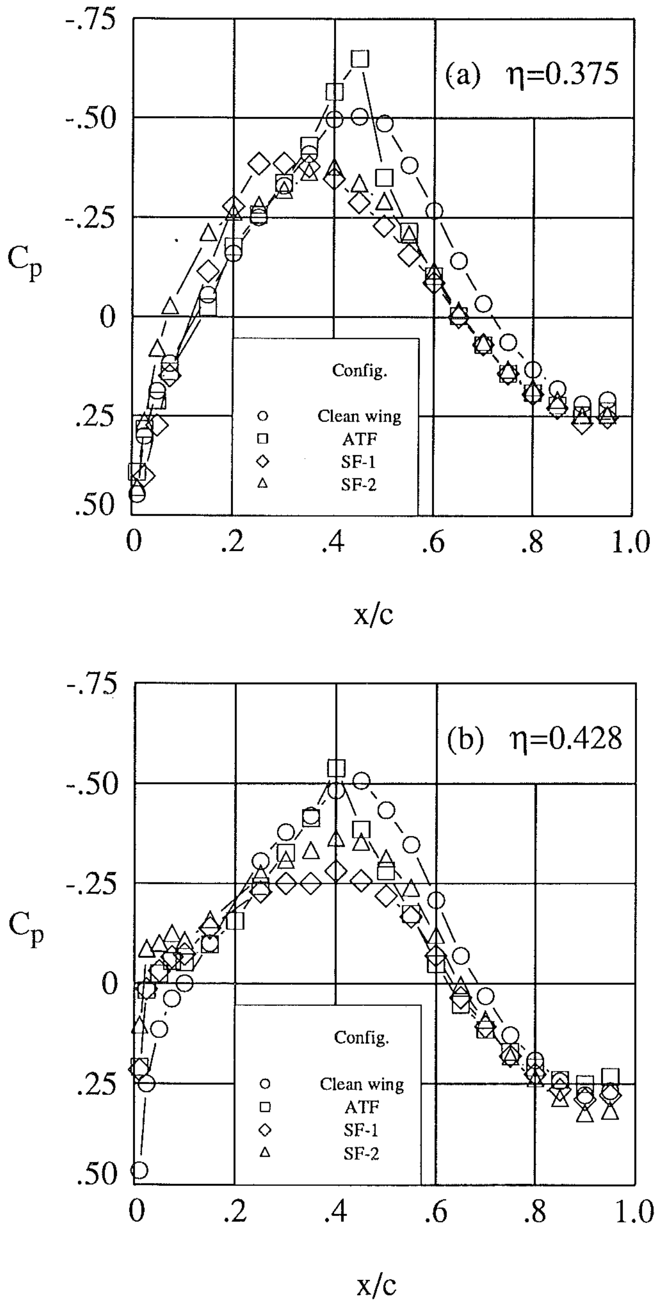

Fig. 12 Lower surface pressure coefficients for the clean wing and with nacelles installed at $\eta = 0.40$ ($M_\infty = 0.80$, Re $= 2.6 \times 10^6$, $C_L \approx 0.55$)

closest to 40 percent semispan nacelle installation location. At this Mach number, there appears to be little difference in wing pressure distributions between the three nacelle installations. Figure 11 presents the C_p plots for the same orifice rows at $M_\infty = 0.77$. There are some noticeable differences between the nacelle installations at the cruise Mach number. Figure 11(*a*) shows that the ATF installation induced higher peak velocities on the wing inboard of the pylon than either the SF-1 or SF-2 nacelles, but still not much higher than those for the clean wing configuration. Euler calculations have indicated that the inboard wing/pylon junction region typically has the worst interference effects from nacelle installation [7]. Figure 11(*b*) shows that the SF-1 nacelle had a larger compression effect on the wing outboard of the pylon than the other nacelles. Figure 12 presents the wing lower surface C_p comparisons for Mach 0.8. The ATF nacelle installation shows a sharp peak in the C_p curve at about the midchord location, particularly on the inboard side ($\eta = 0.375$). The critical C_p at Mach 0.8 is -0.44, and supersonic flow exists on the wing lower surface (inboard and outboard of the pylon) for both the clean wing and ATF configurations. For the ATF nacelle installation, there appears to be a wing lower surface shock on the inboard side of the pylon. This supports the idea that the ATF nacelle had higher interference drag due to core-cowl/wing flow interactions. The SF-1 and SF-2 nacelles both had a compressive effect on the wing's local flow at Mach 0.8.

Figures 13–16 present contour plots of the wing pressure coefficients at Mach 0.77. The upper surface plots cannot be compared quantitatively due to the sensitivity of upper surface pressures to lift coefficient, but they do present a qualitative picture of the nacelle installation effects on the wing upper surface flowfield. Figure 13 shows the wing upper and lower

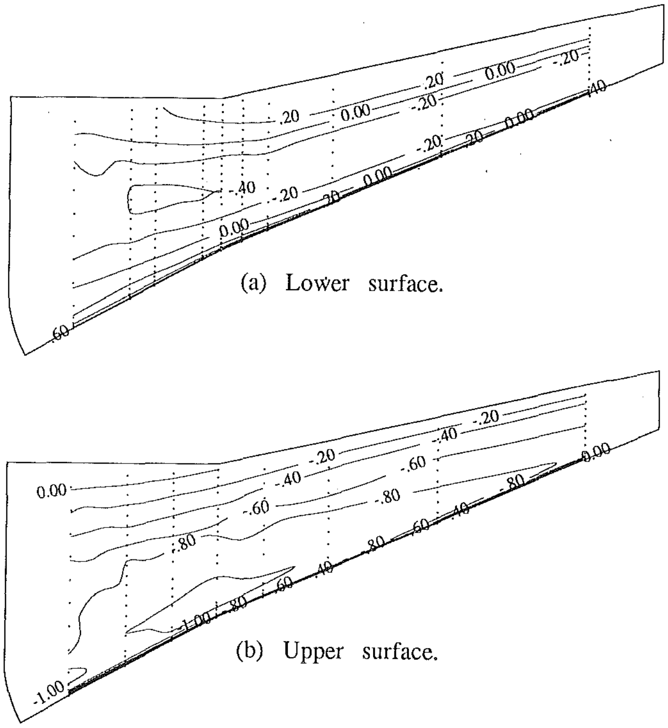
(a) Lower surface.

(b) Upper surface.

Fig. 13 Pressure coefficient contours for the clean wing ($M_\infty = 0.77$, $Re = 2.6 \times 10^6$, $C_L = 0.527$)

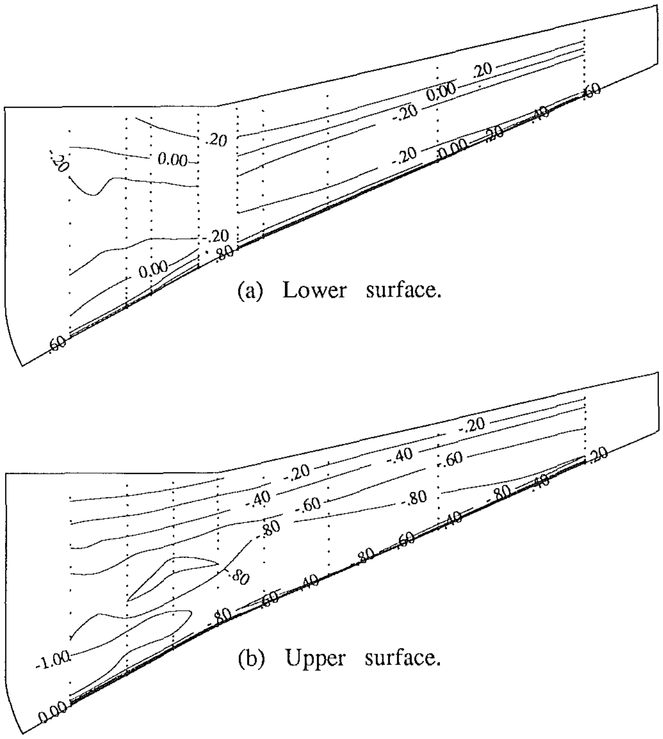
(a) Lower surface.

(b) Upper surface.

Fig. 15 Pressure coefficient contours with the SF-1 nacelle installed at $\eta = 0.40$ ($M_\infty = 0.77$, $Re = 2.6 \times 10^6$, $C_L = 0.527$)

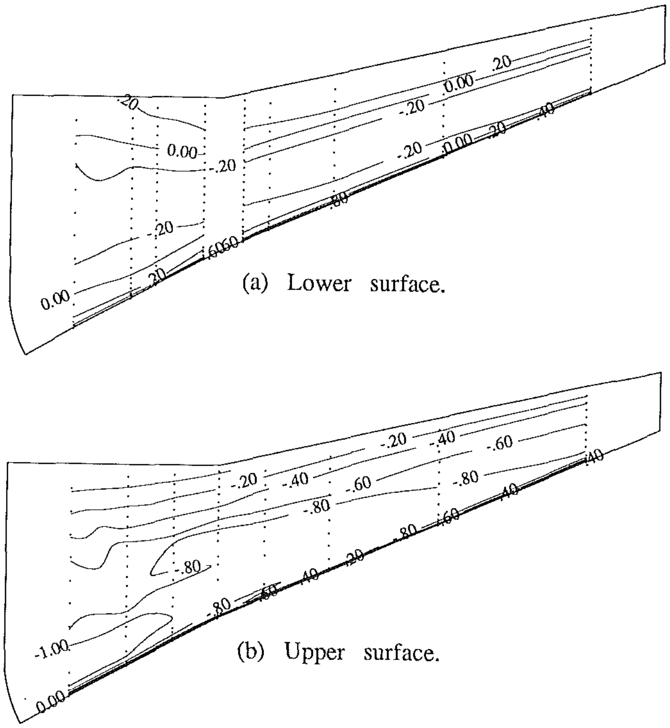
(a) Lower surface.

(b) Upper surface.

Fig. 14 Pressure coefficient contours with the ATF nacelle installed at $\eta = 0.40$ ($M_\infty = 0.77$, $Re = 2.6 \times 10^6$, $C_L = 0.545$)

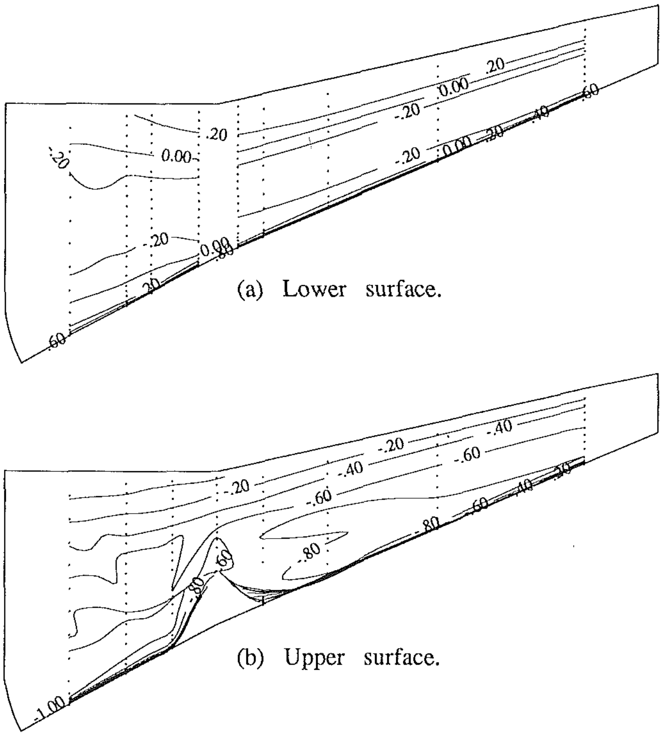
(a) Lower surface.

(b) Upper surface.

Fig. 16 Pressure coefficient contours with the SF-2 nacelle installed at $\eta = 0.40$ ($M_\infty = 0.77$, $Re = 2.6 \times 10^6$, $C_L = 0539$)

surface pressure coefficient contours for the clean wing. Figure 13(*b*) illustrates the supercritical nature of the wing design in that supercritical flow extends far back on the upper surface ($C_{p_{\text{critical}}}$ at Mach 0.77 is -0.53). Figure 14(*a*) shows that the lower surface flowfield with the ATF nacelle installation was very similar to the clean wing flowfield. Figures 15(*a*) and 16(*a*) indicate that both superfan nacelle designs had compressive effects over a fairly large region of the wing lower surface. Figures 13(*b*), 14(*b*), and 15(*b*) indicate only small differences between the upper surface flowfields with ATF and SF-1 nacelles installed and the clean wing. This is because the leading edge of the pylons for these nacelles intersected the wing on the lower surface (i.e., below the wing leading edge). Figure 16(*b*) shows the wing upper surface flow with the SF-2 nacelle installed. The large effect of the pylon wrapping over the wing leading edge is apparent.

Table 1 Data points closest to the cruise lift coefficient; nacelle data shown for $\eta = 0.40$

Configuration	Mach	C_L
Clean Wing	0.50	0.564
	0.77	0.527
	0.80	0.556
with ATF	0.50	0.557
	0.77	0.545
	0.80	0.545
with SF-1	0.50	0.544
	0.77	0.527
	0.80	0.532
with SF-2	0.50	0.556
	0.77	0.539
	0.80	0.554

Conclusion

The results of a wind tunnel test using flow-through nacelles indicate that the current trend toward increased turbofan bypass ratios does not present an insurmountable nacelle flow interference problem. Two superfan nacelle installations were compared with a conventional turbofan nacelle installation during the investigation. The test results show that a nacelle for a large diameter turbofan with a bypass ratio of about 18 (a superfan) can be installed on a low-wing transport and compare favorably, from an aerodynamic standpoint, with a nacelle installation for a current technology engine with a bypass ratio of about 6. Results also indicate that pylon shaping plays a significant role in the overall aerodynamic performance of a nacelle installation.

References

1 Pendergraft, O. C., et al., "Nacelle/Pylon Interference Study on a 1/17th Scale, Twin-Engine, Low-Wing Transport Model," Paper No. AIAA-89-2480, 1989.

2 Steiner, A. L., "Design and Analysis of a Large-Plug Inlet ADP Nacelle and Pylon," AIAA Paper No. 90-2015, 1990.

3 Braslow, A. L., Hicks, R. M., and Harris, R. V., Jr., "Use of Grit-Type Boundary-Layer-Transition Trips on Wind Tunnel Models," NASA TN D-3579, 1966.

4 Mercer, C. E., et al., "Computations for the 16-Foot Transonic Tunnel," NASA TM-86319, 1987.

5 Putnam, L. E., "Effects of Upper-Surface Nacelles of Longitudinal Aerodynamic Characteristics of High-Wing Transport Configuration," NASA TP-2579, 1986.

6 Lamb, M., and Abeyounis, W. K., "Integration Effects of Underwing Forward- and Rearward-Mounted Separate-Flow, Flow-Through Nacelles on a High-Wing Transport," NASA TM-87627, 1986.

7 Naik, D. A., et al., "Euler Analysis of Turbofan/Superfan Integration for a Transport Aircraft," AGARD Symposium on Engine-Airframe Integration, Fort Worth, TX, Oct. 1991.

J. M. Seiner

J. C. Manning

F. J. Capone

O. C. Pendergraft, Jr.

NASA Langley Research Center,
Hampton, VA 23665

Study of External Dynamic Flap Loads on a 6 Percent B-1B Model

The origin of dynamic pressure loads on external divergent engine nozzle flaps of the B-1B aircraft was investigated in the NASA/LaRC 16-ft transonic tunnel using a 6 percent full-span model with powered engine nacelles. External flap dynamic loads and afterbody drag associated with flap removal were measured using this model. Both dry and maximum A/B power nozzles were evaluated in this study. As a result of this study, the principle mechanisms responsible for high dynamic external flap loads were determined along with performance penalty associated with flap removal.

Introduction

The B-1B, a four-engine aircraft with two twin engine nacelles, has experienced excessive dynamic loads on its external engine nozzle flaps, leading to premature failure rates of the flap attachment system. The present study was initiated to determine the origins of these high dynamic pressure loads and to evaluate the performance penalty associated with removal of the external nozzle flaps. A 6 percent full-span model of the B-1B aircraft with powered engine nacelles was mounted in the NASA/LaRC 16-ft. Transonic Wind Tunnel to determine the effect of flight on the dynamic loads. Several methods for suppression of the dynamic loads were also investigated. This paper presents the major findings associated with this model scale aeroacoustic study of the B-1B aircraft aft-end dynamic loads. This work was part of a joint wind tunnel and full-scale flight investigation of dynamic outer nozzle flap loads conducted with Rockwell International and the USAF in the fall of 1987.

In a previous investigation of this model Berndt (1984) found that the spatial region of the highest dynamic pressures on the twin jet nacelles matched that of the area where structural damage occurred in full scale. This area was found to be primarily associated with the internozzle region of the twin jet nacelle. Narrow band surface pressure spectra in this region contained high-amplitude discrete peaks, whose amplitude could be minimized by installation of a fencelike device between the two nozzles. The origin of these fluctuations was not uncovered in Berndt's study.

As a result of Berndt's work, Seiner et al. (1988) investigated the dynamic pressure environment associated with the operation of a choked tube twin jet nacelle operating at static conditions (i.e., $M_\infty = 0$). This study revealed the presence of high-amplitude discrete dynamic pressure peaks in the internozzle region. The investigation showed that these discrete peaks were produced by shock noise processes associated with the interaction of turbulence and shock waves in the supersonic plumes. This study also revealed that, as a consequence of the nacelle's close jet centerline spacing (i.e., approximately 1.9 dry power nozzle diameters), the twin jet plumes would dynamically couple to produce intense pressure waves in the internozzle region, similar to those found previously by Berndt.

Further investigations of the twin jet supersonic plume resonance phenomenon were conducted by Wlezien (1987) and Shaw (1989), who investigated the effects of initial jet spacing on plume coupling. Both investigators found that, even with initial jet spacings of seven nozzle diameters, weak coupling of each plume's pressure field was still evident. Their results also indicated that the preferred spatial mode of plume oscillation was dependent on nozzle spacing. Using the F-15 aircraft at NASA/Dryden, Seiner et al. (1987) also reported evidence of twin plume supersonic resonance in full scale.

More recently Seiner et al. (1990) were able to show from a NASA/LaRC 16-ft Wind Tunnel aeroacoustic study of a model F-15 S/MTD (Short Take-Off and Landing Maneuver Technology Demonstrator) that nozzle external flap dynamic pressures were produced by two major mechanisms. At low flight Mach numbers, typically below Mach 0.5, flap dynamic pressures were dominated by the supersonic plume resonance phenomenon. At higher flight Mach numbers, the flap dynamic pressures were dominated by large-scale vorticity shed from the aircraft forebody. This result was found to be configuration dependent. When the model was fitted with twin STOL rectangular nozzles, shock noise processes dominated the surface dynamic pressure spectra to a flight Mach number of 0.72. When round nozzles were installed in the model, shock noise dominated flap dynamic pressures to a flight Mach number of 0.5.

In the present study, surface dynamic pressures of the B-1B model were obtained for a wide range of operating conditions to determine the relative importance of the two fundamental source mechanisms for dynamic flap loads. The twin nozzles of the right engine nacelle were instrumented with flush-mounted dynamic pressure sensors; both dry and maximum *A/B* (maximum afterburner) nozzles were evaluated. The left nacelle was tested with dry power nozzles with and without flaps. This nacelle contained a three-component balance to

---

Contributed by the International Gas Turbine Institute and presented at the 36th International Gas Turbine and Aeroengine Congress and Exposition, Orlando, Florida, June 3–6, 1991. Manuscript received at ASME Headquarters March 4, 1991. Paper No. 91-GT-236. Associate Technical Editor: L. A. Riekert.

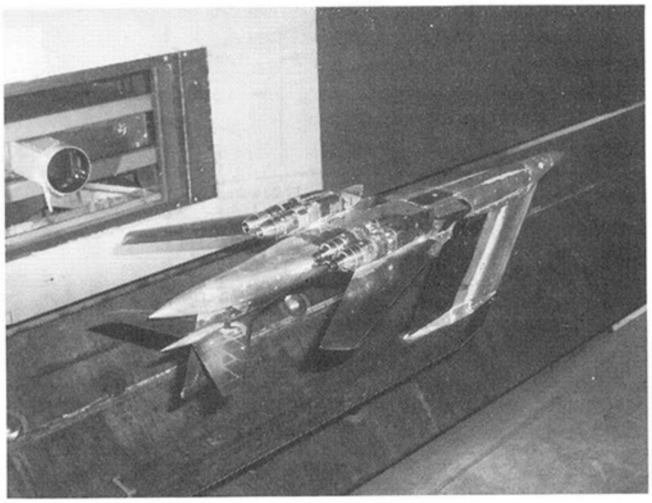

Fig. 1 Full-span 6 percent scale model in the 16-ft Transonic Tunnel

enable assessment of afterbody drag with and without external nozzle flaps.

A comprehensive database was established covering flight Mach numbers from 0 to 1.2 with nozzle pressure ratios ranging from 1 to 5. The effect of aircraft angle of attack was also investigated with alpha sweeps ranging from $\alpha=0$ deg to 6 deg. The model was studied using a fixed swept wing angle of 67.5 deg. Flow visualization using a tracer dye was obtained using a powered 1/72 scale model in the NASA/LaRC 16×24 in. Water Tunnel. These flow measurements were used to assist in determination of the origin of large-scale vorticity shed from upstream forebody locations. To enable the investigation of the suppression potential of tabs, notches, and tube jets, the right hand nacelle was installed in the NASA/LaRC Jet Noise Laboratory (JNL) and tested with plume total temperatures to 250°F. The results showed dependence of supersonic plume resonance on jet temperature. A 4.2 percent twin jet nacelle was thus constructed to test jet total temperatures to 800°F.

Experimental Configurations

Wind Tunnel and Model. The 6 percent B-1B full-span model was mounted inverted by a sting-strut system in the Langley 16-ft Transonic Wind Tunnel. This wind tunnel is a single return, continuous flow, atmospheric wind tunnel with continuous air exchange. The test section Mach number, M_j, is continuously variable from 0.2 to 1.3. High-pressure air, used to power the model, is routed through the support system along with all necessary instrumentation. The tunnel and support system are more fully described by Peddrew (1981).

The model is shown mounted inverted in the tunnel in Fig. 1 with external flaps removed from the nozzles in the left-hand nacelle and with instrumented nozzles in the right-hand nacelle. Figure 2 shows schematically the differences in nozzle contour for the three basic nozzles tested. Figure 2 also shows the method used to simulate flap removal from the dry power nozzles. The table lists both internal and external nozzle coordinates for the three basic nozzles. In the table, the distance X is the axial distance from the nozzle exit plane. Based on these coordinates, dry and maximum power nozzles are de-

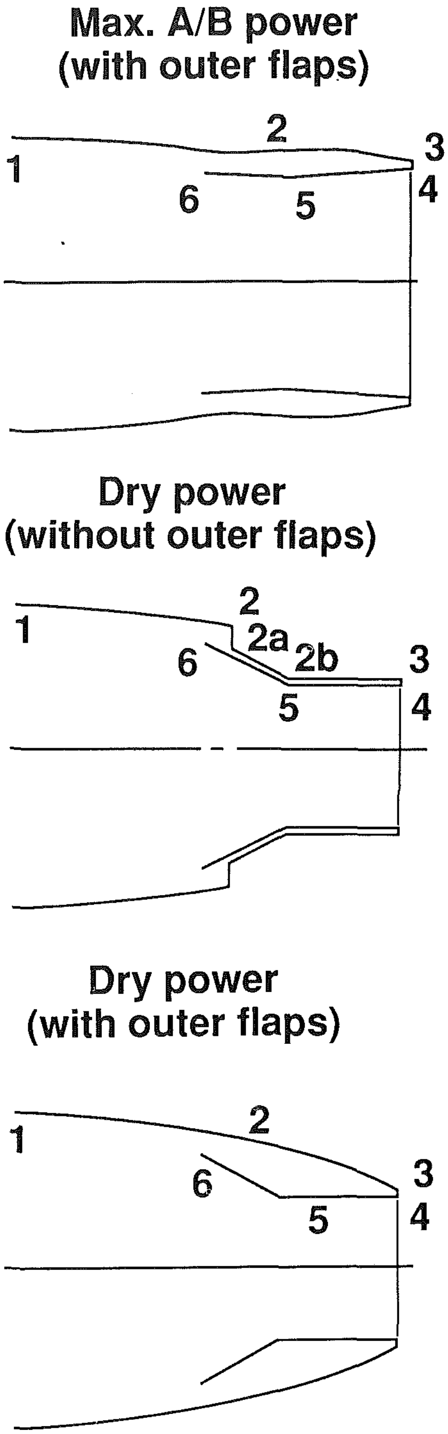

Fig. 2 Shroud and nozzle contours for drag studies

Nomenclature

C_x = axial wave propagation/convection speed, ft/sec
f_s = jet plume screech frequency, Hz
m = azimuthal mode number
M_d = nozzle design Mach number
M_j = fully expanded jet Mach number
M_∞ = wind tunnel Mach number
NPR = jet nozzle pressure ratio
Q = aircraft dynamic pressure, psf
r = radial coordinate
R_o = jet nozzle radius
T_j = jet total temperature
T_t = probe total temperature
α = aircraft angle of attack, deg
θ = phase spectrum angle, deg
ϕ = azimuthal nozzle coordinate, deg

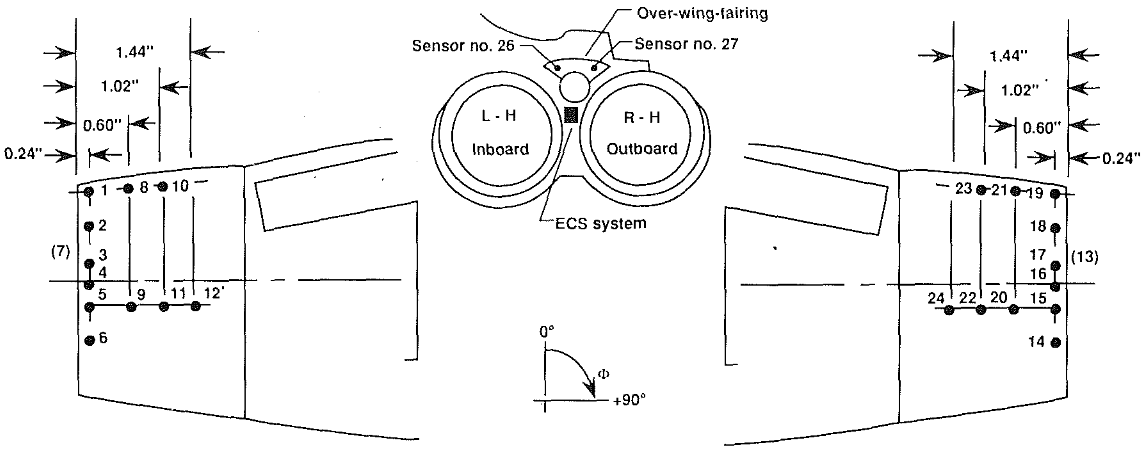

Left-hand inboard nozzle

Sensor	Distance from T.E.	Φ degrees
1	0.24"	15
2	|	45
3	|	75
4	|	90
5	|	105
6	|	135
7	|	285
8	0.60"	15
9	0.60"	105
10	1.02"	15
11	1.02"	105
12	1.44"	105

Right-hand outboard nozzle

Sensor	Distance from T.E.	Φ degrees
13	0.24"	75
14	|	225
15	|	255
16	|	270
17	|	285
18	|	315
19	|	345
20	0.60"	255
21	0.60"	345
22	1.02"	255
23	1.02"	345
24	1.44"	255

a) Alternate dry/cruise power nozzles - wind tunnel tests

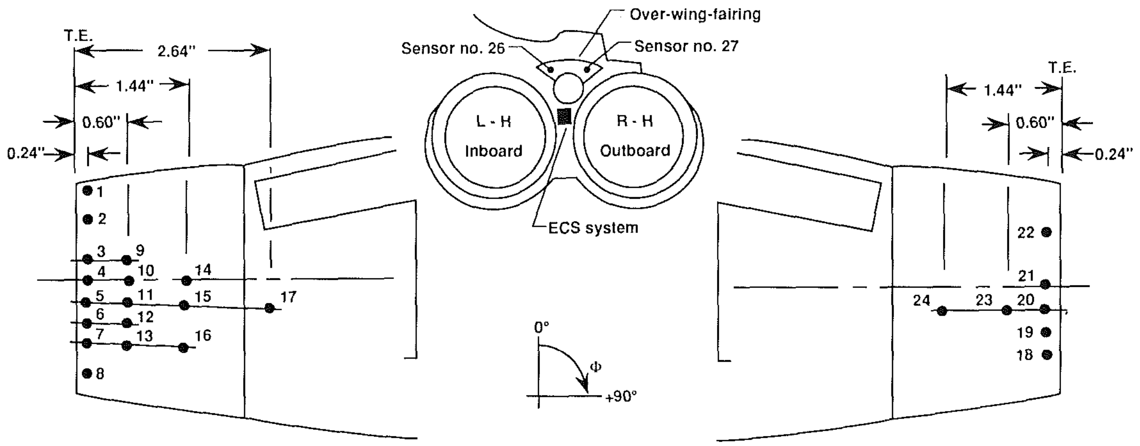

Left-hand inboard nozzle

Sensor	Distance from T.E.	Φ A/B	Φ Cruise
1	0.24"	15	10 *
2	|	45	43 *
3	|	75	74 *
4	|	90	90 *
5	|	105	103 *
6	|	120	117
7	|	135	133
8	|	165	160
9	0.60"	75	74 *
10	|	90	88 *
11	|	105	100
12	|	120	115

Right-hand outboard nozzle

Sensor	Distance from T.E.	Φ A/B	Φ Cruise
13	0.60"	135	133
14	1.44"	90	90
15	|	105	103*
16	|	135	135
17	2.64"	105	100*
18	0.24"	225	222
19	|	240	237
20	|	255	254
21	|	270	267*
22	|	315	305
23	0.60"	255	253
24	1.44"	255	253

* Data obtained in JNL

b) Max A/B power nozzles (wind tunnel tests) and cruise power (isolated nacelle static tests)

Fig. 3 Dynamic pressure sensor locations on right-hand twin jet nacelles

signed to achieve fully expanded flow at respective Mach numbers of $M_d = 1.13$ and 1.55.

The test matrix for the wind tunnel investigation included flight Mach numbers $M_\infty = 0$ (tunnel off), 0.2, 0.3, 0.4, 0.5, 0.6, 0.8, 0.85, 0.9, and 1.24. Jet nozzle pressure ratios included the following NPR = 1. (jet off), 1.5, 2.0, 2.1, 2.4, 2.6, 2.7, 2.9, 3.0, 3.4, 3.5, 4.2, and 5.0. At select M_∞ and NPR settings the aircraft angle of attack, α, was swept from 0 to 6 deg in 2-deg increments. A fixed wing sweep angle of 67.5 deg was used throughout the tests. All together 330 discrete runs were recorded for this series.

For both dry and maximum *A/B* nozzle installations a total of 24 surface dynamic pressure transducers were flush mounted on the nozzle external flap of each configuration. Figure 3(*a*) shows the location for transducers associated with the dry power nozzles in the 16-ft Tunnel tests. The table in this figure provides a location for the transducers. The angle, ϕ, is measured clockwise in degrees from the nozzle top-dead-center. Figure 3(*b*) provides similar information for the maximum *A/B* nozzles. As is evident, the majority of transducers are located in the internozzle region, where previous studies indicated peak levels occur. Two transducers were mounted in the over-the-wing-fairing located between and at the top of each nozzle. Transducers were mounted on the over-the-wing-fairing to measure the effects of large-scale vorticity shed from the forebody that might be swept into the internozzle region.

The data were recorded on a 28-channel FM tape recorder to 20 kHz, permitting postprocessing of narrow band spectra and transfer functions. The transfer function measurements were used to determine the direction of propagation or convection of pressure waves along the nozzle external flaps. The narrow band spectra were integrated to provide overall rms surface pressure. All data runs were made with the Environmental Control System (ECS) operating at 0.12 lb/sec. The ECS exhausts air into the internozzle region, as shown in Fig. 3.

Three-component aft nacelle/nozzle force data were measured using a Rockwell International shell balance located in the left-hand nacelle. The nozzle external shell and part of the aft-end nacelle were machined to be metric. The balance was located in the nacelle just upstream of these machined surfaces. Internal model airflow was monitored by 26 static pressure orifices. The nozzle afterbody and exhaust region static pressures were surveyed by 89 static pressure orifices. An auxiliary high-pressure air source was also available to study its effect on suppression of the twin supersonic plume resonance phenomenon previously discussed.

Models in the Jet Noise (JNL). Before testing the full-span model in the wind tunnel, a similar nacelle with dry power nozzles was mounted in the NASA/LaRC JNL to study various suppression methods. Both the internal and external nozzle geometry followed the contours shown in Fig. 2 and listed in Table 1. The dynamic sensors were located on the exterior nozzle surfaces as indicated in Fig. 3(*b*) for cruise power nozzles. The locations for these sensors were slightly different from those used with dry power nozzles in the wind tunnel. Data obtained in the JNL involved only the 10 locations as indicated in Fig. 3(*b*). The model was mounted in the JNL as shown in Fig. 4. In addition to the 10 surface sensors, three microphones were located off the body in the exhaust plane along the major axis through both nozzles. The flow to each nozzle originated from a common plenum. This was also the condition in the wind tunnel study. The rectangular exhaust of the ECS, located slightly to the right between the nozzles, is shown in Fig. 4.

The twin jet nacelle was tested at fully expanded Mach numbers of $M_j = 0.79$, 1.05, 1.13, 1.18, 1.22, 1.27, 1.32, and 1.38. These Mach numbers correspond closely to those used in the wind tunnel study. Jet total temperatures were varied using electric heating, 250°F being the maximum allowable for this model. Five total temperatures were investigated as follows: $T_j = 67$, 104, 150, 192, and 250°F.

Table 1 Contours for 6 percent scale nozzles

	DRY POWER (with flaps)		DRY POWER (without flaps)		MAX. A/B POWER	
Location	X(In.)	R(In.)	X(In.)	R(In)	X(In.)	R(In.)
1	4.377	1.742	4.377	1.742	4.480	1.742
2	1.905	1.554	1.905	1.554	2.008	1.554
2a			1.905	1.554		
2b			1.208	0.960		
3	0.	0.947	0.	0.960	0.	1.462
4	0.	0.869	0.	0.869	0.	1.386
5	1.329	0.863	1.329	0.863	1.335	1.255
6	2.213	1.313	2.213	1.313	2.316	1.313

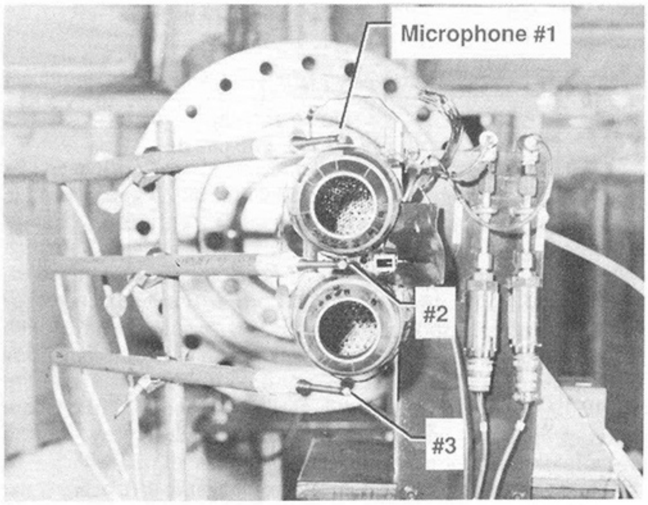

Fig. 4 JNL installation of 6 percent twin jet nacelle

Due to the limitation in jet total temperature with the 6 percent model, a 4.2 percent twin jet nacelle was constructed that would enable testing to at least 680°F, dry power jet total temperature. Figure 5 shows the model surrounded by six off-body microphones, which are positioned in the nozzle exhaust plane. These microphones were positioned azimuthally at major quadrants of each nozzle. For the lower nozzle in Fig. 5, the microphones were located at angles $\phi = 0$, 90, 180, and 270 deg. For the upper nozzle the angles were $\phi = 0$, 90, 270 deg.

This model permitted operation of each nozzle at a different M_j and T_j. This feature provided the opportunity to study the sensitivity of jet plume coupling to minor mismatch in jet operating conditions. This model was tested at 15 fully expanded jet exit Mach numbers ranging from $M_j = 0.79$ to 1.77. Jet total temperatures investigated include $T_j = 104$, 250, 400, 500, 680, and 800°F. The exit velocity profiles of both this hot model and the 6 percent nacelle were measured in the JNL. Plume resonance suppression methods examined included a tab, notch, and small ancillary air jet.

Experimental Results

Static 6 Percent Nacelle. In this section, select aeroacoustic data are presented from the studies using the 6 percent in-

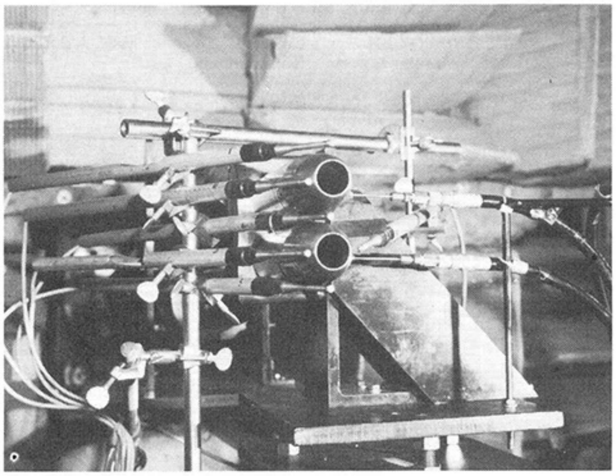

Fig. 5 JNL installation of hot jet 4.2 percent twin nacelle

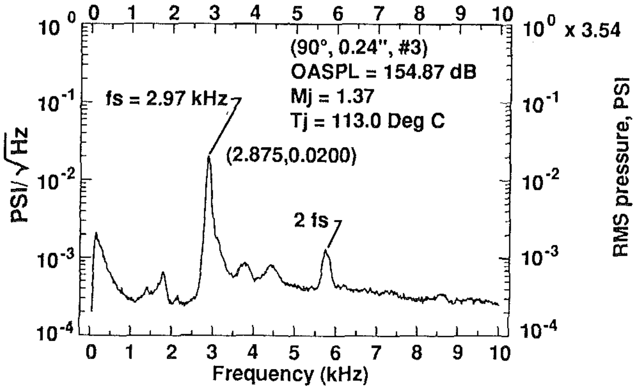

Fig. 6 Load spectrum for 6 percent nacelle test in JNL using cruise point nozzles

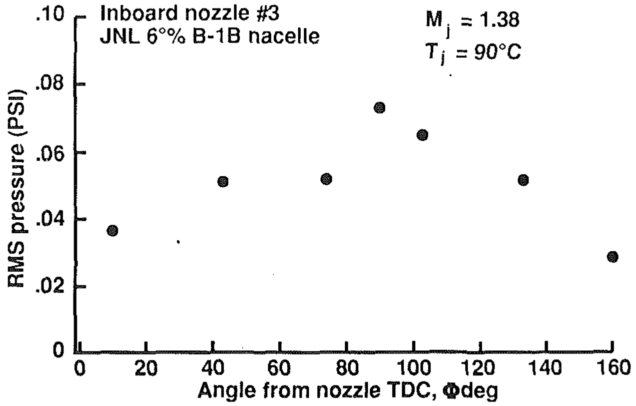

Fig. 7 Screech tone amplitude azimuthal distribution on nozzle outer flaps

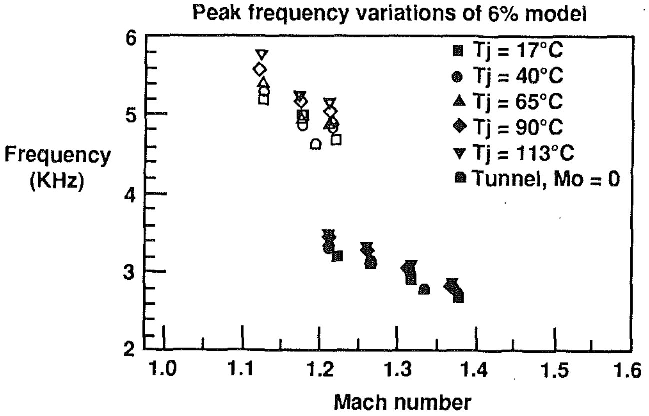

Fig. 8 Dependence of screech frequency on jet plume Mach number and temperature; open symbols (axisymmetric mode) and closed symbols (helical mode)

strumented right hand nacelles. Wind-off tunnel results are presented along with the JNL data to determine difference that may exist between facilities.

Figure 6 shows a characteristic narrow band surface pressure spectrum obtained by operating the model at NPR = 3.05 and jet total temperature of 250°F. This spectrum is associated with trailing edge sensor 4 located on the inboard nozzle (i.e., upper nozzle in Fig. 4) at $\phi = 90$ deg. The left-hand ordinate in Fig. 6 shows the pressure amplitude corrected to the spectrum level. This is obtained by dividing the computed spectral amplitudes by 3.54, the square root of the 12.5 Hz analysis bandwidth. The broadband features of this spectrum will then appear with correct spectrum amplitudes. Narrowband processes, such as the tone at 2.875 kHz, will not appear with the correct amplitude. The right-hand ordinate in Fig. 6 shows the uncorrected pressure spectrum, which provides correct amplitude levels for the discrete tones.

The discrete tone at 2.875 kHz is the dominant spectral feature. Based on the method used by Seiner et al. (1988) for a twin jet configuration, this component can be identified with a jet plume resonance whose predicted frequency is $f_s = 2.97$ kHz. This frequency is also known as the jet plume screech frequency. The azimuthal distribution of this frequency's amplitude for the inboard nozzle is shown in Fig. 7 for $M_j = 1.38$ and jet total temperature of $T_j = 194$°F. These data show that the location for peak amplitude screech occurs at $\phi = 90$ deg. This is close to the region for maximum structural fatigue reported by Berndt (1984) for the B-1B aircraft. While the peak rms amplitude of 0.072 psi may appear small, Miller et al. (1981) detected fracture on a F-15 fuselage with rms dynamic pressures as low as 0.005 psi.

The plume resonance frequency f_s is functionally dependent on the fully expanded plume Mach number M_j and only slightly on the nozzle design Mach number, which for this nozzle is $M_d = 1.135$. Higher plume Mach numbers produce lower frequencies due to greater shock cell spacing in the plume. Figure 8 summarizes the dependence of the plume resonance frequency on jet total temperature. As expected from the previous results of Seiner et al. (1988), plume axisymmetric modal structure appears at values of $M_j < 1.22$, whereas plume helical modal structure appears at values of $M_j > 1.22$. Based on the analysis of Tam and Burton (1984), flow variables associated with the spatial structure of a fixed frequency large-scale wave can be decomposed azimuthally as $\exp(\pm im\phi)$. The coefficient m is zero for axisymmetric structure, and equal to or greater than 1 for helical structure.

For constant M_j, the resonance frequency is shown to increase slightly with jet total temperature, which agrees with theory (Tam et al., 1986). This increase is attributed to an increase in the convection velocity associated with plume large-scale turbulent structure. Figure 8 also presents data that show that the resonance frequencies measured in the wind tunnel and the JNL agree.

The data in Fig. 9 show corresponding amplitudes associated with the frequencies in Fig. 8. From these data, it appears that axisymmetric modes produce amplitude levels that are half those for helical modes when the jet plume is unheated. With only mild jet plume heating, the amplitude for helical modes rises sharply, being 20 times greater than the axisymmetric

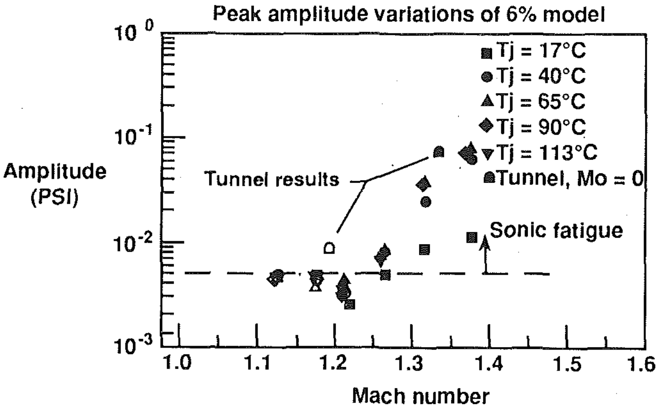

Fig. 9 Dependence of screech frequency amplitude on jet Mach number and temperature; open symbols (axisymmetric mode) and closed symbols (helical mode)

mode amplitude. The helical mode amplitudes are clearly well beyond those found by Miller et al. (1981) to produce sonic fatigue. This is indicated by the dashed line in Fig. 9, which represents the level where they observed fuselage fractures. It should be mentioned that operation of the nacelle in the tunnel produced amplitudes for helical modes that are seven times greater than those found in the JNL. The importance of initial jet boundary layer momentum thickness is known to affect growth of large-scale structures, but current theory cannot yet be used to understand this observation.

The large increase in the jet plume resonance mode amplitude provided strong motivation to construct a twin jet nacelle that was capable of being tested to at least the full scale dry power jet total temperature of 680°F. The primary results using this model are presented in the following section.

High-Temperature Jet Nacelle. To permit testing in the JNL to a jet total temperature of 680°F required sizing the new twin jet nacelle to 4.2 percent. Because of the elevated surface temperatures, only six microphones were used and located off the body, as shown in Fig. 5. Both dry and maximum *A/B* nozzles were constructed for the hot jet study.

Screech tone amplitudes measured by the internozzle microphone of the 4.2 percent model are shown in Fig. 10. The data are associated with operation of dry power nozzles over a range of jet total temperatures from 63 to 800°F. The screech tone amplitudes obtained with the 6 percent nacelle only test and the wind-off tunnel test are also shown with the 4.2 percent data. The 6 percent data are associated with trailing edge sensor 4 at $\phi = 90$ deg for both models. As is evident, the data indicate that the screech tone amplitude is a strong function of not only plume temperature, but also the model and facility used to acquire the data. While in general the data indicate that screech tone amplitudes decrease with increasing plume temperature, the data at 104°F from the three tests show a wide scatter in amplitude. At the present time, no theory exists to predict screech tone amplitude, but several factors are believed to exist that may have produced these discrepancies.

Test in a hard wall chamber, such as a wind tunnel test section at wind-off, should be reverberant with the potential for doubling pressure amplitudes relative to a soft test cell enclosure such as the JNL. This may account for a portion of the increase in amplitude level of the 6 percent model results between the JNL and wind tunnel. Operation of the 6 percent nacelle, however, also requires the use of choke plates. This is due to the air inlet area of the model being smaller than the sum of both nozzle throat areas. The 4.2 percent model contains no choke plates. These choke plates produce high-frequency noise that could affect noise producing characteristics of the jet plume. Based on the spectral results from the 6 percent nacelle only test, new choke plates were designed with smaller holes for the wind tunnel model.

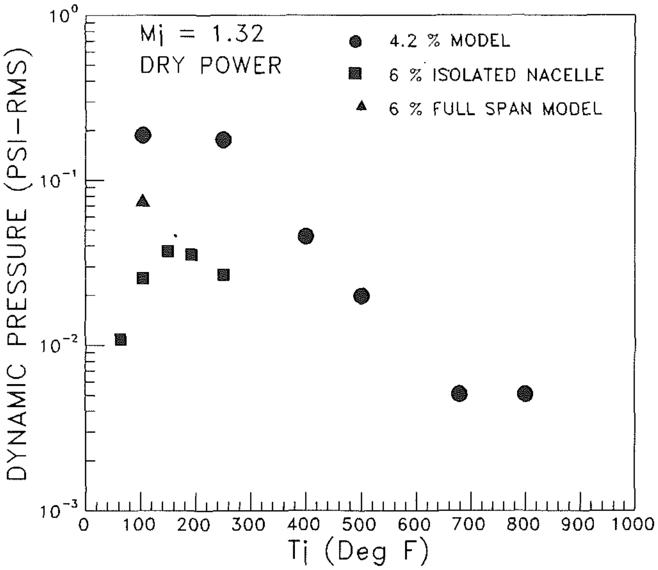

Fig. 10 Dependence of screech frequency amplitude on jet temperature

The nozzle exit boundary layer, for nozzles with internal geometry of Fig. 2, was found to be very thick and dependent on nozzle area ratio. These results are summarized by the nozzle exit total temperature probe surveys in Figs. 11(*a*) and 11(*b*) of both dry and maximum *A/B* power nozzles. The probe surveys extend across the jet exit diameter. Circular symbols denote radial values measured from the nozzle center in positive coordinate direction and the triangular symbols those measured in a negative direction. While the measurements were made on the upper nozzle in Fig. 5, both lower and upper nozzles were operating at a fully expanded jet Mach number $M_j = 1.38$. The measured probe total temperature results are normalized by the jet supply total temperature T_j of 680°F and the nozzle exit radius R_o. The dry power nozzles have a much thicker boundary layer than the maximum *A/B* nozzles, with a discontinuity near the nozzle lipline (i.e., $r = R_o$). For the maximum *A/B* nozzle the boundary layer extends to $r/R_o \sim 1.05$, whereas the dry power nozzle boundary layer extends to $r/R_o \sim 1.10$.

Screech Suppression Methods. The use of the tablike devices in the nozzle exit plane of a supersonic jet has been utilized in the past by numerous researchers to suppress jet screech. In the studies by Seiner et al. (1988), it was determined that a tab must penetrate through the jet exit boundary layer to the supersonic stream to work effectively at reducing screech. For jets with initially thick boundary layers, its requirement may pose a practical limitation for their application. In addition to thrust losses, failure of such a device in the hot jet stream is of much more concern. The thick nozzle exit boundary layer thickness of the dry power nozzle in Fig. 11(*a*) led to the consideration of alternate methods to achieve reduction in screech tone amplitude. In addition to the use of a tab and notch, the present experiments also evaluated a small supersonic stream at the jet exit to achieve suppression of jet screech.

Figure 12 indicates the position and dimensions used for mounting the suppression devices. In the wind tunnel studies, suppression devices were mounted on the right-hand nacelle outboard nozzle. Screech suppression effectiveness is independent of the selection of inboard or outboard nozzle. The tab protruded into the supersonic stream based on the exit plane boundary layer measurements of Fig. 11. Figure 13 shows the tab mounted on the maximum *A/B* nozzles in the 16-ft tunnel. The notch dimensions were 0.2 in. wide by 0.2 in deep.

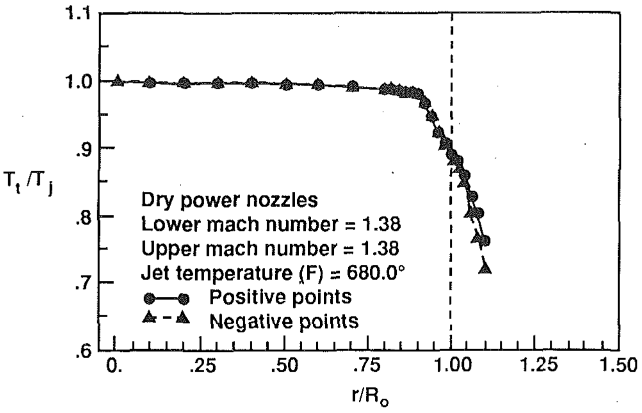

a) Dry power nozzles

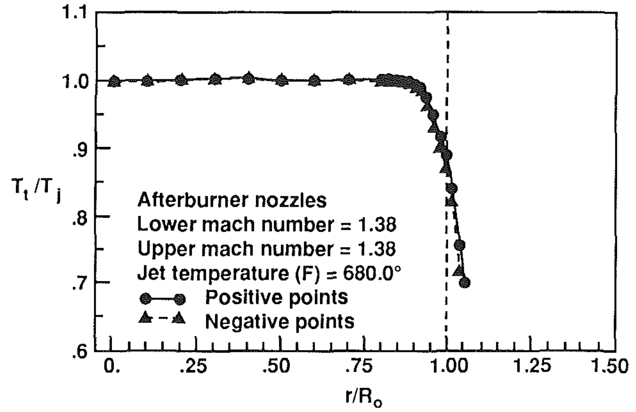

b) Max AB power nozzles

Fig. 11 Jet exit total temperature profile using 4.2 percent model

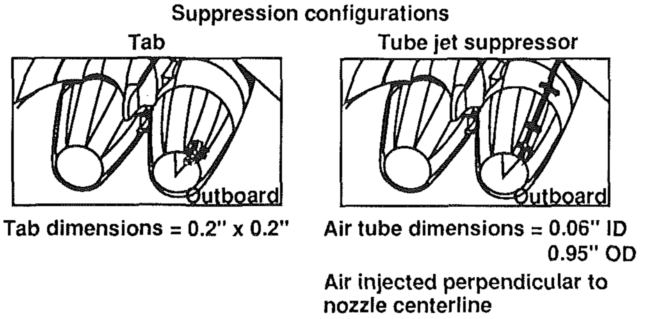

Fig. 12 Location for installation of suppression concepts on outboard nozzle

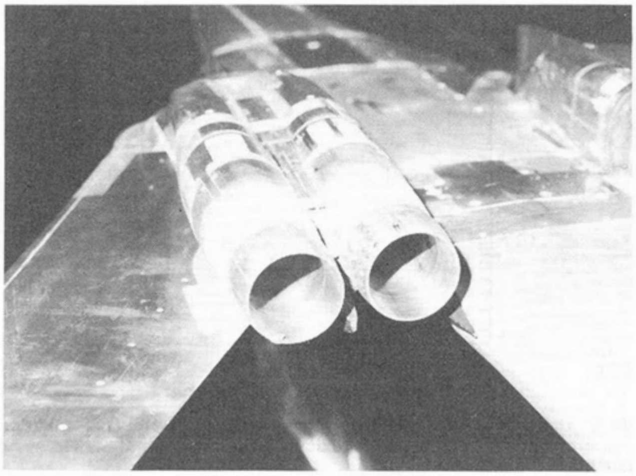

Fig. 13 Photograph of tab installation on maximum *A/B* in 16-ft Transonic Tunnel

Figures 14(*a*), 14(*b*), and 14(*c*) present narrow band spectra for the inboard nozzle sensor located at $\phi = 90$ deg, 0.24 in. back from the trailing edge. Figure 14(*a*) shows the unsuppressed case, Fig. 14(*b*) the tab application, and Fig. 14(*c*) the notch application. These spectra were obtained using the 6 percent dry power nozzles. These data indicate that application of either suppression device increases the overall dynamic pressure level, OASPL. The tab does reduce the screech tone, but spectral amplitudes are increased for frequencies above the screech frequency. The notch increases the overall level considerably, and even increases the screech tone amplitude.

The tube jet suppressor provides positive suppression of jet screech as shown in the narrow band spectra of Figs. 15(*a*) and 15(*b*). These spectra are associated with application of the method to the full-span model in the wind tunnel with dry power nozzles. In this example, the tunnel test section Mach number is 0.2. Figure 15(*a*) presents surface dynamic pressure data for the trailing edge sensor 4 at $\phi = 90$ deg for the unsuppressed case and Fig. 15(*b*) for the tube jet application. The tube jet injection pressure is 100 psig. This high pressure is necessary to overcome significant pressure losses associated with the tube air supply system. Comparison of the Fig. 15 spectra show that both the jet screech component and overall dynamic pressure are significantly reduced through application of the tube jet suppressor.

Figures 16(*a*) and 16(*b*) are phase-averaged schlieren results from the JNL using the 6 percent isolated nacelle, where $M_j = 1.38$ and $T_j = 249$°F. The unsuppressed case of Fig. 16(*a*) shows the presence of large-scale waves in both jet plumes. These waves produce coupled internozzle pressure fields. Figure 16(*b*) shows that application of the tube jet suppressor to the upper nozzle eliminates all large-scale supersonic plume pressure waves and coupling of the twin jet column.

Full-Span Model. A typical narrow-band spectrum obtained from the full-scale aircraft is shown in Fig. 17. The spectrum is associated with the internozzle trailing edge sensor at $\phi = 45$ deg located on the outboard engine of the left-hand nacelle. The flight condition for this example is $M_\infty = 0.85$ and $\alpha = 2$ deg.

The Fig. 17 spectrum shows a high-amplitude discrete tone near 30 Hz. A broadband component appears at twice this frequency. The 400 Hz tone is related to aircraft line power. Taking into account the full-scale engine operating conditions, as well as aircraft flight conditions, the predicted screech frequency for this case is 31 Hz. This agrees well with the measured data. This result provided strong incentive to study the full-span model.

Spectral results from the full-span model in the wind tunnel, using the dry power nozzles, are shown in Figs. 18(*a*), 18(*b*), and 18(*c*), where $M_\infty = 0.85$ and $\alpha = 0$ deg. Differences between flight and model spectra can be attributed to differences in jet plume total temperature, the aircraft dynamic pressure, *Q*, and nozzle expansion ratio. Despite these operational differences, and as will be established below, both spectra contain peak spectral amplitudes that coincide with the predicted jet screech frequency.

Figure 18(*a*) shows the spectrum associated with trailing edge transducer 5 mounted on the inboard nozzle at $\phi = 105$ deg with twin jets operating at NPR = 3.4. The predicted plume resonance frequency for this condition is $f_s = 456$ Hz. Although the Fig. 18(*a*) spectrum contains no discrete tones, the spectrum peak amplitude occurs near f_s. With nozzles powered-off

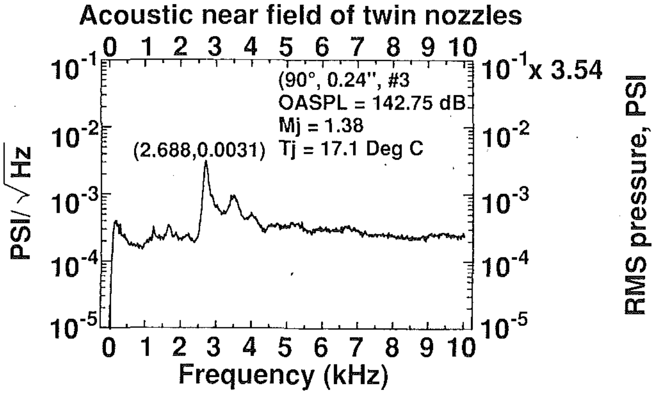

a) Unsuppressed

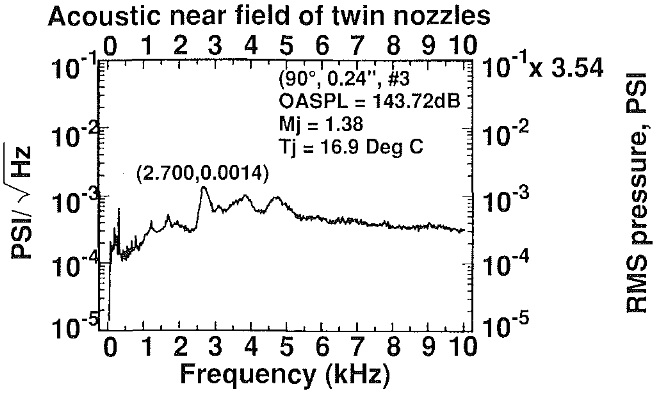

b) Application of tab

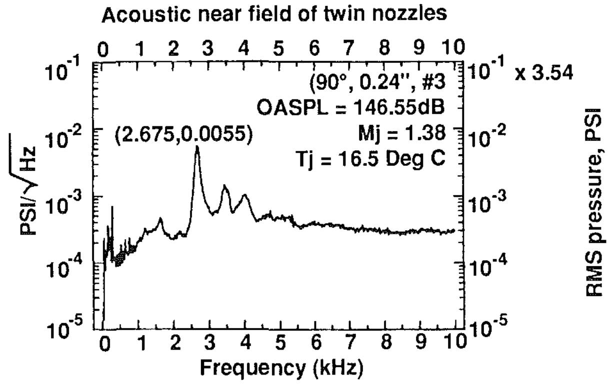

c) Application of notch

Fig. 14 Modification of load spectrum with applied suppression

(NPR = 1), Fig. 18(*b*) shows that a narrow band process begins to form in the vicinity of the predicted f_s. This narrow band process is even more evident in the Fig. 18(*c*) spectrum associated with the over-the-wing fairing sensors when nozzles are powered-off. Despite the coincidence between the predicted plume resonance frequency and that for the narrowband process in Figs. 17, 18(*b*), and 18(*c*), the narrowband process is unrelated to jet screech. To substantiate this observation, Fig. 19 shows a comparison of the directivity patterns between powered and powered-off nozzles for flight data at $M_\infty = 0.85$. Not only are the overall dynamic pressure levels of the same order of magnitude, but the azimuthal distribution shows that maximum pressure amplitudes occur near $\phi = 105$ deg. Thus the narrowband process at $M_\infty = 0.85$ is unrelated to jet screech.

Flow Visualization Study. The azimuthal distribution of dynamic pressure amplitude in Fig. 19 is similar to the plume resonance mechanism as shown in Fig. 7. In order to determine the source of the narrow band process more clearly, a flow visualization experiment was implemented.

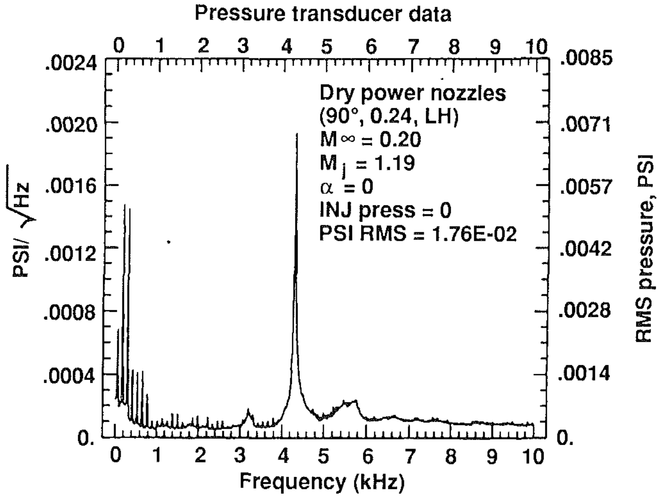

a) Unsuppressed (tube flow off)

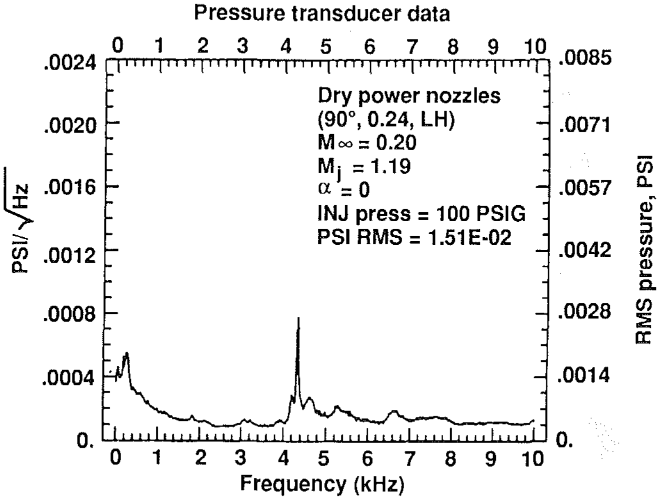

b) Suppressed (tube flow on)

Fig. 15 Modification of load spectrum with application of supersonic tube jet

The flow visualization study was conducted using the NASA/LaRC 16 in. × 24 in. Water Tunnel. A 1/72 scale model was assembled with powered twin jet exhausts and faired over inlets for the left-hand nacelle. Flow-through inlets and exhaust nozzles were used for the right-hand nacelle. Dye tracers were injected at the aircraft nose and at locations just upstream of the nozzles on the over-the-wing fairing. The sweepback angle of the wing was fixed at 67.5 deg and photographs of the dye streaks on the model were taken at $\alpha = 0$ and 2 deg in an attempt to compare to both the wind tunnel and full-scale flight studies. The flow through the powered left-hand nacelle nozzles was adjusted to correspond to a jet to free-stream velocity ratio of 2.07 for comparison to Fig. 18 data and 3.0 for comparison to Fig. 17 data.

Figure 20 shows the flow visualization results. The dye tracer released at the nose indicates smooth, undisturbed flow to a region near the leading edge of the wing body junction. At this point, a vortex rolls up, bursts midchord, and is convected into the internozzle region. The low Reynolds number per foot

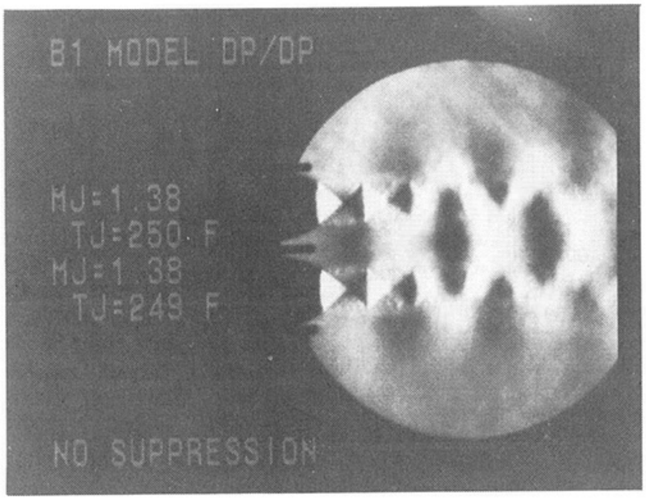

a) Unsuppressed

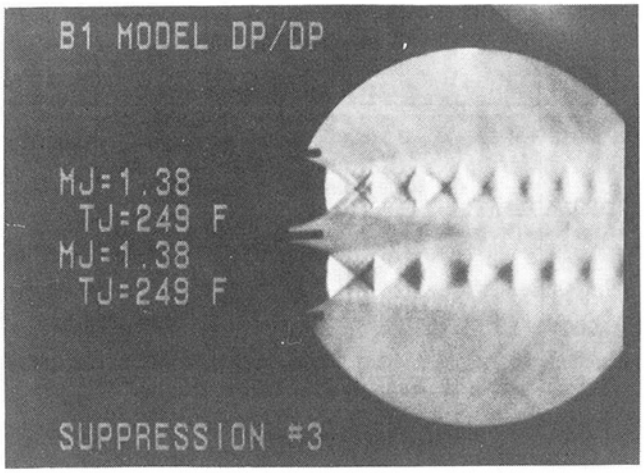

b) Suppressed by application of tube jet in upper nozzle

Fig. 16 Phase-averaged schlieren of 6 percent dry power nozzles in JNL

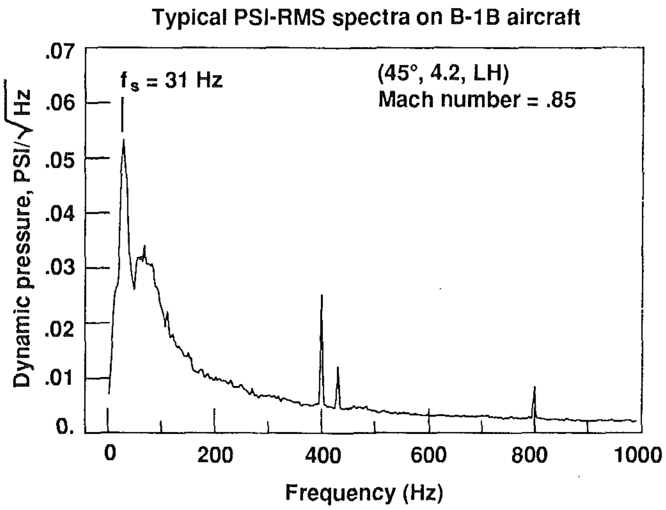

Fig. 17 Full-scale load spectrum on nozzle outer flaps

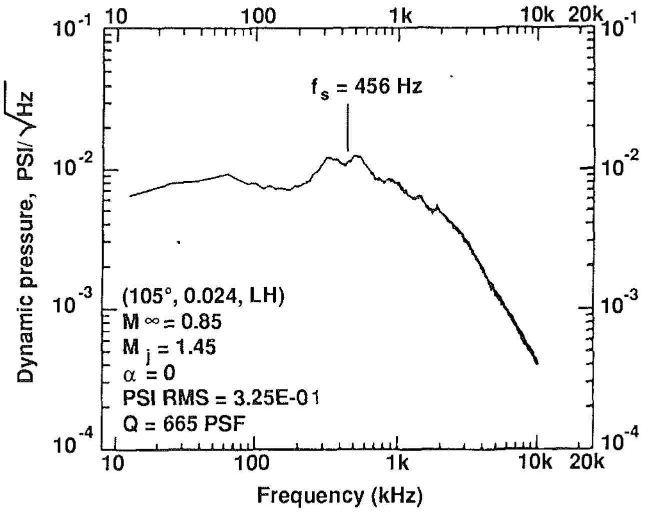

a) Flap spectrum, NPR = 3.4

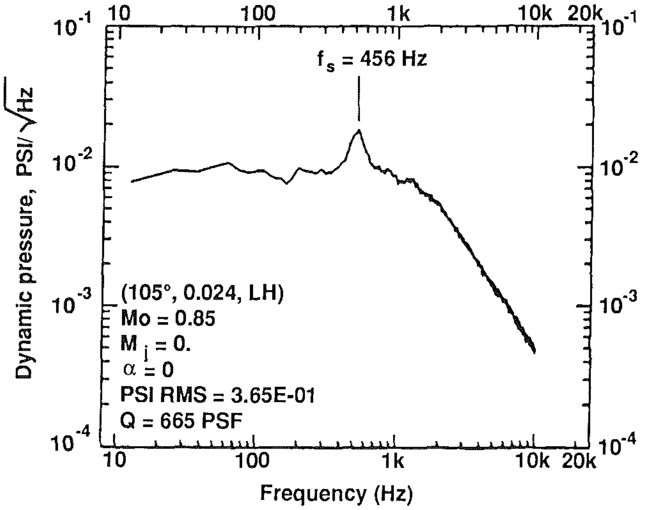

b) Flap spectrum, NPR = 1.0

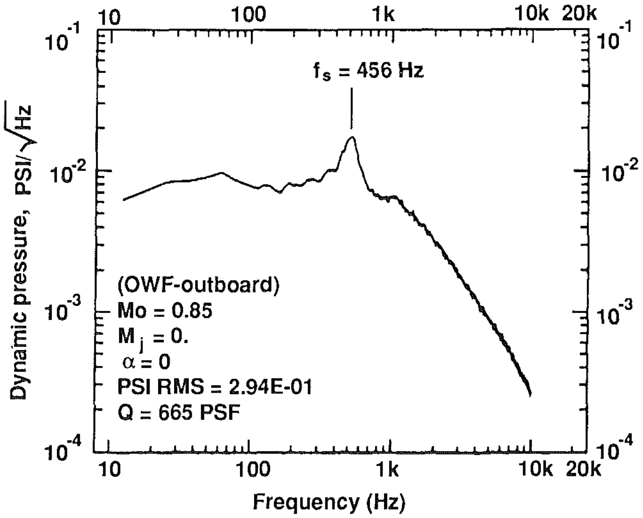

c) Over the wing fairing spectrum, NPR = 1.0

Fig. 18 Model scale load spectrum

of 19 for these tests is of course much less than the one associated with either the wind tunnel or full-scale data. To examine further the nature of the high internozzle dynamic loads required analysis of the dynamic pressure data to determine convective direction of boundary layer disturbances.

Transfer Function Measurements. The direction of propagation or convection of the boundary layer loads mechanism can be determined from computation of the coherence and phase between surface dynamic pressure sensors. As shown in Fig. 21, the wave speed is related to the slope in the phase spectrum according to $C_x = 2\pi x(f/\theta)$. The direction is determined from the sign of the slope in the phase spectrum and the location of the sensor used for reference. Thus for those frequency ranges where the coherence is greater than 0.1, it is possible to determine not only the direction of wave motion but also its speed along the path of the surface sensors.

Figures 22–25 present transfer function measurements associated with the wind tunnel test of the dry power nozzles, where $M_\infty = 0.85$ and with $\alpha = 0$ deg. In the examples of Figs. 22–24, the nozzles are powered-off (i.e., NPR = 1.0). The nozzles are powered in the Fig. 25 data at a value of $M_j = 1.45$.

Recall that the spectrum in Fig. 18(*c*) shows, for powered-off nozzles, a narrow band process near 450 Hz. The analysis in Fig. 22 uses the inboard sensor on the over-the-wing fairing as the reference, and shows the resulting coherence and phase spectrum associated with trailing edge transducer 1 at $\phi = 15$ deg on the inboard nozzle. A high level of coherence exists between these two spatial locations for the narrow band process near 450 Hz. The coherence at this frequency reaches a value of 0.5, which is the dominant correlated process in the spectrum. The phase spectrum has a negative slope in this frequency range, indicating that this narrow band process is being convected from the over-the-wing fairing down into the internozzle region (i.e., the over-the-wing fairing sensor is the reference, so the meaning of the slope is reversed from that in Fig. 21). These results correspond to those observed in the flow visualization studies.

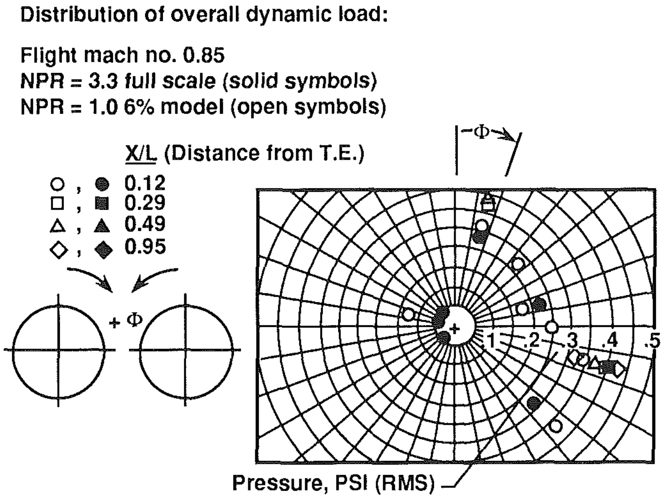

Fig. 19 Azimuthal distribution of flap loads in flight

The transfer function was acquired in Fig. 23 for transducers 5 and 9 at $\phi = 105$ deg on the inboard nozzle. These results additionally show that the narrow band process enters the internozzle region and is convected aft in an axial direction with a speed of 511 ft/sec. In Fig. 23, trailing edge transducer 5 is the reference transducer, so that a positive slope in the phase spectrum indicates aft convection. The coherence data in Fig. 23 indicate a level of coherence near 0.9 at 450 Hz. A broadband range of frequencies above this value is also well correlated to a value near 4 kHz. This good coherence, with small separation of transducers, is indicative of what one expects for a turbulent boundary layer.

The Fig. 24 transfer function data, between the two trailing edge transducers 5 and 15 at $\phi = 105$ deg on the inboard and outboard nozzles, indicates that only the narrow band process at 450 Hz is convected from the direction of the over-the-wing fairing. Higher frequencies are evidently generated by local boundary layer events over each nozzle afterbody. With nozzles powered, the transfer function measurements in Fig. 25, between the same transducers in Fig. 23, show that the convection of the narrow band disturbance into the internozzle region is altered. Not only is there a loss of coherence in the signal of the narrow band process at the 105 deg location, but there is also a loss of coherence of high-frequency boundary layer fluctuations. This provides a rational explanation for the Fig. 18 narrow band spectra, which does not indicate the presence of a narrow band process near 450 Hz with powered nozzles.

Load Mechanisms. Based on the above results, it was possible to piece together an understanding of dynamic loads on nozzle outer flaps for the B-1B aircraft. After acquiring narrow band spectra for a wide range of free-stream Mach numbers, it became apparent that two separate mechanisms were pri-

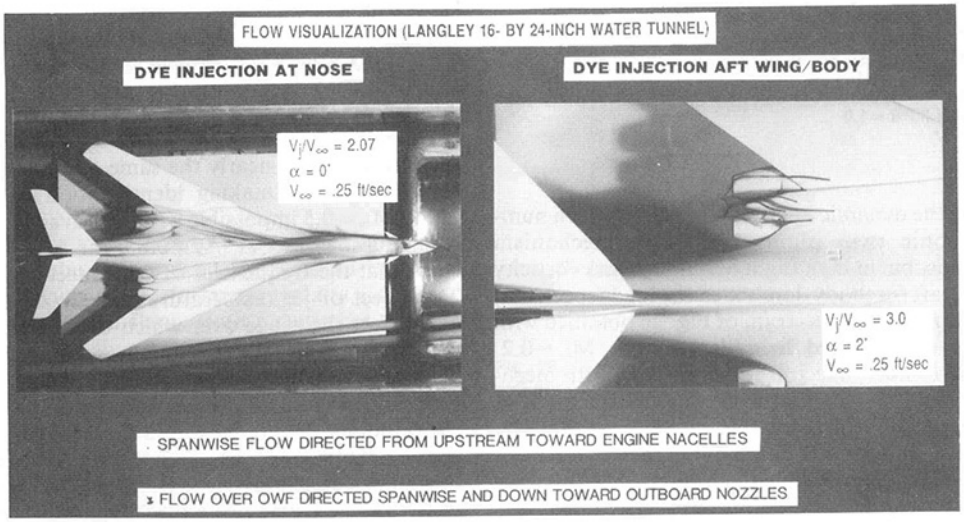

Fig. 20 Flow visualization using dye tracers on 1/72 scale model

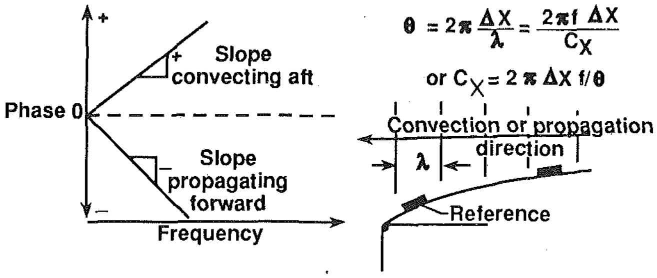

Fig. 21 Method for determining wave speed and direction using transfer function method

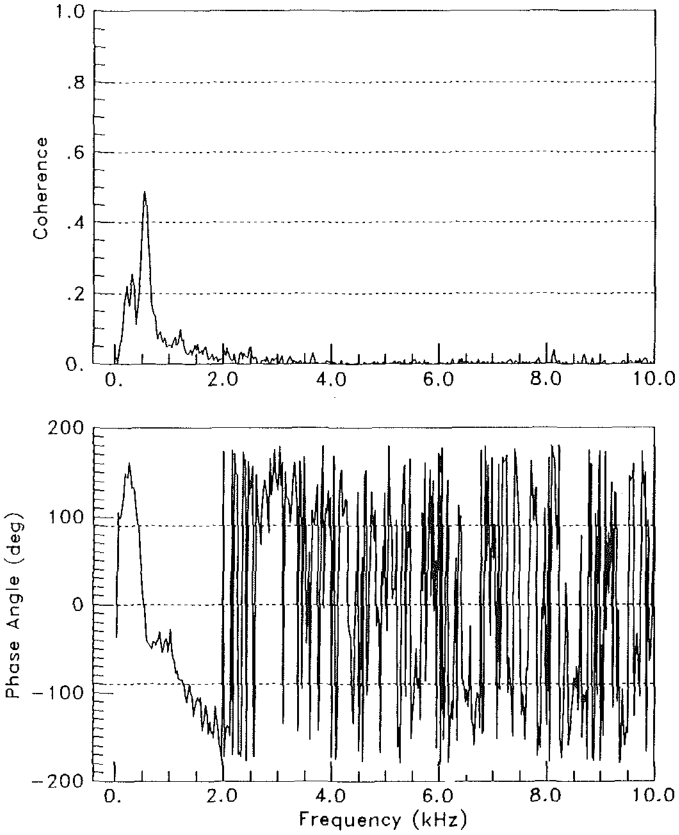

RUN PARAMETERS
(OWF-INBOARD) (15°,0.024, LH)
RH NAC = 1, COMMENT = 4
NPR = 1.00, Mo = 0.85
ALPHA = 0, INJ PRESS = 0

Fig. 22 Transfer function measurement between OWF and trailing edge flap transducer 1 with NPR = 1.0

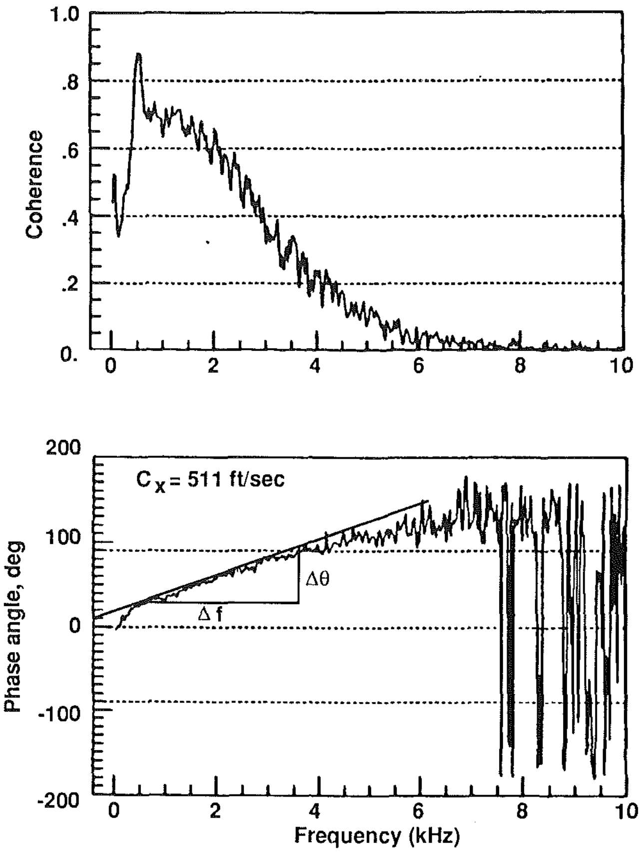

Run parameters
(105°, 0.024, LH) (105°, 0.060, LH)
RH NAC = 1, Comment = 4
NPR = 1.00, Mo = 0.85
Alpha = 0, INJ press = 0

Fig. 23 Transfer function measurement between transducers 5 and 9 at $\phi = 105$ deg with NPR = 1.0

marily controlling the dynamic loads. At low flight Mach numbers, the supersonic twin plume resonance mechanism dominated the loads, but at high flight Mach numbers vorticity shed from the aircraft forebody dominated the loads spectrum.

Consider the narrow band spectrum of Fig. 26 obtained with dry power nozzles and a forward flight Mach number $M_\infty = 0.2$. At this low Mach number, spectral features from both mechanisms can be identified. The vortex-dominated fluctuations occur at low frequency, which for this case is near 300 Hz. Plume shock noise fluctuations dominate higher frequencies above 3000 Hz. Increases in flight Mach number will reduce the shock noise frequencies as previously discussed, but will also decrease the amplitude of this mechanism as shown in Fig. 27. The plume resonance amplitude is reduced at higher values of M_∞ due to the increasing presence of a turbulent boundary layer with separated flow. With twin nozzle geometry, these boundary layers are expected to be nonaxisymmetric, and thus interfere greatly with the generation of plume resonance. Figure 27 also shows that an increase in the forward flight Mach number will increase the amplitude associated with upstream vorticity shed by the aircraft forebody. The spectral data presented above show that the frequency associated with this process increases with increasing flight Mach number.

From Figs. 27 and 18, it is clear that at $M_\infty = 0.5$, both mechanisms have nearly the same amplitude and close to the same frequency, making identification of each mechanism above $M_\infty = 0.5$ impossible without advanced signal processing techniques. In fact at $M_\infty = 0.85$, the spectral data of Fig. 18 show that the frequencies of both mechanisms are the same. The effect of jet temperature and nozzle pressure ratio can also affect the range over which the shock noise mechanism is dominant, since previously it was shown that the amplitude decreases with jet temperature and increases with nozzle pressure ratio. Figure 28 provides a qualitative illustration of the above points. Figure 29 shows the dependence of overall dynamic pressure load on aircraft dynamic pressure for the inboard nozzle trailing edge sensor at $\phi = 105$ deg at several values of NPR. These data show that amplitude levels above 600 psf are independent of the nozzle NPR.

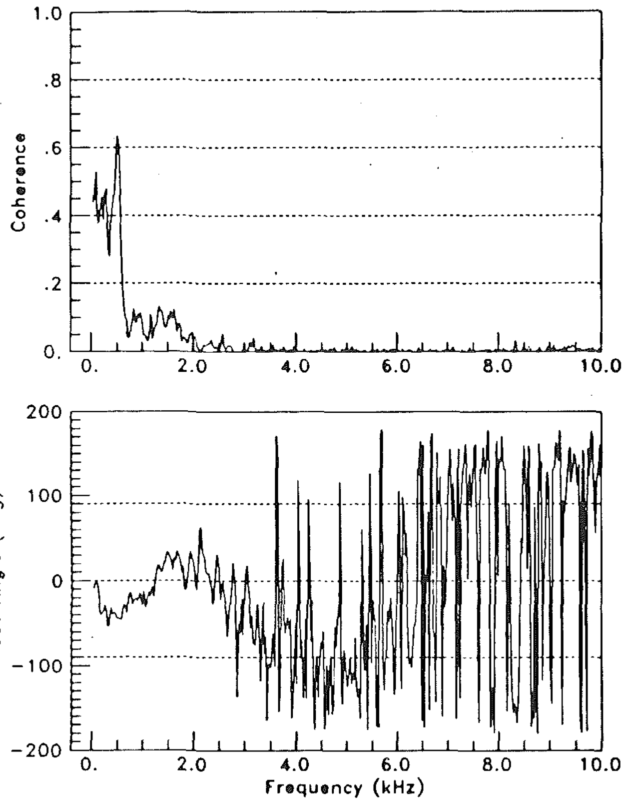

RUN PARAMETERS
(75°,0.024, LH) (285°,0.024, LH)
RH NAC = 1, COMMENT = 4
NPR = 1.00, Mo = 0.85
ALPHA = 0, INJ PRESS = 0

Fig. 24 Transfer function measurement between inboard nozzle transducer 5 and outboard nozzle transducer 15 at NPR = 1.0

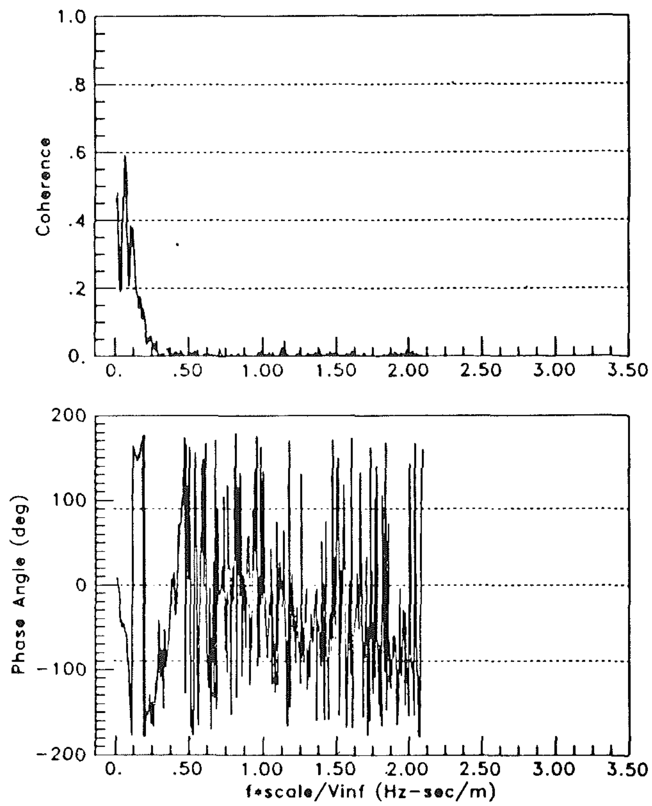

RUN PARAMETERS FOR
6% MODEL IN TUNNEL
(105°,0.24, LH) (105°,0.60, LH)
RH NAC = 1, COMMENT = 0
NPR = 3.40, Mo = 0.85
ALPHA = 0, INJ PRESS = 0

Fig. 25 Transfer function measurements between transducers 5 and 9 at $\phi = 105$ deg with NPR = 3.40

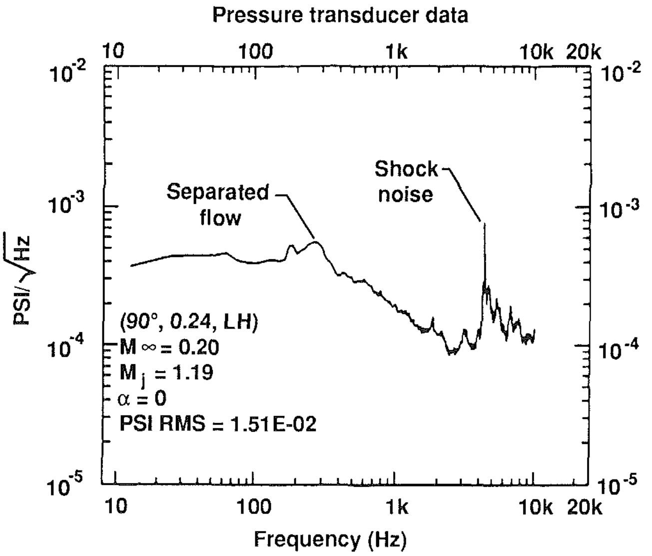

Fig. 26 Narrow band spectrum showing vortex-induced fluctuations and plume resonance

Performance Assessment. In order to investigate the effect of removal of the external nozzle flaps on aircraft performance, the aircraft left-hand nacelle was instrumented with a three-component shell balance. The flaps were removed from both dry power nozzles in the nacelle as illustrated in Fig. 2. The variation of afterbody drag was found to depend only slightly on aircraft angle of attack over the limited range investigated in this study. Figure 30 provides a summary of the performance penalty associated with removal of the outer flaps. A difference of six drag counts is representative of the average difference in nacelle C_d over the Mach number range investigated. The nacelle afterbody drag increases sharply beyond $M_\infty = 0.85$, due to separated flow induced by formation of a shock on the nozzle afterbody. The Fig. 30 results show this Mach number effect occurs with and without outer nozzle flaps.

Conclusions

The objective of this study was to evaluate the origin for dynamic loads on engine external nozzle flaps on the B-1B aircraft, and to determine the performance penalty associated with removal of the external flaps. Both a static hot twin jet nacelle and 6 percent full-span model of the B-1B were investigated along with a model for flow visualization. The results of this investigation are as follows:

1 Twin jet supersonic plume resonance was found to dominate the load spectrum below flight Mach numbers of 0.5. The amplitude associated with this mechanism was found to decrease with increasing flight speed and jet total temperature. Low nozzle pressure ratios, which are dominated by axisymmetric plume structures, have much smaller amplitudes than do helical plume structures, which dominate higher NPR.

2 Vorticity shed from upstream aircraft locations dominates the load spectrum above flight Mach numbers of 0.5.

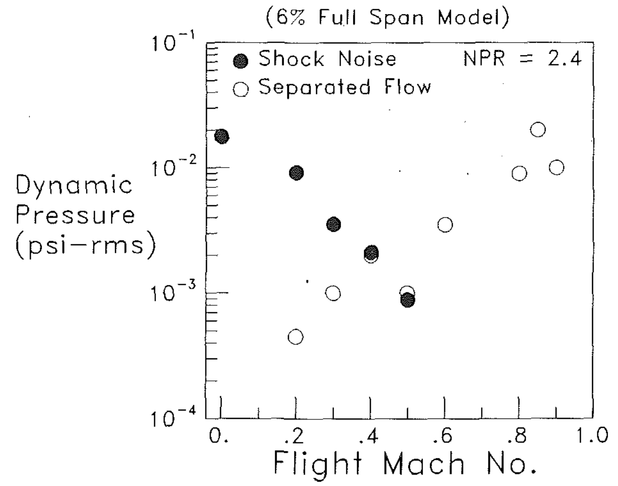

Fig. 27 Amplitude dependence of source mechanisms with flight Mach number

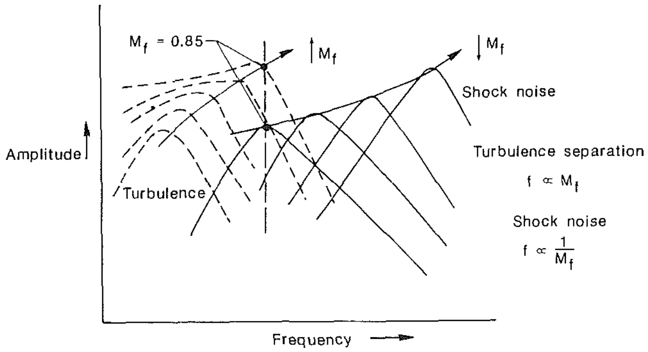

Fig. 28 Illustration of amplitude and frequency dependence of two source mechanisms as a function of flight Mach number

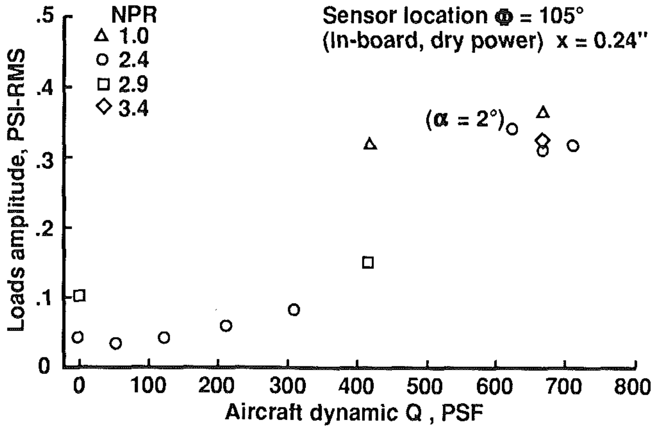

Fig. 29 Loads amplitude relative to aircraft dynamic *Q*

The amplitude of this mechanism continually increases with flight Mach number until $M_\infty = 0.8$, while above this value it remains relatively constant. The frequency of this mechanism increases with flight speed, whereas that for plume resonance decreases. At a flight Mach number of 0.85, both mechanisms have the same frequency.

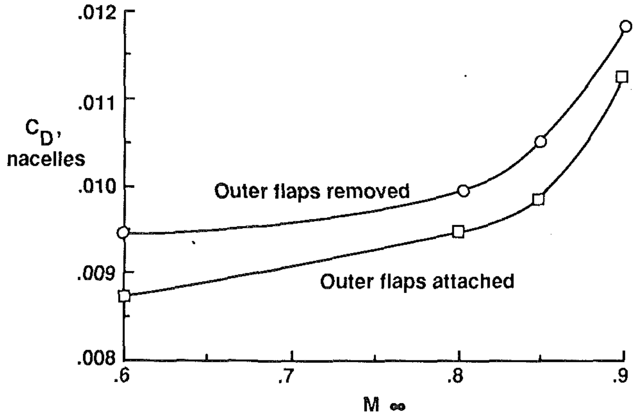

Fig. 30 Performance penalty associated with removal of outer flaps

3 Jet plume resonance was more effectively reduced by use of a small supersonic tube jet compared to the use of a tab or notch. A notch in the nozzle wall was found to enhance plume resonance.

4 Both the supersonic plume resonance mechanism and forebody generated vorticity fluctuations create dynamic loads that are sufficient to produce structural failures.

The results of this study agree in general with the results obtained by Seiner et al. (1990) on the F-15 16-ft Wind Tunnel tests. In that study, dynamic loads produced by the plume resonance mechanism dominated load spectra to a flight Mach number of 0.72 with twin rectangular nozzles. Thus it appears that the dominant mechanism depends on the flight regime and geometry. More research is required to understand better the vortex-dominated flow. CFD time-accurate schemes for full-body calculations need to be investigated along with flow measurements off the aircraft body in the boundary layer. In addition, hot jet models need to be included in the wind tunnel experiments to establish properly the range of importance of each mechanism.

References

Berndt, D. E., 1984, "Dynamic Pressure Fluctuations in the Internozzle Region of a Twin-Jet Nacelle," SAE Paper No. 841540.

Miller, V. R., Plazak, G. A., and Chinn, J. M., 1981, "Acoustic Measurements of F-15 Aircraft Operating in Hush House," AFWAL-TM-81-82-FIBE.

Peddrew, K. H., 1981, "A User's Guide to the Langley 16-Foot Transonic Tunnel," NASA TM-83186.

Seiner, J. M., Manning, J. C., and Ponton, M. K., 1987, "Model and Full Scale Study of Twin Supersonic Plume Resonance," AIAA Paper No. 87-0244.

Seiner, J. M., Manning, J. C., and Ponton, M. K., 1988, "Dynamic Pressure Loads Associated With Twin Supersonic Plume Resonance," *AIAA J.*, Vol. 26, No. 8, pp. 954–960.

Seiner, J. M., Ponton, M. K., Pendergraft, O. C., Jr., Manning, J. C., and Mason, M. L., 1990, "External Nozzle Flap Dynamic Load Measurements on F-15 S/MTD Model," AIAA Paper No. 90-1910.

Shaw, L., 1989, "Twin Jet Screech Suppression," AIAA Paper No. 89-1140.

Tam, C. K. W., and Burton, D. E., 1984, "Sound Generated by Instability Waves of Supersonic Flows. Part 2. Axisymmetric Jets," *J. Fluid Mech.*, Vol. 138, pp. 273–295.

Tam, C. K. W., Seiner, J. M., and Yu, J. C., 1986, "Proposed Relationship Between Broadband Shock Associated Noise and Screech Tones," *Journal of Sound and Vibration*, Vol. 110, pp. 309–321.

Wlezien, R. W., 1987, "Nozzle Geometry Effects on Supersonic Jet Interaction," AIAA Paper No. 87-2694.